



Special Issue Reprint

---

# Characterization of Metallic Materials

Microstructure, Forming, and Heat Treatment

---

Edited by  
Seong-Ho Ha, Shae-Kwang Kim and Hyun-Kyu Lim

[mdpi.com/journal/materials](https://www.mdpi.com/journal/materials)



# **Characterization of Metallic Materials: Microstructure, Forming, and Heat Treatment**





# **Characterization of Metallic Materials: Microstructure, Forming, and Heat Treatment**

Editors

**Seong-Ho Ha**

**Shae-Kwang Kim**

**Hyun-Kyu Lim**



Basel • Beijing • Wuhan • Barcelona • Belgrade • Novi Sad • Cluj • Manchester

*Editors*

Seong-Ho Ha

Industrial Materials and  
Process R&D Department  
Korea Institute of Industrial  
Technology (KITECH)  
Incheon  
Korea, South

Shae-Kwang Kim

Industrial Materials and  
Process R&D Department  
Korea Institute of Industrial  
Technology  
Incheon  
Korea, South

Hyun-Kyu Lim

Industrial Materials and  
Process R&D Department  
Korea Institute of Industrial  
Technology  
Incheon  
Korea, South

*Editorial Office*

MDPI

St. Alban-Anlage 66

4052 Basel, Switzerland

This is a reprint of articles from the Special Issue published online in the open access journal *Materials* (ISSN 1996-1944) (available at: [www.mdpi.com/journal/materials/special\\_issues/Q8R11FSBR8](http://www.mdpi.com/journal/materials/special_issues/Q8R11FSBR8)).

For citation purposes, cite each article independently as indicated on the article page online and as indicated below:

Lastname, A.A.; Lastname, B.B. Article Title. <i>Journal Name</i> <b>Year</b> , <i>Volume Number</i> , Page Range.
--

**ISBN 978-3-7258-1220-2 (Hbk)**

**ISBN 978-3-7258-1219-6 (PDF)**

**[doi.org/10.3390/books978-3-7258-1219-6](https://doi.org/10.3390/books978-3-7258-1219-6)**

© 2024 by the authors. Articles in this book are Open Access and distributed under the Creative Commons Attribution (CC BY) license. The book as a whole is distributed by MDPI under the terms and conditions of the Creative Commons Attribution-NonCommercial-NoDerivs (CC BY-NC-ND) license.

# Contents

<b>About the Editors</b> . . . . .	<b>vii</b>
<b>Abdul Wahid Shah, Seong-Ho Ha, Jabir Ali Siddique, Bong-Hwan Kim, Young-Ok Yoon and Hyun-Kyu Lim et al.</b> Investigating the Influence of Mg Content Variations on Microstructures, Heat-Treatment, and Mechanical Properties of Al-Cu-Mg Alloys Reprinted from: <i>Materials</i> <b>2023</b> , <i>16</i> , 4384, doi:10.3390/ma16124384 . . . . .	<b>1</b>
<b>Yunxiang You, Li Tan, Yuqin Yan, Tao Zhou, Pengfei Yang and Jian Tu et al.</b> Towards Understanding {10-11}-{10-12} Secondary Twinning Behaviors in AZ31 Magnesium Alloy during Fatigue Deformation Reprinted from: <i>Materials</i> <b>2024</b> , <i>17</i> , 1594, doi:10.3390/ma17071594 . . . . .	<b>15</b>
<b>Yuchao Zhao, Qiang Lu, Qudong Wang, Dezhi Li, Feng Li and Yuzhao Luo</b> Corrosion Behavior of Homogenized and Extruded 1100 Aluminum Alloy in Acidic Salt Spray Reprinted from: <i>Materials</i> <b>2024</b> , <i>17</i> , 1279, doi:10.3390/ma17061279 . . . . .	<b>27</b>
<b>Zhixiang Xiao, Guifang Zhang, Daiwei Liu and Chenhui Wu</b> Impact of Electromagnetic Stirring Roller Arrangement Pattern on Magnetic Field Simulation and Solidification Structure of PW800 Steel in the Second Cooling Zone Reprinted from: <i>Materials</i> <b>2024</b> , <i>17</i> , 1038, doi:10.3390/ma17051038 . . . . .	<b>43</b>
<b>Nan Tian, Guifang Zhang, Peng Yan, Pengchao Li, Zhenhua Feng and Xiaoliang Wang</b> Simulation and Experimental Study on the Effect of Superheat on Solidification Microstructure Evolution of Billet in Continuous Casting Reprinted from: <i>Materials</i> <b>2024</b> , <i>17</i> , 682, doi:10.3390/ma17030682 . . . . .	<b>55</b>
<b>Kun Ni, Hanyu Wang, Qianying Guo, Zumin Wang, Wenxi Liu and Yuan Huang</b> The Construction of a Lattice Image and Dislocation Analysis in High-Resolution Characterizations Based on Diffraction Extinctions Reprinted from: <i>Materials</i> <b>2024</b> , <i>17</i> , 555, doi:10.3390/ma17030555 . . . . .	<b>69</b>
<b>Daiwei Liu, Guifang Zhang, Jianhua Zeng and Chenhui Wu</b> Investigation of Solidification Heat Transfer in Slab Continuous Casting Process Based on Different Roll Contact Calculation Methods Reprinted from: <i>Materials</i> <b>2024</b> , <i>17</i> , 482, doi:10.3390/ma17020482 . . . . .	<b>87</b>
<b>Yi-Jin Cheng, Fei-Yi Hung and Jun-Ren Zhao</b> Microstructural Characteristics and Material Failure Mechanism of SLM Ti-6Al-4V-Zn Alloy Reprinted from: <i>Materials</i> <b>2023</b> , <i>16</i> , 7341, doi:10.3390/ma16237341 . . . . .	<b>99</b>
<b>Hwanseok Lee, Hee-Seon Lee, Seonghoon Kim, Kanghee Jo, Ilguk Jo and Heesoo Lee</b> Phase Stability and Slag-Induced Destabilization in MnO <sub>2</sub> and CeO <sub>2</sub> -Doped Calcia-Stabilized Zirconia Reprinted from: <i>Materials</i> <b>2023</b> , <i>16</i> , 7240, doi:10.3390/ma16227240 . . . . .	<b>118</b>
<b>Bo-Chin Huang and Fei-Yi Hung</b> Effect of High Temperature and Thermal Cycle of 4043 Al Alloy Manufactured through Continuous Casting Direct Rolling Reprinted from: <i>Materials</i> <b>2023</b> , <i>16</i> , 7176, doi:10.3390/ma16227176 . . . . .	<b>132</b>
<b>Hao Yang, Jin-Han Yang, Ying Zhao, Han Ma, Yanzhong Tian and Minghui Cai et al.</b> Impact of Mn Alloying on Phase Stabilities, Magnetic Properties and Electronic Structures in Fe Reprinted from: <i>Materials</i> <b>2023</b> , <i>16</i> , 6679, doi:10.3390/ma16206679 . . . . .	<b>155</b>

<b>Jingzhe Wang, Siyu Zhang, Liang Jiang, Shesh Srivatsa and Zaiwang Huang</b> Prediction of Grain Size in a High Cobalt Nickel-Based Superalloy Reprinted from: <i>Materials</i> <b>2023</b> , <i>16</i> , 5776, doi:10.3390/ma16175776 . . . . .	<b>172</b>
<b>Xiaobo Yuan, Ping Zhang, Jianxiang Wang, Biaobiao Yang and Yunping Li</b> Influences of Fe Content and Cold Drawing Strain on the Microstructure and Properties of Powder Metallurgy Cu-Fe Alloy Wire Reprinted from: <i>Materials</i> <b>2023</b> , <i>16</i> , 5180, doi:10.3390/ma16145180 . . . . .	<b>182</b>
<b>Doina Răducanu, Anna Nocivin, Vasile Dănuț Cojocaru, Nicolae Șerban, Nicoleta Zărnescu-Ivan and Raluca Elena Irimescu et al.</b> Microstructural Considerations of a Multi-Pass Rolled Ti-Nb-Ta-Zr Alloy Reprinted from: <i>Materials</i> <b>2023</b> , <i>16</i> , 3208, doi:10.3390/ma16083208 . . . . .	<b>195</b>
<b>Abdul Wahid Shah, Seong-Ho Ha, Jabir Ali Siddique, Bong-Hwan Kim, Young-Ok Yoon and Hyun-Kyu Lim et al.</b> Microstructure Evolution and Mechanical Properties of Al–Cu–Mg Alloys with Si Addition Reprinted from: <i>Materials</i> <b>2023</b> , <i>16</i> , 2783, doi:10.3390/ma16072783 . . . . .	<b>210</b>

# About the Editors

## **Seong-Ho Ha**

Dr. Seong-Ho Ha works at the Industrial Materials and Process R&D Department, Korea Institute of Industrial Technology. His interests are metals and alloys; thermodynamic calculation; phase diagrams; solidification; and metal oxidation.

## **Shae-Kwang Kim**

Dr. Shae-Kwang Kim works at the Industrial Materials and Process R&D Department, Korea Institute of Industrial Technology, Incheon, Republic of Korea. His interests are alloys; magnesium alloys; thermooxidation; and oxidation.

## **Hyun-Kyu Lim**

Hyun-Kyu Lim works at the Industrial Materials and Process R&D Department, Korea Institute of Industrial Technology. His interests are materials; material characterization; mechanical properties; materials engineering; and alloys.



## Article

# Investigating the Influence of Mg Content Variations on Microstructures, Heat-Treatment, and Mechanical Properties of Al-Cu-Mg Alloys

Abdul Wahid Shah <sup>1,2</sup>, Seong-Ho Ha <sup>2,\*</sup>, Jabir Ali Siddique <sup>1,2</sup>, Bong-Hwan Kim <sup>1,2</sup>, Young-Ok Yoon <sup>2</sup>, Hyun-Kyu Lim <sup>2</sup> and Shae K. Kim <sup>1,2</sup>

<sup>1</sup> Industrial Technology Department, University of Science and Technology, Daejeon 34113, Republic of Korea; abdulwahid.shah799@gmail.com (A.W.S.); jabirali94@kitech.re.kr (J.A.S.); bonghk75@kitech.re.kr (B.-H.K.); shae@kitech.re.kr (S.K.K.)

<sup>2</sup> Industrial Materials Processing R&D Department, Korea Institute of Industrial Technology, Incheon 21999, Republic of Korea; veryoon@kitech.re.kr (Y.-O.Y.); hklim@kitech.re.kr (H.-K.L.)

\* Correspondence: shha@kitech.re.kr

**Abstract:** The objective of this study was to examine the impact of varying magnesium levels in the  $\alpha$ -Al + S + T region of the Al-Cu-Mg ternary phase diagram on the solidification process, microstructure development, tensile properties, and precipitation hardening of Al-Cu-Mg-Ti alloys. The outcomes indicate that alloys with 3% and 5% Mg solidified with the formation of binary eutectic  $\alpha$ -Al-Al<sub>2</sub>CuMg (S) phases, whereas in the alloy with 7% Mg, the solidification process ended with the formation of eutectic  $\alpha$ -Al-Mg<sub>32</sub>(Al, Cu)<sub>49</sub> (T) phases. Additionally, a significant number of T precipitates were noticed inside the granular  $\alpha$ -Al grains in all alloys. In the as-cast condition, the 5% Mg-added alloy showed the best combination of yield strength (153 MPa) and elongation (2.5%). Upon T6 heat treatment, both tensile strength and elongation increased. The 7% Mg-added alloy had the best results, with a yield strength of 193 MPa and an elongation of 3.4%. DSC analysis revealed that the increased tensile strength observed after the aging treatment was associated with the formation of solute clusters and S''/S' phases.

**Keywords:** Al-Cu-Mg alloys; microstructure evolution; heat treatment; tensile properties



**Citation:** Shah, A.W.; Ha, S.-H.; Siddique, J.A.; Kim, B.-H.; Yoon, Y.-O.; Lim, H.-K.; Kim, S.K.

Investigating the Influence of Mg Content Variations on Microstructures, Heat-Treatment, and Mechanical Properties of Al-Cu-Mg Alloys. *Materials* **2023**, *16*, 4384. <https://doi.org/10.3390/ma16124384>

Academic Editor: Frank Czerwinski

Received: 23 May 2023  
Revised: 12 June 2023  
Accepted: 12 June 2023  
Published: 14 June 2023



**Copyright:** © 2023 by the authors. Licensee MDPI, Basel, Switzerland. This article is an open access article distributed under the terms and conditions of the Creative Commons Attribution (CC BY) license (<https://creativecommons.org/licenses/by/4.0/>).

## 1. Introduction

Aluminum-silicon (Al-Si)-based casting alloys are widely utilized in the automobile industry for producing various powertrain components because of their excellent castability. However, they can exhibit relatively low strength, which further decreases at elevated temperatures. Because of this, these alloys are not suitable for high temperature applications in the aerospace, automotive, and other industries. Aluminum-copper-magnesium (Al-Cu-Mg) alloys containing high levels of magnesium, such as A240, 242, and 243, are often preferred for higher-temperature applications due to their excellent combination of strength, hardness, and wear resistance at both room and elevated temperatures [1–5]. High Mg-containing Al-Cu-Mg commercial alloys have limited elongation, typically less than 1%, which is significantly lower than the elongation exhibited by low Mg-containing Al-Cu-Mg alloys, such as A206, which typically have an elongation of 8–11% in the T7 temper [6–15]. As a result, these high Mg-containing alloys are typically only used in applications where thermal stability and/or wear resistance are the primary requirements [1,2,12–19]. These alloys, including A240, 242, and 243, are commonly used in aircraft engines and diesel engines due to their excellent thermal stability and wear resistance [1–5]. Despite their desirable thermal stability and wear resistance, these alloys cannot be utilized in applications that necessitate a favorable balance between strength and elongation due to their low elongation. Therefore, further investigation of the Al-Cu-Mg ternary system is necessary to develop novel alloys that exhibit high strength, ductility, and improved castability.



On the aluminum-rich corner of the Al-Cu-Mg ternary phase diagram, multiple phases are in equilibrium with the primary  $\alpha$ -Al phase, including  $\text{Al}_2\text{Cu}$  ( $\theta$ ),  $\text{Al}_2\text{CuMg}$  (S), and  $\text{Al-Mg}_{32}(\text{Al, Cu})_{49}$  (T) [2]. The S phase has an orthorhombic crystal structure (Cmcm space group) with a narrow homogeneity range and a density of  $3.55 \text{ g/cm}^3$ . Its micro-hardness decreases from 4.44 GPa at  $20 \text{ }^\circ\text{C}$  to 2.22 GPa at  $300 \text{ }^\circ\text{C}$ . By contrast, the T phase (~25% Cu, ~28% Mg) has a defective bcc crystal structure with a space group of Im3 and is isomorphic to the  $\text{Al}_2\text{Mg}_3\text{Zn}_3$  phase. It has a slightly higher density ( $4.14 \text{ g/cm}^3$ ) and lower micro-hardness (4.14 GPa) than the S phase at both room and elevated temperatures [2]. Commercially available Al-Cu-Mg alloys mainly exist in the Al + S +  $\theta$  section of the Al-Mg-Cu ternary phase diagram [1,2,16–22].

Commercial Al-Cu-Mg alloys, specifically those with less than 1% Mg content (such as A201 and A206), demonstrate exceptional strength and toughness through precipitation hardening. Nevertheless, these alloys possess certain drawbacks, including a relatively high susceptibility to hot tearing and low resistance to corrosion [1,2,7–9]. Conversely, alloys with higher Mg content (e.g., 240, 242, and 243) exhibit improved fluidity and hot tearing resistance but suffer from very low elongation, rendering them unsuitable for many applications. Consequently, the utilization of Al-Cu-Mg alloys is significantly limited compared to Al-Si-based casting alloys. Hence, there is a need to develop novel Al-Cu-Mg alloys that possess high strength, ductility, and improved castability. In this regard, the current focus lies in exploring compositions within the Al + S + T region of the ternary phase diagram. To the authors' knowledge, no prior attention has been given to the development of Al-Cu-Mg alloys situated in the Al + S + T section of the ternary phase diagram. Therefore, the current study is the first to report on the microstructure evolution, heat treatment response, and mechanical properties of compositions located within the Al + S + T section of the phase diagram.

The aim of this research was to investigate how changes in the Mg composition in the Al + S + T region of the Al-Mg-Cu ternary system affect the solidification process, development of microstructure, mechanical characteristics, and precipitation hardening of Al-Cu-Mg-Ti alloys.

## 2. Materials and Methods

The chemical composition of the examined alloys employed in the investigation is presented in Table 1. The addition of Mg, Cu, and titanium (Ti) to the melts was accomplished using Mg +  $\text{Al}_2\text{Ca}$ , Al-50% Cu, and Al-5% Ti-1% B master alloys (all compositions in mass%), respectively. Once the pure aluminum with 99.99% purity had melted, the alloying process was conducted at a temperature of approximately  $770\text{--}800 \text{ }^\circ\text{C}$ . The gas bubbling filtration (GBF) process was utilized for 15 min to eliminate oxide inclusions and dissolved hydrogen gas using Ar gas. Following the melt treatment, the temperature of the melts was maintained at approximately  $690 \text{ }^\circ\text{C}$  for 5 min before being poured into a steel mold that had been preheated to  $200 \text{ }^\circ\text{C}$ . The chemical composition of developed alloys was examined using optical emission spectroscopy (OES, Bruker model Q2 ION, Bruker, Billerica, MA, USA).

**Table 1.** Nominal and analyzed compositions of the alloys that were investigated.

Alloy	Nominal Composition (Mass %)	Analyzed Compositions (Mass %)					
		Cu	Mg	Ti	Fe	Si	Al
A43	AlCu4.5Ti0.2Mg3	4.30	3.13	0.263	0.0964	0.022	bal.
A45	AlCu4.5Ti0.2Mg5	4.11	5.23	0.287	0.0942	0.010	bal.
A47	AlCu4.5Ti0.2Mg7	4.09	7.44	0.267	0.0952	0.00087	bal.

The experimental alloys underwent a heat treatment process that began with a solution heat treatment at  $477 \text{ }^\circ\text{C}$  for a duration of 10 h. The samples were then water-quenched

and subjected to aging treatment at different temperatures (170 °C and 200 °C) for 20 h. To determine the change in hardness with the aging time, the Brinell hardness machine (Buehler, Uzwil, Switzerland) was employed. Five hardness values were obtained for each specimen at each condition, and the average of these five values is presented.

The microstructure was observed using optical microscopy (OM, Nikon, Tokyo, Japan) and field emission-scanning electron microscopy (FE-SEM, FEI model Quanta 200 F, Hillsboro, OR, USA) with energy dispersive spectroscopy (EDS, EDAX, Pleasanton, CA, USA). Before optical microscopy (OM) was utilized to observe the microstructure, the samples underwent preparation involving grinding and micro-polishing, followed by etching in Keller's reagent. The FE-SEM analysis was carried out under specific conditions, including an accelerating voltage of 20 KV and a working distance of 10.0 mm. The volume fraction of eutectic phases within each alloy was determined using the ImageJ software (version 1.51). Phase analysis was conducted using X-ray diffraction (XRD D8 Discover) with a scanning step size of 0.02 degrees and a speed of 0.5 s per step. The XRD patterns were analyzed using the EVA software program (version 11.0). The samples were prepared in accordance with ASTM standard B557 for tensile testing, and a universal tensile testing machine (DTU-900MHN, Daekyung Tech, Gumisi, Republic of Korea) was used to perform the tests. Throughout all of the tests, a strain rate of 1.5 mm/min was utilized, and the gauge length of the extensometer was 30 mm. The differential scanning calorimetry (DSC, TA Q1000 instrument, TA instruments, Milford, MA, USA) experiments involved heating each alloy's sample at a rate of 10 °C per minute under an argon atmosphere between 100 °C and 700 °C. Theoretical calculations were carried out using *Fact-Sage 7.1* software.

### 3. Results and Discussion

In the Al-Mg-Cu ternary phase diagram, the Al<sub>2</sub>CuMg intermetallic compound acts similarly to Mg<sub>2</sub>Si in the Al-Mg-Si ternary system, dividing the diagram into two regions in the Al-rich corner, which are (1)  $\alpha$ -Al +  $\theta$  + S and (2)  $\alpha$ -Al + T + S (as indicated in Figure 1). In the Al-Cu-Mg ternary system with a Cu/Mg ratio of 2.40, a binary eutectic reaction ( $L \geq \alpha$ -Al + S) takes place, leading to several non-variant reactions in the Al-rich corner of the alloys [2]. FactSage calculations, based on the Scheil model, indicate that the Al + S eutectic phases in the Al-4.5Cu-3.0Mg alloy form at temperatures between 529 °C and 517 °C, after which Al + S +  $\theta$  eutectic phases are formed at 517 °C, representing the solidus temperature of the alloy. By contrast, in the Al-4.5Cu-5.0Mg and Al-4.5Cu-7.0Mg alloys, it is predicted that the formation of Al + S eutectic phases will occur until 468 °C, after which Al + T eutectic phases are formed, followed by the formation of Al-T-Al<sub>3</sub>Mg<sub>2</sub> eutectic phases at 450 °C. Figure 2 shows that the final microstructure of the AlCu4.5Ti0.2Mg3 (A43) alloy is predicted to consist of  $\alpha$ -Al, S, and Al<sub>18</sub>Ti<sub>2</sub>Mg<sub>3</sub> phases. Moreover, when the Mg content increases to 5% and 7% in AlCu4.5Ti0.2Mg5 (A45) and AlCu4.5Ti0.2Mg7 (A47) alloys (respectively), theoretical calculations suggest that T phases (in addition to S- and Ti-based phases) will precipitate out when the temperature decreases to a certain value, depending on the Mg content.

In Figure 3, DSC thermographs of these alloys in the as-cast temper are presented. The thermographs showed two distinct peaks, one indicating the development of primary  $\alpha$ -Al phases and the other representing the eutectic  $\alpha$ -Al-S phases. Additionally, the thermograph of the A47 alloy showed a peak associated to eutectic  $\alpha$ -Al-T phases. The results indicate that the solidification process concluded with a binary eutectic reaction ( $L \geq \alpha$ -Al + S) in the A43 and A45 alloys, while the  $L + S \geq \alpha$ -Al + T reaction completed the solidification in the A47 alloy at a lower solidus temperature than the former alloys [2].

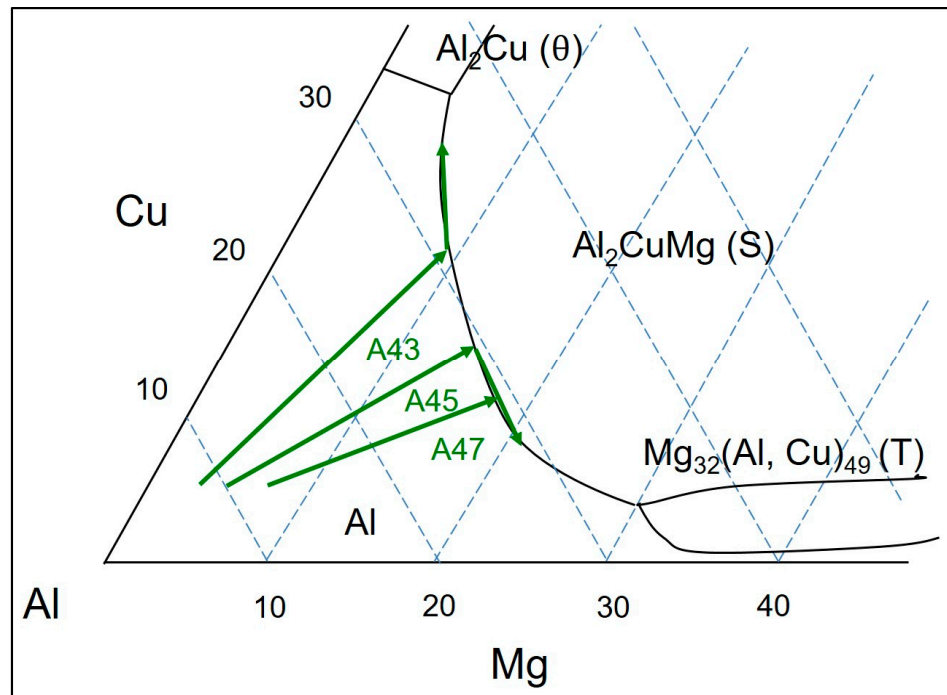


**Figure 1.** The aluminum-rich corner of the ternary liquid projection phase diagram of the Al-Cu-Mg system.

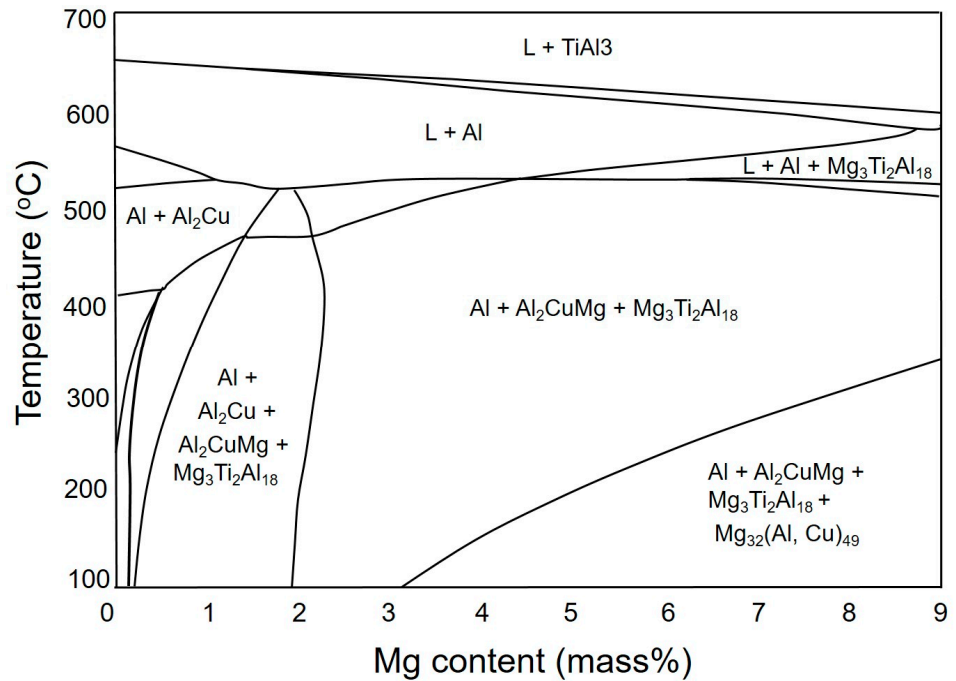


**Figure 2.** The vertical section of the phase diagram for the Al-4.5 wt% Cu-0.2 wt% Ti-0~9 wt% Mg alloy system.

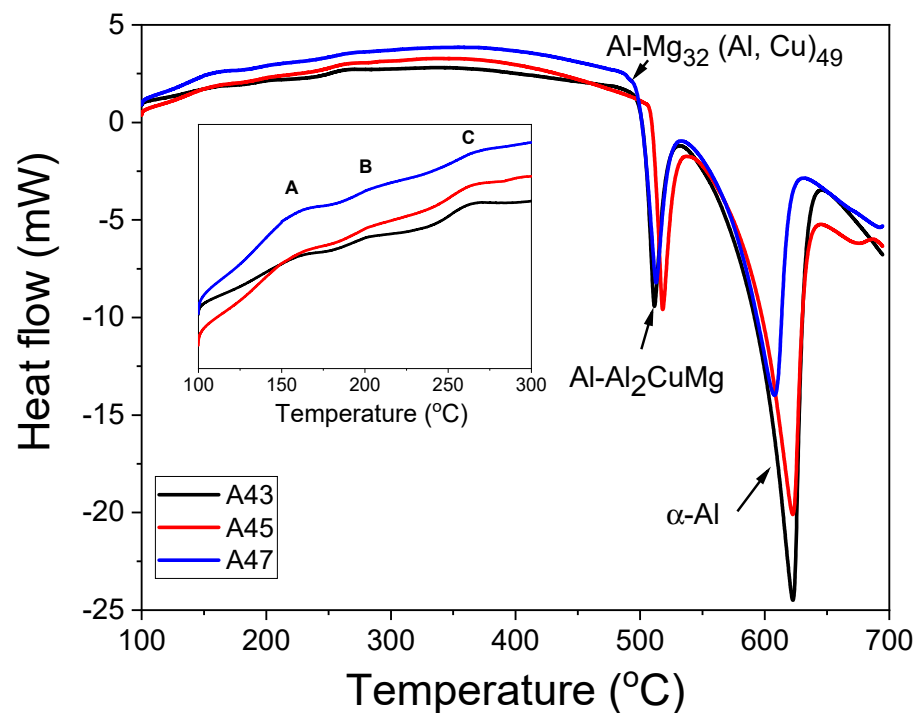


**Figure 3.** Differential scanning calorimetry (DSC) thermograms of the investigated alloys, which were obtained by heating at a rate of 10 °C per minute.

Furthermore, all alloys displayed exothermic peaks between 100 and 300 °C, where peak A was likely to indicate the precipitation of T phases, which is consistent with the phase diagram shown in Figure 2. Surprisingly, all alloys exhibited formation temperatures that were almost similar, in contrast to theoretical calculations. The next exothermic peak B could be connected to the creation of solute clusters. Previous studies suggested that the peak C observed between 250 and 280 °C could potentially be linked to the precipitation of S'' or S' phases [23–26]. The X-ray diffraction (XRD) results of the examined alloys support the conclusions derived from the DSC analysis. The XRD patterns exhibited peaks corresponding to primary aluminum, Al<sub>2</sub>CuMg (S), Mg<sub>32</sub>(Al, Cu)<sub>49</sub> (T), and Ti-based phases in all the investigated alloys, as illustrated in Figure 4. This indicates that, similar to the DSC analysis, the XRD analysis has also confirmed the presence of T precipitates within the A43 alloy, as well as in the other alloys.

Table 2 compares the solidification ranges of the investigated alloys, as obtained from both theoretical calculations and experimental results (Figure 3). As the Mg content increased, there was a notable reduction in the liquidus temperature. According to equilibrium-based theoretical calculations, the A43 alloy was predicted to have a solidification range of 113.8 °C, which increased to 171.4 °C and 157.9 °C in the A45 and A47 alloys, respectively. However, the DSC results showed that the A43 alloy had a solidification range of 134 °C, which decreased significantly in the A45 alloy to 113 °C, before slightly increasing again to 119.5 °C in the A47 alloy. The reason why the A47 alloy has a wider range of freezing compared to the A45 alloy may be due to the creation of eutectic α-Al-Mg<sub>32</sub>(Al,Cu)<sub>49</sub> phases.

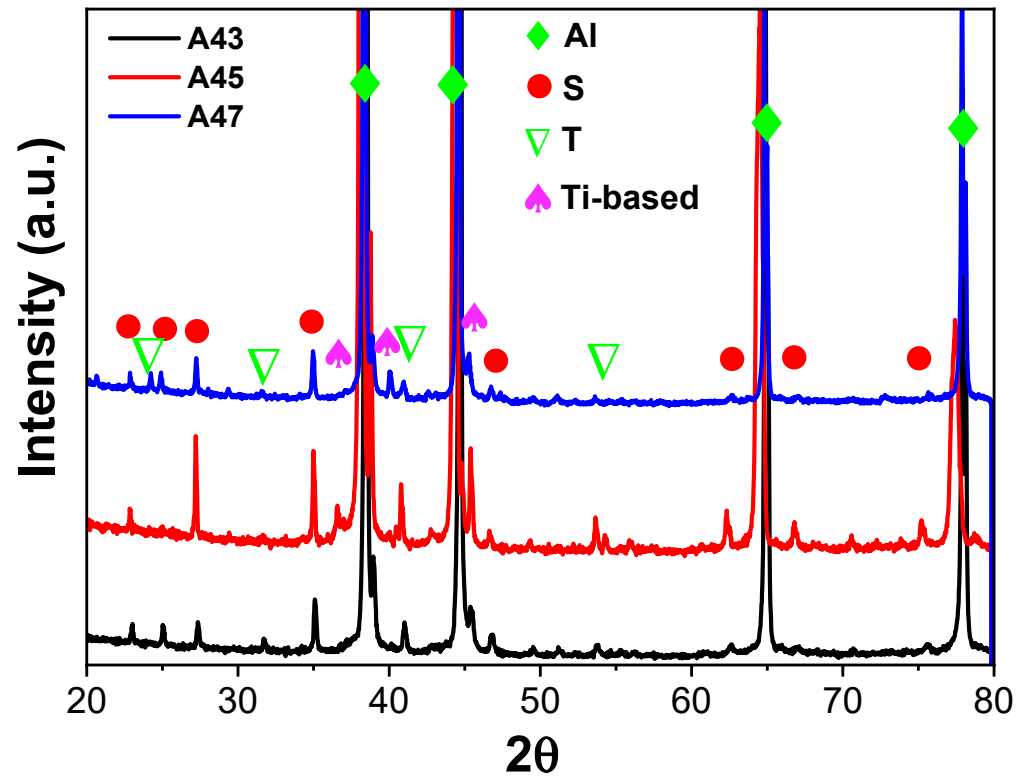


Figure 4. XRD patterns of the as-cast investigated alloys.

Table 2. Liquidus and solidus temperatures, as well as the corresponding solidification range, which were determined through theoretical calculations and differential scanning calorimetry (DSC) analysis.

Alloy	Theoretical Calculations			DSC Analysis		
	$T_L$	$T_S$	$\Delta T$	$T_L$	$T_S$	$\Delta T$
A43	631.54	517	113.8	635.03	500.32	134.71
A45	621.92	450.46	171.4	623.03	509.73	113.3
A47	608.38	450.46	157.9	607.7	488.04	119.6

Figure 5 illustrates that the  $\alpha$ -Al matrix in all the analyzed alloys had a globular grain structure, with eutectic  $\alpha$ -Al-S phases located at the boundaries of the grains and T precipitates present within the globular grains. Additionally, the A45 and A47 alloys showed the presence of  $Mg_3Ti_2Al_{18}$  intermetallic compounds (Figure 6). The FESEM-micrographs of the alloys are presented in Figure 6, with the eutectic  $\alpha$ -Al-S, eutectic  $\alpha$ -Al-T, T precipitates, and  $Mg_3Ti_2Al_{18}$  intermetallic compound denoted as 1, 2, 3, and 4, respectively. Figure 7 displays the EDS analysis results that were used to determine the exact composition of the second phases. During the solidification process, the T phases were seen to precipitate when the temperature dropped below the solidus temperature, as revealed by the DSC results in Figure 3.



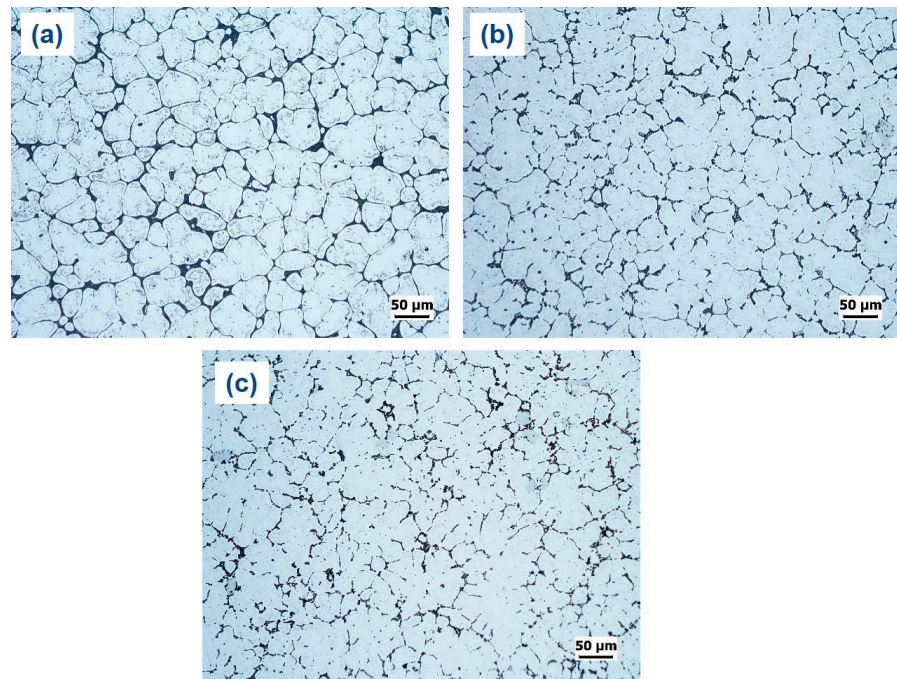


Figure 5. Optical micrographs of as-cast investigated alloys: (a) A43, (b) A45, and (c) A47.

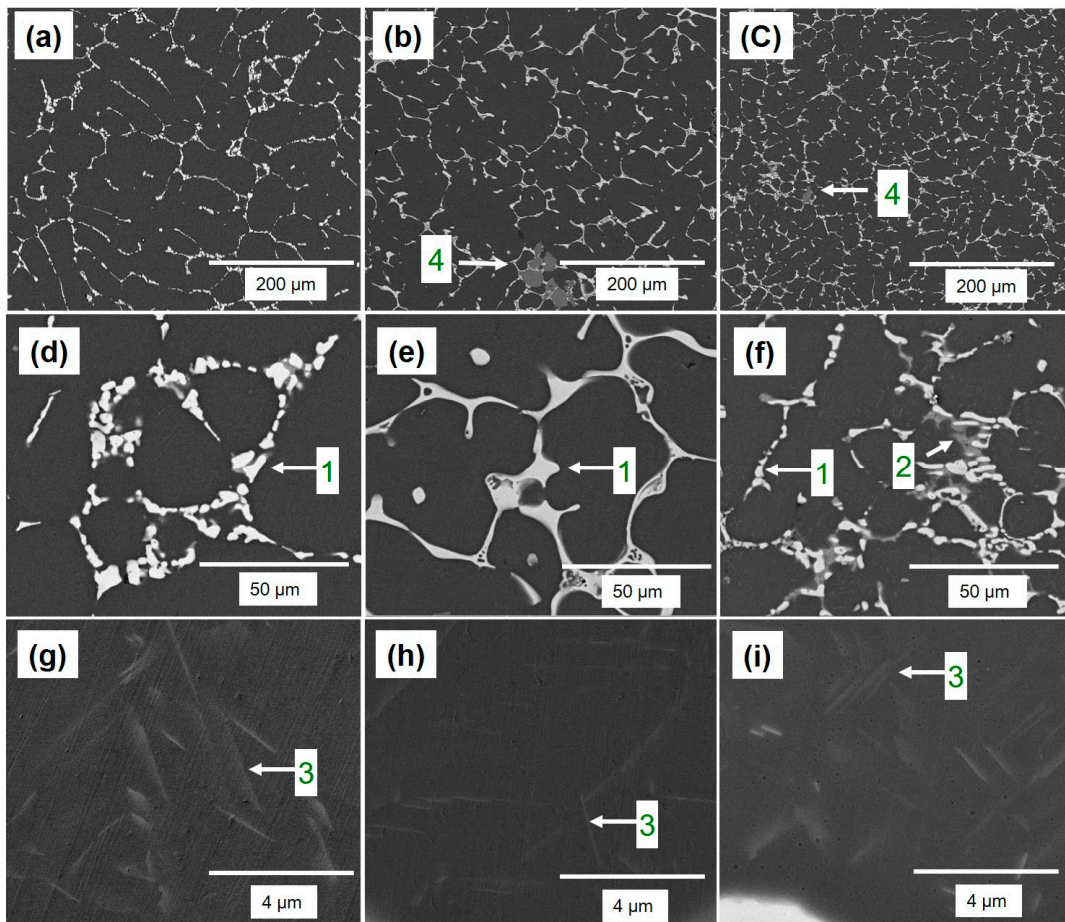
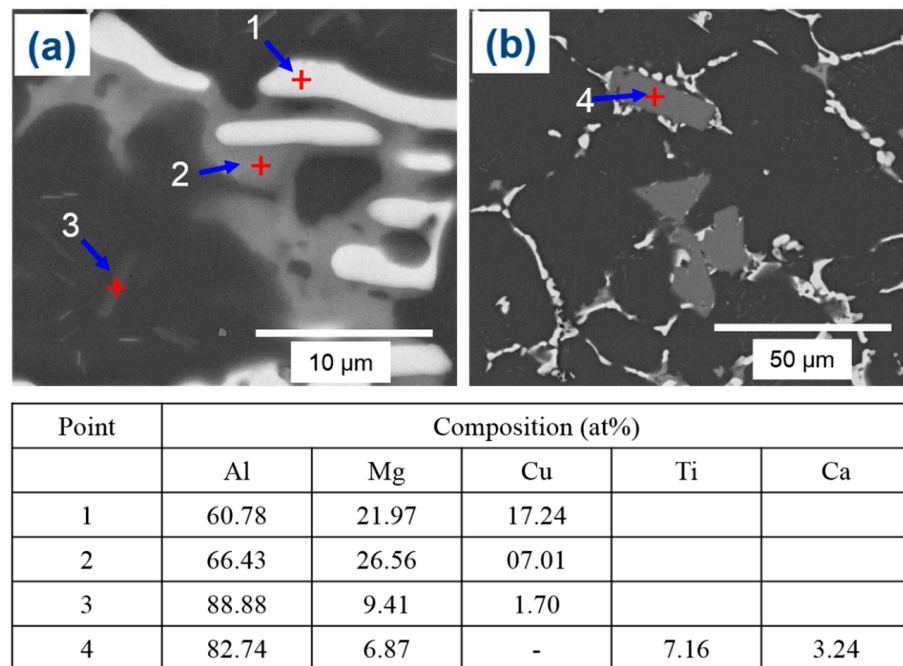
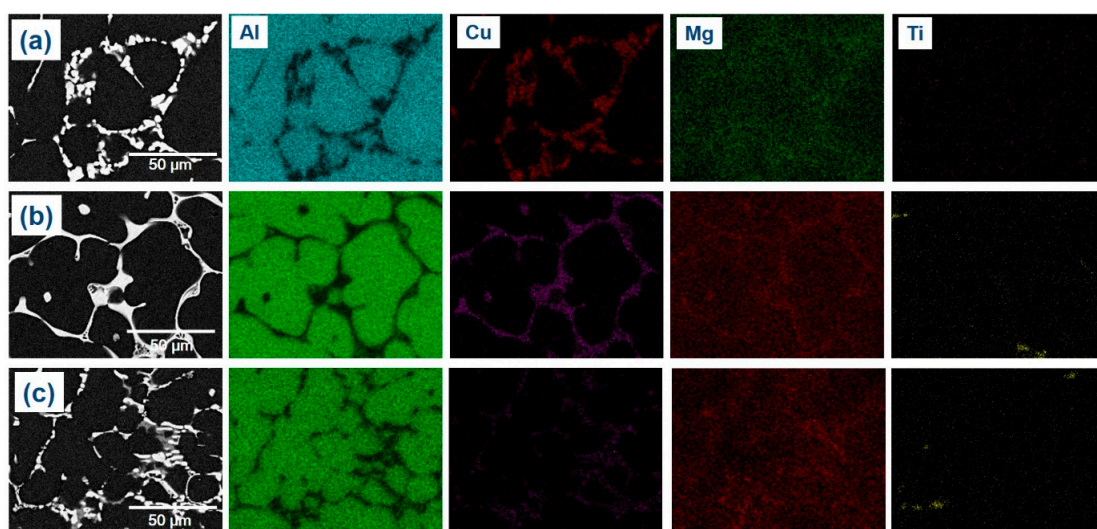


Figure 6. FESEM-micrographs of the as-cast A43, A45, and A47 alloys, with (a–g), (b–h), and (c–i) corresponding to each alloy, respectively. In each micrograph, 1, 2, 3, and 4 are used to indicate the eutectic Al-S, eutectic Al-T, T-precipitates, and Ti-based intermetallic, respectively.



**Figure 7.** FESEM-micrographs (a,b) of the A47 alloy in its as-cast condition, while the corresponding compositions of the points indicated in the micrographs are given in the table below.

The experimental findings presented in Figure 7 are consistent with the theoretical calculations shown in Figure 2. However, there were some discrepancies between the experimental and theoretical results. For example, T phases were detected in the A43 alloy, despite not being predicted by the theoretical calculations. Additionally,  $Mg_3Ti_2Al_{18}$  intermetallic compounds were also observed in all alloys, which was confirmed by EDS mapping analysis (Figure 8). This finding aligns well with the XRD results depicted in Figure 4. EDS analysis (Figure 7) also revealed a considerable quantity of Ca in the  $Mg_3Ti_2Al_{18}$  intermetallic compounds. The A47 alloy also exhibited eutectic  $\alpha$ -Al-T phases in addition to the eutectic  $\alpha$ -Al-S phases, which is consistent with the peak related to this reaction ( $L + S \geq \alpha\text{-Al} + T$ ) observed in the DSC thermograph (Figure 3). The eutectic morphology differed among the alloys, with the A43 and A47 alloys displaying rounded eutectic  $\alpha$ -Al-S phases, while the A45 alloy had interconnected eutectic phases.



**Figure 8.** FESEM-micrographs and the corresponding mapping analysis results of the A43 (a), A45 (b), and A47 (c) alloys.



The microstructures of the as-cast and as-quenched alloys are compared in Figure 9. It can be seen that the eutectic  $\alpha$ -Al-S phases are still present in the as-quenched alloys, indicating that the solution heat treatment did not significantly modify these phases. Similarly, the  $Mg_3Ti_2Al_{18}$  intermetallic compounds remained almost unchanged after the solution treatment. Nevertheless, the solution heat treatment led to a substantial dissolution of T precipitates within the globular grains of primary Al, which suggests that the T precipitates have a greater solubility in the Al matrix at higher temperatures.

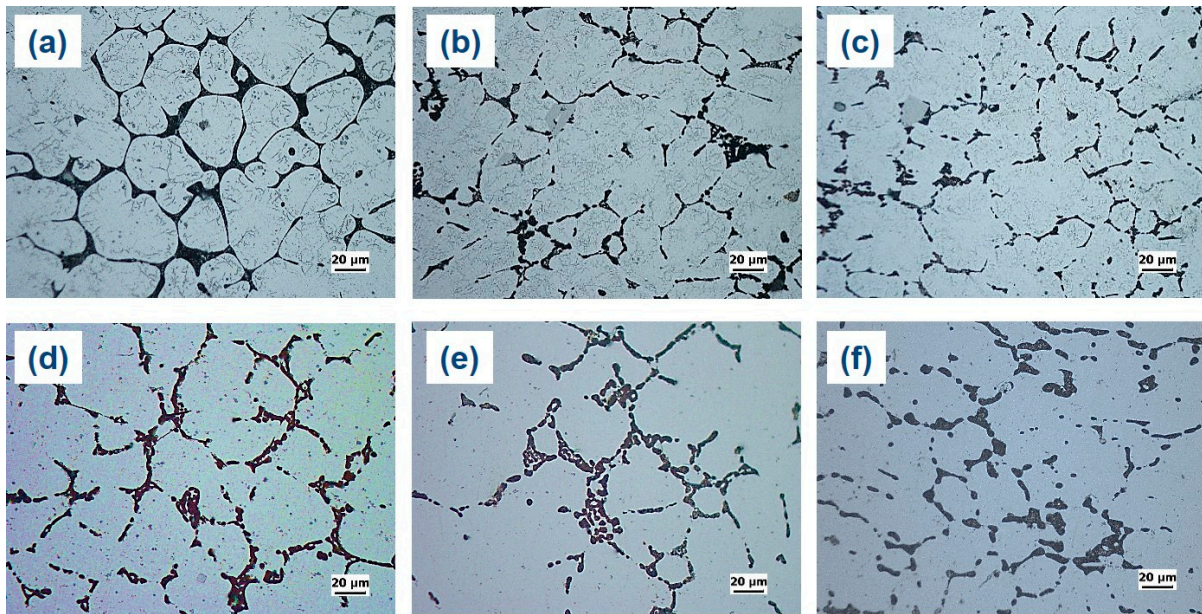


**Figure 9.** Optical micrographs of the investigated alloys in different temper conditions. Specifically, (a–c) depict the microstructures of the A43, A45, and A47 alloys, respectively, in their as-cast condition, while (d–f) reveal the microstructures of the A43, A45, and A47 alloys, respectively, in their as-quenched condition.

Figures 10 and 11 display how the hardness values of the alloys changed over time at various aging temperatures. The as-quenched hardness values were different for the three alloys, with A47 exhibiting the highest initial hardness value of 51 HBR, followed by A45 with a value of 36 HBR, and A43 with the lowest value of 27 HBR (Figure 9). The increment in hardness values after aging was not the same for all alloys, and it was observed to be dependent on the Mg content. The rate of hardness increase was slower for the A47 alloy than for the A43 and A45 alloys, which showed a rapid increase in hardness after 1 h of aging, followed by a slight decrease before increasing gradually up to 10–12 h. Following that time, the hardness values remained relatively constant for the remainder of the aging duration. Previous studies [23–26] on Al-Mg-Cu alloys with higher Mg contents have identified two distinct peaks in the evolution of hardness during aging. The first peak in hardness is associated with the creation of atomic clusters or GPB zones, which contribute to as much as 60% of the overall hardening that takes place during aging. The second stage of precipitation hardening, which happens later in the aging process, corresponds to the precipitation of  $S''$  and  $S'$  phases. Similar findings were observed in this study for the current alloys, where more than 60% of total hardness was achieved after 1 h of aging. Moreover, when aged at a higher temperature of 200 °C, a similar trend was observed, but A43 alloy showed a considerable increase in hardness, and a peak hardness of 65 HRB was obtained after 8 h of aging (Figure 11). In conclusion, the hardness values of the alloys significantly increased after aging, but the rate and magnitude of increase varied with the magnesium content and aging temperature.



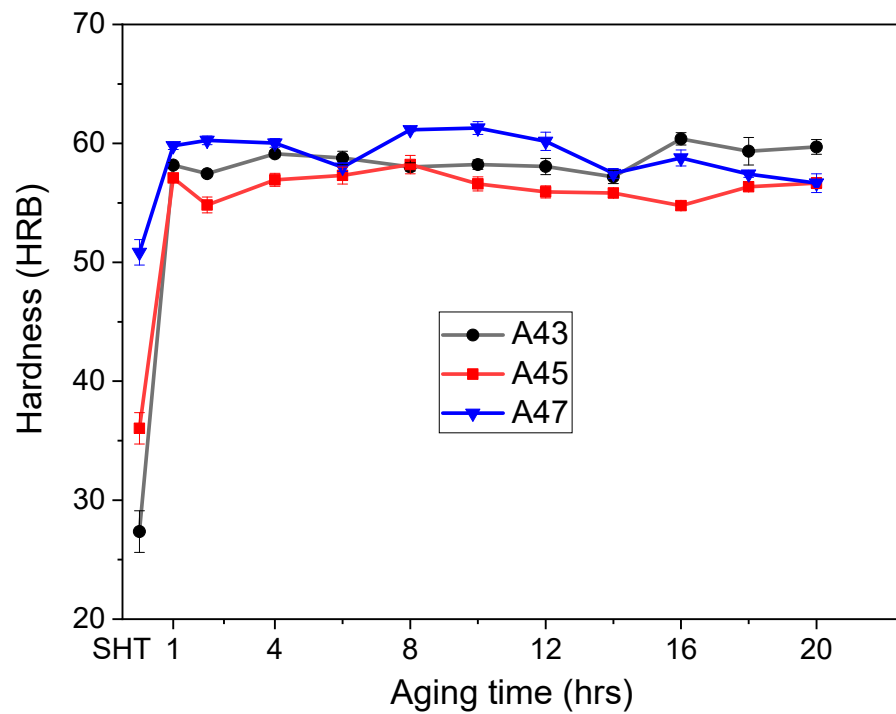


**Figure 10.** The evolution of hardness values for the examined alloys as a function of aging time at 170 °C.

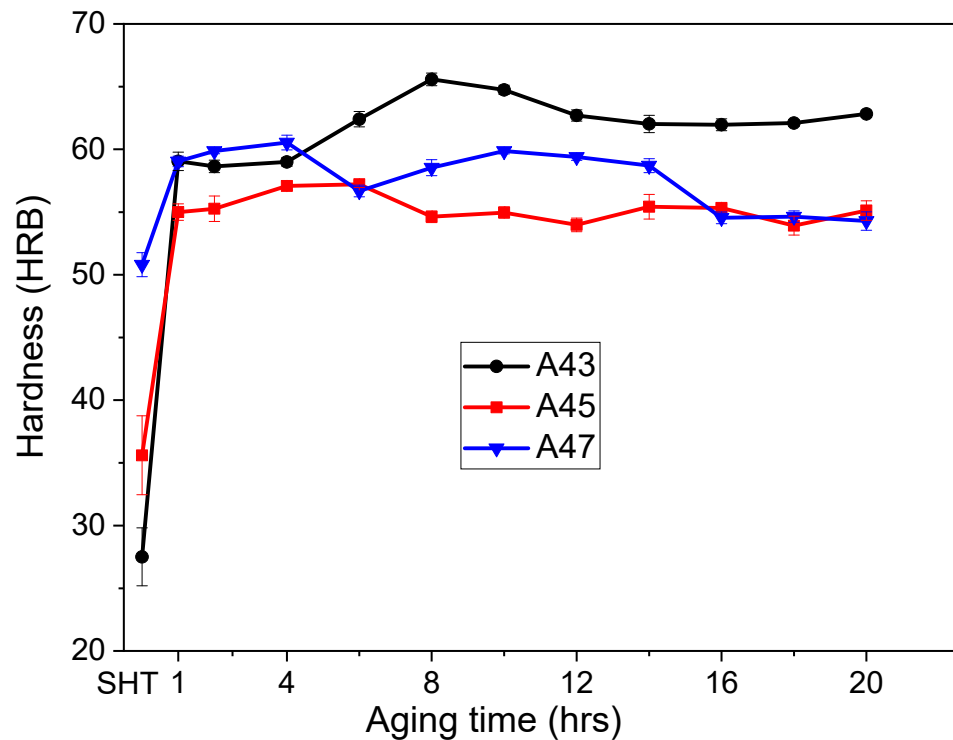


**Figure 11.** The evolution of hardness values for the examined alloys as a function of aging time at 200 °C.

In their as-quenched state, Al-Cu-Mg alloys are made up of a supersaturated solid solution (SSSS), which is a high-energy state [23–26]. During precipitation hardening, this state transforms into solute clusters as the first stage. The growth of these solute clusters regions causes the creation of the  $S''$  metastable phase, which eventually transforms to another  $S'$  (metastable phase) over time. The stable S phase is formed through the growth

of the metastable  $S'$  phase. Figure 12 displays the DSC thermograms of the investigated alloys in their as-quenched tempers, revealing two endothermic peaks (A and C) and one exothermic peak (B) common to all alloys. Previous studies [23–26] have associated endothermic peak A with the dissolution of solute clusters, while exothermic peak B indicates the precipitation of  $S''$  or  $S'$  phases [25]. The DSC curves of A45 and A47 alloys showed a significant decrease in the area of exothermic peak B compared to that of A43, indicating a reduction in precipitation hardening in A45 compared to A43. Peak C represents the dissolution of  $S''$  or  $S'$  phases, and an additional exothermic peak (D) was observed in the A45 alloy, which may be attributed to the formation of T precipitates, as discussed previously. These results demonstrate that the kinetics of precipitate formation vary significantly with changes in the Mg/Cu ratio, leading to substantial differences in the hardness changes with time observed for these alloys, as illustrated in Figures 10 and 11.

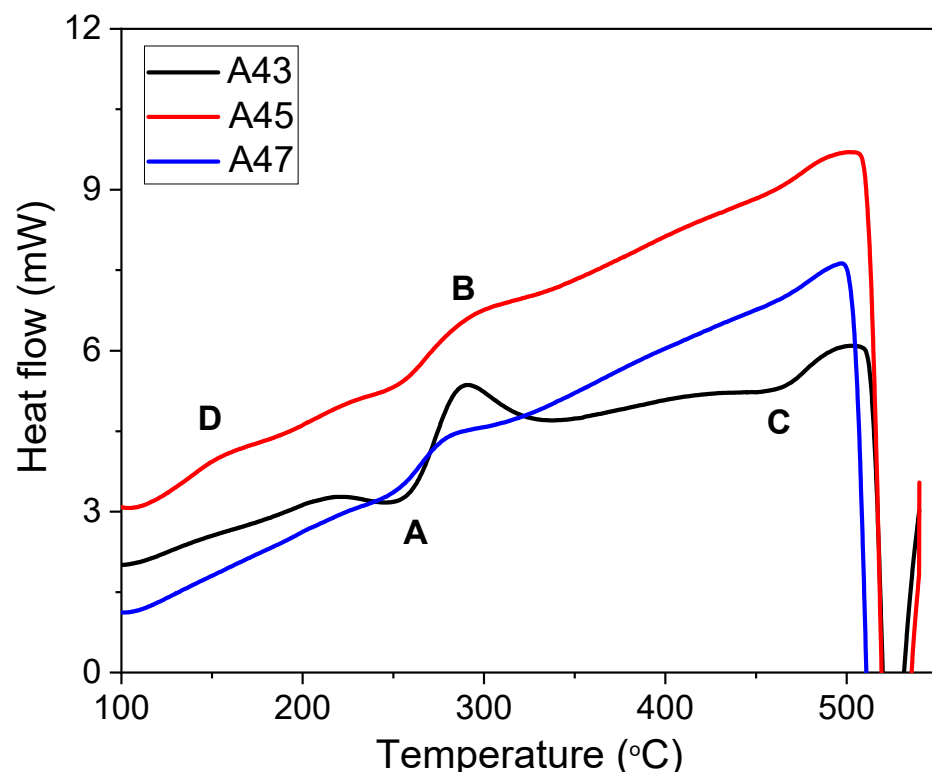


**Figure 12.** Differential scanning calorimetry (DSC) curves of the investigated alloys when heated from 25 °C to 550 °C under argon atmosphere at a rate of 10 °C per minute.

Figure 13 and Table 3 present the tensile properties of these examined alloys under different conditions. In the as-cast state, the A43 and A45 alloys showed similar yield strength values of around 150 MPa (Figure 13a), but the A45 alloy showed a higher elongation of 2.5%, indicating a better combination of strength and ductility compared to commercial alloys [1–3]. The enhanced elongation of the A45 alloy might be attributed to the variation in the morphology of the eutectic phases present in this alloy compared to other alloys (Figure 6). Additionally, the higher Mg content in the A47 alloy increased the yield strength to 167 MPa but reduced the elongation to 0.76%. The increase in yield strength with increasing Mg content is likely due to the increasing amount of eutectic phases in the A47 alloy. The volume fraction of eutectic phases was approximately 6.7% in the A43 alloy. This fraction increased to 9.5% in the A45 alloy and further to 15.1% in the A47 alloy. The overall tensile strength of the as-cast alloys is expected to have been contributed to by grain boundary strengthening from the granular primary Al matrix and strengthening induced by eutectic phases and T precipitates (via thermal mismatch, load transfer, and Orowan looping). Following solution heat treatment, the yield strength of the

alloys decreased, while the ultimate tensile strength and elongation increased (Figure 13b). Enhanced elongation in the as-quenched state of these alloys may arise from the T phases dissolving within the aluminum matrix, a uniform dispersion of solute atoms, and the rounding of eutectic phases. Additionally, the A47 alloy showed a higher yield strength of 146 MPa, which aligns with the hardness findings presented in Figures 10 and 11. The increased yield strength observed in the A47 alloy can be attributed to its larger quantity of remnant phases in the as-quenched state compared to the other alloys. This higher concentration of remnant phases can be directly linked to the fact that the A47 alloy had a greater amount of eutectic phases in the as-cast condition. Aging treatments for 1 h at 170 °C (Figure 13c) and 200 °C (Figure 13d) resulted in a significant improvement in tensile strength for all alloys along with an increase in elongation. A longer exposure of 8 h at 200 °C further improved yield strength in all alloys with no significant impact on elongation (Figure 13e). The improvement in the strength of the aged samples compared to the as-quenched tempers can be attributed to precipitation strengthening induced by the formation of solute clusters and the creation of  $S''$  or  $S'$  phases. The A47 alloy exhibited the best results, with a yield strength of 193 MPa and an elongation of 3.4%, surpassing the yield strength–ductility combinations achieved in commercially available high Mg-added Al-Cu-Mg alloys (e.g., 240, A242, and 243) used for aircraft engine parts [1–3].

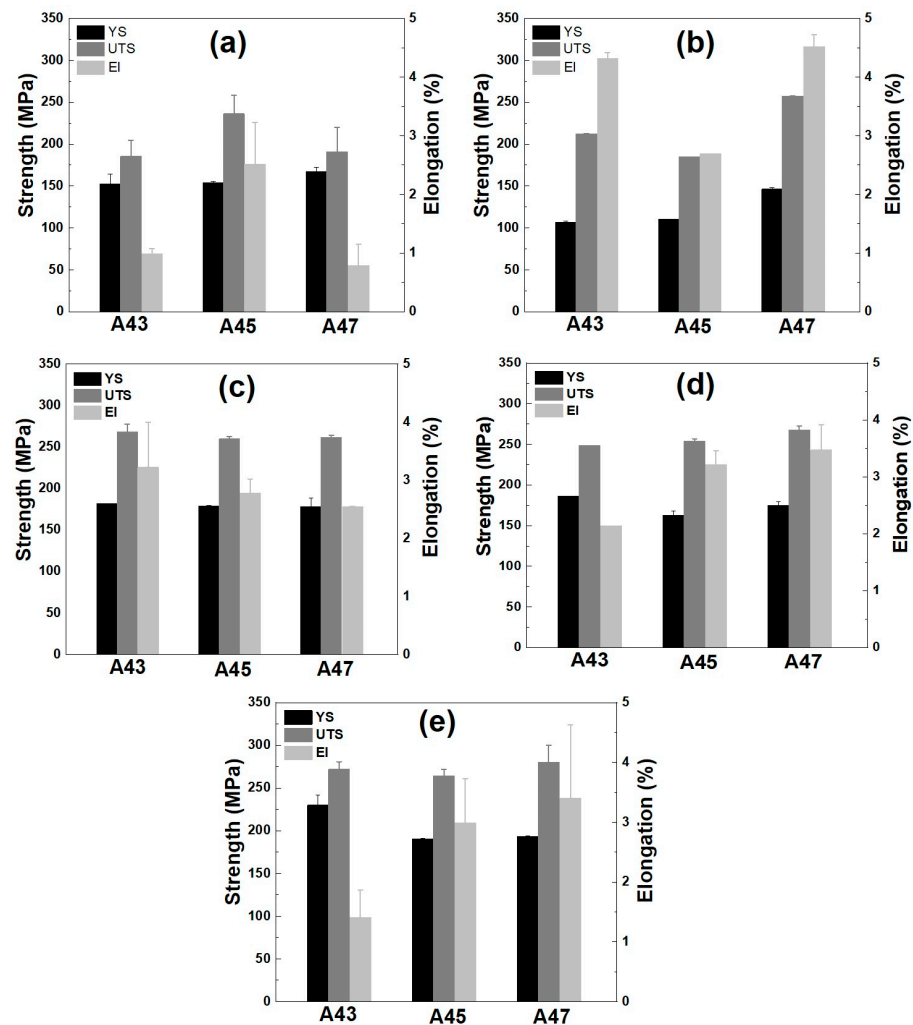


**Figure 13.** Tensile properties of the investigated alloys in different tempers, including (a) as-cast, (b) as-quenched, (c) T6 temper-aged at 170 °C for 1 h, (d) T6 temper-aged at 200 °C for 1 h, and (e) T6 temper-aged at 200 °C for 8 h.

**Table 3.** Tensile properties of the alloys that were examined in both their as-cast and heat-treated conditions.

Temper	Alloy	Yield Strength (MPa)	Ultimate Tensile Strength (MPa)	Elongation (%)
As-cast	A43	152.59 ± 11.9	185.55 ± 18.9	0.985 ± 0.09
	A45	153.79 ± 1.8	236.21 ± 21.8	2.515 ± 0.71
	A47	167.27 ± 5.03	191.0 ± 28.9	0.79 ± 0.36
As-quenched	A43	107 ± 1.4	212.51 ± 0.2	4.32 ± 0.1
	A45	110.7 ± 0.0	184.9 ± 0.0	3.70 ± 0.0
	A47	146.36 ± 1.9	257.4 ± 0.5	4.52 ± 0.2
T6 (170 °C × 1 h)	A43	181.92 ± 0.00	268.36 ± 8.96	3.22 ± 0.77
	A45	179.13 ± 0.03	259.64 ± 2.59	2.78 ± 0.24
	A47	178.23 ± 10.4	261.57 ± 2.10	2.54 ± 0.01
T6 (200 °C × 1 h)	A43	186.29 ± 0.00	248.69 ± 0.00	2.14 ± 0.00
	A45	162.82 ± 4.82	253.73 ± 3.17	3.22 ± 0.24
	A47	174.90 ± 4.70	267.61 ± 4.84	3.47 ± 0.44
T6 (200 °C × 8 h)	A43	230.15 ± 11.6	271.91 ± 8.97	1.41 ± 0.46
	A45	190.68 ± 0.34	264.3 ± 7.24	2.99 ± 0.74
	A47	193.23 ± 0.70	280.13 ± 19.74	3.4 ± 1.23

#### 4. Conclusions

The aim of this research was to investigate how changes in the Mg composition in the  $\alpha$ -Al + S + T region of the Al-Mg-Cu ternary phase diagram affect the solidification process, development of microstructure, precipitation hardening, and mechanical characteristics of Al-Cu-Mg-Ti alloys. The outcomes indicated that alloys with 3% and 5% Mg solidified with the creation of binary eutectic  $\alpha$ -Al-Al<sub>2</sub>CuMg (S) phases, whereas in the alloy with 7% Mg, the solidification process ended with the creation of eutectic  $\alpha$ -Al-Mg<sub>32</sub>(Al, Cu)<sub>49</sub> (T) phases. Additionally, a significant number of T precipitates were noticed inside the granular  $\alpha$ -Al grains in all alloys. In the as-cast condition, the 5% Mg-added alloy showed the best combination of yield strength (153 MPa) and elongation (2.5%). Upon T6 heat treatment, both tensile strength and elongation increased. The 7% Mg-added alloy had the best results, with a yield strength of 193 MPa and an elongation of 3.4%. These mechanical properties have not been previously observed in commercially available Al-Cu-Mg alloys with high Mg content. DSC analysis revealed that the increased tensile strength observed after the aging treatment was associated with the formation of solute clusters and S''/S' phases.

**Author Contributions:** Conceptualization: A.W.S. and S.-H.H.; methodology: A.W.S.; Data curation: A.W.S. and J.A.S.; Formal analysis: A.W.S. and J.A.S.; Original draft preparation: A.W.S. and S.-H.H. writing—review and editing: B.-H.K., Y.-O.Y., H.-K.L. and S.K.K.; supervision: S.-H.H., B.-H.K., Y.-O.Y., H.-K.L. and S.K.K. All authors have read and agreed to the published version of the manuscript.

**Funding:** This study has been conducted with the support of the Ministry of Trade, Industry and Energy as “Automotive Technology Development Program (20019047)”.

**Institutional Review Board Statement:** Not applicable.

**Informed Consent Statement:** Not applicable.

**Data Availability Statement:** Available upon request from the corresponding author.


**Conflicts of Interest:** The authors declare no conflict of interest.

## References

- Hatch, J.E. *Aluminum: Properties and Physical Metallurgy*; ASM International: Geauga County, OH, USA, 1984; pp. 333–338.
- Glazoff, M.V.; Khvan, A.; Zolotarevsky, V.S.; Belov, N.A.; Dinsdale, A.T. *Castings Aluminum Alloys: Their Physical and Mechanical Metallurgy*, 2nd ed.; Elsevier: Oxford, UK, 2018; pp. 56–58, 85–87.
- Çadırlı, E.; Kaya, H.; Büyük, U.; Ustun, E.; Gunduz, M. Effect of Heat Treatment on the Microstructures and Mechanical Properties of Al–4Cu–1.5Mg Alloy. *Int. J. Metalcast.* **2022**, *16*, 1020–1033. [CrossRef]
- Rezaei, M.; Jamshidi Aval, H. Effect of Li Micro-Alloying on Microstructure and Corrosion Resistance of Non-Isothermal Aged Al–Cu–Mg Cast Alloy with Different Cu/Mg Ratios. *Int. J. Metalcast.* **2023**, 1–15. [CrossRef]
- Elgallad, E.; Samuel, F.; Samuel, A.; Doty, H. Development of New Al–Cu Based Alloys Aimed at Improving the Machinability of Automotive Castings. *Int. J. Metalcast.* **2009**, *3*, 29–41. [CrossRef]
- Zamani, M.; Toschi, S.; Morri, A.; Ceschini, L.; Seifeddine, S. Optimisation of heat treatment of Al–Cu–(Mg–Ag) cast alloys. *J. Ther. Anal. Calor.* **2020**, *139*, 3427–3440. [CrossRef]
- Kamga, H.; Larouche, D.; Bourmane, M.; Rahem, A. Mechanical Properties of Aluminum–Copper B206 Alloys with Iron and Silicon Additions. *Int. J. Cast Met. Res.* **2012**, *25*, 15–25. [CrossRef]
- Mihara, M.; Kobayashi, E.; Sato, T. Rapid age-hardening behavior of AlMgCu (Ag) alloys and incubation stage in the low temperature aging. *Mater. Trans.* **2013**, *54*, 1898–1904. [CrossRef]
- Mihara, M.; Marioara, C.D.; Andersen, S.J.; Holmestad, R.; Sato, E.T. Precipitation in an Al–Mg–Cu alloy and the effect of a low amount of Ag. *Mater. Sci. Eng. A* **2016**, *658*, 91–98. [CrossRef]
- Ringe, S.P.; Hono, K.; Polmear, I.J.; Sakurai, T. Precipitation processes during the early stages of ageing in Al–Cu–Mg alloys. *Appl. Surf. Sci.* **1996**, *94/95*, 253–260. [CrossRef]
- Novelo-Peralta, O.; Gonzalez, G.; Lara-Rodriguez, G.A. Characterization of precipitatio-n in Al–Mg–Cu alloys by X-ray diffraction peak broadening analysis. *Mater. Charact.* **2008**, *59*, 773–780. [CrossRef]
- Zheng, Y.; Xiao, W.; Ge, S.; Zhao, W.; Hanada, S.; Ma, C. Effects of Cu content and Cu/Mg ratio on the microstructure and mechanical properties of Al–Si–Cu–Mg alloys. *J. Alloys Compd.* **2015**, *649*, 291–296. [CrossRef]
- Stemper, L.; Tunes, M.A.; Dumitraschkewitz, P.; Mendez-Martin, F.; Tosone, R.; Marchand, D.; Curtin, W.A.; Uggowitzner, P.J.; Pogatscher, S. Giant hardening response in AlMgZn(Cu) alloys. *Acta Mater.* **2021**, *206*, 116617. [CrossRef]
- Liu, T.W.; Wang, Q.D.; Tang, H.P.; Li, Z.Y.; Chuan, L.E.I.; Ebrahimi, M.; Jiang, H.Y.; Ding, D.W.J. Microstructure and mechanical properties of squeeze-cast Al–5.0 Mg–3.0 Zn–1.0 Cu alloys in solution-treated and aged conditions. *Trans. Nonferrous Met. Soc. Chin.* **2020**, *30*, 2326–2338. [CrossRef]
- DeVaucorbeil, A.; Sinclair, C.W.; Poole, W.J. Atomistic insights into cluster strengthening in aluminum alloys. *Materialia* **2018**, *4*, 566–574. [CrossRef]
- Girgis, A.; Samuel, A.M.; Doty, H.W.; Valtierra, S.; Samuel, F.H. On the Elevated Temperature, Tensile Properties of Al–Cu Cast Alloys: Role of Heat Treatment. *Adv. Mater. Sci. Eng.* **2019**, *2019*, 1–15. [CrossRef]
- Girgis, A.; Abdelaziz, M.H.; Samuel, A.M.; Valtierra, S.; Samuel, F.H. On the Enhancement of the Microstructure and Tensile Properties of an Al–Cu Based Cast Alloy. *Metall. Microstruct. Anal.* **2019**, *8*, 757–769. [CrossRef]
- Kamga, H.K.; Larouche, D.; Bourmane, M.; Rahem, A. Solidification of Aluminum–Copper B206 alloys with Iron and Silicon Additions. *Metall. Mater. Trans. A* **2010**, *41*, 2844–2855. [CrossRef]
- Fentazi, S.; Bourmane, M.; Ragab, K.A.; Mehdi, B. Influence of Mg Additions on Solidification and Performance of B206-Type Aluminum Castings of High Fe and Si Contents. *Int. J. Cast Met. Res.* **2018**, *31*, 14–19. [CrossRef]
- Liu, K.; Cao, X.; Chen, X. Effect of Mn, Si, and Cooling Rate on the Formation of Iron-Rich Intermetallics in 206 Al–Cu Cast Alloys. *Metall. Mater. Trans. B* **2012**, *43*, 1231–1240. [CrossRef]
- D’Elia, F.; Ravindran, C.; Sediako, D.; Kainer, K.U.; Hort, N. Hot Tearing Mechanisms of B206 Aluminum–Copper Alloy. *Mater. Des.* **2014**, *64*, 44–180. [CrossRef]
- D’Elia, F.; Ravindran, C.; Sediako, D. Interplay Among Solidification, Microstructure, Residual Strain and Hot Tearing in B206 Aluminum Alloy. *Mater. Sci. Eng. A* **2015**, *624*, 169–180. [CrossRef]
- Shah, A.W.; Ha, S.H.; Kim, B.H.; Yoon, Y.O.; Lim, H.K.; Kim, S.K. Effect of Cu Addition on the Precipitation Hardening and Mechanical Properties of Al–Mg Based Cast Alloys. *J. Nanosci. Nanotechnol.* **2021**, *21*, 1943–1947.
- Li, C.; Sha, G.; Gun, B.; Xia, J.H.; Liu, X.F.; Wu, Y.Y.; Birbilis, N.; Ringer, S.P. Enhanced age-hardening response of Al–4 Mg–1 Cu (wt.%) microalloyed with Ag and Si. *Scr. Mater.* **2013**, *68*, 857–860. [CrossRef]
- Wang, S.C.; Starink, M.J.; Gao, N. Precipitation hardening in Al–Cu–Mg alloys revisited. *Scr. Mater.* **2006**, *54*, 287–291. [CrossRef]
- Wang, S.C.; Starink, M.J. Two types of S phase precipitates in Al–Cu–Mg alloys. *Acta Mater.* **2007**, *55*, 933–941. [CrossRef]

**Disclaimer/Publisher’s Note:** The statements, opinions and data contained in all publications are solely those of the individual author(s) and contributor(s) and not of MDPI and/or the editor(s). MDPI and/or the editor(s) disclaim responsibility for any injury to people or property resulting from any ideas, methods, instructions or products referred to in the content.

# Towards Understanding {10-11}-{10-12} Secondary Twinning Behaviors in AZ31 Magnesium Alloy during Fatigue Deformation

Yunxiang You <sup>1</sup> , Li Tan <sup>1,2,\*</sup>, Yuqin Yan <sup>1</sup>, Tao Zhou <sup>1,\*</sup>, Pengfei Yang <sup>3</sup>, Jian Tu <sup>1</sup> and Zhiming Zhou <sup>1</sup>

<sup>1</sup> School of Materials Science and Engineering, Chongqing University of Technology, Chongqing 400054, China; youyunxiang@stu.cqut.edu.cn (Y.Y.)

<sup>2</sup> Chongqing Yujiang Die-Casting Co., Ltd., Chongqing 400000, China

<sup>3</sup> College of Engineering, Zhejiang Normal University, Jinhua 321004, China

\* Correspondence: tanli@cqut.edu.cn (L.T.); zt19811118@cqut.edu.cn (T.Z.)

**Abstract:** Tensile-compression fatigue deformation tests were conducted on AZ31 magnesium alloy at room temperature. Electron backscatter diffraction (EBSD) scanning electron microscopy was used to scan the microstructure near the fatigue fracture surface. It was found that lamellar {10-11}-{10-12} secondary twins (STs) appeared inside primary {10-11} contraction twins (CTs), with a morphology similar to the previously discovered {10-12}-{10-12} STs. However, through detailed misorientation calibration, it was determined that this type of secondary twin is {10-11}-{10-12} ST. Through calculation and analysis, it was found that the matrix was under compressive stress in the normal direction (ND) during fatigue deformation, which was beneficial for the activation of primary {10-11} CTs. The local strain accommodation was evaluated based on the geometric compatibility parameter ( $m'$ ) combined with the Schmid factor (SF) of the slip system, leading us to propose and discuss the possible formation mechanism of this secondary twin. The analysis results indicate that when the local strain caused by basal slip at the twin boundaries cannot be well transmitted, {10-11}-{10-12} STs are activated to coordinate the strain, and different loading directions lead to different formation mechanisms. Moreover, from the microstructure characterization near the entire fracture surface, we surmise that the presence of such secondary twins is not common.

**Keywords:** magnesium alloy; {10-11}-{10-12} secondary twins; local strain accommodation; fatigue deformation



**Citation:** You, Y.; Tan, L.; Yan, Y.; Zhou, T.; Yang, P.; Tu, J.; Zhou, Z. Towards Understanding {10-11}-{10-12} Secondary Twinning Behaviors in AZ31 Magnesium Alloy during Fatigue Deformation.

*Materials* **2024**, *17*, 1594.

[https://doi.org/](https://doi.org/10.3390/ma17071594)

[10.3390/ma17071594](https://doi.org/10.3390/ma17071594)

Academic Editors: Seong-Ho Ha, Shae-Kwang Kim and Hyun-Kyu Lim

Received: 2 March 2024

Revised: 21 March 2024

Accepted: 25 March 2024

Published: 31 March 2024



**Copyright:** © 2024 by the authors. Licensee MDPI, Basel, Switzerland. This article is an open access article distributed under the terms and conditions of the Creative Commons Attribution (CC BY) license (<https://creativecommons.org/licenses/by/4.0/>).

## 1. Introduction

Magnesium alloys have characteristics such as low density, good damping properties, high specific stiffness, and good processability, which have attracted increasing attention from scholars, mainly for uses in aerospace, automobiles, and 3C electronic products [1–3]. Among all reported twinning modes of magnesium alloys, {10-12} extension twinning is the most common activation mode, usually occurring when tensile stress is applied along the *c*-axis of the grain [4]. When the loading direction is parallel to the *c*-axis compression or perpendicular to the *c*-axis tension, {10-11} contraction twins and {10-11}-{10-12} STs will occur to coordinate deformation [5–7].

At present, some scholars have reported on {10-11}-{10-12} STs. Wu et al. [8] studied the twinning mode of the AZ31 magnesium alloy under uniaxial compression loading, and the results revealed that {10-11} contraction twinning and {10-11}-{10-12} secondary twinning are the main twinning modes during compression along the *c*-axis. When a uniaxial compressive stress is applied to the magnesium alloy along the normal direction (ND), dislocation pile-ups at the grain boundaries cause stress concentration, leading to the activation of primary {10-11} CTs, and as deformation continues, {10-11}-{10-12} STs activate and grow within the primary {10-11} CT to coordinate deformation. During tensile-compression fatigue deformation, traces of {10-11}-{10-12} STs can be found on the fatigue fracture surface, and some scholars have indicated that cyclic hardening phenomena will

activate a large number of STs in the fatigue deformation, and the stress concentration at the boundaries of STs leads to crack initiation and ultimate fracture failure [9]. In a fully reversed strain-controlled fatigue test, Yu et al. [10] found that fatigue microcracks initiate at the {10-12} twin boundaries, but macroscopic crack propagation leading to final fracture occurs along the {10-11}-{10-12} secondary twin boundaries. The authors pointed out that the type of twin cannot be accurately determined solely by the deformation degree of the fracture surface, and it should only be judged based on the trace of the cleavage plane. Yang et al. [2] investigated the secondary twinning behavior during fatigue tests and proposed several local stress-induced secondary twinning mechanisms. The results showed that the interaction between the basal slip within primary twins and the twin boundaries plays an important role in the activation of secondary twins. Compared to slip–twin interaction, the local strain associated with twin–twin interaction may not directly induce the activation of such {10-12}-{10-12} STs. But, to date, our understanding of the induced mechanism of the {10-11}-{10-12} ST during fatigue tests is still incomplete.

In the previous study [11], we also found the presence of {10-11}-{10-12} STs in the fatigue fracture region, but as their quantity was relatively small, the activation mechanism of these twins was not revealed. Therefore, this paper analyzes the formation mechanism of {10-11}-{10-12} STs during fatigue deformation, elucidating this using the Schmid factor and geometric compatibility parameter. The findings provide insight into the activation of {10-11}-{10-12} STs with a low or negative SF in magnesium.

## 2. Materials and Methods

The stress–strain curves for the first cycle, the second cycle, and the half-life cycle were charted in the previous study, and the specific fatigue test parameters were also detailed [12]. The same as-rolled AZ31 Mg alloy sheet underwent fully reversed tension–compression fatigue tests at a total strain amplitude of 1% (fatigue testing machine model: MTS809, Metes Industrial Systems, Inc, Eden Prairie, MN, USA). One electro-polished with commercial AC2 solution, subsequently, the microstructure of the fatigue samples was characterized by scanning electron microscopy (SEM) and electron backscatter diffraction (EBSD) techniques. EBSD examination was performed using the HKL channel 5 system (Technology-Oxford Instruments, Abingdon, UK) in a scanning electron microscope (SEM, FEI Nova 400, Hillsboro, OR, USA).

## 3. Results

The hysteresis loops of the fatigue deformation process were discussed in the previous study [12]. This article only discusses the {10-11}-{10-12} STs that can be observed on the fatigue fracture surface. The IPF map in Figure 1a exhibits the microstructural features of the fracture surface after tensile–compression fatigue, with a specific region selected for subsequent analysis. The AZ31 sample shows a strong basal texture, as shown in Figure 1b. Table 1 lists the twinning types in magnesium alloy, the misorientation angles between twins and the matrix, and the corresponding rotation axes. The color legend for the IPF maps includes low-angle grain boundaries ( $2\text{--}15^\circ$ ), high-angle grain boundaries ( $>15^\circ$ ), and seven possible twinning boundaries [13], shown in different colors in Figure 2d. The six variants generate three types of misorientation, which are  $60.01^\circ <10\text{-}10>$ ,  $60.41^\circ <8\text{-}1\text{-}70>$ , and  $7.41^\circ <1\text{-}210>$ , and the identification of the active twin variant is performed by analyzing the twin plane traces and misorientation [14].

**Table 1.** Common twin types and their angles and axes in magnesium (Mg) [15].

Type of Twin	Twin Plane	Misorientation Axis	Misorientation Angle
Extension twin	{10-12}	$<1\text{-}210>$	$86.3^\circ$
Contraction twin	{10-11}	$<1\text{-}210>$	$56^\circ$
	{10-13}	$<1\text{-}210>$	$64^\circ$



Table 1. Cont.

Type of Twin	Twin Plane	Misorientation Axis	Misorientation Angle
Secondary twin	{10-11}-{10-12}	$\langle 1-210 \rangle$	$38^\circ$
	{10-13}-{10-12}	$\langle 1-210 \rangle$	$22^\circ$
	{10-12}- $\{-1012\}$	$\langle 1-210 \rangle$	$7.4^\circ$
	{10-12}-{01-12}	$\langle 1-210 \rangle$	$60^\circ$
	{10-12}- $\{0-112\}$	$\langle 8-1-70 \rangle$	$60.4^\circ$

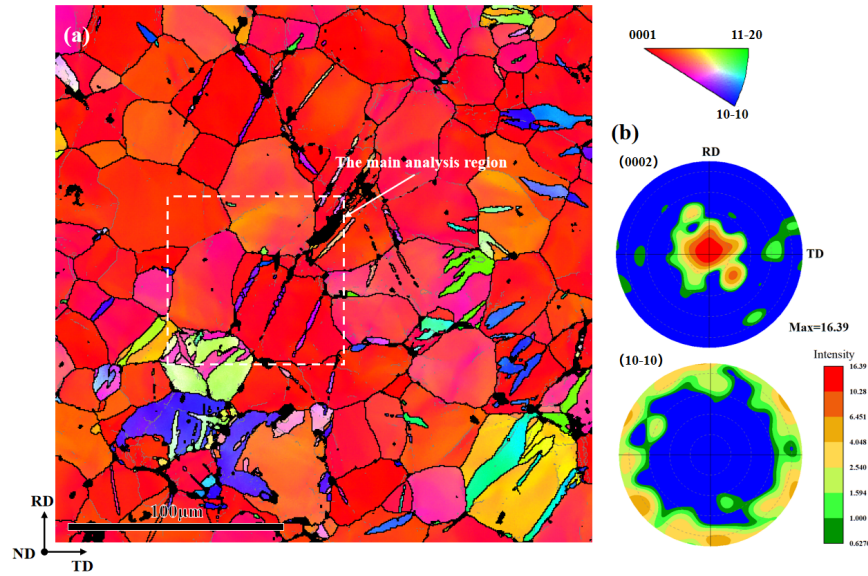


Figure 1. (a) Inverse pole figure map displaying the microstructural characteristics of the fatigued specimens used in the current work. (b) The corresponding pole figure showing a basal texture.

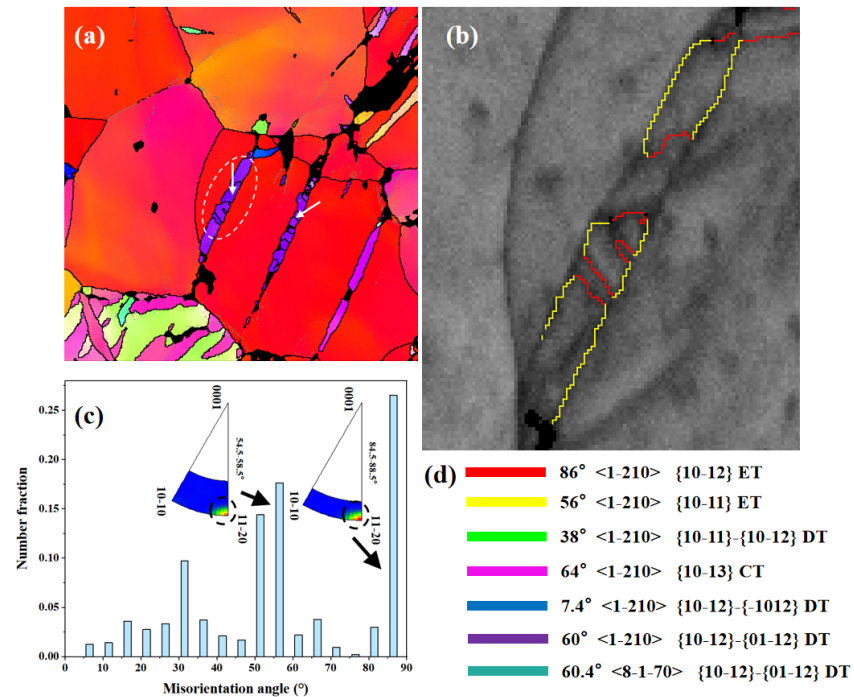


Figure 2. (a) IPF map of the main analysis region; (b) enlarged image of the region shown by the ellipse; (c) misorientation angle map corresponding to the region; (d) boundary color, axis, and twin type. The white arrows in the figure represent the direction of the point-to-point misorientation line profiles. The colorful lines represent the colors of different twin boundaries.



Figure 2 shows the EBSD maps of the main analysis region. Figure 2b depicts an irregular lamellar structure composed of different colored boundaries. The red lines represent the twinning boundaries of {10-12} extension twins (ETs), and the yellow lines represent the twin boundaries of {10-11} CTs. There are two typical types of twins: one is the {10-11} CTs activated by the matrix, and the other type is the {10-11}-{10-12} STs activated within the {10-11} twins. And the {10-11} primary twin boundaries are composed of {10-12}, {10-11}, and {10-11}-{10-12} twin boundaries. In Figure 2c, a peak at around 15° can be observed, which may be caused by low-angle grain boundaries. The distribution peak at around 86° is associated with {10-12} ETs (86°/<1-210>), the peak near 56° is associated with {10-11} CTs (56°/<1-210>), and the peak near 38° is related to {10-11}-{10-12} STs (38°/<1-210>) [16].

The orientation relationship between the matrix and twins in Figure 2b is shown in Figure 3, where the matrix and twins are represented by different symbols. Pt1 (primary twin) is the primary {10-11} CTs activated by the matrix, while St1 (secondary twin) is the {10-11}-{10-12} STs activated within Pt1. From the (0001) and (10-12) pole figures, it can be observed that the CT variant V5 (Pt1) is activated in the matrix by compression along the ND, causing the orientation to tilt from ND to the rolling direction (RD). Subsequently, ET variant V3 (St1) is activated in Pt1 during the subsequent deformation process. Therefore, it can be identified that these lamellar structures are secondary twins. In this work, the identification of {10-11}-{10-12} STs is determined by the misorientation angle that occurs in the primary {10-11} CTs, as shown in Figure 4.

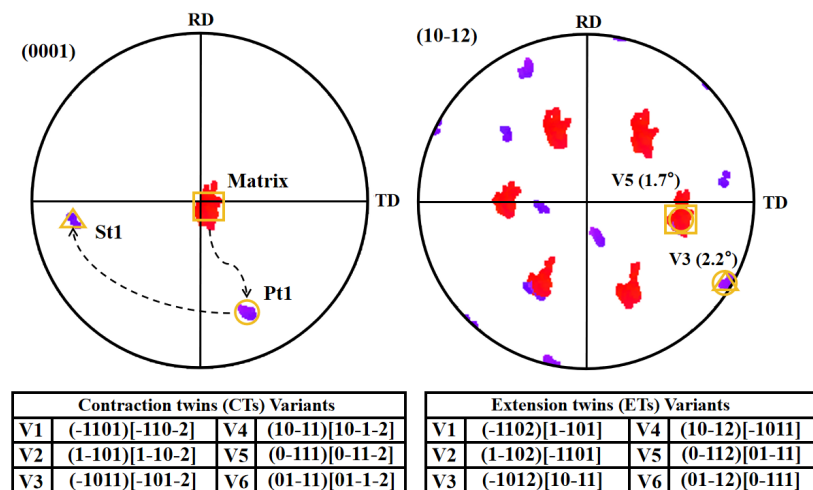


Figure 3. Corresponding orientation relationship of the tagged twin (Matrix, Pt1, St1) and the matrix in Figure 2b, respectively. The symbols indicate the experimentally projected sites of both twins and the matrix by EBSD.

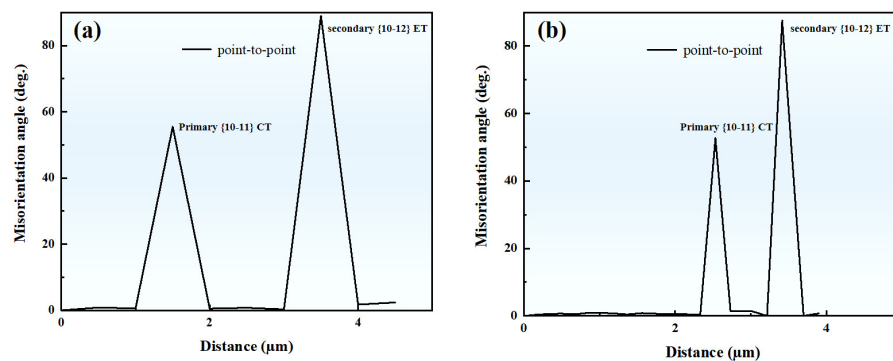


Figure 4. Point-to-point misorientation line profiles along the direction indicated by the white arrows in Figure 2a. (a) represents the white line on the left, and (b) represents the white line on the right.

## 4. Discussion

### 4.1. Analyses of Schmid Factors

In order to reveal the activation mechanism of the observed {10-11}-[10-12] STs, the Schmid factors (SFs) of the primary {10-11} CTs, {10-12} ETs, and {10-11}-[10-12] STs are calculated. The Euler angle values are extracted from the EBSD results. Due to the rapid fracture of the specimen when cracks initiate [10], the final loading direction before fracture during fatigue deformation is uncertain. Therefore, two loading directions are considered in the calculation process: tension and compression along the ND. The twins in Figure 2a are represented by different numbers as shown in Figure 5a, and Figure 5b is a grain boundary map identified based on the axis and angle. The SF is defined as

$$m = \cos\phi \times \cos\lambda$$

where  $\lambda$  represents the angle between the loading axis and the normal twinning plane and  $\phi$  stands for the angle between the loading axis and shear direction. When compressed along the ND, the loading direction is parallel to the c-axis, primary {10-11} CTs are activated when the loading direction is parallel to the c-axis, and {10-11}-[10-12] STs are activated after re-twinning within the primary twin. The SF values of the six potential {10-11} CT variants for the marked grains are shown in Table 2, and the SF values of the actual activated primary twin variants are highlighted in yellow in the table. The SF values of the six potential {10-11} CT variants for grains 1, 4, and 7 are all relatively high, indicating that compression along the ND is favorable for the activation of {10-11} CTs. Table 3 shows the SF values of the six potential {10-12} ET variants for the marked grains. From the data in the table, it can be observed that the SF values of both potential {10-12} ET variants of the matrix and the actual activated variants are negative, indicating that compression along the ND is unfavorable for activating {10-12} ETs within the matrix. The SF values of the actual activated {10-12} ET variants of primary twin 2 and twin 5, whether under compressive stress ( $-0.011$ ,  $-0.008$ ) or tensile stress ( $0.011$ ,  $0.008$ ), do not comply with the Schmid law. Therefore, when the matrix is under compressive stress along the ND, {10-11} CTs 2, 5, and 8 are activated, with their SFs being 0.343, 0.304, and 0.451, respectively. As the SF values of all six variants are relatively high, the variants (0-111)[0-11-2] (V5) and (01-11)[01-1-2] (V6) are activated. Twins 2 and 5 activate the {10-11}-[10-12] ST variants (10-12)[-1011] (V4) during subsequent deformation processes, which possibly coordinate the local strain generated by the interaction between the twins or slip systems, which will be discussed further in the following paragraphs.

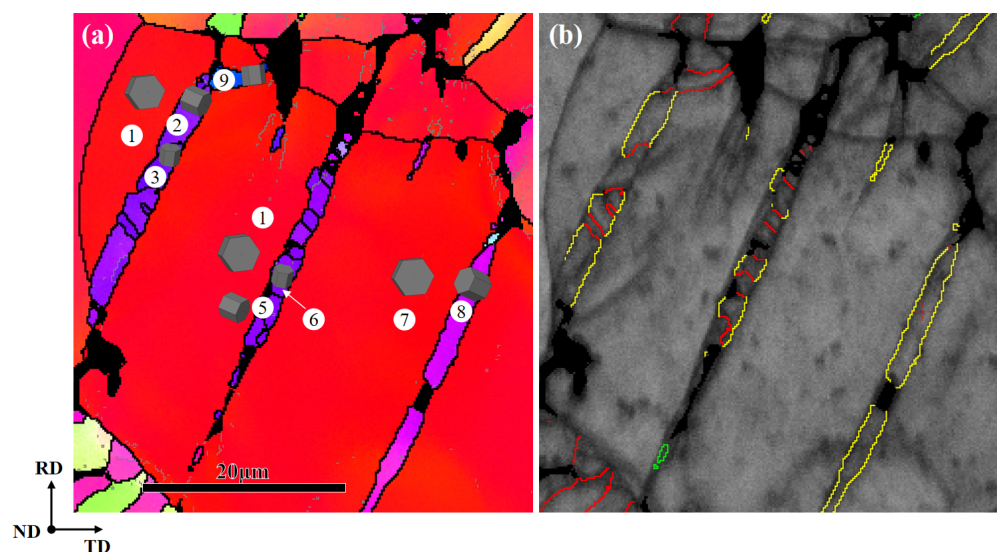


**Figure 5.** (a) IPF map indicating different twin variants with numerical labels; (b) grain boundary map.

**Table 2.** SF values of the six potential {10-11} contraction twin variants labeled by number (compressive loading).

SF	(01-11)[01-1-2]	(10-11)[10-1-2]	(1-101)[1-10-2]	(0-111)[0-11-2]	(-1011)[-101-2]	(-1101)[-110-2]
1 (Matrix)	0.466	0.428	0.365	② 0.343	0.390	0.450
2 (PT)	-0.004	0.127	-0.124	-0.464	-0.088	0.121
3 (ST)	-0.057	0.095	-0.125	-0.481	-0.113	0.092
4 (Matrix)	0.482	0.445	0.356	⑤ 0.304	0.358	0.447
5 (PT)	0.013	0.135	-0.104	-0.458	-0.099	0.134
6 (ST)	0.013	0.133	-0.095	-0.458	-0.107	0.135
7 (Matrix)	⑧ 0.451	0.435	0.394	0.370	0.390	0.430
8	-0.343	-0.022	0.251	0.207	0.251	-0.027
9	-0.393	-0.054	-0.164	-0.421	-0.065	-0.146

The circled numbers represents the actual secondary twin variant activated by this parent/cube. The number indicates which variant of parent/cube is observed.

**Table 3.** SF values of the six potential {10-12} extension twin variants labeled by number (compressive loading).

SF	(0-112)[01-11]	(-1012)[10-11]	(-1102)[1-101]	(01-12)[0-111]	(10-12)[-1011]	(1-102)[-1101]
1	-0.493	-0.494	-0.485	-0.479	-0.490	-0.495
2	0.255	-0.035	0.016	0.308	-0.011	-0.012
3	0.299	-0.001	0.032	0.348	0.023	0.007
4	-0.483	-0.488	-0.477	-0.463	-0.478	-0.488
5	0.240	-0.035	-0.005	0.294	-0.008	-0.032
6	0.240	-0.030	-0.011	0.294	-0.002	-0.037
7	-0.498	-0.498	-0.494	-0.489	-0.493	-0.498
8	0.113	-0.122	-0.151	0.050	-0.153	-0.119
9	0.488	0.071	0.187	0.491	0.072	0.185

When tensile along the ND, the SF values of the potential six {10-11} CT variants of the marked grains are as shown in Table 4, and the SF values of the six potential {10-12} ET variants are as listed in Table 5. The SF values of the activated ST variants are highlighted in the table. The data in the table indicate that the SF values of the six potential {10-11} CT variants for the matrixes 1, 4, and 7 are negative, confirming that the {10-11} CTs are activated by compression along the ND. However, the SF values of these {10-11}-{10-12} ST variants are relatively low, displaying non-Schmid behavior. This indicates that compared with the external stress, the internal stress (or local effect) should play a more important role in the formation of the {10-11}-{10-12} STs.

**Table 4.** SF values of the six potential {10-11} contraction twin variants labeled by number (tensile loading).

SF	(01-11)[01-1-2]	(10-11)[10-1-2]	(1-101)[1-10-2]	(0-111)[0-11-2]	(-1011)[-101-2]	(-1101)[-110-2]
1	-0.466	-0.428	-0.365	-0.343	-0.390	-0.450
2	0.004	-0.127	0.124	0.464	0.088	-0.121
3	0.057	-0.095	0.125	0.481	0.113	-0.092
4	-0.482	-0.445	-0.356	-0.304	-0.358	-0.447
5	-0.013	-0.135	0.104	0.458	0.099	-0.134
6	-0.013	-0.133	0.095	0.458	0.107	-0.135
7	-0.451	-0.435	-0.394	-0.370	-0.390	-0.430
8	0.343	0.022	-0.251	-0.207	-0.251	0.027
9	0.393	0.054	0.164	0.421	0.065	0.146

**Table 5.** SF values of the six potential {10-12} extension twin variants labeled by number (tensile loading).

SF	(0-112)[01-11]	(-1012)[10-11]	(-1102)[1-101]	(01-12)[0-111]	(10-12)[-1011]	(1-102)[-1101]
1	0.493	0.494	0.485	0.479	0.490	0.495
2	-0.255	0.035	-0.016	-0.308	③ 0.011	0.012
3	-0.299	0.001	-0.032	-0.348	-0.023	-0.007
4	0.483	0.488	0.477	0.463	0.478	0.488
5	-0.240	0.035	0.005	-0.294	⑥ 0.008	0.032
6	-0.240	0.030	0.011	-0.294	0.002	0.037
7	0.498	0.498	0.494	0.489	0.493	0.498
8	-0.113	0.122	0.151	-0.050	0.153	0.119
9	-0.488	-0.071	-0.187	-0.491	-0.072	-0.185

The circled numbers represents the actual secondary twin variant activated by this parent/cube. The number indicates which variant of parent/cube is observed.

For magnesium alloys, the contraction of the c-axis is mainly regulated by the formation of {10-11}-{10-12} STs, which will result in the reorientation of  $37.5^\circ$  and  $30.1^\circ$  twin/matrix [17]. Studies have shown that the SF usually controls the selection of variants for initial twin nucleation [15], and twin variants with higher SF values are more easily activated in plastic deformation [18]. However, at least half of the twin activation during certain deformation processes does not follow Schmid's law, and even twin variants with lower or negative SF values can be activated [17,19].

Research has shown that when the shear strain caused by dislocation slip within a grain cannot be accommodated, twins within the same or neighboring grains can be activated to accommodate the local strain caused by dislocation slip or twinning [20–22]. Therefore, two possible mechanisms have been proposed for the formation of secondary twins with lower SF values: (i) when the strain caused by dislocation slip within the primary twin (PT) cannot be well transmitted to the matrix, the secondary twin (ST) is activated to accommodate the local strain; (ii) the strain induced by dislocation slip within the matrix at the primary twin boundary causes the formation of the secondary twin (ST).

The schematic diagrams of these two possible mechanisms are shown in Figure 6. In order to evaluate the effectiveness of these mechanisms for the formation of a secondary twin, a geometric compatibility parameter ( $m'$ ) is employed here and defined as  $m' = \cos\varphi \times \cos\kappa$ , where  $\varphi$  is the angle of the twin or slip plane normal and  $\kappa$  presents the angle between the shear directions of twin or dislocation slip. This factor was successively applied to elucidate the occurrence of the twin with a low SF or for variant selection of the paired twins in magnesium and titanium, where a relatively high  $m'$  value indicates a better accommodation effect [2]. Therefore,  $m'$  and SF values related to the twin variants and slip systems (the geometric relationship in the plane as shown in grain 1–6 in Figure 5a) associated with the two mechanisms mentioned above were calculated and will be discussed in more detail.

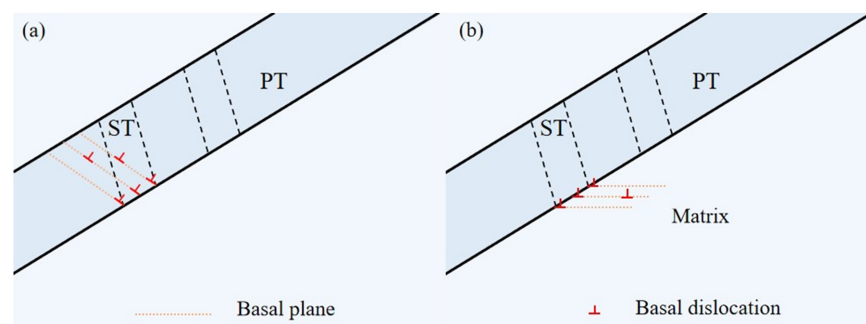


**Figure 6.** Schematics showing the possible formation mechanisms of a secondary twin within the primary twin. (a) The first mechanism above: Primary Twin (PT) basal slip-induced Secondary Twin (ST); (b) The second mechanism above: Matrix basal slip-induced Secondary Twin (ST).

#### 4.2. $m'$ Associated with Secondary Twin and Basal Slip within the Primary Twin

{10-11}-{10-12} STs can be activated within the primary {10-11} CTs, and a large number of dislocations pile up at the twin boundaries. Studies have shown that when the dislocation slip generated by the primary twin encounters a “hard” grain boundary, which occurs when the shear strain caused by the dislocation slip within the primary twin cannot be accommodated by its neighboring twin or matrix, the secondary twin can be activated within the same twin to accommodate the strain [21,22]. Therefore, taking secondary twins in the research region (Figure 5a) as an example, Table 6 lists the  $m'$  values between the basal slip system of the primary twin and the secondary twin variants within twin 2, and Table 7 lists the  $m'$  values between the basal slip system of the primary twin and the secondary twin variants within twin 5, with the corresponding SF values of the basal slip system within the primary twin also in Table 7.

**Table 6.** The  $m'$  values of the basal slip system within the primary twin 2 and the secondary twin variant, and the corresponding SF values of the two kinds of systems.

$M'$	Secondary Twin Variant		(01-12)[0-111]	(10-12)[-1011]	(1-102)[-1101]	(0-112)[01-11]	(-1012)[10-11]	(-1102)[1-101]
basal slip system within primary twin	SF (tensile loading)	SF (compressive loading)	-0.308/0.308	0.011/-0.011	0.012/-0.012	-0.255/0.255	0.035/-0.035	-0.016/0.016
(0001)[2-1-10]	-0.015	0.015	0.000	-0.461	-0.461	0.000	0.461	0.461
(0001)[11-20]	-0.365	0.365	-0.461	-0.461	0.000	0.461	0.461	0.000
(0001)[1-210]	0.349	-0.349	0.461	0.000	-0.461	-0.461	0.000	0.461
(0001)[-12-10]	-0.349	0.349	-0.461	0.000	0.461	0.461	0.000	-0.461
(0001)[-1-120]	0.365	-0.365	0.461	0.461	0.000	-0.461	-0.461	0.000
(0001)[-2110]	0.015	-0.015	0.000	0.461	0.461	0.000	-0.461	-0.461

**Table 7.** The  $m'$  values of the basal slip system within the primary twin 5 and the secondary twin variant, and the corresponding SF values of the two kinds of systems.

$m'$	Secondary Twin Variant		(01-12)[0-111]	(10-12)[-1011]	(1-102)[-1101]	(0-112)[01-11]	(-1012)[10-11]	(-1102)[1-101]
basal slip system within primary twin	SF (tensile loading)	SF (compressive loading)	0.295/-0.295	-0.002/0.002	-0.037/0.037	0.24/-0.24	-0.03/0.03	-0.011/0.011
(0001)[2-1-10]	-0.005	0.005	0.000	-0.461	-0.461	0.000	0.461	0.461
(0001)[11-20]	-0.368	0.368	-0.461	-0.461	0.000	0.461	0.461	0.000
(0001)[1-210]	0.363	-0.363	0.461	0.000	-0.461	-0.461	0.000	0.461
(0001)[-12-10]	-0.363	0.363	-0.461	0.000	0.461	0.461	0.000	-0.461
(0001)[-1-120]	0.368	-0.368	0.461	0.461	0.000	-0.461	-0.461	0.000
(0001)[-2110]	0.005	-0.005	0.000	0.461	0.461	0.000	-0.461	-0.461

From the table data, it can be seen that when the loading direction is tensioned along the ND, the SF values of the basal slip systems (0001) [1-210] and (0001) [-1-120] in the primary twin are higher, and the accommodation between the basal slip system (0001) [-1-120] and the secondary twin variant is also better ( $m' = 0.461$ ). The  $m'$  value between the basal slip system (0001)[-1-120] (the basal slip system with the maximum SF value) within the twin and the secondary ET variant is 0.461, as shown in Figure 7b, indicating that in this case, the secondary twins 3 and 6 are activated to accommodate the local strain incompatibility at the primary twin boundary caused by the basal slip. Similar to previous studies, the activation of secondary twins can reduce the strain incompatibility caused

by the basal slip within the primary twins to the greatest extent [22]. Therefore, it can be inferred that the first type of proposed mechanism for the formation of secondary twins is effective under tensile loading.

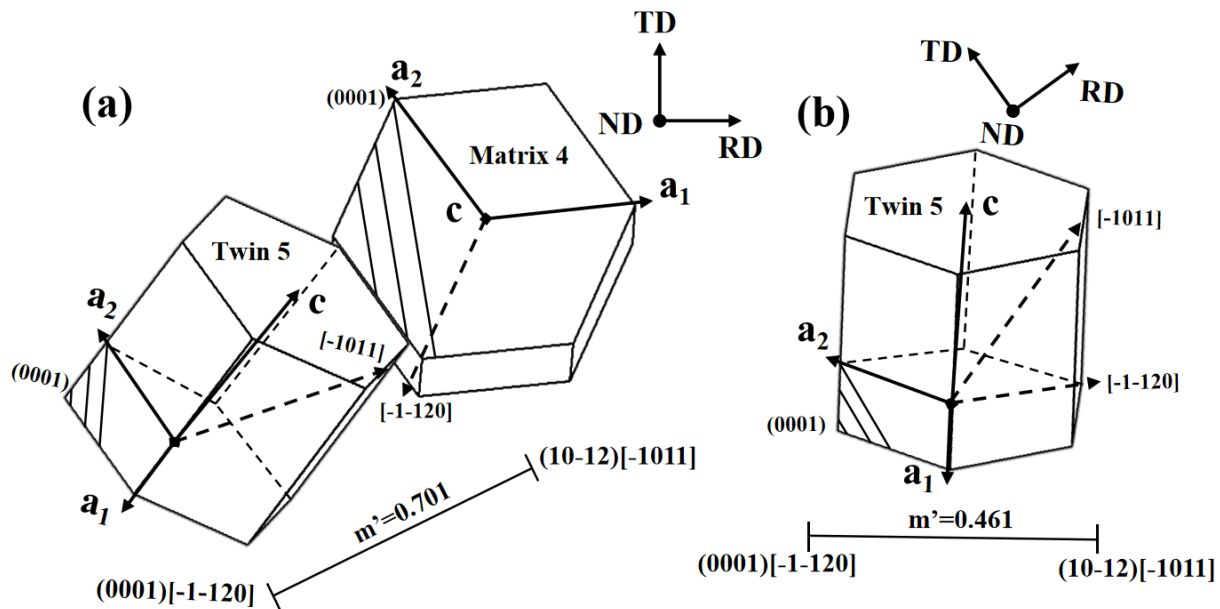


**Figure 7.** Two induced mechanism diagrams under different loading directions: (a) the compressive loading is along the ND direction; (b) the tensile loading is along the ND direction.

#### 4.3. $m'$ Associated with Secondary Twin and Basal Slip in the Matrix

The second mechanism of formation is the local strain-induced secondary twin (ST) at the primary twin boundary caused by the basal slip within the matrix. Previous studies have found that stress concentration induced by basal slip at the grain boundary within the matrix can induce twins, known as the matrix slip-induced twin mechanism [23–25]. From the data in Table 8, it can be seen that the SF values of the slip systems within matrix 1 are relatively low when the stress is applied along the ND, with the basal system (0001)[1-210] being the highest at 0.107. In the process of plastic deformation, a low value of the Schmid factor typically indicates that the system is inactive in this loading direction [14,26]. Therefore, in this loading direction, the orientation of the primary twin is more favorable for the activation of basal slip systems than the original matrix orientation, as shown in Figure 4, so the SF of the basal slip systems within the primary twin is higher than that within the matrix. At the same time, it was found through calculations that when the compressive loading is along the ND, the accommodation between the basal slip systems within the primary twin and the secondary twin variants is unfavorable, with  $m'$  values being zero or negative. The  $m'$  values between the basal slip systems within the matrix and the six potential secondary twin variants are listed in Table 9. In this case, the basal slip systems (0001)[1-210] and (0001)[-1-120] in matrix 4 are more easily activated (under compressive loading in matrix 4:  $SF(0001)[-1-120] = 0.137$ ,  $SF(0001)[1-210] = 0.139$ ). And the  $m'$  value between the slip system (0001)[-1-120] and the secondary twin variant 6 is 0.701, as shown in Figure 7a, which shows good accommodation. In conclusion, this study has found that the activation of most basal slip systems within the matrix is unfavorable, while basal slip systems within the matrix show good accommodation with the secondary twin variants when the compressive loading is along the ND. Therefore, it can be inferred that the second type of proposed mechanism for the formation of secondary twins is effective under compressive loading.

**Table 8.** The  $m'$  values of the basal slip system within matrix 1 and the secondary twin variant within twin 2, and the corresponding SF values of the two kinds of systems.

$m'$	Secondary Twin Variant		(01-12)[0-111]	(10-12)[-1011]	(1-102)[-1101]	(0-112)[01-11]	(-1012)[10-11]	(-1102)[1-101]
basal slip system within matrix	SF (tensile loading)	SF (compressive loading)	-0.308/0.308	0.011/-0.011	0.012/-0.012	-0.255/0.255	0.036/-0.036	-0.016/0.016
(0001)[2-1-10]	-0.024	0.024	-0.037	-0.456	-0.079	0.000	0.080	0.418
(0001)[11-20]	0.083	-0.083	-0.842	-0.674	-0.076	0.022	-0.003	-0.269
(0001)[1-210]	-0.107	0.107	0.805	0.218	-0.004	-0.021	0.083	0.687
(0001)[-12-10]	0.107	-0.107	-0.805	-0.218	0.004	0.021	-0.083	-0.687
(0001)[-1-120]	-0.083	0.083	0.842	0.674	0.076	-0.022	0.003	0.269
(0001)[-2110]	0.024	-0.024	0.037	0.456	0.079	0.000	-0.080	-0.418

**Table 9.** The  $m'$  values of the basal slip system within matrix 4 and the secondary twin variant within twin 5, and the corresponding SF values of the two kinds of systems.

$m'$	Secondary Twin Variant		(01-12)[0-111]	(10-12)[-1011]	(1-102)[-1101]	(0-112)[01-11]	(-1012)[10-11]	(-1102)[1-101]
basal slip system within matrix	SF (tensile loading)	SF (compressive loading)	-0.295/0.295	0.002/-0.002	0.037/-0.037	-0.24/0.24	0.03/-0.03	0.011/-0.011
(0001)[2-1-10]	-0.002	0.002	-0.012	-0.460	-0.115	0.000	0.114	0.448
(0001)[11-20]	0.137	-0.137	-0.852	-0.701	-0.105	0.007	0.007	-0.256
(0001)[1-210]	-0.139	0.139	0.840	0.240	-0.009	-0.007	0.108	0.705
(0001)[-12-10]	0.139	0.139	-0.840	-0.240	0.009	0.007	-0.108	-0.705
(0001)[-1-120]	-0.137	0.137	0.852	0.701	0.105	-0.007	-0.007	0.256
(0001)[-2110]	0.002	-0.002	0.012	0.460	0.115	0.000	-0.114	-0.448

Finally, it should be pointed out that the change in loading direction can lead to different accommodation mechanisms. In this study, under tensile loading along the ND, the second accommodation mechanism is unfavorable, and the dislocation slip within the primary twin plays an important role in the activation of {10-11}-{10-12} STs. Meanwhile, under compressive loading along the ND, the first accommodation mechanism is unfavorable, and the dislocation slip within the matrix plays an important role in the activation of {10-11}-{10-12} STs. Through analysis, it is shown that although the SF values of the secondary twin variants are very low under the tensile-compression loading, the different loading direction determines the activation of different slip systems, which plays a crucial role in subsequent strain accommodation.

## 5. Conclusions

This paper has studied the AZ31 magnesium alloy through tension-compression fatigue tests at room temperature and provided EBSD characterization of the microstructure near the fatigue fracture, and the conclusions are as follows:

- (1) The lamellar secondary twin is activated inside the primary {10-11} CT. This morphological feature is similar to the previously discovered {10-12}-{10-12} STs. After misorientation calibration, it is found that this type of secondary twin is a {10-11}-{10-12} ST.
- (2) Local strain accommodation plays an important role in the formation of the unusual {10-11}-{10-12} ST. The calculation analysis using the Schmid factor and geometric compatibility parameter concludes that during tensile loading, when the strain caused



by the basal slip within the {10-11} primary twin cannot be effectively transmitted to the matrix, it induces the {10-11}-{10-12} secondary twin within the primary twin to reduce the local strain incompatibility at the twin boundary. Under compressive loading, the activation of certain slip systems within the matrix induces local strain at the primary twin boundary, leading to the activation of {10-11}-{10-12} secondary twins.

**Author Contributions:** Writing—original draft preparation, software, Y.Y. (Yunxiang You); validation, investigation, Y.Y. (Yuqin Yan); methodology, data curation, P.Y.; writing—review and editing, L.T. and T.Z.; conceptualization, J.T. and Z.Z. All authors have read and agreed to the published version of the manuscript.

**Funding:** This work was co-supported by the National Natural Science Foundation of China (51901030, 52274374), Natural Science Foundation of Chongqing (cstc2020jcyj-msxmX0877), Science and Technology Research Program of the Chongqing Municipal Education Commission (KJQN202201160), Cultivation Plan of Scientific Research and Innovation Team of Chongqing University of Technology (No.2023TDZ010), and Postdoctoral Research Project of the Chongqing Human Resources and Social Security Bureau (2022CQBSHTB3110).

**Institutional Review Board Statement:** Not applicable.

**Informed Consent Statement:** Not applicable.

**Data Availability Statement:** Data are contained within the article.

**Conflicts of Interest:** Author Li Tan was employed by the company Chongqing YuJiang Die-Casting. The remaining authors declare that the research was conducted in the absence of any commercial or financial relationships that could be construed as a potential conflict of interest.

## References

- Carneiro, L.; Culbertson, D.; Yu, Q.; Jiang, Y.Y. Twinning in Rolled AZ31B Magnesium Alloy under Free-End Torsion. *Mater. Sci. Eng. A* **2021**, *801*, 140405. [CrossRef]
- Yang, P.F.; Yang, Z.Y.; Li, L.; Sun, Q.; Tan, L.; Ma, X.K.; Zhu, M.H. Towards Understanding Double Extension Twinning Behaviors in Magnesium Alloy during Uniaxial Tension Deformation. *J. Alloys Compd.* **2022**, *894*, 162491. [CrossRef]
- Liu, H.; Lin, F.X.; Liu, P.; Yue, Y.; Shin, K.S.; Peng, L.M.; Delannay, L.; Nie, J.F.; Moelans, N. Variant Selection of Primary–Secondary Extension Twin Pairs in Magnesium: An Analytical Calculation Study. *Acta Mater.* **2021**, *219*, 117221. [CrossRef]
- Park, S.H.; Hong, S.G.; Lee, J.H.; Huh, Y.H. Texture Evolution of Rolled Mg–3Al–1Zn Alloy Undergoing a {10-12} Twinning Dominant Strain Path Change. *J. Alloys Compd.* **2015**, *646*, 573–579. [CrossRef]
- Sandlöbes, S.; Zaeferrer, S.; Schestakow, I.; Yi, S.; Gonzalez-Martinez, R. On the Role of Non-Basal Deformation Mechanisms for the Ductility of Mg and Mg–Y Alloys. *Acta Mater.* **2011**, *59*, 429–439. [CrossRef]
- Hou, X.L.; Liu, X.Q.; Wang, D.L.; Liu, Y.F.; Zhao, Q.Y.; Sun, Z.; Shang, Z.X.; Sun, Z.K. Insight into Double Twinning Behavior of Mg–Gd Rolled Alloy at the Nano Scale: Role of Micro-Texture Entropy. *J. Alloys Compd.* **2024**, *983*, 173835. [CrossRef]
- Chaudry, U.M.; Tariq, H.M.R.; Zubair, M.; Ansari, N.; Jun, T.S. Implications of Twinning on the Microstructure Development, Crystallographic Texture and Mechanical Performance of Mg Alloys—A Critical Review. *J. Magnes. Alloys* **2023**, *11*, 4146–4165. [CrossRef]
- Wu, B.L.; Wan, G.; Zhang, Y.D.; Esling, C. Twinning Characteristics in Textured AZ31 Alloy under Impact Loading along Specified Direction. *Mater. Lett.* **2010**, *64*, 636–639. [CrossRef]
- Koike, J.; Fujiyama, N.; Ando, D.; Sutou, Y. Roles of Deformation Twinning and Dislocation Slip in the Fatigue Failure Mechanism of AZ31 Mg Alloys. *Scr. Mater.* **2010**, *63*, 747–750. [CrossRef]
- Yu, Q.; Jiang, Y.Y.; Wang, J. Cyclic Deformation and Fatigue Damage in Single-Crystal Magnesium under Fully Reversed Strain-Controlled Tension–Compression in the [101 $\bar{0}$ ] Direction. *Scr. Mater.* **2015**, *96*, 41–44. [CrossRef]
- Li, L.; Yang, J.; Yang, Z.Y.; Sun, Q.; Tan, L.; Zeng, Q.H.; Zhu, M.H. Towards Revealing the Relationship between Deformation Twin and Fatigue Crack Initiation in a Rolled Magnesium Alloy. *Mater. Charact.* **2021**, *179*, 111362. [CrossRef]
- Tan, L.; Huang, X.Y.; Wang, Y.Z.; Sun, Q.; Zhang, Y.B.; Tu, J.; Zhou, Z.M. Activation Behavior of {10-12}-{10-12} Secondary Twins by Different Strain Variables and Different Loading Directions during Fatigue Deformation of AZ31 Magnesium Alloy. *Metals* **2022**, *12*, 1433. [CrossRef]
- Dang, K.; Graham, J.; McCabe, R.J.; Taupin, V.; Tomé, C.N.; Capolungo, L. Atomistic and Phase Field Simulations of Three Dimensional Interactions of {101-2} Twins with Grain Boundaries in Mg: Twin Transmission and Dislocation Emission. *Materialia* **2021**, *20*, 101247. [CrossRef]





14. Guo, C.F.; Xin, R.L.; Ding, C.H.; Song, B.; Liu, Q. Understanding of Variant Selection and Twin Patterns in Compressed Mg Alloy Sheets via Combined Analysis of Schmid Factor and Strain Compatibility Factor. *Mater. Sci. Eng. A* **2014**, *609*, 92–101. [CrossRef]
15. Mu, S.J.; Jonas, J.J.; Gottstein, G. Variant Selection of Primary, Secondary and Tertiary Twins in a Deformed Mg Alloy. *Acta Mater.* **2012**, *60*, 2043–2053. [CrossRef]
16. Guan, D.K.; Rainforth, W.M.; Gao, J.H.; Sharp, J.; Wynne, B.; Ma, L. Individual Effect of Recrystallisation Nucleation Sites on Texture Weakening in a Magnesium Alloy: Part 1—Double Twins. *Acta Mater.* **2017**, *135*, 14–24. [CrossRef]
17. Cizek, P.; Barnett, M.R. Characteristics of the Contraction Twins Formed Close to the Fracture Surface in Mg–3Al–1Zn Alloy Deformed in Tension. *Scr. Mater.* **2008**, *59*, 959–962. [CrossRef]
18. Yin, D.D.; Boehlert, C.J.; Long, L.J.; Huang, G.H.; Zhou, H.; Zheng, J.; Wang, Q.D. Tension-Compression Asymmetry and the Underlying Slip/Twinning Activity in Extruded Mg–Y Sheets. *Int. J. Plast.* **2021**, *136*, 102878. [CrossRef]
19. Shi, Z.Z.; Zhang, Y.D.; Wagner, F.; Juan, P.A.; Berbenni, S.; Capolungo, L.; Lecomte, J.S.; Richeton, T. On the Selection of Extension Twin Variants with Low Schmid Factors in a Deformed Mg Alloy. *Acta Mater.* **2015**, *83*, 17–28. [CrossRef]
20. Zhou, B.J.; Wang, L.Y.; Jin, P.P.; Jia, H.L.; Roven, H.J.; Zeng, X.Q.; Li, Y.J. Revealing Slip-Induced Extension Twinning Behaviors Dominated by Micro Deformation in a Magnesium Alloy. *Int. J. Plast.* **2020**, *128*, 102669. [CrossRef]
21. Agnew, S.R.; Tomé, C.N.; Brown, D.W.; Holden, T.M.; Vogel, S.C. Study of Slip Mechanisms in a Magnesium Alloy by Neutron Diffraction and Modeling. *Scr. Mater.* **2003**, *48*, 1003–1008. [CrossRef]
22. Liu, G.D.; Xin, R.L.; Shu, X.G.; Wang, C.P.; Liu, Q. The Mechanism of Twinning Activation and Variant Selection in Magnesium Alloys Dominated by Slip Deformation. *J. Alloys Compd.* **2016**, *687*, 352–359. [CrossRef]
23. Homayonifar, M.; Mosler, J. On the Coupling of Plastic Slip and Deformation-Induced Twinning in Magnesium: A Variationally Consistent Approach Based on Energy Minimization. *Int. J. Plast.* **2011**, *27*, 983–1003. [CrossRef]
24. Guan, D.K.; Wynne, B.; Gao, J.H.; Huang, Y.H.; Rainforth, W.M. Basal Slip Mediated Tension Twin Variant Selection in Magnesium WE43 Alloy. *Acta Mater.* **2019**, *170*, 1–14. [CrossRef]
25. Wang, L.; Yang, Y.; Eisenlohr, P.; Bieler, T.R.; Crimp, M.A.; Mason, D.E. Twin Nucleation by Slip Transfer across Grain Boundaries in Commercial Purity Titanium. *Metall. Mater. Trans. A* **2010**, *41*, 421–430. [CrossRef]
26. Nan, X.L.; Wang, H.Y.; Zhang, L.; Li, J.B.; Jiang, Q.C. Calculation of Schmid Factors in Magnesium: Analysis of Deformation Behaviors. *Scr. Mater.* **2012**, *67*, 443–446. [CrossRef]

**Disclaimer/Publisher’s Note:** The statements, opinions and data contained in all publications are solely those of the individual author(s) and contributor(s) and not of MDPI and/or the editor(s). MDPI and/or the editor(s) disclaim responsibility for any injury to people or property resulting from any ideas, methods, instructions or products referred to in the content.

## Article

# Corrosion Behavior of Homogenized and Extruded 1100 Aluminum Alloy in Acidic Salt Spray

Yuchao Zhao <sup>1</sup>, Qiang Lu <sup>1</sup>, Qudong Wang <sup>1,\*</sup> , Dezhi Li <sup>2</sup> , Feng Li <sup>3</sup> and Yuzhao Luo <sup>3</sup>

<sup>1</sup> National Engineering Research Center of Light Alloy Net Forming, State Key Laboratory of Metal Matrix Composites, School of Materials Science and Engineering, Shanghai Jiao Tong University, Shanghai 200240, China; zhaoyuchao@sjtu.edu.cn (Y.Z.); luqiang951127@sjtu.edu.cn (Q.L.)

<sup>2</sup> Warwick Manufacturing Group, University of Warwick, Coventry CV4 7AL, UK; dezhi.li@warwick.ac.uk

<sup>3</sup> GD Midea Heating & Ventilating Equipment Co., Ltd., Foshan 528308, China; lifeng3@midea.com (F.L.); luoyz1@midea.com (Y.L.)

\* Correspondence: wangqudong@sjtu.edu.cn

**Abstract:** The 1100 aluminum alloy has been widely used in many industrial fields due to its high specific strength, fracture toughness, excellent thermal conductivity, and corrosion resistance. In this study, the corrosion behavior of the homogenized and hot-extruded 1100 aluminum alloy in acid salt spray environment for different time was studied. The microstructure of the 1100 aluminum alloy before and after corrosion was characterized by an optical microscope (OM), scanning electron microscopy (SEM), X-ray photoelectron spectroscopy (XPS), and a laser scanning confocal microscope (LSCM). The difference in corrosion resistance between the homogenized and extruded 1100 aluminum alloy was analyzed via the electrochemical method. The results indicate that after hot extrusion at 400 °C, the microstructure of the 1100 aluminum alloy changes from an equiaxed crystal structure with (111) preferentially distributed in a fibrous structure with (220) preferentially distributed. There was no obvious dynamic recrystallization occurring during extrusion, and the second-phase particles containing Al-Fe-Si were coarse and unevenly distributed. With the increase in corrosion time, corrosion pits appeared on the surface of the 1100 aluminum alloy, and a corrosion product layer was formed on the surface of the homogenized 1100 aluminum alloy, which reduced the corrosion rate. After 96 h of corrosion, the CPR of the extruded samples was 0.619 mm/a, and that of the homogenized samples was 0.442 mm/a. The corrosion resistance of the extruded 1100 aluminum alloy was affected by the microstructure and the second phase, and no protective layer of corrosion products was formed on the surface, resulting in a faster corrosion rate and deeper corrosion pits.

**Keywords:** 1100 aluminum alloy; homogenized; hot-extruded; acid salt spray; pitting corrosion



**Citation:** Zhao, Y.; Lu, Q.; Wang, Q.; Li, D.; Li, F.; Luo, Y. Corrosion Behavior of Homogenized and Extruded 1100 aluminum Alloy in Acidic Salt Spray. *Materials* **2024**, *17*, 1279. <https://doi.org/10.3390/ma17061279>

Academic Editors: Helena Otmačić Čurković, Seong-Ho Ha, Shae-Kwang Kim and Hyun-Kyu Lim

Received: 11 January 2024

Revised: 4 March 2024

Accepted: 7 March 2024

Published: 10 March 2024



**Copyright:** © 2024 by the authors. Licensee MDPI, Basel, Switzerland. This article is an open access article distributed under the terms and conditions of the Creative Commons Attribution (CC BY) license (<https://creativecommons.org/licenses/by/4.0/>).

## 1. Introduction

The 1100 alloy is a pure aluminum alloy with high specific strength, high fracture toughness, excellent thermal conductivity, and strong chemical corrosion resistance and weathering resistance. It has become one of the most versatile, cost-effective, and attractive metal materials being widely used in different industrial fields [1,2]. With the advocacy for global energy conservation and emission reduction, research on the corrosion performance of designed aluminum parts has found that the corrosion rate of aluminum alloys under acidic condensation conditions is much lower than that of certain steel grades [3].

It is well known that the corrosion resistance of aluminum alloy depends on the formation of alumina passive films on its surface [4,5]. In the pH range of about 4.5–8, this surface film is usually stable [6]. However, most strong acids and alkalis can dissolve the oxide layer, resulting in faster corrosion of aluminum. The alumina layer is also eroded by atmospheric chlorides or sulfides. The adsorption of chloride ions (Cl<sup>-</sup>) in the protective film faults and the penetration and accumulation of Cl<sup>-</sup> in these defects are considered to be triggering factors for the pitting nucleation process [7,8]. Therefore, it is of great

significance to study the rate and mechanism of oxidation layer degradation in the presence of chloride or sulfide in highly acidic environments.

In the past, the research on the corrosion behavior of 1100 aluminum alloys was more focused on the corrosion behavior under near-neutral conditions after immersion in simulated seawater solution (3.5 wt.% NaCl). For example, S. A. Zakaria et al. [9] studied the effects of annealing and solution treatment on the mechanical properties and corrosion properties of cold-rolled Al-1100 alloys in 3.5 wt.% NaCl solution and discussed the effect of microstructure on the corrosion properties. Marlon L. Mopon et al. [7] studied the corrosion behavior of anodic aluminum oxide in simulated seawater solution by anodizing AA-1100 aluminum alloys. Hosni Ezuber et al. [10] studied the corrosion behavior of AA5083 and AA1100 aluminum alloys in seawater at 23 and 60 °C, and showed that the types of intermetallic particles in the aluminum alloy played a major role in passivity breakdown and pit morphology in seawater. Vasundhara Shinde et al. [11] studied the corrosion of Al 1100 alloys in an acidic condensation environment and found that the formation of acidic condensation droplets led to uneven corrosion of Al 1100 samples. Thus, immersion corrosion is a kind of uniform corrosion which cannot effectively characterize the corrosion behavior of metal materials in an atmospheric environment.

The salt spray test is an environmental test that uses artificially simulated salt spray environmental conditions created by salt spray test equipment to confirm the corrosion resistance of products or metal materials, and the relevant standards are ASTM G 85-2011, ISO 9227:2022, etc. [12,13]. Some articles have reported the corrosion of aluminum alloys in salt spray environments. Jing-zhen Qiao et al. [14] studied the corrosion behavior and microstructure of 2024 aluminum alloy sheets after shot peen forming in a salt spray environment. Surendarnath et al. [15] used traditional and new equal-channel angular pressing (ECAP) molds to process commercial pure aluminum, and studied the corrosion of annealed and ECAP-treated samples using the immersion test and salt spray test. However, most studies have used the neutral salt spray test, which corrodes slowly and takes a long time. In order to quickly evaluate the corrosion resistance of aluminum alloys, an acidic environment can be used to accelerate corrosion [16–19].

The purpose of this study is to study the corrosion of aluminum 1100 alloys in an acidic salt spray environment. In this study, the homogenized 1100 aluminum alloy ingots were prepared and hot-extruded. The corrosion resistances of homogenized and extruded 1100 aluminum alloys after acid salt spray for different times were compared and analyzed according to the microstructure, corrosion morphology, and an electrochemical test. It is believed that the results of this work will help to provide anti-corrosion data and a theoretical basis for the practical engineering application of 1100 aluminum alloys in acidic environments, such as in the marine engineering and chemical industries.

## 2. Materials and Methods

### 2.1. Materials

Homogenized 1100 aluminum alloy was obtained through homogenizing heat treatment of commercial 1100 aluminum alloy ingots with diameters of 178 mm. The commercial 1100 aluminum alloy ingots were provided by Henan Runze Light Alloy Technology Co., Ltd. (Pingdingshan City, China), and their composition is shown in Table 1. The homogenizing heat treatment process was as follows: the ingots were placed in a furnace (KSL-1200X-J, Sino-us Joint Venture Hefei Kejing Material Technology Co., LTD, Hefei City, China) at  $595 \pm 5$  °C for 12 h, followed by air cooling to 250 °C and rapid cooling with strong wind until room temperature was reached. Then, the homogenized 1100 aluminum alloy ingots were hot-extruded to make a strip sample with a cross-section of 25 mm × 2 mm. The extrusion process was as follows: the homogenized 1100 aluminum alloy was held at 540 °C for 0.5 h before extrusion, the extrusion cylinder temperature was 400 °C, and the extrusion was carried out at a maximum extrusion ratio of 55:1.

**Table 1.** Chemical compositions of 1100 aluminum alloy (wt.%).

Specimen	Fe	Si	Cu	Mn	Al
1100 aluminum alloy	0.28	0.09	0.13	0.01	Balance

### 2.2. Acid Salt Spray Test

The samples for the salt spray corrosion test were divided into 5 groups and tested for different durations, i.e., 0, 24, 48, 72, and 96 h, with 5 samples in each group. Samples were cleaned with anhydrous ethanol solution and dried before corrosion, and the initial mass of each sample was weighed using an analytical balance (XPR106DUH/AC, Mettler-Toledo, Switzerland) with a range of 120 g and a readability of 0.005 mg. The acetic acid salt spray (AASS) corrosion test was conducted in accordance with the ISO 9227:2022 standard. The exposure zone of the acetic acid–salt spray fog chamber was maintained at  $35 \pm 2$  °C, and the temperature in the saturator tower was 47 °C. The salt solution was 50 g/L sodium chloride (NaCl), and the pH of around 3 was adjusted by a few drops of acetic acid. The block-shaped samples were tilted and placed in a V-shaped groove at a 30° angle to the vertical direction. The samples for salt spray testing could be recovered at different time intervals, up to a maximum of 96 h.

The weight loss analysis was calculated according to the difference in the weight of the samples before and after corrosion. After the acid salt spray test, the samples were ultrasonically cleaned in distilled water to remove the corrosion products in the corrosion pit before weighing.

### 2.3. Electrochemical Tests

Electrochemical tests were performed on DH3000 electrochemical workstation (Donghua Analytical Instruments Co., Ltd., Jingjiang City, China) in 50 g/L NaCl acetic acid solution (with pH = 3.0–3.1) using the conventional three-electrode system. The platinum sheet was used as the counter electrode, and the saturated calomel electrode was used as the reference electrode. The 1100 aluminum alloy samples were used as the working electrodes. The samples were immersed in electrolyte solution for at least 30 min, and then the open circuit potential (OCP) was measured until it became stable. All the other electrochemical tests were conducted based on a stable OCP.

Electrochemical impedance spectroscopy (EIS) was used to evaluate the corrosion behavior of the alloys in a frequency range from 100 kHz to 10 mHz. The potentiodynamic polarization tests were carried out in a potential range of  $-0.6 \sim 0.4$  V vs. OCP, with a scanning rate of 1.0 mV/s. The polarization curves of the dynamic potential were measured to characterize the corrosion behavior of the samples.

### 2.4. Microstructural Characterization

An optical microscope (OM, LEICA DM 4000, Wetzlar, Germany) was used to examine the metallographic structure of the samples. Field emission scanning electron microscopy (SEM, Nova Nano SEM 230, Waltham, MA, USA) equipped with X-ray energy-dispersive spectroscopy (EDS) was used to characterize the corrosion morphology and corrosion product composition. The crystal structure of the samples was analyzed via X-ray diffraction (XRD, Rigaku UltimaIV, Tokyo, Japan). The three-dimensional morphology of the corrosion pits was characterized using a laser scanning confocal microscope (LSCM, Keyence VK-X3000, Osaka, Japan).

### 2.5. Surface Composition Analysis

The composition of corrosion products of the homogenized and extruded 1100 aluminum alloys were determined by X-ray photoelectron spectroscopy (XPS). The XPS experiments were carried out using ESCALAB Xi+ (Thermo Scientific, Waltham, MA, USA). The X-ray source was monochromatic Al K $\alpha$  (1486.6 eV), with a power of 150 W and a flux of 20 eV. The signal in the vertical exit direction of the sample was collected. The C 1s peak

from adventitious carbon at 284.8 eV was used as a reference to correct the charging shifts. Thermo Avantage software v5.99 was used to fit the data of the XPS experiment. In order to extract more reliable information, we recorded only core level spectra for the elements with the highest photoionization cross sections.

### 3. Results and Discussion

#### 3.1. Microstructure Analysis

Prior to the corrosion test, the microstructure of the homogenized and extruded 1100 aluminum alloy was analyzed, as shown in Figure 1. The grains of the homogenized 1100 aluminum alloy were equiaxed with a grain size of about 300  $\mu\text{m}$ , while the microstructure of the extruded 1100 aluminum alloy showed an elongated, fibrous structure along the extrusion direction with uneven grain size and no obvious dynamic recrystallization.

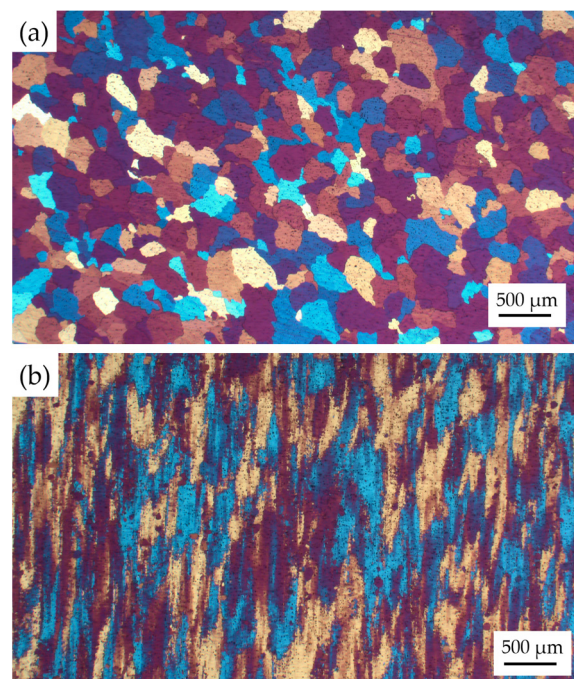


**Figure 1.** Microstructure of the homogenized (a) and extruded (b) 1100 aluminum alloy.

Figure 2 shows the X-ray diffraction patterns of the homogenized and extruded 1100 aluminum alloy. The results indicate that the preferred orientation of the homogenized 1100 aluminum alloy was along the plane (111), and the grain arrangement orientation changed after hot extrusion, in which the plane (220) had the highest intensity, indicating that the preferred orientation of the extruded 1100 aluminum alloy was along the plane (220).

The 1100 aluminum alloy is composed of industrial pure aluminum, and usually contains iron and silicon as impurities. Iron is almost insoluble in aluminum and exists in the form of the intermetallic compound  $\text{FeAl}_3$  [20]. When silicon coexists, it exists in the form of Fe-Al-Si intermetallic compounds, such as  $\alpha(\text{Fe, Si})$  and  $\beta(\text{Fe, Si})$  [21]. The SEM images of the homogenized (a,b) and extruded (c,d) 1100 aluminum alloy are shown in Figure 3. The microstructure of 1100 aluminum alloy after homogenization was uniform and dense, and the particles of the second phase (Al-Fe-Si) in the alloy were fine and presented a network distribution. After hot extrusion, the Al-Fe-Si phase particles in the extruded 1100 aluminum alloy were coarsened and dispersed in the aluminum matrix in a short rod-like form, with voids introduced and evenly distributed in the matrix. There is a large extrusion ratio during hot extrusion, which introduces a large number of dislocations in the aluminum matrix and some voids and defects around the second-phase particles. In the meantime, the heating from the extrusion mold (400  $^\circ\text{C}$ ) and the heat generated during

the extrusion causes the second phases to grow (coarsening). This coarse intermetallic particle feature has been reported in the literature [20], where the coarse typical composition of AA1100 alloy has been identified as containing (Al, Fe) and (Al, Fe, Si) particles. Through EDS spectrum analysis, as shown in Figure 3b,d, we found that the second phase of the 1100 aluminum alloy used in this study corresponded to  $Al_{12}Fe_3Si_2$ ,  $Al_6Fe$ , or  $Al_3Fe$ .

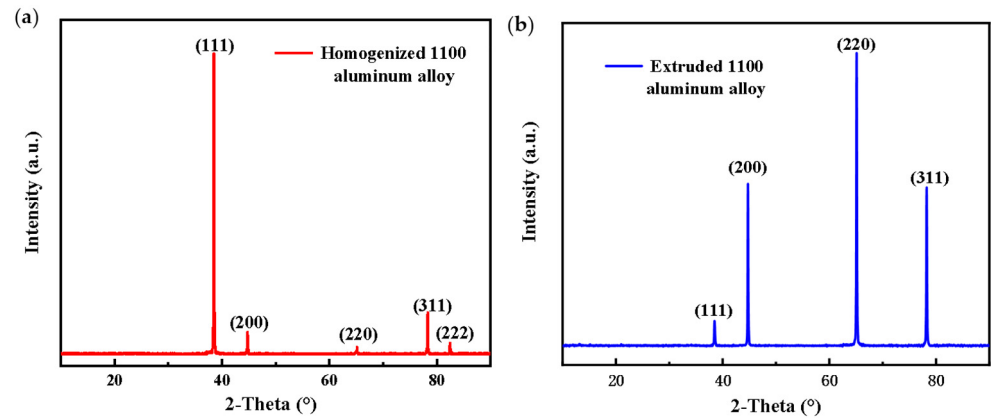


**Figure 2.** X-ray diffraction pattern of the homogenized (a) and extruded (b) 1100 aluminum alloy.

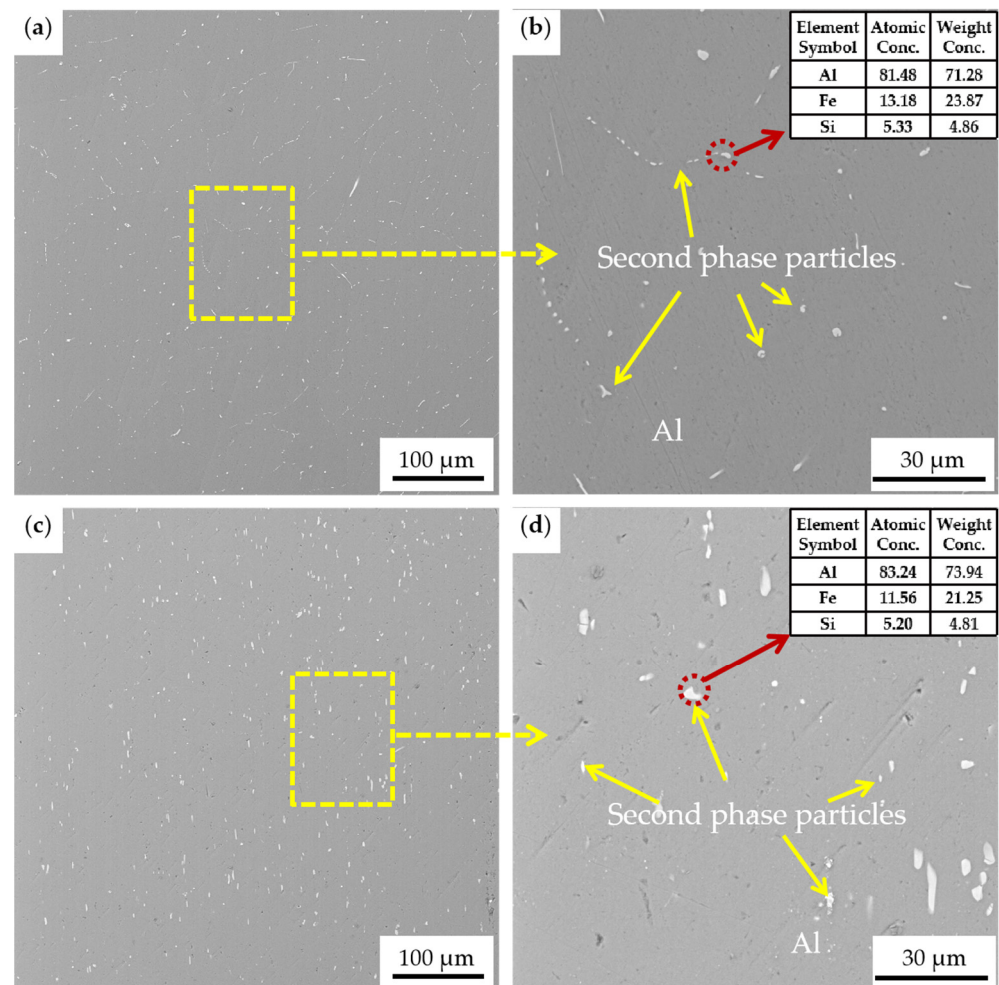


**Figure 3.** SEM images of the homogenized (a,b) and extruded (c,d) 1100 aluminum alloy; (b) and (d) are the enlarged areas of the yellow boxes in (a,c), respectively.

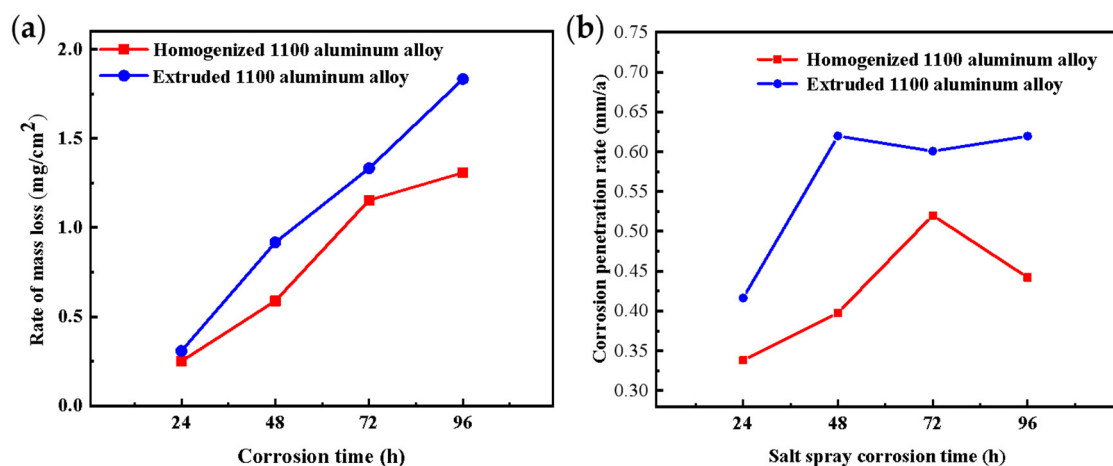


### 3.2. Rate of Mass Loss and Corrosion Penetration

After the corrosion test, weight loss analysis was carried out on the sample, and the results are shown in Figure 4a. The results of corrosion weight loss corresponded to the results of corrosion morphology, and the corrosion of the extruded 1100 aluminum alloy was more severe. After 96 h of corrosion, the weight loss rate of the extruded samples was 1.83 mg/cm<sup>2</sup>, and that of the homogenized samples was 1.31 mg/cm<sup>2</sup>. The corrosion penetration rate (CPR) of the samples was calculated according to the following equation [22]:

$$\text{CPR} = KW/\rho At \quad (1)$$

where  $W$  is the weight loss of the sample after exposure time  $t$ ;  $\rho$  and  $A$  represent the density and the area of the exposed specimen, respectively; and  $K$  is a constant whose magnitude depends on the unit area used. CPR represents the depth of material loss per unit of time, which can be conveniently expressed in millimeters per year (mm/a), where  $K = 87.6$ , and  $W$ ,  $\rho$ ,  $A$ , and  $t$  are expressed in milligrams (mg), grams per cubic centimeter (g/cm<sup>3</sup>), square centimeters (cm<sup>2</sup>), and hours (h), respectively.



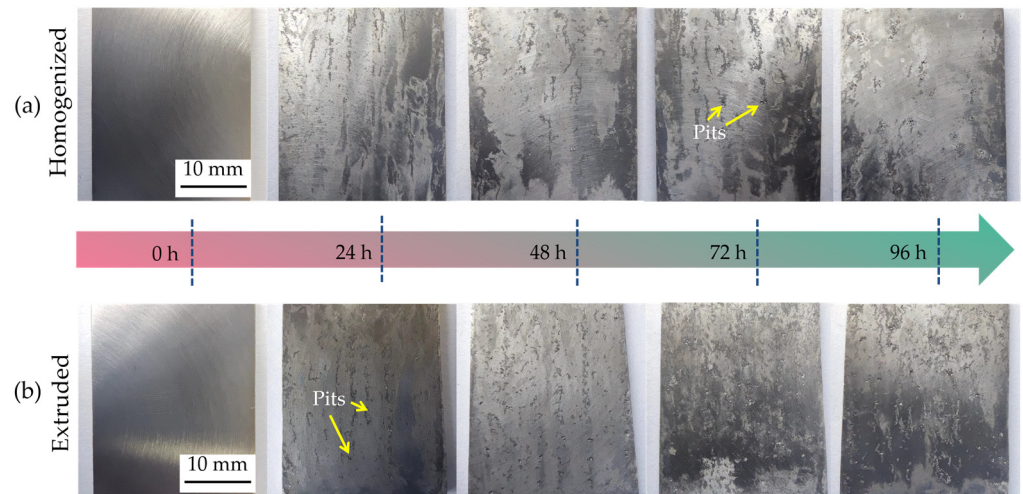
**Figure 4.** The rate of mass loss (a) and corrosion penetration (b) of the homogenized and extruded 1100 aluminum alloy for different acidic salt spray corrosion times.

Figure 4b shows the CPR of the homogenized and extruded 1100 aluminum alloy after different acidic salt spray corrosion times. The CPR of the extruded 1100 aluminum alloy was greater than that of the homogenized aluminum alloy. After 96 h of corrosion, the CPR of the extruded samples was 0.619 mm/a, and that of the homogenized samples was 0.442 mm/a. The CPR of the homogeneous 1100 aluminum alloy reached the maximum after 72 h, while the CPR of the extruded 1100 aluminum alloy reached the maximum after 48 h, and then the CPR decreased. This is also the reason for the greater weight loss of the extruded 1100 aluminum alloy.

### 3.3. Surface Morphology and Corrosion Products

Figure 5 shows the macroscopic morphology of the homogenized and extruded 1100 aluminum alloy samples corroded by acid salt spray at different times. Aluminum alloys have a stable and tough oxide layer on the surface to protect them from corrosion, but when there are defects, such as cracks and scratches, in the oxide layer, these defects cannot be repaired due to dissolution, as pitting corrosion will happen. It can be seen from Figure 5 that the surface of the sample before salt spray corrosion was smooth, bright, and without corrosion pits. After corrosion, the surface color of the sample changed obviously, losing its smooth and shining appearance, due to the growth of corrosion pits and the deposition of corrosion products. With the increase in corrosion time, the number, depth, and diameter of pits gradually increased, and various corrosion pits began to connect with each other. After being placed in the salt spray tests for 24 h, there was no obvious pitting point on the surface

of the homogeneous 1100 aluminum alloy, but there were obvious small corrosion pits on the surface of the extruded 1100 aluminum alloy. In addition, under the same corrosion time, there were more pits on the surfaces of the extruded 1100 aluminum alloy samples, which were deeper and larger. This indicates that the extruded structure is more prone to corrosion, and the corrosion rate is faster than the homogeneous 1100 aluminum alloy.



**Figure 5.** Macroscopic morphology of the homogenized (a) and extruded (b) 1100 aluminum alloys for different acidic salt spray corrosion times.

In order to further analyze the corrosion situation and corrosion products of the specimen, SEM was used to observe the corrosion surface of the homogenized and extruded 1100 aluminum alloy, as shown in Figure 6. It can be seen that, with the increase in the corrosion time, the number of corrosion pits formed on the surface and the size and depth of the corrosion pits increased. At the same corrosion time, the corrosion pits of the extruded 1100 aluminum alloy were larger and deeper than that of the homogeneous 1100 aluminum alloy. In the homogeneous 1100 aluminum alloy, no obvious deep corrosion pit was formed within 48 h of corrosion, but the corrosion pits showed significant growth at 72 h. Moreover, pitting preferentially occurred around the second-phase particles; it spread along the direction of the distribution of the second phase, indicating that the corrosion rate of the homogeneous 1100 aluminum alloy was first slow and then accelerated.

The corrosion layers of the homogenized and extruded 1100 aluminum alloys and the products in the corrosion pits were analyzed by energy spectrum analysis (EDS), and the results are shown in Table 2. According to the results of the energy spectrum analysis, it can be seen that in the initial stage of corrosion, the surface corrosion layers of 1100 aluminum alloys mainly consisted of  $\text{Al}_2\text{O}_3$  and  $\text{Al}(\text{OH})_3$ . The corrosion product in the corrosion pits after 96 h was a mixture of  $\text{Al}_2\text{O}_3$ ,  $\text{Al}(\text{OH})_3$ , and  $\text{AlCl}_3$ , as well as a possible intermediate substance,  $\text{Al}(\text{OH})\text{Cl}_2$  [9,16]. There is naturally a stable and tough aluminum oxide film on the surfaces of aluminum alloys to protect the alloy from corrosion, but this oxide film is only stable at pH values between 4 and 8 [8,23], below and above this range, the oxide film can be locally dissolved. The AASS corrosion solution contains a large number of  $\text{Cl}^-$ , which can be absorbed on the oxide film, and when the  $\text{Cl}^-$  reach a certain concentration, it gathers together and destroys the oxide film in the acidic environment, allowing the salt spray solution to contact and corrode the aluminum alloy matrix. This is a typical pitting corrosion that creates pits on the surface of an aluminum alloy. Dissolved  $\text{Al}^{3+}$  does not diffuse easily. As  $\text{Al}^{3+}$  increases in the pits,  $\text{Cl}^-$  enters the mine to maintain electrical neutrality. At this point, the corrosion pits form an  $\text{AlCl}_3$  solution, thus maintaining the activity of the aluminum alloy surface. In addition, the acidity of the solution increases due to the hydrolysis of  $\text{Cl}^-$  and  $\text{Al}^{3+}$  ions. The increase in acidity in the pit accelerates the dissolution rate of the anode.



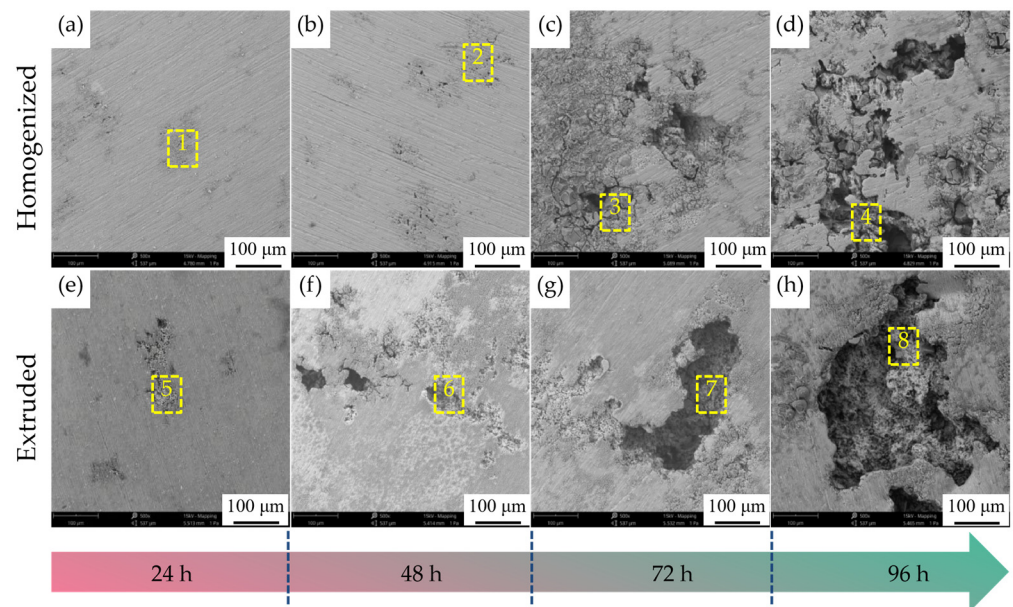


**Figure 6.** SEM images of the homogenized (a–d) and extruded (e–h) 1100 aluminum alloys for different acidic salt spray corrosion times (24 h, 48 h, 72 h, 96 h). The yellow area marked 1–8 in (a–h) indicates the EDS test area.

**Table 2.** EDS results for corrosion products in selected areas in Figure 6.

Specimen	Points	Al		O		Cl	
		wt. %	at. %	wt. %	at. %	wt. %	at. %
Homogenized 1100 aluminum alloy	1	57.59	44.61	42.41	55.39	-	-
	2	37.46	27.25	56.62	69.47	5.92	3.28
	3	27.51	21.17	51.03	66.25	21.47	12.58
	4	44.47	36.07	39.53	54.06	16.00	9.87
Hot-extruded 1100 aluminum alloy	5	74.14	62.96	25.86	37.04	-	-
	6	37.34	26.92	58.01	70.53	4.66	2.55
	7	37.23	31.44	36.12	51.43	22.66	17.13
	8	27.24	21.14	49.96	65.39	22.79	13.46

In order to determine the composition of the corrosion products, surface analysis was performed with XPS. Figure 7 shows the XPS analysis of Al 2p, O 1s, and Cl 2p for corrosion products on the surfaces of the homogenized and extruded 1100 aluminum alloys after 96 h of acidic salt spray corrosion. Figure 7a,b exhibit the XPS spectra of Al 2p on the surfaces of the homogenized and extruded 1100 aluminum alloys, respectively, both having peaks at about 75 eV (relative to C 1s = 284.6 eV), corresponding to the oxidized Al ( $Al^{3+}$ ). Figure 7c,d show the XPS spectra of O 1s for corrosion products, and the peaks at binding energies of 531.8, 532.2, and 533.3 eV correspond to  $O^{2-}$ ,  $OH^-$ , and  $H_2O$ , respectively [24]. Combined with the Al 2p spectra, it is evident that the corrosion product layer consisted mainly of  $Al(OH)_3$  and  $Al_2O_3$ . However, the difference is that the corrosion products of the homogenized 1100 aluminum alloy were mainly  $Al(OH)_3$ , while the corrosion products of the extruded 1100 aluminum alloy were mainly  $Al_2O_3$ . Figure 7e,f show the Cl 2p spectra, indicating that the corrosion products of the homogenized and extruded 1100 aluminum alloys both contained a small amount of  $Cl^-$ . The results of XPS are consistent with those of the EDS analysis above, and are similar to the generally accepted aluminum corrosion products of aluminum.

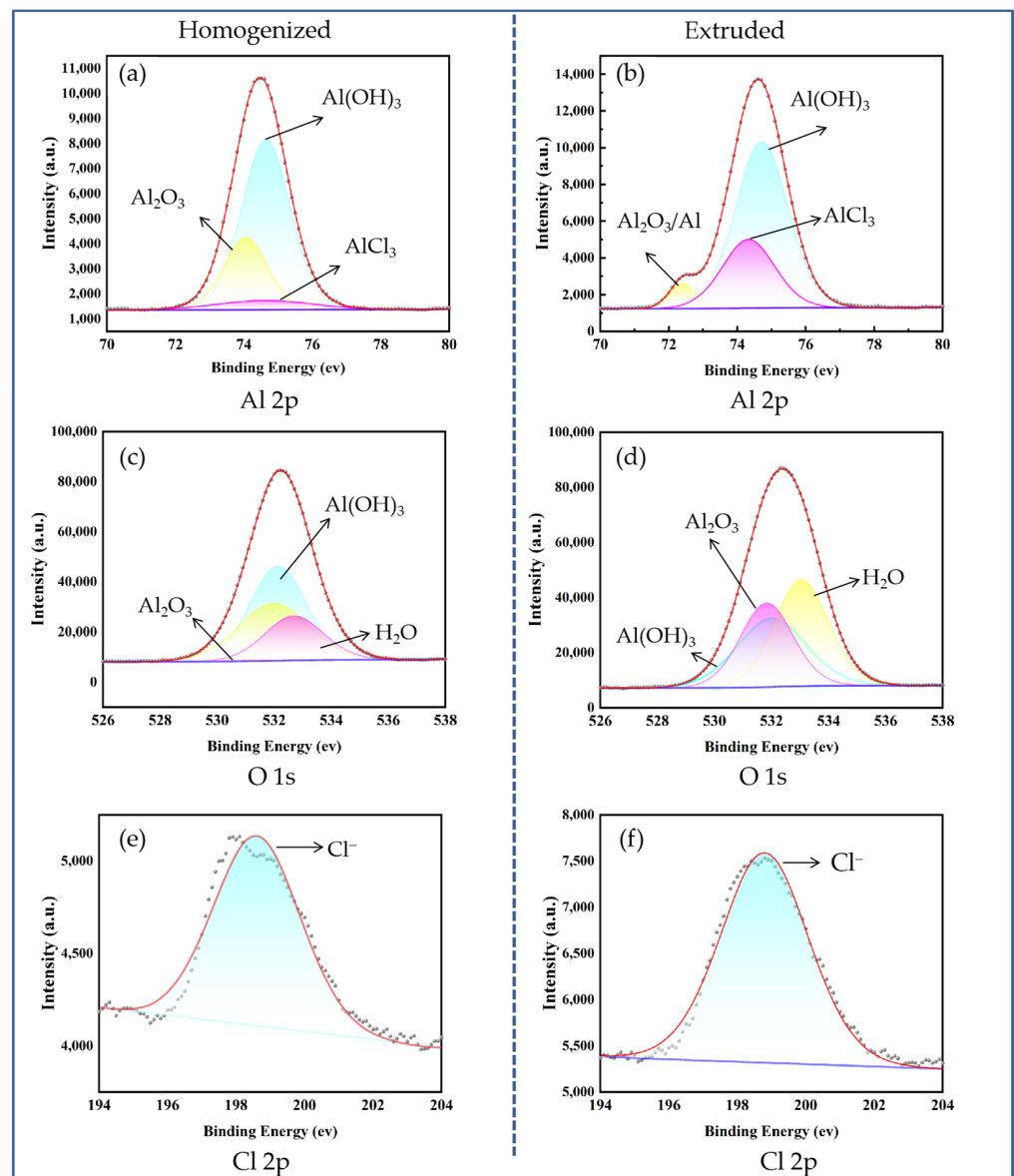


**Figure 7.** XPS spectra of Al 2p, O 1s, and Cl 2p for corrosion products formed on the homogenized (a,c,e) and extruded (b,d,f) 1100 aluminum alloys after 96 h of acidic salt spray corrosion.

Confocal microscopy was used to measure the depth and area of the corrosion pit of the homogenized and extruded 1100 aluminum alloy. VK-X3000 multi-file analysis software (<https://www.keyence.com/products/microscope/laser-microscope/vk-x3000/>) was used for data analysis. Figure 8 shows the localized corrosion morphology of the homogenized and extruded 1100 aluminum alloy after 96 h of acidic salt spray corrosion. Figure 8a,b show the optical images and corresponding surface profiles of the homogenized 1100 aluminum alloy; Figure 8c,d are the optical images and corresponding surface profiles of the extruded 1100 aluminum alloy. It can be seen that the corrosion pits of the extruded 1100 aluminum alloy were larger and deeper than those of the homogeneous 1100 aluminum alloy. Figure 9 shows the maximum pitting depth of the homogenized and extruded 1100 aluminum alloy with different salt spray corrosion times. The maximum pitting depth of the homogenized 1100 aluminum alloy was only 5.51  $\mu\text{m}$  after 24 h of acid salt spray corrosion and 10.3  $\mu\text{m}$  after 48 h of corrosion, and the pitting depth increased slowly. Then, the pitting depth increased rapidly, reaching 62.7  $\mu\text{m}$  after 72 h of corrosion, and subsequently slowed down to reach 73.5  $\mu\text{m}$  after 96 h of corrosion. The maximum pitting depth of the extruded 1100 aluminum alloy was initially 27.8  $\mu\text{m}$  after 24 h of corro-

sion, then gradually increased with the increase in corrosion time. After 96 h of corrosion, the maximum pitting depth reached 154  $\mu\text{m}$ . The results show that the corrosion rate of the extruded 1100 aluminum alloy in acid salt spray was higher than that of the homogeneous 1100 aluminum alloy, which is consistent with the corrosion surface morphology.

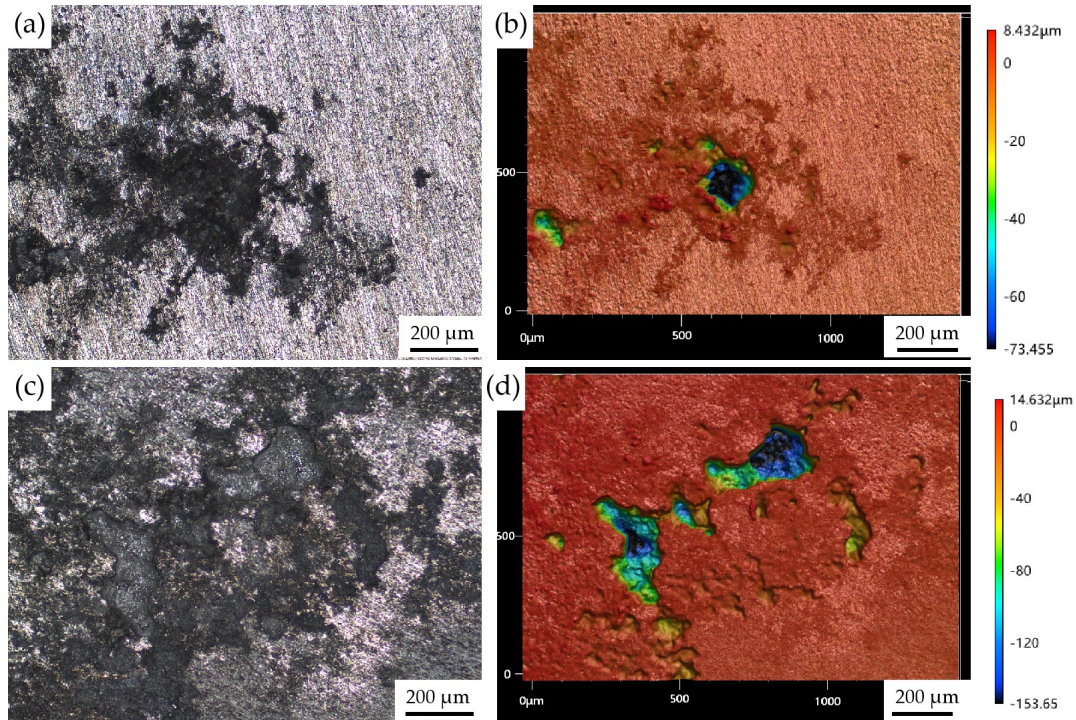


**Figure 8.** Typical surface morphology of the homogenized (a,b) and extruded (c,d) 1100 aluminum alloy after 96 h of acidic salt spray corrosion using laser scanning confocal microscopy.

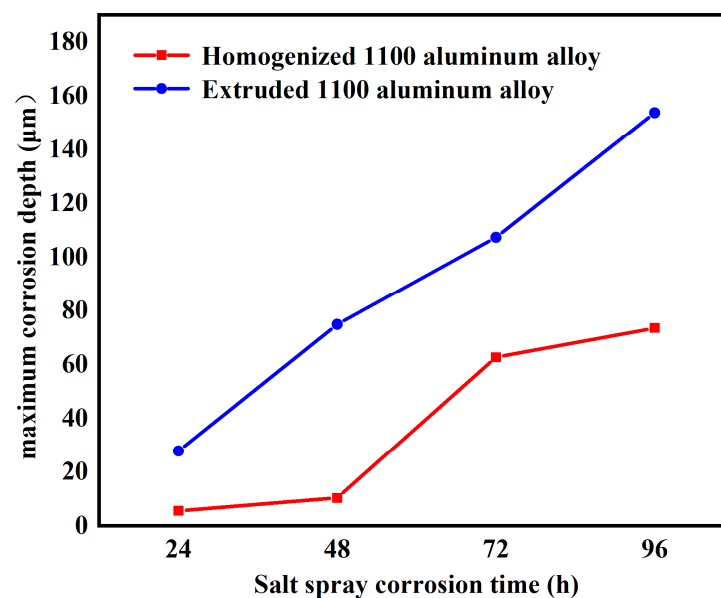


**Figure 9.** The maximum pitting depth of the homogenized and extruded 1100 aluminum alloy with different salt spray corrosion times.

The microstructure analysis shows that the particles of the second phase were coarse in the microstructure of the extruded 1100 aluminum alloy, which affected the perfection of the surface oxide film, and the corrosion began preferably around the particles of the

second phase. The extruded 1100 aluminum alloy was more prone to corrosion, which is the reason why the corrosion rate of the extruded 1100 aluminum alloy was fast.

### 3.4. Electrochemical Analysis

Figure 10 shows the potentiodynamic polarization curves of the homogenized and extruded 1100 aluminum alloy measured in acid salt spray corrosion solution. By fitting the polarization curves, the corrosion potential ( $E_{\text{corr}}$ ) and corrosion current density ( $I_{\text{corr}}$ ) of the 1100 aluminum alloy were calculated, as shown in Table 3. The corrosion potential of the homogenized 1100 aluminum alloy was  $-0.505$  V, and the corrosion current density was  $19.3 \mu\text{A}/\text{cm}^2$ . The corrosion potential of the extruded 1100 aluminum alloy was  $-0.496$  V, and the corrosion current density was  $18.0 \mu\text{A}/\text{cm}^2$ . The corrosion potential of the homogenized 1100 aluminum alloy was slightly lower than that of the extruded aluminum alloy, indicating that the homogenized 1100 aluminum alloy had a higher corrosion tendency. The potentiodynamic polarization curve of the extruded 1100 aluminum alloy had no passivation phenomenon, showing good activation dissolution characteristics.

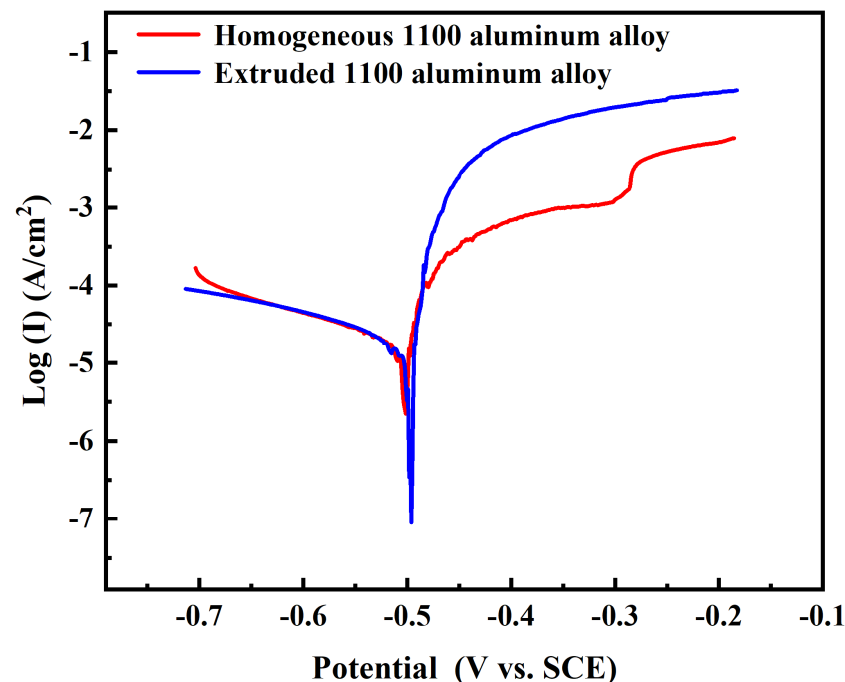


**Figure 10.** Potentiodynamic polarization curves of homogenized and extruded 1100 aluminum alloy.

**Table 3.** The polarization curve fitting parameter values of homogenized and extruded 1100 aluminum alloy.

Specimen	$E_{\text{corr}}$ ( $V_{\text{SCE}}$ )	$I_{\text{corr}}$ ( $\mu\text{A}/\text{cm}^2$ )
Homogenized 1100 aluminum alloy	$-0.505$	19.275
Extruded 1100 aluminum alloy	$-0.496$	17.766

In the acidic salt spray corrosion solution, the current density of the homogenized 1100 aluminum alloy increased sharply when the potential increased above  $-505$  mV, and the sample was in the active dissolution stage. In the range of  $-356$ ~ $-307$  mV, the current density basically did not change. At this stage, pitting corrosion slowed down due to the forming of a corrosion product layer on the surface of the aluminum, which slowed the ion diffusion speed. Then, in the range of  $-307$ ~ $-278$  mV, the current density increased sharply again with the increase in potential, indicating the dissolving of the corrosion product layer. After  $-278$  mV, the characteristic of this interval was that the current density increased



slightly with the increase in potential, indicating that the further corrosion products formed on the surface had a protective effect and that the corrosion reaction was weakened.

The corrosion rate can be judged according to the corrosion current density, and the higher the corrosion current density, the higher the corrosion rate [14,25,26]. Under the same corrosion potential, the corrosion current density of the extruded 1100 aluminum alloy was higher than that of the homogenized 1100 aluminum alloy, indicating that the corrosion rate of the extruded 1100 aluminum alloy was fast in the middle and late stages of corrosion, which was also the reason for the significant loss of the extruded 1100 aluminum alloy. This is consistent with the results of the acid salt spray test and the weight loss analysis.

Electrochemical impedance spectroscopy (EIS) is an electrochemical measurement method using a small amplitude sinusoidal potential (or current) as a disturbance signal. Figure 11 shows the EIS of the homogenized and extruded 1100 aluminum alloy. It was found that the Nyquist diagram shapes of the two different alloy states were completely different, indicating that the different microstructures led to different corrosion mechanisms. Figure 12 shows the effective fitting circuit diagram of the electrochemical impedance spectrum.  $R_s$  is the resistance of the bulk solution,  $R_f$  and  $Q_f$  are the resistance and constant phase element (CPE) of the oxide film or corrosion product,  $R_{ct}$  and  $Q_{dl}$  are the charge transfer resistance and constant phase element of the double electric layer, and  $W$  is the Warburg impedance.  $L$  represents the inductance. The Nyquist diagram of the homogenized 1100 aluminum alloy consists of a capacitance semicircle in the high-frequency region and a diffusion tail in the low-frequency region, while the EIS of the extruded 1100 aluminum alloy in the acid salt spray corrosion solution shows a nearly completely circular inductance spectrum. The high-frequency capacitance semicircle represents the charge transfer reaction of the 1100 aluminum alloys with the oxide film, while the low-frequency diffusion impedance is related to the diffusion of oxygen [27]. The diameter of the semicircle in the high-frequency region of the EIS of the homogenized 1100 aluminum alloy is larger than that of the extruded 1100 aluminum alloy, which indicates that the corrosion rate of the homogenized 1100 aluminum alloy was lower than that of the extruded 1100 aluminum alloy under the acid salt spray condition. The EIS of the extruded 1100 aluminum alloy shows a circular inductance impedance, which is due to the absence of a product layer in the corrosion process and the adsorption of intermediate compounds [9,17]. This result is consistent with the morphology of the corrosion products mentioned above.

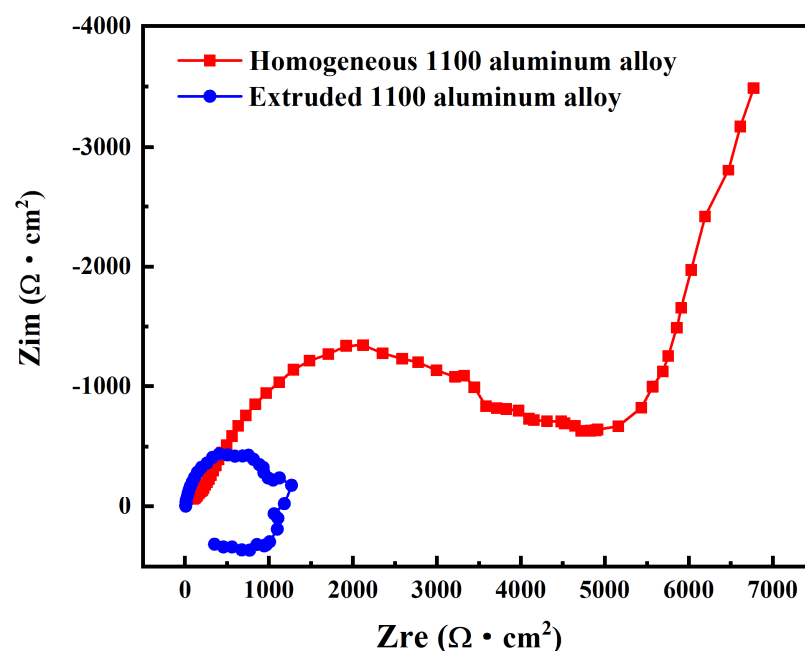
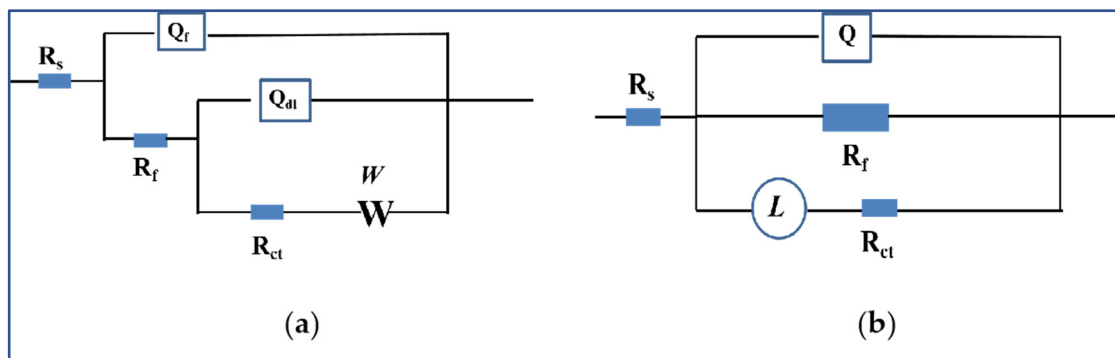
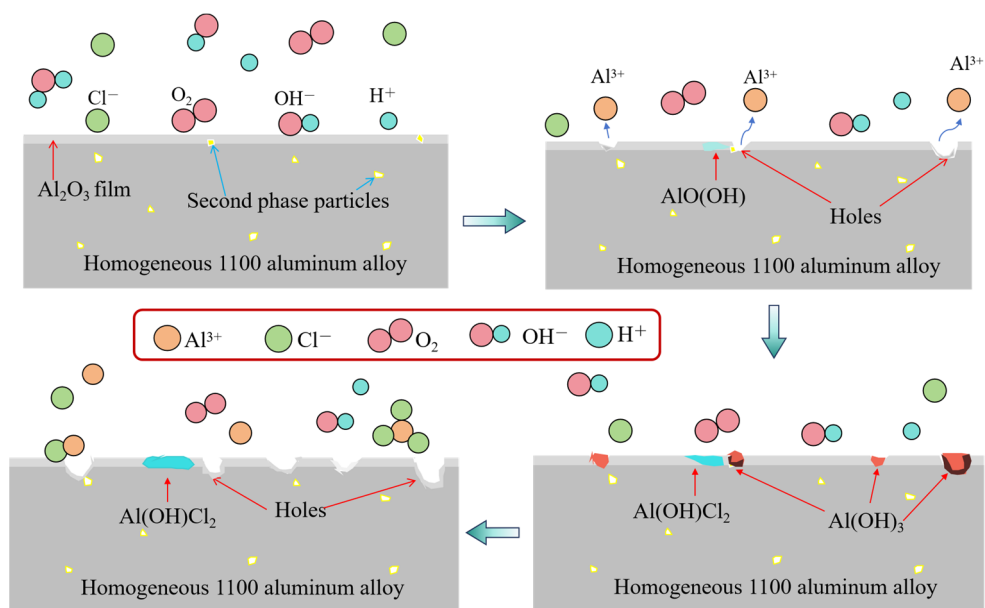


Figure 11. Nyquist diagram of homogenized and extruded 1100 aluminum alloy.



**Figure 12.** Effective fitting circuit diagram of electrochemical impedance spectra of homogenized (a) and extruded (b) 1100 aluminum alloys.

In summary, the corrosion mechanisms of 1100 aluminum alloys in different states are different, and the corrosion mechanisms of homogenized 1100 aluminum alloys in acid salt spray samples are shown in Figure 13. In the acid salt spray test, Al and the trace Al<sub>2</sub>O<sub>3</sub> protective film on the alloy surface were easily dissolved due to the presence of H<sup>+</sup> and Cl<sup>-</sup>. An anodic reaction occurred to form Al<sup>3+</sup>.



**Figure 13.** Corrosion reaction mechanism of homogenized 1100 aluminum alloy.

According to the electrochemical test results, the corrosion potential of the homogenized 1100 aluminum alloy was lower than that of the extruded 1100 aluminum alloy, indicating that the corrosion dissolution trend of the homogenized 1100 aluminum alloy was higher, and the concentration of Al<sup>3+</sup> on the surface of the sample increased with the increase in corrosion time. A corrosion product film formed due to the meeting of Al<sup>3+</sup> ions from the anode reaction with the OH<sup>-</sup> generated from the cathode reaction to cover the sample surface close to the Al<sub>2</sub>O<sub>3</sub> particles, and to prevent the dissolution of Al.

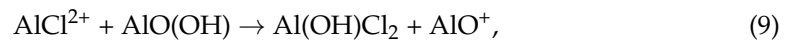
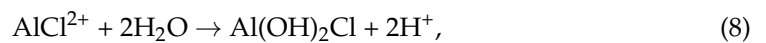




Subsequently, part of  $\text{Al}(\text{OH})_3$  reacted with  $\text{H}_2\text{O}$  and was converted to  $\text{Al}_2\text{O}_3 \cdot n\text{H}_2\text{O}$  ( $\text{AlO}(\text{OH})$ ). With the increase in corrosion time, more and more corrosion products were formed.  $\text{Cl}^-$  did not easily penetrate into the fresh Al substrates, which led to surface enrichment. Then,  $\text{Al}(\text{OH})_3$  reacted with  $\text{Cl}^-$  to form  $\text{Al}^{3+}$ , forming a corrosion pit.



After the forming of corrosion pits, the corrosion product of  $\text{Al}(\text{OH})_3$  started to form at the periphery of the pits. Meanwhile, the side effects were as follows:



The corrosion mechanism of the extruded 1100 aluminum alloy is shown in Figure 14. The corrosion reaction and corrosion products of the extruded 1100 aluminum alloy in salt spray were similar to those of the homogenized aluminum alloy, but the difference is that the corrosion rate of the extruded 1100 aluminum alloy was faster than that of the homogenized aluminum alloy. The corrosion product layer on the extruded 1100 aluminum alloy surface did not play a protective role, and large corrosion pits were directly formed. This is because the microstructure of the aluminum alloy after extrusion was not uniform, with defects around the second phases. The microstructure defects made it easy for  $\text{Cl}^-$  to erode the aluminum matrix. In addition, due to the potential difference between the second phase and the matrix, a large gap around the second phase particles was easily formed through an electrochemical reaction, increasing the corrosion rate and the depth of the corrosion pit. As a result, the corrosion products fell off or dissolved quickly.

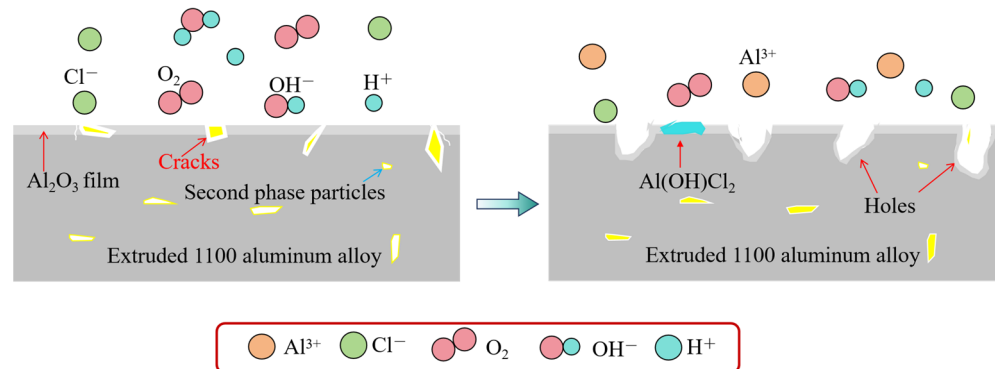


**Figure 14.** Corrosion reaction mechanism of extruded 1100 aluminum alloy.

#### 4. Conclusions

- (1) There were second-phase particles containing Al-Fe-Si in the microstructure of the 1100 aluminum alloy, which were network-distributed fine particles in the homogenized microstructure. No dynamic recrystallization occurred during hot extrusion. The microstructure was fibrous, and the second phase was coarse and rod-like.
- (2) The surface corrosion morphology of the extruded 1100 aluminum alloy in salt spray was more severe than that of the homogenized 1100 aluminum alloy. The corrosion loss and penetration rate of the homogeneous 1100 aluminum alloy were relatively slow within 48 h, and then rapid corrosion occurred, whereas the initial corrosion rate

of the extruded 1100 aluminum alloy was very fast. The results show that the change in microstructure and second-phase particles during hot extrusion accelerated the corrosion rate and deteriorated the corrosion resistance.

- (3) With the increase in corrosion time, a layer of corrosion products was formed on the surface of the homogenized 1100 aluminum alloy, which covered the surface of the alloy and slowed the corrosion process. The pitting corrosion of the homogeneous and extruded 1100 aluminum alloys occurred in the initial corrosion stage, but the corrosion rate of the extruded alloy was faster, and deeper corrosion pits were formed.
- (4) The corrosion mechanisms of different forms of 1100 aluminum alloys in acid salt spray conditions were different. The corrosion products formed in the initial corrosion stage of the homogeneous 1100 aluminum alloy protected the Al matrix and inhibited the corrosion reaction. With the increase in the corrosion time, the corrosion products dissolved and fell off, an obvious pitting phenomenon occurred, and then the corrosion rate became faster. However, in the initial corrosion stage of the extruded 1100 aluminum alloy, pitting occurred, and the number and depth of corrosion pitting pits increased with the increase in the corrosion time.
- (5) In this study, the corrosion behavior of the 1100 aluminum alloy in homogenized and hot-extruded states was compared through an acid salt spray test. The results are expected to help to evaluate the corrosion resistance of the 1100 aluminum alloy in acidic environments, such as in marine engineering, the chemical industry, acid rain, etc.

**Author Contributions:** Conceptualization, Y.Z., Q.L., Q.W. and D.L.; methodology, Q.L., Y.L. and F.L.; validation, F.L. and D.L.; formal analysis, Y.L. and F.L.; investigation, Q.L. and Y.Z.; resources, Q.W.; data curation, Y.Z. and D.L.; writing—original draft preparation, Y.Z.; writing—review and editing, all authors; visualization, Y.Z., F.L. and Y.L.; supervision, D.L. and Q.W.; project administration, Q.W.; funding acquisition, Q.W. All authors have read and agreed to the published version of the manuscript.

**Funding:** This research was funded by National Key Research and Development Program of China, grant number 2021YFB3701303, National Natural Science Foundation of China, grant numbers U1902220 and 51674166, and SJTU-Warwick Joint Seed Fund, grant number SJTU2210.

**Institutional Review Board Statement:** Not applicable.

**Informed Consent Statement:** Not applicable.

**Data Availability Statement:** Data is contained within the article.

**Conflicts of Interest:** Authors F.L. and Y.L. were employed by the company GD Midea Heating & Ventilating Equipment Co., Ltd. The remaining authors declare that the research was conducted in the absence of any commercial or financial relationships that could be construed as potential conflicts of interest.

## References

1. Fouad, D.M.; El-Garaihy, W.H.; Ahmed, M.M.Z.; El-Sayed Seleman, M.M.; Salem, H.G. Influence of multi-channel spiral twist extrusion (MCSTE) processing on structural evolution, crystallographic texture and mechanical properties of AA1100. *Mater. Sci. Eng. A* **2018**, *737*, 166–175. [CrossRef]
2. Li, D.; Slater, C.; Cai, H.; Hou, X.; Li, Y.; Wang, Q. Joining Technologies for Aluminium Castings—A Review. *Coatings* **2023**, *13*, 958. [CrossRef]
3. Ramaswamy, V.; Pareeka, R.; Girib, A.; Anugulab, G.; Srivastavab, V.; Adhikarib, S. Corrosion Performance Evaluation of Aluminum Alloys for Automotive Applications. In Proceedings of the Conference: 16th National Congress on Corrosion Control, Salt Lake City, UT, USA, 11–15 March 2012.
4. De la Fuente, D. Corrosion of Aluminum, Aluminum Alloys, and Composites. In *Encyclopedia of Materials: Metals and Alloys*; Caballero, F.G., Ed.; Elsevier: Oxford, UK, 2022; pp. 160–169.
5. Orłowska, M.; Ura-Bińczyk, E.; Olejnik, L.; Lewandowska, M. The effect of grain size and grain boundary misorientation on the corrosion resistance of commercially pure aluminium. *Corros. Sci.* **2019**, *148*, 57–70. [CrossRef]
6. Son, I.; Nakano, H.; Oue, S.; Kobayashi, S.; Fukushima, H.; Horita, Z. Effect of Equal-Channel Angular Pressing on Pitting Corrosion of Pure Aluminum. *Int. J. Corros.* **2012**, *2012*, 450854. [CrossRef]



7. Mopon, M.L.; Garcia, J.S.; Manguerra, D.M.; Narisma, C.J.C. Corrosion Behavior of AA 1100 Anodized in Gallic-Sulfuric Acid Solution. *Coatings* **2021**, *11*, 405. [CrossRef]
8. Adams, F.V.; Akinwamide, S.O.; Obadele, B.; Olubambi, P.A. Comparison study on the corrosion behavior of aluminum alloys in different acidic media. *Mater. Today Proc.* **2021**, *38*, 1040–1043. [CrossRef]
9. Zakaria, S.A.; Anasyida, A.S.; Zuhailawati, H.; Dhindaw, B.K.; Jabit, N.A.; Ismail, A. Characterization of mechanical and corrosion properties of cryorolled Al 1100 alloy: Effect of annealing and solution treatment. *Trans. Nonferrous Met. Soc. China* **2021**, *31*, 2949–2961. [CrossRef]
10. Ezuber, H.; El-Houd, A.; El-Shawesh, F. A study on the corrosion behavior of aluminum alloys in seawater. *Mater. Des.* **2008**, *29*, 801–805. [CrossRef]
11. Shinde, V.; Argade, G.; Chilukuri, A.; Gehrich, M.; Parikh, C. *TMS 2022 151st Annual Meeting & Exhibition Supplemental Proceedings*; Springer International Publishing AG: Cham, Switzerland, 2022; pp. 640–648.
12. *ISO 9227:2022*; Corrosion Tests in Artificial Atmospheres-Salt Spray Tests. International Organization for Standardization: Geneva, Switzerland, 2022.
13. *ASTM G85-11*; Standard Practice For Modified Salt Spray (Fog) Testing. ASTM International: West Conshohocken, PA, USA, 2011.
14. Qiao, J.-Z.; Fu, X.-S.; Gai, P.-T.; Chen, G.-Q.; Zhou, W.-L. Corrosion Behavior and Microstructure of 2024 Aluminum Alloy Sheets by Shot Peen Forming in a Salt Spray Environment. *J. Mater. Eng. Perform.* **2022**, *32*, 4124–4137. [CrossRef]
15. Surendarnath, S.; Ramesh, G.; Ramachandran, T.; Ravisankar, B. Corrosion Behavior of Commercially Pure Aluminum Processed through Conventional and New ECAP Dies. *J. Mater. Eng. Perform.* **2023**, 1–14. [CrossRef]
16. Zhao, J.; Zhang, H.; Yang, X.; Gu, Y.; Liu, Y. Local Electrochemical Corrosion of 6061 Aluminum Alloy with Nano-SiO<sub>2</sub>/MAO Composite Coating. *Materials* **2023**, *16*, 6721. [CrossRef]
17. Jokar, M.; Boerstler, J.T.; Frankel, G.S. Use of impressed current for accelerated corrosion testing of aluminium alloy panels. *Corros. Eng. Sci. Technol.* **2022**, *57*, 32–43. [CrossRef]
18. Alfattani, R.; Yunus, M.; Mohamed, A.F.; Alamro, T.; Hassan, M.K. Assessment of the corrosion behavior of friction-stir-welded dissimilar aluminum alloys. *Materials* **2021**, *15*, 260. [CrossRef]
19. Prabhuraj, P.; Rajakumar, S.; Balasubramanian, V.; Sonar, T.; Ivanov, M.; Elil Raja, D. Effect of pH value, chloride ion concentration and salt spraying time on salt fog corrosion resistance of friction stir welded AA7075-T651 alloy joints. *Int. J. Interact. Des. Manuf.* **2023**, 1–13. [CrossRef]
20. Yasakau, K.A.; Zheludkevich, M.L.; Ferreira, M.G.S. 15-Role of intermetallics in corrosion of aluminum alloys. Smart corrosion protection. In *Intermetallic Matrix Composites*; Mitra, R., Ed.; Woodhead Publishing: Sawston, UK, 2018; pp. 425–462.
21. Wu, Y.; Shen, Y.; Wang, Q.; Liu, Y.; Shi, D.; Liu, Y.; Su, X. Effect of Si Content on Microstructures and Electrochemical Properties of Al-xSi-3.5Fe Coating Alloy. *Materials* **2023**, *16*, 7407. [CrossRef] [PubMed]
22. Oshionwu Lucky, C.; Idenyi, N.E.; Ugwu Emmanuel, I. Quadra-Statistical Modeling Of Corrosion Penetration Rate (CPR) Of Martensitic and Annealed Stainless Steel in H<sub>2</sub>SO<sub>4</sub> and HCl. *Math. Theory Model.* **2015**, *5*, 161–170.
23. Abdulstaar, M.; Mhaede, M.; Wagner, L.; Wollmann, M. Corrosion behaviour of Al 1050 severely deformed by rotary swaging. *Mater. Des.* **2014**, *57*, 325–329. [CrossRef]
24. Can, P.E.N.G.; Liu, Y.W.; Guo, M.X.; Gu, T.Z.; Chuan, W.A.N.G.; Wang, Z.Y.; Cheng, S.U.N. Corrosion and pitting behavior of pure aluminum 1060 exposed to Nansha Islands tropical marine atmosphere. *Trans. Nonferrous Met. Soc. China* **2022**, *32*, 448–460.
25. Miramontes, J.C.; Gaona Tiburcio, C.; García Mata, E.; Esneider Alcála, M.Á.; Maldonado-Bandala, E.; Lara-Banda, M.; Nieves-Mendoza, D.; Olguín-Coca, J.; Zambrano-Robledo, P.; López-León, L.D.; et al. Corrosion Resistance of Aluminum Alloy AA2024 with Hard Anodizing in Sulfuric Acid-Free Solution. *Materials* **2022**, *15*, 6401. [CrossRef] [PubMed]
26. Wang, G.; Tuo, X.; Kou, L.; Zhao, W.; Zhu, X. Research on corrosion performance of 6061 aluminum alloy in salt spray environment. *Mater. Werkst.* **2020**, *51*, 1686–1699. [CrossRef]
27. Fan, L.; Wang, F.; Wang, Z.; Hao, X.; Yang, N.; Ran, D. Study on the Influence of Surface Treatment Process on the Corrosion Resistance of Aluminum Alloy Profile Coating. *Materials* **2023**, *16*, 6027. [CrossRef] [PubMed]

**Disclaimer/Publisher’s Note:** The statements, opinions and data contained in all publications are solely those of the individual author(s) and contributor(s) and not of MDPI and/or the editor(s). MDPI and/or the editor(s) disclaim responsibility for any injury to people or property resulting from any ideas, methods, instructions or products referred to in the content.

## Article

# Impact of Electromagnetic Stirring Roller Arrangement Pattern on Magnetic Field Simulation and Solidification Structure of PW800 Steel in the Second Cooling Zone

Zhixiang Xiao <sup>1</sup>, Guifang Zhang <sup>1,\*</sup>, Daiwei Liu <sup>1</sup> and Chenhui Wu <sup>2</sup>

<sup>1</sup> Faculty of Metallurgical and Energy Engineering, Kunming University of Science and Technology, Kunming 650093, China; xiaozhixiang1998@163.com (Z.X.); liudaiwei@pzhhu.edu.cn (D.L.)

<sup>2</sup> Panzhihua Iron and Steel Co., Ltd., Panzhihua 617000, China; wch\_neu@126.com

\* Correspondence: guifangzhang65@163.com

**Abstract:** Strand electromagnetic stirring (S-EMS), a technique applied in the secondary cooling zone, enhances the solidification structure of casting slabs. This study examines how the arrangement pattern of electromagnetic stirring rollers—face-to-face, side-to-side or up-down misalignment produces this enhancement. It uses simulations to analyze the electromagnetic field distribution in these configurations. The findings demonstrate that: (1) The magnetic flux density distribution in the casting slab is related to the arrangement pattern of the electromagnetic stirring rollers. (2) The face-to-face arrangement produces the largest and most concentrated electromagnetic force compared to the other two arrangement patterns. (3) S-EMS can effectively improve the equiaxed grain ratio of casting slabs. Before and after EMS is turned on, casting slabs' average equiaxed grain ratio goes up from 8% to 33%.

**Keywords:** continuously cast slab; strand electromagnetic stirring; secondary cooling zone; magnetic field; numerical simulation



**Citation:** Xiao, Z.; Zhang, G.; Liu, D.; Wu, C. Impact of Electromagnetic Stirring Roller Arrangement Pattern on Magnetic Field Simulation and Solidification Structure of PW800 Steel in the Second Cooling Zone. *Materials* **2024**, *17*, 1038. <https://doi.org/10.3390/ma17051038>

Academic Editors: Seong-Ho Ha, Shae-Kwang Kim and Hyun-Kyu Lim

Received: 24 December 2023

Revised: 14 February 2024

Accepted: 22 February 2024

Published: 23 February 2024



**Copyright:** © 2024 by the authors. Licensee MDPI, Basel, Switzerland. This article is an open access article distributed under the terms and conditions of the Creative Commons Attribution (CC BY) license (<https://creativecommons.org/licenses/by/4.0/>).

## 1. Introduction

As consumers' demands for high-quality casting slabs grow, it is essential to improve their quality accordingly. Prior research has demonstrated that the implementation of electromagnetic stirring in continuous casting manufacturing may significantly enhance the quality of casting slabs. This includes augmenting the ratio of equiaxed grain, removing central shrinkage cavities and minimizing the extent of casting slab segregation [1,2]. Due to the high temperature of molten steel, many parameters in the continuous casting process cannot be directly measured, so researchers introduced numerical simulation technology, which is widely used to simulate and predict the flow and temperature fields of the molten steel in the continuous casting process [3–8].

Correlation research has been developed in recent decades by some scholars to elucidate the effect of various factors of electromagnetic stirring on S-EMS. For example, Zhang et al. [9] conducted numerical simulations to analyze the electromagnetic field and molten steel flow field in a continuous casting machine under three stirring modes: double butterfly, double ring and three rings. Their findings indicate that near the electromagnetic stirring rolls, the magnetic induction intensity's distribution is similar across all three modes. However, the electromagnetic force in the double-ring mode is approximately double that of the double-butterfly and three-ring modes. In the longitudinal cross-section at the casting slab's center, the flow field is symmetrical for all stirring modes, with the double-ring mode generating a larger reflux zone. Li et al. [10] explored the advantages and disadvantages of double-ring and double-butterfly stirring modes under different electromagnetic stirring roller spacings by means of numerical simulation and concluded that the double-ring is better when the spacing of the two sets of electromagnetic stirring

roller is five times the roller diameter and the double-butterfly is better when the spacing is 0 [10]. Xiao et al. [11,12] observed a substantial end effect when the electromagnetic stirring roller was installed parallel to the casting slab section, leading to solidification organization asymmetry at both casting slab ends. Based on segmental simulation, they concluded that a 150-mm electromagnetic stirring roller bias achieves near symmetry in solidification. Additionally, they found that increasing the electromagnetic roll pair notably augmented the electromagnetic force in the casting direction and at the roll's center. Under specific parameters (400 A, 7 Hz), this enhancement increased the equiaxed grain ratio in the casting slab's center to 69%, facilitating a uniform, dense solidification structure produced, thereby improving hot working properties. Fang et al. [13] conducted a study on the impact of electromagnetic stirring in the second cooling zone of ultrawide casting slabs. The research focused on how different methods of energizing electromagnetic stirring rolls affect the flow of molten steel within the casting slab. Gong et al. [14] observed that varying electromagnetic stirring parameters in their study, notably current intensity, frequency and the stirring mode of electromagnetic stirring rollers, significantly influenced the intensity of stirring and the pattern of steel flow in the casting slab. These factors are intricately linked to the metallurgical efficacy of the stirrer, as they directly impact the temperature distribution within the casting slab and, consequentially, the final solidification structure.

These studies indicate that although lots of research has been done on the effect of the stirring mode, stirring current strength, frequency and electromagnetic stirring roll pairs on S-EMS, the effects of the electromagnetic stirring roller arrangement pattern on the S-EMS are rarely reported. Hence, this study utilizes simulation methods, incorporating the development of a three-dimensional transient magnetic field model to a 1300 mm × 230 mm casting slab to investigate the impact of electromagnetic stirring roller alignments, including face-to-face, side-to-side and up-down misalignment arrangements, on the magnetic field. The research findings offer a reference for optimizing the location of the electromagnetic stirring roller in the secondary cooling zone.

## 2. Model Descriptions

### 2.1. Assumptions

Typically, while performing numerical calculations for electromagnetic fields, certain assumptions are made to simplify the calculations while still guaranteeing that the desired results match the necessary criteria as follows [13,15]:

1. Given the ample space surrounding the electromagnetic stirring device, there is assurance that the magnetic field lines can form a closed loop and are not significantly affected by the external magnetic field. Therefore, it is assumed that the magnetic field in the proximity of the magnetic pole is uniformly distributed, with the magnetic field lines passing through the pole oriented at a right angle to the surface of the pole;
2. The physical parameters are time-invariant constants due to the small variation in the physical parameters of the molten steel during the continuous casting process;
3. Considering the magnetic Reynolds number being less than 1 during electromagnetic stirring in the continuous casting process, it is assumed that the electromagnetic field is barely affected by the slow flow of molten steel (0.9 m/min) [16];
4. The electromagnetic field generated by electromagnetic stirring can be considered a quasistatic field due to the low frequency of the alternating current (5–9 Hz).

### 2.2. Governing Equations

The linear electromagnetic stirring method employs a low-frequency alternating current to exert an electromagnetic force on the sluggish flow of molten steel within the casting slab, enhancing the recirculating flow of the molten metal. The mechanism of this method is shown in the following text and Figure 1. After the application of the alternating current, an alternating magnetic field  $\vec{B}$  is induced by the electromagnetic stirring roller. This alternating magnetic field  $\vec{B}$  manifests as a traveling wave magnetic field moving unidirectionally at a specified velocity. Within the casting slab, this traveling wave magnetic field generates

induced eddy currents  $\vec{J}$ . Subsequently, the interplay between these induced currents  $\vec{J}$  and the alternating magnetic field  $\vec{B}$  results in the emergence of electromagnetic forces  $\vec{F}$  within the molten steel in the casting slab. For the theoretical modeling of this process, a set of simplified Maxwell's equations is utilized as delineated in multiple scholarly sources [17–20].

$$\nabla \times \vec{H} = \vec{J} + \frac{\partial \vec{D}}{\partial t} \approx \vec{J} \tag{1}$$

$$\nabla \times \vec{E} = -\frac{\partial \vec{B}}{\partial t} \tag{2}$$

$$\nabla \cdot \vec{B} = 0 \tag{3}$$

$$\vec{J} = \sigma \vec{E} \tag{4}$$

$$\vec{F} = \frac{1}{2} Re \left( \vec{J} \times \vec{B}^* \right) \tag{5}$$

where,  $\vec{H}$  represents the magnetic field intensity, A/m;  $\vec{J}$  represents the current density, A/m<sup>2</sup>;  $\vec{E}$  represents the electric field intensity, V/m<sup>2</sup>;  $\vec{B}$  represents the magnetic induction intensity, mT;  $\vec{D}$  is the electrical induction intensity, C/m<sup>2</sup>;  $\sigma$  is the conductivity, S/m;  $Re$  represents the real part of the complex number;  $\vec{B}^*$  represents the conjugate complex of  $\vec{B}$ ; and  $\vec{F}$  represents time-averaged electromagnetic force, N/m<sup>3</sup>.

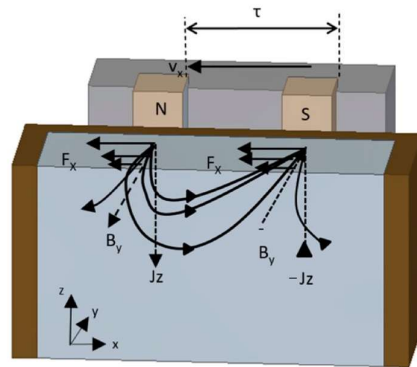


Figure 1. Working principle of the linear stirrer [12].

### 2.3. Electromagnetic Stirring Device

Under different electromagnetic stirring modes, the separation between the centers of the two electromagnetic stirring rollers in the secondary cooling zone is determined to be twice their diameter, equating to a distance of  $2 \times 240$  mm between each roller. The coils are energized through the application of a two-phase alternating current. The formula for computing the current density within a coil energized by an alternating current is expressed as

$$\vec{J}_1 = \vec{J}_0 \sin(\omega t) \tag{6}$$

$$\vec{J}_2 = \vec{J}_0 \sin(\omega t + 90^\circ) \tag{7}$$

where  $\omega$  represents the angular velocity,  $\omega = 2\pi f = \frac{2\pi}{T}$ , rad/s;  $f$  represents frequency, Hz;  $T$  represents the period, s;  $t$  represents time, s;  $\vec{J}_0$  is the amplitude of the coil current, A/m<sup>2</sup>; and  $\vec{J}_1$  and  $\vec{J}_2$  are the current densities of the first and second phases.

A schematic representation of the electromagnetic stirring roller, along with the power supply methodology, is depicted in Figure 2. It is necessary here to explain simply the role of each part in the picture, as follows:

1. Coil: the coil produces an alternating magnetic field when an alternating current is applied to it;
2. Iron core: the iron core is the carrier of magnetic lines of force, which can enhance and concentrate magnetic fields;
3. Slab: the slab is composed of an externally solidified shell and internal molten steel, with the flow field of the internal molten steel to changes in the electromagnetic force.

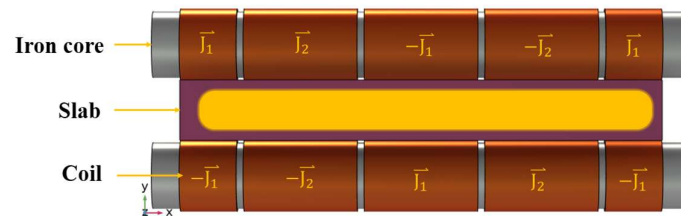


Figure 2. Electromagnetic stirring roller and its electrification method.

### 3. Results and Discussion

#### 3.1. Model Validation

The precision and dependability of the constructed model were verified by conducting a thorough comparison and validation of the data obtained from Xiao et al.'s [12] measurement of the casting slab magnetic field against the results produced by the model in this study. Figure 3 illustrates that the magnetic induction values simulated at the centerline of the electromagnetic stirring roller in the wide direction of the continuous casting slab closely align with those measured in the literature. Specifically, at 0.16 m on the centerline, the peak magnetic induction intensity is noted at 57.9 mT measured and 56.5 mT simulated, with a minor difference of 1.4 mT. The general agreement of measured and simulated values, coupled with a calculation error within acceptable limits, lends credibility to the numerical simulation results.

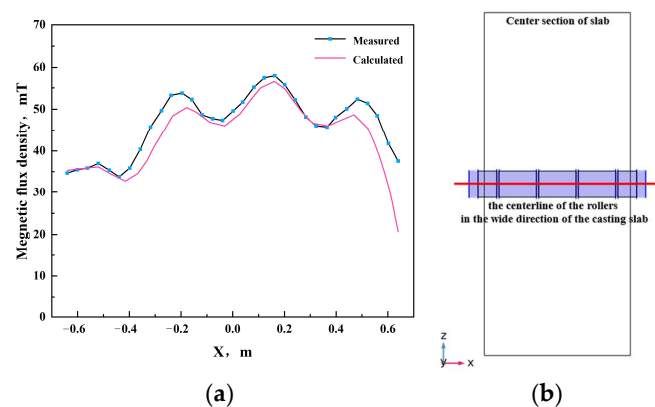


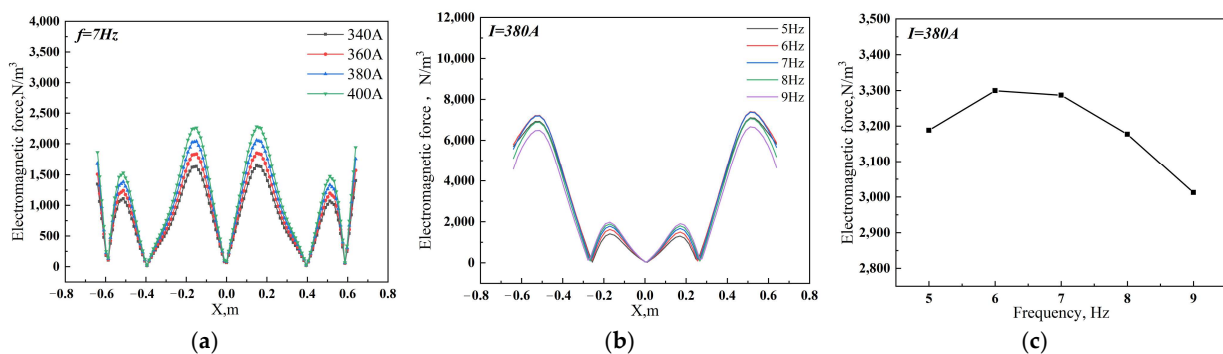
Figure 3. (a) Distribution of magnetic field density along the centerline of the electromagnetic stirring roller in the wide direction of the casting slab under electromagnetic stirring. (b) The centerline of the rollers in the wide direction of the casting slab schema.

#### 3.2. Selection of Optimal Stirring Current and Frequency

Based on the rated current and frequency parameters of an electromagnetic stirrer in a specific steel plant, where a pair of electromagnetic stirring rollers were arranged in a face-to-face configuration, two sets of simulations were conducted. In the initial series of simulations, the stirring frequency was uniformly established at 7 Hz, while the stirring currents were assigned values of 340 A, 360 A, 380 A and 400 A, respectively. The optimal stirring current was determined based on the magnitude of the generated electromagnetic force. In the subsequent series of simulations, the stirring current was uniformly established as the optimal value identified from the first series, with the stirring frequencies being set

at 5 Hz, 6 Hz, 7 Hz, 8 Hz and 9 Hz, respectively. The optimal stirring frequency was also determined based on the magnitude of the electromagnetic force generated.

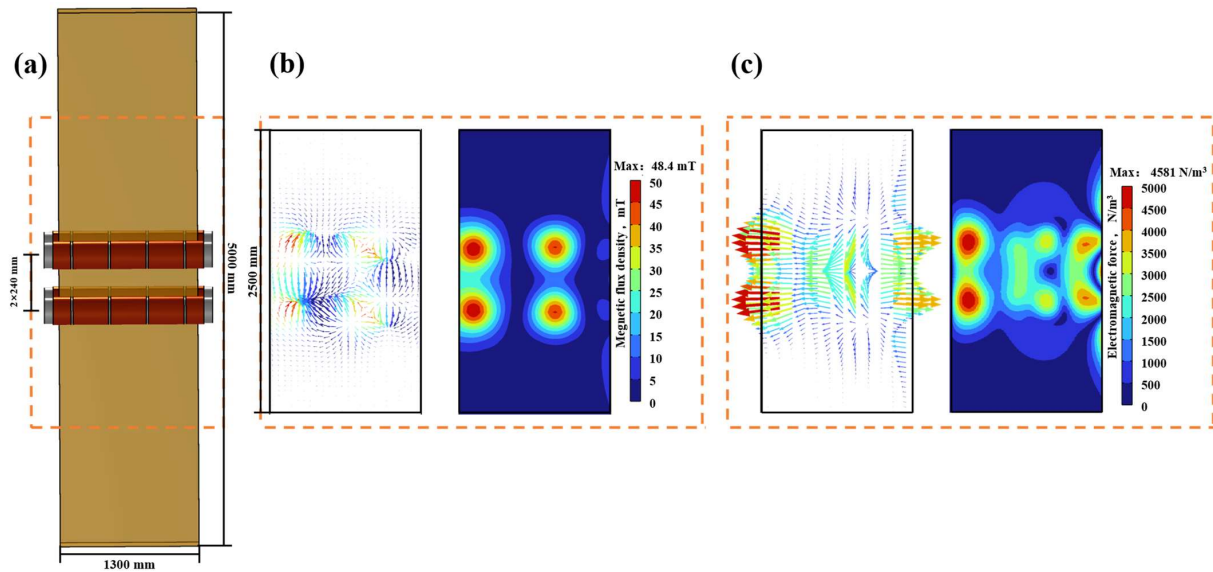
Figure 4 demonstrates that the greatest electromagnetic force generated by the electromagnetic stirring roller occurs when the current is set at 400 A. Given the minimal disparity in electromagnetic force between 400 A and 380 A, and considering that excessive electromagnetic force may deteriorate casting slab segregation and impair the solidification structure, 380 A has been selected as the optimal stirring current. Excessive electromagnetic force may lead to the breakthrough of the solidification shell by electromagnetic force-driven molten steel flow, resulting in molten steel leakage. Additionally, elevated frequencies contribute to increased energy loss through the skin effect. Taking a conservative approach, the optimal frequency is determined to be 5 Hz.



**Figure 4.** Distribution of electromagnetic force along the centerline of the rollers in the casting slab wide direction: (a) different currents; (b) different frequencies; (c) the average electromagnetic force at different frequencies.

### 3.3. Distribution of Electromagnetic Force and Magnetic Flux Density When Two Pairs of Electromagnetic Stirring Rollers Are Arranged Face-to-Face

The geometric schematic diagram depicting the two pairs of electromagnetic stirring rollers arranged face-to-face is presented in Figure 5a. Figure 5b presents the magnetic flux density distribution in the longitudinal section of the casting slab center at a current of 380 A, a frequency of 5 Hz and during a period of  $5/8$  T. The presence of the para-position electromagnetic stirring roller causes the magnetic field to close at the coil's corresponding position inside the casting slab, resulting in a localized peak in magnetic flux density where the coil is situated.



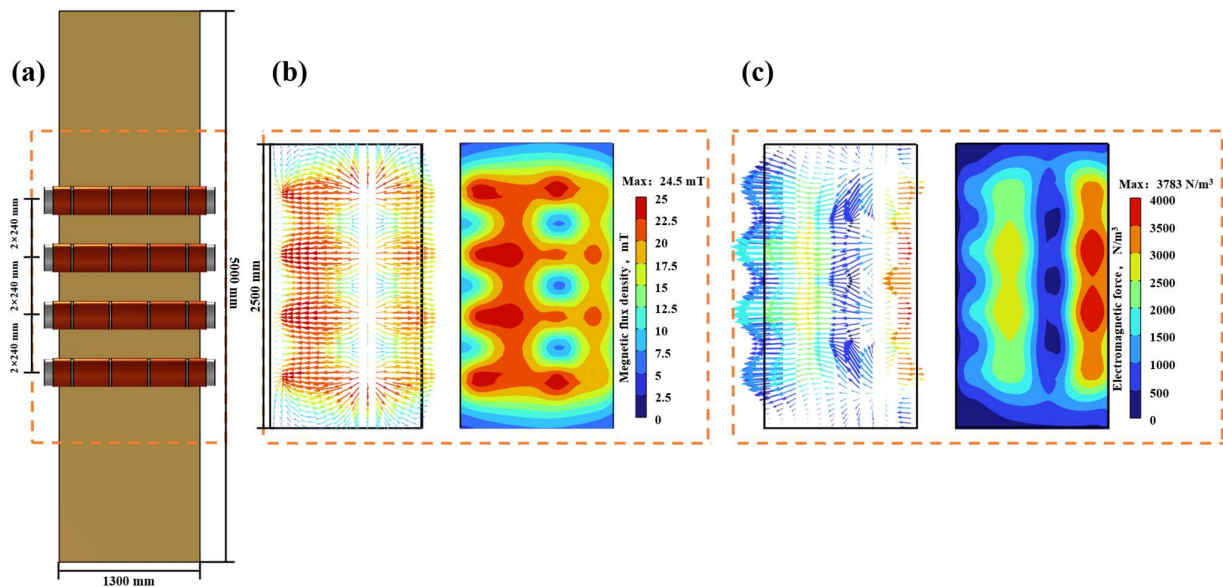
**Figure 5.** Distribution of magnetic induction intensity inside continuous casting slab under electromagnetic stirring arranged face-to-face: (a) geometric schematic diagram; (b) magnetic flux density cloud diagram and vector diagram; (c) electromagnetic force cloud diagram and vector diagram.

Figure 5c depicts the distribution of electromagnetic force in the central longitudinal section of the casting slab. The concentration of the magnetic field generated by the coil at this position, interacting with the molten steel in the casting slab, results in an increased local electromagnetic force. So, the electromagnetic force at the location of the electromagnetic stirring roller is observed to be higher than that in the surrounding areas, with a peak in electromagnetic force manifesting at the coil position of the roller.

### 3.4. Distribution of Electromagnetic Force and Magnetic Flux Density When Two Pairs of Electromagnetic Stirring Rollers Are Arranged Side-to-Side

The geometric schematic diagram depicting the two pairs of electromagnetic stirring rollers arranged side-to-side is presented in Figure 6a. Figure 6b presents the magnetic flux density distribution in the longitudinal section of the casting slab center at a current of 380 A, a frequency of 5 Hz and during a period of  $5/8$  T. When electromagnetic stirring rollers are arranged side-to-side, the lack of opposing rollers leads to the magnetic flux density vector being oriented predominantly in a single direction. This specific orientation results in the magnetic induction lines passing through the casting slab at a certain angle and closing at the external electromagnetic stirring rollers. Consequently, this results in a higher magnetic flux density near the rollers compared to a face-to-face arrangement, with the exception of the coil position.





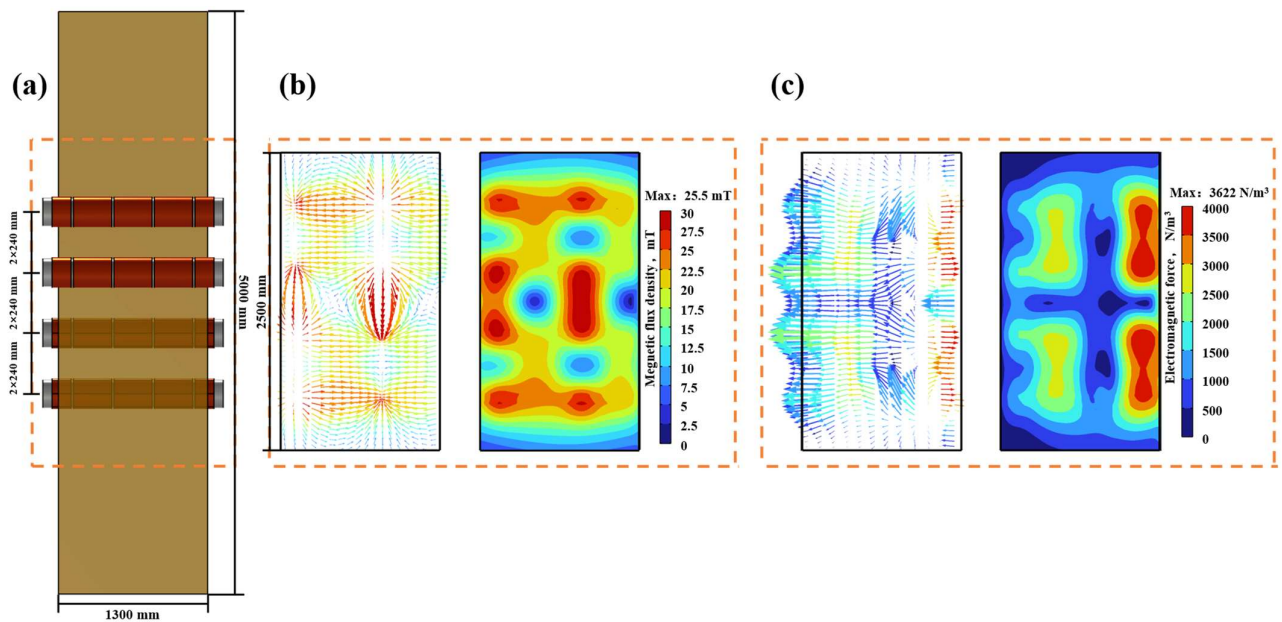
**Figure 6.** Distribution of magnetic flux density and electromagnetic force in the casting slab with two pairs of electromagnetic stirring rollers arranged side-to-side: (a) geometric schematic diagram; (b) magnetic flux density cloud diagram and vector diagram; (c) electromagnetic force cloud diagram and vector diagram.

Figure 6c depicts the distribution of electromagnetic force in the central longitudinal section of the casting slab. Besides the component force aligned with the direction of magnetic field movement, significant upward and downward components of electromagnetic force are also present. The mechanism entails the generation of a magnetic field through the side-to-side arrangement of electromagnetic stirring rollers, resulting in the formation of a curved magnetic induction line. It exhibits a semicircular distribution within the casting slab (referring to Figure 1). As the molten steel within the casting slab flows, it cuts through the magnetic induction line that is not perpendicular to the wide side of the casting slab, generating a significant electromagnetic component force.

### 3.5. Distribution of Electromagnetic Force and Magnetic Flux Density When Four Electromagnetic Stirring Rollers Are Arranged in an Up-Down Misalignment

The geometric schematic diagram depicting the two pairs of electromagnetic stirring rollers arranged in an up-down misalignment is presented in Figure 7a. Figure 7b presents the magnetic flux density distribution in the longitudinal section of the casting slab center at a current of 380 A, a frequency of 5 Hz and during a period of 5/8 T. In the up-down misalignment arrangement, the flux density is higher near the electromagnetic stirring rollers and the peak flux density happens at the coil position, similar to what was seen in the side-to-side arrangement. However, this increased flux density is more pronounced in the up-down misalignment than in the side-to-side configuration. Furthermore, a pair of oppositely misaligned rollers leads to the closure of the magnetic field within the casting slab at a distinct tilt angle. This tilt angle is determined by the angle between the oppositely misaligned rollers and the casting slab's wide surface, resulting in the peak magnetic flux density area intersecting near the closest misaligned roller.





**Figure 7.** The distribution of magnetic flux density and electromagnetic force in the casting slab with two pairs of electromagnetic stirring rollers arranged in an up-down misalignment: (a) geometric schematic diagram; (b) magnetic flux density cloud diagram and vector diagram; (c) electromagnetic force cloud diagram and vector diagram.

Figure 7c depicts the distribution of electromagnetic force in the central longitudinal section of the casting slab. From the figure, it can be seen that the overall electromagnetic force is higher when the electromagnetic stirring rollers are arranged in an up-down misalignment compared to when they are arranged side-to-side. There is also the electromagnetic component force when the electromagnetic stirring rollers are arranged in an up-down misalignment and the mechanism of generating this component is the same as that of generating electromagnetic component force when they are arranged side-to-side.

The study selected the centerline in different directions as the data value line to compare the distribution of electromagnetic force under different arrangement patterns of the electromagnetic stirring roller. Figure 8 displays the results. At a cycle of  $1/2 T$ , the observed maximum electromagnetic force on the casting slab's centerline for the face-to-face, side-to-side and up-down misalignment arrangements is  $2378 \text{ N/m}^3$ ,  $31607 \text{ N/m}^3$  and  $1516 \text{ N/m}^3$ , respectively. The corresponding average electromagnetic forces for these arrangements are  $432 \text{ N/m}^3$ ,  $646 \text{ N/m}^3$ , and  $604 \text{ N/m}^3$ . In addition, the maximum electromagnetic force exerted on the wide centerline of the electromagnetic stirring roller casting slab reaches  $9850 \text{ N/m}^3$ ,  $4779 \text{ N/m}^3$  and  $4629 \text{ N/m}^3$ , respectively. The average electromagnetic force measures  $4712 \text{ N/m}^3$ ,  $2766 \text{ N/m}^3$  and  $2696 \text{ N/m}^3$ , respectively. It is evident that face-to-face arrangements have the smallest component of electromagnetic force, suggesting that this arrangement generates the largest and most concentrated electromagnetic force.

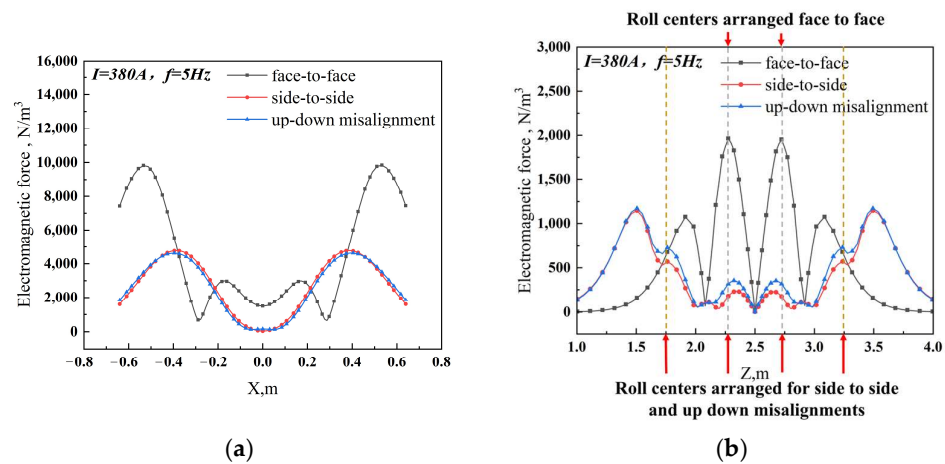


**Figure 8.** Distribution of electromagnetic force with different arrangement patterns (a) along the centerline of the upper pair of rollers of face-to-face arrangement in the casting slab wide direction; (b) along the centerline in the casting direction.

### 3.6. The Impact of Electromagnetic Field on PW800 Steel’s Solidification Structure

In the S-EMS industrial experiment, two pairs of electromagnetic stirring rollers were selected for the face-to-face arrangement of PW800 steel casting slab continuous casting. PW800 steel belongs to the category of electrical steel and its chemical composition is presented in Table 1.

**Table 1.** Chemical compositions of PW800 steel (wt.%).

C	Si	Mn	P	S	Al	Cr	Cu	Ni
0.003	1.05	0.32	0.012	0.005	0.31	0.0285	0.041	0.033

The electromagnetic stirring rollers are arranged in the following ways: face-to-face, side-to-side and in an up-down misalignment. Among them, the face-to-face arrangement generates the largest electromagnetic force and the smallest area of effect on the casting slab. This phenomenon accelerates the erosion speed of molten steel at the solidification front and is conducive to the formation of equiaxed grains.

As shown in Figure 9a,b, the solidification structures of casting slabs, produced with or without S-EMS, were compared in industrial experiments. Figure 9c illustrates a schematic diagram for calculating the equiaxed grain ratio. The grain aspect ratio less than or equal to 3 was defined as an equiaxed grain and the zone where equiaxed grains exist is the equiaxed grain zone. According to the measured thickness of the equiaxed grain zone and Equation (8), the equiaxed grain ratio at 1/4, 2/4 (center) and 3/4 of the casting slab width was calculated and the average value was taken to obtain the equiaxed grain ratio of the casting slab.

$$\Phi = \frac{H_e}{H} \times 100 \tag{8}$$

where  $\Phi$  is the equiaxed grain ratio, %;  $H_e$  is the thickness of the equiaxed grain zone, mm; and  $H$  is the thickness of the casting slab, constant, 230 mm.

In the absence of S-EMS, the heat transfer from the interior of the casting slab to the surface transpires at a more gradual pace, leading to a slower dissipation of superheat. Superheat is defined as the difference between the actual temperature of the molten steel and its liquidus temperature. As long as the molten steel remains superheated above the temperature of the liquid phase line, it solidifies in the form of dendritic grains growing along the direction of the temperature gradient. Consequently, the macrostructure of the casting slab reveals more developed columnar grains [21,22]. During the solidification process, the interdendritic liquid enriched in alloying elements migrates to the center before

solidification. Because the center of the liquid pool lacks equiaxed grains to decentralize the enriched liquid, the flow of the residual enriched liquid will gather in the center of the slab. This led to serious center segregation after the solidification process was completed [21,23]. When using S-EMS with 380 A and 5 Hz electromagnetic stirring parameters, on the one hand, the electromagnetic force generated by the traveling wave magnetic field causes the molten steel to flow violently and wash away the solidification front, which homogenizes the temperature at the solidification front of the casting slab and accelerates the dissipation of superheat. This suppresses the growth of columnar grains and promotes the formation of equiaxed grains [21,24,25]. On the other hand, under the action of electromagnetic force-driven molten steel flow washing, the tips of columnar grains are remelted or broken. The growth of columnar grains is inhibited and broken tips of columnar grains are washed into the molten steel, serving as nuclei for equiaxed grain nucleation and promoting the formation of equiaxed grains [26]. The thickness of the equiaxed grain zone  $H_e$  at  $1/4$ ,  $2/4$  (center) and  $3/4$  of the casting slab width measured from Figure 9a are 16 mm, 21 mm and 18 mm. From Equation (8), the equiaxed grain ratios are calculated as 7%, 9% and 8%, respectively. The average equiaxed grain ratio of the casting slab is 8%.

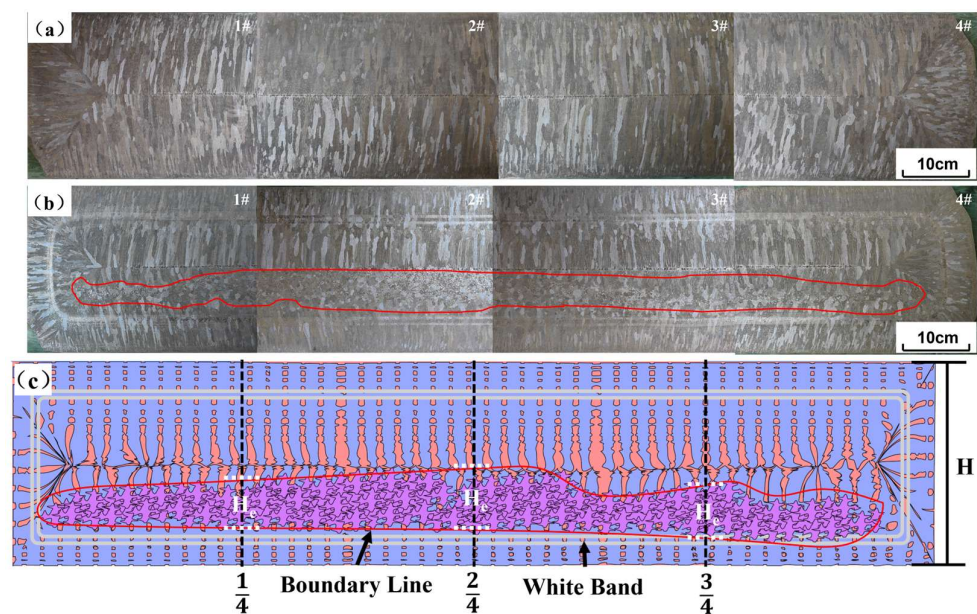


**Figure 9.** Cross-section macrostructure photos of continuous casting slabs and a schematic diagram of equiaxed grain ratio calculation: (a) without S-EMS; (b) with S-EMS (face-to-face); (c) schematic diagram for calculating the equiaxed grain ratio of the cross-section of the casting slab.

Upon observation of the macroscopic structure of the casting slab following the application of S-EMS, two distinct white light bands are clearly visible as a result of electromagnetic stirring. Additionally, the amount of equiaxed grains in the casting slab is noticeably enhanced. The thickness of the equiaxed grain zone  $H_e$  at  $1/4$ ,  $2/4$  (center) and  $3/4$  positions of the casting slab width exhibit an increase to 78 mm, 81 mm and 69 mm. From Equation (8), the equiaxed grain ratios  $\Phi$  are calculated as 34%, 35% and 30%, respectively. The average ratio of equiaxed grain in the casting slab ranged from 8% to 33%. However, the resulting grain structure distribution is unequal, with a concentration of equiaxed grains on one side while the other side is predominantly composed of columnar grains. This effect is caused by the arc-shaped construction of the continuous casting machine. The curve in the curved structural segment of the continuous casting machine (usually mold and secondary cooling zone) has a certain curvature. The casting slab is accordingly divided into two sides: the loose side and fixed side. The term “loose side” denotes the inner arc of the casting slab, whereas the term “fixed side” designates the outer arc of the casting slab. Because the loose side surface of the casting slab is a water accumulation surface, the cooling speed on the

loose side is faster than the cooling speed on the fixed side during the water spray cooling process, promoting the formation of columnar grains on the loose side. This accelerates the formation of columnar grains on the loose side. At the same time, the primary grain nucleus deposits at the solidification front of the fixed side due to gravity, impeding the formation of columnar grains. The amalgamation of these two events leads to an irregular distribution of grain structure within the casting slab [27].

After the application of S-EMS, the equiaxed grain ratio of the casting slab is significantly increased. Previous studies have shown that, for electrical steels, a higher equiaxed grain ratio is closely related to better overall mechanical and magnetic properties [28].

#### 4. Conclusions

1. The distribution of magnetic flux density in the casting slab is determined by the arrangement pattern of the electromagnetic stirring roller. In face-to-face, side-to-side and up-down misalignment arrangements, peak magnetic flux density occurs at the coil position. Furthermore, the flux density adjacent to the electromagnetic stirring roller in the side-to-side and up-down misalignment arrangements is observed to be higher than in the face-to-face arrangement.
2. The electromagnetic force of the face-to-face arrangement generated by the largest and most concentrated produces almost no upward and downward components of electromagnetic force. Therefore, the face-to-face arrangement is superior to the remaining two types of arrangement patterns. The arrangement of side-to-side and up-down misalignment will produce large upward or downward components of electromagnetic force. These component forces lead to a reduction in the force applied to the stirring process and could potentially disturb the vortex, thereby compromising the effectiveness of the stirring.
3. Using S-EMS significantly enhances the equiaxed grain ratio of casting slabs. Before and after the use of S-EMS, the equiaxial grain thickness of casting slabs increased from 16 mm, 21 mm and 18 mm to 78 mm, 81 mm, and 69 mm and the equiaxed grain ratio of casting slabs increased from 7%, 9% and 8% to 34%, 35% and 30%, respectively. The average equiaxed grain ratio of the casting slabs increased from 8% to 33%. Additionally, in actual production, the presence of curvature in the casting slabs leads to nonuniform heat transfer, causing the growth of columnar grains to be promoted on the loose side while hindering their growth on the fixed side.

**Author Contributions:** Conceptualization, Z.X. and G.Z.; validation, Z.X. and C.W.; Analysis, Z.X.; writing, Z.X., G.Z. and D.L.; project administration, G.Z.; funding acquisition, G.Z. All authors have read and agreed to the published version of the manuscript.

**Funding:** This work is supported by the Special Steel Continuous Casting MEMS+FEMS Project from Hunan Zhongke Electric Co., Ltd. [grant number HZ2021F0529A].

**Institutional Review Board Statement:** Not applicable.

**Informed Consent Statement:** Not applicable.

**Data Availability Statement:** The data presented in this study are available on request from the corresponding author due to the project policy.

**Conflicts of Interest:** Author Chenhui Wu was employed by the company Panzhihua Iron and Steel Co., Ltd. The remaining authors declare that the research was conducted in the absence of any commercial or financial relationships that could be construed as a potential conflict of interest.

#### References

1. Cho, S.-M.; Thomas, B.G. Electromagnetic Effects on Solidification Defect Formation in Continuous Steel Casting. *JOM* **2020**, *72*, 3610–3627. [CrossRef]
2. Liu, T.Y. Numerical Simulation of Electromagnetic Stirring of Rolls in Sub-Section of Ultra-Wide Slab Second Cooling Zone. Master's Thesis, Northeastern University, Boston, MA, USA, 2019.

3. de León, B.M.; Castillejos, E.A.H. Physical and Mathematical Modeling of Thin Steel Slab Continuous Casting Secondary Cooling Zone Air-Mist Impingement. *Metall. Mater. Trans. B* **2015**, *46*, 2028–2048. [CrossRef]
4. Zappulla, M.L.S.; Cho, S.-M.; Koric, S.; Lee, H.-J.; Kim, S.-H.; Thomas, B.G. Multiphysics Modeling of Continuous Casting of Stainless Steel. *J. Mater. Process. Technol.* **2020**, *278*, 116469. [CrossRef]
5. Liang, M.; Cho, S.-M.; Ruan, X.; Thomas, B.G. Modeling of Multiphase Flow, Superheat Dissipation, Particle Transport, and Capture in a Vertical and Bending Continuous Caster. *Processes* **2022**, *10*, 1429. [CrossRef]
6. Thomas, B.G. Review on Modeling and Simulation of Continuous Casting. *Steel Res. Int.* **2018**, *89*, 1700312. [CrossRef]
7. Thomas, B.G.; Zhang, L. Mathematical Modeling of Fluid Flow in Continuous Casting. *ISIJ Int.* **2001**, *41*, 1181–1193. [CrossRef]
8. Yoon, J.-K. Applications of Numerical Simulation to Continuous Casting Technology. *ISIJ Int.* **2008**, *48*, 879–884. [CrossRef]
9. Zhang, K.; Chen, S.F.; Yang, B.; Liu, T.Y.; Zhao, Y.; Lei, H. Electromagnetic stirring roller arrangement in the second cooling zone of slab. *J. Liaoning Univ. Sci. Technol.* **2018**, *41*, 335–340+350.
10. Li, J.C.; Yin, Y.C.; Wang, B.F. Numerical Simulation of Stirring Modes for Roll-type Electromagnetic Stirring in the Secondary Cooling Zone of the Continuous Casting Slab. *Spec. Cast. Nonferrous Alloys* **2013**, *33*, 302–305.
11. Xiao, H.; Wang, P.; Zheng, Q.; Liu, S.; Chen, X.Q.; Zhang, Q. Influence of roll electromagnetic stirring coil position on solidification behavior of slabs. *Steel* **2023**, *58*, 79–88.
12. Xiao, H.; Wang, P.; Yi, B.; Chen, X.; Li, A.; Tang, H.; Li, W.; Zhang, J. A Numerical and Experimental Study on the Solidification Structure of Fe–Cr–Ni Steel Slab Casting by Roller Electromagnetic Stirring. *Metals* **2020**, *11*, 6. [CrossRef]
13. Fang, L.; Liu, T.; Huang, Y.; Wu, W.; Feng, W.; Lei, H. Numerical Simulation for Magnetohydrodynamic Flow and Solidification in an Ultra-Wide Slab Continuous Caster with Electromagnetic Stirring Roller. *ISIJ Int.* **2022**, *62*, 2294–2300. [CrossRef]
14. Gong, J.; Liu, H.; Wang, X.; Bad, Y. Numerical Simulation of Electromagnetic Field and Flow Pattern in a Continuous Slab Caster with In-Roll Type Strand Electromagnetic Stirring. *J. Iron Steel Res. Int.* **2015**, *22*, 414–422. [CrossRef]
15. Yu, Y.; Li, B.K. Calculation of electromagnetic force in electromagnetic stirring process for continuous casting of steel. *J. Metals*. **2006**, *42*, 540–544.
16. Barna, M.; Javurek, M.; Wimmer, P. Numeric Simulation of the Steel Flow in a Slab Caster with a Box-Type Electromagnetic Stirrer. *Steel Res. Int.* **2020**, *91*, 9. [CrossRef]
17. Wang, Y.; Chen, W.; Jiang, D.; Zhang, L. Effect of the Gap Between Copper Mold and Solidified Shell on the Fluid Flow in the Continuous Casting Strand with Mold Electromagnetic Stirring. *Steel Res. Int.* **2020**, *91*, 1900470. [CrossRef]
18. Kunstreich, S. Electromagnetic Stirring for Continuous Casting-Part 1. *Rev. Met. Paris* **2003**, *100*, 395–408. [CrossRef]
19. Goman, V.; Sokolov, I.; Fedoreev, S. Modeling Electromagnetic Stirring Processes during Continuous Casting of Large-Format Slabs. In Proceedings of the 2019 International Conference on Industrial Engineering, Applications and Manufacturing (ICIEAM), Sochi, Russia, 25–29 March 2019; pp. 1–5.
20. Jiang, D.B.; Zhu, M.Y.; Zhang, L.F. Numerical Simulation of Solidification Behavior and Solute Transport in Slab Continuous Casting with S-EMS. *Metals* **2019**, *9*, 452. [CrossRef]
21. Kunstreich, S. Electromagnetic Stirring for Continuous Casting-Part 2. *Rev. Met. Paris* **2003**, *100*, 1043–1061. [CrossRef]
22. Drożdż, P. The Influence of the Superheat Temperature on the Slab Structure in the Continuous Steel Casting Process. *Arch. Metall. Mater.* **2019**, *64*, 1287–1293. [CrossRef]
23. Ayçiçek, İ.; Solak, N. Optimization of Macro Segregation and Equiaxed Zone in High-Carbon Steel Use in Prestressed Concrete Wire and Cord Wire Application. *Metals* **2023**, *13*, 1435. [CrossRef]
24. Choudhary, S.K.; Ganguly, S.; Sengupta, A.; Sharma, V. Solidification Morphology and Segregation in Continuously Cast Steel Slab. *J. Mater. Process. Technol.* **2017**, *243*, 312–321. [CrossRef]
25. Yao, C.; Wang, M.; Ni, Y.; Gong, J.; Xing, L.; Zhang, H.; Bao, Y. Effects of Secondary Cooling Segment Electromagnetic Stirring on Solidification Behavior and Composition Distribution in High-Strength Steel 22MnB5. *JOM* **2022**, *74*, 4823–4830. [CrossRef]
26. Cho, S.-M.; Thomas, B.G. Electromagnetic Forces in Continuous Casting of Steel Slabs. *Metals* **2019**, *9*, 471. [CrossRef]
27. Shibata, H.; Itoyama, S.; Kishimoto, Y.; Takeuchi, S.; Sekiguchi, H. Prediction of Equiaxed Crystal Ratio in Continuously Cast Steel Slab by Simplified Columnar-to-Equiaxed Transition Model. *ISIJ Int.* **2006**, *46*, 921–930. [CrossRef]
28. Li, J.; Deng, B.; Yang, X.; Liang, L.; Wang, H.; Wu, T. Microstructure Control of Continuous Casting Slab of Grain Oriented Silicon Steel. *Mater. Trans.* **2022**, *63*, 112–117. [CrossRef]

**Disclaimer/Publisher’s Note:** The statements, opinions and data contained in all publications are solely those of the individual author(s) and contributor(s) and not of MDPI and/or the editor(s). MDPI and/or the editor(s) disclaim responsibility for any injury to people or property resulting from any ideas, methods, instructions or products referred to in the content.



## Article

# Simulation and Experimental Study on the Effect of Superheat on Solidification Microstructure Evolution of Billet in Continuous Casting

Nan Tian <sup>1</sup>, Guifang Zhang <sup>1,2,\*</sup>, Peng Yan <sup>1</sup>, Pengchao Li <sup>1,3</sup>, Zhenhua Feng <sup>1</sup> and Xiaoliang Wang <sup>1</sup>

- <sup>1</sup> Faculty of Metallurgical and Energy Engineering, Kunming University of Science and Technology, Kunming 650093, China; tian1852558@163.com (N.T.); yanp\_km@163.com (P.Y.); 13696392999@163.com (P.L.); fengzhenhua666@126.com (Z.F.); wangxiaoliang@kust.edu.cn (X.W.)
- <sup>2</sup> Key Laboratory of Clean Metallurgy for Complex Iron Resources in Colleges and Universities of Yunnan Province, Kunming University of Science and Technology, Kunming 650093, China
- <sup>3</sup> Linyi Iron and Steel Investment Group Special Steel Co., Ltd., Linyi 276000, China
- \* Correspondence: guifangzhang65@163.com

**Abstract:** The control of the solidification structure of a casting billet is directly correlated with the quality of steel. Variations in superheat can influence the transition from columnar crystals to equiaxed crystals during the solidification process, subsequently impacting the final solidification structure of the billet. In this study, a model of microstructure evolution during billet solidification was established by combining simulation and experiment, and the dendrite growth microstructure evolution during billet solidification under different superheat was studied. The results show that when the superheat is 60 K, the complete solidification time of the casting billet from the end of the 50 mm section is 252 s, when the superheat is 40 K, the complete solidification time of the casting billet is 250 s, and when the superheat is 20 K, the complete solidification time of the casting billet is 245 s. When the superheat is 20 K, the proportion of the equiaxed crystal region is higher—the highest value is 53.35%—and the average grain radius is 0.84556 mm. The proportion of the equiaxed crystal region decreases with the increase of superheat. When the superheat is 60 K, the proportion of the equiaxed crystal region is the lowest—the lowest value is 46.27%—and the average grain radius is 1.07653 mm. Proper reduction of superheat can obviously reduce the size of equiaxed crystal, expand the area of equiaxed crystal and improve the quality of casting billet.

**Keywords:** square billet; superheat; solidification structure; dendrite growth; numerical simulation



**Citation:** Tian, N.; Zhang, G.; Yan, P.; Li, P.; Feng, Z.; Wang, X. Simulation and Experimental Study on the Effect of Superheat on Solidification Microstructure Evolution of Billet in Continuous Casting. *Materials* **2024**, *17*, 682. <https://doi.org/10.3390/ma17030682>

Academic Editor: Jordi Sort

Received: 8 January 2024

Revised: 23 January 2024

Accepted: 25 January 2024

Published: 31 January 2024



**Copyright:** © 2024 by the authors. Licensee MDPI, Basel, Switzerland. This article is an open access article distributed under the terms and conditions of the Creative Commons Attribution (CC BY) license (<https://creativecommons.org/licenses/by/4.0/>).

## 1. Introduction

The microstructure simulation of the solidification process refers to the simulation of the solidification process of castings on the grain scale, through which only a few experiments can be conducted to predict the solidification microstructure and mechanical properties of castings [1–3]. With the rapid development of computer simulation technology, numerical simulation technology has become an efficient and convenient means to simulate the solidification process of casting and predict the evolution of the solidification process organization. At present, the numerical simulation methods that can be used to predict the microstructure evolution of casting during solidification, include deterministic method, stochastic method, phase-field method, etc. [4–6]. In recent years, the stochastic model closest to crystal growth in the solidification process is mainly based on cellular automation (CA) and its derivative simulation methods. The basic idea is that the primitive cell changes the state of the primitive cell according to the change rules of the cell in the similar field, and affects the change of the next cell, so it constantly evolves. This is similar to the process of metal solidification. Zhong et al. [7] studied the effect of superheating and cooling intensity on the solidification structure and macro-segregation of 6Cr13Mo stainless steel

billet. The cooling conditions of the continuous casting billet were determined through numerical simulation. The 6Cr13Mo steel sample was solidified in the thermal simulator under simulated cooling conditions. Sheng et al. [8] established a finite element coupled model of cellular automata and studied the effects of cooling spray state and process conditions on the solidification structure of continuous casting slabs. The model is verified. The solidification structure under different cooling spray schemes, superheat and pouring speed was simulated. Cao et al. [9] introduced fractal dimension and specific surface area to quantitatively describe the overall morphology of the solidified structure of continuous casting billet of GCr15 bearing steel, and calculated the permeability of dendrite channel based on this. The results show that the fractal dimension can describe the self-similar complexity and the specific surface area can describe the coarsening degree of the solidified structure. Zhao et al. [10] adopted a two-dimensional cellular automaton (CA) model and finite element (FE) method to simulate solidification structure formation during continuous casting of beam billet, which represents the growth of columnar and equiaxial dendrites under detailed secondary cooling boundary conditions. An et al. [11] established the CAFE model and SDAS model in order to study the evolutionary behavior of macrostructure and secondary dendrites, respectively, on a  $220 \times 260 \text{ mm}^2$  bloom cross-section of GCr15 bearing steel. Based on numerical simulation and experiments, the effects of process parameters on center ECR and SDAS are investigated. Xiao et al. [12] researched the grain growth process of X15CrNiSi20-12 austenitic stainless steel in the process of investment casting by using the cellular automaton finite element (CAFE) model, and studied the effects of shell thickness, shell temperature, pouring temperature and cooling rate on the solidification structure via orthogonal test. The results show that the cooling method has an important effect on the formation of axial crystals. The effect of shell temperature, shell thickness and pouring temperature on the formation of axial crystals is small. Yamazaki et al. [13] used the cellular automata method to simulate the solidification structure of steel during continuous casting, and the influence of electromagnetic stirring was also considered in the model.

Based on the production data of casting billet with a carbon content of 0.20wt.%, the potential influence of continuous casting parameters on the solidification process was systematically studied by using the CAFE model. By combining the actual field statistics, we successfully verified the high accuracy of the numerical simulation model by using the low superheat structure test of continuous casting billet.

Continuous casting superheat refers to the temperature above its equilibrium liquidus before pouring molten metal into a mold in a continuous casting process. The setting of the superheat has an important influence on the whole continuous casting process and the properties of the final continuous casting billet. On the basis of model verification, the effects of different superheat parameters on the solidification structure were studied. This study not only contributes to a comprehensive understanding of the solidification behavior of 20# steel under specific process conditions, but also provides practical guidance for industrial production. Through numerical simulation and experimental verification of the system, we provide a new research idea for the optimization of on-site continuous casting parameters, which is expected to play a positive role in improving production efficiency and product quality. The aim of this research is to provide engineers and decision makers in the relevant fields with strong support to better understand the influence of superheat parameters on the solidification structure of 20# steel, and to flexibly apply this knowledge in actual production. Through this research, we expect to contribute to the technological advancement and process optimization of the steel industry and promote innovation and development in related fields.



## 2. Materials and Methods

### 2.1. Nucleation Model

Based on the theory of continuous nucleation, refs. [14,15] finite element (FE) method was used to solve the differential equation of heat conduction [16], and the governing equation of 3D macroscopic temperature field heat conduction is shown as Equation (1).

$$\frac{\partial}{\partial x} \left( \lambda \frac{\partial T}{\partial x} \right) + \frac{\partial}{\partial y} \left( \lambda \frac{\partial T}{\partial y} \right) + \frac{\partial}{\partial z} \left( \lambda \frac{\partial T}{\partial z} \right) + \rho L \frac{\partial f_s}{\partial t} = \rho c \frac{\partial T}{\partial t} \quad (1)$$

In Equation (1),  $T$  is the thermodynamic temperature, K;  $\rho$  is the density,  $\text{kg}/\text{m}^3$ ;  $c$  is the specific heat capacity,  $\text{J}/(\text{kg} \cdot ^\circ\text{C})$ ;  $\lambda$  is the thermal conductivity,  $\text{W}/(\text{m}\cdot\text{K})$ ; and  $L$  is the latent heat of solidification,  $\text{J}/\text{g}$ .

In order to more accurately reflect the actual situation and take into account the influence of other solidification conditions on the final grain size and grain shape distribution during solidification, the continuous nucleation model based on Gaussian distribution proposed by GANDIN et al. [17,18] was adopted in this study, assuming that nucleation occurs at a series of different nucleation locations. A continuous rather than discrete distribution function  $dn/d\Delta T$  was used to describe the change in nucleation density [19], where  $dn$  is an increase in grain density caused by an increase in subcooling  $\Delta T$ . The density  $n(\Delta T)$  of the grains formed at a certain degree of subcooling  $\Delta T$  can be obtained by integrating the distribution curve [20], as shown in Equation (2).

$$n(\Delta T) = \int_0^{\Delta T} \frac{dn}{d(\Delta T)} d(\Delta T) \quad (2)$$

The Gaussian distribution of Equation (2) is used to obtain Equation (3):

$$\frac{dn}{d(\Delta T)} = \frac{N_s}{\sqrt{2\pi}\Delta T_\sigma} \exp \left[ -\frac{1}{2} \left( \frac{\Delta T - \Delta T_N}{\Delta T_\sigma} \right)^2 \right] \quad (3)$$

In Equation (3),  $n(\Delta T)$  is the nucleus density at subcooling degree  $\Delta T$ , where  $\Delta T = T_L - T$  ( $T_L$  is liquidus temperature, K);  $N_s$  is the maximum nucleation density; and  $\Delta T_N$  and  $\Delta T_\sigma$  are the maximum nucleation supercooling and standard variance supercooling of the alloy, respectively.

### 2.2. Dendrite Growth Model

The transformation from columnar crystals to equiaxed crystals in dendrite growth represents two distinct conditions of crystal growth morphology during the solidification process of continuous casting billets. These conditions are influenced by a multitude of factors, some of which can induce either dendrite growth or the formation of columnar crystals. The temperature gradient is an essential factor that affects crystal growth morphology. A larger temperature gradient typically promotes dendrite growth, as crystals tend to grow faster on one side under high-temperature gradients, resulting in a branched structure. Conversely, a smaller temperature gradient is more conducive to the formation of equiaxed crystals. Simultaneously, the solidification rate plays a crucial role in determining crystal growth morphology. A faster solidification rate generally favors dendritic structures because rapid solidification leads to increased crystal growth rates and facilitates the formation of dendrites. On the other hand, a slower solidification rate is more favorable for the development of columnar equiaxed crystals.

This paper primarily focuses on investigating how changes in superheat influence dendrite growth within the solidified tissue during continuous casting processes. In conclusion, variations in superheat effectively impact both the temperature gradient and solidification rate within casting billets, thereby significantly influencing dendrite growth under different superheating conditions.

In this study, the KGT model [21,22] was used to calculate the dendrite tip growth rate. The KGT model is a dendrite growth model established by Kurz, Giovanola and Trivedi in 1986 on a steady-state basis [23]. According to the boundary stability criterion [24], Equation (4) can be obtained:

$$V^2 \frac{\pi^2 \Gamma}{P^2 D^2} + V \frac{m C_0 (1 - k_0)}{D [1 - (1 - k_0) Iv(P)]} + G = 0 \quad (4)$$

In Equation (4),  $V$  is the growth rate of the dendrite tip,  $m \cdot s^{-1}$ ;  $\Gamma$  is the Gibbs–Thompson coefficient,  $m \cdot K$ ;  $P$  is the Peclet number of solute diffusion;  $D$  is the diffusion coefficient of solute element in liquid,  $m^2 \cdot s^{-1}$ ;  $m$  is the liquidus slope,  $K \cdot (wt.\%)^{-1}$ ;  $C_0$  is the initial concentration of solute elements,  $wt.\%$ ;  $k_0$  is the distribution coefficient;  $Iv(P)$  is the Ivantsov function; and  $G$  is the temperature gradient,  $K \cdot m^{-1}$ . Ivantsov function is the steady state diffusion solution of dendrite tip obtained strictly from mathematics by mathematician Ivantsov on the basis of assuming that the solid–liquid interface is isothermal or isoconcentration parabola. Since the temperature gradient has little effect on the growth rate of the dendrite tip, the value of  $G$  is set to zero.

In order to increase the universality of the above KGT model in solidification simulation [25], the KGT model is extended in multiple components, and Equations (5)–(7) are obtained:

$$c_0 = \sum c_i \quad (5)$$

$$m = \sum \frac{m_i c_i}{c_0} \quad (6)$$

$$k = \sum \frac{m_i c_i k_i}{m c_0} \quad (7)$$

In Equations (5)–(7),  $c_i$  is the mass fraction of the alloy element;  $m_i$  is the liquidus slope of the alloy element; and  $k_i$  is the solute equilibrium partition coefficient of the alloying element.

According to the theory of metal solidification [26], there is a supercooled melt at the dendrite front during grain growth, and the dendrite growth is affected by dynamic supercooling, compositive supercooling, thermal supercooling, curvature supercooling and other factors, as shown in Equation (8):

$$\Delta T = \Delta T_c + \Delta T_t + \Delta T_k + \Delta T_r \quad (8)$$

In Equation (8),  $\Delta T_c$  is the component subcooling degree,  $K$ ;  $\Delta T_t$  is the degree of thermodynamic undercooling,  $K$ ;  $\Delta T_r$  is the curvature subcooling degree of solid–liquid interface,  $K$ ; and  $\Delta T_k$  is growth dynamic subcooling,  $K$ . For most metals, the latter three values are small and negligible compared to the subcooling  $\Delta T_c$ .

To simplify the calculation, Rappaz and Kurz give a simplified relationship between dendrite tip growth rate and subcooling degree based on the KGT model, and the following polynomial fitting Equation (9) is obtained.

$$v(\Delta T) = a_2 \Delta T^2 + a_3 \Delta T^2 \quad (9)$$

In Equation (9),  $a_2$  and  $a_3$  are polynomial coefficients, respectively, which are alloy-related constants,  $m \cdot s^{-1} \cdot K^{-2}$ ; and  $\Delta T$  is the degree of subcooling of the dendrite tip,  $K$ .

### 2.3. Model Parameters and Boundary Conditions

In this paper, the three-dimensional modeling software SolidWorks 2019 was used to model the casting billet. The overall dimension cross-section of the casting billet was 200 mm × 200 mm. The established stereoscopic model of the casting billet was imported

into the ProCAST software 17.5 to grid the model with tetrahedral mesh, and the total number of grids of the model was 1372037.

In this paper, the Scheil model was selected for simulation. It is a mathematical model used to simulate the solidification process of alloys. Named after the German metallurgist Theodor Scheil, the model is used to describe the changes in the composition of the solid and liquid phases of alloys during solidification.

To limit the computational time, the model relies on the following assumptions:

- (1) The solidification shrinkage was not taken into account;
- (2) The self-nucleation was not taken into consideration;
- (3) The model assumes that the solidification process was carried out under equilibrium conditions, and each solid phase and liquid phase in the alloy were formed under their equilibrium conditions;
- (4) The model ignores the reverse reaction between the solid phase and liquid phase, and the formed solid phase no longer reacts with the liquid phase;
- (5) The simulation assumes that the elements in the alloy are ideally mixed, and the effect of element diffusion on the solidification structure was ignored.

In this study, the billet elements from a steel mill were imported into ProCAST software 17.5, and  $c_i$ ,  $m_i$ ,  $k_i$  and other values required for simulation could be calculated, as shown in Table 1. The G-T coefficient of 20# steel is  $2 \times 10^{-7} \text{ m}\cdot\text{K}$ , and the growth kinetic parameter  $a_2 = 1.798 \times 10^{-6} \text{ m}\cdot\text{s}^{-1}\cdot\text{K}^{-2}$ .  $a_3 = 3.529 \times 10^{-6} \text{ m}\cdot\text{s}^{-1}\cdot\text{K}^{-2}$ .

**Table 1.** Simulation calculation parameter.

Element	Content (wt.%)	k	m	$D/\text{m}^2\cdot\text{s}^{-1}$
C	0.200	0.170784	−82.6456	$3 \times 10^{-9}$
Si	0.270	0.594312	−16.3372	$3 \times 10^{-9}$
Mn	0.500	0.710554	−5.22204	$3 \times 10^{-9}$
P	0.035	0.310875	−27.0198	$3 \times 10^{-9}$
S	0.035	0.036319	−39.9102	$3 \times 10^{-9}$
Cr	0.010	0.884948	−2.20964	$3 \times 10^{-9}$
Ni	0.010	0.818543	−3.33588	$3 \times 10^{-9}$
Cu	0.010	0.827207	−3.48933	$3 \times 10^{-9}$

The thermal physical parameters used in the simulation process include enthalpy change, density thermal conductivity, solid phase ratio, etc., as shown in Figure 1. The liquidus is 1786 K, and the solid phase is 1751 K.

Considering the efficiency and accuracy of numerical simulation, appropriate simplification was conducted in the process of numerical simulation. The filling process was ignored in the simulation, and the initial state of the model was assumed to be full of melt. Specific nucleation simulation parameters in the simulation process are shown in Table 2. The nucleation parameters adopted in the simulation mainly refer to the values provided by ESI Company, and the influence of electromagnetic stirring on nucleation parameters is considered [27]; where  $n_{v, \max}$  is the maximum volume nucleation density;  $\Delta T_{v, \max}$  is the maximum supercooling of volume nucleation,  $\Delta T_{v, \sigma}$  is the maximum supercooling standard deviation of volume nucleation.  $n_{s, \max}$  is the maximum surface nucleation density,  $\Delta T_{s, \max}$  is the maximum supercooling of surface nucleation,  $\Delta T_{s, \sigma}$  is the maximum supercooling standard deviation of surface nucleation. The values in Table 2 are derived from the experience of searching ESI companies and publishing-related papers [24–26]. These references are all publicly published books. When the values were cited in the manuscript, we significantly added reference numbers with full source information. Therefore, under the terms of the Creative Commons CC BY license, we believe that these references could be cited without permission.

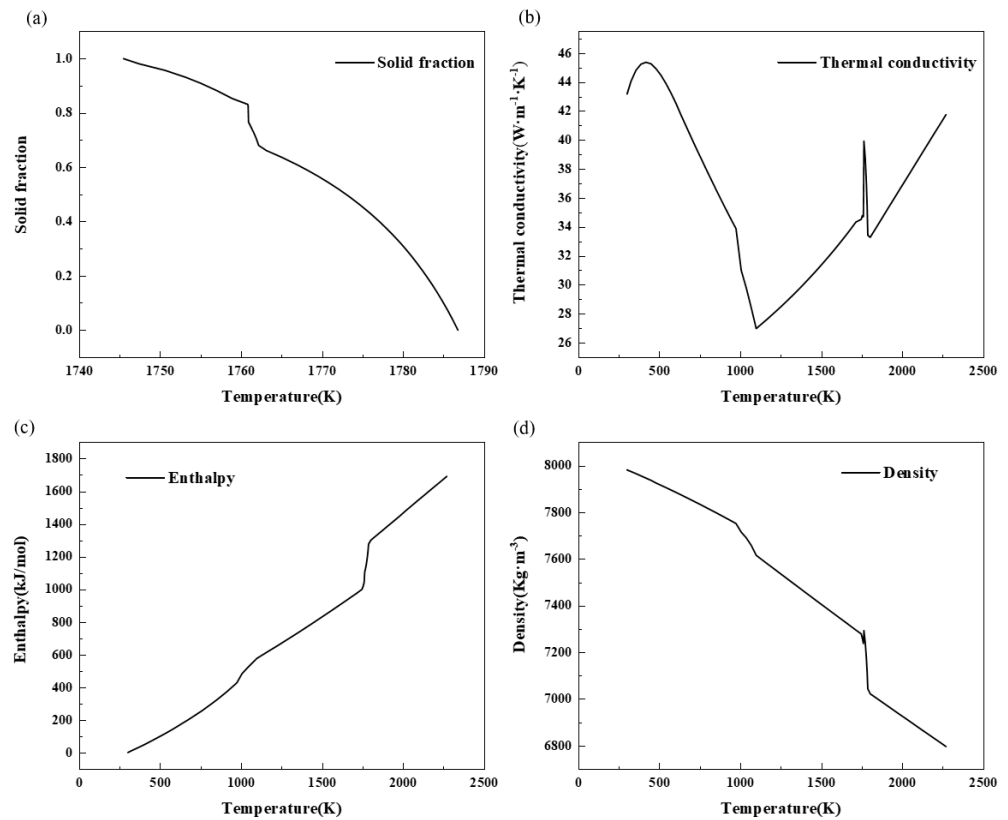


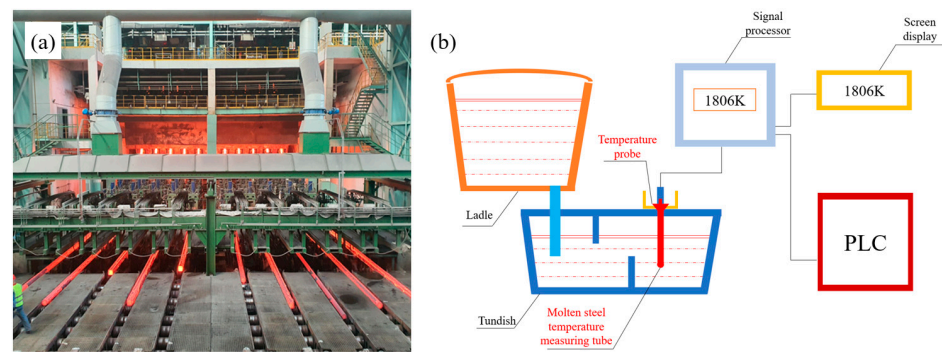
Figure 1. Thermophysical property parameters.

Table 2. Nucleation simulation parameters.

Nucleation Parameter	$n_{v, \max}/K$	$\frac{\Delta T_{v, \max}}{\sigma/K}$	$\Delta T_{v, \sigma}/K$	$n_{s, \max}/K$	$\Delta T_{s, \max}/K$	$\Delta T_{s, \sigma}/K$
Value	$1 \times 10^9$	10	1	$3 \times 10^7$	10	1

### 3. Experimental Implementation

On the basis of simulation, experiments were carried out using a small billet continuous casting machine in a steel plant. The main parameter of the continuous casting machine is a 10-flow full arc square billet continuous casting machine, and the main parameters of the cooling system are the use of segmented water cooling as well as aerosol cooling. The main composition of the billet is 20# steel. Figure 2a shows the continuous casting production site, and Figure 2b shows the superheat continuous temperature measurement equipment, and superheat measurement using BCT-V-A continuous temperature measurement device. This device is manufactured in China Shenyang Taihe Metallurgical Measurement and Control Technology Co., Ltd. (Shenyang, China). The cast billet was processed by grinding machine and pickling to treat the low-power structure. We used 30% hydrochloric acid and water to mix 1:1. We heated the acid solution to 328 K and let the cast billet stand for 5–10 min to obtain the low-power structure, then we observed and measured the equiaxed crystal region.



**Figure 2.** Billet production: (a) Continuous casting production site; (b) Continuous temperature measuring equipment.

## 4. Results and Discussion

### 4.1. Simulation Verification

A full-size model of continuous casting was established, with a cross-section of  $200\text{ mm} \times 200\text{ mm}$  and an arc radius of  $10,000\text{ mm}$ . The wall heat transfer parameters were adjusted, and the inlet temperature was set to  $1806\text{ K}$ , that is, the superheat was  $20\text{ K}$ . The surface temperature was simulated, and the actual temperature was measured with an infrared temperature gun on the basis of the simulation. The measured data were compared with the simulated data, as shown in Figure 3.

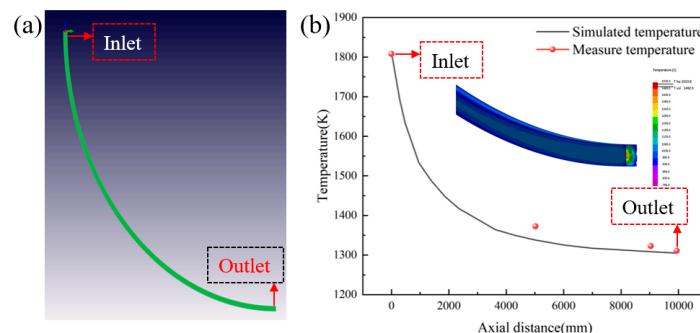


**Figure 3.** Comparison between simulated surface temperature and measured value: (a) Continuous casting model; (b) Comparison of test and simulation results.

From Figure 3, the simulation data match at both ends. At the axial distance of  $5500\text{ mm}$ , the measured temperature is  $1373\text{ K}$ , while the simulated temperature is  $1338\text{ K}$ ; the reason for the error is in the measurement using the infrared thermometer, which measures the surface fluctuations and the temperature difference is large. The measured temperature at the axial distance of  $10,000\text{ mm}$  is  $1311\text{ K}$ , and the simulated temperature here is  $1305\text{ K}$ ; the relative error is  $0.58\%$ , and it can be considered that the model verification is accurate. After simulation verification, the calculation results of the final  $50\text{ mm}$  of the whole process model were intercepted for analysis.

### 4.2. Simulation of Solidification Structure Evolution with Different Superheat

Columnar crystal evolution is a form of crystal growth during solidification, usually along a certain direction or axial growth, forming columnar grains. Temperature gradient and solidification rate are the key factors affecting the solidification structure and evolution of columnar crystals. Smaller temperature gradients and slower solidification rates are more conducive to the formation of equiaxed crystals. Therefore, in this study, by controlling the superheat parameters of the continuous casting process, the growth of columnar crystals and the transformation of columnar crystals to equiaxed crystals in continuous casting steel were simulated.

Low-temperature casting can reduce the internal and external temperature gradient of the billet and inhibit the growth of columnar crystals. This study simulated the solidification structure of the casting billet by changing the superheat [28,29]. In order to simplify the calculation of the simulation, the simulated temperature calculated in the model validation was used to simulate the model with a thickness of 50 mm. Figure 4 is the schematic diagram of the cross-sectional solidification process of the billet when the superheat is 60 K. Figure 5 is the schematic diagram of the cross-sectional solidification process of the billet when the superheat is 40 K. Figure 6 is the schematic diagram of the cross-sectional solidification process of the billet when the superheat is 20 K.



**Figure 4.** Superheat 60 K billet solidification process: (a) 1 s; (b) 42 s; (c) 92 s; (d) 202 s; (e) 252 s.

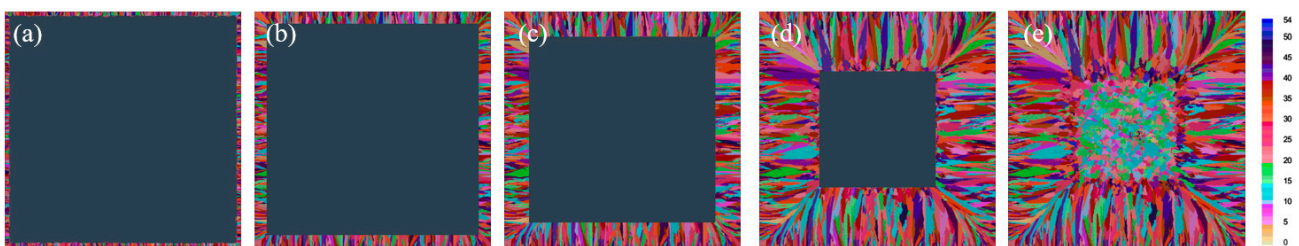


**Figure 5.** Superheat 40 K billet solidification process: (a) 1 s; (b) 42 s; (c) 92 s; (d) 202 s; (e) 250 s.

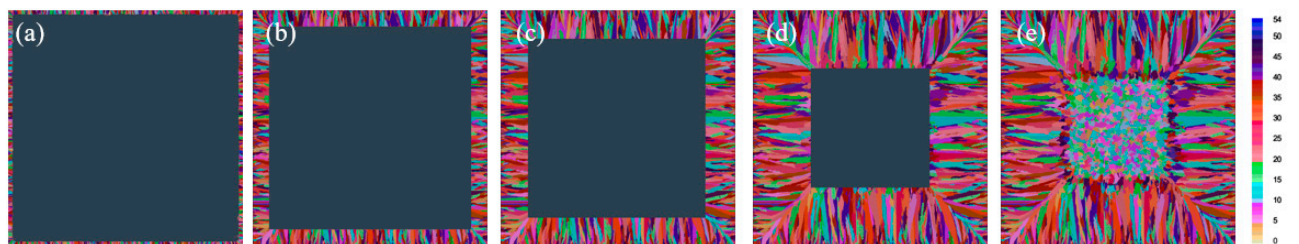


**Figure 6.** Superheat 20 K billet solidification process: (a) 1 s; (b) 42 s; (c) 92 s; (d) 202 s; (e) 245 s.

From Figure 4, at the 1 s mark, the presence of substantial heat exchange at the wall initiates rapid solidification, giving rise to the formation of an excitatory cooling layer. This process results in the development of a thin, finely crystallized zone. By the 42 s mark, columnar crystal growth becomes evident in Figure 4b, originating from the fine crystal zone. Notably, the orientation of columnar crystal growth exhibits inconsistency, attributed to the anisotropy arising from inconsistent cooling intensity along the heat flow direction. As time progresses to 92 s, the columnar crystals reach full growth. Subsequently, at 202 s, a significant transformation known as the columnar-to-equiaxed transition (CET) occurs at the conclusion of columnar crystal growth. This transition marks the shift from columnar crystal morphology to equiaxed crystal formation. Finally, at the 252 s mark, the cast billet undergoes complete solidification, signifying the culmination of the observed stages in the continuous casting process. These temporal landmarks, elucidated through the sequential analysis of Figure 4, offer crucial insights into the dynamic evolution of microstructural features during the solidification process. The observed phenomena,



including the development of the excitatory cooling layer, fine crystal zone, and the subsequent CET transformation, contribute to a comprehensive understanding of the intricate interactions taking place in the continuous casting of billets.

From Figure 5, when the time is 1 s, the grain growth of the section is compared and the chilling layer of the wall is fully grown at the same time. When the time is 42 s, the columnar crystal starts to grow, and the growth rate of the columnar crystal will be different due to the different superheat. When the time is 92 s, the cylindrical crystal in the corner begins to grow to the center position, which promotes the formation of equiaxed crystals to a certain extent. When the time is 202 s, the columnar crystals have grown completely, and CET transformation is carried out at the apex of the columnar crystals. Compared with the superheat of 60 K, the transition trend of columnar crystals to equiaxed crystals is different due to the temperature difference at the same time point. When the time is 250 s, the casting billet is completely solidified, and there is a tendency to expand in the central equiaxed crystal region when the superheat is 60 K, and the complete solidification time is reduced by 2 s when the superheat is 60 K, indicating that the decrease of superheat also slows down the growth rate of the solidified structure cylindrical crystals and equiaxed crystals.

From Figure 6, when the time is 1 s, compared with the superheat of 60 K and 40 K, the chill layer of 20 K is fully grown, and a fine crystal zone of about 5 mm is formed on the wall. When the time is 42, the growth rate of columnar crystals is faster because of the low superheat. When the time is 92 s, the growth of corner columnar crystals accelerates the growth of wall columnar crystals to the center position. Compared with the superheat conditions of 60 K and 40 K, the maximum distance between the growth end of columnar crystals and the wall is 26 mm. When the time is 202 s, the columnar crystal achieves complete growth and CET transition occurs at the end of columnar crystal growth. When the time is 245 s, the complete solidification time is reduced by 7 s compared with the casting billet with 60 K superheat, 5 s compared with the casting billet with 40 K superheat, and the central equiaxed crystal rate is increased, the superheat is further reduced, the equiaxed crystal area is expanded and the performance of the casting billet is improved. Figure 7 shows the dendrite growth of solidified tissue at the section of casting billet with superheat of 20 K, 40 K and 60 K.

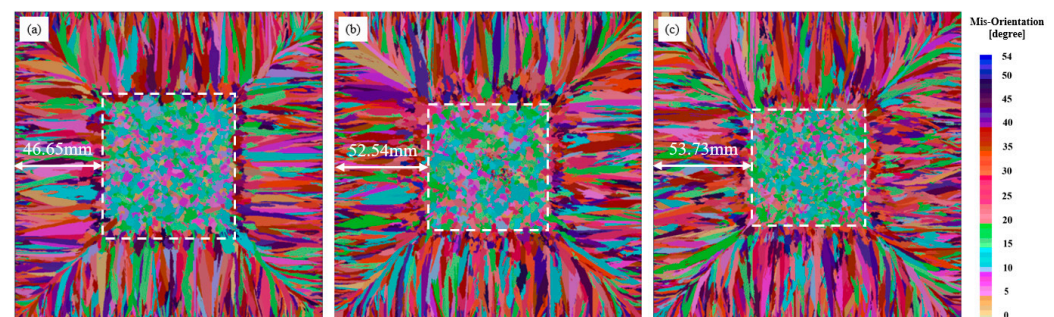


**Figure 7.** Simulation results of different superheat degrees on solidification organization: (a) Superheat 20 K; (b) Superheat 40 K; (c) Superheat 60 K.

From Figure 7, the solidification organization is divided into three regions, the surface fine crystal region, the columnar crystal region and the central equiaxed crystal region. The evolution rule is that the fine crystal zone on the surface of the ingot gradually develops into a coarse columnar crystal zone along the radial direction, while the central part of the ingot is the equiaxed crystal zone, and the simulated solidification tissue evolution is in accordance with the solidification theory. It is obvious from the solidification tissue growth state that the size of columnar crystals becomes larger and larger as the superheat increases, and the original growth area of equiaxed crystals is occupied by columnar crystals, while the growth area of equiaxed crystals decreases in scope and the size of equiaxed crystals also increases slightly. In order to analyze the simulation results in detail, the isometric crystal size measurements were performed using ImageJ 1.8.0 software. Table 3 shows the



calculation results about the number of grains, etc., under different superheat degrees, and Figure 8 shows the effect of different superheat degrees on the isometric crystal size.

**Table 3.** Calculated the number of grains at different superheats.

Statistical Items	Superheat 20 K	Superheat 40 K	Superheat 60 K
Number of grains	25,662	23,146	22,476
Average grain area/mm <sup>2</sup>	1.104	1.295	1.398
Average grain radius/mm	0.84556	0.94281	1.07653
Percentage of radial equiaxed crystal region/%	53.35	47.46	46.27

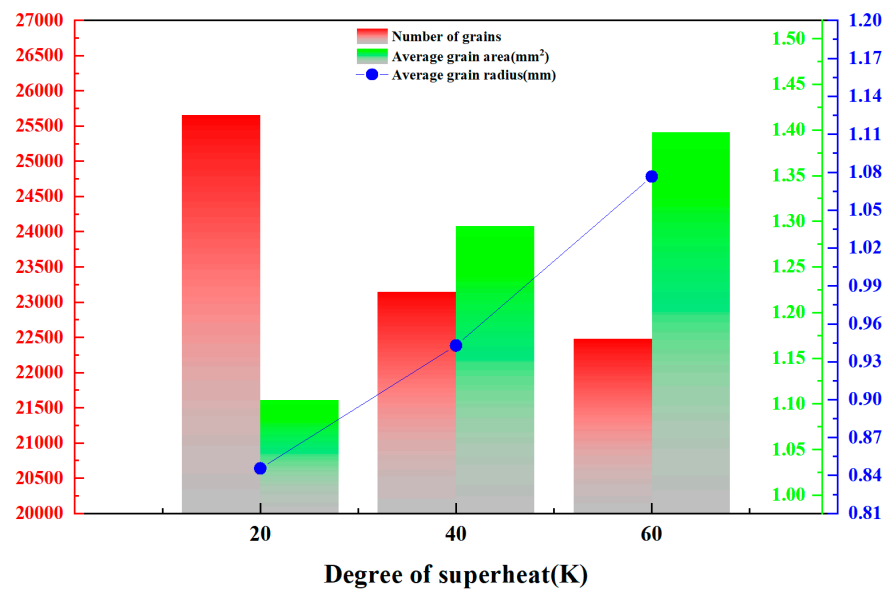


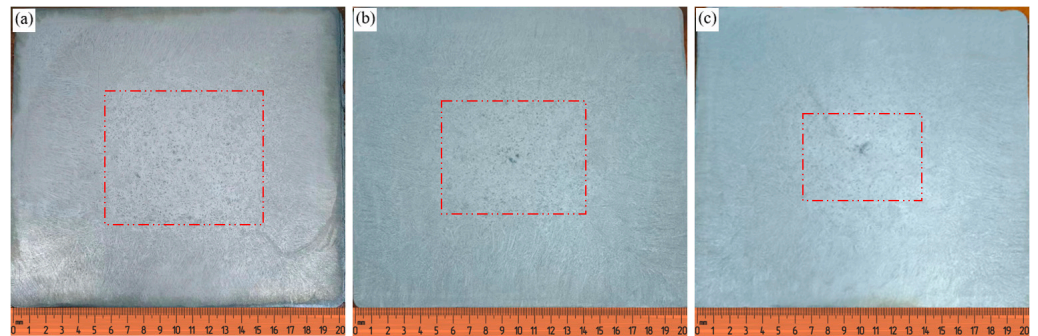
**Figure 8.** Statistics on the effect of different superheat degrees on the size of equiaxed crystals.

From Table 3, the percentage of equiaxed crystal zone decreases from 53.35% to 46.27% when the superheat degree increases from 20 K to 60 K. With the increase of superheat degree, the temperature gradient in the liquid metal increases, which is not conducive to the formation of nuclei inside the melt, resulting in the decrease of the percentage of equiaxed crystal zone. With the increase of superheat degree, a larger temperature gradient exists in the solid–liquid phase dendrite front, which promotes the growth of columnar crystals and expands the proportion of columnar crystals. From Figure 8, the red number represents the number of grains, the green number represents the average grain area, and the blue number represents the average grain radius. The number of grains decreases when the superheat degree increases from 20 K to 60 K, the number of grains decreases from the maximum value of 25,662 to 22,476, the average grain area increases from 1.104 mm<sup>2</sup> to 1.398 mm<sup>2</sup>, and the average grain size increases from 0.84556 mm to 1.07653 mm, which reduces the heat transfer efficiency of the steel due to the increase of superheat degree. In this case, the degree of nucleation supercooling is not sufficient to provide isometric nucleation growth force, resulting in columnar crystal growth and reduction of isometric crystal area. On the other hand, the increase in temperature causes the solidified columnar crystals to remelt and inhibits the growth of equiaxed crystals.

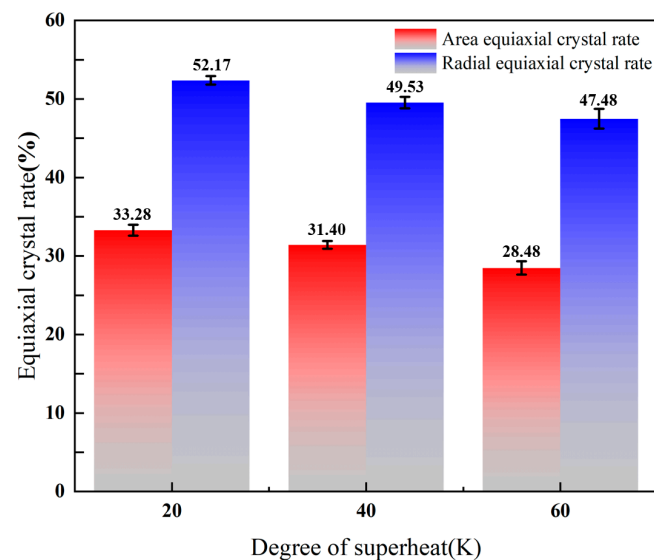
#### 4.3. Experiment of Influence of Different Superheat on Solidification Structure

Figure 7 shows the pictures of the low power structure of a 200 mm × 200 mm small billet at superheat degrees of 20 K, 40 K and 60 K. The low power structure is divided into equiaxed crystal areas using ImageJ 1.8.0 software, and the area divided by the red line

in Figure 9 is the equiaxed crystal area. The comparison of the low power structure at superheat 20 K with the simulation results is shown in Figure 10.



**Figure 9.** Test results of cast billets at different superheat levels: (a) Superheat 20 K; (b) Superheat 40 K; (c) Superheat 60 K.



**Figure 10.** The influence of superheat on the area equiaxed crystal rate and radial equiaxed crystal rate of casting billet.

From Figure 9, it can be seen that under different superheat conditions, there is a big difference in the growth morphology of the cast billet low times, when the superheat is lower, the difference of the melt temperature gradient is smaller, the columnar crystal grows more slowly in the solidification front, and the supercooled liquid zone in front of the columnar crystal tip also widens, which inhibits the growth of columnar crystal and increases the proportion of equiaxed crystal zone. In Figure 9b,c, it is obvious that high superheat degree casting will cause central shrinkage defects in the cast billet.

From Figure 10, with the increase of superheat, the area equiaxed crystal rate decreases from 33.28% to 28.48%, and the radial equiaxed crystal rate decreases from 52.17% to 47.48%. Therefore, the equiaxed crystal rate decreases with the increase of superheat. The change of superheat mainly affects the growth of columnar crystals and the formation of equiaxed crystal regions. In the case of low superheat, the grain growth may be more random, resulting in a more uniform grain orientation distribution in the final billet, leading to a more dense equiaxed grain [30]. At the same time, a lower superheat may produce a relatively uniform texture. The formation of texture is closely related to the orientation of grain, which has a significant effect on the anisotropy and mechanical properties of the material [31]. The effect of superheat on crystal direction is realized by adjusting the mode and orientation of grain growth. In the continuous casting process, the orientation

distribution of the crystals during solidification can be adjusted by controlling the superheat, thus affecting the microstructure and macroscopic properties of the final casting billet [32]. Figure 11 shows the effect of different superheat degrees on the equiaxed crystal rate of cast billets. Figure 12 shows the comparison between the simulated results and the test results on the equiaxed crystal rate of the casting billet under different superheat conditions.

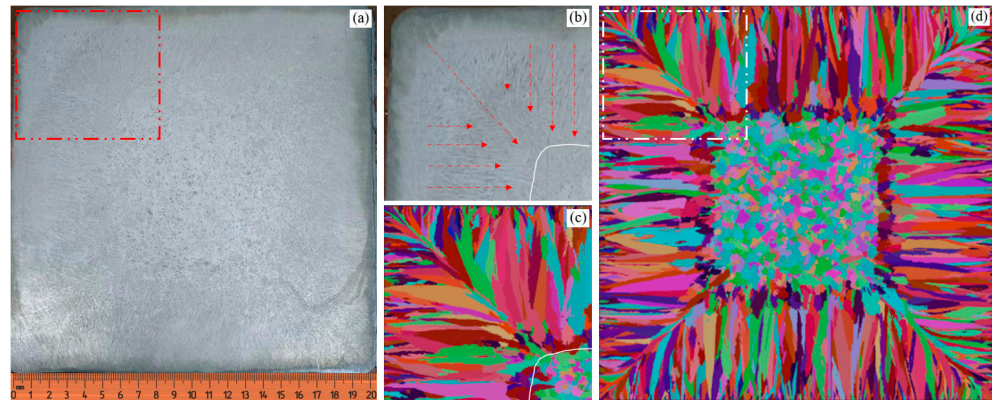


**Figure 11.** Comparison of test and simulation results under 20 K superheat condition: (a) Test results; (b) Test results corner; (c) Corners of simulation results; (d) Simulation results.

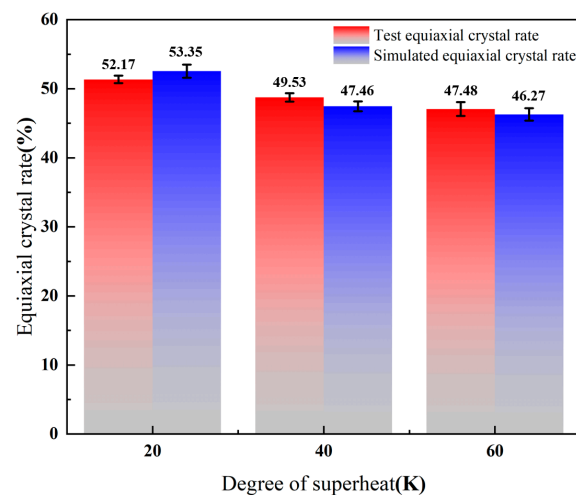


**Figure 12.** The effect of superheat on the equiaxed crystal rate of casting billet is compared between simulation results and test results.

From Figure 11, the red arrow in the figure indicates the growth direction of the columnar crystal, and the edge area is enlarged. We combine Figures 11 and 12 for analysis, it can be seen that the solidification organization of the small billet tends to be consistent with the simulation results under the same superheat degree, which confirms the feasibility of the simulation. When the superheat is 20 K, the simulated equiaxed crystal rate reaches the highest value, which is 53.35%, and the standard deviation is 0.55%. When the superheat is 40 K, the simulated equiaxed crystal rate decreases to 47.46% and the standard deviation is 0.61%. When the superheat is 60 K, the simulated equiaxed crystal rate reaches the lowest value, which is 46.27%, and the standard deviation is 1.01%. It can be seen that billet defects such as shrinkage are prone to occur at high superheat, so a lower superheat should be controlled in practice to expand the area of the isometric crystal zone and improve the quality of the billet.

## 5. Conclusions

- (1) The simulation results of solidification microstructure evolution during the solidification process of casting billet with different superheats indicate that increasing superheat can inhibit the growth of equiaxed crystals and reduce the size of equiaxed crystals. The lower the superheat, the lower the edge temperature gradient, and the slower the solidification rate of the billet, which is more conducive to the growth of the medium axis of the billet. When the superheat increases from 20 K to 60 K, the proportion of the equiaxed crystal region decreases from 53.35% to 46.27%. This relationship reflects the influence of superheat on the solidification process of casting billet.
- (2) The experimental study of the effect of different superheats on the solidification structure of the casting billet shows that under the same conditions, the difference in equiaxed crystal rate is not significant between the simulated results and the field test results. The proportion of the equiaxed crystal region at low magnification shows that the equiaxed crystal region decreases and the columnar crystal region increases when the superheat is increased from 20 K to 60 K. Under the test condition that the superheat is increased from 20 K to 60 K, the equiaxed crystal rate decreases from 52.17% to 47.48%. When the simulated superheat increases from 20 K to 60 K, the equiaxed crystal rate decreases from 53.35% to 46.27%, indicating that the effect of different superheats on the solidification structure is consistent with the simulated results.

**Author Contributions:** Conceptualization, N.T., G.Z., P.Y. and P.L.; Formal analysis, N.T., G.Z. and P.L.; Funding acquisition, G.Z.; Methodology, N.T., Z.F. and X.W.; Project administration, G.Z.; Validation, N.T. and P.L.; Writing—original draft, N.T.; Writing—review & editing, G.Z. All authors have read and agreed to the published version of the manuscript.

**Funding:** The work was supported by the Special Steel Continuous Casting MEMS+FEMS Project from Hunan Zhongke Electric Co., Ltd., grant number “HZ2021F0529A” and the Scientific Research Fund of Education Department of Yunnan Province, China, grant number “2023J0130”.

**Institutional Review Board Statement:** Not applicable.

**Informed Consent Statement:** Not applicable.

**Data Availability Statement:** The data presented in this study are available on request from the corresponding author.

**Conflicts of Interest:** Author Pengchao Li was employed by the company Linyi Iron and Steel Investment Group Special Steel Co., Ltd. The remaining authors declare that the research was conducted in the absence of any commercial or financial relationships that could be construed as a potential conflict of interest.

## References

1. Zaeem, M.A.; Yin, H.; Felicelli, S.D. Modeling dendritic solidification of Al–3%Cu using cellular automaton and phase-field methods. *Appl. Math. Model.* **2013**, *37*, 3495–3503. [CrossRef]
2. Böttger, B.; Apel, M.; Santillana, B.; Eskin, D. *Phase-Field Modelling of Microstructure Formation during the Solidification of Continuously Cast Low Carbon and HSLA Steels*; IOP Conference Series: Materials Science and Engineering; IOP Publishing: Bristol, UK, 2012; p. 012107.
3. Reuther, K.; Rettenmayr, M. Perspectives for cellular automata for the simulation of dendritic solidification—A review. *Comput. Mater. Sci.* **2014**, *95*, 213–220. [CrossRef]
4. Sun, T.; Yue, F.; Wu, H.J.; Guo, C.; Li, Y.; Ma, Z.C. Solidification Structure of Continuous Casting Large Round Billets under Mold Electromagnetic Stirring. *J. Iron Steel Res.* **2016**, *23*, 9. [CrossRef]
5. Fang, Q.; Ni, H.; Zhang, H.; Wang, B.; Liu, C. Numerical Study on Solidification Behavior and Structure of Continuously Cast U71Mn Steel. *Metals* **2017**, *7*, 483. [CrossRef]
6. Stefanescu, D.M. *Science and Engineering of Casting Solidification*; Springer: Berlin/Heidelberg, Germany, 2015.
7. Zhong, H.; Wang, R.; Han, Q.; Fang, M.; Yuan, H.; Song, L.; Xie, X.; Zhai, Q. Solidification structure and central segregation of 6Cr13Mo stainless steel under simulated continuous casting conditions. *J. Mater. Res. Technol.* **2022**, *20*, 3408–3419. [CrossRef]
8. Sheng, Y.; Meng, X.; Liu, X.; Zhou, Z. Numerical Simulation of Solidification Structures Influenced by Cooling Spraying and Process Parameters Based on Cellular Automaton Finite-Element Model. *Steel Res. Int.* **2023**, *94*, 2200874. [CrossRef]


9. Cao, J.; Hou, Z.; Guo, Z.; Guo, D.; Tang, P. Effect of Superheat on Integral Morphology Characteristics of Solidification Structure and Permeability in Bearing Steel Billet. *Acta Met. Sin.* **2021**, *57*, 586–594.
10. Zhao, Y.; Chen, D.; Ma, M.; Wan, X.; Li, Y.; Qin, R. A Cellular Automaton Model Coupled with Finite Element Method for Solidification Process of Beam Blank Continuous Casting. In Proceedings of the EPD Congress 2015, Orlando, FL, USA, 15–18 May 2015; Springer: Berlin/Heidelberg, Germany, 2016; pp. 41–47.
11. An, H.; Bao, Y.; Wang, M.; Yang, Q.; Dang, Y. Numerical and experimental investigation of solidification structure evolution and reduction of centre segregation in continuously cast GCr15 bloom. *Ironmak. Steelmak.* **2020**, *47*, 1063–1077. [CrossRef]
12. Xiao, Z.; Dong, S.; Nie, S.; Ma, Z.; Lv, Z. *Simulation of the Solidification Organization of X15CrNiSi20-12 Alloy Castings during Investment Casting Based on the CAFE Model*; IOP Publishing Ltd.: Bristol, UK, 2023.
13. Yamazaki, M.; Natsume, Y.; Harada, H.; Ohsasa, K. Numerical simulation of solidification structure formation during continuous casting in Fe-0.7mass% C alloy using cellular automaton method. *ISIJ Int.* **2018**, *46*, 903–908. [CrossRef]
14. Kalikmanov, V.I. Classical nucleation theory. In *Nucleation Theory*; Springer: Berlin/Heidelberg, Germany, 2012; pp. 17–41.
15. Domitner, J.; Kharicha, A.; Wu, M.; Ludwig, A. Application of microprobe analysis to the reconstruction and characterization of dendritic structures. *Metall. Mater. Trans. A* **2013**, *44*, 607–616. [CrossRef]
16. Yasuda, H.; Yamamoto, Y.; Nakatsuka, N.; Yoshiya, M.; Nagira, T.; Sugiyama, A.; Ohnaka, I.; Uesugi, K.; Umetani, K. In situ observation of solidification phenomena in Al–Cu and Fe–Si–Al alloys. *Int. J. Cast Met. Res.* **2009**, *22*, 15–21. [CrossRef]
17. Davis, S.H. *Theory of Solidification*; Cambridge University Press: Cambridge, UK, 2001.
18. Fallah, V.; Amoozazei, M.; Provatias, N.; Corbin, S.; Khajepour, A. Phase-field simulation of solidification morphology in laser powder deposition of Ti–Nb alloys. *Acta Mater.* **2012**, *60*, 1633–1646. [CrossRef]
19. Böttger, B.; Schmitz, G.; Santillana, B. Multi-phase-field modeling of solidification in technical steel grades. *Trans. Indian Inst. Met.* **2012**, *65*, 613–615. [CrossRef]
20. Elahi, S.; Tavakoli, R.; Romero, I.; Tourret, D. Grain growth competition during melt pool solidification—Comparing phase-field and cellular automaton models. *Comput. Mater. Sci.* **2023**, *216*, 111882. [CrossRef]
21. Saunders, N.; Miodownik, A. *CALPHAD (Calculation of Phase Diagrams): A Comprehensive Guide*; Pergamon Materials Series; Pergamon: Oxford, UK, 1998; p. 465.
22. Soar, P.; Kao, A.; Pericleous, K. The impact of two and three dimensional assumptions on coupled structural mechanics and microstructure solidification modelling. *Crystals* **2023**, *13*, 114. [CrossRef]
23. Kurz, W.; Giovanola, B.; Trivedi, R. Theory of microstructural development during rapid solidification. *Acta Metall.* **1986**, *34*, 823–830. [CrossRef]
24. Esaka, H.; Wakabayashi, T.; Shinozuka, K.; Tamura, M. Origin of equiaxed grains and their motion in the liquid phase. *ISIJ Int.* **2003**, *43*, 1415–1420. [CrossRef]
25. Sterkhova, I.; Kamaeva, L.V.; Lad'yanov, V.I.; Chtchelkatchev, N. Structure and solidification of the (Fe<sub>0.75</sub>B<sub>0.15</sub>Si<sub>0.1</sub>)<sub>100-x</sub>Tax (x = 0–2) melts: Experiment and machine learning. *J. Phys. Chem. Solids* **2023**, *174*, 111143. [CrossRef]
26. Khosroaghayani, M.; Khorasani, M.; Alavi Zaree, S.; Eskandari, M. Investigation of microstructure and mechanical properties of AZ91 magnesium alloy produced by directional solidification method in different angles using cafe simulation. *Int. J. Met.* **2023**, *17*, 195–209. [CrossRef]
27. Ji, K.; Dorari, E.; Clarke, A.J.; Karma, A. Microstructural pattern formation during far-from-equilibrium alloy solidification. *Phys. Rev. Lett.* **2023**, *130*, 026203. [CrossRef]
28. Mohammed, W.; Firoozbakht, M.; Bührig-Polaczek, A. Study of the Solidification Behavior and Homogenization Heat Treatment of the Investment-Cast Al–Cu Foams: Experimental and Modelling Investigations. In Proceedings of the TMS Annual Meeting & Exhibition, San Diego, CA, USA, 19–23 March 2023; Springer: Berlin/Heidelberg, Germany, 2023; pp. 627–634.
29. Jeong, J.J.; Lee, H.; Yun, D.W.; Jeong, H.W.; Yoo, Y.-S.; Seo, S.-M.; Lee, J.H. Analysis of a Single Crystal Solidification Process of an Ni-based Superalloy using a CAFE Model. *Korean J. Met. Mater.* **2023**, *61*, 126–136. [CrossRef]
30. Cao, J.; Zeng, Z.; Zhang, F.; Guo, D.; Hou, Z. Effect of Cooling Rates on the Local—Overall Morphology Characteristics of Solidification Structure at Different Stages for High Carbon Steel. *Metals* **2021**, *11*, 1291. [CrossRef]
31. Cao, J.; Hou, Z.; Guo, D.; Guo, Z.; Tang, P. Morphology characteristics of solidification structure in high-carbon steel billet based on fractal theory. *J. Mater. Sci.* **2019**, *54*, 12851–12862. [CrossRef]
32. Wang, W.; Hou, Z.-B.; Chang, Y.; Cao, J.-H. Effect of superheat on quality of central equiaxed grain zone of continuously cast bearing steel billet based on two-dimensional segregation ratio. *J. Iron Steel Res. Int.* **2018**, *25*, 9–18. [CrossRef]

**Disclaimer/Publisher's Note:** The statements, opinions and data contained in all publications are solely those of the individual author(s) and contributor(s) and not of MDPI and/or the editor(s). MDPI and/or the editor(s) disclaim responsibility for any injury to people or property resulting from any ideas, methods, instructions or products referred to in the content.



## Article

# The Construction of a Lattice Image and Dislocation Analysis in High-Resolution Characterizations Based on Diffraction Extinctions

Kun Ni, Hanyu Wang, Qianying Guo, Zumin Wang, Wenxi Liu and Yuan Huang \* 

School of Materials Science and Engineering, Tianjin University, Tianjin 300354, China

\* Correspondence: tju\_huangyuan@163.com

**Abstract:** This paper introduces a method for high-resolution lattice image reconstruction and dislocation analysis based on diffraction extinction. The approach primarily involves locating extinction spots in the Fourier transform spectrum (reciprocal space) and constructing corresponding diffraction wave functions. By the coherent combination of diffraction and transmission waves, the lattice image of the extinction planes is reconstructed. This lattice image is then used for dislocation localization, enabling the observation and analysis of crystal planes that exhibit electron diffraction extinction effects and atomic jump arrangements during high-resolution transmission electron microscopy (HRTEM) characterization. Furthermore, due to the method's effectiveness in localizing dislocations, it offers a unique advantage when analyzing high-resolution images with relatively poor quality. The feasibility of this method is theoretically demonstrated in this paper. Additionally, the method was successfully applied to observed edge dislocations, such as  $1/6[21\bar{1}]$ ,  $1/6[\bar{2}11]$ , and  $1/2[0\bar{1}1]$ , which are not easily observable in conventional HRTEM characterization processes, in electro-deposited Cu thin films. The Burgers vectors were determined. Moreover, this paper also attempted to observe screw dislocations that are challenging to observe in high-resolution transmission electron microscopy. By shifting a pair of diffraction extinction spots and superimposing the reconstructed images before and after the shift, screw dislocations with a Burgers vector of  $1/2[01\bar{1}]$  were successfully observed in electro-deposited Cu thin films.



**Citation:** Ni, K.; Wang, H.; Guo, Q.; Wang, Z.; Liu, W.; Huang, Y. The Construction of a Lattice Image and Dislocation Analysis in High-Resolution Characterizations Based on Diffraction Extinctions. *Materials* **2024**, *17*, 555.

<https://doi.org/10.3390/ma17030555>

Academic Editor: Antonio Polimeni

Received: 26 December 2023

Revised: 18 January 2024

Accepted: 22 January 2024

Published: 24 January 2024



**Copyright:** © 2024 by the authors. Licensee MDPI, Basel, Switzerland. This article is an open access article distributed under the terms and conditions of the Creative Commons Attribution (CC BY) license (<https://creativecommons.org/licenses/by/4.0/>).

**Keywords:** HRTEM; dislocation; Fourier transform; Burgers vector

## 1. Introduction

The high-resolution transmission electron microscope (HRTEM) is a widely used technique for characterizing the microstructures of materials [1–7]. It is an imaging technique that is based on the phase contrast principle [8] and comprises two fundamental processes: the incident electron beam scatters after passing through a thin crystal specimen and undergoes Fourier transformation in the back focal plane of the objective lens, forming a diffraction pattern that carries crystal structure information. Subsequently, interference between the transmitted beam and multiple diffracted beams occurs, leading to Fourier inverse transformation to reconstruct high-resolution images of the crystal structure in the image plane of the objective. Clearly, the formation of high-resolution images involves the two mathematical processes of Fourier transformation and inverse transformation [9].

Using high-resolution transmission electron microscopy, one can obtain one- and two-dimensional lattice images and structural images, with two-dimensional lattice images and structural images being directly applicable to the observation of crystal defects such as dislocations within the crystal. Due to the abundance of information in actual lattice and structural images, it is often challenging to visually discern the distribution and features of certain crystal planes. Simultaneously, in cases where the dislocation analysis of specific regions of lattice images is required, there may be difficulties due to poor image clarity. In such cases, Fourier transformation can be applied to the regions of interest in



the lattice images, specific diffraction spots of particular crystal planes can be selected, noise can be filtered, and Fourier inverse transformation can be performed to reconstruct the fringe images of specific crystal planes, facilitating the localization and analysis of dislocations on those planes. However, due to the limitations of transmission electron microscopy principles, the information of certain crystal planes may be hidden, even if they satisfy Bragg diffraction conditions, causing diffraction extinction phenomena. Diffraction extinction is a very common phenomenon during TEM observations. It is characterized by the absence of an extinction spot at a location where it should theoretically exist. For different crystal structures, diffraction extinction shows different patterns. This is manifested during specific microscopic observations as the inability to find corresponding diffraction spots for these crystal planes in the diffraction pattern, making it challenging to directly analyze the arrangement patterns of these crystal planes. For example, in face-centered cubic (FCC) crystal structures, crystal planes with indices like  $\{011\}$  and  $\{012\}$  follow the “odd-even mixed” extinction rule, leading to the absence of corresponding spots in the electron diffraction pattern and Fourier transform spectrum. Thus, these spots cannot be directly selected for Fourier inverse transformation to reconstruct the corresponding fringe images, making it difficult to observe their dislocation distribution. Nevertheless, it is crucial to observe these types of crystal planes, as comprehensive analyses of full dislocations such as  $a/2\langle 110 \rangle$  and partial dislocations such as  $a/6\langle 112 \rangle$  and  $a/3\langle 112 \rangle$  are essential for a more detailed understanding of phenomena such as dislocation reactions [10,11], stacking faults, twinning mechanisms [12,13], and the strengthening mechanisms of certain metals [14,15].

Furthermore, the atomic arrangement on crystal planes that exhibit diffraction extinction often features a jumping arrangement under certain crystal zone axes, such as the distribution of the  $(\bar{1}12)$  plane in an FCC crystal under the  $[110]$  zone axis, as illustrated in Figure 1. This particular atomic arrangement makes direct observation of these crystal planes in lattice images challenging. In such cases, it becomes even more necessary to rely on fringe images for localization. However, in conventional approaches, due to the disappearance of corresponding diffraction spots, it becomes impossible to reconstruct fringe images, rendering localization operations unfeasible. Additionally, there is an ongoing challenge in the current high-resolution lattice imaging techniques concerning the observation of edge dislocations, which is relatively easier to achieve, while the observation of screw dislocations remains more challenging.

This research introduces a novel method for characterizing metal dislocations, termed the “High-Resolution Lattice Image Reconstruction and Dislocation Analysis Based on Diffraction Extinction” (HRLIRDE). This method is designed around a series of steps involving Fourier transformation, extinction position identification, the construction of extinction diffraction wave functions, filtering, lattice image reconstruction, and real image comparison analysis. Additionally, this study provides theoretical derivations for this method based on phase contrast dynamics [8,16] and high-resolution imaging principles, establishing its theoretical foundation.

Finally, the proposed method was applied to analyze edge and screw dislocations in HRTEM images of electro-deposited copper thin films. The results indicate that this method can effectively identify and determine the Burgers vectors of edge dislocations and screw dislocations. Its main advantage lies in the fact that it only requires high-resolution transmission electron microscopy (HRTEM) images for the analysis of edge and screw dislocations with Burgers vectors  $\langle 110 \rangle$  and  $\langle 112 \rangle$ . This reduces the complexity and cost of the research. Additionally, this method can also be applied to analyze high-resolution images with reduced clarity, where the dislocation positions are difficult to directly determine using conventional analysis techniques.

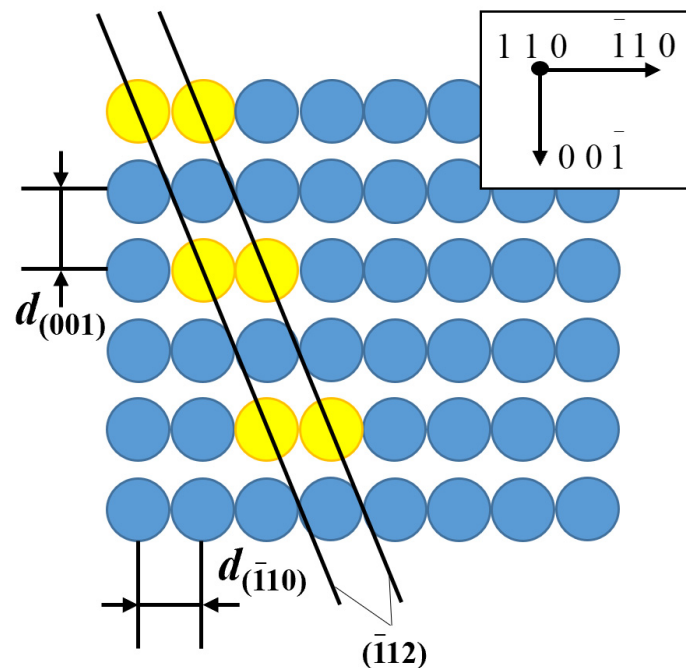


**Figure 1.** Schematic diagram of face-centered cubic crystal plane ( $\bar{1}12$ ) and its atom arrangement without diffraction spots but with extinction.

## 2. Method

### 2.1. Experimental Preparation for High-Resolution Transmission Electron Microscopy Observation

In this study, Cu films were prepared using the electro-deposition method for HRTEM observations. For the electro-deposition process, a high-purity titanium (Ti) foil (purity  $\geq 99.99\%$ , Zhongnuo New Material Company, Beijing, China) was used as the cathode. The choice of Ti as the cathode material was motivated by its inertness, which provides excellent corrosion resistance in both acidic and alkaline environments. Additionally, Ti is easily separable from the electro-deposited layer after deposition compared to steel substrates. Prior to electro-deposition, both the anode material (Cu plate) and cathode material (Ti foil, etc.) underwent pre-treatment procedures, including grinding, polishing, and cleaning, to remove oxide layers from the sample surfaces, ensuring smooth surfaces that are suitable for HRTEM observation.

An acid-based copper sulfate electro-deposition solution was employed, consisting primarily of  $\text{CuSO}_4 \cdot 5\text{H}_2\text{O}$  (200 g/L, Komeo Chemical Reagent Company, Tianjin, China), concentrated  $\text{H}_2\text{SO}_4$  (98%, Komeo Chemical Reagent Company, Tianjin, China), and trace amounts of additives, all of which were analytical-grade reagents. During electro-deposition, the solution was continuously stirred at a rate of 300 rpm in a temperature-controlled water bath to maintain uniform composition. The anode and cathode were positioned 10 cm apart, and the electro-deposition was conducted at a constant current density of  $30 \text{ mA/cm}^2$  at  $25^\circ\text{C}$  for 1 h to obtain the copper film. Subsequently, the film was cleaned and removed from the Ti substrate for TEM characterization. The equipment used in this study was a transmission electron microscope (Tecnai G2 F20 S-Twin, FEI Company, Eindhoven, The Netherlands).

### 2.2. HRTEM Observation and Analysis

Cu is an FCC metal, and its full dislocation Burgers vector is  $a/2\langle 110 \rangle$ , while partial dislocations have Burgers vectors such as  $a/6\langle 112 \rangle$  and  $a/3\langle 112 \rangle$  [12]. To observe the distribution, decomposition, and synthesis of these dislocations using HRTEM, it is advisable to align the incident electron beam along the zone axis  $\langle 110 \rangle$  [16]. Therefore, before observation, the zone axis  $[110]$  should be adjusted to ensure that it is parallel to the direction of the incident electron beam.

Since this paper primarily focuses on the proposed HRLIRDE method, it is necessary to first locate the dislocations. Due to the potential presence of numerous dislocations within or around the twin boundaries during the formation of twins (the growth mechanism of  $a/6\langle 112 \rangle$  partial dislocations within twin boundaries [12]) and the relatively common occurrence of Cu metal twinning, this study initially used the electron diffraction contrast imaging (EDCI) technique in TEM to identify the twinning structures in electro-deposited Cu thin films. Subsequently, the analysis mode was switched to high-resolution imaging to obtain HRTEM images. Figure 2 shows the EDCI image of the twinning structure (see Figure 2a) and the corresponding high-resolution image of the twin layers (see Figure 2b).

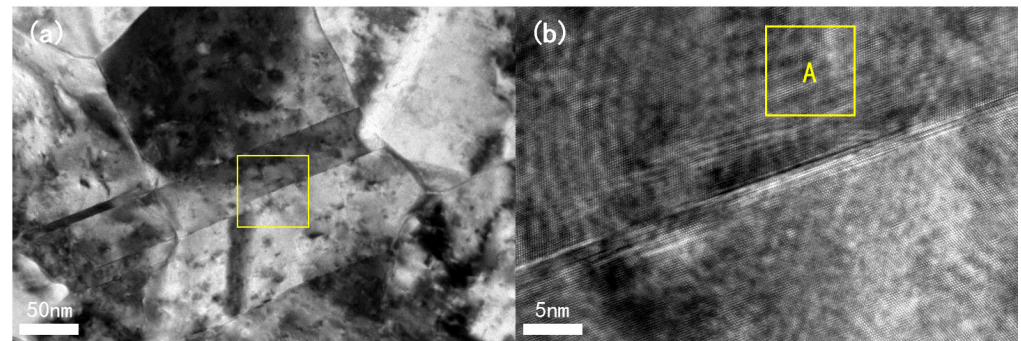


**Figure 2.** (a) Electron diffraction contrast image of twin structure in electroplated copper thin film. An enlarged image of the yellow box is shown in (b); (b) high-resolution image of the twinned lamella. Region A is the analytical part of the text.

After obtaining HRTEM images of the twinning in the electro-deposited Cu thin films, we performed the HRLIRDE method. The specific steps are as follows: (1) Perform a Fast Fourier Transform (FFT) on a selected region within the twinning area (e.g., the yellow-boxed region A in Figure 2b) to obtain the Fourier transform spectrum (approximately equivalent to the reciprocal space). (2) Calculate and determine the positions of the Fourier spectrum spots (reciprocal lattice points) corresponding to extinction crystal planes such as  $\{110\}$  and  $\{112\}$  based on the crystallographic angle formula. Virtualize diffraction wave functions corresponding to the extinction spots based on phase contrast dynamics theory, assigning a certain diffraction intensity to these extinction spots. (3) In the Fourier transform spectrum, the diffraction wavefunction corresponding to the extinction point is added to the transmission wavefunction corresponding to the center point, causing mutual interference between the extinction point and the center point. Through the above process, an image of lattice fringes belonging only to the extinction crystal plane is obtained, which helps in the identification of dislocations. This step mainly involves the Fourier inverse transform process. (4) Overlay the obtained fringe images with actual HRTEM images to further confirm the presence and type of dislocations, completing the localization of dislocations. (5) Measure the Burgers vectors of the identified dislocations.

### 2.3. Theoretical Proof of the Analysis Method

Based on the steps described earlier, this study presents the HRLIRDE method, which can be summarized as a process of “transforming high-resolution images into diffraction patterns in reciprocal space through Fourier transformation, selecting diffraction spots corresponding to specific crystal planes, performing an inverse Fourier transform to obtain one-dimensional lattice fringe images corresponding to these crystal planes, and intuitively locating the positions of dislocations”. This process involves existing theories in HRTEM imaging principles, phase contrast dynamics, and diffraction optics. Therefore, this study utilizes the principles of high-resolution transmission electron microscopy imaging, phase contrast dynamics, and diffraction optics to theoretically justify the feasibility of the proposed method. The theoretical proof primarily focuses on whether the interference between the virtualized extinction spot diffraction wave function and the transmission wave func-

tion of the central spot in the Fourier transform spectrum can yield periodic lattice fringe images of extinction crystal planes.

Figure 3a illustrates the schematic process of imaging using HRTEM with phase contrast imaging. In Figure 3b, a schematic representation depicts the relationship between the incident beam and diffracted beam during diffraction under the assumption of a column and double-beam approximation (assuming that there is only one diffracted beam in addition to the transmitted beam) [17]. Figure 3c illustrates the relationship between the incident beam and the extinguished diffracted beam with a structure under the column and double-beam approximation during extinction.

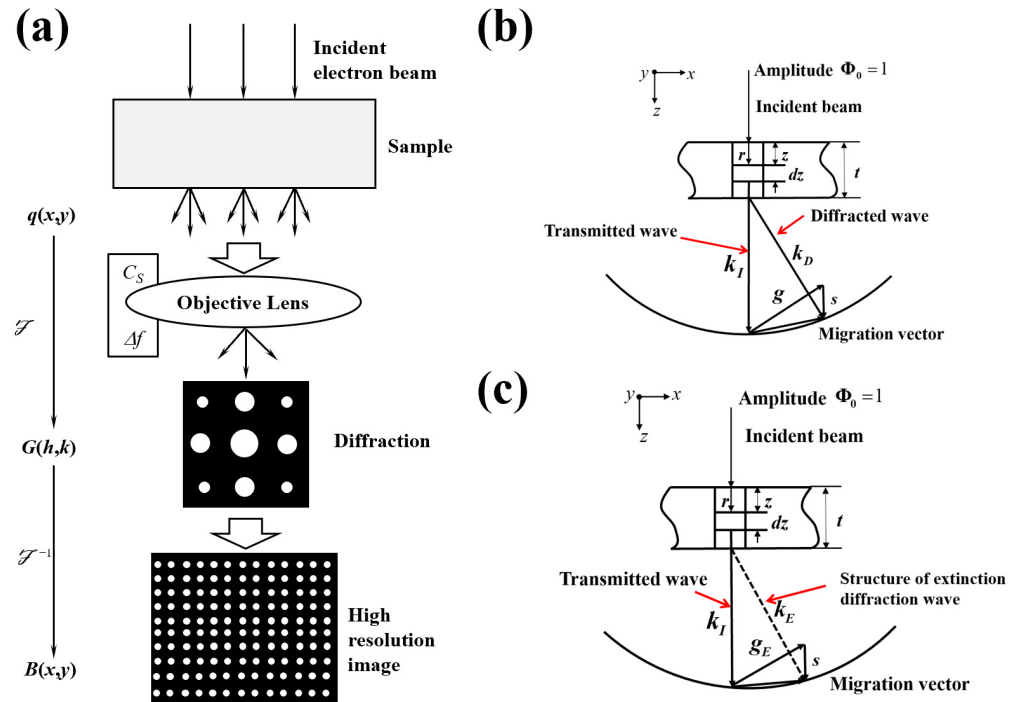


**Figure 3.** (a) Imaging process of HRTEM [18]; (b) schematic diagram illustrating the relationship between the transmitted beam and diffracted beam during diffraction under the assumption of the singlecrystal and double-beam approximations; (c) schematic diagram illustrating the relationship between the transmitted beam and the extinction-diffracted beam during diffraction extinction under the assumption of the single-crystal and double-beam approximations.

According to Figure 3a, the general imaging process of HRTEM is as follows:

The objective lens performs a Fourier transformation on the surface wave  $q(x,y)$  of the sample’s lower surface, resulting in a diffraction wave  $G(h,k)$  on the back focal plane:

$$F\{q(x,y)\} = G(h,k) = G(g) \tag{1}$$

Considering the objective lens aberration ( $C_s$ ) and defocus ( $\Delta f$ ), the diffraction wave  $G(h,k)$  is multiplied by a correction factor (phase contrast transfer function  $\exp(i\chi(g))$ ):

$$G(h,k) = F\{q(x,y)\} \cdot \exp(i\chi(g)) \tag{2}$$

$$\chi(g) = \chi_s + \chi_d = \pi(0.5C_s\lambda^3g^4 - \Delta f\lambda g^2) = -\pi\Delta f\lambda g^2 + \frac{\pi}{2}C_s\lambda^3g^4. \tag{3}$$

where  $\chi(g)$  is the phase difference (distortion) function,  $\chi_s$  and  $\chi_d$  represent the phase shifts caused by the defocus and aberrations of the HRTEM electromagnetic lens,  $\lambda$  is the electron beam wavelength, and  $g$  is the reciprocal vector length.

On the back focal plane, multiple diffraction orders, including the zeroth-order diffraction (corresponding to the transmitted beam), were selectively filtered using the objective

aperture. Coherence was established among these diffraction orders by the objective aperture, and this coherence corresponds to the second Fourier transformation of the acquired  $G(h, k)$ . In comparison to the initial Fourier transformation process, this transformation represents a Fourier inverse transformation:

$$B(x, y) = F^{-1}\{G(h, k)\} \quad (4)$$

By performing two Fourier transformations, final lattice and structure images are obtained. At this point, the region of interest in the lattice or structure image can be Fourier transformed; then, select the diffraction spots corresponding to specific crystal planes in the Fourier transform spectrum, filter out noise, and perform an inverse Fourier transform to reconstruct fringe images corresponding to specific crystal planes. Finally, dislocation analysis for specific crystal planes can be conducted based on these fringe images. The inverse Fourier transform process involves coherent implementation using computer programming or existing analysis software and is essentially similar to the aperture coherence in experiments. If the transmitted beam and diffraction spot with reciprocal vector  $\vec{g}$  are selected in the Fourier spectrum, coherent analysis is conducted using the transmitted beam and diffraction wave functions, with reciprocal vector  $\vec{g}$  corresponding to the selected crystal plane. Therefore, the inverse Fourier transformation process can be specifically written as

$$\psi = \phi_0(z) \exp 2\pi i \left( \vec{k}_I \cdot \vec{r} \right) + \phi_{\vec{g}}(z) \exp 2\pi i \left( \vec{k}_D \cdot \vec{r} \right) \quad (5)$$

In the equation,  $\psi$  represents the interference wave function,  $\phi_0(z)$  denotes the amplitude of the transmitted electron beam wave,  $\phi_{\vec{g}}(z)$  stands for the amplitude of the diffracted electron beam wave,  $z$  represents the coordinate along the depth direction of the sample, and  $\vec{k}_I$  and  $\vec{k}_D$  are, respectively, the wave vectors of the transmitted and diffracted electron beams.  $\exp 2\pi i \left( \vec{k}_I \cdot \vec{r} \right)$  can be considered the phase factor of the transmitted wave, and  $\exp 2\pi i \left( \vec{k}_D \cdot \vec{r} \right)$  can be considered the phase factor of the diffracted wave. Clearly, Equation (5) satisfies the definition of Fourier (inverse) transformation.

Suppose the reciprocal vector is  $\vec{g}$ , and the deviation vector from the reciprocal point is  $\vec{s}$ , as shown in Figure 3b. Then, according to the definition of the deviation vector [17], we can obtain the following:

$$\vec{k}_D = \vec{k}_I + \vec{g} + \vec{s} \quad (6)$$

Introducing the double-beam approximation [17], based on phase contrast dynamics [17], it can be stated that

$$\phi_{\vec{g}} = i \exp(\pi i s z) \sin \beta \sin(\pi \Delta K z) \quad (7)$$

where  $z$  is the depth into the crystal from the upper surface;  $\beta = \arccot \omega$ ,  $\omega = s \xi_{\vec{g}}$ , and  $\xi_{\vec{g}}$  are extinction distances;  $\Delta K = \frac{\sqrt{1+\omega^2}}{\xi_{\vec{g}}}$ .

For a sample with thickness  $t$ , in Equation (7),  $z = t$ . Additionally, based on trigonometric relationships, it can be obtained that

$$\sin \beta = \sin(\arccot \omega) = \frac{1}{\sqrt{1+\omega^2}} = \frac{1}{\sqrt{1+s^2\xi_{\vec{g}}^2}} = \frac{1}{\xi_{\vec{g}} \sqrt{\xi_{\vec{g}}^{-2} + s^2}} = \frac{1}{\xi_{\vec{g}}^{eff}} \quad (8)$$

where  $s_{eff}$  is the effective deviation vector:

$$s_{eff} = \sqrt{s^2 + \xi_{\vec{g}}^{-2}} \tag{9}$$

The effective deviation vector defined by Equation (9) is represented by  $\Delta K = s_{eff}$ , and according to Euler’s formula, we have that

$$\sin(\pi\Delta Kz) = \sin(\pi s_{eff}t) \tag{10}$$

$$\begin{aligned} \phi_{\vec{g}} &= \phi_{\vec{g}} = i \exp(\pi isz) \sin \beta \sin(\pi\Delta Kz) = \frac{1}{\xi_{\vec{g}} s_{eff}} \sin(\pi s_{eff}t) (-\sin(\pi st) + i \cos(\pi st)) \\ &= \left( \frac{\pi t}{\xi_{\vec{g}}} \cdot \frac{\sin(\pi s_{eff}t)}{\pi s_{eff}t} \right) \exp i \left( \frac{\pi}{2} + \pi st \right) \end{aligned} \tag{11}$$

Substituting Equations (6), (7), and (11) into Equation (5) and using complex variable conjugate transformations as well as trigonometric functions, it can be derived that

$$\psi = \exp 2\pi i (k_I \cdot \vec{r}) \left[ \phi_0(z) + \left( \frac{\pi t}{\xi_{\vec{g}}} \frac{\sin(\pi s_{eff}t)}{\pi s_{eff}t} \right) \exp i \left( (\vec{g} + \vec{s}) \cdot \vec{r} + \frac{\pi}{2} + \pi st \right) \right] \tag{12}$$

When approximating that  $\vec{g} + \vec{s}$  is parallel to the  $x$ -axis, the final result yields the intensity of the interference wave as

$$I = |\psi|^2 = \psi^* \cdot \psi = \phi_0^2(z) + \left( \frac{\pi t}{\xi_{\vec{g}}} \frac{\sin(\pi s_{eff}t)}{\pi s_{eff}t} \right)^2 - 2\phi_0(z) \left( \frac{\pi t}{\xi_{\vec{g}}} \frac{\sin(\pi s_{eff}t)}{\pi s_{eff}t} \right) \sin(2\pi |\vec{g} + \vec{s}|x + \pi st) \tag{13}$$

From Equation (13), it can be observed that the image obtained by interfering the transmitted beam with the diffracted beam with a reciprocal vector of  $\vec{g}$  is an intensity distribution with sinusoidal oscillations, and its period is

$$\frac{2\pi}{2\pi \cdot |\vec{g} + \vec{s}|} = 1/|\vec{g} + \vec{s}| \tag{14}$$

Since  $|\vec{s}|$  is much smaller than  $|\vec{g}|$  by up to three orders of magnitude [19], it can be assumed that the period of the interference image is approximately  $1/|\vec{g}|$ . According to the properties of the reciprocal lattice, the length of the reciprocal vector is equal to the reciprocal of the lattice spacing  $d$  of the corresponding crystallographic plane, which implies that  $1/|\vec{g}| = d$ . Therefore, it can be inferred that when the transmitted beam is interfered with the diffracted beam that has a reciprocal vector of  $\vec{g}$ , the period of the resulting interference image can be approximately considered to be the spacing of the crystallographic plane corresponding to the selected reciprocal vector  $\vec{g}$ , and the interference image represents the fringes corresponding to the reciprocal vector  $\vec{g}$  that is associated with the crystallographic plane.

Based on the above derivation, if the position of the extinction spot is calculated in the diffraction pattern at this point, it corresponds to  $\vec{g}_E$ . At this stage, the diffraction beam’s wave function corresponding to the extinction spot can be constructed according to Equation (11):

$$\phi_{\vec{g}_E} = B \exp i \left( \frac{\pi}{2} + \pi st \right) \exp 2\pi i (k_E \cdot \vec{r}) \tag{15}$$



In Equation (15),  $\vec{k}_E$  is the wave vector of the constructed diffraction wave, and its relationship with the wave vector of the incident wave  $\vec{k}_I$  is shown in Figure 3c and can be written as

$$\vec{k}_E = \vec{k}_I + \vec{g}_E + \vec{s} \quad (16)$$

After derivation, it can be determined that the intensity of the interference between the extinction spots and the transmission spots is given by

$$I = \phi_0^2(z) + B^2 - 2\phi_0(z)B \sin\left(2\pi\left|\vec{g}_E + \vec{s}\right|x + \pi st\right) \quad (17)$$

From Equation (17), it can be deduced that the obtained interference image is also an intensity distribution with sinusoidal oscillations, and its period is  $1/\left|\vec{g}_E + \vec{s}\right|$ . Clearly, this period spacing is approximately equal to the lattice spacing of the extinction crystallographic plane. Therefore, the obtained image can be regarded as the fringe image of the extinction crystallographic plane. At this point, the obtained image contains only the fringe patterns of the extinction crystallographic plane, which is suitable for analyzing full dislocations and partial dislocations that are involved in the extinction crystallographic plane.

In summary, the proposed HRLIRDE is theoretically valid.

#### 2.4. Extinction Speckle Reconstruction and Dislocation Verification Methods

Region A in the HRTEM image shown in Figure 2 was subjected to a Fast Fourier Transform (FFT) to obtain the corresponding Fourier transform spectrum, as shown in Figure 4. This Fourier transformation is equivalent to transforming Equation (4) into  $G(h, k)$  in Equation (2). The resulting Fourier transform spectrum closely resembles the reciprocal lattice. After calibrating the Fourier transform spectrum, it can be observed that there are no spots corresponding to  $\{112\}$  and  $\{110\}$  crystallographic planes. Therefore, it is not possible to directly observe the periodic information of the  $\{112\}$  and  $\{110\}$  crystallographic planes, as well as the corresponding dislocations such as full dislocations like  $a/2\langle 110 \rangle$  and partial dislocations like  $a/6\langle 112 \rangle$  and  $a/3\langle 112 \rangle$ , through subsequent filtering and inverse Fourier transformation in the HRTEM image.

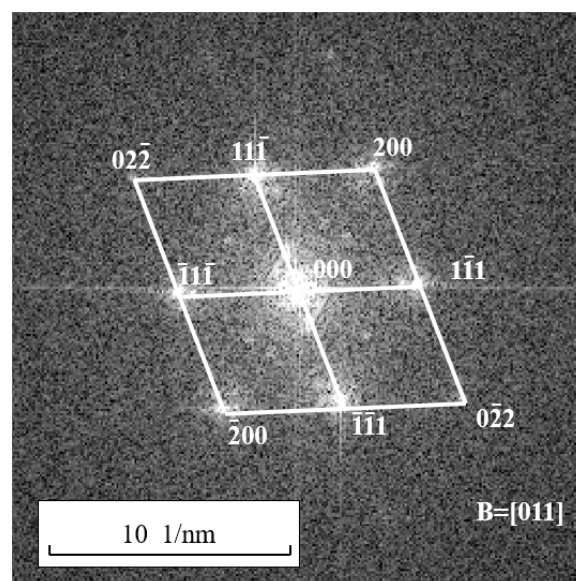


**Figure 4.** The Fourier transform spectrum of region A in Figure 2b.

At this point, the HRLIRDE proposed in this study can be employed to address this issue.

It should be noted that, according to the HRLIRDE method proposed in this study, after locating the position of the extinction spots, it is necessary to virtually construct

diffraction wavefunctions for the extinction spots based on the theory of diffraction contrast and assign a certain diffraction intensity to these extinction spots.

Taking the  $(21\bar{1})$  plane in the FCC  $\{211\}$  crystal family as an example, according to the formula [12] for interplanar spacing in cubic crystal systems,

$$d = a / \sqrt{h^2 + k^2 + l^2} \quad (18)$$

where  $d$  represents the interplanar spacing;  $a$  is the lattice constant of the Cu crystal, which is 0.36 nm [20]; and  $h$ ,  $k$ , and  $l$  are the Miller indices for the plane, and in this case, they are taken as 2, 1, and  $-1$ , respectively. Using these values, the interplanar spacing for the  $(21\bar{1})$  plane can be calculated as 0.15 nm. According to the formula [12] for the angular relationship between crystal planes in a cubic crystal system,

$$\cos \varphi = (h_1 h_2 + k_1 k_2 + l_1 l_2) / \sqrt{(h_1^2 + k_1^2 + l_1^2)(h_2^2 + k_2^2 + l_2^2)} \quad (19)$$

The angle between the  $(21\bar{1})$  plane and the  $(11\bar{1})$  plane is calculated to be  $19^\circ$ , and the angle between the  $(21\bar{1})$  plane and the  $(200)$  plane is calculated to be  $35^\circ$ . Based on this information, the positions of the extinction spots corresponding to the  $(21\bar{1})$  plane can be determined in the reciprocal lattice, along with the positions of another extinction spot  $(\bar{2}11)$  that is symmetrically opposite to it through the center of the Fourier transform spectrum, as shown in Figure 5a. Wave functions are constructed for these two points, and filtering is applied. The results are shown in Figure 5b, where the two symmetric spots in Figure 5b represent the shapes of the  $(\bar{2}11)$  plane extinction spots after filtering.

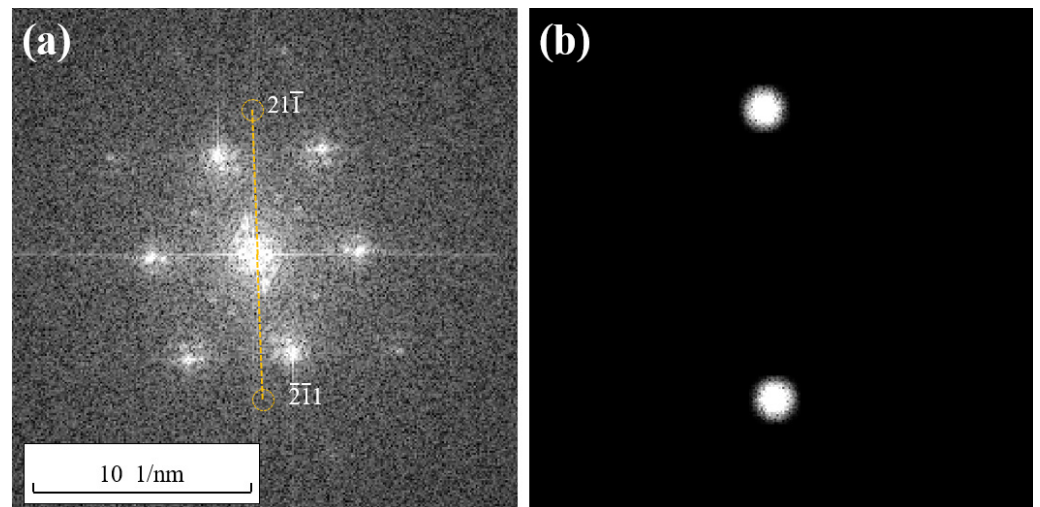


**Figure 5.** (a) The position of  $(21\bar{1})$  plane dimming spot in a reciprocal lattice (extinction spots symmetrical to the center and their connecting lines are identified in the figure); (b) the filtered image.

Consider another  $(2\bar{1}1)$  crystal plane within the  $\{211\}$  crystallographic family. Similar to the calculation process described earlier, the angle between the planes  $(2\bar{1}1)$  and  $(11\bar{1})$  can be calculated using Equations (18) and (19) to be  $90^\circ$ . When the angle between the planes  $(2\bar{1}1)$  and  $(200)$  is  $35^\circ$ , and the interplanar spacing of the  $(2\bar{1}1)$  crystal planes is 0.15 nm, the position is determined, and filtering is applied. The resulting  $(2\bar{1}1)$  spots' positions in the Fourier transform spectrum and the construction of the wave function, as well as the filtered spot morphology, are shown in Figure 6a,b. The positions and filtered spot morphology of other crystal plane spots within the  $\{211\}$  crystallographic family in the Fourier transform spectrum are not further elaborated.

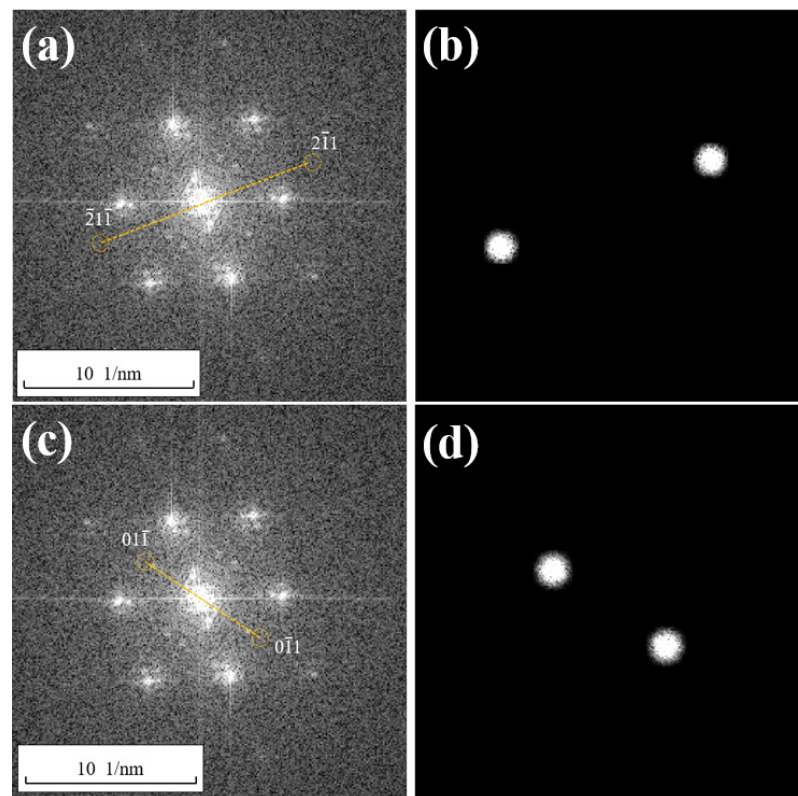


**Figure 6.** The position of  $(2\bar{1}1)$  (a) and  $(01\bar{1})$  (c) (extinction spots symmetrical to the center and their connecting lines are identified in the figure) dimming spot in a reciprocal lattice; the filtered image of  $(2\bar{1}1)$  (b) and  $(01\bar{1})$  (d).

Finding spots on  $(01\bar{1})$  crystal planes that are extinguished due to odd–even mixing is relatively simple. They can be directly derived from the unextinguished  $(02\bar{2})$  spots in the Fourier transform spectrum, located at the midpoint between the  $(02\bar{2})$  and transmitted spots, as shown in Figure 6c. After filtering the extinguished  $(01\bar{1})$  spots, their spot morphology is as shown in Figure 6d.

Finally, after observing the dislocations using the method proposed in this study, the observed dislocation Burgers vector lengths can be compared with the theoretically calculated Burgers vector lengths, which can be used to verify the correctness of the dislocation analysis. In FCC crystals, their length can be calculated using formula [12]:

$$|b| = a/n \cdot \sqrt{u^2 + v^2 + w^2} \quad (20)$$

In Equation (20),  $a/n$  represents a fractional multiple of the lattice constant;  $u$ ,  $v$ , and  $w$  are the Miller indices of the crystallographic plane.

### 3. Result Analysis and Discussion

#### 3.1. Observation and Analysis of Edge Dislocations

After the construction of wave functions and filtering, the  $(21\bar{1})$  extinction spot in Figure 5 was interfered with the central spot in the Fourier transform spectrum using Equations (5)–(17). This process is also known as an Inverse Fast Fourier Transform (IFFT) process. The resulting fringe pattern is shown in Figure 7, and according to Equation (17), it can be considered the lattice fringe pattern of the  $(21\bar{1})$  crystallographic plane. Moreover, through the above approach, Figure 7 primarily displays the lattice fringe pattern of the  $(21\bar{1})$  crystallographic plane, containing the periodic information that is enhanced by the crystallographic plane. This is more conducive to locating positions with incomplete periodicity in the lattice fringe pattern through analysis, and thereby determining the distribution of edge dislocations that are generated by the  $(21\bar{1})$  crystallographic plane.

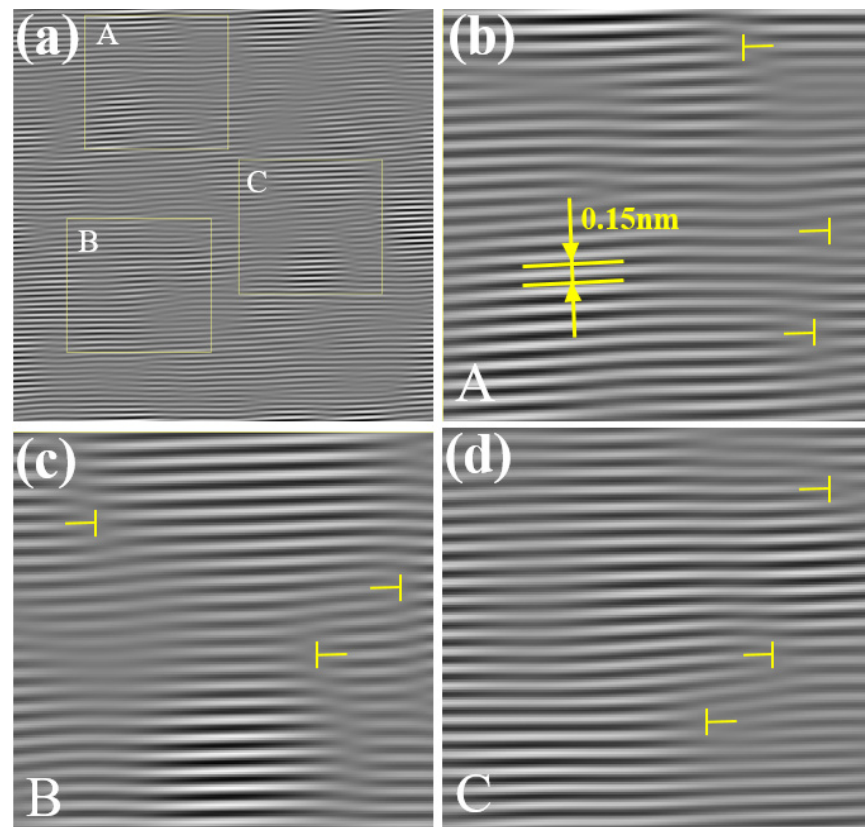


**Figure 7.** A wide distribution of dislocations (marked with a yellow “T”) and plane spacing can be seen in the inverse Fourier transform of the filtered dimming spots on the  $(21\bar{1})$  plane; (a) is the original image, (b–d) are magnified images of regions A, B, and C, respectively, identified in (a).

The lattice fringe pattern shown in Figure 7 was subjected to fringe spacing measurements, and the measured spacing was determined to be 0.153 nm, which is essentially the same as the previously calculated spacing of 0.15 nm for the  $(21\bar{1})$  crystallographic plane. This confirms that Figure 7 represents the lattice fringe pattern of the  $(21\bar{1})$  crystallographic plane. From Figure 7, it can be visually observed that there are numerous edge dislocations within the entire region, which may be related to the selected area being near a twin boundary [12,13].

To further analyze the dislocation morphology in region A of Figure 7, which contains lattice distortions at the center of the image, the various crystal planes that make up a dislocation in region A are marked with lines, as shown in Figure 8a. Then, these lines that are used for marking are placed in the corresponding positions within the two-dimensional lattice image, as shown in Figure 8b. Since the one-dimensional fringe pattern essentially retains the information of crystal planes in one direction, the distribution and position information of the atoms remain unchanged. Therefore, as long as the relative positions of the marking lines in the field of view remain unchanged, it is possible to identify the corresponding atoms in Figure 8b based on the lines and depict the specific morphology of the dislocation. The total amount of lattice distortion caused by this dislocation is the magnitude of the Burgers vector of the dislocation, which can be measured to be 0.15 nm in size in the direction of vector  $[21\bar{1}]$ .

In FCC crystals, the Burgers vector of a Shockley partial dislocation is denoted as  $a/6\langle 112 \rangle$  [12], and its length can be calculated using Formula (20). From this, the magnitude of the Burgers vector for the Shockley partial dislocation  $a/6\langle 112 \rangle$  can be calculated as  $\sqrt{6}a/6$ . Using the previously provided lattice constant  $a$  for Cu, which is 0.36 nm, the calculated magnitude of the Burgers vector  $|b|$  for the Shockley partial dislocation  $a/6\langle 112 \rangle$  in Cu is 0.15 nm. This result is in excellent agreement with the magnitude of



the Burgers vector that was measured from the Burgers circuit in Figure 8b. Thus, it can be concluded that a Shockley partial dislocation has been identified in region A of Figure 7b, and its Burgers vector has been determined to be  $1/6[2\bar{1}\bar{1}]$ .

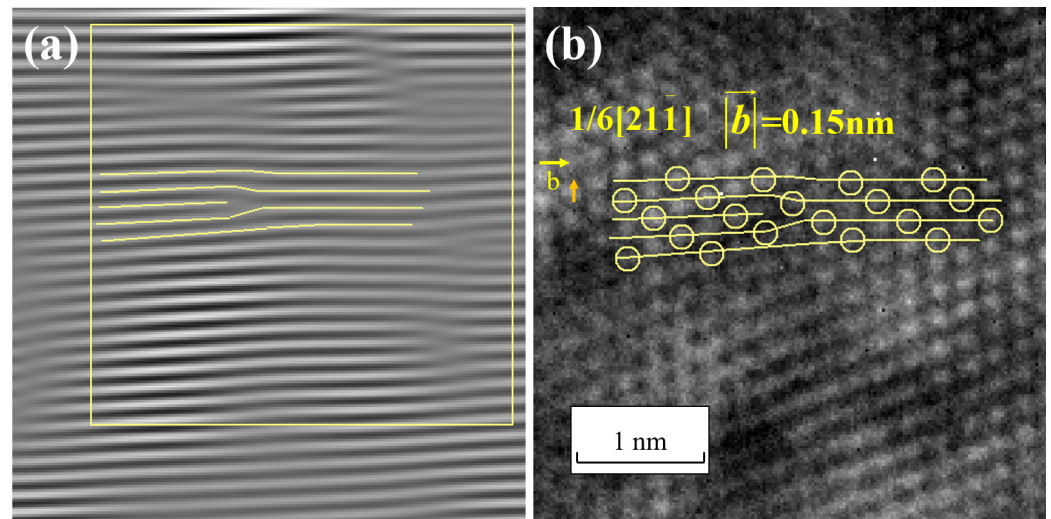


**Figure 8.** Morphology of  $1/6[2\bar{1}\bar{1}]$  dislocation in one-dimensional lattice fringe image (a) and two-dimensional lattice image (b).

After performing the interference between the  $(2\bar{1}\bar{1})$  extinction spots that were obtained from Figure 6b through the construction of the wave function and filtering and the central spot in the Fourier transform spectrum using Equations (5)–(17), the lattice fringe pattern shown in Figure 9a is obtained. Region A from Figure 9a is selected and enlarged to produce Figure 9b, which is then compared to the experimental HRTEM lattice image, as shown in Figure 9c. From the lattice fringe pattern, the interplanar spacing is measured to be 0.15 nm, which is consistent with the calculated interplanar spacing of the  $(2\bar{1}\bar{1})$  crystal plane. This confirms that the lattice fringe pattern belongs to the crystallographic family of the  $(2\bar{1}\bar{1})$  crystal plane.

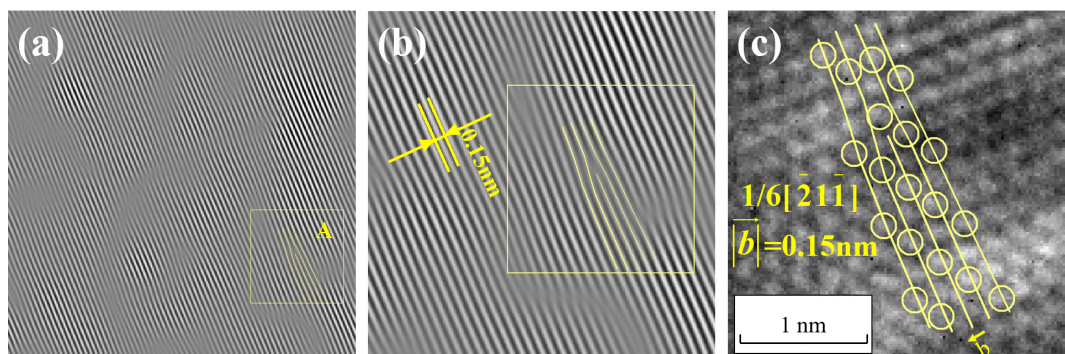


**Figure 9.** Morphology of  $1/6[2\bar{1}\bar{1}]$  dislocation in one-dimensional lattice fringe image (a,b) and two-dimensional lattice image (c).

By selecting the boxed area for the dislocation analysis and using the previously described dislocation analysis method, the morphology of the dislocation can be observed in the two-dimensional lattice image, and the magnitude of the Burgers vector is measured to be 0.15 nm in the direction of vector  $[\bar{2}\bar{1}\bar{1}]$ . This Burgers vector magnitude matches the Burgers vector magnitude of the Shockley partial dislocation  $a/6 \langle 112 \rangle$  in Cu, and it can be concluded that a Shockley partial dislocation with a Burgers vector  $1/6[2\bar{1}\bar{1}]$  has been found in Figure 9c.

After performing the interference between the  $(0\bar{1}\bar{1})$  extinction spots that were obtained from Figure 6d through the construction of the wave function and filtering and the

central spot in the Fourier transform spectrum using Equations (5)–(17), the lattice fringe pattern shown in Figure 10a is obtained. Region A from Figure 10a is selected and enlarged, and then compared to the experimental HRTEM lattice image, as shown in Figure 10c. The measured interplanar spacing is found to be 0.25 nm, which matches the calculated interplanar spacing of the  $(0\bar{1}1)$  crystal plane. This confirms that the lattice fringe pattern in Figure 10 corresponds to the lattice fringe pattern of the  $(0\bar{1}1)$  crystal plane.

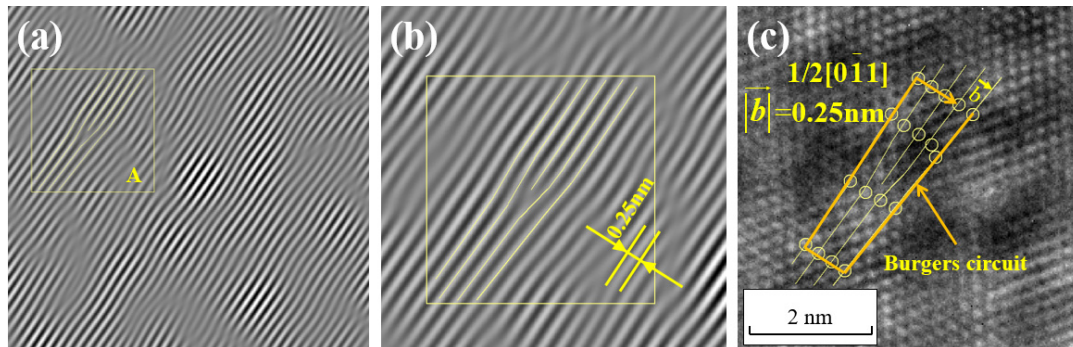


**Figure 10.** Morphology of  $1/2[0\bar{1}1]$  dislocation in one-dimensional lattice fringe image (a,b) and two-dimensional lattice image (c).

For the boxed area, a dislocation analysis is conducted. The Burgers vector magnitude of the dislocation is measured to be 0.25 nm in the direction of vector  $[0\bar{1}1]$ . This Burgers vector magnitude matches the magnitude of the Burgers vector for a full dislocation  $a/2 < 110 >$  in Cu. Therefore, it can be concluded that a full dislocation with a Burgers vector  $1/2[0\bar{1}1]$  has been found in Figure 10c.

In Figures 8b and 9c, it can be observed that the atoms constituting the  $(2\bar{1}\bar{1})$  and  $(\bar{2}\bar{1}\bar{1})$  exhibit a discontinuous distribution, making it challenging to directly discern their distribution characteristics. It is difficult to identify, assess, and measure the Burgers vector directly from the atomic arrangement. Clearly, the HRLIRDE method proposed in this study can effectively address this issue and offers unique advantages.

### 3.2. Observation and Analysis of Screw Dislocations

Screw dislocations are a crucial type of defect in metals [21–26]. Although their presence can be determined through conventional electron diffraction two-beam methods [19], observing screw dislocations at the atomic scale has remained challenging. Yang et al. achieved atomic-scale imaging of screw dislocations in a scanning transmission electron microscope using a method involving aberration-corrected electron optical slicing [27]. This method involved controlling the depth of each scan to obtain the positional information of several atomic layers and reconstructing the complete structural image. However, this approach is relatively complex and places high requirements on the equipment. In this paper, we present a relatively simple and universally applicable high-resolution transmission electron microscopy method for observing screw dislocations, based on the HRLIRDE method.

Screw dislocations [28] essentially involve the upper-layer atoms sliding parallel to the dislocation line relative to the lower-layer atoms. This results in lattice distortion in the upper layer, as shown in Figure 11a. From the schematic diagram, it can be seen that while the overall lattice undergoes twisting and distortion, local periodic arrangements still exist, specifically, periodic arrangements on the left side of the dislocation line and distorted lattice on the right side of the dislocation line. The angle between the lattices on either side of the periodic arrangement is denoted as  $\alpha$ , as depicted in Figure 11b. Consequently, for upper-layer atoms, the spacing between the regular lattice and the distorted lattice planes can be approximated as identical, with an angle  $\alpha$  existing in that direction. In reciprocal space, this is manifested as two reciprocal lattice points that are equidistant from the reciprocal origin and with an  $\alpha$  angle in the connecting line.



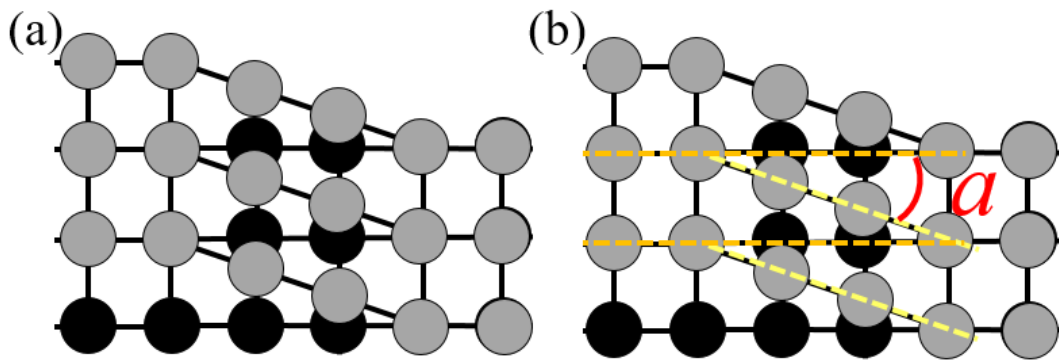


**Figure 11.** Periodic structure (a) of screw dislocation and schematic diagram (b).

Common in FCC metals are  $a/2\langle 110 \rangle$  screw dislocations [18,28]. The  $\{110\}$  crystallographic plane, perpendicular to the  $\langle 110 \rangle$  direction, is the extinction crystallographic plane. Therefore, we still employ the approach outlined in Section 3.2 to identify the  $01\bar{1}$  extinction spots in the Fourier transform spectrum and their symmetric counterparts  $0\bar{1}1$ . Subsequently, we rotate a reciprocal lattice vector connecting the  $01\bar{1}$  extinction spots, the center of the Fourier transform spectrum, and the  $0\bar{1}1$  spots by an angle, such as  $5^\circ$ , to obtain two new symmetric spots, as illustrated in Figure 12. Evidently, the reciprocal vector lengths of these two new spots remain unchanged, and they can be regarded as the extinction spots corresponding to the  $01\bar{1}$  crystal planes rotated by an angle. Coherently combining these two sets of extinction spots, which have an angle of  $5^\circ$ , in a reciprocal space with the central spot in the Fourier spectrum generates periodic fringe patterns as an attempt to identify whether the patterns resemble those shown in Figure 11. Since the extent of lattice distortion caused by screw dislocations cannot be predicted, multiple attempts may be required if coherent combinations of the two sets of spots do not yield periodic structures resembling those shown in Figure 11. In this case, a  $5^\circ$  rotation was chosen, which produced the expected results.

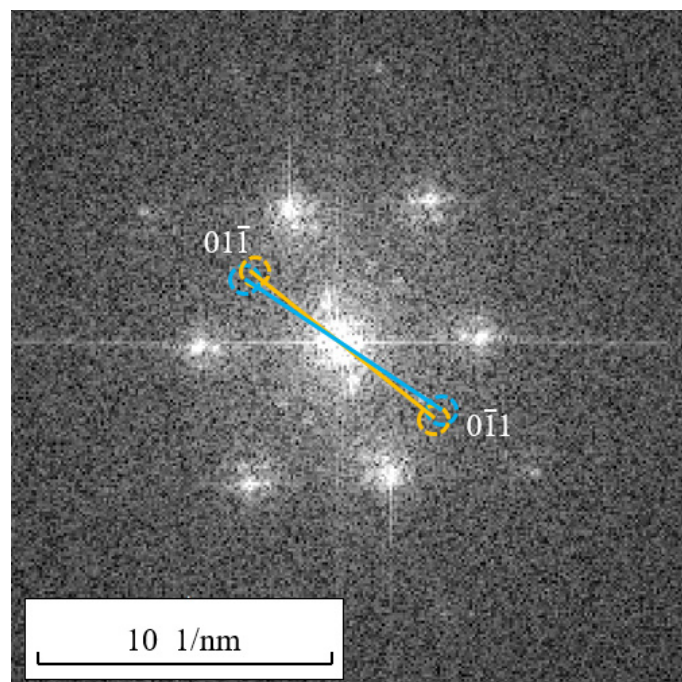


**Figure 12.** Filtering of two pairs of reciprocal points with similar angles.

After constructing the diffraction wave functions and performing filtering, the periodic fringe patterns that were obtained by interfering the two pairs of  $01\bar{1}$  extinction spots with

the center spot of the Fourier transform spectrum, as shown in Equations (5)–(17), are depicted separately in Figure 13a,b. To observe the periodic relationship more clearly between the two images, the lattice fringe patterns from both figures are superimposed, as shown in Figure 13c. In the superimposed image, the typical lattice arrangement of upper-layer atoms in a screw dislocation is discernible. It is marked and magnified, as depicted in Figure 14.

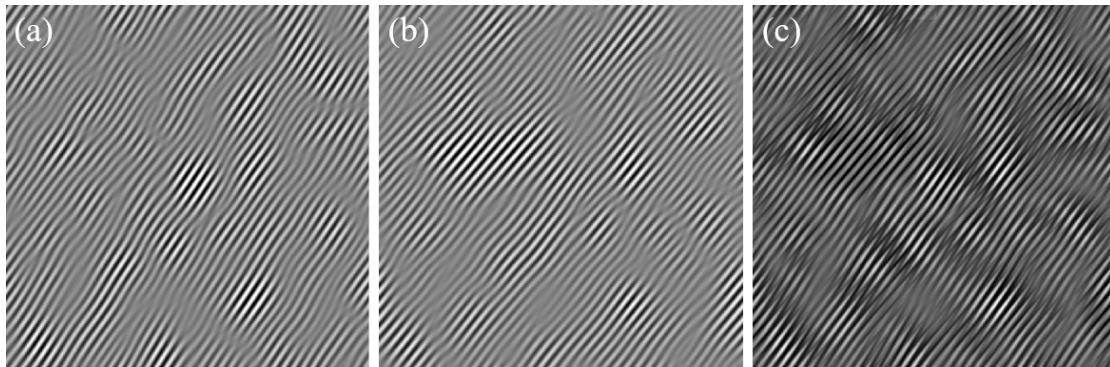


**Figure 13.** Lattice fringe images (a,b) and superimposed lattice fringe image (c).

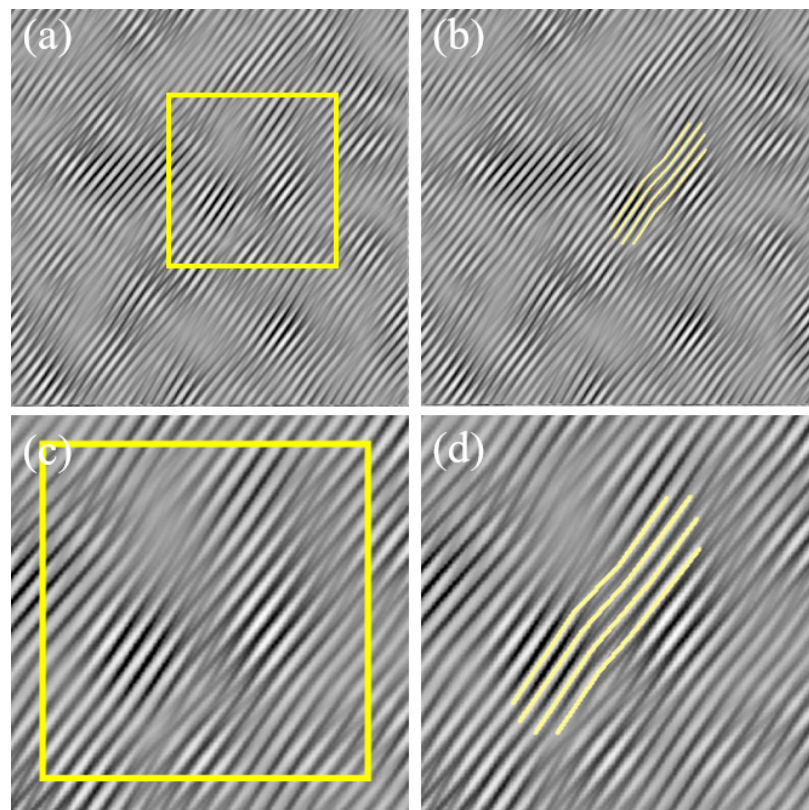


**Figure 14.** Lattice fringe superposition image (a,c) and part of it with screw dislocation morphology (b,d).

Furthermore, the distorted crystal planes are marked at the corresponding positions in the lattice image, as depicted in Figure 15. The total amount of lattice distortion can be measured from the image, yielding a value of 0.25 nm. This indicates that the Burgers vector magnitude for this screw dislocation is 0.25 nm, which is identical to the size of  $a/2 < 110 >$  dislocations in Cu. The direction of the Burgers vector is  $[01\bar{1}]$ , confirming the identification of a screw dislocation with a Burgers vector of  $1/2[01\bar{1}]$ .

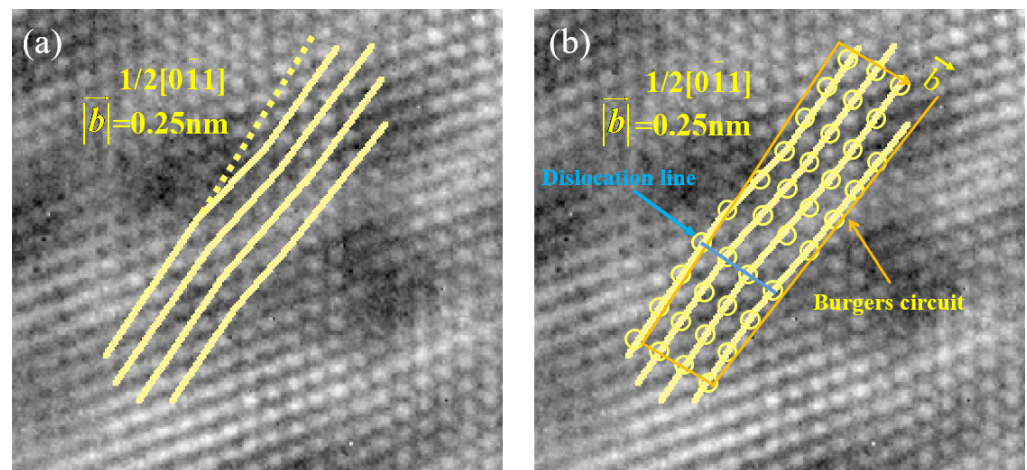


**Figure 15.** (a) A screw dislocation in two-dimensional lattice images; (b) The Burgers circuit of the screw dislocation.

Obviously, for this method of finding and measuring screw dislocation, it is necessary to use a computer to carry out continuous calculation and reconstruction with different angles and compare with the real HRTEM structural image. It is worth mentioning that since the method of analyzing screw dislocations involves some repetitive work, the workload may be greatly enhanced by the experimental purpose and experimental conditions, and perhaps the efficiency of the analysis can be improved by combining this method with some AI algorithms, just as AI algorithms are used in other fields [29,30].

#### 4. Conclusions

This paper presents a method for high-resolution lattice image reconstruction and dislocation analysis based on diffraction extinction. The approach primarily involves locating extinction spots in the Fourier transform spectrum (reciprocal space) and virtually constructing the corresponding diffraction wave functions. Subsequently, the filtered diffraction and transmission waves are coherently combined to reconstruct the lattice image of the extinction planes. This enables the observation of crystal facets that exhibit electron diffraction extinction effects and an atomic jump arrangement during high-resolution transmission electron microscopy (HRTEM) characterization. Simultaneously, since this method can be used to locate dislocations based on lattice fringe images, it can also facilitate dislocation analysis in high-resolution images with suboptimal quality.

- (1) Based on the principles of high-resolution transmission electron microscopy, diffraction dynamics, and diffraction optics, it can be deduced that after constructing diffraction wave functions for extinction spots, the overlaid interference of the diffraction wave functions and transmission wave functions yields the periodic lattice image of the extinction crystal plane, with a period that is approximately equal to the crystal plane spacing. This demonstrates the theoretical feasibility of the method that is proposed in this paper.
- (2) Using the diffraction extinction-based high-resolution lattice image reconstruction and metal dislocation analysis method, this study characterized edge dislocations within Cu films that were prepared by electrodeposition. It successfully observed dislocations like  $1/6[21\bar{1}]$ ,  $1/6[\bar{2}1\bar{1}]$ , and  $1/2[0\bar{1}1]$ , which are challenging to observe in conventional high-resolution transmission electron microscopy characterization.
- (3) Building upon the above method, this paper also characterized screw dislocations that are difficult to observe in high-resolution transmission electron microscopy. Through repeated attempts to superimpose lattice fringe images that were obtained by reconstructing extinction spots with a certain angular deviation, a screw dislocation with a Burgers vector of  $1/2[01\bar{1}]$  was successfully observed.



- (4) The method described in this paper can theoretically be widely used in transmission electron microscopy-based dislocation analysis, but it may be necessary to find appropriate substitutions for Formulas (18)–(20) and to substitute suitable parameters in the individual formulas when the crystals are not FCC-structured.

The research method presented in this paper allows for the analysis and study of dislocations with Burgers vectors of  $\langle 110 \rangle$  and  $\langle 112 \rangle$  based solely on high-resolution images captured by HRTEM. This reduces the complexity and cost of research, expanding the application of general high-resolution transmission electron microscopy in microscale observations.

**Author Contributions:** Conceptualization, Y.H.; Data curation, H.W.; Methodology, H.W. and Y.H.; Supervision, Q.G., Z.W. and W.L.; Validation, K.N.; Writing—original draft, K.N.; Writing—review and editing, K.N. and Y.H. All authors have read and agreed to the published version of the manuscript.

**Funding:** This work is supported by a grant from the Key Program of the National Science Foundation of China (No: U23B2073).

**Institutional Review Board Statement:** Not applicable.

**Informed Consent Statement:** Not applicable.

**Data Availability Statement:** Data are contained within the article.

**Acknowledgments:** The authors thank Yuan Huang for his careful guidance and Hanyu Wang for her suggestions and corrections to the drawing.

**Conflicts of Interest:** The authors declare no conflicts of interest.

## References

1. Yehliu, K.; Vander Wal, R.L.; Boehman, A.L. Development of an HRTEM image analysis method to quantify carbon nanostructure. *Combust. Flame* **2011**, *158*, 1837. [CrossRef]
2. Vander Wal, R.L.; Tomasek, A.J.; Pamphlet, M.I.; Taylor, C.D. Analysis of HRTEM images for carbon nanostructure quantification. *J. Nanopart. Res.* **2004**, *6*, 555. [CrossRef]
3. Deiseroth, H.J.; Aleksandrov, K.; Reiner, C.; Kienle, L.; Kremer, R.K. Fe<sub>3</sub>GeTe<sub>2</sub> and Ni<sub>3</sub>GeTe<sub>2</sub>—Two New Layered Transition-Metal Compounds: Crystal Structures, HRTEM Investigations, and Magnetic and Electrical Properties. *Eur. J. Inorg. Chem.* **2006**, *2006*, 1561–1567. [CrossRef]
4. Galindo, P.L.; Kret, S.; Sanchez, A.M.; Laval, J.-Y.; Yáñez, A.; Pizarro, J.; Guerrero, E.; Ben, T.; Molina, S.I. The Peak Pairs algorithm for strain mapping from HRTEM images. *Ultramicroscopy* **2007**, *107*, 1186. [CrossRef] [PubMed]
5. Kovarik, L.; Gouma, P.I.; Kisielowski, C.; Court, S.A.; Mills, M.J. A HRTEM study of metastable phase formation in Al–Mg–Cu alloys during artificial aging. *Acta Mater.* **2004**, *52*, 2509. [CrossRef]
6. Lee, C.; Maresca, F.; Feng, R.; Chou, Y.; Ungar, T.; Widom, M.; An, K.; Poplawsky, J.D.; Chou, Y.-C.; Liaw, P.K.; et al. Strength can be controlled by edge dislocations in refractory high-entropy alloys. *Nat. Commun.* **2021**, *12*, 5474. [CrossRef] [PubMed]
7. Sivasankaran, S.; Ramkumar, K.R.; Ammar, H.R.; Al-Mufadi, F.A.; Alaboodi, A.S.; Irfan, O.M. Microstructural evolutions and enhanced mechanical performance of novel Al–Zn die-casting alloys processed by squeezing and hot extrusion. *J. Mater. Process. Technol.* **2021**, *292*, 117063. [CrossRef]
8. Kandeegan, R.; Manojkumar, K.; Saminathan, K. *Non-Destructive Material Characterization Methods*; Elsevier: Amsterdam, The Netherlands, 2024; pp. 167–188.
9. Ann-Katrin, F.; Maximilian, T.; Stefan, L.; Hans-Joachim, K. *Encyclopedia of Materials: Technical Ceramics and Glasses*; Elsevier: Amsterdam, The Netherlands, 2021; pp. 578–599.
10. Byun, T.S. On the stress dependence of partial dislocation separation and deformation microstructure in austenitic stainless steels. *Acta Mater.* **2003**, *51*, 3063. [CrossRef]
11. Ishikawa, Y.; Sugawara, Y.; Yao, Y.; Noguchi, N.; Takeda, Y.; Yamada, H.; Shimizu, M.; Tadamoto, K. Generation of dislocations from scratches on GaN formed during wafer fabrication and dislocation reactions during homoepitaxial growth. *Jpn. J. Appl. Phys.* **2021**, *60*, 115501. [CrossRef]
12. Lu, G.X.; Hou, Z.S. *Metal Science Course*; Science and Technology Press: Shanghai, China, 1985; p. 238.
13. Riaz, T.; Das, S.; Sahu, T.; Chakraborti, P.C.; Sahu, P. Dislocation substructures in tensile deformed Fe–Mn–Al–C steel. *Mater. Lett.* **2021**, *282*, 128691. [CrossRef]
14. Kwasiak, P.; Fedorov, M.; Muzyk, M.; Wrobel, J.; Garbacz, H. Interaction of O, N, C and H interstitials with screw dislocations in hexagonal titanium. *Mater. Sci. Eng. A* **2023**, *875*, 145070. [CrossRef]
15. Mitchell, T.E.; Anderson, P.M.; Baskes, M.I.; Chen, S.P.; Hoagland, R.G.; Misra, A. Nucleation of kink pairs on partial dislocations: A new model for solution hardening and softening. *Philos. Mag.* **2003**, *83*, 1329. [CrossRef]

16. Imito, D.; Hiraga, K. *High Resolution Electron Microscopy Method for Material Evaluation*; Liu, A.S., Translator; Metallurgical Industry Press: Beijing, China, 1998; p. 38.
17. Peter, H.; Erwin, K. *Principles of Electron Optics*, 2nd ed.; Academic Press: Cambridge, MA, USA, 2022; Volume 3, pp. 1521–1540.
18. Spence, J.C.H. *Experimental High Resolution Electron Microscopy*; Zhang, C.G.; Zhu, Y., Translators; Higher Education Press: Beijing, China, 1988; p. 118.
19. Huang, X.Y. *Transmission Electron Microscopy*; Science and Technology Press: Shanghai, China, 1987; Volume 326.
20. Trong, D.N.; Long, V.C.; Saraç, U.; Quoc, V.D.; Tãlu, Ş. First-Principles Calculations of Crystallographic and Electronic Structural Properties of Au-Cu Alloys. *Compos. Sci.* **2022**, *6*, 383. [CrossRef]
21. D’Anna, G.; Benoit, W. *Fundamental Aspects of Dislocation Interactions*; Elsevier: Amsterdam, The Netherlands, 1993; pp. 191–195.
22. Alexander, M.K. *A Teaching Essay on Residual Stresses and Eigenstrains*; Butterworth-Heinemann: Oxford, UK, 2017; pp. 79–92.
23. Xia, J.; Zhu, D.D.; Wang, L.; Huang, B.; Huang, X.; Meng, X.-M. Large-Scale Growth of Two-Dimensional SnS<sub>2</sub> Crystals Driven by Screw Dislocations and Application to Photodetectors. *Adv. Funct. Mater.* **2015**, *25*, 4255. [CrossRef]
24. Jin, Z.H.; Gumbsch, P.; Ma, E.; Albe, K.; Lu, K.; Hahn, H.; Gleiter, H. The interaction mechanism of screw dislocations with coherent twin boundaries in different face-centred cubic metals. *Scr. Mater.* **2013**, *54*, 1163. [CrossRef]
25. Maresca, F.; Curtin, W.A. Theory of screw dislocation strengthening in random BCC alloys from dilute to “High-Entropy” alloys. *Acta Mater.* **2020**, *182*, 144. [CrossRef]
26. Morin, S.A.; Bierman, M.J.; Tong, J.; Jin, S. Mechanism and Kinetics of Spontaneous Nanotube Growth Driven by Screw Dislocations. *Science* **2010**, *328*, 476. [CrossRef] [PubMed]
27. Fey, L.T.W.; Hunter, A.; Beyerlein, I.J. Phase-field dislocation modeling of cross-slip. *Mater. Sci.* **2022**, *57*, 10585–10599. [CrossRef]
28. Cui, Z.Q. *Metal Science and Heat Treatment*; China Machine Press: Beijing, China, 1989; p. 23.
29. Dučić, N.; Manasijević, S.; Jovičić, A.; Čojbašić, Ž.; Radiša, R. Casting Process Improvement by the Application of Artificial Intelligence. *Appl. Sci.* **2022**, *12*, 3264. [CrossRef]
30. Sawilla, I.; Weber, C.; Schmidt, B.; Ulrich, M. Industrial challenges for AI systems engineering: Towards autonomous industrial systems. *Automatisierungstechnik* **2022**, *70*, 805–814. [CrossRef]

**Disclaimer/Publisher’s Note:** The statements, opinions and data contained in all publications are solely those of the individual author(s) and contributor(s) and not of MDPI and/or the editor(s). MDPI and/or the editor(s) disclaim responsibility for any injury to people or property resulting from any ideas, methods, instructions or products referred to in the content.

## Article

# Investigation of Solidification Heat Transfer in Slab Continuous Casting Process Based on Different Roll Contact Calculation Methods

Daiwei Liu <sup>1,2</sup>, Guifang Zhang <sup>1,\*</sup>, Jianhua Zeng <sup>3</sup> and Chenhui Wu <sup>3</sup>

<sup>1</sup> Faculty of Metallurgical and Energy Engineering, Kunming University of Science and Technology, Kunming 650093, China; liudaiwei158@163.com

<sup>2</sup> School of Electrical and Information Engineering, Panzhihua University, Panzhihua 617000, China

<sup>3</sup> Pangang Group Research Institute Co., Ltd., Panzhihua 617000, China; zengjianhua68@163.com (J.Z.); wch\_neu@126.com (C.W.)

\* Correspondence: guifangzhang65@163.com

**Abstract:** The heat transfer of a slab is significantly influenced by roll contact during the continuous casting process. The influence of roll contact calculation methods on the predicted heat transfer results has not been previously investigated. In this work, the non-uniform solidification of the wide-thick slab was studied with a 2D heat transfer model using real roll contact method (R. method) and equivalent roll contact method (E. method). The predicted slab surface temperature and shell thickness were verified with the measured results of the infrared camera and nail shooting experiments, respectively. Then, the predicted heat transfer results (including the slab surface temperature, mushy region length, and solidification end position) for the wide-thick slab with different thicknesses and different casting speeds were calculated using the E. method and R. method, and the influence of these two roll contact methods on the predicted heat transfer results was discussed for the first time. The results show that both these two roll contact methods could be applied to accurately predict the slab surface temperature without considering the transient temperature dips in the roll–slab contact regions. However, the deviation of the predicted mushy region length and solidification end position using the E. method are obvious. Compared with the R. method, the predicted mushy region length obtained using the E. method is larger and the solidification end obviously subsequently moves along the casting direction.

**Keywords:** wide-thick slab; heat transfer; uneven cooling; roll contact



**Citation:** Liu, D.; Zhang, G.; Zeng, J.; Wu, C. Investigation of Solidification Heat Transfer in Slab Continuous Casting Process Based on Different Roll Contact Calculation Methods. *Materials* **2024**, *17*, 482. <https://doi.org/10.3390/ma17020482>

Academic Editor: Francesco Iacoviello

Received: 9 December 2023

Revised: 10 January 2024

Accepted: 17 January 2024

Published: 19 January 2024



**Copyright:** © 2024 by the authors. Licensee MDPI, Basel, Switzerland. This article is an open access article distributed under the terms and conditions of the Creative Commons Attribution (CC BY) license (<https://creativecommons.org/licenses/by/4.0/>).

## 1. Introduction

In the continuous casting process, the heat of the liquid steel is sequentially removed in the mold, the secondary cooling region, and the air cooling region, which is closely related to the quality and productivity of the casting steel [1–3]. Many researchers [4–13] have studied the heat transfer behavior of casting steel using numerical calculation methods in order to optimize the cooling and other process parameters. Based on the predicted slab surface temperature and the target temperature, the cooling water amount or nozzle arrangement in the secondary cooling region was optimized to eliminate the slab surface defects of transverse cracks [4–7]. Furthermore, according to the predicted features of the mushy region and the strand position of the solidification end, a reasonable position for implementing strand/final electromagnetic stirring (S/F-EMS) [8–10] or soft/heavy reduction (S/HR) [11–13] was determined to effectively improve the internal defects of centerline segregation and porosity.

Roll contact (shown in Figure 1), as one of the main cooling methods after the mold, removes about 10% [14] of the heat of the casting steel and thus significantly influences the heat transfer of the continuously cast steel. In the previous works, two main calculation



methods were adopted to deal with the cooling boundary condition between rolls and strand in the numerical study of the strand heat transfer behavior: the equivalent roll contact method (E. method) and the real roll contact method (R. method). For the E. method [11,15,16], all the heat extracted via roll contact is regarded as a uniformly releasing process along the casting direction, and for the R. method [14,17,18], the cooling boundary condition for roll contact is applied in each roll–slab contact region. For the numerical calculation process of heat transfer using the R. method, the calculation time step should be strictly limited to ensure that all the roll–slab contacts can be detected in order to accurately apply the corresponding cooling boundary condition in the contact regions. If the calculation time step is too large, some roll–slab contact regions cannot be detected, and the cooling effect of some detected roll contacts on the slab heat transfer will be excessively enlarged. Furthermore, due to the high cooling intensity in the roll–slab contact regions (the heat transfer coefficient in the roll–slab contact regions approximately reaches  $1000\text{--}1300\text{ w}/(\text{m}^2\cdot^\circ\text{C})$  [14]), finer grids should be applied to discretize the calculation domain of the mathematical heat transfer model in order to more accurately consider the cooling effect of the rolls. For the reasons outlined above, the R. method is more complicated, and obviously, the corresponding computational cost consequently increases, whereas because the cooling effect of the roll contact can be considered more practically using the R. method, the accuracy of the predicted heat transfer results obtained using this method are undoubtedly better than those obtained using the E. method.

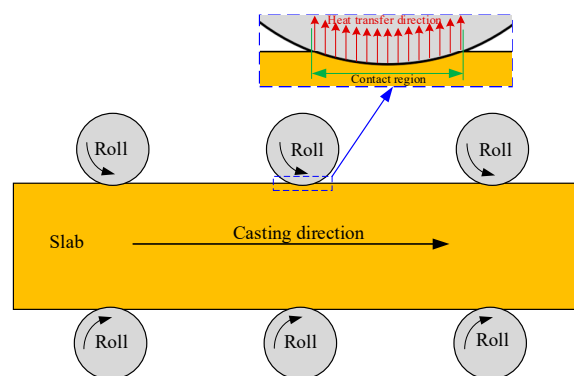


**Figure 1.** Schematic of heat transfer in roll–slab contact region.

The present work focuses on the numerical calculation of the wide-thick slab heat transfer under uneven cooling conditions in the continuous casting process and mainly studies the influence of calculation method for roll contact on the predicted slab surface temperature, strand position of the solidification end, and the mushy region length, aiming to provide a theoretical basis for choosing an appropriate roll contact method to accurately and rapidly calculate the relevant heat transfer results during the optimization of some process parameters.

## 2. Heat Transfer Model

### 2.1. Model Description

In the present work, the peritectic steel slab produced by a commercial wide-thick continuous caster was taken as the specific research object. Based on some simplified assumptions [19], one quarter of the slab transverse section was chosen as the calculation domain to establish the 2D heat transfer model. Four-node rectangular elements with a mesh size of  $2\text{ mm} \times 2\text{ mm}$  were used to discretize the calculation domain, and the final finite element model is shown in Figure 2. During the calculation process, the time step is  $0.2\text{ s}$ , and Table 1 lists more detailed parameters about the casting process and the continuous cast.

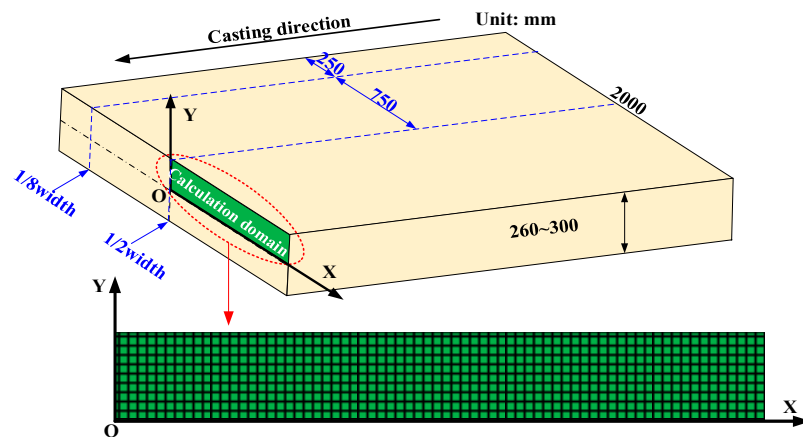


Figure 2. Schematic of the 2D heat transfer model.

Table 1. Parameters about the casting process and the continuous caster.

Items	Unit	Value
Steel composition	wt%	C: 0.17 Si: 0.15 Mn: 0.6 P: 0.015 S: 0.01
Liquidus temperature	°C	1517.7
Solidus temperature	°C	1467.5
Slab width	mm	2000
Slab thickness	mm	260~300
Casting speed	m/min	0.7~0.9
Casting temperature	°C	1548
Effective length of mold	mm	800
Each secondary cooling zone length	mm	Zone 1: 240; Zone 2: 560; Zone 3: 1110; Zone 4: 1550; Zone 5: 1920; Zone 6: 3840; Zone 7: 3840; Zone 8: 6725
Air cooling zone length	mm	9840

The heat transfer behavior of the mathematical model can be described by the two-dimensional transient heat conduction equation:

$$\rho c \frac{\partial T}{\partial t} = \frac{\partial}{\partial x} \left( \lambda \frac{\partial T}{\partial x} \right) + \frac{\partial}{\partial y} \left( \lambda \frac{\partial T}{\partial y} \right) \quad (1)$$

where  $T$  and  $t$  are, respectively, the temperature in °C and calculation time in s;  $\rho$ ,  $c$ , and  $\lambda$  are the temperature-dependent density, specific heat, and conductivity in  $\text{kg}/\text{m}^3$ ,  $\text{J}/(\text{kg}\cdot^\circ\text{C})$ , and  $\text{W}/(\text{m}\cdot^\circ\text{C})$ , respectively.

To accurately acquire the thermal material properties of the peritectic steel, a microsegregation model that has been described in detail in a previous work [11] was employed to calculate the phase fraction evolution, and the phase fraction evolution is shown in Figure 3a.  $f_\delta$ ,  $f_\gamma$ ,  $f_s$ , and  $f_L$  in Figure 3a respectively represent the fraction of  $\delta$ -Fe,  $\gamma$ -Fe, solid, and liquid, and  $f_s$  is equal to the sum of  $f_\delta$  and  $f_\gamma$ . With the temperature decrease, the amount of liquid phase continuously decreases from the liquidus temperature of 1517.7 °C; meanwhile, the amount of solid phase (including  $\delta$ -Fe and  $\gamma$ -Fe) continuously increases. During this process,  $\delta$ -Fe precipitate first and  $\gamma$ -Fe forms subsequently. When the temperature decreases to the solidus temperature of 1467.5, liquid steel disappears, and the solidification process finishes.

Based on the phase evolution in Figure 3a, the thermal material properties of the research steel, including density, conductivity, and enthalpy, were calculated using weighted phase fraction equations [20] and are respectively shown in Figure 3b, Figure 3c, and Figure 3d. With the temperature increase, density in Figure 3b continuously decreases, while conductivity in Figure 3c and enthalpy in Figure 3d present an overall increasing trend. It should be noted that the thermal conductivity of the liquid steel is magnified

by 1.5 times compared to that in the solid state when considering the improving effect of molten steel flow on heat conduction of steel [4,11].

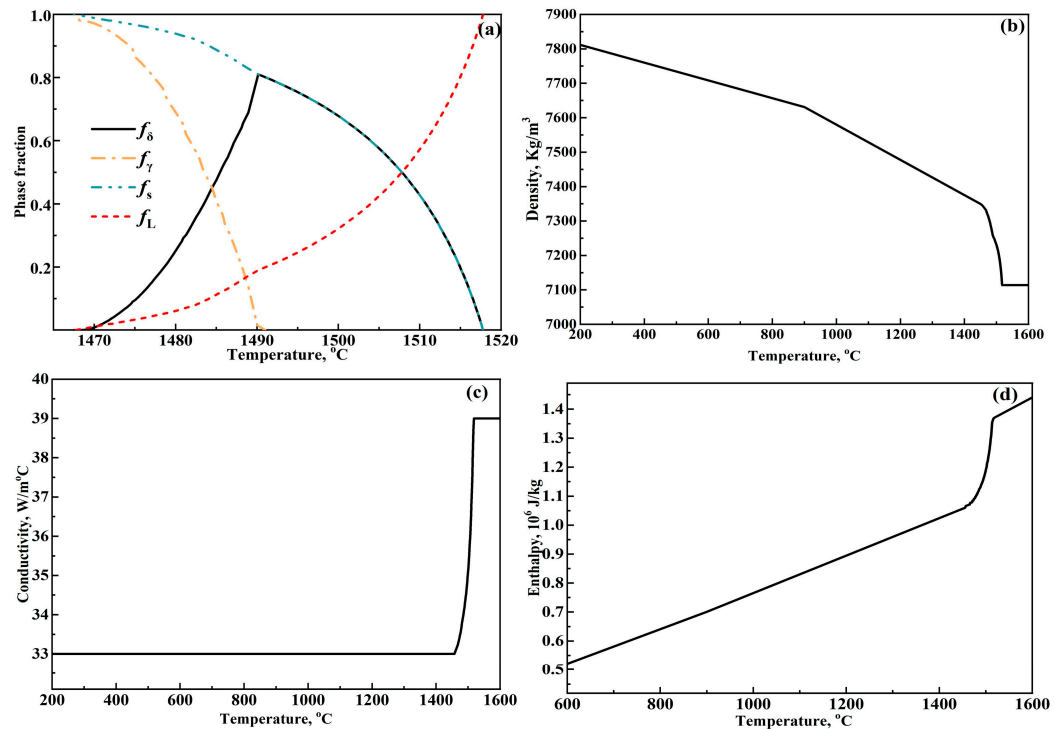


**Figure 3.** Phase fraction and thermal material properties of peritectic steel: (a) phase fraction, (b) density, (c) conductivity, and (d) enthalpy.

## 2.2. Boundary Conditions

The casting temperature, 1548 °C, is taken as the initial temperature of the heat transfer model, and heat flux at symmetrical sides (OX, OY) is set as zero. During the calculation process, the 2D heat transfer model was assumed to move with casting speed from meniscus to the continuous caster end. Corresponding cooling boundary conditions are applied according to the strand position of the 2D heat transfer model, and the calculation methods for cooling boundary conditions in mold and out of mold are described as follows:

### (1) In mold:

The heat flux between the strand surface and mold can be calculated with the following equation proposed by Savage and Pritchard [21]:

$$q = A - B\sqrt{t} \quad (2)$$

where  $q$  is heat flux between the solidified shell and mold,  $Mw/m^2$ ;  $A$  and  $B$  are coefficients depending on the mold cooling condition;  $t$  is calculation time in mold, s.

### (2) Out of mold:

When the slab moves out of mold, heat of the strand is mainly taken away by sprayed cooling water, roll contact, and radiation.

#### (i) For sprayed cooling water [19]:

$$h_{spray}^i = \alpha_i \cdot W_i^{0.55} (1 - 0.075T_w) \quad (3)$$

where  $i$  denotes the  $i$ th secondary cooling zone;  $h_{spray}^i$  is the heat transfer coefficient between the strand surface and cooling water,  $w/(m^2 \cdot ^\circ C)$ ;  $T_w$  is the cooling water temperature, °C;  $W_i$  represents the cooling water flux density,  $L/(m^2 \cdot min)$ .

As the water flux distribution along the slab width direction in secondary cooling Zone 5~Zone 8 is obviously non-uniform, the water flux distribution in these secondary cooling zones was measured and applied in the calculation of  $h_{spray}^i$ . Figures 4a and 4b show the nozzle arrangement and the corresponding measured water flux distribution, respectively.

(ii) For roll contact [16,17] with the E. method:

$$\bar{h}_{con}^i = \frac{h_{R/s}^i \cdot N_R^i \cdot L_{R/S}}{L^i} \tag{4}$$

where  $i$  denotes the  $i$ th secondary cooling zone;  $\bar{h}_{con}^i$  is the equivalent heat transfer coefficient between the strand surface and rolls,  $w/(m^2 \cdot ^\circ C)$ ;  $N_R^i$  is the number of rolls;  $h_{R/s}^i$  denotes the real heat transfer coefficient between the slab and rolls,  $w/(m^2 \cdot ^\circ C)$ ;  $L_{R/S}$  is the length of each roll–slab contact region, m. According to a previous work [14],  $h_{R/s}^i$  ranges from 1000  $w/(m^2 \cdot ^\circ C)$  to 1300  $w/(m^2 \cdot ^\circ C)$ , and  $L_{R/S}$  was set as 0.02 m;  $L^i$  represents the length of the  $i$ th cooling zone, m.

(iii) For radiation:

$$h_{rad} = \varepsilon \cdot \sigma \cdot (T_{surf}^2 + T_{env}^2) \cdot (T_{surf} + T_{env}) \tag{5}$$

where  $h_{rad}$  is the heat transfer coefficient of radiation,  $w/(m^2 \cdot K)$ ;  $\varepsilon$  is the emissivity, 0.8 [16];  $\sigma$  is the Stefan–Boltzmann coefficients,  $5.67 \times 10^{-8} (w/m^2 K^4)$ ;  $T_{surf}$  and  $T_{env}$  denote the temperature of strand surface and the environment, respectively, K.

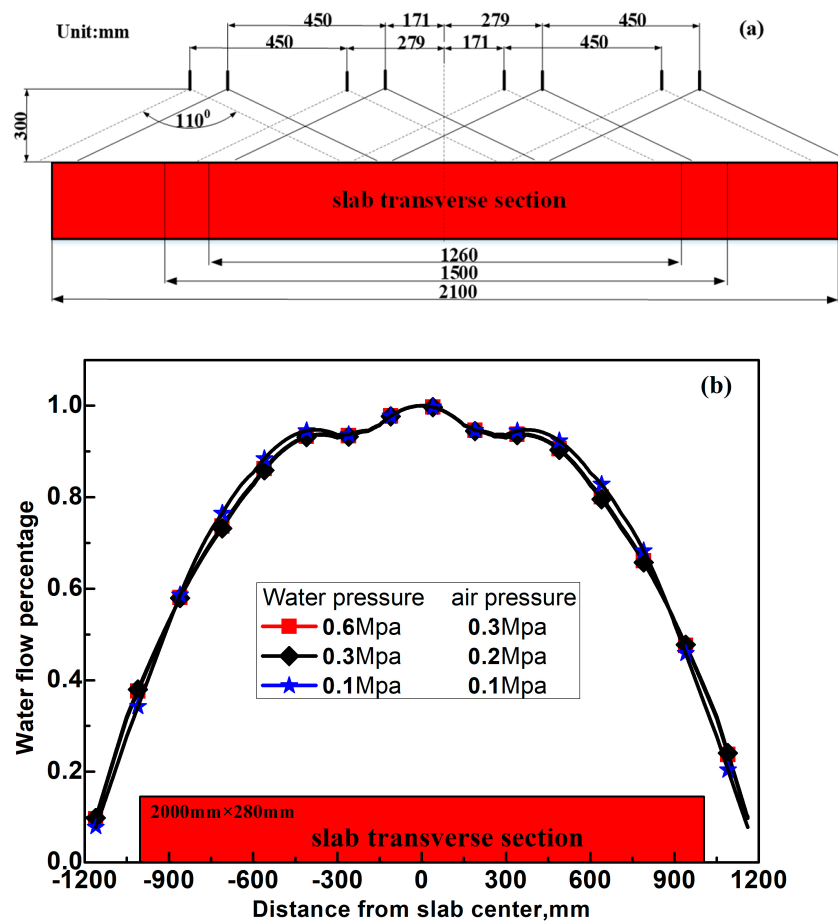


Figure 4. (a) Nozzle arrangement and (b) the corresponding measured water flux distribution along the slab width in zones 5–8.

Based on the abovementioned calculation formulas for the heat transfer coefficients of sprayed cooling water, roll contact, and radiation, the cooling boundary conditions out of mold can be expressed with two forms of equations according to the adopted calculation method for roll contact:

E. method:

$$-\lambda \frac{\partial T}{\partial n} = \left( h_{spray}^i + \bar{h}_{con}^i + h_{rad} \right) \cdot \left( T_{surf} - T_{env} \right) \quad (6)$$

R. method:

$$-\lambda \frac{\partial T}{\partial n} = (1 - k) \cdot \left( h_{spray}^i + h_{rad} \right) \cdot \left( T_{surf} - T_{env} \right) + k \cdot h_{R/s} \cdot \left( T_{surf} - T_{Roll} \right) \quad (7)$$

where  $T_{Roll}$  is the roll surface temperature and set as 150 °C according to the previous work of Xia [14];  $k$  denotes whether the 2D heat transfer model is in the roll–slab contact regions: if in, then  $k = 1$ , but if not in, then  $k = 0$ . Additionally, because the cooling water sprayed on the strand surface disappears in the air cooling zone,  $h_{spray}^i$  is equal to zero in this cooling region.

### 2.3. Model Validation

To evaluate the calculation accuracy of the R. method and E. method, the slab surface temperature and shell thickness were measured via infrared camera and nail shooting experiments at different locations in the transverse direction and casting direction; the 2000 mm × 280 mm slab was cast at 0.8 m/min. Table 2 shows the specific parameters about the measuring positions, and the measured results are compared with the calculated ones using the R. method and E. method in Figure 5a–d.

**Table 2.** Strand positions for temperature measuring.

Measuring No.	Strand Position for Temperature Measuring, m	Strand Position for Shell Thickness Measuring, m
1#	9.87	20.38
2#	13.72	23.25
3#	20.38	24.50
4#	25.30	/

1#–4# means the number of measuring position.

In Figure 5, the temperature and shell thickness at 1/8 width of the wide-thick slab are, respectively, higher and thinner than that at 1/2 width due to the continuously declining cooling water flux from the slab surface center to corner as shown in Figure 4b. In Figure 5a, transient slab surface temperature dips can be observed in roll–slab contact regions because the cooling effect of the slab surface is dramatically enhanced in these regions.

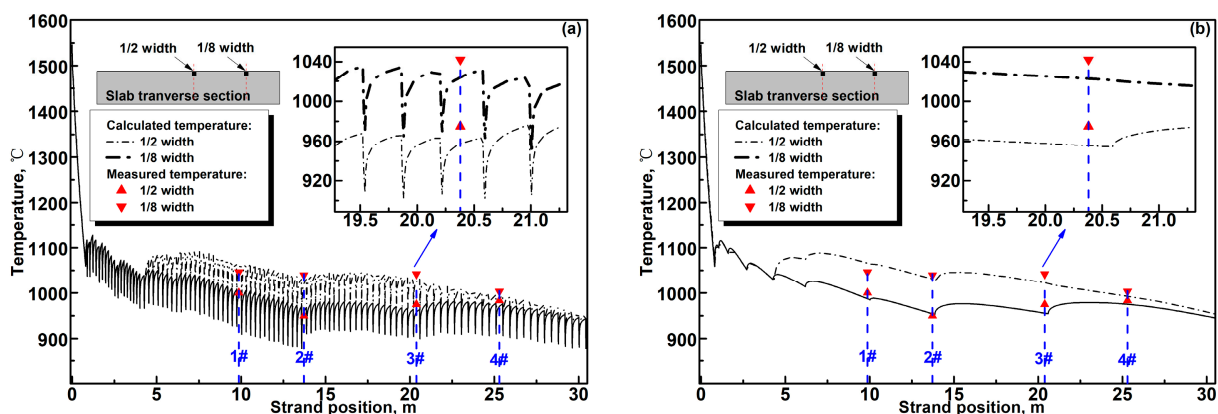


**Figure 5.** Cont.

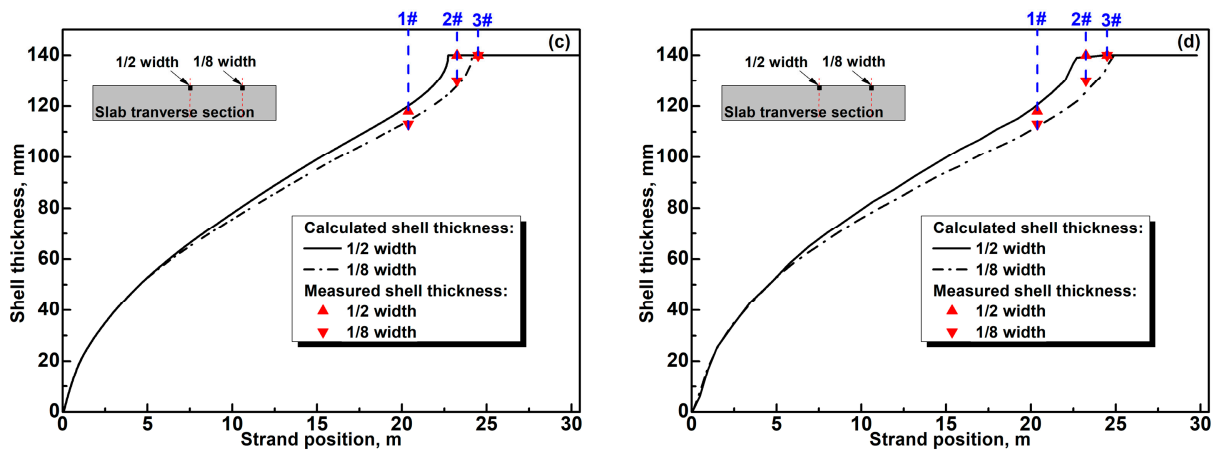


**Figure 5.** Comparison of the calculated and measured results: (a) calculated temperature using the R. method, (b) calculated temperature using the E. method, (c) calculated shell thickness using the R. method, and (d) calculated shell thickness using the E. method.

It can be seen from Figure 5a–c that the predicted slab surface temperature using the R. method and E. method and the predicted shell thickness obtained using the R. method agrees well with the measured ones. The maximum absolute value of relative error between the measured slab surface temperature and the predicted ones are less than 1.9% for the R. method and less than 2.6% for the E. method. The maximum absolute value of relative error between the measured shell thickness and the predicted ones obtained using the R. method is less than 1.7%. However, the relative deviation between the measured shell thickness and the predicted ones obtained using the E. method is relatively obvious, and the maximum absolute value of relative error of the predicted shell thickness obtained using the E. method reaches 3.2%.

### 3. Results and Discussion

#### 3.1. Difference between the R. Method and E. Method on the Predicted Heat Transfer Results

As the slab surface temperature are closely related to the optimization of secondary cooling process [4–7] and the mushy region and solidification end are an important theoretical basis for determining reasonable process parameters for S/F-EMS [8–10] and S/HR [11–13], slab surface temperature, mushy region length, and strand position of solidification end are calculated, respectively, using the R. method and E. method in order to study the difference between these two roll contact methods. Figure 6 illustrates the solidification end and mushy region length.

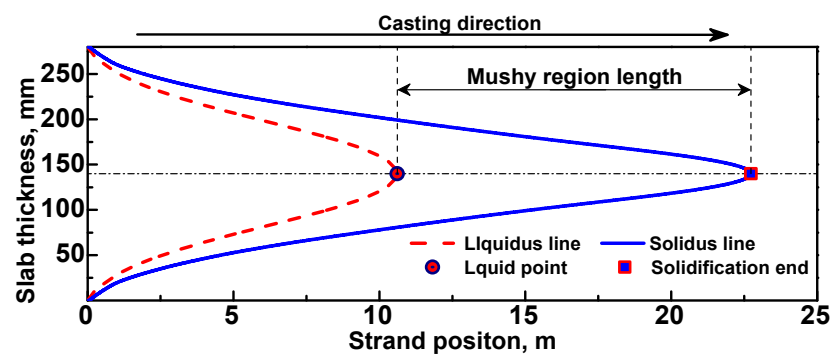


**Figure 6.** Illustration of the mushy region length and solidification end at the mid-width (1/2 width) plane of a 2000 mm × 280 mm slab produced under a casting speed of 0.8 m/min.

Figures 7a and 7b, respectively, compare the calculated surface temperature at 1/2 and 1/8 width of the slab using two different calculation methods for roll contact. Compared



with the R. method, the transient surface temperature dip in each roll–slab contact region disappears when the calculation was carried out using the E. method. This is because the heat extracted via roll–slab contact was regarded as a uniformly releasing process along the casting direction for the E. method. However, without considering the transient temperature dip in each roll–slab contact region, the predicted slab surface temperature obtained using the E. method is essentially consistent with the predicted results obtained using the R. method, and agree well with the measured results. Therefore, these two calculation methods for roll contact are both applicable for accurately predicting the slab surface temperature during the optimization of secondary cooling process, but the E. method is preferable due to its simplicity and high efficiency.

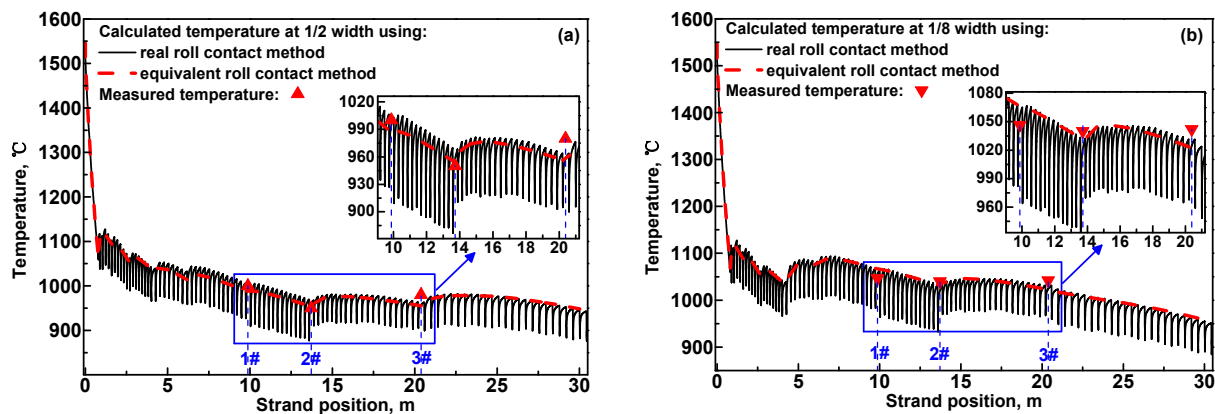


**Figure 7.** Comparison of the predicted slab surface temperature obtained using different roll contact methods with the measured results at (a) 1/2 width and (b) 1/8 width.

Figures 8a and 8b, respectively, compare the calculated solidification end position and mushy region length using the R. method and E. method at 1/2 width and 1/8 width plane of the wide-thick slab. It is obvious that the predicted strand positions of the solidification end obtained using the E. method shift along the casting direction compared with that predicted using the R. method, which is caused by the neglect of the transient temperature dips in the roll–slab contact regions when the E. method is employed. Figure 7b shows that the calculated solidification end position obtained using the E. method at 1/8 width plane of the slab is 24.95 m. However, the measured shell thickness in Figure 5c,d indicates that the solidification end at 1/8 width plane of the slab is before the 3# measuring position of 24.50 m, which is obviously inconsistent with the predicted result of 24.95 m obtained using the E. method. This proves that the predicted solidification end obtained using the E. method obviously lags behind the real solidification end.

Although both the predicted liquid point and solidification end in Figure 8a,b obtained using the E. method shift along the casting direction compared with that predicted using the R. method, the solidification end shifts more obviously. As a result, the predicted mushy region using the E. method is longer than that predicted using the R. method. Furthermore, the deviation of the predicted solidification end and mushy region length obtained using the E. method are more obvious at 1/8 width plane of the wide-thick slab compared with that at 1/2 width. This is mainly caused by two factors: (1) the higher surface temperature at 1/8 width increases the temperature difference between the slab surface and rolls surface and thus enhances the cooling effect of the rolls; (2) as indicated in Figure 5c,d, the solidification end at 1/8 width is located behind that at 1/2 width due to the continuously declining cooling intensity from the slab surface center to the corner. This leads to the fact that more roll–slab contact regions exist before the solidification end at 1/8 width, which further increases the total heat amount extracted via roll–slab contact.

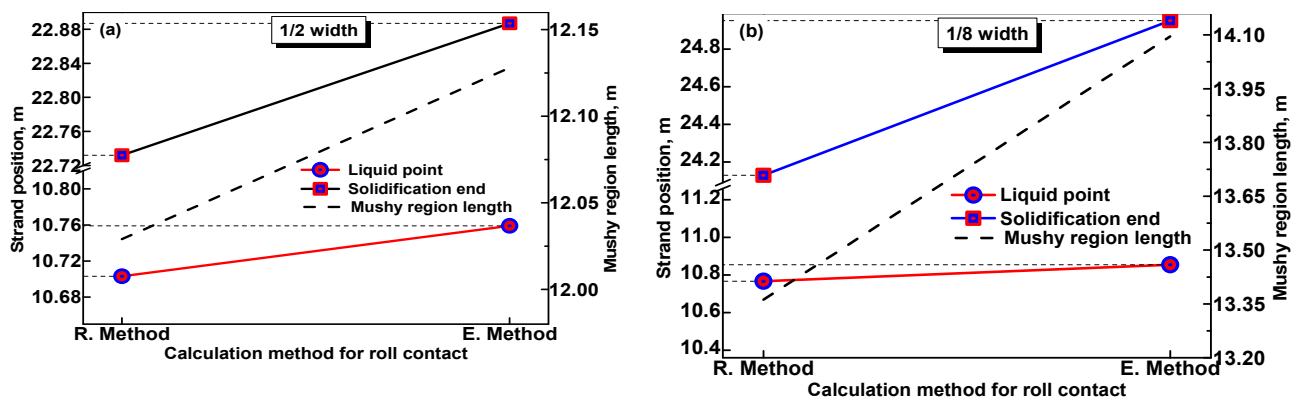


**Figure 8.** Comparison of the calculated strand position of solidification end and mushy region length using the R. method and E. method at (a) 1/2 width and (b) 1/8 width plane of a 2000 mm × 280 mm slab produced under the casting speed of 0.8 m/min.

As the deviation of the predicted solidification end position and mushy region length obtained using the E. method, especially the predicted results at 1/8 width plane of the wide-thick slab, are obvious, it is preferable to adopt the R. method to predict the solidification end position and the features of the mushy region, which could provide more reliable data for determining a reasonable location to implement S/HR or S/F-EMS.

### 3.2. Effect of Casting Speeds on the Deviation of the Predicted Results Using the E. Method and R. Method

As the deviation of the predicted solidification end position and the mushy region length obtained using the E. method and R. method are especially obvious at 1/8 width plane of the wide-thick slab, these two results were calculated and compared using the E. method and R. method, respectively, under different casting speeds in order to investigate the influence of casting speeds on the deviation degree of the predicted results obtained using the E. method.

Figure 9 shows the deviation degree (the deviation degree is defined as that the predicted strand position of solidification end or mushy region length obtained using the E. method minus the predicted ones obtained using the R. method) of the predicted results obtained using the E. method and R. method under different casting speeds. It can be seen that the deviation degree of solidification end position are overall larger than the deviation degree of mushy region length, and the variation trend of the deviation degree of these two predicted results obtained using the E. method are similar. With the increase in casting speed, two main factors significantly influence the tendency of the deviation degree: (a) the increase in casting speed dramatically shortens the contact time in each roll–slab contact region, which helps to decrease the deviation degree of the predicted results obtained using the E. method which is caused by neglect of the transient temperature dips in roll–slab contact regions. (b) However, with the increase in casting speed, the solidification end subsequently moves along the casting direction, and thus the mushy region length simultaneously increases. This means more roll–slab contact regions exist before the strand solidification end, which tend to enlarge the deviation degree of the predicted results obtained using the E. method. In Figure 9, with the increase in casting speed, the deviation degree first shows a decreasing tendency between 0.7 m/min and 0.8 m/min and then continuously increases in the range of 0.8–0.9 m/min. This indicates that the above-mentioned Factor (a) plays a more significant role in influencing the tendency of the deviation degree when the casting speed is in the range of 0.7–0.8 m/min. However, Factor (b) influences the variation of the deviation degree more obviously when the casting speed is in the range of 0.8–0.9 m/min.

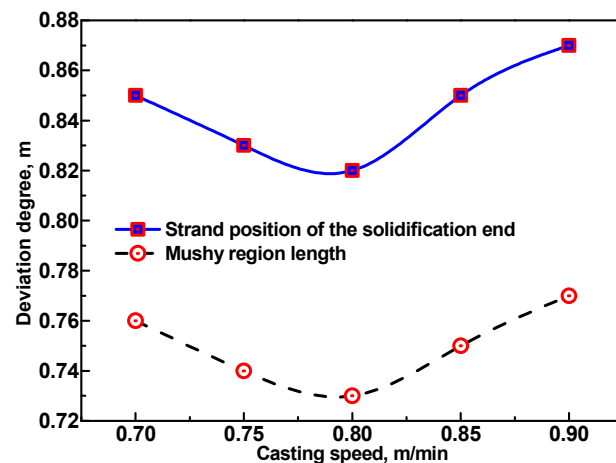


**Figure 9.** Deviation degree of the predicted strand position of solidification end and mushy region length using the E. method and R. method at 1/8 width plane of the 2000 mm × 280 mm slab under different casting speeds.

### 3.3. Effect of Slab Thickness on the Deviation of the Predicted Results Using the E. Method and R. Method

In order to study the influence of slab thickness on the deviation degree of the predicted strand position of solidification end and mushy region length obtained using the E. method and R. method, these two results at 1/8 width plane of the wide-thick slab with different thickness were calculated and compared using the E. method and R. method, respectively. Figure 10 shows the variation of deviation degree with slab thickness. With the increase in slab thickness, the solidification end subsequently moves along the casting direction, and the mushy region length is also increased. This results in more roll–slab contact regions before the strand solidification end and thus tends to enlarge the deviation degree of the predicted results obtained using the E. method and R. method. However, the increase in slab thickness means more heat per unit length of strand to be extracted during the solidification process due to the amount of secondary cooling water increasing correspondingly, which results in a tendency to decrease the ratio of the heat extracted via roll–slab contact. As a result, the increase in slab thickness also has an effect of helping to decrease the deviation degree of the predicted results obtained using the E. method and R. method. Affected more significantly by the former of the two factors mentioned above, both the deviation degree of the predicted solidification end position and mushy region length obtained using the E. method and R. method continuously increase with the increasing slab thickness. However, the increase in the deviation degree continuously grows slower.

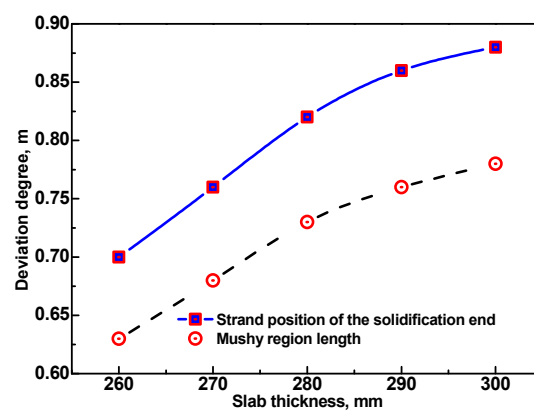


**Figure 10.** Deviation degree of the predicted solidification end position and mushy region length using the E. method and R. method at 1/8 width plane of the wide-thick slab with different thickness produced at 0.8 m/min.

#### 4. Conclusions

- (1) Both the R. method and the E. method can be used to accurately predict the wide-thick slab surface temperature without considering the transient temperature dips in the roll–slab contact regions, and the E. method is preferable during the optimization of the secondary cooling process due to its simplicity and high efficiency;
- (2) With the casting speed increased from 0.7 m/min to 0.9 m/min for the 280 mm thick slab, the deviation of the predicted results obtained at 1/8 width using the E. method ranges from 0.82 m to 0.87 m for the solidification end position and ranges from 0.73 m to 0.77 m for the mushy region length. With the slab thickness increased from 260 mm to 300 mm at the casting speed of 0.8 m/min, the deviation increases from 0.70 m to 0.88 m for the solidification end position and increases from 0.63 m to 0.78 m for the mushy region length;
- (3) Deviation of the predicted solidification end position and mushy region length obtained using the E. method is obvious. It is preferable to adopt the R. method to predict the solidification end position and mushy region length in order to provide more reliable data to determine a reasonable location for implementing S/HR or S/F-EMS.

In order to predict the solidification end position and mushy region length more accurately and efficiently using the E. method, a data rectification algorithm for the E. method on predicting solidification end position and mushy region length will be investigated in our future work based on the present work.

**Author Contributions:** Conceptualization, D.L. and G.Z.; experimental setup design, D.L., G.Z. and C.W.; validation, D.L., J.Z. and C.W.; analysis, G.Z., J.Z. and C.W.; writing, D.L., G.Z., J.Z. and C.W.; project administration, D.L. and G.Z.; funding acquisition, G.Z. All authors have read and agreed to the published version of the manuscript.

**Funding:** The work was supported by Hunan Zhongke Electric Co., Ltd., grant number “HZ2021F0529A”.

**Institutional Review Board Statement:** Not applicable.

**Informed Consent Statement:** Not applicable.

**Data Availability Statement:** Data are contained within the article.

**Conflicts of Interest:** Author Jianhua Zeng and Chenhui Wu were employed by the company Pangang Group Research Institute Co., Ltd. The remaining authors declare that the research was conducted in the absence of any commercial or financial relationships that could be construed as a potential conflict of interest.

#### References

1. El-Bealy, M.; Leskinen, N.; Fredrikson, H. Simulation of cooling conditions in secondary cooling zones in continuous casting process. *Ironmak. Steelmak.* **1995**, *22*, 246–255.
2. Quinelato, F.; Garção, W.; Paradela, K.; Sales, R.; Baptista, L.; Ferreira, A. An experimental investigation of continuous casting process: Effect of pouring temperatures on the macrosegregation and macrostructure in steel slab. *Mater. Res.* **2020**, *23*, e20200023. [CrossRef]
3. Lee, Y.S.; Kim, S.; Jang, D.W.; Lee, S.B. Mechanism of crack initiation and propagation in high-alloy steel slabs during the cooling and scarfing processes after the continuous casting process. *Mech. Mater.* **2022**, *166*, 104240. [CrossRef]
4. Ji, C.; Cai, Z.Z.; Wang, W.W.; Zhu, M.Y.; Sahai, Y. Effect of transverse distribution of secondary cooling water on corner cracks in wide thick slab continuous casting process. *Ironmak. Steelmak.* **2014**, *41*, 360–368. [CrossRef]
5. Hou, A.G.; Zhang, Q.; Xu, G.D.; Jiang, M.-F. Study and application of advanced secondary control model for continuous casting at baosteel. *J. Iron Steel Res. Int.* **2015**, *22*, 98–103. [CrossRef]
6. Norrena, J.; Louhenkilpi, S.; Visuri, V.V.; Alatarvas, T.; Bogdanoff, A.; Fabritius, T. Assessing the effects of steel composition on surface cracks in continuous casting with solidification simulations and phenomenological quality criteria for quality prediction applications. *Steel Res. Int.* **2023**, *5*, 2200746. [CrossRef]
7. Wang, X.; Liu, Q.; Wang, B.; Qing, J.-S.; Hu, Z.-G.; Sun, Y.H. Optimal control of secondary cooling for medium thickness slab continuous casting. *Ironmak. Steelmak.* **2011**, *38*, 552–560. [CrossRef]
8. Ding, N.; Bao, Y.P.; Sun, Q.S.; Wang, L.F. Location determination of final electromagnetic stirring and its effect on central carbon segregation for SWRH82B steel. *J. Univ. Sci. Technol. Beijing* **2011**, *1*, 17–21.

9. Wang, R.; Bao, Y.P.; Li, Y.H.; An, H.H. Optimization of strand and final electromagnetic stirrers of round bloom casters with multiple sections. *Int. J. Miner. Metall. Mater.* **2016**, *23*, 1150–1156. [CrossRef]
10. Kumar, R.; Jha, P.K. Effect of electromagnetic stirring on the transient flow, solidification and inclusion movements in the continuous casting slab mold. *Int. J. Numer. Methods Heat Fluid Flow* **2023**, *33*, 3716–3733. [CrossRef]
11. Ji, C.; Luo, S.; Zhu, M.Y.; Sahai, Y. Uneven solidification during wide-thick slab continuous casting process and its influence on soft reduction zone. *ISIJ Int.* **2014**, *54*, 103–111. [CrossRef]
12. Jiang, M.; Yao, T.; Yang, E.; Wang, X. Decreasing Central Porosities in a Continuous Casting Thick Slab by Heavy Mechanical Reduction Near the Solidification End. *Metall. Mater. Trans. B* **2022**, *53*, 3322–3333. [CrossRef]
13. Han, Z.; Chen, D.; Feng, K.; Long, M. Development and application of dynamic soft-reduction control model to slab continuous casting process. *ISIJ Int.* **2010**, *50*, 1637–1643. [CrossRef]
14. Xia, G.; Schiefermüller, A. The influence of support rollers of continuous casting machines on heat transfer and on stress-strain of slabs in secondary cooling. *Steel Res. Int.* **2010**, *81*, 652–659. [CrossRef]
15. Wang, H.; Li, G.; Lei, Y.; Zhao, Y.; Dai, Q.; Wang, J. Mathematical heat transfer model research for the improvement of continuous casting slab temperature. *ISIJ Int.* **2005**, *45*, 1291–1296. [CrossRef]
16. Xu, Z.; Wang, X.; Jiang, M. Investigation on improvement of center porosity with heavy reduction in continuously cast thick slabs. *Steel Res. Int.* **2017**, *88*, 1600061. [CrossRef]
17. Zhang, J.; Chen, D.F.; Zhang, C.Q.; Wang, S.G.; Hwang, W.S. Dynamic spray cooling control model based on the tracking of velocity and superheat for the continuous casting steel. *J. Mater. Process. Technol.* **2016**, *229*, 651–658. [CrossRef]
18. Louhenkilpi, S.; Mäkinen, M.; Vapalahti, S.; Räisänen, T.; Laine, J. 3D steady state and transient simulation tools for heat transfer and solidification in continuous casting. *Mater. Sci. Eng. A* **2005**, *413*, 135–138. [CrossRef]
19. Nozaki, T.; Matsuno, J.; Murata, K.; Ooi, H.; Kodama, M. A secondary cooling pattern for preventing surface cracks of continuous casting slab. *Trans. Iron Steel Inst. Jpn.* **1978**, *18*, 330–338. [CrossRef]
20. Li, C.; Thomas, B.G. Thermomechanical finite-element model of shell behavior in continuous casting of steel. *Metall. Mater. Trans. B* **2004**, *35*, 1151–1172. [CrossRef]
21. Wang, B.; Zhang, J.M.; Yin, Y.B.; Dong, Q.-P.; Xiao, C. Study on the reduction efficiency of soft reduction on continuous casting bloom. *Metall. Res. Technol.* **2016**, *113*, 406. [CrossRef]

**Disclaimer/Publisher’s Note:** The statements, opinions and data contained in all publications are solely those of the individual author(s) and contributor(s) and not of MDPI and/or the editor(s). MDPI and/or the editor(s) disclaim responsibility for any injury to people or property resulting from any ideas, methods, instructions or products referred to in the content.

Article

# Microstructural Characteristics and Material Failure Mechanism of SLM Ti-6Al-4V-Zn Alloy

Yi-Jin Cheng, Fei-Yi Hung \*  and Jun-Ren Zhao

Department of Materials Science and Engineering, National Cheng Kung University, Tainan 701, Taiwan; a2x346yz03@gmail.com (J.-R.Z.)

\* Correspondence: fyhung@mail.ncku.edu.tw; Tel.: +886-6-275-7575 (ext. 62950)

**Abstract:** This study focuses on the additive manufacturing technique of selective laser melting (SLM) to produce Ti-6Al-4V-Zn titanium alloy. The addition of zinc at 0.3 wt.% was investigated to improve the strength and ductility of SLM Ti-6Al-4V alloys. The microstructure and mechanical properties were analyzed using different vacuum heat treatment processes, with the 800-4-FC specimen exhibiting the most favorable overall mechanical properties. Additionally, zinc serves as a stabilizing element for the  $\beta$  phase, enhancing the resistance to particle erosion and corrosion impedance of Ti-6Al-4V-Zn alloy. Furthermore, the incorporation of trace amounts of Zn imparts improved impact toughness and stabilized high-temperature tensile mechanical properties to SLM Ti-6Al-4V-Zn alloy. The data obtained serve as valuable references for the application of SLM-64Ti.

**Keywords:** Ti-6Al-4V; selective laser melting (SLM); mechanical properties; oxidation; phase transformation; particle erosion; 3D printing



**Citation:** Cheng, Y.-J.; Hung, F.-Y.; Zhao, J.-R. Microstructural Characteristics and Material Failure Mechanism of SLM Ti-6Al-4V-Zn Alloy. *Materials* **2023**, *16*, 7341. <https://doi.org/10.3390/ma16237341>

Academic Editors: Seong-Ho Ha, Shae-Kwang Kim and Hyun-Kyu Lim

Received: 30 October 2023

Revised: 21 November 2023

Accepted: 23 November 2023

Published: 25 November 2023



**Copyright:** © 2023 by the authors. Licensee MDPI, Basel, Switzerland. This article is an open access article distributed under the terms and conditions of the Creative Commons Attribution (CC BY) license (<https://creativecommons.org/licenses/by/4.0/>).

## 1. Introduction

The advantage of additive manufacturing lies in its ability to customize products with complex shapes or unique structures while saving on tooling costs and material waste, thereby reducing production costs [1,2]. Currently, this technology has been widely applied in industries such as automotive, aerospace, and medical fields [2,3]. While additive manufacturing technology offers the above advantages, it is crucial to select appropriate processing technology and parameters to ensure the attainment of desirable properties [4,5]. In this study, Selective Laser Melting (SLM) was chosen as the additive manufacturing technology, using metal powder as the raw material [6]. The process involves melting the metal powder by high-energy laser scanning on a powder bed and rapidly cooling it to solidify into a specific shape [7,8]. The selected material is Ti-6Al-4V-Zn titanium alloy, which exhibits high strength-to-weight ratio, low elastic modulus, excellent corrosion resistance, and fatigue properties [9]. It is extensively used in industrial, aerospace, and medical applications [10], and is even employed in military applications [11]. With the development of modern industry, there is an increasing demand for titanium alloy products with higher dimensional accuracy and complex shapes. Therefore, the use of SLM as a forming technology for titanium alloys not only maintains the advantages of titanium alloys but also leverages the benefits of the SLM process, making it the preferred choice for industrial products. Furthermore, zinc metal is widely utilized across various industries. The addition of zinc elements and zinc coatings is prevalent in various fields, with galvanized coating being particularly common in industries due to its effective enhancement of corrosion and erosion resistance [12,13]. Moreover, the incorporation of trace amounts of zinc has been shown to enhance the strength, corrosion resistance, and processability of alloys [14–16]. Due to their similar hexagonal close-packed structures and electronegativity, the addition of zinc has minimal influence on the original Ti-6Al-4V alloy [17]. However, given the different atomic radii of Ti and Zn [18], it is important to note that the amount of added Zn should not be excessive.



In this study, zinc metal was chosen as an additive element in the Ti-6Al-4V titanium alloy, and an investigation into the microstructure and mechanical properties of the resulting Ti-6Al-4V-Zn titanium alloy was conducted [19]. Given that parts or equipment made of titanium alloys are susceptible to corrosion and damage at the metal/solution interface when exposed to corrosive media [20], we also conducted corrosion resistance investigations. Different vacuum heat treatments were applied to improve the properties of the Ti-6Al-4V-Zn alloy and to explore the effects of high temperature and oxygen content on its properties [21]. Furthermore, erosion wear is the phenomenon of gas- or liquid-driven particles impacting the surface of a material [22,23]. In numerous industrial applications of titanium alloys, including automotive and aerospace sectors, erosional wear caused by solid particles can lead to the failure of mechanical equipment and parts [23,24]. Despite the significance of particle erosion wear, there is a scarcity of studies on the erosion wear of SLM Ti-6Al-4V, let alone the SLM Ti-6Al-4V-Zn alloy investigated in this study. Therefore, it is crucial to establish particle erosion wear data and mechanisms for this alloy. Consequently, the changes in the structure, phase composition, and various properties of the alloy before and after particle erosion were examined [25,26]. Prior to this study, there were no related investigations on Ti-6Al-4V-Zn. Therefore, we conducted a comprehensive study on the SLM Ti-6Al-4V-Zn titanium alloy to obtain an in-depth understanding of the impact of zinc addition on SLM Ti-6Al-4V material properties. The generated data can offer valuable references for engineering or military applications of SLM-64Ti [27].

## 2. Materials and Methods

The experimental material in this study is the Ti-6Al-4V-Zn alloy fabricated using selective laser melting (SLM). The powder, provided by Circle Metal Powder Co., Ltd. in Tainan, Taiwan, is illustrated in Figure 1 to showcase its morphology. The specimens were fabricated using an EOS M290 400 W machine manufactured by EOS in Krailing, Germany. The process parameters are presented in Table 1. The fabrication process took place in an inert gas (argon) atmosphere. The composition of the alloy elements is shown in Table 2, with a zinc content of 0.3 wt.%. According to the titanium-zinc alloy phase diagram [28], when the Zn content is 0.3 wt.%,  $\alpha$ -Ti is the primary alloy phase rather than other titanium-zinc compounds. Additionally, the Zn content influences the phase transformation temperature of the titanium alloy. At this content, the phase transition temperature can be maintained between 800 and 900 °C. According to Chen et al. [29], the heat treatment at 850 °C leads to Ni<sub>3</sub>Ti precipitation and an increase in hardness, providing a basis for comparison with this study. Consisting of spherical particles with an average diameter of approximately 30  $\mu$ m. Figure 2 illustrates the schematic and dimensions of the standard tensile specimens and erosion specimens obtained by wire-cutting the SLM Ti-6Al-4V-Zn alloy. The specimens include an SD surface perpendicular to the laser incidence direction and an ND surface parallel to the laser incidence direction. The dimensions of the tensile specimens are 20 mm in length, 5 mm in width, and 3 mm in thickness. The erosion specimens measure 48 mm in length, 28 mm in width, and 4 mm in thickness.

**Table 1.** Parameters of the process for SLM Ti-6Al-4V-Zn alloy.

Particle Size	Laser Power	Laser Radius	Scanning Velocity	Layer Thickness
15–53 $\mu$ m	170 W	35 $\mu$ m	1000 mm/s	60 $\mu$ m

**Table 2.** Chemical composition of SLM Ti-6Al-4V-Zn alloy (wt.%).

Element	Al	V	Zn	O	C	N	Ti
Wt.%	5.7	3.7	0.3	0.2	0.1	0.1	Bal.

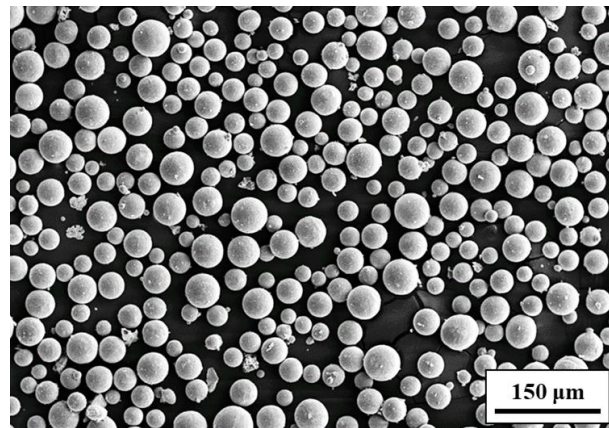


**Figure 1.** Morphology of Ti-6Al-4V-Zn powders.

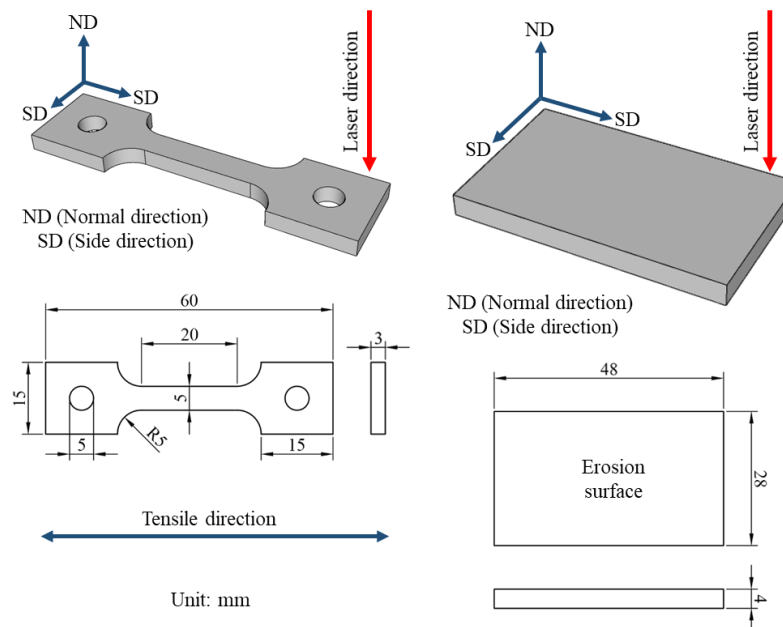


**Figure 2.** Schematic diagram of the dimensions for SLM processed tensile specimens and erosion test specimens.

After subjecting the SLM Ti-6Al-4V-Zn tensile specimens to different vacuum heat treatment processes (800 °C and 900 °C), the microstructure and phase composition were analyzed using optical microscopy (OM, OLYMPUS BX41M-LED, Tokyo, Japan), scanning electron microscopy (SEM, HITACHI SU-5000, Hitachi, Tokyo, Japan), transmission electron microscopy (TEM, JEOL JEM-2100F, Hillsboro, OR, USA), and X-ray diffraction (XRD, Bruker AXS GmbH, Karlsruhe, Germany). The mechanical properties were evaluated using a Rockwell hardness tester (Rockwell hardness machine, RH, Mitutoyo, Kawasaki-shi, Japan), universal testing machine (HT-8336, Hung-Ta, Taichung, Taiwan), and impact testing machine (HT-8041A, Hung-Ta, Taichung, Taiwan). Fracture surfaces and sub-surfaces were examined, and the high-temperature effects, as well as the oxygen content effects, were investigated by considering variations in oxygen content among different batches of powder. Erosion experiments were conducted using alumina particles as shown in Figure 3a, and erosion properties of the SLM Ti-6Al-4V-Zn titanium alloy were analyzed using the schematic in Figure 3b [30]. The mechanical property differences after particle erosion were investigated by subjecting the tensile test specimens to double-sided erosion on the parallel portion, as shown in Figure 3c. Finally, the alloy polarization curves were

measured and plotted to analyze the corrosion resistance properties. Based on multiple test results, application data for the SLM Ti-6Al-4V-Zn titanium alloy system were established.

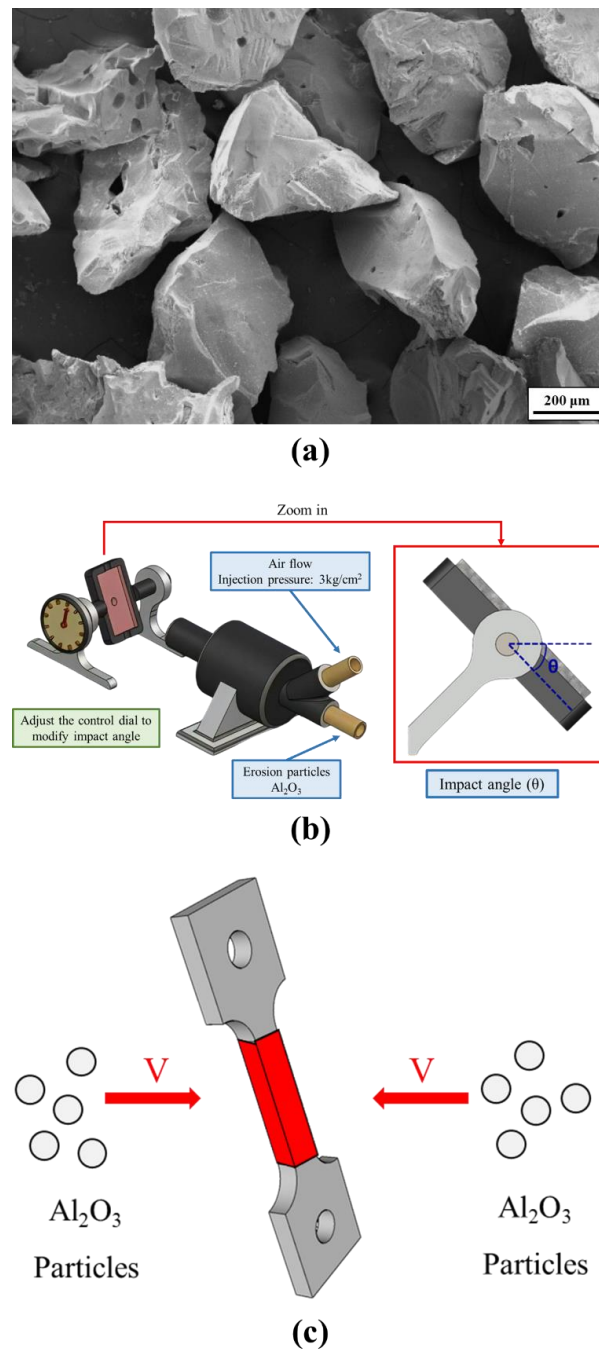


**Figure 3.** Particle erosion test: (a) morphology of erosion particles ( $\text{Al}_2\text{O}_3$ ), (b) schematic diagram of the equipment, and (c) schematic diagram of double-sided erosion on parallel portion during tensile testing [30].

### 3. Results and Discussion

In this study, the SLM Ti-6Al-4V-Zn titanium alloy, designated as the AS material, was used as the raw material. Figure 4 illustrates the microstructure of the ND and SD surfaces of the AS material. Both surfaces exhibit a needle-like microstructure, but the distribution on the ND surface is relatively more uniform. Therefore, the subsequent analysis of the heat-treated material focuses on the ND direction. The microstructure differs from the equiaxed primary  $\beta$  grain morphology observed in traditional cast Ti-6Al-4V

alloy [31]. In comparison with the SLM Ti-6Al-4V alloy we previously studied [32], the needle-like phases in this study appear denser. Figure 5 shows the microstructure of the material after vacuum heat treatment at 800 °C. With increasing heat treatment time, the needle-like microstructure gradually transforms into a combination of needle-like and lamellar structures. The needle-like structure corresponds to the  $\alpha$  phase, whereas the lamellar structure consists of alternating light-colored  $\alpha$  phase and dark-colored  $\beta$  phase. Figure 6 displays the microstructure of the material after vacuum heat treatment at 900 °C, demonstrating an increased proportion of the lamellar structure with prolonged heat treatment time.

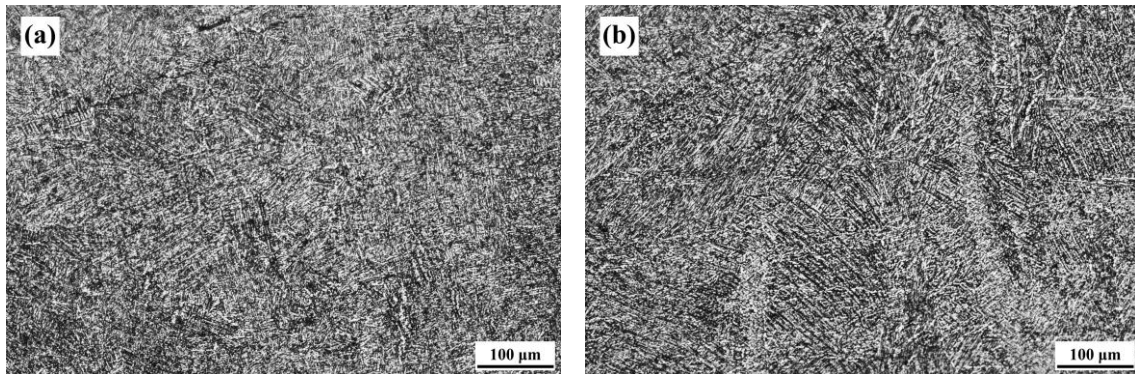


**Figure 4.** Microstructure of AS-printed material: (a) ND surface and (b) SD surface.

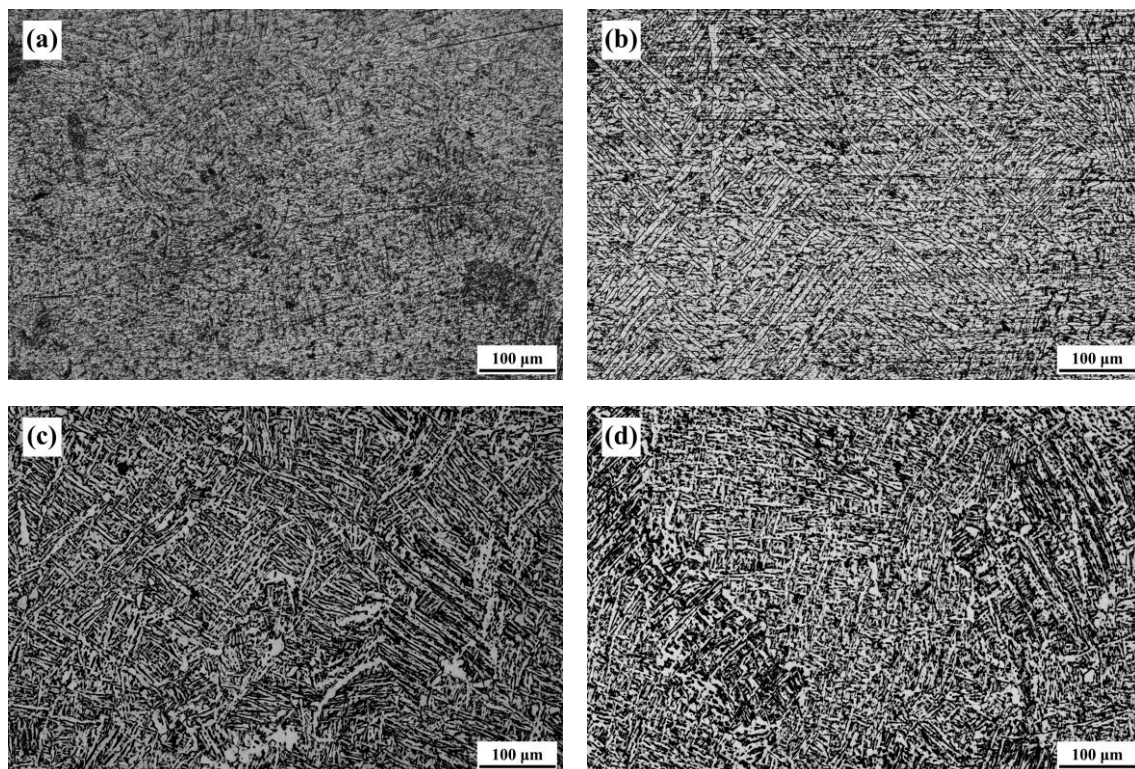


**Figure 5.** Microstructure of 800-FC material: (a) 1 h, (b) 2 h, (c) 4 h, and (d) 8 h.

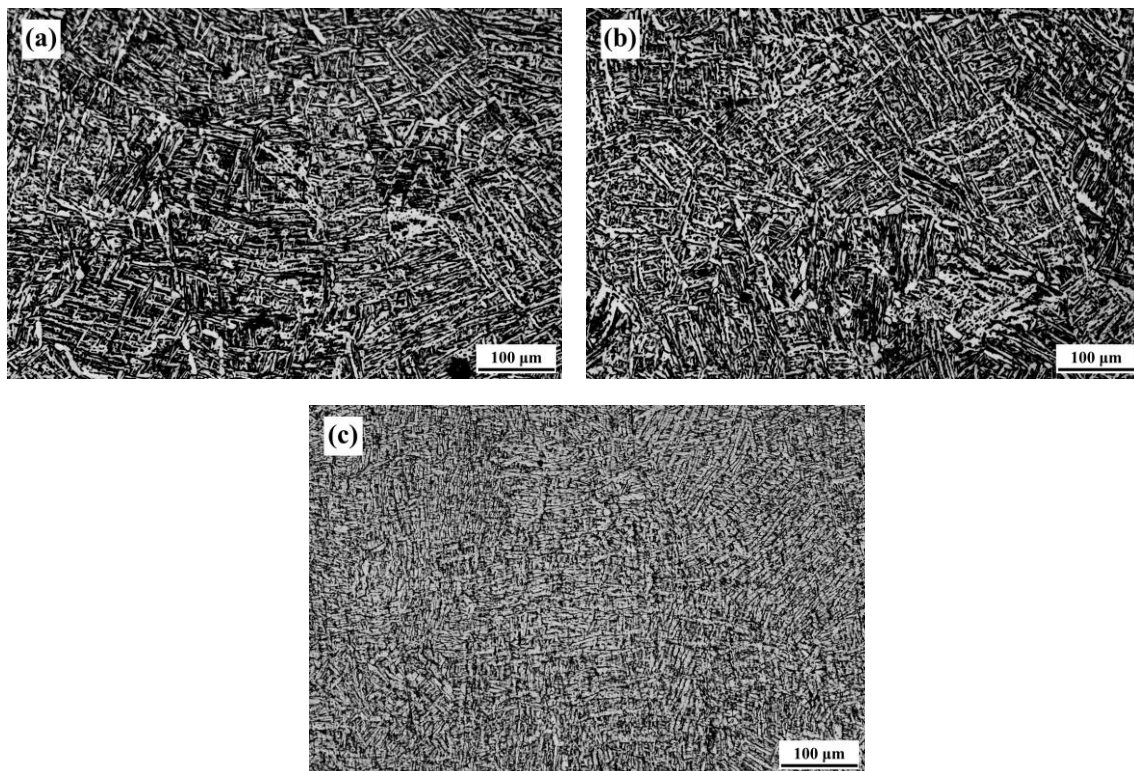


**Figure 6.** Microstructure of 900-FC material: (a) 1 h, (b) 2 h, and (c) 4 h.

Figure 7 shows the XRD diffraction analysis of AS material, 800-4-FC material, and 900-4-FC material. In the AS material, only  $\alpha$ -phase peaks are observed. In contrast, both  $\alpha$ -phase and  $\beta$ -phase peaks are detected in the 800-4-FC and 900-4-FC materials. However, no zinc-related peaks are detected in all three samples, indicating that the zinc content (only 0.3 wt.%) is relatively low. Figure 8 focuses on the TEM analysis of the 800-4-FC material (as it exhibits the best overall mechanical properties). It shows the uniform distribution of titanium and aluminum, with vanadium clustering in the light-colored regions. The 0.3 wt.% of zinc is primarily in a uniform solid solution, with only a very small amount accumulating at specific locations, as seen in Figure 8 at point 1. On the other hand, Figure 8 at point 2 only detects titanium, aluminum, and vanadium, without detecting any zinc. The elemental contents at these two points are shown in Table 3. Further analysis of point 1 reveals that the dark-colored regions in Figure 9 correspond to  $\alpha$  phase titanium, while the light-colored regions correspond to  $\beta$  phase titanium. It can be inferred that the majority of zinc is uniformly dissolved in the titanium, with only a small portion of zinc accumulating around the  $\beta$  phase near the grain boundaries of the needle-like  $\alpha$  phase. This zinc accumulation prevents the transformation of the needle-like  $\alpha$  phase to the lamellar  $\alpha + \beta$  phase during heat treatment, indicating that zinc addition helps stabilize the  $\beta$  phase.

**Table 3.** TEM elemental analysis of the 800-4-FC specimen.

Element		Ti	Al	V	Zn
at. %	1	75.27	3.58	21.09	0.07
	2	87.26	9.42	3.32	0.00



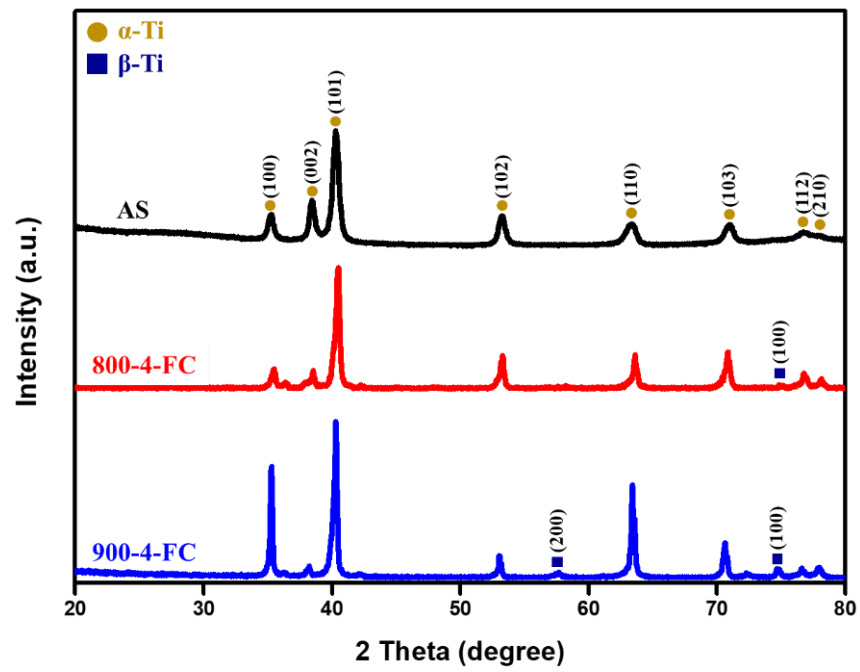


Figure 7. XRD analysis of AS, 800-4-FC, and 900-4-FC material.

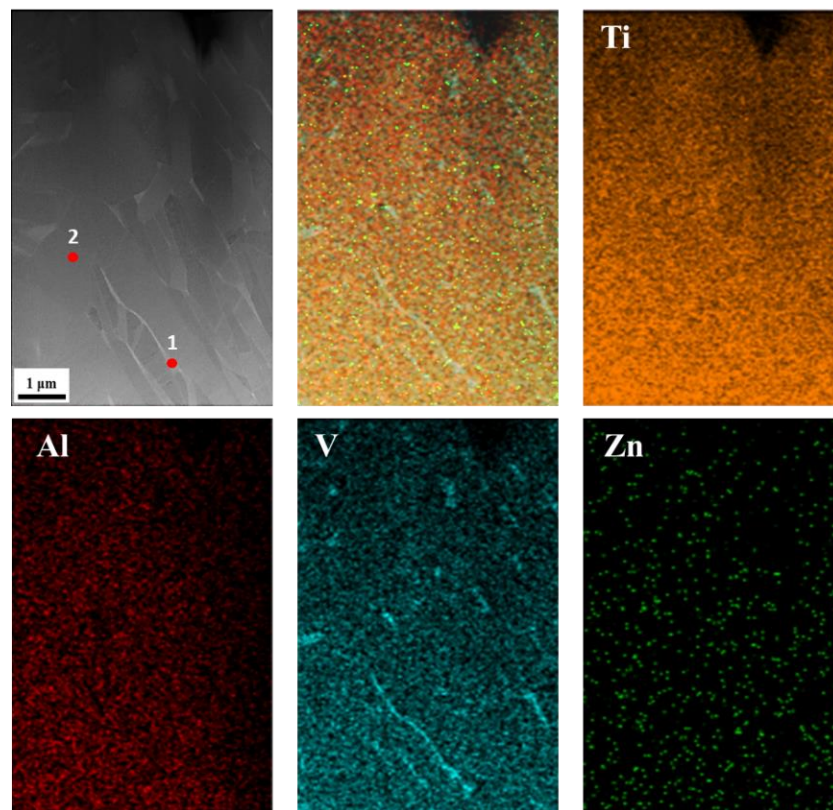
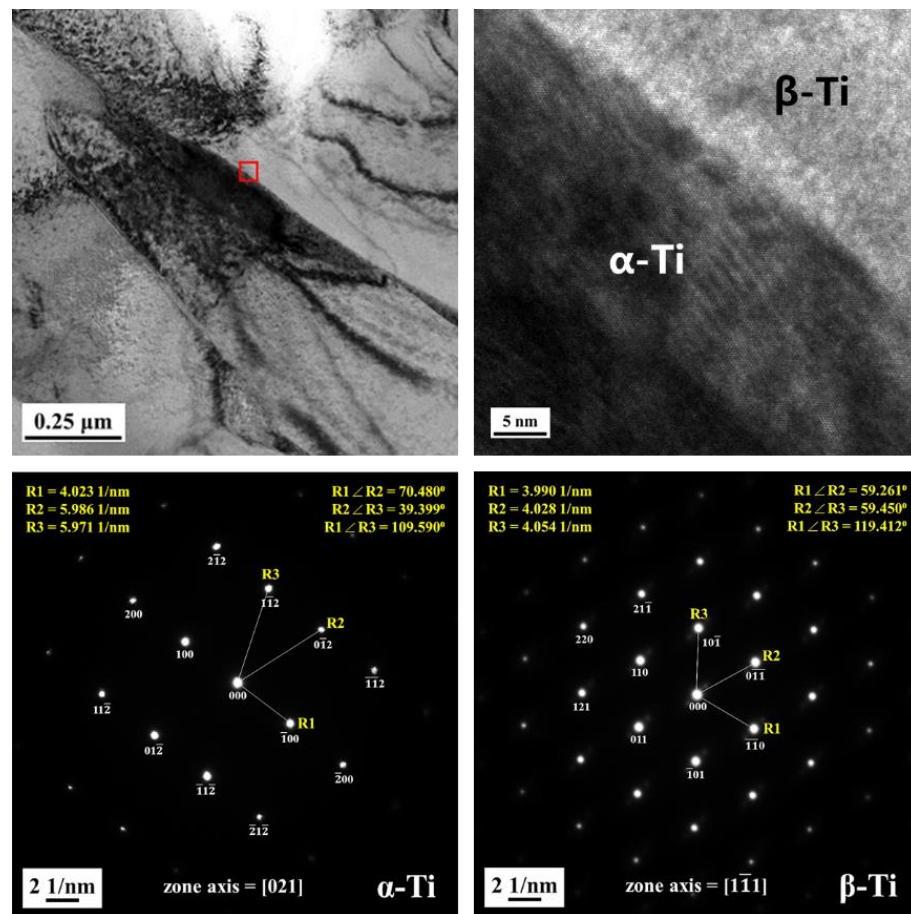


Figure 8. TEM specimen and elemental distribution of 800-4-FC material.





**Figure 9.** TEM phase identification analysis and atomic lattice with crystallographic axis analysis of 800-4-FC material.

Figure 10 presents the mechanical property data of the AS material and various heat-treated materials. In Figure 10a, a comparison of hardness is presented, showing that the AS material has a higher hardness (HRC 45) compared to all heat-treated materials (HRC 40). Figure 10b–d displays the tensile property data. The AS material exhibits the highest strength but poor ductility. The 800-4-FC material demonstrates the best overall tensile properties, combining both strength and ductility. The main reason for this is the coexistence of the needle-like  $\alpha$  phase and lamellar  $\alpha + \beta$  phase in the microstructure, as shown in Figure 11. The 800-4-FC material exhibits the optimal ratio of the needle-like to layered  $\alpha + \beta$  phases, resulting in a combination of strength and ductility. Therefore, subsequent analysis mainly focuses on the AS and 800-4-FC materials. Figure 12 shows the fracture surfaces of the AS and 800-4-FC materials after tensile testing. Both fracture surfaces exhibit a combination of dimple-like structures and flat cleavage surfaces. The samples with higher ductility display a higher proportion of dimple-like structures, whereas flat cleavage surfaces dominate in the less ductile samples. Overall, when compared to traditional casting and SLM Ti-6Al-4V alloy [31,32], the failure mechanism of SLM Ti-6Al-4V-Zn is characterized by brittle dominance and poor ductility.

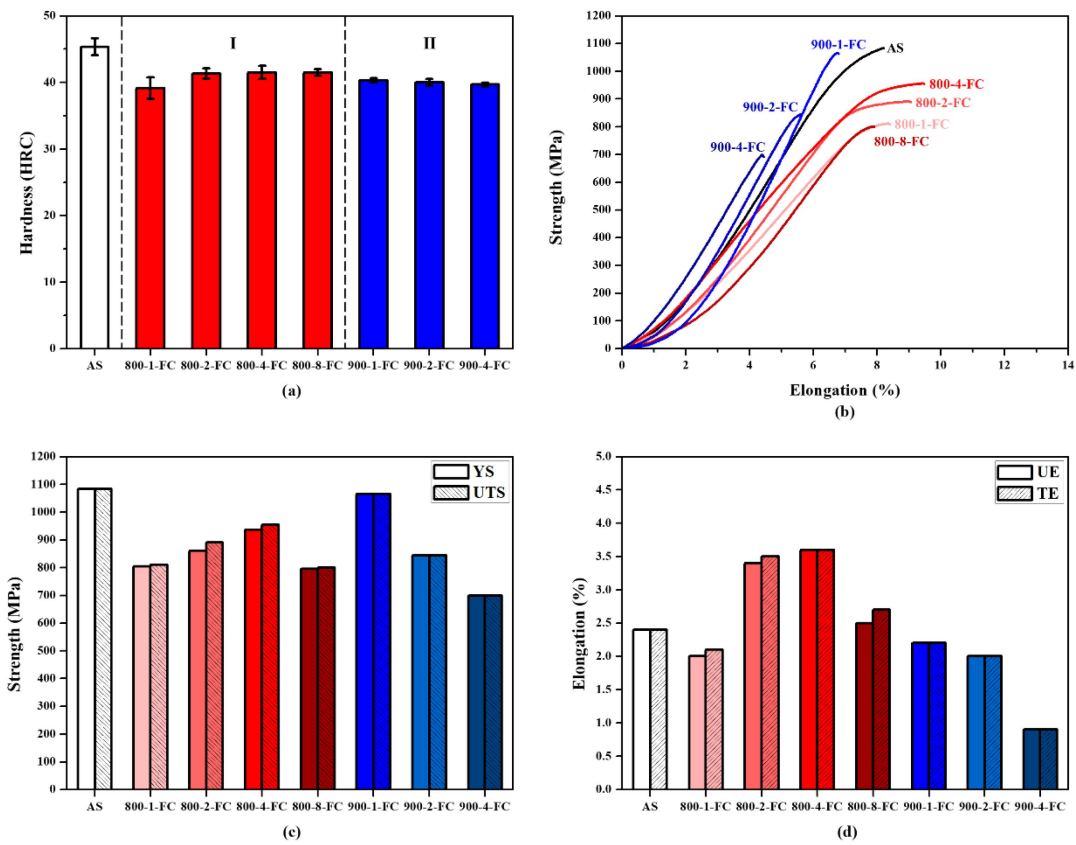


Figure 10. Mechanical properties of AS, 800-FC, and 900-FC material: (a) hardness, (b) tensile curve, (c) yield strength (YS) and ultimate tensile strength (UTS), and (d) uniform elongation (UE) and total elongation (TE).

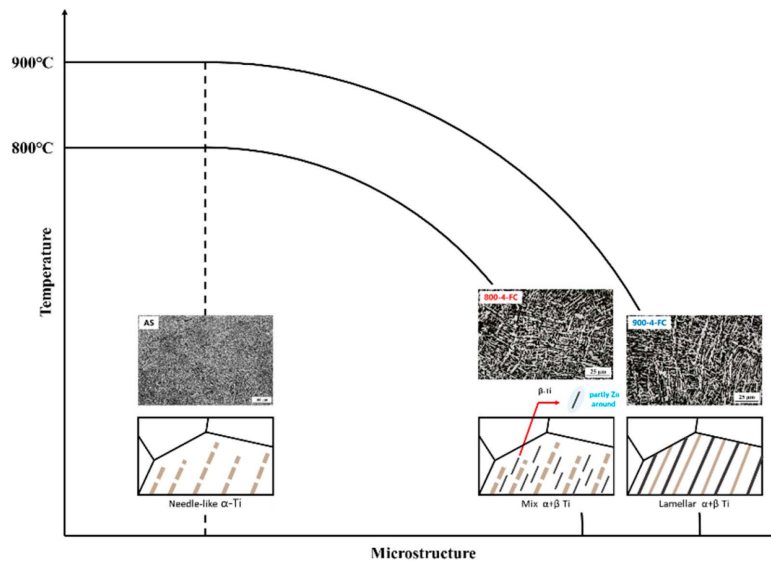
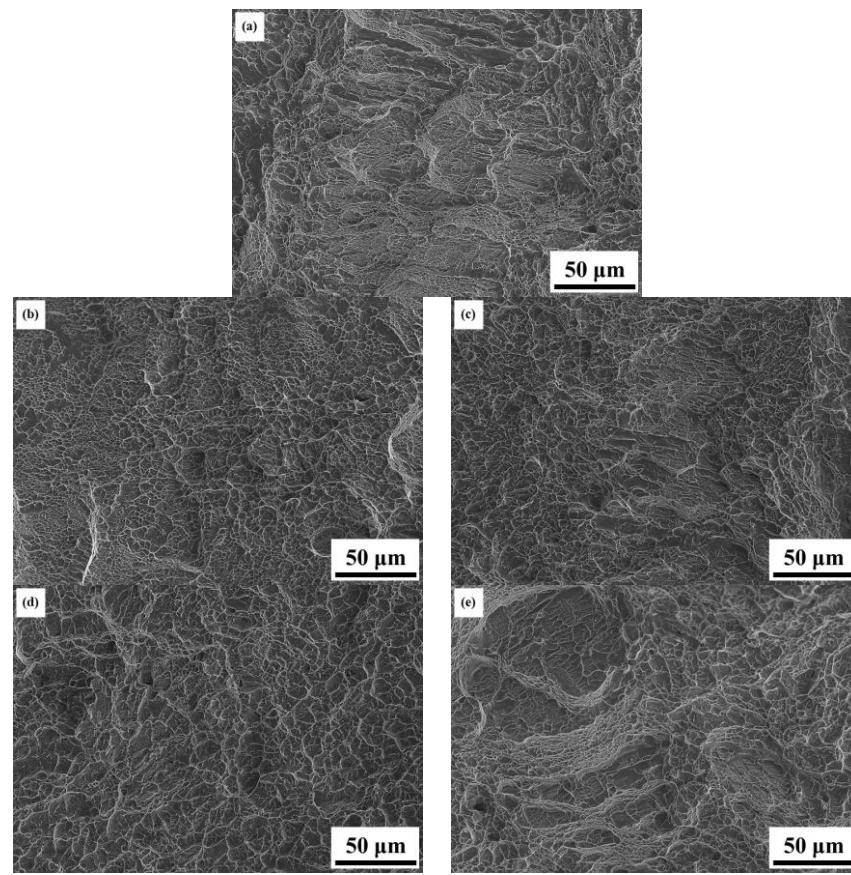
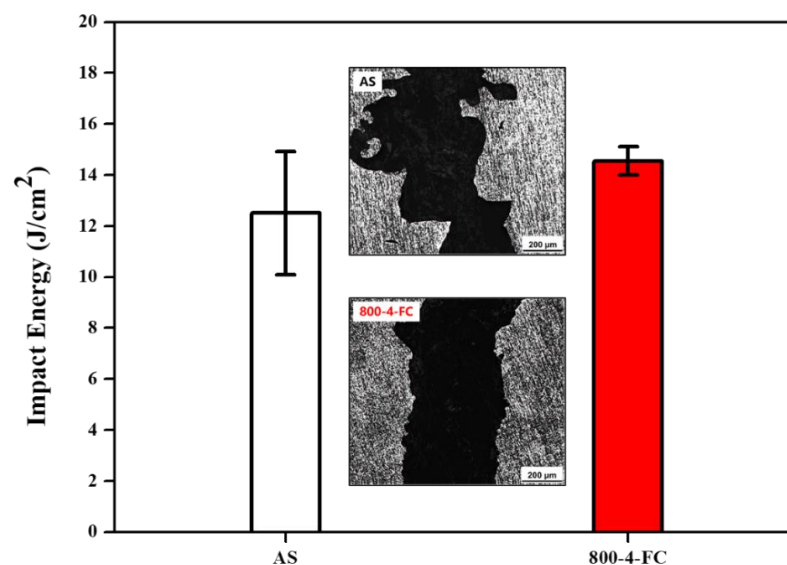


Figure 11. The mechanism of zinc addition on the tensile properties of AS, 800-FC, and 900-FC material.



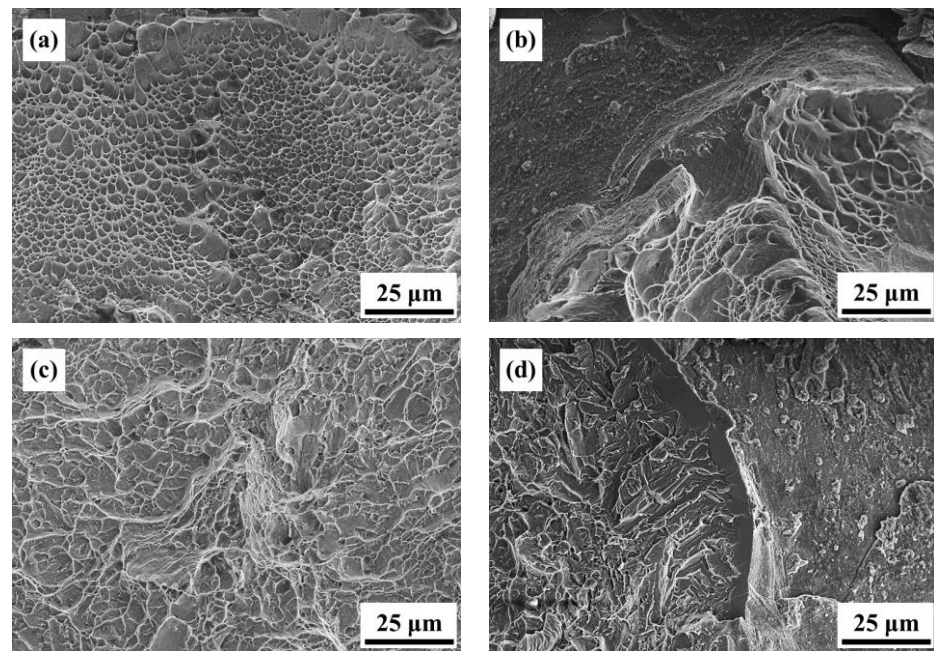
**Figure 12.** Room temperature tensile fracture surface morphology: (a) AS, (b) 800-1-FC, (c) 800-2-FC, (d) 800-4-FC, and (e) 800-8-FC.

Figure 13 presents the impact values and fracture sub-surfaces of the AS and 800-4-FC materials. The fracture sub-surface of the AS material shows numerous sharp fracture surfaces indicating crack propagation paths, with longer crack propagation distances. On the other hand, the fracture surface of the 800-4-FC material, (Figure 14), exhibits a layered structure with perpendicular fracture cracks, which effectively hinders crack propagation [32].



**Figure 13.** Impact energy and impact fracture sub-surface of AS and 800-4-FC material.





**Figure 14.** Impact fracture surfaces: (a) AS flat region, (b) AS cracked region, (c) 800-4-FC flat region, and (d) 800-4-FC cracked region.

Figure 15 displays the high-temperature tensile data of the AS material in the range of 250 °C to 400 °C. It can be observed that an increase in temperature leads to a decrease in strength and an improvement in ductility. Overall, the material still retains its applicability. Figure 16 illustrates the fracture surfaces of the AS material under high-temperature tensile testing. The proportion of dimple-like structures, which represents the ductile behavior of the material, increases with temperature. The size of the dimples is inversely proportional to the ductility. Moreover, the increase in temperature does not result in significant high-temperature oxidation effects in the AS material. The differences in fracture surfaces at different temperatures are minimal, indicating that the SLM Ti-6Al-4V-Zn titanium alloy can maintain stability at high temperatures [32].

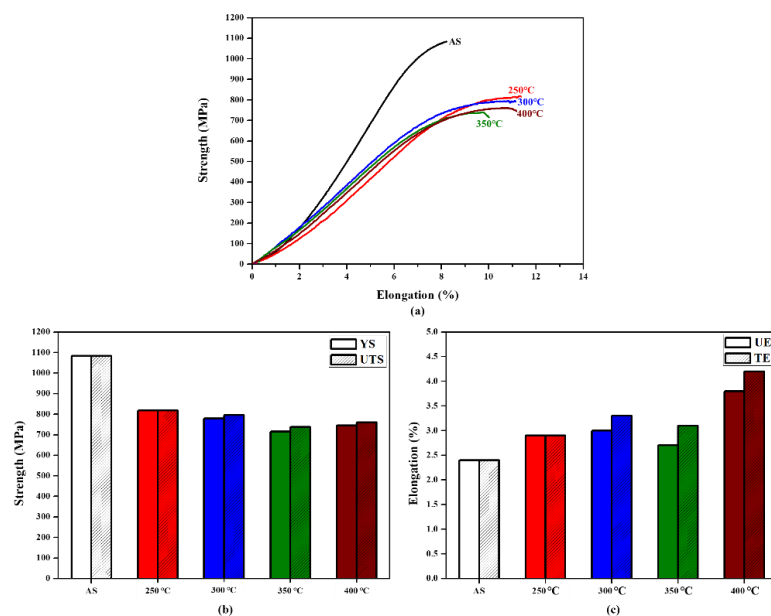


**Figure 15.** High-temperature tensile properties of AS material: (a) tensile curve, (b) yield strength and ultimate tensile strength, and (c) uniform elongation and total elongation.

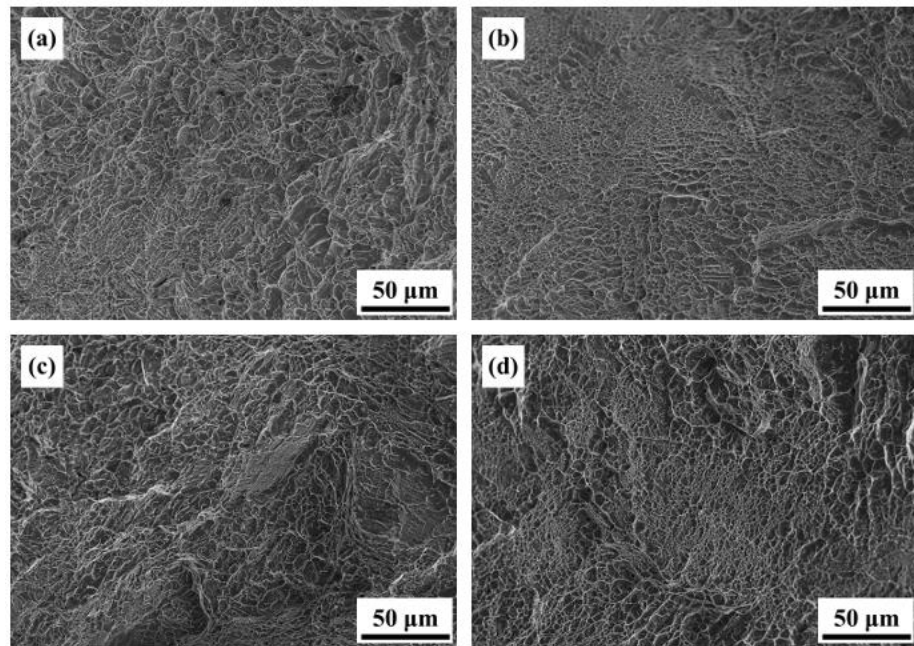


**Figure 16.** High-temperature tensile fracture surface morphology of AS material: (a) 250 °C, (b) 300 °C, (c) 350 °C, and (d) 400 °C.

Figure 17 presents the particle erosion weight loss rates of the AS material and the 800-4-FC material. Both materials exhibit peak erosion rates at 30° and the lowest rates at 90°. The erosion behavior in both cases is dominated by ductile deformation [30]. Moreover, for any erosion angle, the 800-4-FC material demonstrates lower erosion rates compared to the AS material. This indicates that the 800-4-FC material, which consists of a combination of the needle-like  $\alpha$  phase and lamellar  $\alpha + \beta$  phase, exhibits superior erosion resistance compared to the AS material, which consists only of the needle-like  $\alpha$  phase. Furthermore, the erosion rates of SLM Ti-6Al-4V gradually decrease from 30° to 90°.

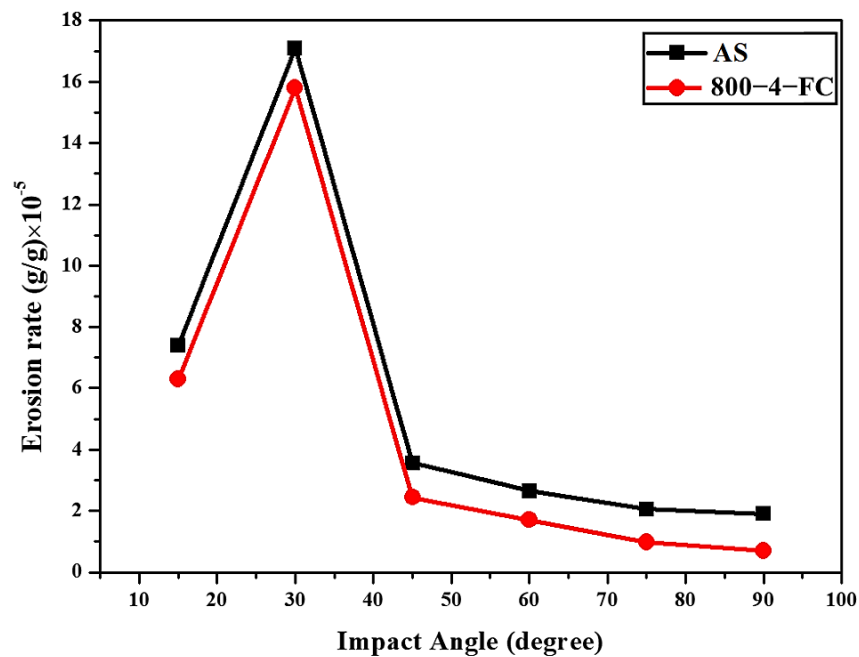


**Figure 17.** Erosion rates of AS and 800-4-FC material.

Figure 18 illustrates the XRD analysis of the AS material and the 800-4-FC material before and after particle erosion at 90°. The appearance of peaks corresponding to Al<sub>2</sub>O<sub>3</sub> and Al<sub>3</sub>Ti can be observed. This is attributed to the reaction between the sample surface and the eroded particles during the particle erosion process, as the surface temperature of the sample can reach up to 500 °C [32]. It is also possible that residual eroded particles remain on the sample surface, leading to the formation of these new phases. Furthermore, the peaks corresponding to Al<sub>2</sub>O<sub>3</sub> and Al<sub>3</sub>Ti are more pronounced in the AS-E material compared to the 800-4-FC-E material. This is attributed to the transformation of the microstructure into a combination of needle-like and lamellar structures after heat treatment, which effectively prevents the impact of particles. This mechanism has been reported in our previous study [32].

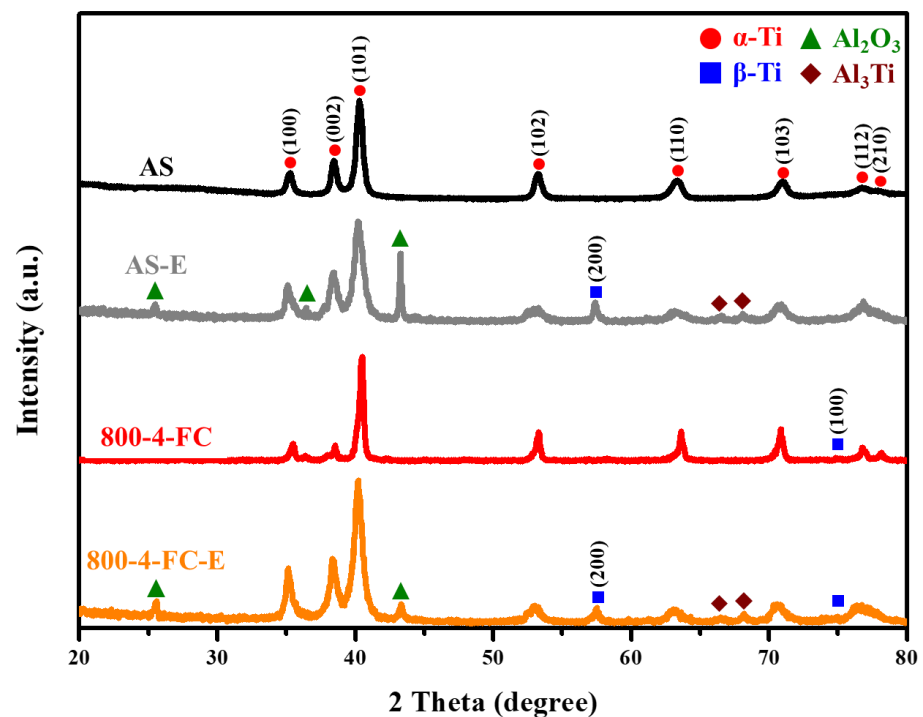
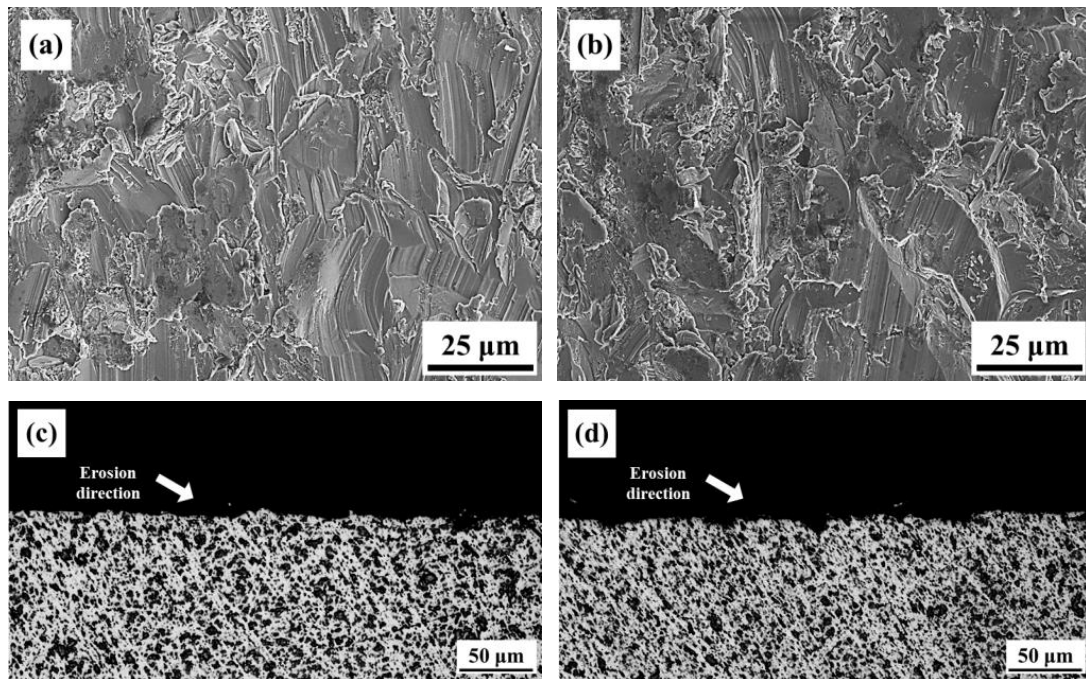


Figure 18. XRD analysis of AS and 800-4-FC material before and after particle erosion.

Observations were made on the eroded surfaces at 30° and 90° angles. After erosion at 30°, distinct and directional scratches were observed on the surface of the specimens, and localized plowing features were also present, as shown in Figure 19a,b. A comparison between the two angles revealed that the 800-4-FC material exhibited fewer surface scratches and plowing features. Similar observations were made on the sub-surface after erosion at 30°, as depicted in Figure 19c,d, with the sub-surface of the 800-4-FC material appearing relatively smoother, whereas the AS material exhibited more pronounced damage. For erosion at 90°, the eroded surfaces and sub-surfaces also exhibited less damage in the case of the 800-4-FC material. A comparison of the erosion surfaces in Figure 20a,b showed that the AS material exhibited more pits and larger scratched areas. On the other hand, in Figure 20c,d, which represents the sub-surfaces after 90° erosion, the AS material had narrower and deeper pits, whereas the 800-4-FC material had shallower and wider pits. The observations from Figures 19 and 20 collectively show that the 800-4-FC material possesses superior erosion resistance properties [33].





**Figure 19.** Surface and sub-surface morphology after 30° erosion: (a) AS surface, (b) 800-4-FC surface, (c) AS sub-surface, and (d) 800-4-FC sub-surface.

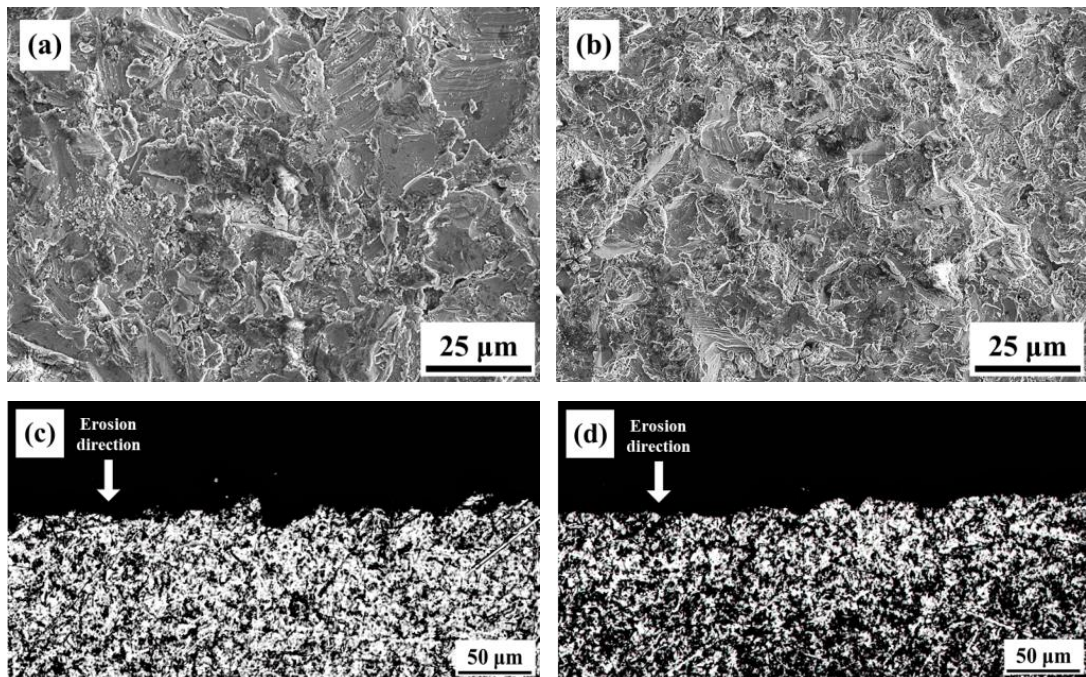


**Figure 20.** Surface and sub-surface morphology after 90° erosion: (a) AS surface, (b) 800-4-FC surface, (c) AS sub-surface, and (d) 800-4-FC sub-surface.

Figure 21 illustrates the differences in tensile properties between the AS and 800-4-FC materials before and after particle erosion. Compared to the AS material, the 800-4-FC material exhibited less deterioration in tensile properties after erosion, although both materials experienced a decrease in tensile strength following the erosion process. Figure 22 displays the tensile fracture surfaces of the AS and 800-4-FC materials after erosion. The 800-4-FC material exhibited predominantly cleavage fracture, whereas the AS material

showed only the localized regions of ductile dimples. The reduction in tensile properties can be attributed to the formation of new phases at high temperatures during particle erosion and the damage caused to the specimens during the erosion process.

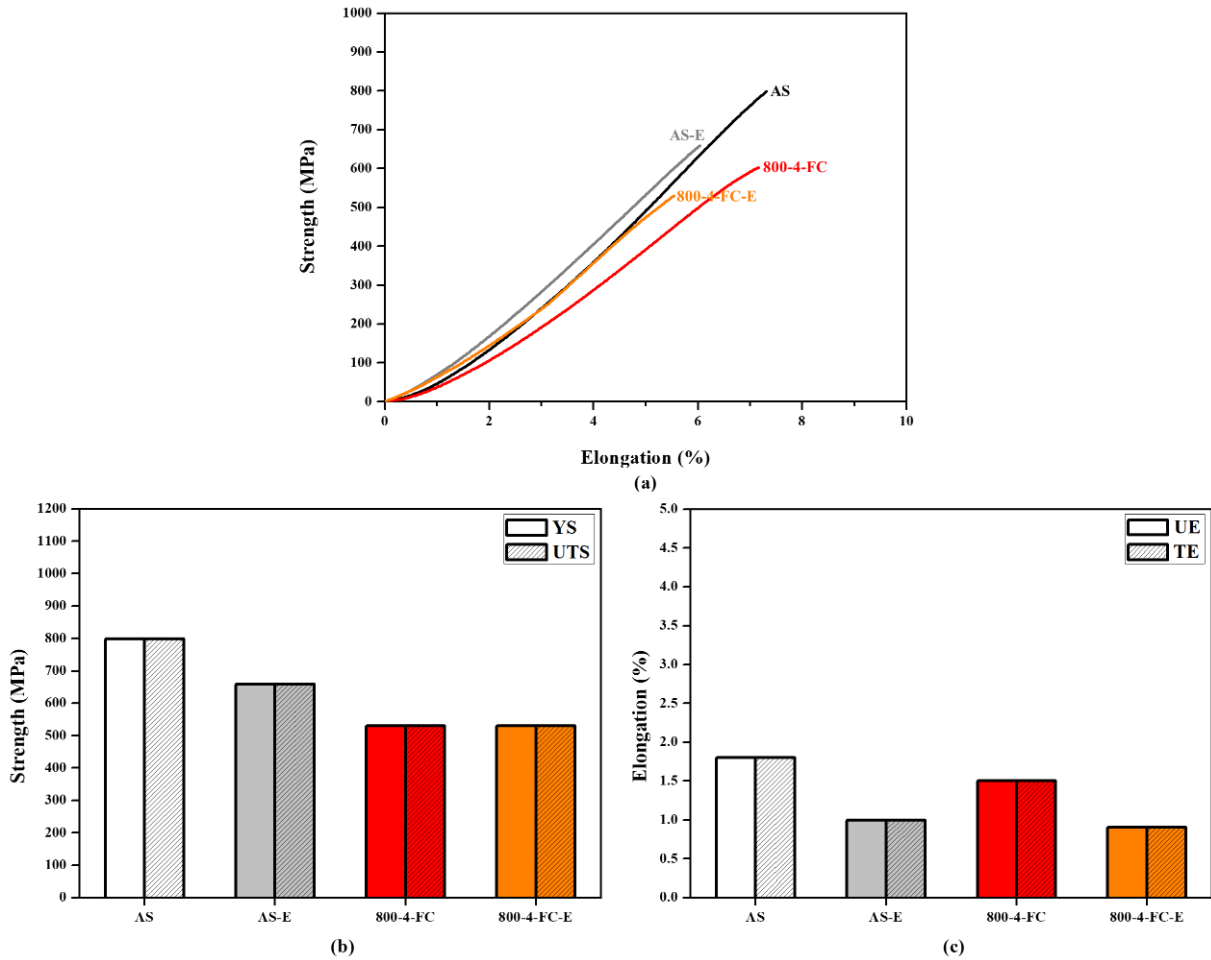


Figure 21. Tensile properties before and after particle erosion in AS and 800-4-FC material: (a) tensile curve, (b) yield strength and ultimate tensile strength, and (c) uniform elongation and total elongation.

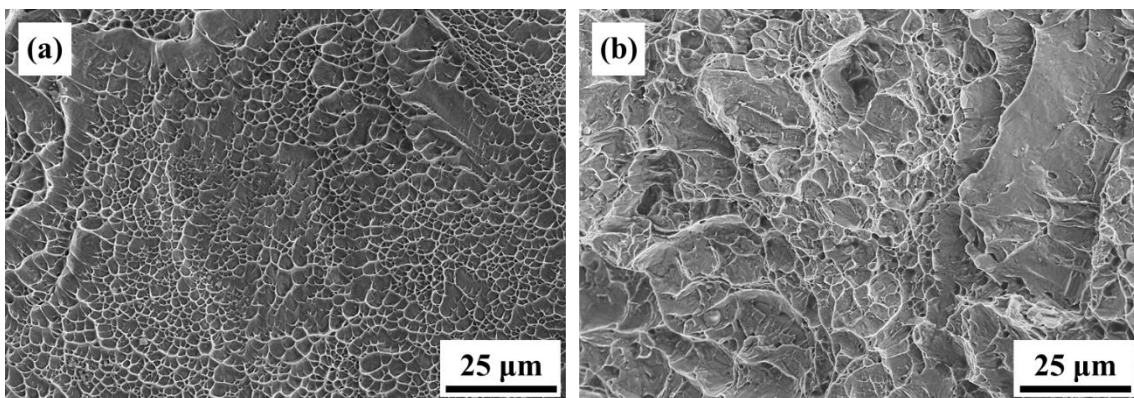
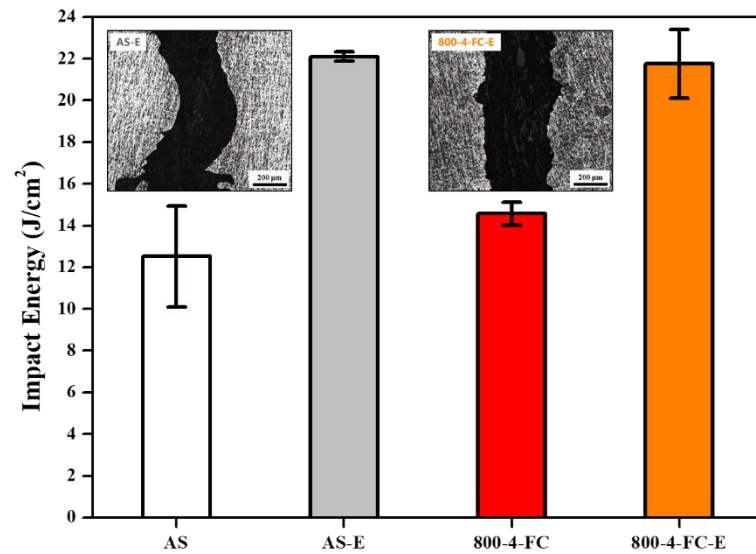


Figure 22. Tensile fracture surfaces after particle erosion: (a) AS and (b) 800-4-FC.

Figure 23 presents the differences in impact values and impact fracture sub-surfaces of the AS and 800-4-FC materials before and after particle erosion. It can be observed that the impact values increased after erosion, but there were no significant differences in the crack propagation path compared to before erosion. The increase in energy absorption is



attributed to the surface work hardening and the formation of a surface layer induced by particle erosion, which helps to absorb and disperse the impact energy [34].



**Figure 23.** Impact energy and impact fracture sub-surfaces before and after particle erosion of AS and 800-4-FC material.

Figure 24 compares the polarization curves of SLM Ti-6Al-4V-Zn AS material and SLM Ti-6Al-4V AS material [35]. Zinc itself is a corrosion-resistant metal, and according to our TEM results (Figures 8 and 9), most of the zinc in SLM Ti-6Al-4V-Zn is uniformly dissolved in titanium. Consequently, it effectively enhances corrosion resistance, resulting in a lower corrosion current density for SLM Ti-6Al-4V-Zn alloy ( $0.029 \text{ A/cm}^2$ ) compared to SLM Ti-6Al-4V alloy ( $0.039 \text{ A/cm}^2$ ).

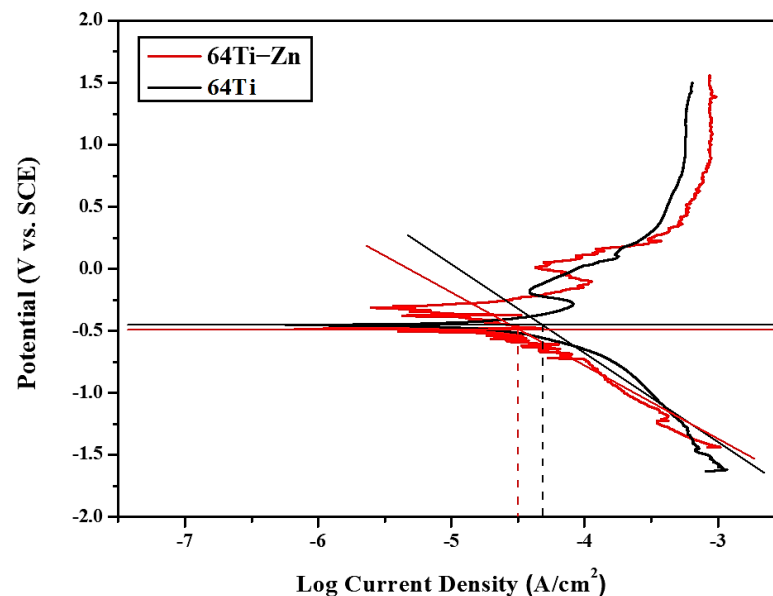


**Figure 24.** Polarization curves of SLM Ti-6Al-4V AS material and SLM Ti-6Al-4V-Zn AS material.

Based on several tests evaluating practical applicability and analyzing mechanisms, the 800-4-FC material demonstrates the best overall mechanical properties. It exhibits a combination of strength and ductility, maintains stability in high-temperature environments, and improves erosion and corrosion resistance compared to other materials.

#### 4. Limitations

The influence of the phase transformation layer on the tensile and impact properties after particle erosion can be further studied, including the thickness, phase structure, and high-temperature stability of the phase transformation layer.

#### 5. Conclusions

The microstructural characteristics of SLM Ti-6Al-4V-Zn exhibit a uniform distribution of needle-shaped  $\alpha$  phase in the ND plane. With increasing heat treatment temperature, this structure gradually transforms into a layered structure of  $\alpha + \beta$  phases. Zinc in the SLM Ti-6Al-4V-Zn titanium alloy is primarily distributed in a homogeneous solid solution within the titanium matrix, with only a small portion clustering and inhibiting the phase transformation of the needle-shaped  $\alpha$  phase. Therefore, the addition of zinc effectively stabilizes the  $\beta$  phase, and the incorporation of trace amounts of zinc does not impact its industrial applicability.

The vacuum heat treatment at 800 °C for 4 h followed by furnace cooling (800-4-FC) enhances ductility while maintaining strength in SLM Ti-6Al-4V-Zn. This is attributed to the coexistence of needle-shaped  $\alpha$  phase and layered  $\alpha + \beta$  phase in the optimal proportion, resulting in the best combination of tensile mechanical properties and impact energy. Additionally, the heat treatment improves the high-temperature oxidation resistance of the alloy, thereby enabling its industrial applicability even at elevated temperatures.

Particle erosion leads to the formation of new phases on the surface of SLM Ti-6Al-4V-Zn specimens due to high-temperature phase transformation and the reaction with eroded particles. Particle erosion induces surface work hardening, resulting in the formation of a hardened layer and improved impact toughness. The industrial applicability of SLM Ti-6Al-4V-Zn is enhanced by the addition of zinc, which improves its resistance to erosion and corrosion. Furthermore, its application performance is further enhanced via heat treatment.

**Author Contributions:** Conceptualization, F.-Y.H.; Validation, Y.-J.C. and J.-R.Z.; Investigation, Y.-J.C.; Resources, F.-Y.H.; Data curation, F.-Y.H. and J.-R.Z.; Writing—original draft, Y.-J.C.; Writing—review & editing, F.-Y.H. and J.-R.Z.; Supervision, F.-Y.H. All authors have read and agreed to the published version of the manuscript.

**Funding:** This research received no external funding.

**Institutional Review Board Statement:** Not applicable.

**Informed Consent Statement:** Not applicable.

**Data Availability Statement:** Data is contained within the article.

**Acknowledgments:** The authors are grateful to the Instrument Center of National Cheng Kung University and the Ministry of Science and Technology of Taiwan for their financial support. The authors also thank the Taiwan Circle Metal Powder Co., Ltd. and Taiwan ANJI Technology Co., Ltd. for providing the alloy powder and SLM printer, respectively.

**Conflicts of Interest:** The authors declare no conflict of interest.

#### References

- Jiang, J. A survey of machine learning in additive manufacturing technologies. *Int. J. Comput. Integr. Manuf.* **2023**, *36*, 1258–1280. [CrossRef]
- Nazir, A.; Gokcekaya, O.; Billah, K.M.M.; Ertugrul, O.; Jiang, J.; Sun, J.; Hussain, S. Multi-material additive manufacturing: A systematic review of design, properties, applications, challenges, and 3D Printing of materials and cellular metamaterials. *Mater. Des.* **2023**, *226*, 111661. [CrossRef]
- Peters, M.; Kumpferr, J.; Ward, C.H.; Leyens, C. Titanium alloys for aerospace applications. *Adv. Eng. Mater.* **2003**, *5*, 419–427. [CrossRef]
- Niu, X.; Zhu, S.P.; He, J.C.; Liao, D.; Correia, J.A.; Berto, F.; Wang, Q. Defect tolerant fatigue assessment of AM materials: Size effect and probabilistic prospects. *Int. J. Fatigue* **2022**, *160*, 106884. [CrossRef]

5. Fang, J.X.; Wang, J.X.; Wang, Y.J.; He, H.T.; Zhang, D.B.; Cao, Y. Microstructure evolution and deformation behavior during stretching of a compositionally inhomogeneous TWIP-TRIP cantor-like alloy by laser powder deposition. *Mater. Sci. Eng. A* **2022**, *847*, 143319. [CrossRef]
6. Nandhakumar, R.; Venkatesan, K. A process parameters review on Selective laser melting-based additive manufacturing of Single and Multi-Material: Microstructure, Properties, and machinability aspects. *Mater. Today Commun.* **2023**, *35*, 105538. [CrossRef]
7. Yap, C.Y.; Chua, C.K.; Dong, Z.L.; Liu, Z.H.; Zhang, D.Q.; Loh, L.E.; Sing, S.L. Review of selective laser melting: Materials and applications. *Appl. Phys. Rev.* **2015**, *2*, 041101. [CrossRef]
8. Peng, J.; Li, J.; Liu, B.; Wang, J.; Chen, H.; Feng, H.; Zeng, X.; Duan, H.; Cao, Y.; He, J. Formation process and mechanical properties in selective laser melted multi-principal-element alloys. *J. Mater. Sci. Technol.* **2023**, *133*, 12–22. [CrossRef]
9. Liu, S.; Shin, Y.C. Additive manufacturing of Ti6Al4V alloy: A review. *Mater. Des.* **2019**, *164*, 107552. [CrossRef]
10. Wang, Z.; Zhou, W.; Luo, K.; Lu, H.; Lu, J. Strengthening mechanism in thermomechanical fatigue properties of Ti6Al4V titanium alloy by laser shock peening. *Int. J. Fatigue* **2023**, *172*, 107631. [CrossRef]
11. Zochowski, P.; Bajkoruk, M.; Grygoruk, R.; Magier, M.; Burian, W.; Pyka, D.; Jamroziak, M.B.K. Ballistic impact resistance of bulletproof vest inserts containing printed titanium structures. *Metals* **2021**, *11*, 225. [CrossRef]
12. Yao, H.L.; Hu, X.Z.; Yi, Z.H.; Xia, J.; Tu, X.Y.; Li, S.B.; Yu, B.; Zhang, M.X.; Bai, X.B.; Chen, Q.Y.; et al. Microstructure and improved anti-corrosion properties of cold-sprayed Zn coatings fabricated by post shot-peening process. *Surf. Coat. Technol.* **2021**, *422*, 127557. [CrossRef]
13. Maniam, K.K.; Paul, S. Corrosion performance of electrodeposited zinc and zinc-alloy coatings in marine environment. *Corros. Mater. Degrad.* **2021**, *2*, 163–189. [CrossRef]
14. Pola, A.; Tocci, M.; Goodwin, F.E. Review of microstructures and properties of zinc alloys. *Metals* **2020**, *10*, 253. [CrossRef]
15. Arun, S.; Lim, B.-S.; Ahn, S.-G.; Choe, H.-C. Osteoconductive element-doped, porous, and low-elastic-modulus duplex coatings on a Ti-6Al-4V alloy: A hybrid coating system for accelerating cell growth. *J. Alloys Compd.* **2023**, *943*, 169131. [CrossRef]
16. Liu, W.; Zhao, Y.; Zhang, Y.; Shuai, C.; Chen, L.; Huang, Z.; Hou, H. Deformation-induced dynamic precipitation of 14H-LPSO structure and its effect on dynamic recrystallization in hot-extruded Mg-Y-Zn alloys. *Int. J. Plast.* **2023**, *164*, 103573. [CrossRef]
17. Zhang, Y.; Chen, X.; Jayalakshmi, S.; Singh, R.A.; Deev, V.B.; Prusov, E.S. Factors determining solid solution phase formation and stability in CoCrFeNiX<sub>0.4</sub> (X = Al, Nb, Ta) high entropy alloys fabricated by powder plasma arc additive manufacturing. *J. Alloys Compd.* **2021**, *857*, 157625. [CrossRef]
18. Xu, C.; Wu, Q.; Hua, Y.; Li, J. The electrodeposition of Zn-Ti alloys from ZnCl<sub>2</sub>-urea deep eutectic solvent. *J. Solid State Electrochem.* **2014**, *18*, 2149–2155. [CrossRef]
19. Saidi, R.; Ashrafizadeh, F.; Raeissi, K.; Kharaziha, M. Electrochemical aspects of zinc oxide electrodeposition on Ti6Al4V alloy. *Surf. Coat. Technol.* **2020**, *402*, 126297. [CrossRef]
20. Wang, N.X.; Wang, Y.S.; Zheng, K.; Zhi, J.Q.; Zhou, B.; Wu, Y.X.; Xue, X.P.; Ma, Y.; Cheng, F.; Gao, J.; et al. Achieving CVD diamond films on Mo<sub>0.5</sub> (TiZrTaW)<sub>0.5</sub> highly concentrated alloy for ultrastrong corrosion resistance. *Surf. Coat. Technol.* **2023**, *466*, 129620. [CrossRef]
21. Gogia, A. High-temperature titanium alloys. *Def. Sci. J.* **2005**, *55*, 149–173. [CrossRef]
22. Finnie, I. Some observations on the erosion of ductile metals. *Wear* **1973**, *23*, 87–96. [CrossRef]
23. Dai, W.S.; Chen, L.H.; Lui, T.S. A study on SiO<sub>2</sub> particle erosion of flake graphite and spheroidal graphite cast irons. *Wear* **2000**, *239*, 143–152. [CrossRef]
24. Cai, F.; Huang, X.; Yang, Q. Mechanical properties, sliding wear and solid particle erosion behaviors of plasma enhanced magnetron sputtering CrSiCN coating systems. *Wear* **2015**, *324–325*, 27–35. [CrossRef]
25. Khoddami, A.; Salimi-Majd, D.; Mohammadi, B. Finite element and experimental investigation of multiple solid particle erosion on Ti-6Al-4V titanium alloy coated by multilayer wear-resistant coating. *Surf. Coat. Technol.* **2019**, *372*, 173–189. [CrossRef]
26. Saidi, R.; Raeissi, K.; Ashrafizadeh, F.; Kharaziha, M. The effect of zinc oxide coating morphology on corrosion performance of Ti-6Al-4V alloys. *J. Alloys Compd.* **2021**, *883*, 160771. [CrossRef]
27. Lv, Z.; Li, H.; Che, L.; Chen, S.; Zhang, P.; He, J.; Wu, Z.; Niu, S.; Li, X. Effects of HIP Process Parameters on Microstructure and Mechanical Properties of Ti-6Al-4V Fabricated by SLM. *Metals* **2023**, *13*, 991. [CrossRef]
28. Okamoto, H. Ti-Zn (titanium-zinc). *J. Phase Equilibria Diffus.* **2008**, *29*, 211–212. [CrossRef]
29. Chen, Y.; Sun, S.; Zhang, T.; Zhou, X.; Li, S.S. Effects of post-weld heat treatment on the microstructure and mechanical properties of laser-welded NiTi/304SS joint with Ni filler. *Mater. Sci. Eng. A* **2020**, *771*, 138545. [CrossRef]
30. Zhao, J.R.; Hung, F.Y.; Lui, T.S. Particle erosion induced phase transformation of different matrix microstructures of powder bed fusion Ti-6Al-4V alloy flakes. *Metals* **2019**, *9*, 730. [CrossRef]
31. Elshaer, R.N.; Ibrahim, K.M. Study of microstructure; mechanical properties, and corrosion behavior of as-cast Ni-Ti and Ti-6Al-4V alloys. *J. Mater. Eng. Perform.* **2023**, *32*, 7831–7845. [CrossRef]
32. Zhao, J.R.; Hung, F.Y.; Lui, T.S.; Wu, Y.L. The relationship of fracture mechanism between high temperature tensile mechanical properties and particle erosion resistance of selective laser melting Ti-6Al-4V alloy. *Metals* **2019**, *9*, 501. [CrossRef]
33. Huang, B.C.; Chang, K.C.; Hung, F.Y.; Microstructure, S.O. Mechanical Properties and Erosion Characteristics of Al-Si Alloy Manufactured by Continuous Casting Direct Rolling Process. *Appl. Sci.* **2021**, *11*, 8351. [CrossRef]

34. Chen, H.; Zhao, D.; Wang, Q.; Qiang, Y.; Qi, J. Effects of impact energy on the wear resistance and work hardening mechanism of medium manganese austenitic steel. *Friction* **2017**, *5*, 447–454. [CrossRef]
35. Zhang, Q.; Duan, B.; Zhang, Z.; Wang, J.; Si, C. Effect of ultrasonic shot peening on microstructure evolution and corrosion resistance of selective laser melted Ti–6Al–4V alloy. *J. Mater. Res. Technol.* **2021**, *11*, 1090–1099. [CrossRef]

**Disclaimer/Publisher’s Note:** The statements, opinions and data contained in all publications are solely those of the individual author(s) and contributor(s) and not of MDPI and/or the editor(s). MDPI and/or the editor(s) disclaim responsibility for any injury to people or property resulting from any ideas, methods, instructions or products referred to in the content.



## Article

# Phase Stability and Slag-Induced Destabilization in MnO<sub>2</sub> and CeO<sub>2</sub>-Doped Calcia-Stabilized Zirconia

Hwanseok Lee <sup>1,†</sup>, Hee-Seon Lee <sup>1,2,†</sup> , Seonghoon Kim <sup>1</sup>, Kanghee Jo <sup>1</sup>, Ilguk Jo <sup>3,\*</sup> and Heesoo Lee <sup>1,\*</sup>

<sup>1</sup> School of Materials Science and Engineering, Pusan National University, Busan 46241, Republic of Korea; hwanseok@pusan.ac.kr (H.L.); lhs9693@kriect.re.kr (H.-S.L.); seonghoonkim@pusan.ac.kr (S.K.); jokanghee@pusan.ac.kr (K.J.)

<sup>2</sup> Reliability Assessment Center, Korea Research Institute of Chemical Technology, Daejeon 34114, Republic of Korea

<sup>3</sup> Advanced Materials Engineering, Dong-Eui University, Busan 47340, Republic of Korea

\* Correspondence: ijo@deu.ac.kr (I.J.); heesoo@pusan.ac.kr (H.L.); Tel.: +82-51-890-1698 (I.J.); +51-510-2388 (H.L.)

† These authors contributed equally to this work.

**Abstract:** MnO<sub>2</sub> and CeO<sub>2</sub> were doped to improve the corrosion resistance of CSZ (calcia-stabilized zirconia), and we studied the phase formation, mechanical properties, and corrosion resistance by molten mold flux. The volume fraction of the monoclinic phase gradually decreased as the amount of MnO<sub>2</sub> doping increased. The splitting phenomenon of the t(101) peak was observed in 2Mn\_CSZ, and in 4Mn\_CSZ, it was completely split, forming a cubic phase. The relative density increased and the monoclinic phase decreased as the doping amount increased, leading to an increase in Vickers hardness and flexural strength. However, in 3Mn\_CSZ and 4Mn\_CSZ, where cubic phase formation occurred, the tetragonal phase decreased, leading to a reduction in these properties. MnO<sub>2</sub>-doped CSZ exhibited a larger fraction of the monoclinic phase compared to the original CSZ after the corrosion test, indicating worsened corrosion resistance. These results are attributed to the predominant presence of Mn<sup>3+</sup> and Mn<sup>2+</sup> forms, rather than the Mn<sup>4+</sup> form, which has a smaller basicity difference with SiO<sub>2</sub>, and due to the low melting point. The monoclinic phase fraction decreased as the doping amount of CeO<sub>2</sub> increased in CeO<sub>2</sub>-doped CSZ, but the rate of decrease was lower compared to MnO<sub>2</sub>-doped CSZ. The monoclinic phase decreased as the doping amount increased, but the Vickers hardness and flexural strength showed a decreasing trend due to the low relative density. The destabilization behavior of Ca in SEM-EDS images before and after corrosion was difficult to identify due to the presence of Ca in the slag, and the destabilization behavior of Ce due to slag after corrosion was not observed. In the XRD data of the specimen surface after the corrosion test, the fraction of the monoclinic phase increased compared to before the test but showed a lower monoclinic phase fraction compared to CSZ. It is believed that CeO<sub>2</sub> has superior corrosion resistance compared to CaO because Ce predominantly exists in the form of Ce<sup>4+</sup>, which has a smaller difference in basicity within the zirconia lattice.

**Keywords:** calcia-stabilized zirconia; slag; submerged entry nozzle; immersion resistance; phase stability; stabilizing agents



**Citation:** Lee, H.; Lee, H.-S.; Kim, S.; Jo, K.; Jo, I.; Lee, H. Phase Stability and Slag-Induced Destabilization in MnO<sub>2</sub> and CeO<sub>2</sub>-Doped Calcia-Stabilized Zirconia. *Materials* **2023**, *16*, 7240. <https://doi.org/10.3390/ma16227240>

Academic Editor: Chih-Chun Hsieh

Received: 1 November 2023

Revised: 12 November 2023

Accepted: 17 November 2023

Published: 20 November 2023



**Copyright:** © 2023 by the authors. Licensee MDPI, Basel, Switzerland. This article is an open access article distributed under the terms and conditions of the Creative Commons Attribution (CC BY) license (<https://creativecommons.org/licenses/by/4.0/>).

## 1. Introduction

The submerged entry nozzle (SEN) is a functional refractory material that plays a crucial role in the final stage of continuous casting, situated between the tundish and the mold [1]. It prevents contact between the molten metal and air while ensuring a steady flow of molten metal into the mold and stabilizing the flow of the molten metal [2]. The SEN must possess excellent thermal shock resistance to withstand rapid temperature changes and sufficient strength to bear the pressure of the molten metal. Additionally, it requires high corrosion resistance and wear resistance against molten metal and slag for prolonged

usage [3,4]. The body of the SEN primarily utilizes  $\text{Al}_2\text{O}_3\text{-C}$ -based refractories, but in the areas that contact slag,  $\text{ZrO}_2\text{-C}$ -based refractories are used due to their superior corrosion resistance and abrasion resistance [5]. In  $\text{ZrO}_2\text{-C}$ -based refractories,  $\text{ZrO}_2$  is chemically stable, resistant to forming low-melting-point compounds, and has excellent thermal spalling resistance. Graphite minimizes thermal shock by providing excellent thermal conductivity and reduces contact and reactions between slag and the refractory material due to its low wettability with slag [6]. However,  $\text{ZrO}_2\text{-C}$ -based refractories are known to be eroded by slag [7]. It is commonly understood that erosion occurs due to the flow at the interface between slag and molten metal [8,9]. The interface between slag and molten metal fluctuates, causing the  $\text{ZrO}_2\text{-C}$  refractory to alternately come into contact with the molten metal and slag. When the molten metal rises, graphite dissolves into the molten metal, exposing the surface of  $\text{ZrO}_2$ . When the molten metal descends,  $\text{ZrO}_2$  is exposed to the slag without graphite, and it is known that  $\text{ZrO}_2$  dissolves into the slag, leading to erosion. The dissolution of  $\text{ZrO}_2$  by the slag is known to be the rate-determining step, given the rapid dissolution of graphite into the molten metal in this erosion mechanism [10]. However, this mechanism explains erosion at the interface between slag and molten metal, but it does not explain erosion that occurs further up from the interface. Therefore, Hauck and Potschke proposed a localized corrosion mechanism due to interfacial tension gradients [11]. This mechanism suggests that slag covers  $\text{ZrO}_2$  due to surface tension, forming a slag film and eroding  $\text{ZrO}_2$ . In this manner, the submerged entry nozzle is explained by complex erosion mechanisms, and ultimately, since the erosion rate of  $\text{ZrO}_2$  determines the life of the submerged entry nozzle, research is being conducted to reduce the erosion rate of  $\text{ZrO}_2$  and to decrease the graphite content [12]. However, the reduction in graphite content causes a lower thermal conductivity in  $\text{ZrO}_2\text{-C}$  refractories, which can lead to a decrease in thermal shock resistance. Therefore, there is a need to secure thermal shock resistance through the improvement of the mechanical properties of zirconia.

Partially stabilized zirconia (PSZ), which exhibits excellent thermal shock resistance due to transformation toughening as cubic or tetragonal phases transform to the monoclinic phase, is used for submerged entry nozzles [13,14]. PSZ is obtained by stabilizing high-temperature phases at room temperature by adding stabilizers such as  $\text{MgO}$ ,  $\text{CaO}$ , and  $\text{Y}_2\text{O}_3$ . Primarily,  $\text{CaO}$ -stabilized zirconia (CSZ) is used for submerged entry nozzles [15]. However, CSZ has issues with corrosion caused by slag, and the destabilization of zirconia due to reactions with slag is known to be the main cause.  $\text{SiO}_2$  present in the slag reacts with  $\text{CaO}$  to form a low-melting-point glass, and it is known to transform cubic or tetragonal phases of zirconia into the monoclinic phase, breaking up the zirconia grains [16,17]. To improve the durability of submerged entry nozzles, it is necessary to address the destabilization of zirconia caused by slag, and progress is being made in enhancing corrosion resistance through co-doping.

Corrosion of refractories by slag is related to the basicity and viscosity of the slag, and Hirata et al. have presented an experimental equation to predict the corrosion rate of ceramic materials by slag [18].

$$\log \Delta D = 0.18 \log \Delta B - 0.55 \log \eta + C \quad (1)$$

where  $\Delta D$  is the depth of corrosion ( $\mu\text{m}$ ),  $\Delta B$  is the basicity gap between slag and ceramics,  $\eta$  is the viscosity of the slag, and  $C$  is a constant that varies depending on the corrosion conditions. The basicity gap can be calculated through the  $\Delta B$  parameter proposed by Morinaga et al., estimated as follows [19]:

$$B = \sum n_i B_i \quad (2)$$

$$B_i = \frac{\left( \frac{(r_i + 1.40)^2}{Z_i \times 2} \right) - 0.405}{1.023} \quad (3)$$

where  $n_i$  represents the fraction of cation  $i$  for all cations, and  $r_i$  and  $Z_i$  represent the ionic radius and charge of cation  $i$ , respectively. This parameter can represent the basicity of completely molten oxides, assuming that the bond between cations and anions in the slag is ionic. From this equation, we can deduce that the basicity increases as the ionic radius increases and the charge decreases, and to reduce reactivity with  $\text{SiO}_2$ , it is necessary to dope with acidic elements.

In this study, we aimed to enhance the corrosion resistance of CaO-stabilized zirconia (CSZ) by doping it with acidic  $\text{CeO}_2$  and  $\text{MnO}_2$  and analyzing the resultant mechanical properties. XRD analysis was performed to investigate the changes in crystal structure due to doping, including variations in monoclinic phase fraction and peak shifts/corrosion tests were conducted to assess the corrosion resistance of  $\text{CeO}_2$  and  $\text{MnO}_2$ -doped CSZ and analyze the associated destabilization behavior.

## 2. Experimental Procedures

CaO-stabilized zirconia (CSZ) is a commercial refractory powder, and its chemical composition is listed in Table 1.  $\text{MnO}_2$  (Junsei Chemical Co., Ltd., Kanto, Japan, 90%) powder and  $\text{CeO}_2$  (Kanto Chemical Co., Inc., Tokyo, Japan, 99.99%) were used as dopants. The particle size distribution characteristics and SEM images of the powders are shown in Figures 1 and 2.  $\text{MnO}_2$ -doped CSZ and  $\text{CeO}_2$ -doped CSZ were prepared as shown in Table 2.  $\text{MnO}_2$  and  $\text{CeO}_2$  were introduced into CSZ powders by the mechanical mixing method. The mixed powders were ball milled in ethanol for 24 h. Mixed solutions were then dried at  $100^\circ\text{C}$  using a dry oven, calcinated for 24 h using a dry oven, and then calcined at  $1200^\circ\text{C}$  for 2 h in a box-type electric furnace. Powder was uniaxially pressed at  $3\text{ ton/m}^2$  to produce a 20 mm disk specimen, and the green body was sintered at  $5^\circ\text{C}/\text{min}$  to various temperatures ( $1300\text{--}1600^\circ\text{C}$ ) for 4 h. The bar-type specimens ( $3.5\text{ mm} \times 4.5\text{ mm} \times 36\text{ mm}$ ) were uniaxially pressed at  $3.2\text{ ton/m}^2$  in a steel die and heated up to  $1600^\circ\text{C}$  with a heating rate of  $5^\circ\text{C}/\text{min}$  for 4 h.

**Table 1.** Chemical composition of CSZ powder (mol. %).

ZrO <sub>2</sub>	CaO	HfO <sub>2</sub>	SiO <sub>2</sub>	Al <sub>2</sub> O <sub>3</sub>	TiO <sub>2</sub>
81.818	13.707	1.739	1.894	0.324	0.517

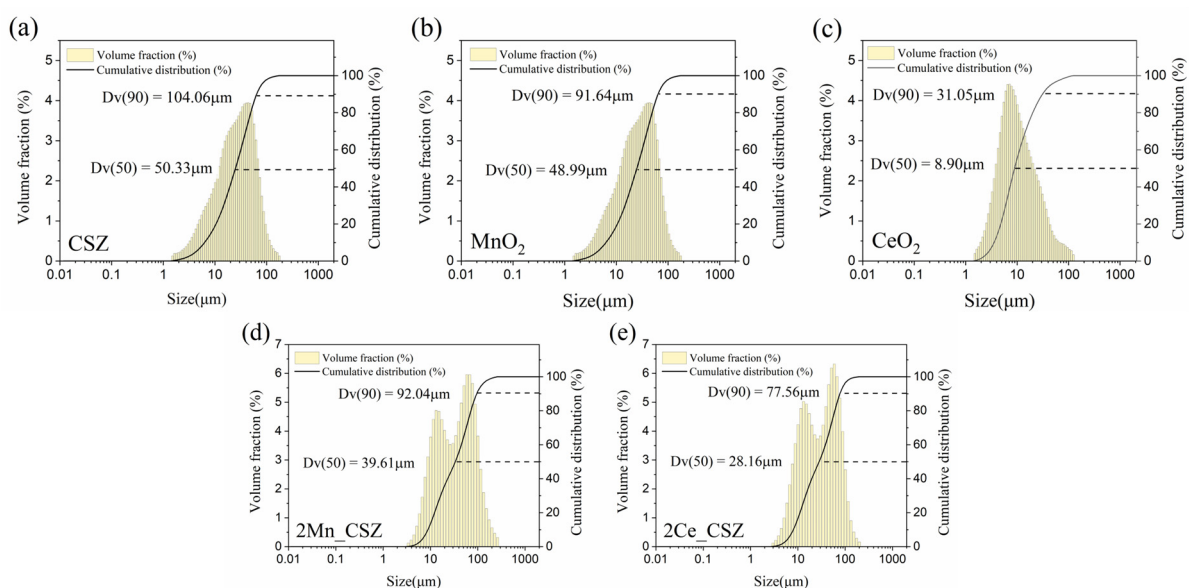


**Figure 1.** Particle size distribution of (a) CSZ powder, (b)  $\text{MnO}_2$  powder, (c)  $\text{CeO}_2$  powder, (d) 2Mn\_CSZ powder after calcination and (e) 2Ce\_CSZ powder after calcination.

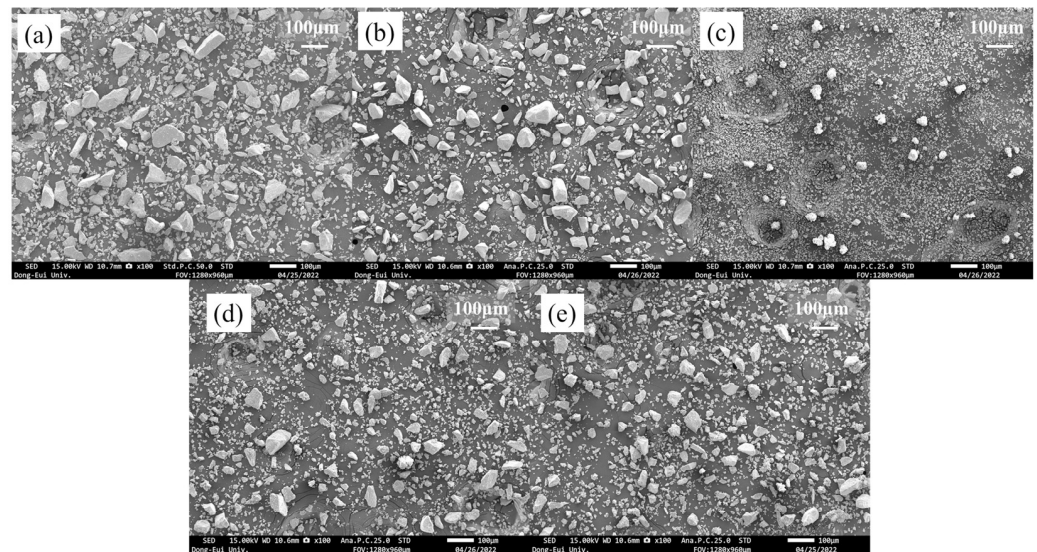


**Figure 2.** (a) CSZ powder, (b)  $\text{MnO}_2$  powder, (c)  $\text{CeO}_2$  powder, (d) 2Mn\_CSZ powder after calcination, and (e) 2Ce\_CSZ powder after calcination.

**Table 2.** Composition of the CSZ specimens with different amounts of  $\text{MnO}_2$  and  $\text{CeO}_2$ .

Compound	Composition		
	$\text{MnO}_2$ (mol%)	$\text{CeO}_2$ (mol%)	CSZ
1Mn_CSZ	1	-	Balance
2Mn_CSZ	2	-	
3Mn_CSZ	3	-	
4Mn_CSZ	4	-	
1Ce_CSZ	-	1	
2Ce_CSZ	-	2	
3Ce_CSZ	-	3	
4Ce_CSZ	-	4	

A corrosion test was performed using slag powder, and the composition of the slag powder is indicated in Table 3. 0.7 g of the slag powder was formed into pellets using a cylindrical 15 mm mold with a pressure of 1 ton/ $\text{m}^2$ . The slag pellets were then placed on sintered zirconia specimens and heat-treated in a box furnace at 1550 °C for 10 h in an air atmosphere.

**Table 3.** Chemical composition of slag powder (mol. %).

Slag Powder	$\text{SiO}_2$	$\text{CaO}$	$\text{Na}_2\text{O}$	$\text{MgO}$	$\text{Al}_2\text{O}_3$
Composition (mol. %)	35.500	35.919	23.897	2.940	1.743

The densities of sintered pellets were determined using the Archimedes' method, which involved immersing the samples in distilled water. X-ray diffraction (XRD) patterns of the specimens were collected at room temperature using a step scan procedure ( $2\theta = 10\text{--}90^\circ$ , with a step interval of  $0.02^\circ$ ) and  $\text{Cu-K}\alpha$  radiation on a Rigaku Ultima-IV XRD instrument (Rigaku Corporation, Tokyo, Japan) at the Converging Materials Core Facility. The XRD data obtained for phase analysis was analyzed using Rigaku SmartLab Studio II software version 4.3.101.0.

Monoclinic phase was determined from the integrated intensity of the X-ray diffraction scan based on ISO 5803 [20].

$$X = \frac{I\left(\bar{1}11\right)_m + I(111)_m}{I\left(\bar{1}11\right)_m + I(111)_M + I(101)_t} \quad (4)$$

$$X = \frac{I\left(\bar{1}11\right)_m + I(111)_m}{I\left(\bar{1}11\right)_m + I(111)_M + I_{ttc}} \quad (5)$$

Formular (4) is for a two-phase system (monoclinic and tetragonal phases), and Formular (5) is for multi-phase system (a mixture of monoclinic, tetragonal, and cubic).  $X$  is an integrated intensity ratio. Where  $I\left(\bar{1}11\right)_m$  and  $I(111)_m$  refer to the integral intensity of the X-ray diffraction pattern of monoclinic. The  $I(101)_t$  refers to the integral intensity from the (101) plane of tetragonal and  $I_{ttc}$  is total integrated intensity of tetragonal phase (101) and cubic phase (111) reflection. Calculate the volume fraction of the monoclinic phase using Formular (6):

$$f_m = \frac{PX}{1 + (P - 1)X} \quad (6)$$

$f_m$  is the volume fraction of the monoclinic phase and the  $P$  is the intensity factor. In the monoclinic-tetragonal  $ZrO_2$  system,  $P = 1.219$  is used, while in the multiphase system,  $P = 1.265$  is used.

A nano indenter (FISCHERSCOPE, HM2000, Sindelfingen, Germany) was used to measure the Vickers hardness. Flexural strength was measured with the three-point bending method using test specimens measuring  $3.5 \text{ mm} \times 4.5 \text{ mm} \times 36 \text{ mm}$ . The SEM images of the samples were obtained by using a scanning electron microscope (JEOL Ltd., JSM-IT800, Tokyo, Japan).

### 3. Results and Discussion

Figure 1 presents the particle size analysis (PSA) data of the powders. CSZ and  $MnO_2$  consisted of coarser particles with average diameters of  $50.33 \mu\text{m}$  and  $48.99 \mu\text{m}$ , respectively, while  $CeO_2$  comprised finer particles with an average diameter of  $8.90 \mu\text{m}$ . This trend is well illustrated in Figure 2, where CSZ and  $MnO_2$  exhibit non-uniform, coarse single particles. Figure 1d,e presents the PSA data of 2Mn\_CSZ and 2Ce\_CSZ powders, which were wet ball milled and calcined at  $1200 \text{ }^\circ\text{C}$ , demonstrating a reduction in average diameter compared to the original CSZ. Figure 2d,e displays smaller particle sizes compared to the original CSZ. Additionally, the average particle diameter of 2Ce\_CSZ, which is doped with the relatively finer  $CeO_2$ , was  $28.16 \mu\text{m}$ , smaller than that of 2Mn\_CSZ at  $39.61 \mu\text{m}$ .

Figure 3 shows the XRD patterns of  $MnO_2$ -doped CSZ sintered at  $1600 \text{ }^\circ\text{C}$  for 4 h. In CSZ, both the monoclinic phase (ICSD 98-006-0900, space group of  $P1\ 21/c\ 1$ ) and the tetragonal phase (ICSD 98-007-0014, space group of  $P\ 42/nmc$ ) were observed, with the monoclinic volume fraction reaching 33.7%. As shown in Figure 3b, the monoclinic peak gradually decreased with the increase in  $MnO_2$  doping amount. The monoclinic volume fraction was 19.7% in 1Mn\_CSZ, while the monoclinic phase was not observed in 3Mn\_CSZ and 4Mn\_CSZ. In 2Mn\_CSZ, the phenomenon of peak splitting at the t(101) peak was observed, and as the doping amount increased, the peak splitting became more distinct. In 4Mn\_CSZ, complete splitting was confirmed, and the formation of a cubic phase (ICSD 98-010-5553, space group  $Fm\bar{3}m$ ) was verified through Figure 2c, with the cubic phase fractions in 3Mn\_CSZ and 4Mn\_CSZ being determined to be 4.6% and 9.1%, respectively (Table 4). In addition, a higher angle shift was observed with the increase in doping amount, suggesting a change in the valence state of Mn during doping. Clavel et al. reported that

when the content of Mn is less than 1.4%, Mn exists mainly in the form of  $\text{Mn}^{2+}$  (96 Å) in zirconia, which is larger than  $\text{Zr}^{4+}$  (84 Å). However, as the Mn content increases, Mn mainly exists as  $\text{Mn}^{3+}$  (64.5 Å), which has a smaller ionic radius than  $\text{Zr}^{4+}$ , inducing lattice distortion [21]. Thus, the doped Mn mainly forms a substitutional solid solution as  $\text{Mn}^{3+}$ , creating oxygen vacancies and stabilizing the monoclinic phase into tetragonal and cubic phases [22].

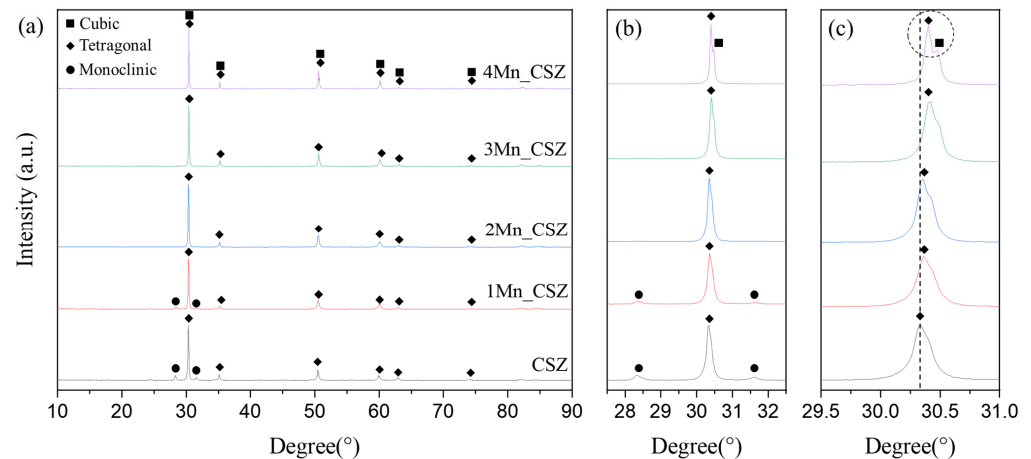


**Figure 3.** (a) XRD diffraction patterns (b)  $m(111)$  and  $m(111)$  peaks and (c)  $t(101)$  and  $C(111)$  peaks of  $\text{MnO}_2$ -doped CSZ.

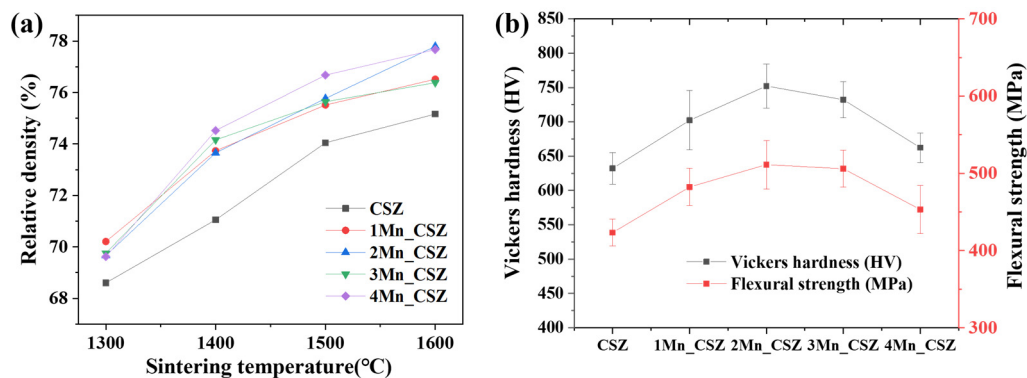
**Table 4.** Monoclinic volume fraction of  $\text{MnO}_2$ -doped CSZ.

Specimen	Volume Fraction (%)		
	Monoclinic ( $V_m$ )	Tetragonal ( $V_t$ )	Cubic ( $V_c$ )
CSZ	33.7	66.3	-
1Mn_CSZ	19.7	80.3	-
2Mn_CSZ	2.8	97.2	-
3Mn_CSz	-	95.4	4.6
4Mn_CSZ	-	90.9	9.1

Figure 4a shows the graph of the relative density changes of  $\text{MnO}_2$ -doped CSZ with temperature. The relative density appearing in the 70% range is believed to be attributed to the larger particle size of the zirconia refractory powder, as shown in Figure 1a, resulting in incomplete densification. In the SEM images of the specimen sintered at 1600 °C (Supplementary Figure S1), it was difficult to observe microstructural changes due to density changes because the overall density was low. It was observed that the relative density increased with the doping of  $\text{MnO}_2$ , while CSZ displayed a relative density of 75.16% at 1600 °C, 4Mn-doped CSZ exhibited a higher relative density of 77.68%.  $\text{MnO}_2$ , having a low melting point of 535 °C, acted as an additive, enhancing the relative density [23]. Figure 4b presents the Vickers hardness and flexural strength of  $\text{MnO}_2$ -doped CSZ. As  $\text{MnO}_2$  was doped, the Vickers hardness steadily increased from 632.12 Hv (CSZ) to 752.12 Hv (2Mn\_CSZ), and the flexural strength increased from 423.25 MPa (CSZ) to 511.23 MPa (2Mn\_CSZ). These results are attributed to the increase in relative density and the decrease in monoclinic phase fraction due to  $\text{MnO}_2$  doping [24]. However, as the doping amount of  $\text{MnO}_2$  increased further, the mechanical properties decreased. The Vickers hardness dropped to 732.26 Hv (3Mn\_CSZ) and 662.35 Hv (4Mn\_CSZ), and the flexural strength decreased to 505.89 MPa (3Mn\_CSZ) and 453.25 MPa (4Mn\_CSZ). Despite the increase in relative density, the decrease in mechanical properties is considered to be related to the formation of the cubic phase. The formation of the cubic phase reduces the tetragonal

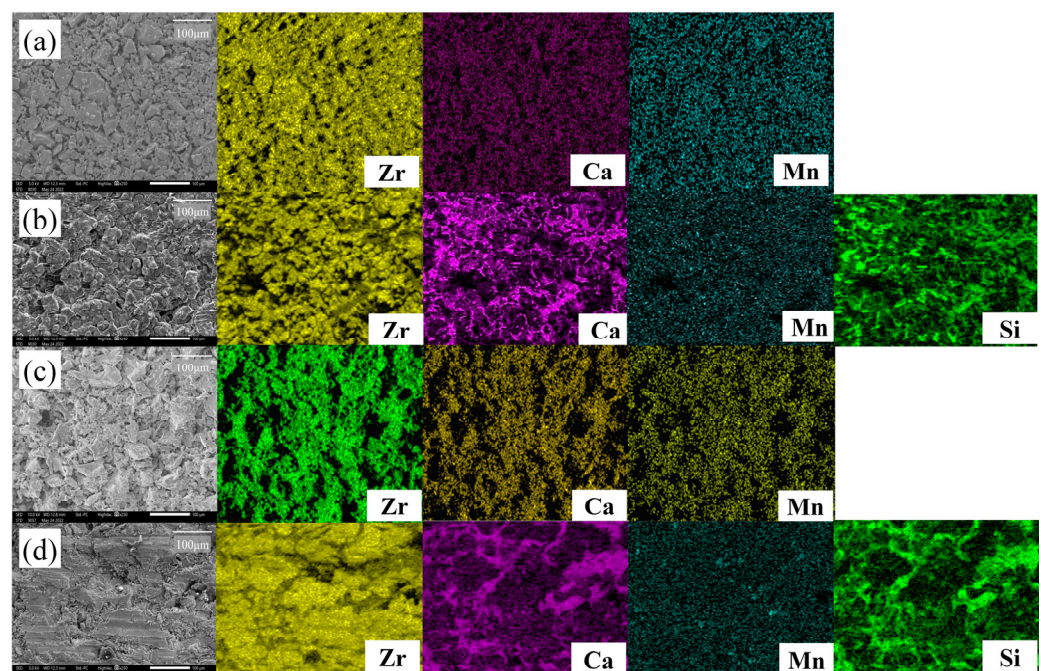


phase, diminishing the transformation toughening effect arising from the martensitic phase transformation from tetragonal to monoclinic phases [25].



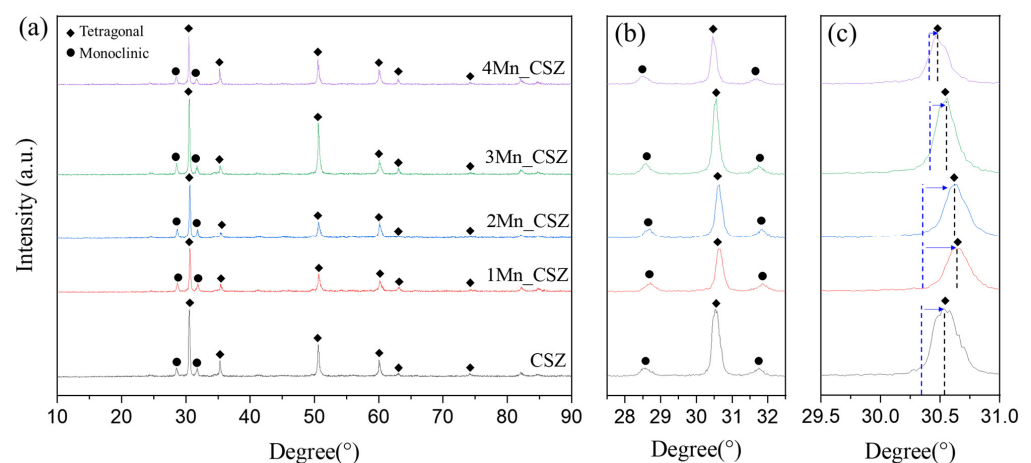
**Figure 4.** (a) Relative density vs. sintering temperature, and (b) Vickers hardness and flexural strength of MnO<sub>2</sub>-doped CSZ.

Figure 5 shows SEM-EDS images of 2Mn\_CSZ magnified 250 times before and after corrosion, where the specimen sintered at 1600 °C was subjected to corrosion in slag at 1550 °C for 10 h. In the pre-corrosion surface image of 2Mn\_CSZ (Figure 5a), it is apparent that full densification has not occurred due to the coarse particle size, and EDS scanning revealed that Ca and Mn were uniformly dispersed without agglomeration. Figure 5b shows the surface of 2Mn\_CSZ after corrosion, and the EDS scans of Ca and Si indicate that residues of slag remain on the surface. The presence of slag residues made it difficult to observe the destabilization behavior due to the leaching of Mn and Ca from 2Mn\_CSZ caused by the slag. The post-corrosion cross-sectional SEM-EDS images of 2Mn\_CSZ (Figure 5d) reveal that the slag has penetrated the interior due to the high porosity of the specimen, making it impossible to evaluate the internal corrosion resistance through the assessment of the penetration depth of the slag.



**Figure 5.** SEM-EDS surface images of 2Mn\_CSZ (a) before corrosion, and (b) after corrosion and SEM-EDS corrosion cross-sectional images of 2Mn\_CSZ (c) before corrosion, and (d) after corrosion test (same magnification).

Figure 6 shows the XRD data of the MnO<sub>2</sub>-doped CSZ specimens' surface after corrosion. After the corrosion, only the tetragonal and monoclinic peaks were observed in MnO<sub>2</sub>-doped CSZ, while no slag peaks were detected. This is due to the formation of a glass phase during the rapid cooling process following the corrosion test [26]. In 4Mn\_CSZ, although a cubic peak was initially observed, no cubic phase was detected after corrosion. As indicated in Table 5, the cubic volume fraction decreased from 9.1% before corrosion to 0% after corrosion, which is considered to be a phase transition caused by destabilization. In Figure 6c, it can be seen that the CSZ has shifted to a higher angle after corrosion (from 30.34° to 30.52°), indicating that Ca<sup>2+</sup> ions, which are larger than Zr<sup>4+</sup> ions, have leached out from the lattice due to reactions with the slag. Before the corrosion test, the MnO<sub>2</sub>-doped CSZ showed a low-angle shift due to the doping of smaller Mn<sup>3+</sup> and Mn<sup>4+</sup> ions, positioning the t(101) at a lower angle compared to CSZ. In particular, the 1Mn\_CSZ exhibited the largest shift from 30.36° before corrosion to 30.66° after corrosion. However, after the corrosion test, the t(101) position was at a higher angle than that in the undoped case. These results corresponded with the monoclinic phase fraction results, with 1Mn\_CSZ showing the highest monoclinic phase fraction of 42.7% after corrosion. As the amount of MnO<sub>2</sub> doping increased, the angle shift to a higher angle after corrosion decreased, with the 4Mn\_CSZ shifting from 30.40° before corrosion to 30.46° after corrosion. These results suggest that Mn, being smaller than the zirconia ions, has also leached out from the zirconia lattice due to destabilization, resulting in a combined effect of a lower angle shift due to Mn leaching and a higher angle shift due to Ca leaching. All specimens with Mn doping showed a higher fraction of the monoclinic phase compared to the original CSZ, indicating a decrease in corrosion resistance. As mentioned earlier, the corrosion of stabilized zirconia by slag is primarily due to the leaching of stabilizers by SiO<sub>2</sub> [16,17]. The  $B_i$  values of SiO<sub>2</sub> and CaO calculated using Equation (3) are 0.470 and 1.613, respectively. Since SiO<sub>2</sub> and CaO not only form a glass phase but also have a large difference in basicity, a significant reaction can be expected. The  $B_i$  values for MnO<sub>2</sub>, Mn<sub>2</sub>O<sub>3</sub>, and MnO are 0.536, 0.796, and 1.563, respectively. Although the  $B_i$  of MnO<sub>2</sub> does not differ significantly from that of SiO<sub>2</sub>, it is expected that the reaction will be minimal. However, since Mn in the zirconia lattice mainly exists in the form of Mn<sup>3+</sup>, there is a difference in basicity, leading to potential instability. Additionally, the melting points of MnO<sub>2</sub> and Mn<sub>2</sub>O<sub>3</sub> are 535 °C and 940 °C, respectively, which are significantly lower than the 2572 °C of CaO, suggesting that leaching into the slag would be easier.

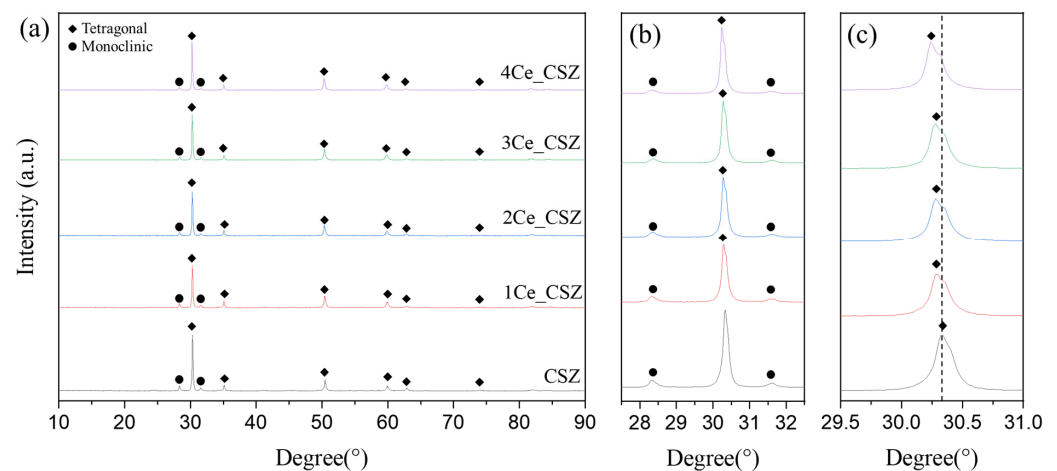


**Figure 6.** (a) XRD diffraction patterns, (b)  $m(111)$  and  $m(111)$  peaks, and (c)  $t(101)$  peaks of MnO<sub>2</sub>-doped CSZ after corrosion test.

**Table 5.** Monoclinic volume fraction of MnO<sub>2</sub>-doped CSZ after corrosion test.

Specimen	Volume Fraction (%)		
	Monoclinic (V <sub>m</sub> )	Tetragonal (V <sub>t</sub> )	Cubic (V <sub>c</sub> )
CSZ	33.7 → 39.4	66.3 → 33.7	-
1Mn_CSZ	19.7 → 42.7	80.3 → 57.3	-
2Mn_CSZ	2.8 → 42.5	91.2 → 57.5	-
3Mn_CSz	- → 40.0	95.4 → 60.0	4.6 → -
4Mn_CSZ	- → 42.4	90.9 → 57.6	9.1 → -

Figure 7 presents the XRD patterns of CeO<sub>2</sub>-doped CSZ, which was sintered at 1600 °C for 4 h. Both monoclinic and tetragonal phases were observed in the CeO<sub>2</sub>-doped CSZ. As seen in Figure 7b, the monoclinic peak gradually decreased with the increase of CeO<sub>2</sub> doping, resulting in a decrease in the monoclinic volume fraction from 29.5% in 1Ce\_CSZ to 21.8% in 4Ce\_CSZ (Table 6). In Figure 7c, a lower angle shift occurred with the increase in doping amount, indicating that the lattice expanded due to the doping of Ce<sup>4+</sup> (97 Å), which is larger than Zr<sup>4+</sup> (84 Å) [27]. When compared to MnO<sub>2</sub>-doped CSZ, the rate of decrease in the monoclinic phase was lower. This is because when MnO<sub>2</sub> is doped, it mainly forms a substitutional solid solution in the form of Mn<sup>3+</sup> (64.5 Å), creating oxygen vacancies to maintain charge neutrality, leading to a significant stabilization effect due to the formation of these vacancies [28]. On the other hand, when CeO<sub>2</sub> is doped, both Ce<sup>3+</sup> and Ce<sup>4+</sup> exist, predominantly in the form of Ce<sup>4+</sup>. Thus, stabilization primarily occurs due to lattice stress caused by the ionic radius difference between Zr<sup>4+</sup> and Ce<sup>4+</sup>, resulting in a weaker effect on stabilizing the tetragonal phase compared to MnO<sub>2</sub> [29].

**Figure 7.** (a) XRD diffraction patterns, (b) m (111) and m (111) peaks, and (c) t(101) of CeO<sub>2</sub>-doped CSZ.**Table 6.** Monoclinic volume fraction of CeO<sub>2</sub>-doped CSZ after corrosion test.

c	Volume Fraction (%)		
	Monoclinic (V <sub>m</sub> )	Tetragonal (V <sub>t</sub> )	Cubic (V <sub>c</sub> )
CSZ	33.7	66.3	-
1Ce_CSZ	29.5	70.5	-
2Ce_CSZ	27.9	72.1	-
3Ce_CSz	24.6	75.4	-
4Ce_CSZ	21.8	78.2	-

Figure 8a illustrates the graph of relative density changes in CeO<sub>2</sub>-doped CSZ, indicating a trend of decreasing relative density with increasing amounts of CeO<sub>2</sub> doping.

The SEM images of the specimen sintered at 1600 °C (Supplementary Figure S2) show that, due to the overall low density, it was challenging to observe microstructural changes associated with density changes. The relative density gradually decreased from 75.1% (CSZ) to 72.23% (4Ce\_CSZ) at 1600 °C, and this result is attributed to the fact that CeO<sub>2</sub> generates a low sinterability system [30]. Figure 8b illustrates the Vickers hardness and flexural strength of CeO<sub>2</sub>-doped CSZ. The Vickers hardness decreased from 612.57 Hv (1Ce\_CSZ) to 586.35 Hv (4Ce\_CSZ), and the flexural strength also reduced from 412.63 MPa (1Ce\_CSZ) to 392.22 MPa. Even though an increase in tetragonal phase was observed with an increase in CeO<sub>2</sub> doping, the sinterability deteriorated, leading to a decrease in mechanical properties.

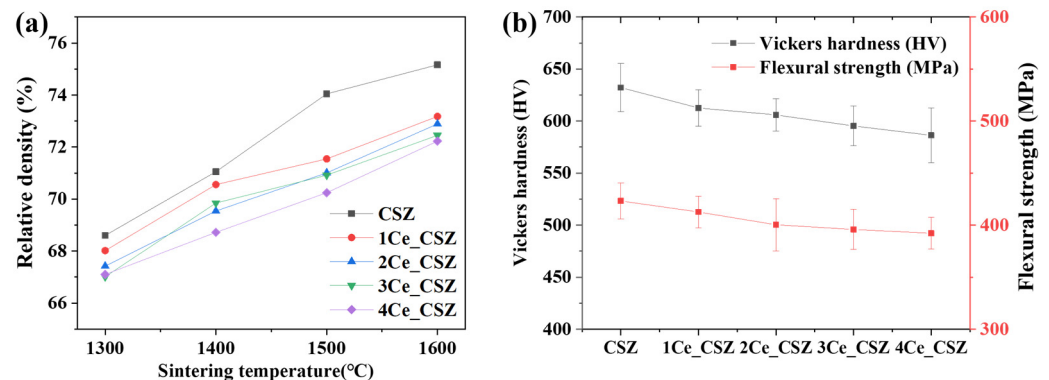
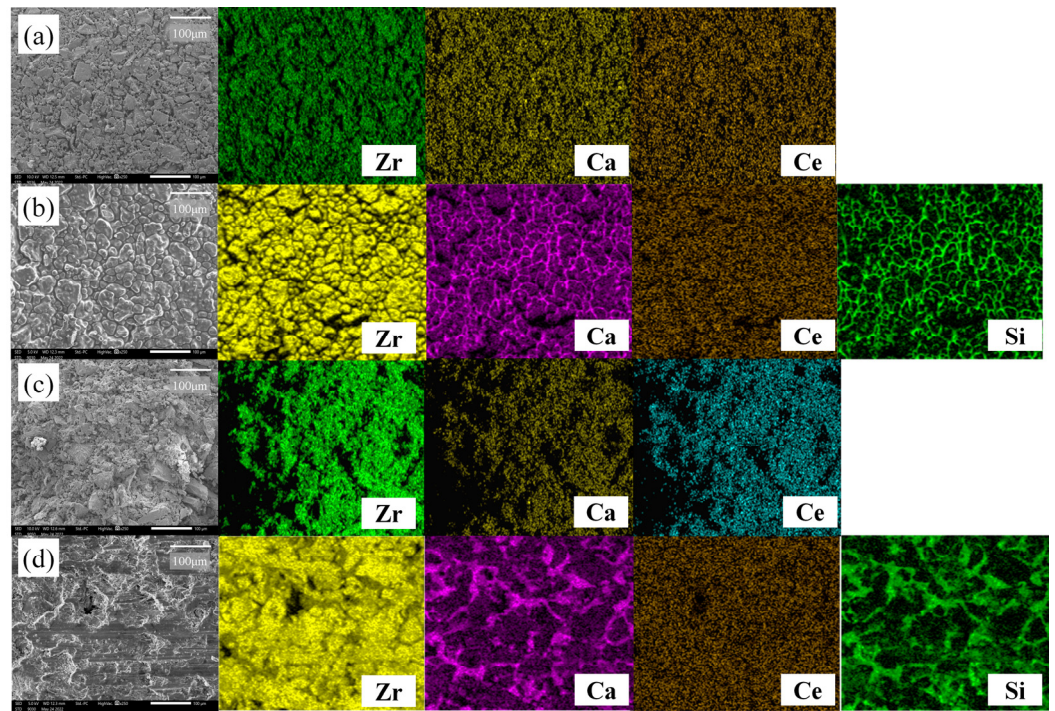


**Figure 8.** (a) Relative density vs. sintering temperature, and (b) Vickers hardness and flexural strength of CeO<sub>2</sub>-doped CSZ.

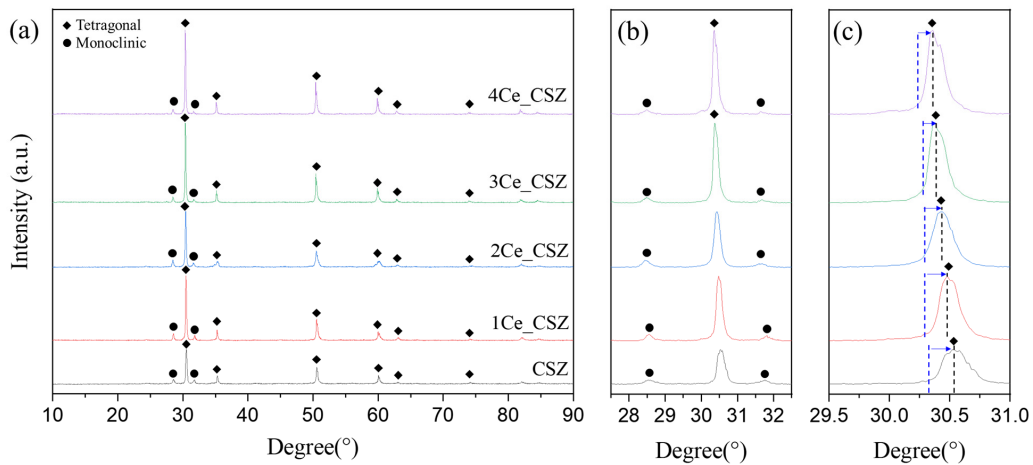
Figure 9 shows the SEM-EDS images of 2Ce\_CSZ magnified 250 times before and after corrosion. In the pre-corrosion surface image of 2Ce\_CSZ, Figure 9a, it is observable that complete densification has not occurred due to the coarse particle size, and the EDS scan confirmed that Ca and Ce were evenly dispersed without agglomeration. After corrosion, the surface of 2Ce\_CSZ shows signs of deterioration due to the slag. The EDS scans of Ca and Si reveal remnants of slag left on the surface, particularly concentrated near the grain boundaries that formed post-corrosion. Discerning the destabilization behavior of Ca was challenging due to the presence of Ca in the slag, and no destabilization behavior of Ce due to slag post-corrosion was observed. Figure 9d presents the cross-sectional SEM-EDS images of 2Ce\_CSZ after corrosion, where the infiltration of slag into the interior due to high porosity can be seen.

Figure 10 shows the surface XRD data of CeO<sub>2</sub>-doped CSZ after corrosion. Similar to MnO<sub>2</sub>-doped CSZ, no slag peaks were observed in CeO<sub>2</sub>-doped CSZ post-corrosion; instead, tetragonal and monoclinic peaks were present. After corrosion, the monoclinic phase fraction calculated through the integrated intensity of X-ray diffraction increased due to destabilization, though it remained lower than that of CSZ (Table 7). Additionally, as the doping amount of CeO<sub>2</sub> increased, the monoclinic phase fraction further decreased. In Figure 10c, the *t*(101) peak exhibited a high angle shift due to destabilization, with less shift occurring as the Ce doping amount increased. The calculated *B<sub>i</sub>* value for CeO<sub>2</sub> using Equation (3) is 0.702, not significantly different from the *B<sub>i</sub>* value of SiO<sub>2</sub> (0.470), indicating a small basicity gap. Consequently, it is inferred that CeO<sub>2</sub>-doped CSZ demonstrates superior corrosion resistance compared to CaO, and unlike MnO<sub>2</sub>-doped CSZ, Ce is not easily leached by the slag, allowing the tetragonal phase to be maintained.





**Figure 9.** SEM-EDS surface images of 2Ce\_CSZ (a) before corrosion, and (b) after corrosion and SEM-EDS corrosion cross-sectional images of 2Ce\_CSZ (c) before corrosion, and (d) after corrosion test (same magnification).



**Figure 10.** (a) XRD diffraction patterns, (b) m (111) and m (111) peaks, and (c) t(101) of CeO<sub>2</sub>-doped CSZ after corrosion.

**Table 7.** Monoclinic volume fraction of CeO<sub>2</sub>-doped CSZ after corrosion.

Specimen	Volume Fraction (%)		
	Monoclinic (V <sub>m</sub> )	Tetragonal (V <sub>t</sub> )	Cubic (V <sub>c</sub> )
CSZ	33.7 → 39.4	66.3 → 60.6	-
1Ce_CSZ	29.5 → 33.5	70.5 → 66.5	-
2Ce_CSZ	27.9 → 31.2	72.1 → 68.8	-
3Ce_CSz	24.6 → 27.5	75.4 → 72.5	-
4Ce_CSZ	21.8 → 24.8	78.2 → 75.2	-

#### 4. Conclusions

We doped CSZ with MnO<sub>2</sub> and CeO<sub>2</sub>, respectively, to enhance its corrosion resistance and investigated the mechanical properties and slag-induced destabilization behavior. The monoclinic phase volume fraction decreased from 33.7% (CSZ) to 0% (3Mn\_CSZ, 4Mn\_CSZ) as the doping amount of MnO<sub>2</sub> increased. A splitting phenomenon of the t(101) peak was observed in 2Mn\_CSZ, and a complete splitting resulting in a cubic phase occurred in 4Mn\_CSZ. It was noted that the relative density increased with MnO<sub>2</sub> doping, showing a relative density of 77.68% in 4Mn-doped CSZ compared to 75.16% in CSZ at 1600 °C. The increase in relative density and decrease in monoclinic phase fraction with MnO<sub>2</sub> doping resulted in an increase in Vickers hardness and flexural strength, though these properties decreased in 3Mn\_CSZ and 4Mn\_CSZ, where a cubic phase was formed. The monoclinic phase fraction of CSZ increased from 33.7% to 39.4% after the corrosion test. The MnO<sub>2</sub>-doped CSZ had a higher monoclinic phase fraction compared to CSZ after the corrosion test, resulting in reduced corrosion resistance, and the monoclinic phase fraction of 4Mn\_CSZ increased from 0% to 42.4%. These results are attributed to the predominant existence of Mn in the forms of Mn<sup>3+</sup> and Mn<sup>2+</sup>, rather than Mn<sup>4+</sup>, and their low melting points due to the small basicity gap with SiO<sub>2</sub>. With CeO<sub>2</sub>-doped CSZ, an increase in the CeO<sub>2</sub>-doping amount led to a decrease in the monoclinic phase fraction, though at a lower rate than in MnO<sub>2</sub>-doped CSZ. This is because Ce in the zirconia lattice mainly exists in the form of Ce<sup>4+</sup>, and the stabilization of the tetragonal phase is mainly due to the lattice stress caused by the ionic radius difference between Zr<sup>4+</sup> and Ce<sup>4+</sup>, resulting in a less significant stabilizing effect than MnO<sub>2</sub>. CeO<sub>2</sub>-doped CSZ showed a lower relative density compared to CSZ due to its low sinterability, leading to a decrease in Vickers hardness and flexural strength. Pre- and post-corrosion SEM-EDS images indicated that the destabilizing behavior of Ca was challenging to observe due to the presence of Ca in the slag, and no post-corrosion destabilizing behavior of Ce due to slag was observed. The XRD data from the specimen surface post-corrosion exhibited a lower monoclinic phase fraction compared to CSZ, decreasing progressively with increased CeO<sub>2</sub> doping. These results suggest that CeO<sub>2</sub> primarily exists in the form of Ce<sup>4+</sup> within the zirconia lattice, demonstrating superior slag resistance compared to CaO due to the small basicity gap. For further study, we aim to conduct research on simultaneously doping MnO<sub>2</sub> and CeO<sub>2</sub> to combine the high phase stability of MnO<sub>2</sub> for improved thermal shock resistance and enhanced corrosion resistance from CeO<sub>2</sub>.

**Supplementary Materials:** The following supporting information can be downloaded at: <https://www.mdpi.com/article/10.3390/ma16227240/s1>, Figure S1: SEM surface images of (a) CSZ, (b) 1Mn\_CSZ, (c) 2Mn\_CSZ, (d) 3Mn\_CSZ and (e) 4Mn\_CSZ sintered at 1600 °C. Figure S2: SEM surface images of (a) CSZ, (b) 1Ce\_CSZ, (c) 2Ce\_CSZ, (d) 3Ce\_CSZ and (e) 4Ce\_CSZ sintered at 1600 °C.

**Author Contributions:** Conceptualization, H.L. (Hwanseok Lee); data curation, H.L. (Hwanseok Lee), H.-S.L. and K.J.; formal analysis, H.L. (Hwanseok Lee), H.-S.L. and S.K.; acquisition, H.L. (Heesoo Lee); investigation, H.L. (Hwanseok Lee), S.K. and H.-S.L.; methodology, H.L. (Hwanseok Lee) and K.J.; projection administration, H.L. (Heesoo Lee); supervision, I.J.; visualization, I.J.; writing—original draft preparation, H.L. (Hwanseok Lee); writing—review and editing, I.J. and H.L. (Heesoo Lee). All authors have read and agreed to the published version of the manuscript.

**Funding:** This work was supported by Korea Institute for Advancement of Technology (KIAT) grant funded by the Korea Government (MOTIE) (P0008335, HDR Program for Industrial Innovation).

**Institutional Review Board Statement:** Not applicable.

**Informed Consent Statement:** Not applicable.

**Data Availability Statement:** The data and analysis in this study are available on request from the corresponding authors.

**Conflicts of Interest:** The authors declare no conflict of interest.



## References


1. Zhao, P.; Piao, R.; Zou, Z. Mesoscopic Fluid-Particle Flow and Vortex Structural Transmission in a Submerged Entry Nozzle of Continuous Caster. *Materials* **2022**, *15*, 2510. [CrossRef] [PubMed]
2. Sunwoo, S.; Kim, H.; Lee, J.K. Corrosion mechanism of zirconia/graphite SEN by molten steel and slag. *J. Korean Cryst. Growth Cryst.* **2000**, *10*, 226–232.
3. Colin, S.; Jeannot, F.; Dupre, B.; Gleitzer, C.; Kaerle, M.C.; Le Coq, X. Ceria-doped zirconia-graphite as possible refractory for tundish nozzles in steelmaking. *J. Eur. Ceram. Soc.* **1993**, *11*, 515–521. [CrossRef]
4. Kondo, H. Submerged entry nozzle which prevents alumina clogging. *Shinagawa Tech. Rep.* **1997**, *40*, 29–34.
5. Peirani, M.V.; Brandaleze, E. Corrosion mechanisms caused on a submerged nozzle applied in steel billet production by mold fluxes with and without fluorine. *Sch. J. Eng. Technol.* **2017**, *5*, 280–289.
6. Nakamura, Y.; Ando, T.; Kurata, K.; Ikeda, M. Effect of chemical composition of mold powder on the erosion of submerged nozzles for continuous casting of steel. *Trans. Iron Steel Inst. Jpn* **1986**, *26*, 1052–1058. [CrossRef]
7. Yan, W.; Chen, W.; Li, J. Quality control of high carbon steel for steel wires. *Materials* **2019**, *12*, 846. [CrossRef]
8. Dick, A.F.; Yu, X.; Pomfret, R.J.; Coley, K.S. Attack of submerged entry nozzles by mould flux and dissolution of refractory oxides in the flux. *ISIJ Int.* **1997**, *37*, 102–108. [CrossRef]
9. Cirilli, F.; Di Donato, A.; Martini, U.; Miceli, P.; Guillo, P.; Simoes, J.; Song, Y.J. Corrosion mechanisms of zirconia/carbon based refractory materials by slag in presence of steel. *Metallurgia Italiana* **2008**, *10*, 43–50.
10. Sharma, M.; Mu, W.; Dogan, N. In situ observation of dissolution of oxide inclusions in steelmaking slags. *Jom* **2018**, *70*, 1220–1224. [CrossRef]
11. Hauck, F.; Pötschke, J. Der Verschleiß von Tauchausgüssen beim Stranggießen von Stahl. *Arch. Für Das Eisenhüttenwesen* **1982**, *53*, 133–138. [CrossRef]
12. Zhang, S.; Yuan, H.; Gan, M.; Wang, Q.; He, S.; Wang, Q. Wetting and Erosion of ZrO<sub>2</sub>-Graphite Refractory by CaO-SiO<sub>2</sub> and CaO-Al<sub>2</sub>O<sub>3</sub>-Based Mold Slags for Submerged Entry Nozzle. *Metall. Mater. Trans. B* **2019**, *50*, 1407–1416. [CrossRef]
13. Yoo, H.; Lee, H.; Jo, K.; Kim, J.; Jo, I.; Lee, H. Phase Formation and Stabilization Behavior of Ca-PSZ by Post-Heat Treatment. *Metals* **2002**, *12*, 1479. [CrossRef]
14. Ślęzak, M.; Warzecha, M. Investigations of liquid steel viscosity and its impact as the initial parameter on modeling of the steel flow through the tundish. *Materials* **2020**, *13*, 5025. [CrossRef] [PubMed]
15. Kumar, A.; Khanna, R.; Ikram-ul-Haq, M.; Spink, J.; Sahajwalla, V. Effect of glaze on the corrosion behavior of ZrO<sub>2</sub>-graphite insert of the submerged entry nozzle in the continuous casting of steel. *Steel Res. Int.* **2015**, *86*, 1004–1013. [CrossRef]
16. Strakhov, V.I.; Zhukovskaya, A.E. Slag-resistant products made from stabilized ZrO<sub>2</sub>. *Refractories* **1979**, *20*, 184–188. [CrossRef]
17. Oki, K. Study of corrosion and penetration of zirconia refractories by molten steel and slag (1st report). *Taikabutsu Overseas* **1983**, *3*, 3.
18. Hirata, T.; Morimoto, T.; Ohta, S.; Uchida, N. Improvement of the corrosion resistance of alumina-chromia ceramic materials in molten slag. *J. Eur. Ceram. Soc.* **2003**, *23*, 2089–2096. [CrossRef]
19. Moringa, K.; Yoshida, H.; Takebe, H. Compositional dependence of absorption spectra of Ti<sup>3+</sup> in silicate, borate, and phosphate glasses. *J. Am. Ceram* **1994**, *77*, 3113–3118. [CrossRef]
20. ISO 5803; Fine Ceramics (Advanced Ceramics, Advanced Technical Ceramics)—Test Method for Determination of Monoclinic Phase in Zirconia. International Standards Organization (ISO): Geneva, Switzerland, 2023.
21. Clavel, G.; Willinger, M.G.; Zitoun, D.; Pinna, N. Manganese-Doped Zirconia Nanocrystals. *Eur. J. Inorg. Chem.* **2008**, *2008*, 863–868. [CrossRef]
22. Kim, B.; Lee, H. Valence state and ionic conduction in Mn-doped MgO partially stabilized zirconia. *J. Am. Ceram.* **2018**, *101*, 1790–1795. [CrossRef]
23. Kanghee, J.; Buyoung, K.; Jiseung, R.; Hyeong-Tae, K.; Heesoo, L. Densification of Mn-Doped YSZ for the Solid Oxide Membrane Process and its Surface Corrosion under Fluoride Salt. *J. Ceram. Sci. Technol.* **2020**, *11*, 91–97.
24. Tovar-Vargas, D.; Turon-Vinas, M.; Anglada, M.; Jimenez-Pique, E. Enhancement of mechanical properties of ceria-calcia stabilized zirconia by alumina reinforcement. *J. Eur. Ceram. Soc.* **2020**, *40*, 3714–3722. [CrossRef]
25. Yoshimura, M. Phase stability of zirconia. *Am. Ceram. Soc. Bull* **1988**, *67*.
26. Li, C.; Sun, H.H.; Li, L.T. Glass phase structure of blast furnace slag. *Adv. Mater. Res.* **2011**, *168*, 3–7. [CrossRef]
27. Zhang, Z.; Wang, T.; Dai, C.; Li, Q.; Li, Y.; Kong, J. Preparation and thermal-insulating properties of Ce-doped ZrO<sub>2</sub> hollow fibers derived from a metaplexis template. *Int. J. Appl. Ceram. Technol.* **2019**, *16*, 1581–1589. [CrossRef]
28. Kim, B.; Ryu, J.; Jeon, S.; Lee, H. Oxygen vacancy generation and structural stability of MgO partially-stabilized zirconia upon MnO<sub>2</sub> addition. *Mater. Res. Express* **2017**, *4*, 126309. [CrossRef]

29. Li, P.; Chen, I.W.; Penner-Hahn, J.E. Effect of dopants on zirconia stabilization—An x-ray absorption study: II, tetravalent dopants. *J. Am. Ceram.* **1994**, *77*, 1281–1288. [CrossRef]
30. Nascente, P.A.; de Souza, D.P. XPS characterisation of ceria-stabilised zirconia doped with iron oxide. *Appl. Surf. Sci* **1999**, *144*, 228–232. [CrossRef]

**Disclaimer/Publisher’s Note:** The statements, opinions and data contained in all publications are solely those of the individual author(s) and contributor(s) and not of MDPI and/or the editor(s). MDPI and/or the editor(s) disclaim responsibility for any injury to people or property resulting from any ideas, methods, instructions or products referred to in the content.

## Article

# Effect of High Temperature and Thermal Cycle of 4043 Al Alloy Manufactured through Continuous Casting Direct Rolling

Bo-Chin Huang and Fei-Yi Hung \* 

Department of Materials Science and Engineering, National Cheng Kung University, Tainan 701, Taiwan; n58081060@ncku.edu.tw

\* Correspondence: fyhung@mail.ncku.edu.tw

**Abstract:** CCDD 4043 Al alloys are an outstanding candidate for producing mechanical components for automotive or aircraft engines. Two experimental environments—sustained high temperature and repeated heating–cooling—were simulated in the laboratory to replicate the actual operating conditions of engine components. This research investigated the microstructural evolution, mechanical properties, and fracture characteristics of the 4043 Al alloy manufactured through the continuous casting direct rolling (CCDR) process under different post-processing conditions. The CCDD process combines continuous casting, billet heating, and subsequent continuous rolling in a single equipment of production line, enabling the mass production of Al alloy in a cost-effective and energy-efficient manner. In the present work, the 4043 alloy was subjected to two environmental conditions: a sustained high-temperature environment (control group) and a cyclic heating–cooling environment (experimental group). The maximum temperature was set to 200 °C in the experiment. The experimental results show that, in a sustained high temperature working environment, the strength and elongation of the CCDD 4043 Al alloy tend to be stable. The overall effect involves the Al matrix softening and the spheroidization of eutectic Si caused by prolonged exposure to high temperature. This can enhance its ductility while retaining a certain level of mechanical strength. Comparatively, in the working environment of cyclic heating–cooling (thermal cycle), the direction of Si diffusion was different in each cycle, thus leading to the formation of an irregular Al–Si eutectic structure containing precipitated Si particles of different sizes. The two compositions of Al and Si with very different thermal expansion coefficients may induce defects at the sharp points of Si particles under repeated heating–cooling, thereby reducing the strength and ductility of the material. The results of this work can confirm that the fracture behavior of 4043 Al alloys is obviously controlled by the morphology of the precipitated eutectic Si. In addition, CCDD 4043 Al alloys are not suitable to be used in working environments with a thermal cycle. In practical applications, it is necessary to add traces of special elements or to employ other methods to achieve the purpose of spheroidizing the precipitated eutectic Si and Al–Fe–Si phases to avoid the deterioration of strength and ductility under cyclic heating. To date, no other literature has explored the changes in the microstructure and mechanical properties of CCDD 4043 Al alloys across various time scales under the aforementioned working environments. In summary, the findings provide valuable insights into the effect of thermal conditions on the properties and behavior of CCDD 4043 Al alloys, offering potential applications for it in various engineering fields, such as the automotive and aerospace industries.



**Citation:** Huang, B.-C.; Hung, F.-Y. Effect of High Temperature and Thermal Cycle of 4043 Al Alloy Manufactured through Continuous Casting Direct Rolling. *Materials* **2023**, *16*, 7176. <https://doi.org/10.3390/ma16227176>

Academic Editors: Seong-Ho Ha, Shae-Kwang Kim and Hyun-Kyu Lim

Received: 24 October 2023  
Revised: 11 November 2023  
Accepted: 13 November 2023  
Published: 15 November 2023



**Copyright:** © 2023 by the authors. Licensee MDPI, Basel, Switzerland. This article is an open access article distributed under the terms and conditions of the Creative Commons Attribution (CC BY) license (<https://creativecommons.org/licenses/by/4.0/>).

**Keywords:** continuous casting direct rolling (CCDD); 4043 Al alloy; thermal cycle; eutectic Si; microstructure evolution

## 1. Introduction

In response to growing environmental concerns and the urgent need to combat climate change, automakers have taken aggressive measures to enhance the energy efficiency of their vehicles. This effort aims to reduce carbon emissions and decrease fossil fuel consumption. Utilizing lightweight materials has emerged as a pivotal strategy to address the energy

crisis and mitigate environmental pollution [1]. Among these materials, Al–Si alloys stand out as one of the most extensively employed lightweight options. Their popularity is driven by a combination of advantageous characteristics, including exceptional wear resistance, low density, low thermal expansion coefficient at high temperatures, high specific strength, efficient thermal conductivity, excellent castability, and superb corrosion resistance [2,3]. In the automotive sector, Al–Si alloys find application in the manufacturing of crucial engine components, such as cylinder heads, valve tappets, crankshaft covers, pistons, and rocker arms [4]. Furthermore, they serve as a viable alternative to conventional iron-based materials for constructing structural components in automobile bodies, including doors, hoods, and frames. This substitution significantly reduces the overall vehicle weight, making a substantial contribution to energy conservation [5,6]. Beyond their role in the automotive sector, Al–Si alloys also find extensive application in the aerospace industry, particularly in aircraft fuel storage and supply systems, such as fuel tanks and fuel pipelines. These alloys display remarkable corrosion resistance and sealing properties, allowing them to endure high pressures and meet stringent temperature requirements. As a result, they play a crucial role in ensuring the safety and reliability of fuel storage and supply systems in the aviation industry. In summary, the widespread adoption of Al–Si alloys in both the automotive and aerospace sectors highlights their pivotal role in enhancing energy efficiency and reducing environmental impacts. These alloys have become indispensable components in the pursuit of a more sustainable and eco-friendly future. In this study, a 4043 Al alloy with Si content of 5 wt.% was used. The addition of Si can improve the castability and fluidity of the metal and reduce the shrinkage of the metal during the solidification process, so that the 4043 Al alloy has excellent weldability, fluidity, and castability, and at the same time, eutectic Si precipitated at the matrix of Al can effectively improve the wear resistance. The relevant literature has pointed out that Al–Si alloys solidified under traditional cooling conditions are usually composed of dendrites formed by coarse Al grains, eutectic Al–Si structures, and lamellar eutectic Si. This microstructure leads to poor mechanical properties [7–9]. Therefore, in recent years, there have been many emerging research attempts to manufacture Al–Si alloys using new process technologies.

Owing to the exceptional fluidity of Al–Si alloys in their molten state and their decreased susceptibility to crack during solidification, research teams have increasingly adopted various advanced production techniques in recent years. These techniques are aimed at fabricating 4043 Al alloys and effectively controlling the grain size, the structure of eutectic Al–Si, and the morphology of the precipitated eutectic Si. These techniques encompass continuous casting direct rolling [10–14], additive manufacturing [15–19], chemical inoculation [7,20,21], and the application of external fields during solidification [22,23]. In this study, we utilized continuous casting direct rolling (CCDR) technology for the fabrication of a 4043 Al alloy. CCDR is a comprehensive process that consolidates various production stages into a single line of equipment. This includes the melting of metal blanks, casting, solidification, rolling, temperature control, coiling, and roll forming [24–27]. This integrated approach enables the adjustment of production speed and product size to meet specific application requirements while simultaneously enhancing production efficiency and quality [14]. Al–Si alloys, thanks to their low melting point and excellent fluidity, have traditionally found wide usage in welding materials [28–30]. Significantly, the outstanding fluidity of Al–Si alloys in their molten state renders them exceptionally well-suited for continuous casting and rolling production when compared to other Al alloys. Therefore, in this study, we employed CCDR technology to manufacture 4043 Al alloy wire rods. Following that, we conducted sustained high-temperature and cyclic heating–cooling experiments to examine the effect of eutectic silicon on the alloy's mechanical properties and evaluate its suitability for high-temperature working environments.

CCDR enables the mass production of 4043 Al alloy sheets, strips, or coils, which serve as crucial raw materials in the fabrication of fasteners and wear-resistant mechanical components. These materials find extensive application in both the automotive and aerospace industries. Moreover, beyond the advantages of reducing material waste and

cutting production costs, CCDD ensures a uniform blank structure while effectively eliminating internal defects. However, 4043 Al alloys are a non-heat-treatable Al alloy, which means that improvement through T6 heat treatment is not feasible. To further enhance the mechanical strength of CCDD 4043 Al alloys, the as-manufactured materials underwent a secondary rolling process at a 60% reduction ratio, successfully avoiding any cracks on the edges of the wire rods. It is important to emphasize that maintaining strength and ductility in high-temperature working environments with repeated cycles of heating and cooling is a crucial research focus, especially given the critical role of these materials as core components in engines, cooling systems, and fuel systems. Previous research has demonstrated that Al–Si alloys typically experience reduced strength and increased elongation after prolonged exposure to high-temperature working environments [4]. Additionally, numerous studies have explored the thermal fatigue life of Al–Si alloys in different test conditions [4,31,32]. In this study, the authors utilized a test model resembling thermal fatigue. Test specimens were repeatedly exposed to both high-temperature and normal room temperature conditions, thereby subjecting them to cyclic heating and cooling, commonly referred to as a thermal cycle [33–36]. In this comparative test, CCDD 4043 Al alloy specimens were assigned to the control group and exposed to a sustained high-temperature environment, while those placed in a cyclic heating–cooling environment constituted the experimental group. During the experiment, the CCDD 4043 Al alloy specimens were placed in a heating furnace to maintain a temperature of 200 °C and within a thermal cycle apparatus. The subsequent experimental results include an analysis of the microstructure, XRD patterns, and mechanical properties of both groups. Additionally, to gain insights into the effect of eutectic Si morphology and distribution on mechanical properties and damage characteristics, a scanning electronic microprobe (SEM) was employed to investigate the distribution characteristics of precipitated eutectic Si in the transverse section and fractured subsurface of the specimens.

The metal manufacturing industry is now actively pursuing energy efficiency, sustainability, carbon tax compliance, and adherence to ESG (Environmental, Social, and Governance) values [37,38]. CCDD addresses the drawbacks of the high energy consumption and labor intensity inherent in traditional metal manufacturing. Its advantages lie in simplifying the process, reducing labor costs, increasing metal yield, conserving energy, improving the quality of CCDD billets, and facilitating production automation. Utilizing the CCDD process for the production of Al–Si alloys not only promotes environmental friendliness but also reduces carbon emissions while offering competitive raw materials for the automotive manufacturing industry. CCDD technology provides distinctive advantages, complementing the inherent wear resistance, low thermal expansion coefficient, and excellent thermal conductivity of Al–Si alloys, rendering them highly competitive in the market. To ascertain the suitability of CCDD 4043 Al alloys for use as a manufacturing material for engine parts or fasteners, we employed two experimental environments: continuous high temperature and repeated heating–cooling. These simulations aim to replicate the potential scenarios in which mechanical components operate in high-temperature working environments. A subsequent in-depth analysis of mechanical properties testing and microstructure was conducted to determine whether CCDD 4043 Al is qualified for this task, mitigating the risk of unexpected dangers. However, to date, there has been no comprehensive research that systematically investigates the microstructural evolution of Al–Si alloys manufactured through CCDD in a repetitive heating–cooling environment, which leads to changes in mechanical properties. In light of this, this study is essential and presents a practical set of experimental methods to verify the potential application of CCDD Al 4043 alloys in high-temperature working environments. In order to integrate CCDD 4043 Al alloys into the industrial supply chains of the automotive and aerospace sectors as a reliable mechanical component designed for long-term use in various high-temperature working environments, the results presented in this study possess both theoretical significance and practical necessity. They can serve as a crucial benchmark for the industrial application of CCDD Al–Si alloys.

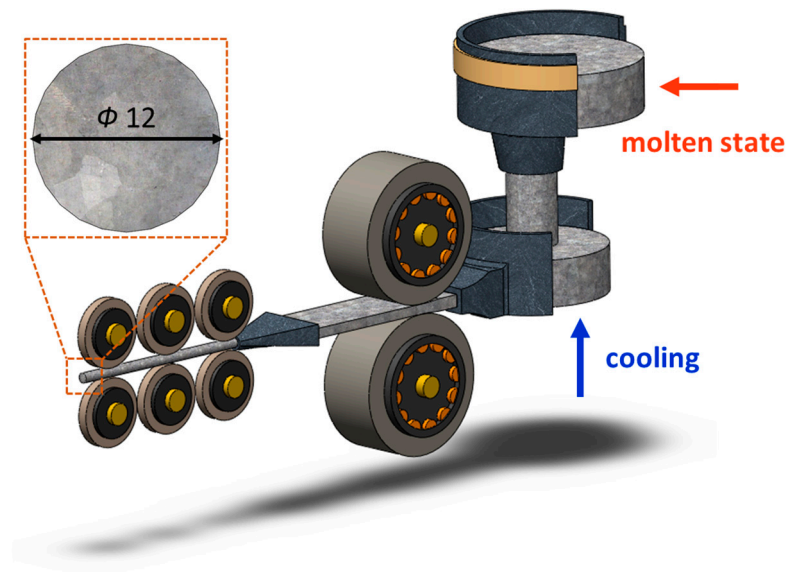


## 2. Materials and Experimental Procedures

The CCDR 4043 Al alloy utilized in this study was provided by Ting Sin Co., Ltd. (Tainan, Taiwan). The chemical composition of this alloy is detailed in Table 1, and the production equipment is depicted in Figure 1.

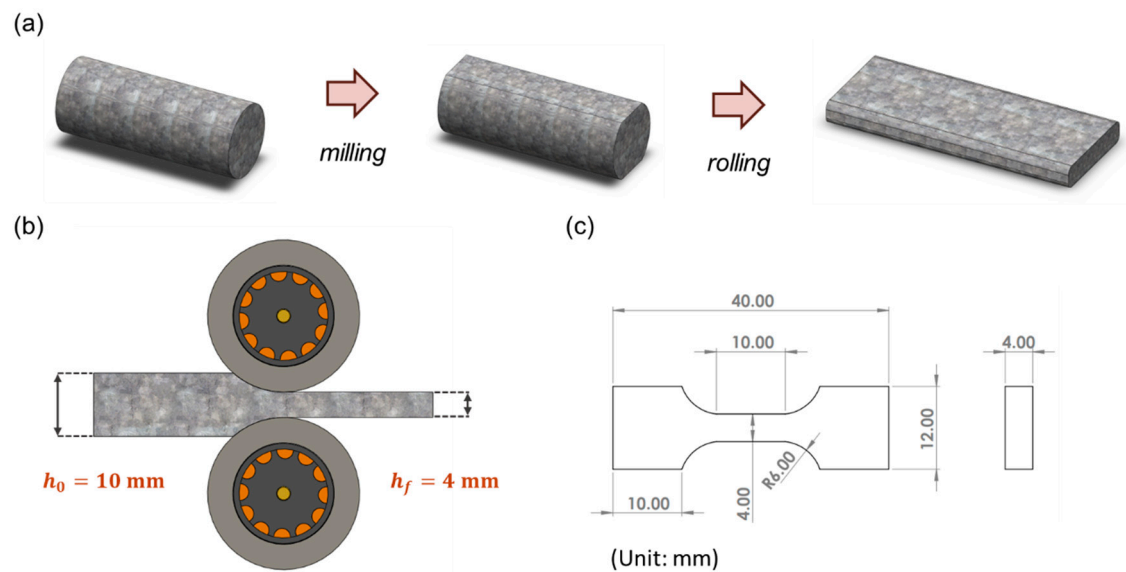
**Table 1.** The chemical composition of the 4043 Al alloy used in this study.

	Al	Si	Fe	Cu	Mn	Mg	Zn	Ti
Composition (wt.%)	Bal.	4.5–6.0	≤0.8	≤0.30	≤0.05	≤0.05	≤0.10	≤0.20
This study	Bal.	4.86	0.23	0.079	0.003	0.002	0.017	0.02



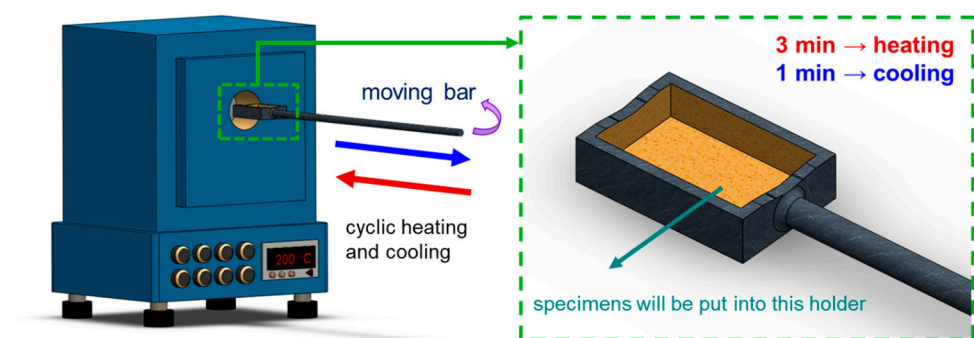
**Figure 1.** CCDR production equipment.

The wire rods produced directly from the CCDR production line, in their initial, as-manufactured state, are denoted as ‘specimen F’. As the 4043 Al alloy is a typical non-heat-treatable Al alloy, its mechanical properties cannot be enhanced through T6 heat treatment. Therefore, this study employed strain hardening to improve its mechanical strength. In the pursuit of maximizing mechanical strength through cold working and ensuring the absence of surface rolling cracks to maintain quality, different reduction ratios were considered as experimental parameters during the preparatory experiments. Ultimately, we determined that a 60% reduction ratio yielded the optimal results [10]. The reduction ratio was calculated as the difference between the original thickness and the rolled thickness, divided by the original thickness. The Ø12 wire rods were initially cut and milled into long strips measuring 10 mm in thickness. These strips were then further reduced to 4 mm in thickness through rolling, resulting in specimens referred to as ‘FR’ (the process and equipment are depicted in Figure 2a,b). The strain rate was about  $0.03 \text{ s}^{-1}$ . Subsequently, dog-bone-shaped specimens, as depicted in Figure 2c, were manufactured through wire electrical discharge machining. In the experiment, ASTM E8/E8M [39] was used as the basis for specimen size modification. Stress–strain curves were subsequently recorded using a uniaxial tensile testing machine. (Hung Ta Instrument Co., Ltd., Taichung, Taiwan). Each set of specimens underwent five tests at a tensile rate of 1 mm/min, from which, the average strength and elongation values were calculated.



**Figure 2.** (a) Milling and rolling process of specimens. (b) Schematic diagram of cold rolling. (c) Engineering drawings of tensile test specimens.

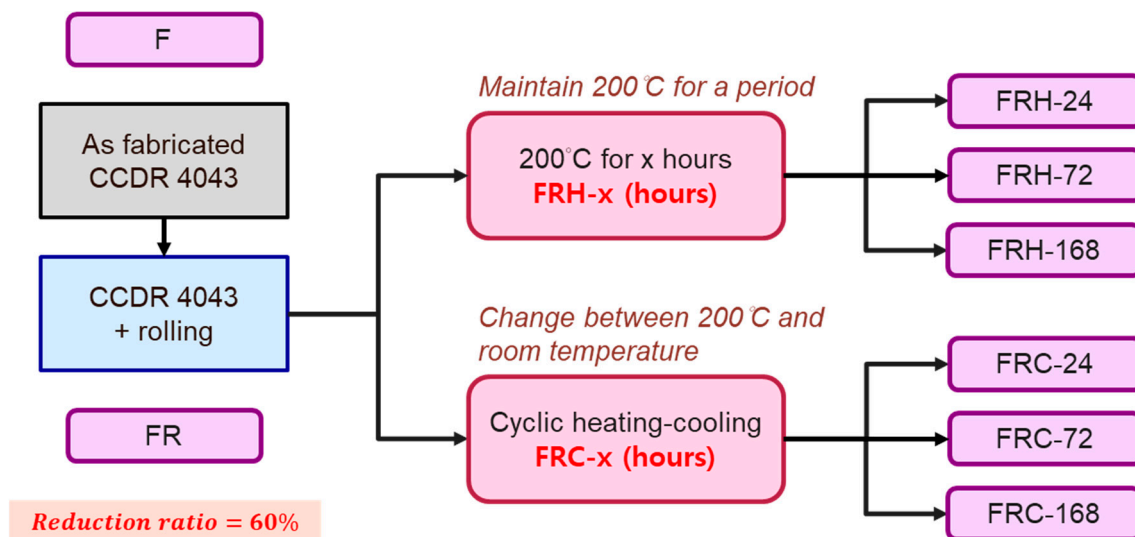
The primary objectives of this study centered on two key aspects: (1) examining the effect of sustained high temperatures, and (2) investigating the effects of cyclic heating and cooling (thermal cycle) on the 4043 Al alloy. In the constant high-temperature experiments, the specimens labeled as FR were placed in a heated furnace and maintained at 200 °C for durations of 24, 72, and 168 h, denoted as FRH-24, FRH-72, and FRH-168, respectively. For the thermal cycling experiment, specimen FR was positioned in the thermal cycle equipment as depicted in Figure 3. In this test, the specimen was subjected to a repetitive cycle of heating at 200 °C for 3 min, followed by natural cooling to room temperature (25 °C) for 1 min. This cycle was repeated continuously for periods of 24, 72, and 168 h, designated as FRC-24, FRC-72, and FRC-168, respectively. The naming conventions for the test specimens are summarized in Table 2, and the process framework is illustrated in Figure 4. The setting of 200 °C as the maximum temperature limit is based on its slight elevation above the artificial aging temperature of typical Al alloys. Beyond this threshold, unpredictable changes in the microstructure may occur, potentially affecting the mechanical properties. Moreover, under elevated temperature conditions, the prolonged use of Al–Si alloys becomes less favorable. In such circumstances, opting for metals with higher temperature resistance, even if sacrificing some lightweight advantages, would be a prudent decision.



**Figure 3.** Schematic diagram of self-developed cyclic heating-cooling equipment.

**Table 2.** The naming principles and post-processing of specimens.

Name	Post-Processing
F	As-manufactured through CCDR
FR	Specimen F rolled at a reduction ratio of 60%
FRH-24	Specimen FR in an environment of 200 °C for 24 h
FRH-72	Specimen FR in an environment of 200 °C for 72 h
FRH-168	Specimen FR in an environment of 200 °C for 168 h
FRC-24	Specimen FR under the thermal cycle for 24 h
FRC-72	Specimen FR under the thermal cycle for 72 h
FRC-168	Specimen FR under the thermal cycle for 168 h

**Figure 4.** The naming conventions and the workflows of specimen treatments.

To examine the metallurgical structure, the specimens mentioned above underwent a sequential process. They were initially ground using SiC sandpaper (3M Company, Maplewood, NJ, USA) with grit sizes ranging from 120 to 4000#. Affixing sandpaper to the rotary disk of the grinding and polishing equipment, the metallographic specimens were then gently pressed on the sandpaper with fingers. Subsequently, the specimens were polished using aqueous solutions of Al<sub>2</sub>O<sub>3</sub> and SiO<sub>2</sub>. Finally, they were immersed in Keller's corrosive solution, composed of 2 mL HF, 3 mL HCl, 5 mL HNO<sub>3</sub>, and 190 mL H<sub>2</sub>O, for approximately 20–25 s. The specimens were then observed under an optical microscope (Olympus BX41M-LED, Tokyo, Japan). This process allowed for the assessment of microstructure characteristics across different sections. In this article, the plane that is perpendicular to the secondary rolling is referred to as the 'transverse section', while the plane parallel to the secondary rolling is termed the 'axial section'. Material hardness was analyzed using a Rockwell hardness testing machine (Mitutoyo AR-10 Hardness Testing Machine, Sakado, Japan), following the HRF test specification (in compliance with ASTM E18-20 [40]). A steel ball indenter with a diameter of 1/16 inches was used as the load source, applying a force of 60 kgf. The hardness measurements were recorded for both the transverse and axial sections of the test specimen. The constituent phases were identified using an X-ray diffractometer (Bruker, Billerica, MA, USA) operating under the following conditions: a voltage of 45 kV, a current of 100 MA, a 2θ range from 20 to 90 degrees, and a scanning speed of 2.4 degrees per minute. The fracture surfaces and precipitated eutectic Si were analyzed using a scanning electron microscope (SEM) (Hitachi SU-5000, Hitachi, Tokyo, Japan) equipped with an energy-dispersive spectroscopy (EDS) instrument. The accelerating voltage of the SEM was from 0.5 KV to 30 KV, and the working distance of SEM was about 160 mm, which was adjusted according to the height of the

specimens. To investigate the effect of the distribution of Si and precipitated crystalline Si morphology on the mechanical properties of the 4043 Al alloy, specimens were extracted from the specimens listed in Table 2. These specimens, taken from the transverse section, were subjected to precision grinding and polishing. The elemental distribution within the transverse cross-section was analyzed using a high-resolution electron probe microanalyzer (EPMA) (JEOL JXA-8530 F, Tokyo, Japan). Additionally, specimens FR, FRH-168, and FRC-168 were specifically chosen for an analysis of the fracture subsurface. Finally, to thoroughly evaluate the atomic-scale precipitation behavior within the internal structure of the 4043 Al alloy under two distinct operating environments (sustained high temperatures and thermal cycle), samples were extracted from specimens FRH-168 and FRC-168 using a focused ion beam (FIB) (Hitachi NX2000, Tokyo, Japan). Phase identification was conducted using a transmission electron microscope (TEM) (FEI Tecnai F20 G2 Field-emission Scanning Transmission Electron Microscope, Hillsboro, OR, USA).

### 3. Results and Discussion

#### 3.1. Microstructure Evolution

The microstructure of the CCDR 4043 Al alloy in its as-manufactured state and after secondary rolling is depicted in Figure 5. The CCDR process induced a texture effect, resulting in distinct microstructures in the directions perpendicular and parallel to the rolling process. In Figure 5a,b, the microstructures of specimens F and FR in the transverse section are presented.

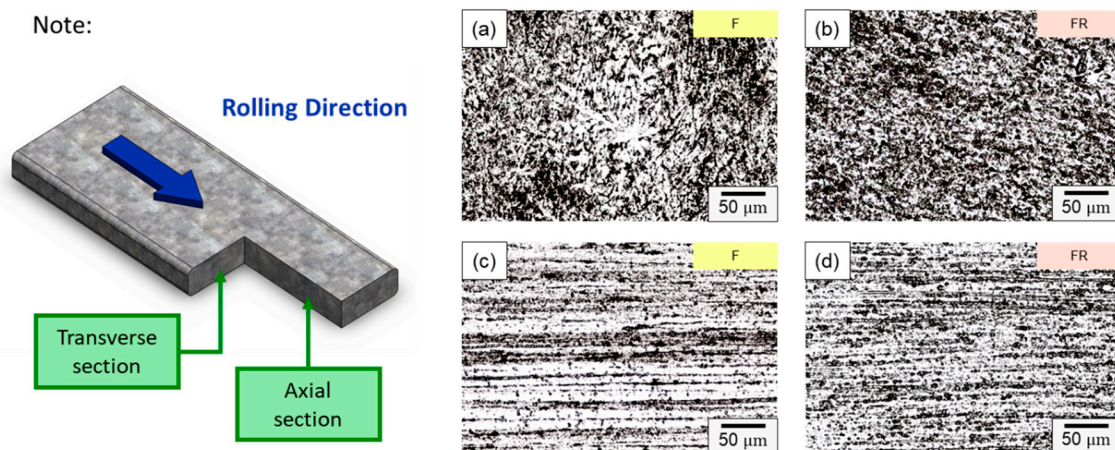


**Figure 5.** Microstructure of specimens F in (a) transverse and (c) axial sections, and specimens FR in (b) transverse and (d) axial sections.

In specimen F, the primary components consisted of  $\alpha$ -Al dendrites and a dark eutectic Al-Si structure. Following the second rolling process (specimen FR), the eutectic Al-Si structure underwent noticeable deformation, forming a Si-rich conglomerate aggregation. Figure 5c,d present the microstructure of the axial section for specimens F and FR. In both instances, Si-rich aggregates that formed along the rolling direction are evident, alongside point-like eutectic Al-Si phases distributed within the matrix. It is worth noting that after the secondary rolling process, specimen FR exhibited a more pronounced long island structure compared to specimen F. According to the literature, eutectic Si in Al-Si alloys precipitates as pure Si crystals [41,42], taking the form of flakes or granules. It also combines to form a eutectic Al-Si structure with Al [43]. This eutectic Al-Si structure is distributed within the darker part of the matrix, and is composed of needles, rods, and branches. In Figure 6, a more detailed analysis of the elemental distribution in the transverse section, performed using EDS, confirmed that the dark regions in Figure 5a,b primarily consisted of highly aggregated Si, with a small amount of Si solidly dissolved in the matrix. Figure 6d demonstrates that Fe was relatively uniformly distributed, with only a few aggregates. The presence of iron in the Al-Si alloy system resulted in the formation



of several intermetallic phases. The existing literature suggests that a significant portion of Fe is solidly dissolved within the  $\alpha$ -Al, while some of it forms the Al-Fe-Si phase in conjunction with Al and Si [44,45]. The sharp corners and incoherent interface of the Al-Fe-Si act as stress concentrators in the  $\alpha$ -Al matrix, leading to severe brittleness in the final Al-Si alloy casting. As the presence of Fe is unavoidable within the 4043 Al alloy, subsequent experiments will meticulously examine the changes in the distribution of Fe using EPMA.

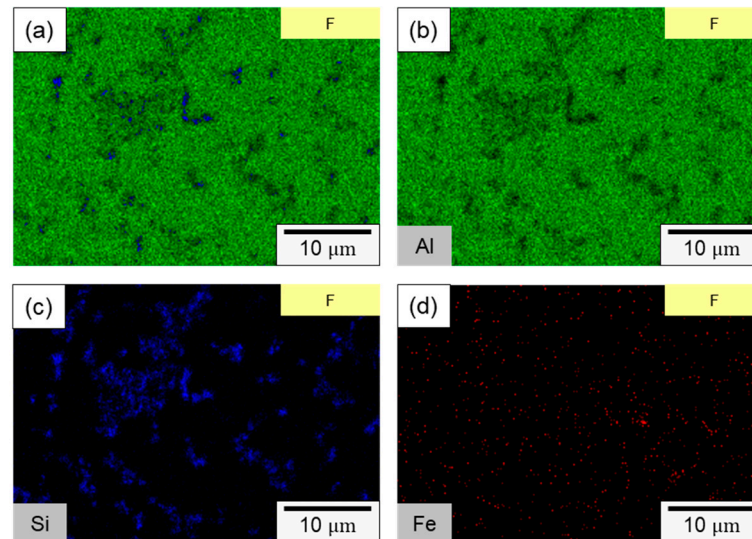


**Figure 6.** SEM element mapping of specimen F: (a) overlaying image, (b) Al, (c) Si, (d) Fe.

Figure 7 illustrates the microstructure evolution of the CCDR 4043 Al alloy at various time intervals of sustained high-temperature exposure. Figure 7a–c reveal that in the transverse section, Si-rich agglomerates gradually diffused and underwent morphological changes at elevated temperatures. Simultaneously, the eutectic Al-Si structure gradually transformed into needle-like and dendritic shapes, closely resembling the original specimen F. Figure 7d–f shows that in the axial section, the microstructure did not change significantly after a long period of high temperature treatment.

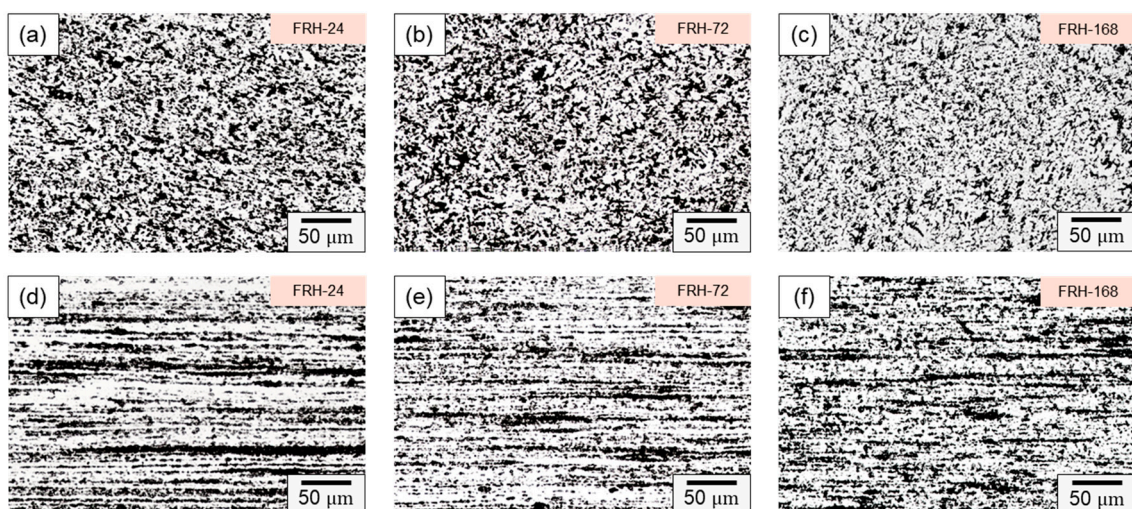


**Figure 7.** Microstructure of specimen FRH-24 in (a) transverse and (d) axial sections; specimen FRH-72 in (b) transverse and (e) axial sections; and specimen FRH-168 in (c) transverse and (f) axial sections.

Figure 8 presents the microstructure evolution of the CCDR 4043 Al alloy within a cyclic heating–cooling environment at various time intervals. In Figure 8a–c, it is evi-

dent that, within the transverse section, the Si-rich agglomerates, initially formed by the secondary rolling, evolved into various structures, including needle-shaped, dendritic, point-like, and irregular forms after varying numbers of thermal cycles. This phenomenon arises from the fact that, under repeated heating–cooling conditions, the Si element spreads out and combines with Al, forming various Al–Si structures. These Al–Si precipitates, which appear as dark-colored regions in the optical microscope image, primarily consist of lamellar Si and Si particles. The sharp edges and corners of the Si phase are particularly susceptible to generating uneven stress, thus becoming the starting point for material failure under stress. Consequently, the control of Si particle morphology and the Al–Si phase to enhance mechanical properties is a crucial metallurgical challenge in the context of Al–Si alloys [46,47]. Figure 8d–f depict the microstructure within the axial section, revealing that the influence of the cyclic heating–cooling environment on the microstructure was relatively subtle. The Si-rich aggregates maintained their original long island shape, with only a portion of the point aggregates re-dissolved into the long island structure due to Si diffusion or formed coarser clusters of Si particle aggregation.

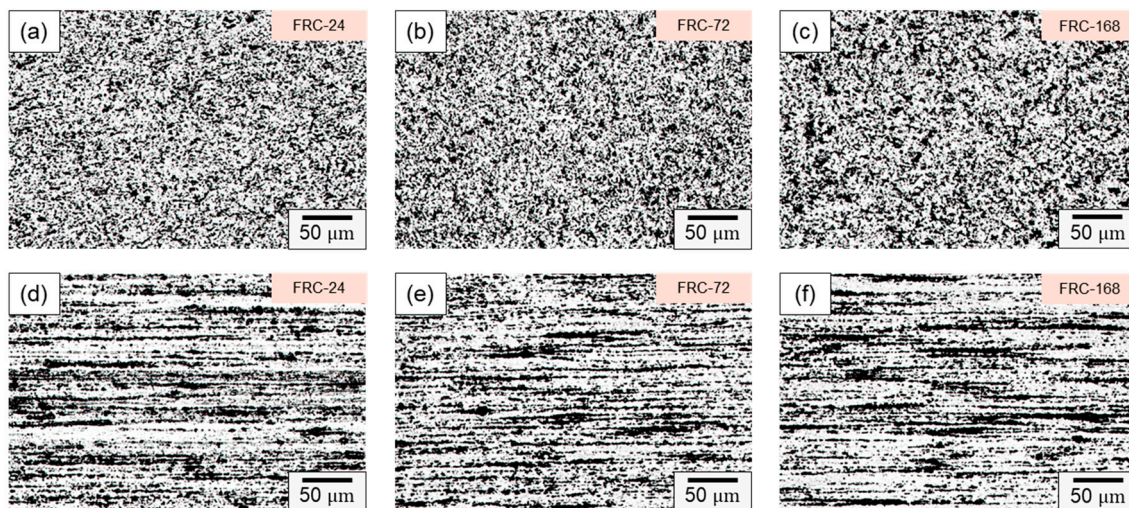


**Figure 8.** Microstructure of specimen FRC-24 in (a) transverse and (d) axial sections; specimen FRC-72 in (b) transverse and (e) axial sections; and specimen FRC-168 in (c) transverse and (f) axial sections.

Figure 9 presents the distribution and size of internal Si particles in the eutectic Al–Si phases within specimens F, FR, FRH-168, and FRC-168. The size distribution of Si particles was about 0.2–1.5  $\mu\text{m}$ . Due to significant variations in the Si particle content depending on the sampling location, we focused solely on discussing the changes in morphology and size in Figure 9. Figure 9a,b illustrate the influence of cold workability on Si precipitation in the pristine state of the 4043 Al alloy specimens after the secondary rolling. The experimental results confirm that both  $\alpha$ -Al dendrites and the eutectic Al–Si structures underwent changes due to compressive stress. Furthermore, the internal flaky and granular Si within the eutectic Al–Si phase transformed into finer Si particles under pressure. Figure 9c,d showcase the microstructure of the CCDR 4043 Al alloy after 168 h of sustained high-temperature and repeated heating–cooling conditions following the secondary rolling. As shown in Figure 9c, prolonged exposure to 200  $^{\circ}\text{C}$  promoted Si diffusion, allowing the Si within the matrix to merge with the originally precipitated Si particles found in specimen FR, resulting in a significant increase in particle size. Conversely, under thermal cycle conditions, repeated heating–cooling led to varying directions of Si diffusion within the microstructure, resulting in a greater difference in sizes between Si particles.



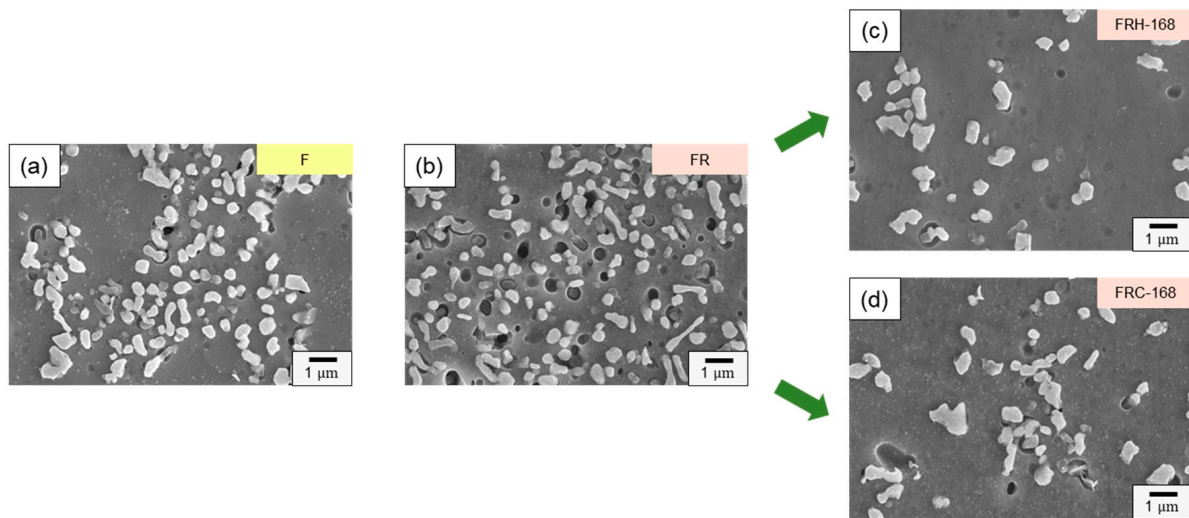


**Figure 9.** Evolution of precipitated Si particles of specimens (a) F, (b) FR, (c) FRH-168, and (d) FRC-168.

Figure 10 provides magnified  $2000\times$  transverse sections of the eight sets of specimens listed in Table 2, allowing for a detailed investigation of the Si distribution evolution under various post-processing conditions. The first, second, and third rows of Figure 10 depict the effect of cold working, sustained high temperature, and thermal cycling on the Si distribution in the microstructure, respectively. Figure 10a,b reveal the formation of clustered aggregates of needle-shaped eutectic Si and Si distributed within the eutectic Al–Si phase due to compression. In Figure 10c–e, it is evident that during sustained high-temperature conditions, a portion of the Si in the eutectic Al–Si phase re-solidified within the  $\alpha$ -Al matrix, while another portion gradually transformed into precipitated Si in the form of rods and particles. Figure 10f–h confirm that the Si within the Si-rich clusters formed unevenly sized particles and irregular structures during thermal cycling. Comparing Figure 9c,d with Figure 10e,h, the sustained high temperature exposure facilitated the formation of spheroidized eutectic Si and short rod-shaped Si clusters, creating a uniform network that enhanced material ductility. In contrast, the cyclic heating–cooling conditions tended to generate irregular Si particles. Therefore, it can be deduced that the thermal expansion coefficients of Al and Si in 4043 Al alloys vary significantly under repeated heating–cooling conditions, inducing defects at the sharp corners of Si particles, leading to reduced strength and decreased material ductility.

Figure 11 displays the X-ray diffraction (XRD) pattern of the CCDR 4043 Al alloy under the various post-treatment conditions. The diffraction pattern primarily consisted of Al and Si crystal planes with different orientations. Notably, the change in crystal orientation due to secondary rolling resulted in a significant increase in peak intensity for Al(111), Al(200), Al(222), and Al(400), accompanied by a decrease in Al(220) peak intensity. Simultaneously, the eutectic Al–Si phase formed Si-rich agglomerates, leading to the appearance of Si(111), Si(220), and Si(311) peaks in the diffraction pattern. In the sustained high-temperature environment, the Si diffusion and homogenization effects within the 4043 Al alloy resulted in a slight decreasing trend in both Al and Si peak intensities. This decreasing trend became more pronounced with longer temperature holding times. In summary, in a cyclic heating–cooling environment, the Si diffusion direction and path vary in each cycle, leading to less significant drops in both Al and Si peaks.

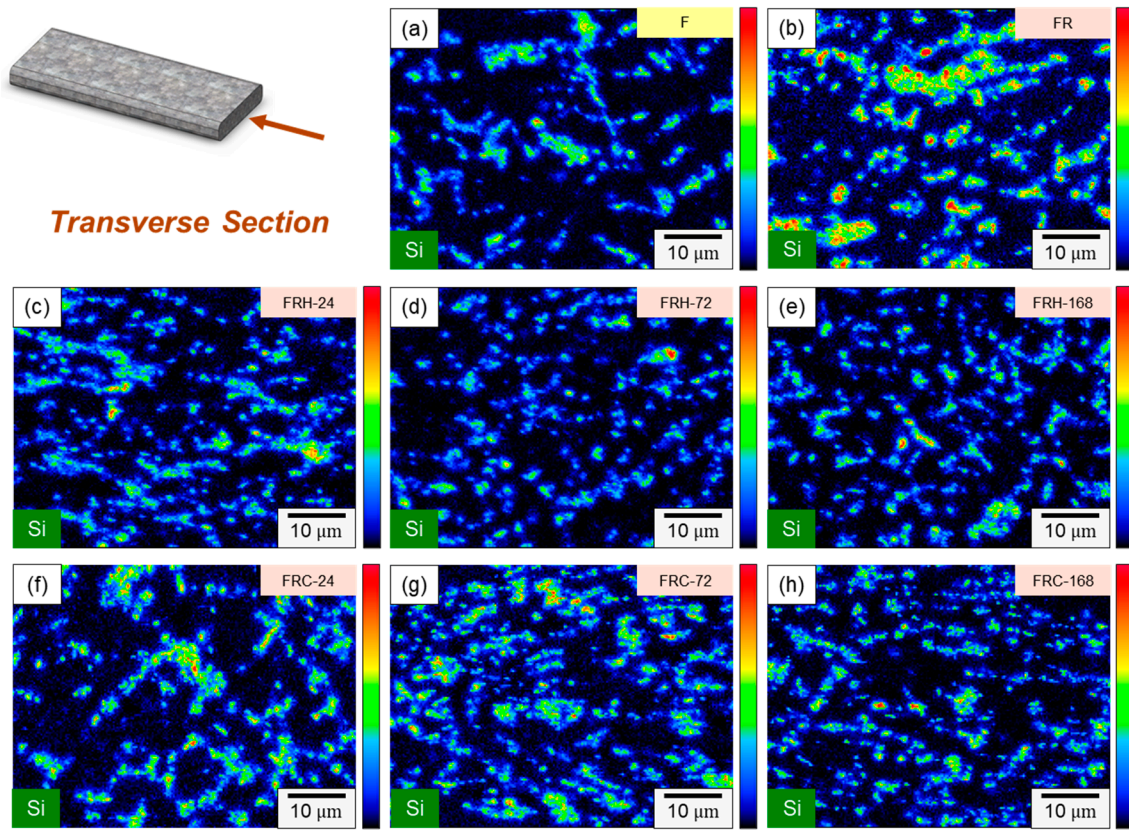


Figure 10. Si distribution evolution of specimens (a) F, (b) FR, (c) FRH-24, (d) FRH-72, (e) FRH-168, (f) FRC-24, (g) FRC-72 and (h) FRC-168.

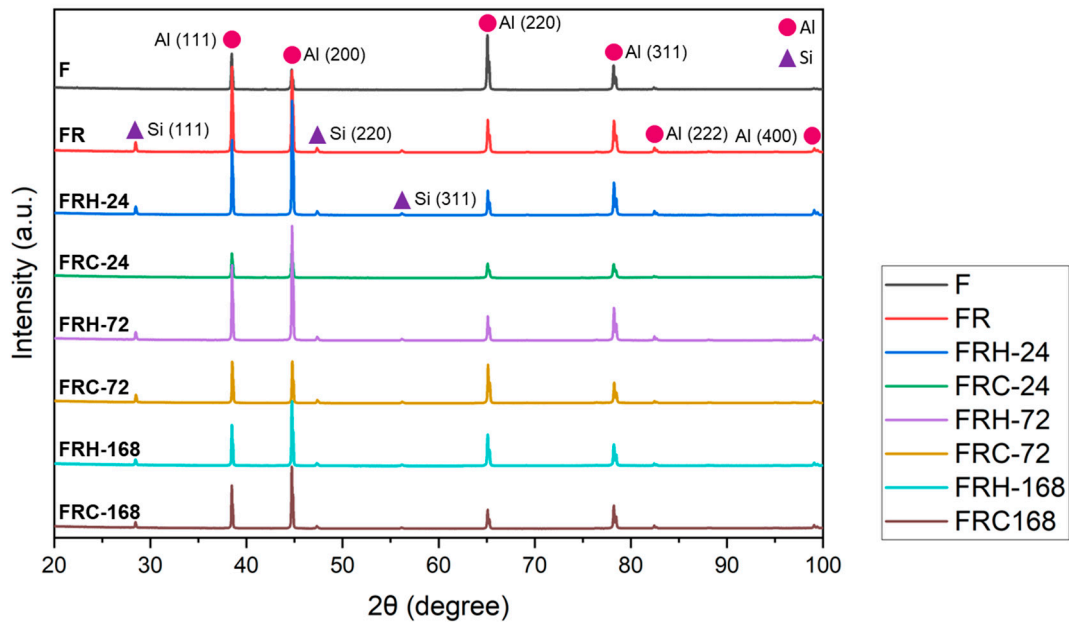
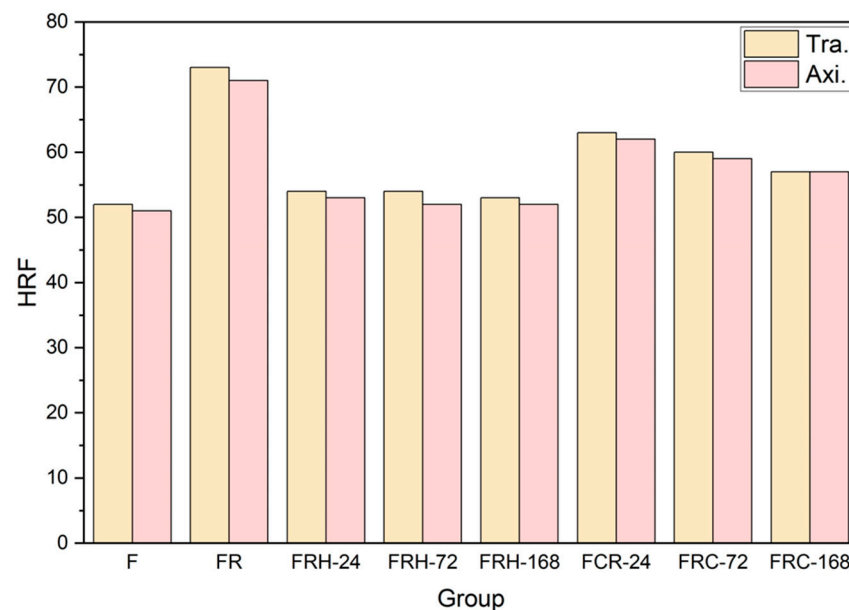


Figure 11. X-ray diffraction pattern of all specimens.

### 3.2. Hardness and Mechanical Properties

Figure 12 illustrates the hardness of the CDDR 4043 Al alloy under the various post-processing conditions. The original 4043 Al alloy (specimen F) exhibited a hardness of HRF 52 in the transverse section and HRF 51 in the axial section. A subsequent secondary rolling led to work hardening and an accumulation of hard silicon, resulting in increased

hardness. Specifically, the transverse section and axial section hardness for specimen FR measured HRF 73 and HRF 71, respectively. The transverse section hardness decreased from HRF 73 to HRF 53 and the axial hardness decreased from HRF 71 to HRF 52 after 168 h of sustained high temperature exposure. After subjecting the material to 168 h of the sustained high temperature treatment at 200 °C, we observed a decrease in hardness. This constant high temperature effectively eliminated the dislocations caused by cold rolling and softened the matrix. The hardness of the specimens stabilizes after 24 h, with minimal changes over the following 168 h. Furthermore, when subjected to cyclic heating–cooling conditions, both the transverse and axial hardness exhibited a gradual decline. The thermal cycle did not provide a stable driving force for grain growth, leading to the multidirectional diffusion of silicon evolving from agglomerates to needle rods. Within the 168 h timeframe, the hardness of the test piece did not reach a stable value, consistent with the observations in Figure 10f–h, indicating that silicon primarily existed in irregular shapes within the eutectic phase.



**Figure 12.** Rockwell hardness (HRF) of all specimens.

Figure 13a confirms that secondary rolling with a 60% reduction rate can enhance both the yield strength and ultimate tensile strength, while maintaining control over uniform and total elongation within acceptable limits. Figure 13b,c, respectively, illustrate the changes in the stress–strain curves of specimen FR under two different working conditions: sustained high temperature and cyclic heating–cooling. The individual effects of each working condition on the strength and elongation of the CCDR 4043 Al alloy after secondary rolling are summarized in Figure 14. It is observed that both sustained high temperature and thermal cycling conditions resulted in a reduction in strength and ultimate tensile strength. The most noteworthy distinction between Figure 13b,c is the matrix softening and the globularization of Si particles induced by sustained high temperature treatment, which contributes to the improved ductility of the 4043 Al alloy [46,48]. Figure 14b reveals that the elongation of specimens FRH-24, FRH-72, and FRH-168 surpassed that of specimen FR. In contrast, cyclic heating–cooling failed to provide sufficient time and stable diffusion for the homogenization of the internal grains in the CCDR 4043 Al alloy. Moreover, it is worth noting that the coefficient of thermal expansion for pure Al is approximately 6.6 times that of Si [49,50]. The cyclic stresses induced by repeated thermal expansion and cold contraction of hard silicon within a soft Al matrix can create defects at the interface between Al and silicon, which can, in turn, impact both strength and elongation.

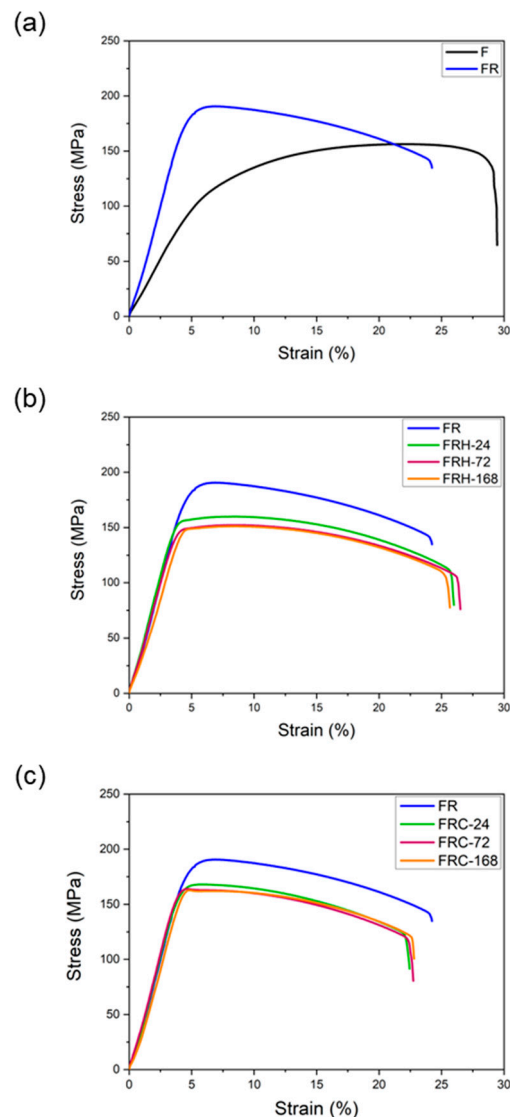


**Figure 13.** Stress–strain curve comparison of (a) specimens F and FR; (b) specimens FR, FRH-24, FRH-72, and FRH-168; (c) specimens FR, FRC-24, FRC-72, and FRC-168.

### 3.3. Fracture Behavior

Figure 15 illustrates the fracture surface characteristics of the specimens listed in Table 2 after undergoing room temperature tensile testing. All specimens exhibited typical ductile fractures dominated by dimple characteristics. The size of these dimples on the fracture surface closely correlated with the material's fracture behavior. A comparison of Figure 15a,b reveals that specimen FR had smaller dimples than specimen F. Larger dimples typically indicate enhanced material ductility since they signify substantial plastic deformation before fracture, resulting in increased elongation. This observation aligns with the findings presented in Figure 13a. Moving on to Figure 15c–e, it is evident that an increase in the holding temperature at 200 °C led to larger dimples on the fracture surface and, concurrently, a decrease in the number of Si particles. These results suggest that spheroidized Si plays a role in restraining crack propagation within the material. Figure 15f–h displays dimples of varying sizes and a higher density of the ridge structure surrounding the dimples. This indicates that the material experienced crack initiation from multiple points under stress, and a greater number of Si particles was evident on the fracture surfaces. When comparing Figure 15e,h, the latter depicts dimples of different sizes, along with numerous tearing ridges and Si particles. This pattern implies that

cracks propagated along the Al–Si interface, a crucial factor contributing to the diminished strength and elongation of the 4043 Al alloy under thermal cycling experimental conditions.

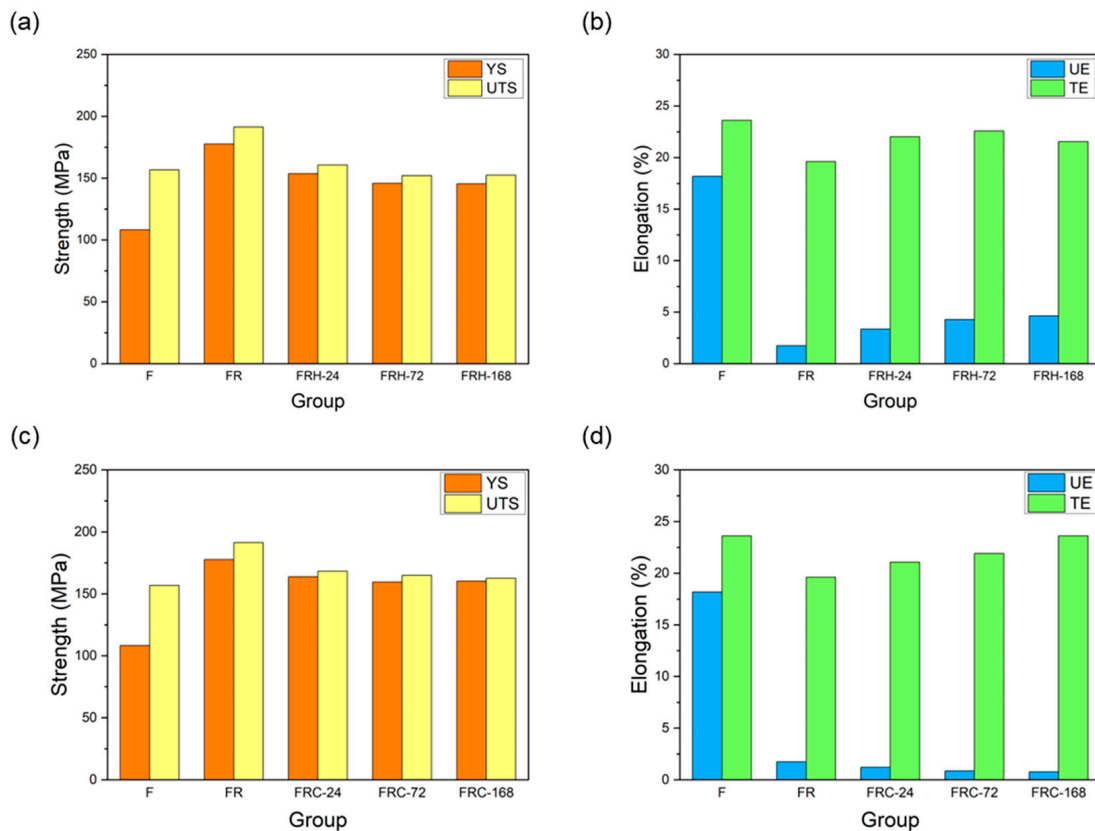


**Figure 14.** Effect of sustained high temperature on (a) strength and (b) elongation. Effect of thermal cycling on (c) strength and (d) elongation.

To elucidate the fracture mechanism of the CCDR 4043 Al alloy, we further conducted a comparison of the elemental distributions on the fracture subsurface of specimens FR, FRH-168, and FRC-168, as depicted in Figure 16. Fe influences crack growth by precipitating a needle-like Al–Fe–Si phase within the Al–Si alloy [51,52]. Previous studies have indicated that the fracture of Al–Si casting alloys with trace amounts of Mg and Cu initiates in the interdendritic regions that contain brittle, Fe-rich intermetallic compounds [53,54]. As such, the phases that affect the fracture behavior in our present study encompassed (1) eutectic Si and (2) Al–Fe–Si phases. The combined effect of the morphology and base softening of these two phases is a pivotal factor in determining the material’s strength and elongation [48]. Comparing the evolution of Si distribution shown in Figure 16a–c, we observed that the thick, island-like precipitated Si, originating from the secondary rolling, gradually transformed into spheroidal and elliptical aggregates after 168 h of exposure to a 200 °C holding temperature. This transformation aided in further impedance of crack propagation. Conversely, after 168 h of cyclic heating and cooling, Si was unevenly distributed in long strips and clusters, resulting in limited ductility improvement and even inducing crack growth at the Al–Si interface, leading to a diminished strength under load. Notably, we can infer from Figure 16a,c that Si closely corresponds to the fracture subsurface profile in BEI, whereas in Figure 16b, Si exhibited a discontinuous distribution at the fracture edge.



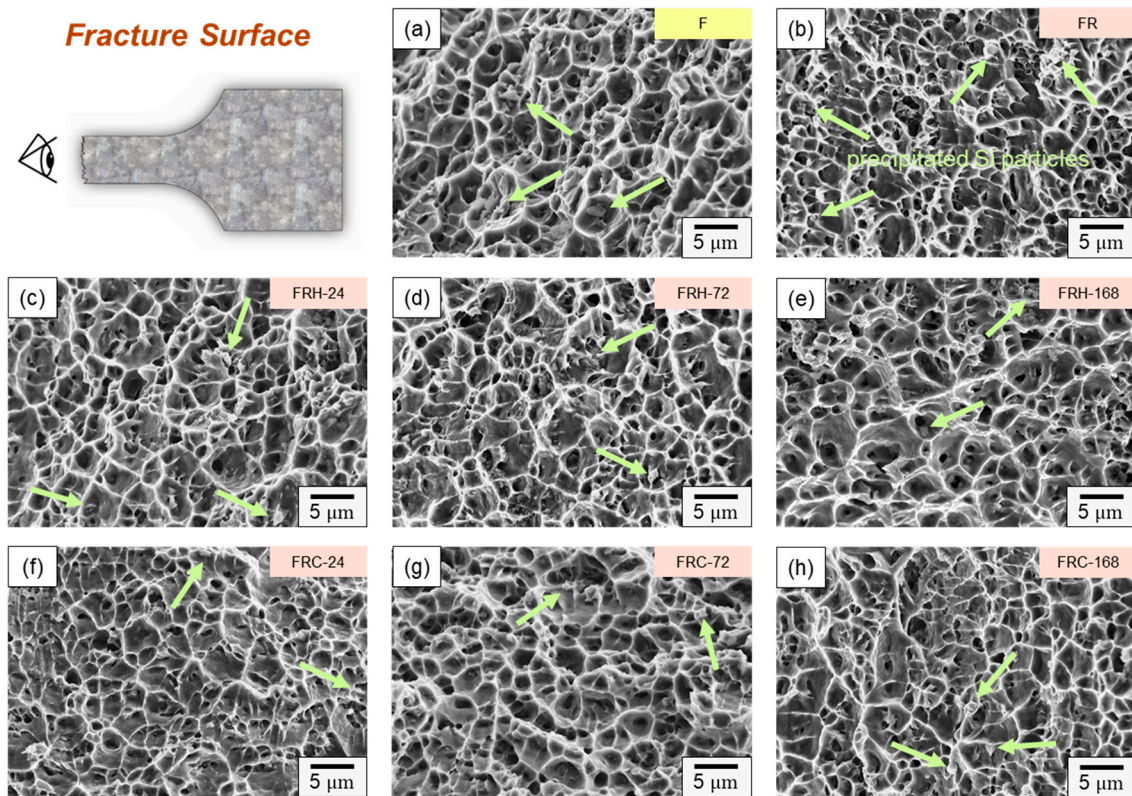


**Figure 15.** Fracture morphology of specimens (a) F, (b) FR, (c) FRH-24, (d) FRH-72, (e) FRH-168, (f) FRC-24, (g) FRC-72, and (h) FRC-168 (Note: The precipitated Si particles on the fractured surface are indicated by bright green arrows).

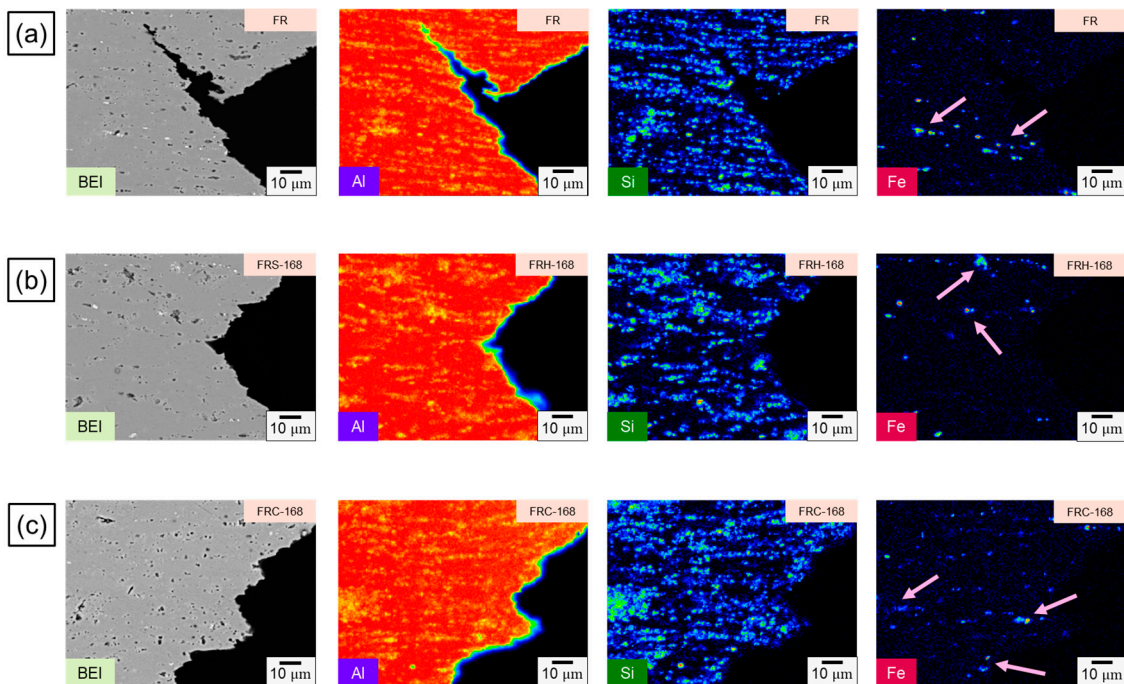


**Figure 16.** EPMA scanning element mapping of specimens (a) FR, (b) FRH-168, and (c) FRC-168. The first, second and third rows of the Figure 16 represent the BEI and the distribution of Al, Si and Fe of specimens FR, FRH-168 and FRC-168 respectively. Fe-rich accumulation on the fracture subsurface is shown by the pink arrows.

The preceding discussion substantiates that the fracture behavior of the 4043 Al alloy is fundamentally governed by the morphology of precipitated Si. On the other hand, the evolution of the Fe distribution in Figure 16a–c sheds light on the needle-like Al–Fe–Si phase within specimen FR. This phase underwent morphological transformations when exposed to a 168 h holding period at 200 °C, effectively mitigating stress concentration points typically induced by the sharp edges of hard secondary phases [55]. Simultaneously, the spheroidized Fe-rich phase acts as an impediment to crack growth [56,57]. However, following 168 h of cyclic heating and cooling, the original needle-like precipitated Al–Fe–Si phase morphed into short rod-like and point-like aggregations with an uneven distribution. This led to non-uniform stress distribution within the material when subjected to mechanical loads. Figure 17a illustrates the dendritic Al–Si eutectic structure with embedded precipitated Si particles. Figure 17b illustrates the evolution of the eutectic Al–Si structure’s morphology in the transverse section of specimens F, FR, FRH-168, and FRC-168.

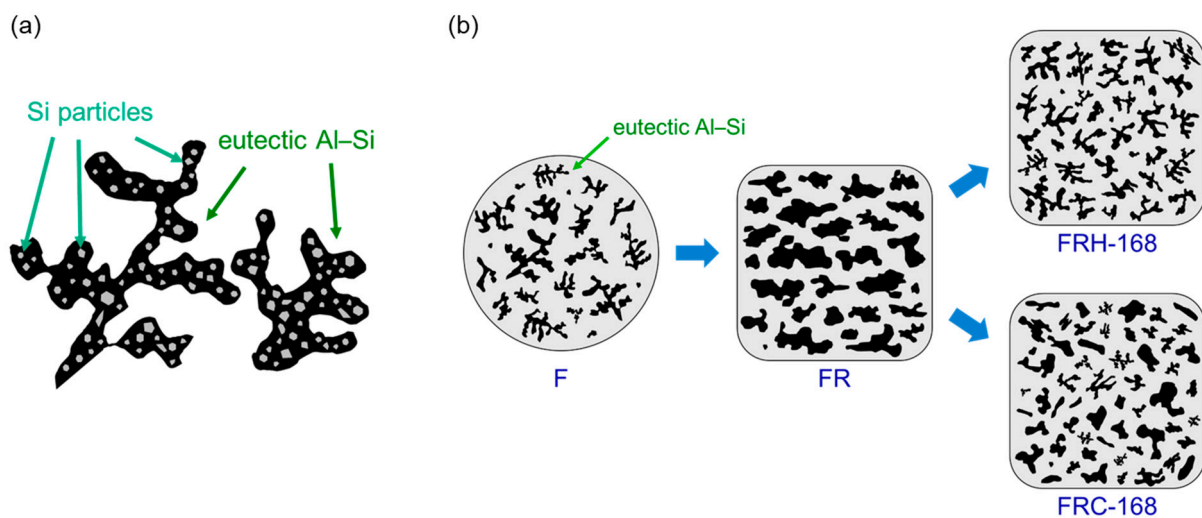


**Figure 17.** Schematic diagrams illustrating (a) the Al–Si eutectic structures and (b) the morphological evolution of precipitated Si.

### 3.4. TEM Diffraction Analysis

Figure 18a,b illustrate the elemental distribution along the FIB sampling profiles for specimen FRH-168 and specimen FRC-168, respectively, revealing the presence of micrometer-scale Si particles in both cases. Moreover, due to the sampling location, the precipitated Al–Fe–Si phase formed by Fe aggregation can be discerned within specimen FRH-168. In contrast, specimen FRC-168 was not sampled in the Fe-rich region, making the Fe signal source in Figure 18b comprise Fe originating from a solid solution within the Al matrix and background signals. Subsequently, Si particle diffraction patterns were employed to examine the crystallization behavior, as showcased in Figure 18.

In Figure 18c, the HRTEM image of specimen FRH-168 reveals a high-density stacking of atoms, indicating that elevated temperatures and extended durations foster stacking faults within the 4043 Al alloy Si particles. Figure 19d represents the diffraction pattern corresponding to Figure 19c, revealing the presence of stacking faults and twins along multiple directions. In Figure 19g, the HRTEM image of specimen FRC-168 displays clearly visible curved grain boundaries. The distinct Si diffusion directions during heating and cooling, coupled with the inability of thermal cycles to provide a stable driving force for grain growth, led Si to solidly dissolve in the Al matrix and precipitate from various nucleation points. Consequently, these Si particles coalesced to form Si particles, with some stacking faults evident within the eutectic Si on either side of the grain boundary. Figure 18h corresponds to the diffraction pattern in Figure 19g. Comparing Figure 19c,d and Figure 19g,h, the experimental results indicate that prolonged exposure to high temperatures results in the development of more stacking faults and defects within the eutectic Si.



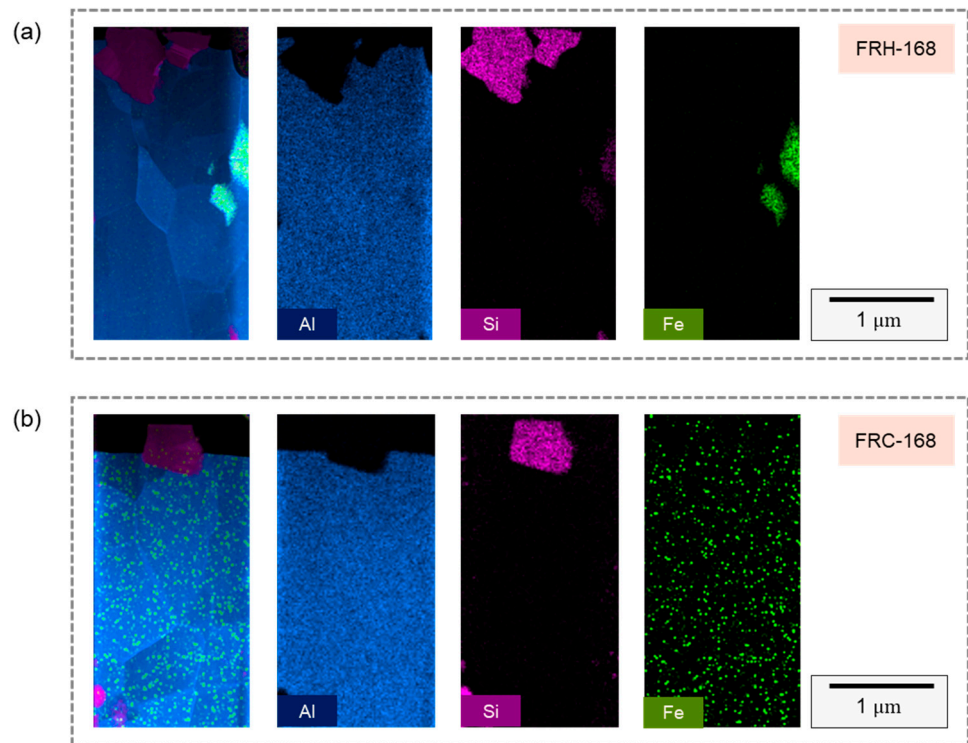


**Figure 18.** TEM analysis of EDS mapping in FIB slice section of specimens (a) FRH-168 and (b) FRC-168.

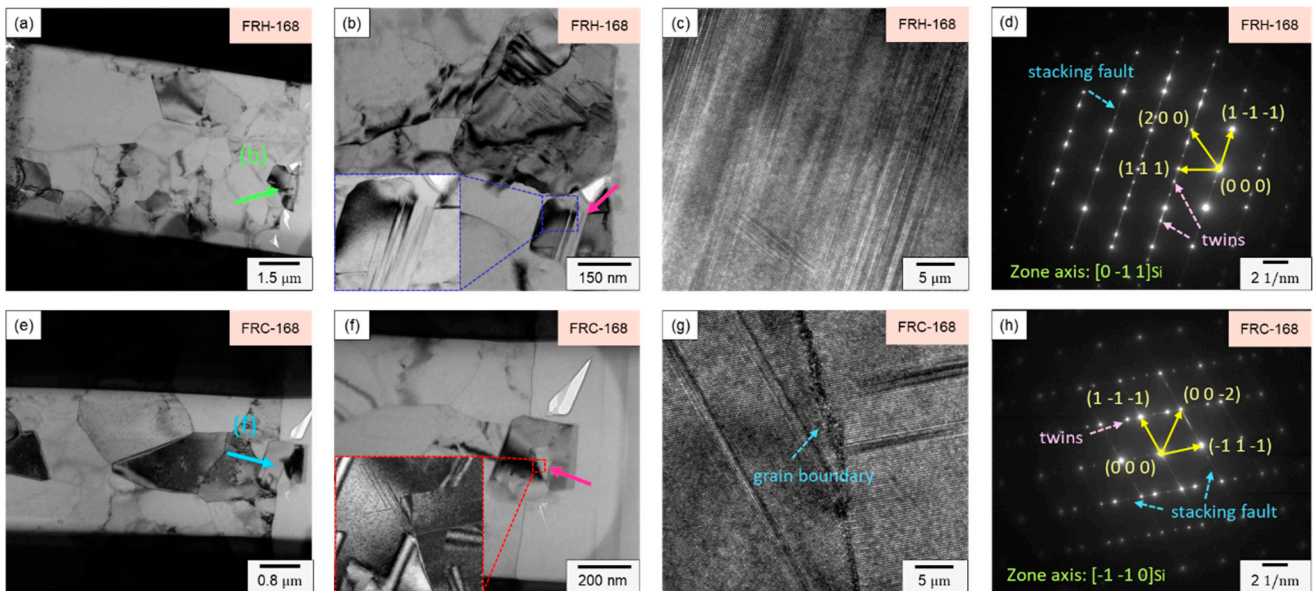


**Figure 19.** (a,e) Bright field TEM images; (b,f) enlarged view of Si particles; (c,g) HRTEM images and (d,h) SAED patterns of specimens FRH-168 and FRC-168.

Figure 20a,b illustrate the Al and Si compositions on both sides of the Al–Si interface, detected using EDX, for specimens FRH-168 and FRC-168. Figure 20c confirms that the Si concentration in the Al matrix of specimen FRH-168 was approximately 2 a.t% lower than that of FRC-168 (compare points 1 and 4). This observation aligns with the results in Figure 10. The prolonged exposure to high temperatures induced the diffusion of solid solution Si from the matrix into the precipitated Si, resulting in a slightly reduced Si

content in the  $\alpha$ -Al. Conversely, the Al and Si contents in the Si particles show only minor differences between the two specimens.

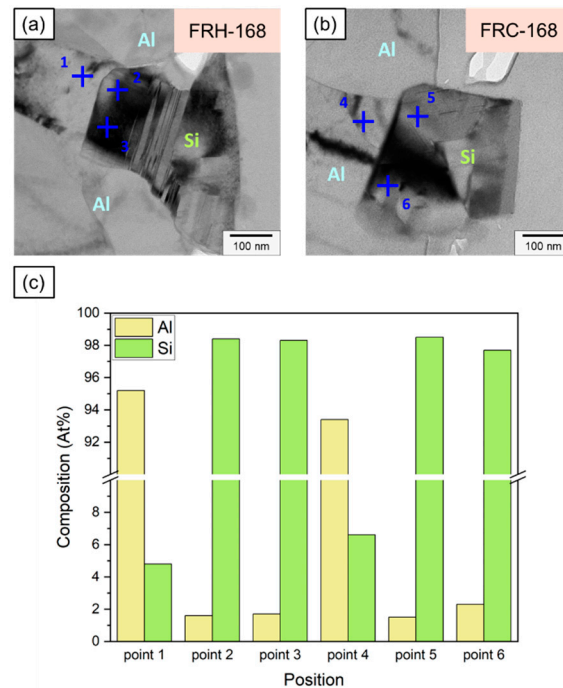


**Figure 20.** Position marking for EDS analysis near Al–Si interface of specimens (a) FRH-168 and (b) FRC-168. (c) Composition analysis of Al and Si at each point.

It is worth noting that past studies on Al–Si alloys have shown that Si is primarily distributed in Al bases as eutectic Si [8,9], which takes the form of flakes and consists of pure Si [58,59]. Figure 21 and Table 3 present the EDX detection results for points 1–6, revealing the presence of approximately 1.6–2.3 at.% of Al solid solution within Si crystals at points 2, 3, 5, and 6. This result may be attributed to scattered electrons impacting the convex areas left by FIB when grinding the thin area on both sides of the TEM specimen, thereby generating weak X-ray signals characteristic of Al. Viewing this result from another perspective, Jiqiang Chen et al. claimed the presence of trace amounts of Al precipitates in the eutectic Si phase in previous research [60]. Nevertheless, the current study was unable to validate this view, and we believe that the precipitated Si particles in the 4043 Al alloy consist of pure Si.

**Table 3.** EDX analysis results of points 1–6.

Point	Composition (at.%)	
	Al	Si
1	95.2	4.8
2	1.6	98.4
3	1.7	98.3
4	93.4	6.6
5	1.5	98.5
6	2.3	97.7

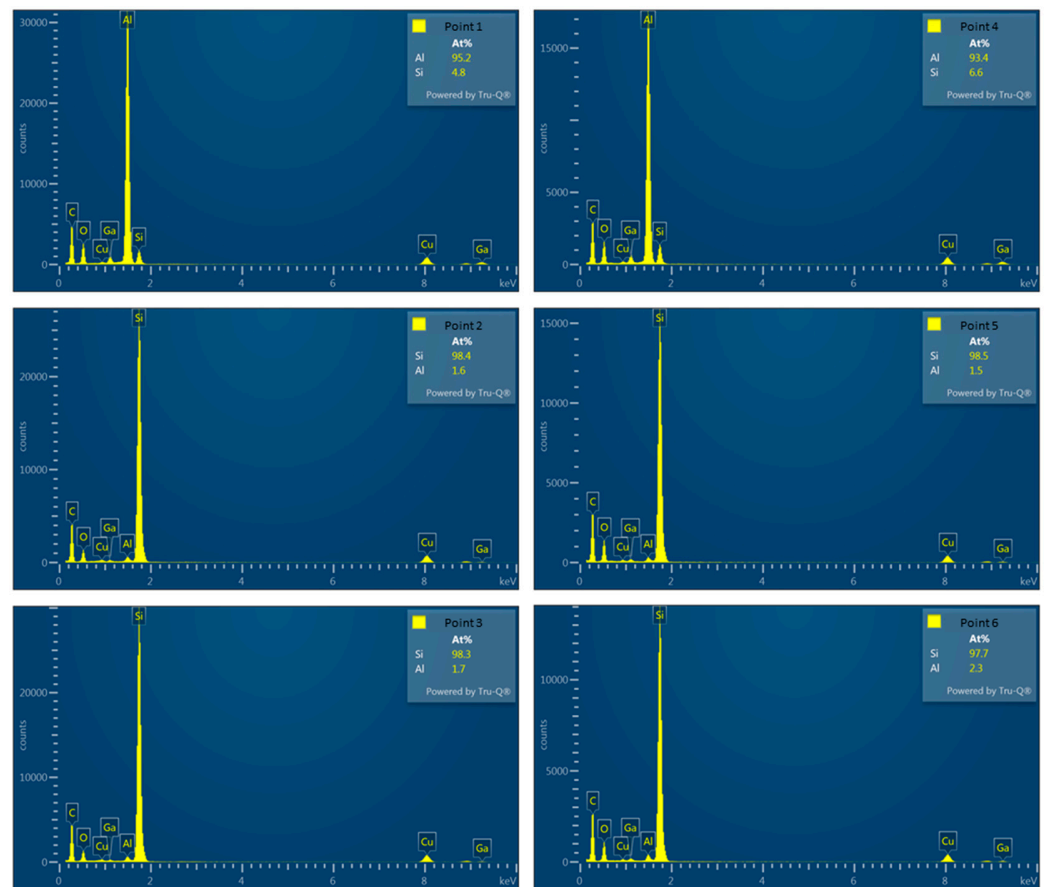


**Figure 21.** Corresponding EDS analysis of each point.

### 3.5. Application Potential and Future Work

The 4043 Al alloy belongs to the 4xxx series of Al alloys and is known for its exceptional characteristics. It exhibits high fluidity at elevated temperatures, resists solidification cracks, and maintains crack resistance during cold processing. As a result, it is well-suited for mass production using the CCDR process compared to other Al alloy types. In this study, we utilized CCDR to produce 4043 Al alloy wire rod coils with the primary goal of developing lightweight, high-quality, and cost-effective raw materials. These materials find applications in the production of fasteners and wear-resistant mechanical components, such as screws, nuts, bolts, sockets, and pins. It is worth noting that the 4043 Al alloy wire rod coils used in our research have achieved IATF16949 certification. This global quality management system certification is crucial for the automotive industry, further underscoring the alloy's potential applicability in this sector.

Furthermore, our experimental findings demonstrated that, in a thermal cycling environment, the inability to achieve spheroidized eutectic Si precipitation and uniform Si particle distribution within the 4043 Al alloy led to a gradual reduction in strength and ductility during repeated heating–cooling cycles. This finding aligns with the observation in Figure 16b, where Si was discontinuously distributed at the fracture edge, indicating that the crack bypasses the spheroidized Si particles during propagation. A closer examination of the third picture in Figure 16a–c can further validate our inference regarding the Si distribution at the edge. As depicted in the evolution process in Figure 17b, the size of the Al–Si eutectic structure in FRC differed significantly from that in FRH. The repeated heating and cooling cycles hindered the effective smoothing and spheroidizing of sharp corners in the Si particles within the structure. In our forthcoming research, we aim to enhance the application potential of CCDR 4043 Al alloys by introducing trace amounts of Sr and Mg to control Si nucleation and precipitation strengthening [61].



#### 4. Conclusions

In this study, a 4043 Al alloy was fabricated by the continuous casting and rolling technique and cold rolling was applied to enhance the mechanical strength. The subsequent testing included (1) sustained high temperature and (2) thermal cycle maintenance for 24, 72, and 168 h to analyze the changes in microstructure and mechanical properties. Finally, a comparison of the Si crystallization behavior of specimens FRH-168 and FRC-168 was made and the following conclusions were obtained:

- (1) Prolonged exposure to 200 °C leads to Si diffusion within the matrix of the 4043 Al alloy, resulting in Si particle coarsening. Additionally, sustained high temperatures eliminate dislocations induced by cold rolling, rendering the matrix more malleable. The uniform network of spheroidized Si and small rod-shaped Si clusters enhances the material's ductility and reduces the concentration effect of hard-phase stress.
- (2) The cyclic heating–cooling environment induces the formation of Al–Si eutectic structures of varying sizes within the 4043 Al alloy, attributed to the diverse directions of the diffusion driving force in each cycle. Sustained high temperature treatment, in comparison with repeated heating and cooling, promotes the spheroidization of more Si particles, particularly at sharp corners.
- (3) The thermal expansion coefficient of Al is approximately 6.6 times that of Si. Repeated cycles of thermal expansion and contraction can readily induce cyclic stress, leading to defects at the Al–Si interface. This, in turn, causes cracks to propagate along the Al–Si interface when the 4043 Al alloy is under load, resulting in a deterioration in strength and elongation.
- (4) When comparing the crystallization behavior of Si under long-term temperature holding and thermal cycling conditions, it becomes evident that a sustained high-temperature environment results in high-density stacking faults and twin crystals forming within the Si particles. In contrast, thermal cycling does not offer a stable driving force for Si growth. Instead, solid solution Si, dissolved in the Al matrix, tends to precipitate from multiple nucleation points, leading to the observation of grain boundaries and dislocations within the Si structure.
- (5) In comparison to repeated heating and cooling conditions, mechanical components manufactured using a CCCR 4043 Al alloy exhibit greater stability under sustained high-temperature conditions. Exploring alternative methods to achieve the spheroidization of precipitated Si and the uniform distribution of Al–Si eutectic structures within the microstructure of Al–Si alloy in a thermal cycle working environment is a crucial engineering challenge that requires further investigation in future research.

**Author Contributions:** Methodology, B.-C.H.; investigation, B.-C.H.; data curation, B.-C.H.; writing—original draft preparation, B.-C.H.; writing—review and editing, F.-Y.H.; supervision, F.-Y.H. All authors have read and agreed to the published version of the manuscript.

**Funding:** This research was funded by the National Science and Technology Council of Taiwan (Grant No. NSTC 112-2740-M-006-001).

**Institutional Review Board Statement:** Not applicable.

**Informed Consent Statement:** Not applicable.

**Data Availability Statement:** The data presented in this study are available on request from the corresponding author.

**Acknowledgments:** The authors would like to express their gratitude to the National Science and Technology Council of Taiwan (Grant No. NSTC 112-2740-M-006-001) for their financial support. The authors also extend their appreciation to Ting Sin Co., Ltd. for supplying the CCCR 4043 wire rods used as the research materials. The authors are particularly thankful for the access to EM000700 under NSTC 112-2740-M-006-001 and the assistance provided by Tsai-Yun Liu, an instrument technology engineer at the Core Facility Center of National Cheng Kung University.

**Conflicts of Interest:** The authors declare no conflict of interest.

## References

- Jiang, D.; Zhang, Q.; Zhao, M.; Xia, H.; Wang, S.; Li, Y. Effects of welds distribution and high-low temperature humidity alternating aging on sealing performance of weld-bonded stainless steel structures. *J. Manuf. Process.* **2019**, *48*, 77–85. [CrossRef]
- Uzun, O.; Karaaslan, T.; Gogebakan, M.; Keskin, M. Hardness and microstructural characteristics of rapidly solidified Al–8–16 wt.% Si alloys. *J. Alloys Compd.* **2004**, *376*, 149–157. [CrossRef]
- Javidani, M.; Larouche, D. Application of cast Al–Si alloys in internal combustion engine components. *Int. Mater. Rev.* **2014**, *59*, 132–158. [CrossRef]
- Xia, F.; Gao, X.S.; Liang, M.X.; Guo, Y.C.; Li, J.P.; Yang, Z.; Wang, J.L.; Zhang, L.L. Effect of thermal exposure on microstructure and high-temperature fatigue life of Al–Si piston alloys. *J. Mater. Res. Technol.* **2020**, *9*, 12926–12935. [CrossRef]
- Wang, J.Y.; Wang, B.J.; Huang, L.F. Structural evolution of Al–8% Si hypoeutectic alloy by ultrasonic processing. *J. Mater. Sci. Technol.* **2017**, *33*, 1235–1239. [CrossRef]
- Hegde, S.; Prabhu, K.N. Modification of eutectic silicon in Al–Si alloys. *J. Mater. Sci.* **2008**, *43*, 3009–3027. [CrossRef]
- Zheng, Q.; Zhang, L.; Jiang, H.; Zhao, J.; He, J.; He, J. Effect mechanisms of micro-alloying element La on microstructure mechanical properties of hypoeutectic Al–Si alloys. *J. Mater. Sci. Technol.* **2020**, *47*, 142–151. [CrossRef]
- Hosch, T.; Napolitano, R. The effect of the flake to fiber transition in silicon morphology on the tensile properties of Al–Si eutectic alloys. *Mater. Sci. Eng. A* **2010**, *528*, 226–232. [CrossRef]
- Riestra, M.; Ghassemali, E.; Bogdanoff, T.; Seifeddine, S. Interactive effects of grain refinement, eutectic modification and solidification rate on tensile properties of Al–10Si alloy. *Mater. Sci. Eng. A* **2017**, *703*, 270–279. [CrossRef]
- Huang, B.-C.; Chang, K.-C.; Hung, F.-Y. Study on microstructure, mechanical properties and erosion characteristics of Al–Si alloy manufactured by continuous casting direct rolling process. *Appl. Sci.* **2021**, *11*, 8351. [CrossRef]
- Huang, B.-C.; Hung, F.-Y. Effect of tensile loading–unloading cyclic plastic deformation on 4043 aluminum alloy manufactured through CCDD. *Mater. Today Commun.* **2023**, *34*, 104979. [CrossRef]
- Antipov, K.V.; Benarieb, I.; Oglodkova, Y.S.; Rudchenko, A.S. Structure and Properties of Industrial Semifinished Products from a Weldable Corrosion-Resistant Aluminum Alloy of the Al–Mg–Si–Cu System. *Inorg. Mater. Appl. Res.* **2022**, *13*, 1200–1208. [CrossRef]
- Zhao, J.-R.; Hung, F.-Y.; Chen, B.-J. Effects of heat treatment on a novel continuous casting direct rolling 6056 aluminum alloy: Cold rolling characteristics and tensile fracture properties. *J. Mater. Res. Technol.* **2021**, *11*, 535–547. [CrossRef]
- Jiang, R.; Zhao, W.; Zhang, L.; Li, X.; Guan, S. Microstructure and corrosion resistance of commercial purity aluminum sheet manufactured by continuous casting direct rolling after ultrasonic melt pre-treatment. *J. Mater. Res. Technol.* **2023**, *22*, 1522–1532. [CrossRef]
- Ding, X.; Li, D.; Zhang, Q.; Ma, H.; Yang, J.; Fan, S. Effect of ambient pressure on bead shape, microstructure and corrosion behavior of 4043 Al alloy fabricated by laser coaxial wire feeding additive manufacturing in vacuum environment. *Opt. Laser Technol.* **2022**, *153*, 108242. [CrossRef]
- Miao, Q.; Wu, D.; Chai, D.; Zhan, Y.; Bi, G.; Niu, F.; Ma, G. Comparative study of microstructure evaluation and mechanical properties of 4043 aluminum alloy fabricated by wire-based additive manufacturing. *Mater. Des.* **2020**, *186*, 108205. [CrossRef]
- He, C.; Wei, J.; Li, Y.; Zhang, Z.; Tian, N.; Qin, G.; Zuo, L. Improvement of microstructure and fatigue performance of wire-arc additive manufactured 4043 aluminum alloy assisted by interlayer friction stir processing. *J. Mater. Sci. Technol.* **2023**, *133*, 183–194. [CrossRef]
- Knapp, G.L.; Gussev, M.; Shyam, A.; Feldhausen, T.; Plotkowski, A. Microstructure, deformation and fracture mechanisms in Al–4043 alloy produced by laser hot-wire additive manufacturing. *Addit. Manuf.* **2022**, *59*, 103150. [CrossRef]
- Ortega, A.G.; Galvan, L.C.; Salem, M.; Moussaoui, K.; Segonds, S.; Rouquette, S.; Deschaux-Beaume, F. Characterisation of 4043 aluminium alloy deposits obtained by wire and arc additive manufacturing using a Cold Metal Transfer process. *Sci. Technol. Weld. Join.* **2019**, *24*, 538–547. [CrossRef]
- Chen, Z.; Kang, H.; Fan, G.; Li, J.; Lu, Y.; Jie, J.; Zhang, Y.; Li, T.; Jian, X.; Wang, T. Grain refinement of hypoeutectic Al–Si alloys with B. *Acta Mater.* **2016**, *120*, 168–178. [CrossRef]
- Bolzoni, L.; Xia, M.; Babu, N.H. Formation of equiaxed crystal structures in directionally solidified Al–Si alloys using Nb-based heterogeneous nuclei. *Sci. Rep.* **2016**, *6*, 39554. [CrossRef] [PubMed]
- Zhang, K.; Bian, X.; Li, Y.; Liu, Y.; Yang, C.; Zhao, X. Chemical diffusion characteristics of Al–Si alloy melts under a transverse magnetic field. *Phys. Lett. A* **2015**, *379*, 1464–1466. [CrossRef]
- Zhang, Z.; Li, J.; Yue, H.; Zhang, J.; Li, T. Microstructure evolution of A356 alloy under compound field. *J. Alloys Compd.* **2009**, *484*, 458–462. [CrossRef]
- Echigo, R.; Yoshida, H.; Mochizuki, T. Temperature equalization by the radiative converter for a slab in continuous casting direct rolling. *JSME Int. J. Ser. 2 Fluids Eng. Heat Transf. Power Combust. Thermophys. Prop.* **1988**, *31*, 545–552. [CrossRef]
- Kase, M.; Matsuzuka, K.; Takahashi, H.; Oba, H.; Hirata, O. Continuous casting direct rolling technology at Nippon Steel’s Sakai Works. *Steel Times* **1985**, *213*, 268.
- Maehara, Y.; Nakai, K.; Yasumoto, K.; Mishima, T. Hot cracking of low alloy steels in simulated continuous casting–direct rolling process. *Trans. Iron Steel Inst. Jpn.* **1988**, *28*, 1021–1027. [CrossRef]
- Kim, M.G.; Lee, G.C.; Park, J.P. Continuous Casting and Rolling for Aluminum Alloy Wire and Rod. In *Materials Science Forum*; Trans Tech Publications: Stafa-Zurich, Switzerland, 2010.





28. Xu, Z.; Zhao, Z.; Han, D.; Chen, Q.; Li, Z. Effects of Si content and aging temperature on wear resistance of surfacing layers welded with 4043 aluminum welding wires. *Rare Met. Mater. Eng.* **2016**, *45*, 71–74.
29. Coniglio, N.; Cross, C.E.; Dörfel, I.; Österle, W. Phase formation in 6060/4043 aluminum weld solidification. *Mater. Sci. Eng. A* **2009**, *517*, 321–327. [CrossRef]
30. Zhao, Z.; Xu, Z.; Wang, G.; Cui, J. Microstructure and property of welding joint weld with micro-Alloying 4043 welding wire. *Acta Met. Sin* **2013**, *49*, 946–952. [CrossRef]
31. Sasaki, K. Low cycle thermal fatigue of aluminum alloy cylinder head in consideration of changing metrology microstructure. *Procedia Eng.* **2010**, *2*, 767–776.
32. Sajedi, Z.; Casati, R.; Poletti, M.C.; Wang, R.; Iranshahi, F.; Vedani, M. Comparative thermal fatigue behavior of AlSi7Mg alloy produced by L-PBF and sand casting. *Int. J. Fatigue* **2021**, *152*, 106424. [CrossRef]
33. Rong, G.; Sha, S.; Li, B.; Chen, Z.; Zhang, Z. Experimental investigation on physical and mechanical properties of granite subjected to cyclic heating and liquid nitrogen cooling. *Rock Mech. Rock Eng.* **2021**, *54*, 2383–2403. [CrossRef]
34. Liu, Q.; Qian, Z.; Wu, Z. Micro/macro physical and mechanical variation of red sandstone subjected to cyclic heating and cooling: An experimental study. *Bull. Eng. Geol. Environ.* **2019**, *78*, 1485–1499. [CrossRef]
35. Lin, H.-M.; Lui, T.-S.; Chen, L.-H. Effect of silicon content on intergranular embrittlement of ferritic spheroidal graphite cast iron suffered from cyclic heating. *Mater. Trans.* **2003**, *44*, 173–180. [CrossRef]
36. Lin, H.-M.; Lui, T.-S.; Chen, L.-H. Effect of microstructural refinement on ductility deterioration of high silicon ferritic spheroidal graphite cast iron caused by cyclic heating. *Mater. Trans.* **2003**, *44*, 1209–1218. [CrossRef]
37. De Winne, R.; Petkeviciute, A. ESG Controversies: How Do They Affect Market Returns and Individual Asset Choices? In Proceedings of the Behavioural Finance Working Group Conference 2022, London, UK, 9–10 June 2022.
38. Trowell, K.; Goroshin, S.; Frost, D.L.; Bergthorson, J.M. Aluminum and its role as a recyclable, sustainable carrier of renewable energy. *Appl. Energy* **2020**, *275*, 115112. [CrossRef]
39. ASTM E8/E8M-22; Standard Test Methods for Tension Testing of Metallic Materials. ASTM International: West Conshohocken, PA, USA, 2022.
40. ASTM E18-20; Standard Test Methods for Rockwell Hardness of Metallic Materials. ASTM International: West Conshohocken, PA, USA, 2022.
41. Qian, G.; Sun, L.; Chen, H.; Wang, Z.; Wei, K.; Ma, W. Enhancing impurities removal from Si by controlling crystal growth in directional solidification refining with Al–Si alloy. *J. Alloys Compd.* **2020**, *820*, 153300. [CrossRef]
42. Nishi, Y.; Kang, Y.; Morita, K. Control of Si crystal growth during solidification of Si–Al melt. *Mater. Trans.* **2010**, *51*, 1227–1230. [CrossRef]
43. Jung, J.-G.; Lee, S.-H.; Lee, J.-M.; Cho, Y.-H.; Kim, S.-H.; Yoon, W.-H. Improved mechanical properties of near-eutectic Al–Si piston alloy through ultrasonic melt treatment. *Mater. Sci. Eng. A* **2016**, *669*, 187–195. [CrossRef]
44. Becker, H.; Bergh, T.; Vullum, P.E.; Leineweber, A.; Li, Y. Effect of Mn and cooling rates on  $\alpha$ -,  $\beta$ - and  $\delta$ -Al–Fe–Si intermetallic phase formation in a secondary Al–Si alloy. *Materialia* **2019**, *5*, 100198. [CrossRef]
45. Basak, C.B.; Babu, N.H. Morphological changes and segregation of  $\beta$ -Al<sub>9</sub>Fe<sub>2</sub>Si<sub>2</sub> phase: A perspective from better recyclability of cast Al–Si alloys. *Mater. Des.* **2016**, *108*, 277–288. [CrossRef]
46. Numan, A.-D.; Marwan, K.; Kozo, S.; Alan, M. Silicon morphology modification in the eutectic Al–Si alloy using mechanical mold vibration. *Mater. Sci. Eng. A* **2005**, *393*, 109–117.
47. Li, Q.; Zhu, Y.; Zhao, S.; Lan, Y.; Liu, D.; Jian, G.; Zhang, Q.; Zhou, H. Influences of Fe, Mn and Y additions on microstructure and mechanical properties of hypoeutectic Al–7% Si alloy. *Intermetallics* **2020**, *120*, 106768. [CrossRef]
48. Li, J.; Cheng, X.; Li, Z.; Zong, X.; Zhang, S.-Q.; Wang, H.-M. Improving the mechanical properties of Al–5Si–1Cu–Mg aluminum alloy produced by laser additive manufacturing with post-process heat treatments. *Mater. Sci. Eng. A* **2018**, *735*, 408–417. [CrossRef]
49. Zhang, B.; Li, X.; Li, D. Assessment of thermal expansion coefficient for pure metals. *Calphad* **2013**, *43*, 7–17. [CrossRef]
50. Watanabe, H.; Yamada, N.; Okaji, M. Linear thermal expansion coefficient of silicon from 293 to 1000 K. *Int. J. Thermophys.* **2004**, *25*, 221–236. [CrossRef]
51. Yang, Y.; Zhong, S.-Y.; Chen, Z.; Wang, M.; Ma, N.; Wang, H. Effect of Cr content and heat-treatment on the high temperature strength of eutectic Al–Si alloys. *J. Alloys Compd.* **2015**, *647*, 63–69. [CrossRef]
52. Cao, X.; Campbell, J. Morphology of  $\beta$ -Al<sub>5</sub>FeSi phase in Al–Si cast alloys. *Mater. Trans.* **2006**, *47*, 1303–1312. [CrossRef]
53. Ceschini, L.; Morri, A.; Morri, A.; Toschi, S.; Johansson, S.; Seifeddine, S. Effect of microstructure and overaging on the tensile behavior at room and elevated temperature of C355-T6 cast aluminum alloy. *Mater. Des.* **2015**, *83*, 626–634. [CrossRef]
54. Firouzidor, V.; Rajabi, M.; Nejati, E.; Khomamizadeh, F. Effect of microstructural constituents on the thermal fatigue life of A319 aluminum alloy. *Mater. Sci. Eng. A* **2007**, *454*, 528–535. [CrossRef]
55. Zhao, B.; Xing, S.; Shan, A.; Yan, G.; Jiang, X. Influence of La addition on Fe-rich intermetallic phases formation and mechanical properties of Al–7Si–4Cu–0.35 Mg–0.2 Fe alloys prepared by squeeze casting. *Intermetallics* **2023**, *153*, 107783. [CrossRef]
56. Phongphisutthinan, C.; Tezuka, H.; Kobayashi, E.; Sato, T. Evolution of Fragmented Fe-Intermetallic Compounds in the Semi-Solid State of Al–Mg–Si–Fe Alloys by Deformation Semi-Solid Forming Process. In *ICAA13 Pittsburgh: Proceedings of the 13th International Conference on Aluminum Alloys, Pittsburgh, PA, USA, 3–7 June 2012*; Springer: Berlin/Heidelberg, Germany, 2016.

57. Jiao, X.; Liu, C.; Wang, J.; Guo, Z.; Wang, J.; Wang, Z.; Gao, J.; Xiong, S. On the characterization of microstructure and fracture in a high-pressure die-casting Al-10 wt% Si alloy. *Prog. Nat. Sci. Mater. Int.* **2020**, *30*, 221–228. [CrossRef]
58. Wang, K.; Jiang, H.Y.; Wang, Q.D.; Ye, B.; Ding, W.J. Nanoparticle-induced nucleation of eutectic silicon in hypoeutectic Al–Si alloy. *Mater. Charact.* **2016**, *117*, 41–46. [CrossRef]
59. Young, K.K.; Sik, S.J.; Wha, P.D. Separation of Pure Silicon from Al–Si Alloy Melts. In *Materials Science Forum*; Trans Tech Publications: Stafa-Zurich, Switzerland, 2014.
60. Chen, J.; Liu, C.; Wen, F.; Zhou, Q.; Zhao, H.; Guan, R. Effect of microalloying and tensile deformation on the internal structures of eutectic Si phase in Al–Si alloy. *J. Mater. Res. Technol.* **2020**, *9*, 4682–4691. [CrossRef]
61. Gan, J.-Q.; Huang, Y.-J.; Cheng, W.; Jun, D. Effect of Sr modification on microstructure and thermal conductivity of hypoeutectic Al–Si alloys. *Trans. Nonferrous Met. Soc. China* **2020**, *30*, 2879–2890. [CrossRef]

**Disclaimer/Publisher’s Note:** The statements, opinions and data contained in all publications are solely those of the individual author(s) and contributor(s) and not of MDPI and/or the editor(s). MDPI and/or the editor(s) disclaim responsibility for any injury to people or property resulting from any ideas, methods, instructions or products referred to in the content.

## Article

# Impact of Mn Alloying on Phase Stabilities, Magnetic Properties and Electronic Structures in Fe

Hao Yang<sup>1,2</sup>, Jin-Han Yang<sup>1</sup>, Ying Zhao<sup>1</sup>, Han Ma<sup>2</sup>, Yanzhong Tian<sup>1,\*</sup>, Minghui Cai<sup>1</sup>, Shuai Tang<sup>1</sup>, Yandong Liu<sup>1</sup>, Xiang Zhao<sup>1</sup>, Hai-Le Yan<sup>1,\*</sup> and Liang Zuo<sup>1</sup>

<sup>1</sup> Key Laboratory for Anisotropy and Texture of Materials (Ministry of Education), School of Material Science and Engineering, Northeastern University, Shenyang 110819, China

<sup>2</sup> Institute of Research of Iron and Steel of Shasteel, Suzhou 215625, China

\* Correspondence: tianyanzhong@mail.neu.edu.cn (Y.T.); yanhaile@mail.neu.edu.cn (H.-L.Y.)

**Abstract:** Impacts of Mn alloying on lattice stabilities, magnetic properties, electronic structures of the bcc and fcc phases and the fcc→bcc phase transition in Fe<sub>16-x</sub>Mn<sub>x</sub> (x = 0, 1 and 2) alloys are studied by first-principles calculations. Results show that the doped Mn atom prefers ferromagnetic and antiferromagnetic interaction with the host Fe atoms in the bcc and fcc phases, respectively. In these two phases, the magnetic moment of Mn is smaller and larger than Fe, respectively. The local moment of Fe is decided by the Fe-Mn distance in the bcc phase, whereas in the fcc phase, it is determined by spatial orientation with Mn. In the different phases, Mn prefers different site occupations, which can be understood from the electronic density of states near Fermi energy, implying a possibility of element redistribution during phase transition. The driving force of phase transition decreases with Mn alloying. Both destabilized bcc phase and stabilized fcc phase contribute to the inhibited phase transition, but the latter plays a dominant role. Antiferromagnetism is recognized as the key reason for the enhanced stability of the fcc phase by Mn alloying.

**Keywords:** Fe; Mn alloying; lattice stability; phase transition; magnetism; first-principles calculations



**Citation:** Yang, H.; Yang, J.-H.; Zhao, Y.; Ma, H.; Tian, Y.; Cai, M.; Tang, S.; Liu, Y.; Zhao, X.; Yan, H.-L.; et al. Impact of Mn Alloying on Phase Stabilities, Magnetic Properties and Electronic Structures in Fe. *Materials* **2023**, *16*, 6679. <https://doi.org/10.3390/ma16206679>

Academic Editors: Seong-Ho Ha, Shae-Kwang Kim and Hyun-Kyu Lim

Received: 8 September 2023

Revised: 28 September 2023

Accepted: 10 October 2023

Published: 13 October 2023



**Copyright:** © 2023 by the authors. Licensee MDPI, Basel, Switzerland. This article is an open access article distributed under the terms and conditions of the Creative Commons Attribution (CC BY) license (<https://creativecommons.org/licenses/by/4.0/>).

## 1. Introduction

Manganese, the fifth most abundant metal in the Earth's crust, is a hard, brittle and silvery white metal. In ferroalloys, Mn represents a key alloying element [1,2] owing to its high solid solubility arising from the similar valence electron configurations of Mn ( $3d^54s^2$ ) and Fe ( $3d^64s^2$ ). In fact, Mn appears in all commercial steels and contributes greatly to strength, ductility, hardenability and high-temperature creep resistance [3,4]. Apart from solid solution strengthening [5–7], owing to significant differences of Mn in stabilizing the different phases of ferroalloys [4,8,9], alloying with Mn greatly affects phase transition temperature and thus microstructure phase constituents. By tuning the content of the doped Mn, many advanced steels with an excellent combination of ductility and strength have been developed [10,11]. Furthermore, the prominent role of Mn alloying in tuning phase transition brings several novel functional properties [12], including the shape memory effect and high damping capacity. As is known, the phase stability is intrinsically decided by valence electron concentration, electronic structure, magnetism, lattice volume and so on [13–19]. Thus, a deep understanding of the impact of Mn alloying on ferroalloys at the level of electronic structure should be helpful for the design of advanced ferroalloys.

To date, the study on the impact of Mn alloying in ferroalloys has focused mainly on magnetism [20–30], elastic properties [31–33] and phase transition from face-centered cubic (fcc) to hexagonal close-packed (hcp) [34,35]. Both experiments and theoretical calculations evidence that the FeMn alloy possesses complex magnetic states, which is mainly attributed to the half-filled  $3d$  orbitals of Mn and Fe. The magnetic moments of both Fe and Mn are sensitive to the local chemical environment. With the alloying of Mn,  $C_{11}$  and  $C_{12}$  of



the FeMn alloy are greatly reduced due to the magnetovolume effect, while  $C_{44}$  is almost unaffected [32]. For the fcc→hcp transformation, the magnetic ordering is found to play a critical role in the behaviors of phase transition [35]. It is evidenced that the doped Mn and the host Fe prefer to be antiferromagnetically coupled in the fcc phase [36]. The appearance of the antiferromagnetism interaction is found to tend to decrease the stacking fault energy of the fcc phase [37,38], which promotes the occurrence of the fcc→hcp phase transition. Different from the extensive studies on the phase transition from fcc to hcp, despite some reports in pure Fe [39], the impact mechanisms of Mn alloying on the phase transition from the fcc ( $\gamma$ ) to the body-centered cubic (bcc,  $\alpha$ ) phase is less studied. As is known, the fcc→bcc phase transition is vital to the ferroalloy (e.g., steel), since the microstructure modification in this material is mainly achieved by tailoring it. Therefore, clarifying the impact of Mn alloying in the fcc phase, the bcc phase and the fcc→bcc phase transition should be greatly meaningful.

In this work, the impact of Mn alloying on phase stabilities, magnetic properties, electronic structures of the bcc and fcc phases and the phase transition from the fcc to the bcc phase in  $\text{Fe}_{16-x}\text{Mn}_x$  ( $x = 0, 1$  and  $2$ ) alloys is systematically studied by first-principles calculation. First, the ground-state magnetic and structural preferences in the bcc phase are determined. Herein, due to the complexity of the magnetic states of the FeMn alloy, a two-stage relaxation strategy, i.e., a sole relaxation of the magnetic state followed by a full structural relaxation, is adopted. With the determined structural models, the impacts of Mn alloying on phase stabilities, magnetic properties and electronic structures are investigated (Section 3.1). Second, in analogy to the study on the bcc phase, the magnetic and structural preferences and the impacts of Mn alloying on the fcc phase are studied (Section 3.2). Last, the impact mechanism of Mn doping on the fcc→bcc phase transition is discussed (Section 3.3).

## 2. Computational Methods

First-principles density functional theory (DFT) calculations were carried out by using the plane-wave pseudopotential method as implemented in Vienna ab initio Simulation Package (VASP). The Perdew–Burke–Erzerh (PBE) exchange correlation functional in the frame of the generalized gradient approximation (GGA) [40] was used to represent the exchange and correlation energy. The electron–ion interactions were described by the projector augmented wave (PAW) [41] approach. The valence electron configurations of  $3d^64s^2$  and  $3d^54s^2$  were utilized for Fe and Mn, respectively. For all calculations, the plane-wave kinetic energy cutoff was set to be 600 eV. The  $k$ -point mesh with an interval of  $0.02 \times 2\pi/\text{\AA}$  was used to integrate the Brillouin zone. During structural relaxation, the energy convergence of  $10^{-5}$  eV and the force convergence of  $10^{-3}$  eV/ $\text{\AA}$  were adopted [28,30]. For calculations of electronic structure, the Brillouin zone integration was carried out using the tetrahedron method with the Blöchl correction [42]. Three alloys with compositions of  $\text{Fe}_{16-x}\text{Mn}_x$  ( $x = 0, 1$  and  $2$ ) with a maximum alloying content of 12.5 at.% are investigated. To accurately clarify the impacts of Mn alloying, for all alloys with different doping concentrations, superstructural models with the same atom number (16) are adopted.

## 3. Results and Discussion

### 3.1. Bcc-Structured $\text{Fe}_{16-x}\text{Mn}_x$

#### 3.1.1. Preferred Structural Model

Figure 1a–c show the 16-atom superstructural models for the bcc phases of pure Fe and the Mn-alloyed  $\text{Fe}_{15}\text{Mn}_1$  and  $\text{Fe}_{14}\text{Mn}_2$ , respectively. For pure Fe, the superstructural model is constituted by stacking eight ( $2 \times 2 \times 2$ ) bcc unit cells (Figure 1a). The superstructural model of  $\text{Fe}_{15}\text{Mn}_1$  is obtained by arbitrarily replacing an Fe atom with Mn in the model of pure Fe, as depicted in Figure 1b. Considering the periodic boundary condition adopted in first-principles calculation, the superstructures in which Mn substitutes different Fe atoms in  $\text{Fe}_{15}\text{Mn}_1$  are equivalent. Using a similar method, the structural models of  $\text{Fe}_{14}\text{Mn}_2$

are built. Nevertheless, when two Fe atoms are replaced by Mn in  $\text{Fe}_{14}\text{Mn}_2$ , there exist multiple nonequivalent substitutions. In this work, four superstructural models, designated as Models I to IV, are established. In Models I (Figure 1c<sub>1</sub>), II (Figure 1c<sub>2</sub>) and III (Figure 1c<sub>3</sub>), the two doped Mn atoms (termed as Mn<sub>1</sub> and Mn<sub>2</sub>) are the first (2.484 Å), second (2.868 Å) and third (4.056 Å) nearest neighbors, respectively. In Model IV (Figure 1c<sub>4</sub>), Mn<sub>1</sub> and Mn<sub>2</sub> atoms with a distance of 4.968 Å exhibit a symmetric site occupation. From Model I to Model IV, the distance between Mn<sub>1</sub> and Mn<sub>2</sub> ( $d_{\text{Mn}_1\text{-Mn}_2}$ ) gradually increases.

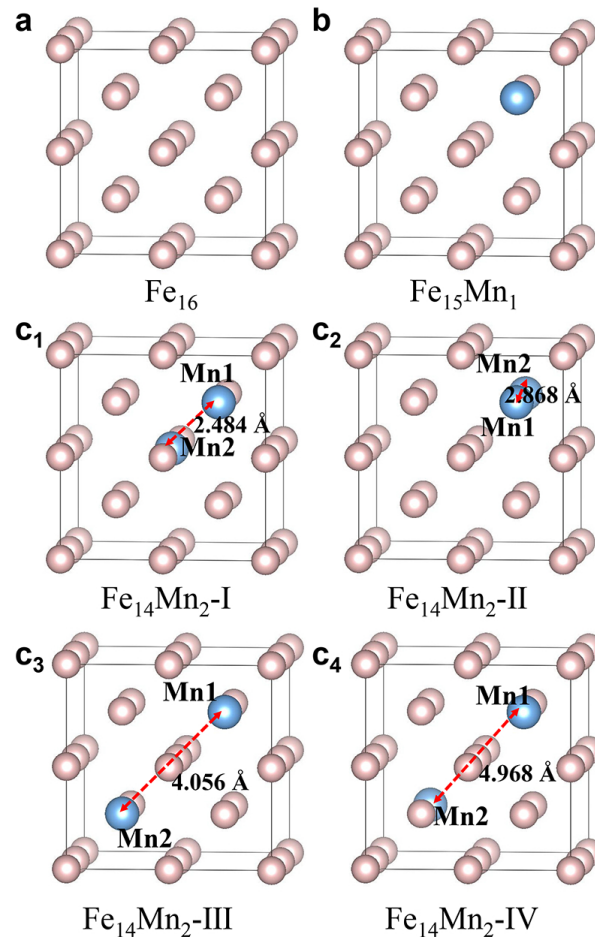


**Figure 1.** Bcc superstructural models of  $\text{Fe}_{16-x}\text{Mn}_x$  ( $x = 0, 1$  and  $2$ ). (a) Pure Fe; (b)  $\text{Fe}_{15}\text{Mn}_1$ ; (c<sub>1</sub>–c<sub>4</sub>) Model I to Model IV of  $\text{Fe}_{14}\text{Mn}_2$ . From Model I to Model IV,  $d_{\text{Mn}_1\text{-Mn}_2}$  increases from 2.484 Å to 2.868 Å, 4.056 Å and 4.968 Å.

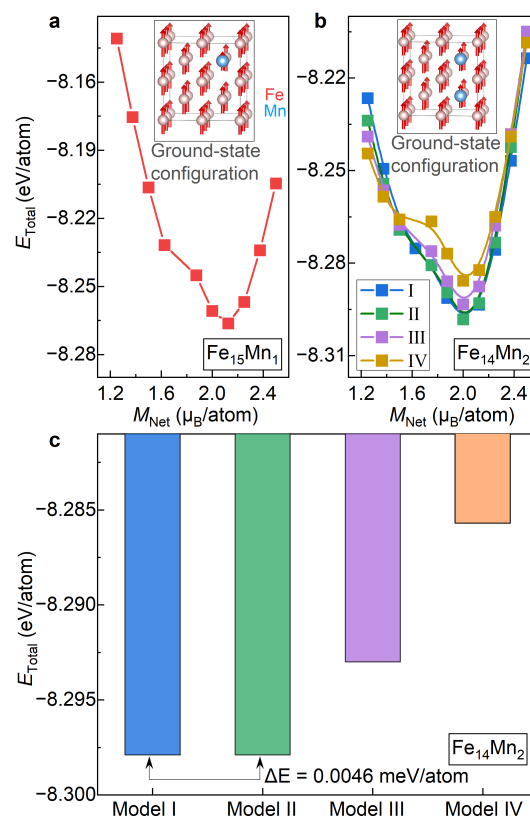
For the bcc phase of pure Fe, the equilibrium lattice constant  $a_0^{\text{bcc}}$  and net magnetization  $M_{\text{Net}}$  are relaxed to be 2.83 Å and 2.19  $\mu_{\text{B}}$ /atom, respectively, as listed in Table 1. This is consistent with the values reported in the literature [24,43,44]. In contrast to pure Fe, the determination of the ground-state structural and magnetic configuration in the FeMn alloy is generally not an easy task, since the FeMn alloy typically possesses multiple metastable magnetic states with similar energies [28–30,45]. To get out from this dilemma, a two-stage relaxation strategy is adopted in this work for the Mn-doped  $\text{Fe}_{16-x}\text{Mn}_x$  alloys. First, the most stable magnetic state is determined by fixing both lattice parameters and atomic positions. Second, with the predetermined magnetic state as the input, a full relaxation is carried out.

**Table 1.** Equilibrium lattice parameter ( $a_0^{\text{bcc}}$ ), net magnetization ( $M_{\text{Net}}$ ) and atom-resolved magnetic moments of Fe ( $M_{\text{Fe}}$ ) and Mn ( $M_{\text{Mn}}$ ) for the bcc phase of the  $\text{Fe}_{16-x}\text{Mn}_x$  ( $x = 0, 1$  and  $2$ ) alloys. The ground-state structural models of  $\text{Fe}_{14}\text{Mn}_2$  are indicated in bold.

Alloy	Model	$a_0^{\text{bcc}}$ Å	$M_{\text{Net}}$ $\mu_{\text{B}}/\text{at.}$	$M_{\text{Fe}}$ $\mu_{\text{B}}/\text{at.}$	$M_{\text{Mn}}$ $\mu_{\text{B}}/\text{at.}$	$E_{\text{Total}}$ eV/at.
Fe	—	2.831	2.19	2.19	—	−8.243
	—	2.84 <sup>a</sup>	2.17 <sup>a</sup>			
	—	2.83 <sup>b</sup>	2.22 <sup>b</sup>			
$\text{Fe}_{15}\text{Mn}_1$	—	2.824	2.11	2.18	1.05	−8.266
	<b>I</b>	<b>2.829</b>	<b>2.02</b>	<b>2.23</b>	<b>0.46</b>	<b>−8.298</b>
$\text{Fe}_{14}\text{Mn}_2$	<b>II</b>	<b>2.820</b>	<b>2.02</b>	<b>2.17</b>	<b>1.02</b>	<b>−8.298</b>
	III	2.819	2.01	2.13	1.06	−8.293
	IV	2.820	2.03	2.07	1.70	−8.286

<sup>a</sup> Ref. [43]; <sup>b</sup> Ref. [24].

Figure 2a presents the total energy ( $E_{\text{Total}}$ ) for the bcc phase of  $\text{Fe}_{15}\text{Mn}_1$  plotted as a function of the fixed net magnetization ( $M_{\text{Net}}$ ). Herein, the change in  $M_{\text{Net}}$ , ranging from  $1.25 \mu_{\text{B}}/\text{atom}$  to  $2.5 \mu_{\text{B}}/\text{atom}$  with an interval of  $0.125 \mu_{\text{B}}/\text{atom}$ , is achieved by using the fixed-spin-moment approach [28]. It is seen that  $E_{\text{Total}}$ , the bcc phase of  $\text{Fe}_{15}\text{Mn}_1$ , roughly exhibits a parabolic trend with the increased  $M_{\text{Net}}$ . The most stable magnetic state of  $\text{Fe}_{15}\text{Mn}_1$  is illustrated in the inset of Figure 2a. Clearly, the bcc phase of  $\text{Fe}_{15}\text{Mn}_1$  prefers to be ferromagnetic at the ground state. Note that there is a kink around  $M_{\text{Net}}$  of  $1.7 \mu_{\text{B}}/\text{atom}$ . This kink, corresponding to a jump in the magnetic moment of the doped Mn, might correspond to a metastable magnetic state.



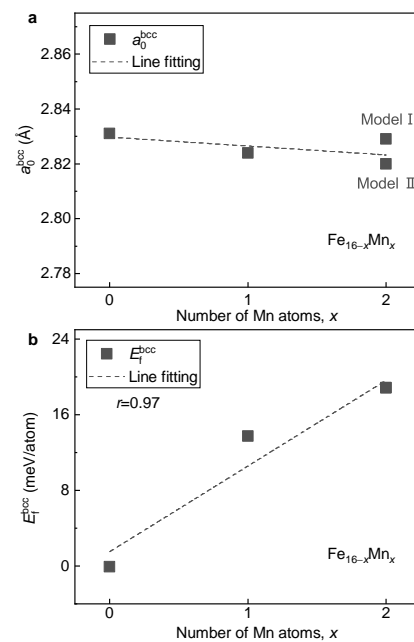
**Figure 2.**  $E_{\text{Total}}$  of the bcc  $\text{Fe}_{16-x}\text{Mn}_x$  ( $x = 1$  and  $2$ ) alloys under different magnetic and structural configurations. (a)  $E_{\text{Total}}$  vs.  $M_{\text{Net}}$  in  $\text{Fe}_{15}\text{Mn}_1$ ; (b)  $E_{\text{Total}}$  vs.  $M_{\text{Net}}$  in  $\text{Fe}_{14}\text{Mn}_2$ ; (c) comparison of  $E_{\text{Total}}$  of Models I, II, III and IV of  $\text{Fe}_{14}\text{Mn}_2$ .

Figure 2b shows the variation in  $E_{\text{Total}}$  for the bcc phase of  $\text{Fe}_{14}\text{Mn}_2$  with respect to  $M_{\text{Net}}$ . Herein, all four site occupations of Mn atoms, i.e., Models I, II, III and IV, are studied. Remarkably, for all four of the examined models,  $E_{\text{Total}}$  shows a roughly parabolic tendency against  $M_{\text{Net}}$ . Like the case of  $\text{Fe}_{15}\text{Mn}_1$ , for all site occupations of Mn, the most stable magnetic state of the bcc phase of  $\text{Fe}_{14}\text{Mn}_2$  is ferromagnetic. The inset of Figure 2b displays the ground-state magnetic configuration of Model II taken as an example. For all the examined four models,  $M_{\text{Net}}$  of the most stable magnetic state are around  $2.0 \mu_{\text{B}}/\text{atom}$ , indicating that  $M_{\text{Net}}$  of the ground-state magnetism state of  $\text{Fe}_{14}\text{Mn}_2$  is independent of the site occupation of Mn. Unlike  $M_{\text{Net}}$ , the kink in the  $E_{\text{Total}}$  vs.  $M_{\text{Net}}$  curve, a signal for a possible metastable state, is sensitive to the site occupation of Mn. The kink in Model IV, originating from a reverse of the magnetic moment of the doped Mn, is prominent, while it almost disappears in Models I and II.

With the determined ground-state magnetic states as the input, lattice parameters and atomic positions of  $\text{Fe}_{15}\text{Mn}_1$  and  $\text{Fe}_{14}\text{Mn}_2$  are fully relaxed, as listed in Table 1. In Figure 2c,  $E_{\text{Total}}$  of Models I, II, III and IV of  $\text{Fe}_{14}\text{Mn}_2$  are compared. Overall, from Model I to Model IV, i.e., with the increase in  $d_{\text{Mn}_1\text{-Mn}_2}$ ,  $E_{\text{Total}}$  of  $\text{Fe}_{14}\text{Mn}_2$  shows an increasing trend. Among various models,  $E_{\text{Total}}$  values of Models I and II are nearly the same, with a discrepancy of less than  $0.01 \text{ meV}/\text{atom}$  (averaged to all atoms in the superstructure), and exhibit the lowest values. Thus, these two site occupations of Mn are more likely to occur in the bcc phase of  $\text{Fe}_{14}\text{Mn}_2$ .  $E_{\text{Total}}$  values of Models III and IV are higher than Model I/II by  $49 \text{ meV}/\text{atom}$  and  $112 \text{ meV}/\text{atom}$ , respectively. In what follows, for the bcc phase of  $\text{Fe}_{14}\text{Mn}_2$ , both Models I and II are considered.

### 3.1.2. Lattice Stabilities and Magnetic Properties

With the determined ground-state magnetic and structural models, the effects of Mn alloying on lattice volume, phase stability and magnetic properties of the bcc phase of the  $\text{Fe}_{16-x}\text{Mn}_x$  alloys are investigated. Figure 3a shows the equilibrium lattice parameter  $a_0^{\text{bcc}}$  of the  $\text{Fe}_{16-x}\text{Mn}_x$  alloys with respect to the Mn content. It is seen that  $a_0^{\text{bcc}}$  of the  $\text{Fe}_{16-x}\text{Mn}_x$  alloys is insensitive to the Mn content, in good agreement with experimental observation [5]. When two Fe atoms are replaced by Mn in  $\text{Fe}_{14}\text{Mn}_2$  with a doping concentration of 12.5 at.%, the variation in  $a_0^{\text{bcc}}$  is less than  $0.01 \text{ \AA}$ . With the increase in Mn content, even though the magnitude is slight,  $a_0^{\text{bcc}}$  shows a gradually decreasing tendency.



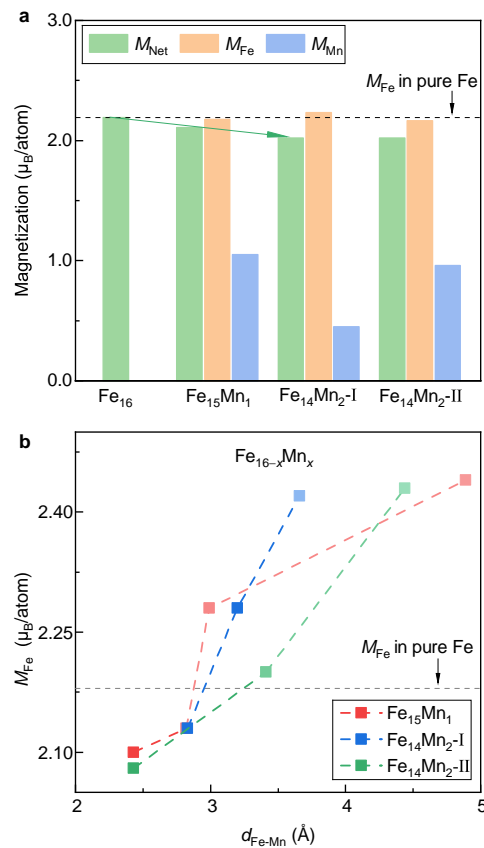
**Figure 3.** Dependence of  $a_0^{\text{bcc}}$  and  $E_f^{\text{bcc}}$  on the Mn content in the bcc  $\text{Fe}_{16-x}\text{Mn}_x$  alloys. (a)  $a_0^{\text{bcc}}$ ; (b)  $E_f^{\text{bcc}}$ .

Figure 3b displays the formation energy  $E_f^{\text{bcc}}$  of the  $\text{Fe}_{16-x}\text{Mn}_x$  alloys with respect to the Mn content. It is seen that with the increase in Mn content,  $E_f^{\text{bcc}}$  shows a monotonically increasing tendency. This result implies that the alloying of Mn tends to destabilize the bcc phase of the FeMn alloy. With the least square method, a roughly linear relation between  $E_f^{\text{bcc}}$  and the content of Mn is fitted as follows:

$$E_f^{\text{bcc}} = 9.1x + 1.5 \quad (1)$$

where  $x$  is the doped number of Mn atoms in the 16-atom superstructure. Clearly, when Mn is doped (corresponding to a concentration of 6.25 at.%), the lattice stability of the bcc phase is decreased by around 10 meV/atom.

Figure 4a displays  $M_{\text{Net}}$  and atom-resolved magnetic moments of Fe ( $M_{\text{Fe}}$ ) and Mn ( $M_{\text{Mn}}$ ) of the bcc phase of the  $\text{Fe}_{16-x}\text{Mn}_x$  alloys. Herein,  $M_{\text{Fe}}$  and  $M_{\text{Mn}}$  are calculated by taking the mean of atom moments of all Fe and Mn atoms in the supercell, respectively. Clearly, as the Mn content increases,  $M_{\text{Net}}$  decreases slightly in a roughly linear manner (indicated in the green arrow). The reduction rate of  $M_{\text{Net}}$  is around  $0.1 \mu_{\text{B}}/\text{atom}$  for every introduction of a Mn atom. Notably,  $M_{\text{Mn}}$  of the doped Mn atom ( $0.5\text{--}1.0 \mu_{\text{B}}/\text{atom}$ ) is much smaller than  $M_{\text{Fe}}$  in pure Fe ( $\sim 2.2 \mu_{\text{B}}/\text{atom}$ ). In contrast,  $M_{\text{Fe}}$  in both  $\text{Fe}_{15}\text{Mn}_1$  and  $\text{Fe}_{14}\text{Mn}_2$  almost equals that in pure Fe. Thus, the decrease in  $M_{\text{Net}}$  with the alloying of Mn should be attributed to a smaller atomic moment of Mn.



**Figure 4.** Net and atom-resolved magnetic moment of the bcc phase. (a) Evolution of magnetization with respect to the doped Mn content. (b) Dependence of  $M_{\text{Fe}}$  on  $d_{\text{Fe-Mn}}$ .

Moreover, the decreased  $M_{\text{Net}}$  gives us a clue to understand the shortened  $a_0^{\text{bcc}}$  with the alloying of Mn. The atom radius of Mn (161 pm) is slightly larger than that of Fe (156 pm) [46]. It is thus expected naively that there would be an increase in the lattice constant with the alloying of Mn, which is opposite to the experimental observation (Figure 3a). Thus, there should be an extra mechanism deciding lattice volume in the

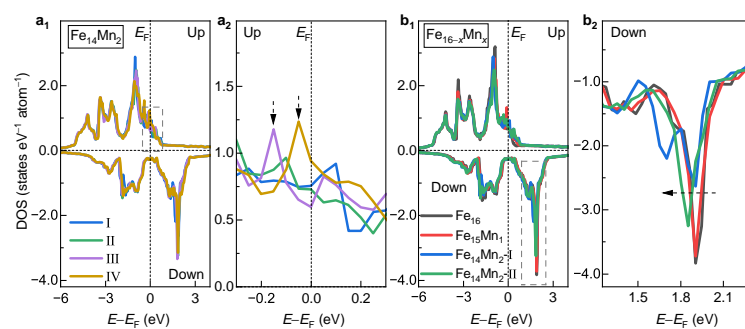


$\text{Fe}_{16-x}\text{Mn}_x$  ( $x = 0, 1$  and  $2$ ) alloys. Apart from atom radius, lattice volume is sensitive to the magnetic moment, i.e., the magnetovolume effect [47]. A decrease in magnetic moment generally tends to cause a shrinkage of lattice volume. Thus, the decreased  $M_{\text{Net}}$  could be responsible for the shortened lattice constant. To verify this, the spin non-polarized calculations are carried out.  $a_0^{\text{bcc}}$  values of Fe,  $\text{Fe}_{15}\text{Mn}_1$  and  $\text{Fe}_{14}\text{Mn}_2$  in the non-magnetic state are determined to be 2.756, 2.761 and 2.770 Å, respectively. Clearly, an opposite trend, i.e., an increase in the lattice constant with the alloying of Mn, is obtained. This result verifies the key role of magnetism in the lattice volume of the bcc phase of the  $\text{Fe}_{16-x}\text{Mn}_x$  ( $x = 0, 1$  and  $2$ ) alloys.

Note that despite the similar  $M_{\text{Net}}$  of Models I and II of  $\text{Fe}_{14}\text{Mn}_2$ ,  $M_{\text{Fe}}$  and  $M_{\text{Mn}}$  in these two models are obviously distinct. It suggests that the site occupation of Mn would greatly affect the local magnetic moments of Fe and Mn, aligning well with the previous investigations [29]. To make it clear, the relation between the moment of Fe and the distance between Fe and Mn (i.e.,  $d_{\text{Fe-Mn}}$ ) is investigated, as shown in Figure 4b. For  $\text{Fe}_{14}\text{Mn}_2$ , the Fe-Mn distance is determined by averaging the distances of the Fe atom from the  $\text{Mn}_1$  and  $\text{Mn}_2$  atoms. As a reference,  $M_{\text{Fe}}$  in pure Fe is plotted in the dashed line. Roughly speaking,  $M_{\text{Fe}}$  is positively correlated to  $d_{\text{Fe-Mn}}$ . When  $d_{\text{Fe-Mn}}$  is less than  $\sim 3$  Å,  $M_{\text{Fe}}$  of the FeMn alloy is smaller than that of pure Fe. Unexpectedly, when  $d_{\text{Fe-Mn}} > 3$  Å,  $M_{\text{Fe}}$  is higher than that of pure Fe. Compared with Model II, the sensitivity of  $M_{\text{Fe}}$  against  $d_{\text{Fe-Mn}}$  in Model I is relatively stronger. At a  $d_{\text{Fe-Mn}}$  of  $\sim 3.6$  Å,  $M_{\text{Fe}}$  equals  $2.42 \mu_{\text{B}}/\text{atom}$ , which is larger than that of pure Fe. This may explain the slightly larger mean  $M_{\text{Fe}}$  in Model I compared to pure Fe (Figure 4a).

### 3.1.3. Electronic Structures

To understand the site occupation preference and magnetic properties, the electronic density of states (DOSs) of the bcc phase of the  $\text{Fe}_{16-x}\text{Mn}_x$  alloys was investigated. Figure 5a<sub>1</sub> displays the DOSs of Models I, II, III and IV of  $\text{Fe}_{14}\text{Mn}_2$ . Overall, the DOS curves of the examined four models with different site occupations of Mn exhibit similar features. A slight difference appears in the majority-spin channel near  $E_{\text{F}}$ , as shown (enlarged) in Figure 5a<sub>2</sub>. Clearly, for both Models III and IV, there exists a prominent state peak near  $E_{\text{F}}$  ( $0 \sim -0.2$  eV), indicated in vertical arrows. Nevertheless, both Models I and II exhibit a much flatter DOS structure near  $E_{\text{F}}$ . As is known, the DOS structure near  $E_{\text{F}}$  strongly affects the lattice stability [14,48]. Generally, the smaller the DOS near  $E_{\text{F}}$ , the more stable the lattice. Thus, the fewer states near  $E_{\text{F}}$  in Models I and II may explain their energy advantages.



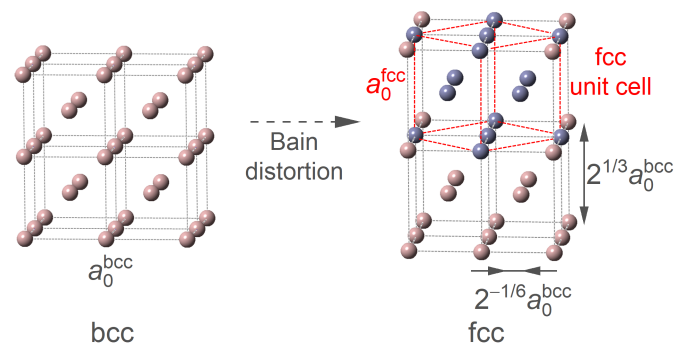
**Figure 5. DOS of the bcc phase.** (a<sub>1</sub>) Comparison of DOSs of Models I, II, III and IV of  $\text{Fe}_{14}\text{Mn}_2$ . (a<sub>2</sub>) Enlarged view of the dashed box in a<sub>1</sub>. (b<sub>1</sub>) Dependence of DOS on the doped Mn content. (b<sub>2</sub>) Enlarged view of the dashed box in b<sub>1</sub>.

Figure 5b<sub>1</sub> compares the DOSs for the bcc phases of the Fe<sub>16-x</sub>Mn<sub>x</sub> ( $x = 0, 1$  and 2) alloys with different Mn contents. For Fe<sub>14</sub>Mn<sub>2</sub>, the DOSs of both Models I and II are plotted. Roughly speaking, it is seen that the DOSs of the bcc phase of different Fe<sub>16-x</sub>Mn<sub>x</sub> alloys are nearly overlapping. The reason could be twofold. First, the difference in valence electron number between the doped Mn and the host Fe is small (1). Second, the doping amount of Mn studied in this work is not huge. Further analyses show that with the increased Mn content, the minority-spin DOS slightly moves towards lower energy, as indicated by the dashed arrow in Figure 5b<sub>2</sub>. The left movement of the minority-spin DOS decreases the asymmetry with the majority-spin DOS, i.e., magnetic exchange splitting, bringing about a decrease in net magnetization [44]. This is in good agreement with the result of the magnetic properties in Figure 4a.

### 3.2. Fcc-Structured Fe<sub>16-x</sub>Mn<sub>x</sub>

#### 3.2.1. Preferred Structural Models

We now shift our attention from the bcc phase to the fcc phase. Herein, to keep the consistency of site occupation of the doped Mn atoms, the superstructures of the fcc phase are obtained by applying the Bain strain on the models of the bcc phase, as illustrated in Figure 6. During the distortion, the  $a$  and  $b$  axes of the bcc phase are shrunk by a normal strain of  $2^{-1/6}$ , while the  $c$  axis is extended with a strain of  $2^{1/3}$ . As indicated by the red dashed lattice, there clearly exists a normal fcc unit cell in the distorted bcc superstructure.



**Figure 6.** Illustration of obtaining the fcc model from the bcc one by Bain distortion.

Starting from the models built by Bain distortion of the fcc phase, the structural relaxations are performed to obtain the ground-state structure and magnetism configuration. In analogy to the study in the bcc phase, a two-stage relaxation strategy, i.e., a sole relaxation of the magnetic state followed by a full relaxation, is adopted. At the relaxation of the magnetic state, considering that  $M_{\text{Net}}$  of the fcc Fe is around  $1.0 \mu_{\text{B}}/\text{atom}$ ,  $M_{\text{Net}}$  scans from  $0.1 \mu_{\text{B}}/\text{atom}$  to  $1.5 \mu_{\text{B}}/\text{atom}$  with an interval of  $0.125 \mu_{\text{B}}/\text{atom}$ . Figure 7a displays  $E_{\text{Total}}$  of Fe<sub>15</sub>Mn<sub>1</sub> with respect to the fixed  $M_{\text{Net}}$ . It is seen that the most stable magnetic state for the fcc phase of Fe<sub>15</sub>Mn<sub>1</sub> appears at  $M_{\text{Net}}$  of  $\sim 0.5 \mu_{\text{B}}/\text{atom}$ . As shown in the inset of Figure 7a, under this magnetic state, the magnetic moment of the doped Mn and the host Fe atoms are antiparallely arranged, i.e., the antiferromagnetic interaction. This is greatly different from the magnetic state in the bcc phase where the moments of the Mn and Fe atoms are ferromagnetically coupled. Figure 7b<sub>1</sub>–b<sub>4</sub> shows the dependence of  $E_{\text{Total}}$  on  $M_{\text{Net}}$  of Fe<sub>14</sub>Mn<sub>2</sub> for Models I, II, III and IV, respectively. The inset in each figure shows the most stable magnetic state. Remarkably, in all models, despite the different  $M_{\text{Net}}$ , the magnetic moments of the doped Mn atoms and the host Fe atoms are antiferromagnetically coupled.

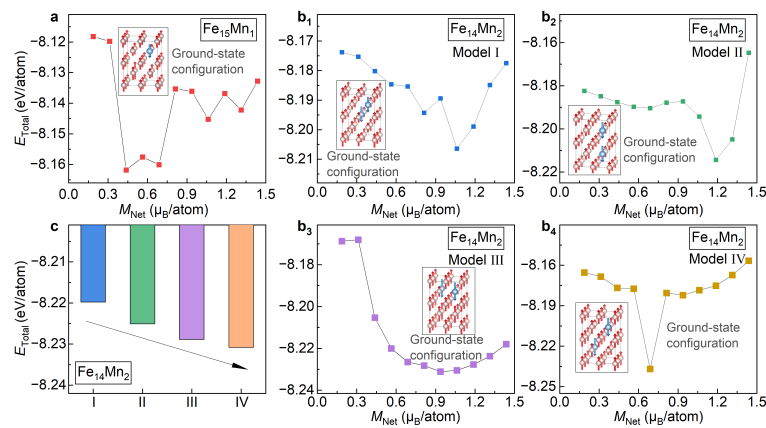


**Figure 7.**  $E_{\text{Total}}$  of the fcc phase under different magnetic and structural configurations. (a)  $E_{\text{Total}}$  vs.  $M_{\text{Net}}$  of  $\text{Fe}_{15}\text{Mn}_1$ ; (b<sub>1</sub>–b<sub>4</sub>)  $E_{\text{Total}}$  vs.  $M_{\text{Net}}$  of Models I, II, III and IV of  $\text{Fe}_{14}\text{Mn}_2$ . The insets in (a,b) illustrate the optimized ground-state configurations. The pink and light blue balls represent Fe and Mn atoms, respectively. (c) Comparison of  $E_{\text{Total}}$  of Models I, II, III and IV of  $\text{Fe}_{14}\text{Mn}_2$ .

Based on the optimized most stable magnetic state as the input, the structural models of  $\text{Fe}_{15}\text{Mn}_1$  and  $\text{Fe}_{14}\text{Mn}_2$ , including the lattice parameter and atomic position and magnetic moment, are fully relaxed, as listed in Table 2. In Figure 7c,  $E_{\text{Total}}$  of the relaxed four structural models of  $\text{Fe}_{14}\text{Mn}_2$  are compared. From Model I to Model IV, i.e., with the increased  $d_{\text{Mn}_1\text{-Mn}_2}$ ,  $E_{\text{Total}}$  shows a monotonically decreasing tendency. This is completely opposite to the trend observed in the bcc lattice (Figure 2c), where  $E_{\text{Total}}$  gradually elevates with the increase in  $d_{\text{Mn}_1\text{-Mn}_2}$  (indicated by the black arrow). The different site occupation preference of Mn in the fcc and bcc phases implies that during the fcc→bcc phase transition, the redistribution of Mn in the Fe matrix would happen. This is in good agreement with experimental observations [1,2]. Among various models, Model IV possesses the lowest energy. Models III, II and I have energies higher than Model IV by 19, 57 and 110 meV/atom, respectively. In what follows, the site occupation of Model IV is considered for  $\text{Fe}_{14}\text{Mn}_2$ .

**Table 2.** Equilibrium lattice parameter ( $a_0^{\text{fcc}}$ ), net magnetization ( $M_{\text{Net}}$ ) and atom-resolved magnetic moments of Fe ( $M_{\text{Fe}}$ ) and Mn ( $M_{\text{Mn}}$ ) for the fcc phase of the  $\text{Fe}_{16-x}\text{Mn}_x$  ( $x = 0, 1$  and  $2$ ) alloys. The ground-state structural model of  $\text{Fe}_{14}\text{Mn}_2$  is indicated in bold.

Alloy	Model	$a_0^{\text{fcc}}$ Å	$M_{\text{Total}}$ μ <sub>B</sub> /at.	$M_{\text{Fe}}$ μ <sub>B</sub> /at.	$M_{\text{Mn}}$ μ <sub>B</sub> /at.	$E_{\text{Total}}$ eV/at.
Fe	–	3.478	1.02	1.02	–	–8.095
	–	3.48 <sup>a</sup>	1.23 <sup>a</sup>			
	–	3.588 <sup>b</sup>	0.75 <sup>b</sup>			
$\text{Fe}_{15}\text{Mn}_1$	–	3.497	0.77	0.98	–2.39	–8.159
	I	3.522	0.93	1.4	–2.33	–8.220
$\text{Fe}_{14}\text{Mn}_2$	II	3.507	0.79	1.26	–2.48	–8.225
	III	3.502	0.75	1.23	–2.37	–8.229
	<b>IV</b>	<b>3.512</b>	<b>0.83</b>	<b>1.34</b>	<b>–2.58</b>	<b>–8.231</b>

<sup>a</sup> Ref. [24]; <sup>b</sup> Ref. [49].

### 3.2.2. Lattice Stabilities and Magnetic Properties

With the relaxed ground-state structure, the impact of Mn content on lattice volume, phase stability and magnetic properties of the fcc phase of the  $\text{Fe}_{16-x}\text{Mn}_x$  ( $x = 0, 1$  and  $2$ ) alloys is investigated. Figure 8a presents the lattice constant ( $a_0^{\text{fcc}}$ ) of the fcc phase of the  $\text{Fe}_{16-x}\text{Mn}_x$  alloys plotted as a function of Mn content. With the increase in Mn content,  $a_0^{\text{fcc}}$  shows a linearly increasing tendency. This change, opposite to what is observed in the bcc structure (Figure 3a), is in agreement with the previous theoretical calculation [34] and experimental measurement [5]. The expanded lattice with Mn alloying could be attributed to the fact that the atom radius of Mn (161 pm) is slightly larger than that of Fe (156 pm) [46].

Note that when two Mn atoms are doped in the 16-atom superstructural model, i.e., from pure Fe to  $\text{Fe}_{14}\text{Mn}_2$ ,  $a_0^{\text{fcc}}$  increases by a value of larger than  $0.03 \text{ \AA}$ . This greatly differs from that of the bcc phase where the variation in  $a_0^{\text{bcc}}$  is less than  $0.01 \text{ \AA}$  under the same doping concentration. Thus, compared to the bcc phase,  $a_0^{\text{fcc}}$  is more sensitive to the alloying of Mn.

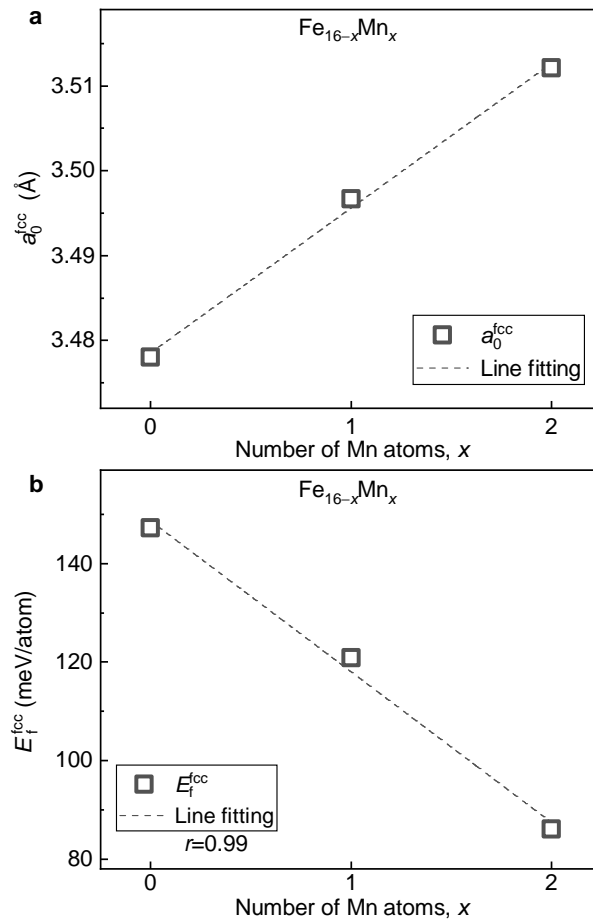


**Figure 8.** Dependence of  $a_0^{\text{fcc}}$  and  $E_f^{\text{fcc}}$  on the Mn content in the fcc  $\text{Fe}_{16-x}\text{Mn}_x$  alloys. (a)  $a_0^{\text{fcc}}$ ; (b)  $E_f^{\text{fcc}}$ .

Figure 8b displays the formation energy of the fcc phase ( $E_f^{\text{fcc}}$ ) of the  $\text{Fe}_{16-x}\text{Mn}_x$  alloys plotted as a function of the Mn content. With the increase in Mn content,  $E_f^{\text{fcc}}$  shows a monotonically decreasing tendency. Thus, the alloying of Mn tends to stabilize the fcc phase, which is in contrast to the destabilized effect on the bcc phase (Figure 3b). By the least square method, a linear relation between  $E_f^{\text{fcc}}$  and the doped Mn content is fitted as follows:

$$E_f^{\text{fcc}} = -30.6x + 148.7 \quad (2)$$

where  $x$  is the doped number of Mn in the 16-atom supercell. From Equation (2), it is clear that when a Mn atom is doped, the lattice stability of the fcc phase increases by a value of around  $-30 \text{ meV/atom}$ . Note that apart from the opposite sign, the variation in formation energy caused by Mn alloying in the fcc phase is around three times larger than that of the bcc phase.

Figure 9a displays  $M_{\text{Net}}$  and atom-resolved  $M_{\text{Mn}}$  and  $M_{\text{Fe}}$  in the fcc phase of the  $\text{Fe}_{16-x}\text{Mn}_x$  ( $x = 0, 1$  and  $2$ ) alloys. Clearly, the signs of  $M_{\text{Mn}}$  and  $M_{\text{Fe}}$  are opposite, indicating an antiferromagnetic interaction between Fe and Mn. In analogy to the bcc phase, with the alloying of Mn,  $M_{\text{Net}}$  of the fcc phase decreases from  $1.02 \mu_{\text{B}}/\text{atom}$  in pure Fe to  $0.77 \mu_{\text{B}}/\text{atom}$  in  $\text{Fe}_{15}\text{Mn}_1$ . However, different from the case in the bcc phase where the reduced  $M_{\text{Net}}$  is attributed to smaller  $M_{\text{Mn}}$  ( $0.5\text{--}1.0 \mu_{\text{B}}/\text{atom}$ ) compared with

$M_{\text{Fe}}$  ( $\sim 2.2 \mu_{\text{B}}/\text{atom}$ ), the decrease in  $M_{\text{Net}}$  arises from antiferromagnetic interactions between Fe and Mn in the fcc phase. Surprisingly, opposite to the case in the bcc phase that  $M_{\text{Mn}}$  is around a half of  $M_{\text{Fe}}$ ,  $M_{\text{Mn}}$  in the fcc phase ( $\sim -2.4 \mu_{\text{B}}/\text{atom}$ ) is about two times larger than that of  $M_{\text{Fe}}$  ( $\sim 1.0 \mu_{\text{B}}/\text{atom}$ ) despite a reversed direction of moment. Furthermore, in contrast to a monotonically decreasing tendency of  $M_{\text{Net}}$  with the Mn doping in the bcc phase,  $M_{\text{Net}}$  of  $\text{Fe}_{14}\text{Mn}_2$  in the fcc phase is slightly larger than that of  $\text{Fe}_{15}\text{Mn}_1$  by  $0.06 \mu_{\text{B}}/\text{atom}$ . Apart from  $M_{\text{Net}}$ , both  $M_{\text{Fe}}$  and  $M_{\text{Mn}}$  in  $\text{Fe}_{14}\text{Mn}_2$  are larger than those in  $\text{Fe}_{15}\text{Mn}_1$ , as highlighted by the arrows in Figure 9a.

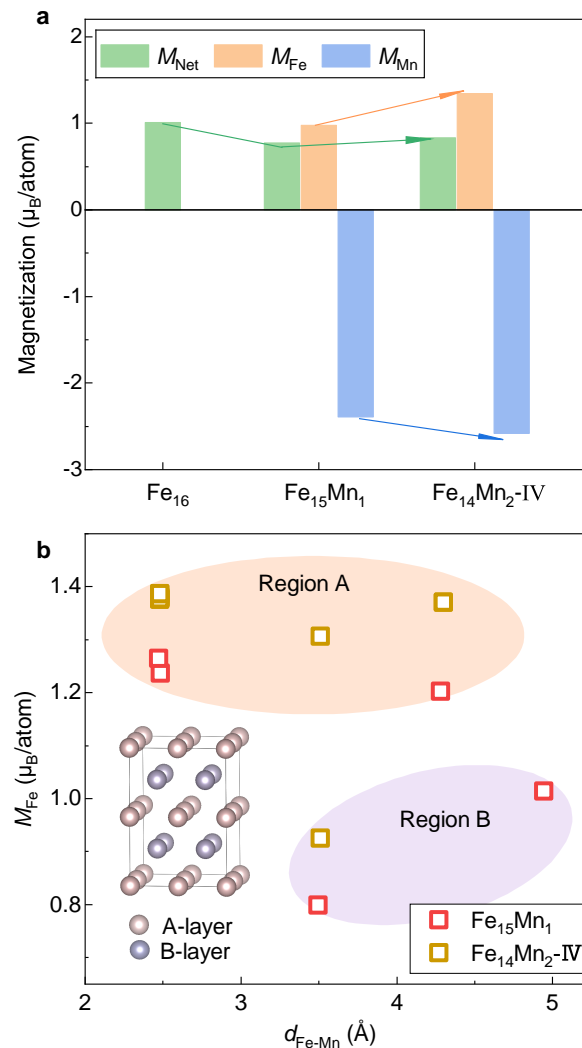


**Figure 9.** Net and atom-resolved magnetic moment of the fcc phase. (a) Evolution of magnetization with respect to the doped Mn content. (b) Dependence of  $M_{\text{Fe}}$  on  $d_{\text{Fe-Mn}}$ .

To clarify the impact of Mn doping on the magnetic moment of Fe,  $M_{\text{Fe}}$  values of different Fe atoms in  $\text{Fe}_{15}\text{Mn}_1$  and  $\text{Fe}_{14}\text{Mn}_2$  alloys are plotted in Figure 9b. Unlike the bcc phase where  $M_{\text{Fe}}$  is roughly positively correlated to  $d_{\text{Fe-Mn}}$ , no clear pattern is seen between  $M_{\text{Fe}}$  and  $d_{\text{Fe-Mn}}$  for the fcc phase. In contrast, in terms of the magnitude of  $M_{\text{Fe}}$ , the Fe atoms in the fcc FeMn alloys can be clearly classified into two categories. One is centered around  $1.3 \mu_{\text{B}}/\text{atom}$  (termed as Region A), while the other is in the range of  $0.8\text{--}1.0 \mu_{\text{B}}/\text{atom}$  (Region B). Amazingly, it is found that the Fe atoms located in Regions A and B come from the layers A and B in the structural model inserted in Figure 9b. The key difference between layers A and B is that the antiferromagnetically coupled Mn atom is located in the B layer and there is no Mn in layer A. Note that the two Mn atoms in  $\text{Fe}_{14}\text{Mn}_2$  are located in the two B layers, respectively, while only one B layer has Mn in



$\text{Fe}_{15}\text{Mn}_1$ . This result shows that different from the  $d_{\text{Fe-Mn}}$  domination in the bcc phase, the local moment of Fe is heavily affected by the spatial orientation of its position with respect to the doped Mn.

### 3.2.3. Electronic Structures

To understand the site occupation preferences of the doped Mn in the fcc phase, the DOSs of Models I, II, III and IV of the fcc  $\text{Fe}_{14}\text{Mn}_2$  alloy are compared in Figure 10a. Overall, the DOS curves of the examined four models show similar features. Detailed analyses show that there exists an obvious difference in the minority-spin DOS near  $E_F$ , as shown (enlarged) in Figure 10b. Clearly, from Model I to Model IV, the state amount near  $E_F$  shows a monotonically decreasing tendency, as indicated by the dashed arrow. This is in excellent agreement with the order of the decreased  $E_{\text{Total}}$  in Figure 7c. Notably, Model IV possesses the fewest electron states near  $E_F$ , which corresponds well with its highest phase stability.

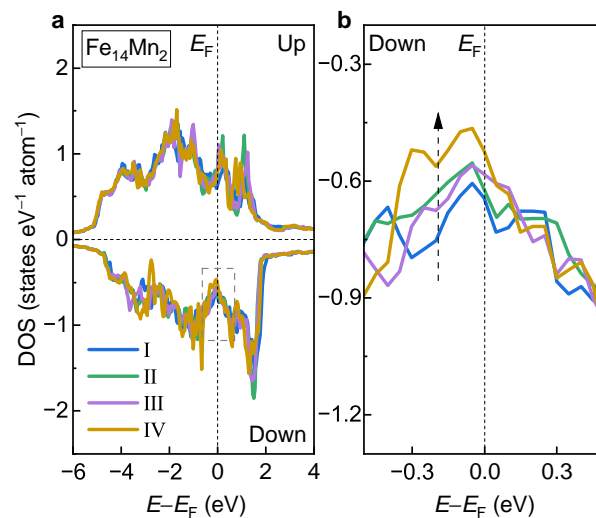


**Figure 10.** (a) DOS of Models I, II, III and IV of the fcc  $\text{Fe}_{14}\text{Mn}_2$  alloy. (b) Enlarged view of the dashed box in (a).

### 3.3. Phase Transition

We now shift our attention from the single bcc/fcc phase to the fcc→bcc phase transition. First, the stabilities of the fcc and the bcc phases are compared and the underlying mechanism in electronic structure is discussed. Second, the impact of the Mn doping on the fcc→bcc phase transition is investigated. Third, the key factors dominating the adjustment of Mn alloying on the fcc→bcc phase transition are discussed.

#### 3.3.1. Phase Transition from fcc to bcc

Tables 1 and 2 list  $E_{\text{Total}}$  of the  $\text{Fe}_{16-x}\text{Mn}_x$  alloys for the bcc and the fcc phase, respectively. For both pure Fe and various Mn-doped FeMn alloys,  $E_{\text{Total}}$  of the bcc phase is obviously smaller than that of the corresponding fcc phase. For instance,  $E_{\text{Total}}$  of  $\text{Fe}_{15}\text{Mn}_1$  at the bcc phase is  $-8.266$  eV/atom, which is smaller than that at the fcc phase ( $-8.159$  eV/atom). Thus, compared with the fcc phase, the bcc phase exhibits a higher phase stability. This is in good agreement with the previous calculations [39,50] and experimental observation [51] that a phase transition from the fcc phase to the ferromagnetic bcc phase occurs in the ferroalloys. In fact, the rich microstructure of steel materials is indeed attributed to the existence of fcc→bcc phase transition.

In Figure 11a–c, the DOSs of the fcc and the bcc phases for pure Fe,  $\text{Fe}_{15}\text{Mn}_1$  and  $\text{Fe}_{14}\text{Mn}_2$  are compared, respectively. For all alloys, the minority-spin DOS near  $E_F$  of the bcc phase is obviously less than that of the fcc phase. The greater the amount of DOS near  $E_F$ , the weaker the phase stability [14,48]. This explains, in view of electronic structure, the phase transition from the high-energy fcc to the low-energy bcc phase. Furthermore, for

all alloys, the exchange splitting of the DOS structure in the bcc phase is obviously greater than that of the fcc phase, which is consistent with the larger  $M_{\text{Net}}$  of the bcc phase.

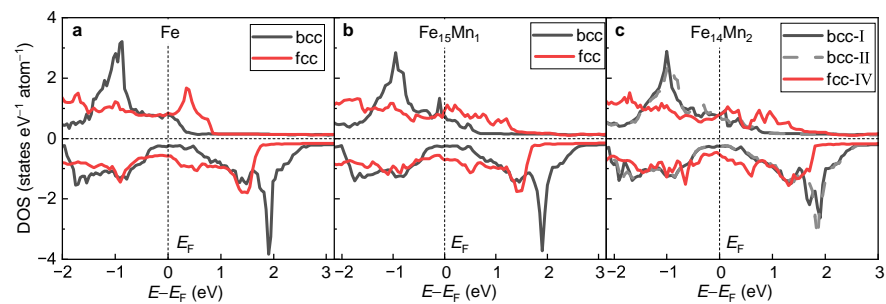


**Figure 11.** Comparison of DOSs of the bcc and fcc phases. (a) Pure Fe; (b)  $\text{Fe}_{15}\text{Mn}_1$ ; (c)  $\text{Fe}_{14}\text{Mn}_2$ .

### 3.3.2. Impact of Mn on Phase Transition

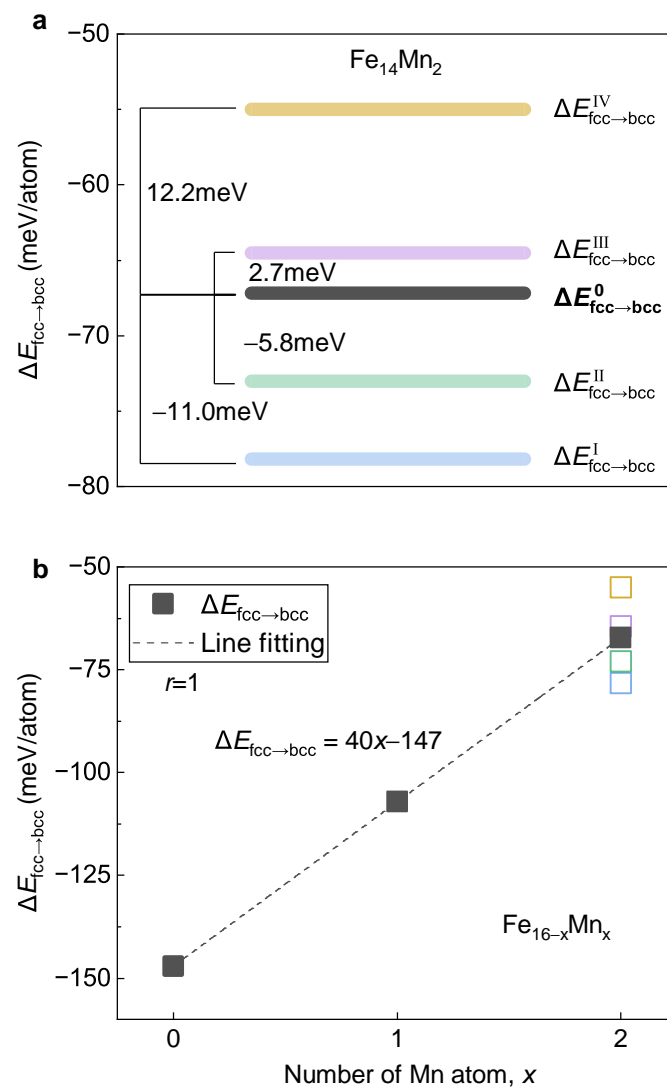
The discrepancy of favorable structural models of the bcc and the fcc phase in  $\text{Fe}_{14}\text{Mn}_2$  implies a possibility of Mn redistribution during the fcc  $\rightarrow$  bcc phase transition. We now focus on its impact on the behavior of phase transition. To make it clear, by using two different approaches, the energy difference  $\Delta E_{\text{fcc} \rightarrow \text{bcc}}$  between the fcc and the bcc phases defined as  $E_{\text{bcc}} - E_{\text{fcc}}$ , i.e., the driving force for the fcc  $\rightarrow$  bcc phase transition, is calculated. First,  $\Delta E_{\text{fcc} \rightarrow \text{bcc}}$  is computed by adopting the most stable structural models for both the fcc (Model IV) and the bcc (Model I/II) phases to represent the case with Mn diffusion during phase transition. For a better illustration,  $\Delta E_{\text{fcc} \rightarrow \text{bcc}}$  calculated in this way is termed as  $\Delta E_{\text{fcc} \rightarrow \text{bcc}}^0$ . Second,  $\Delta E_{\text{fcc} \rightarrow \text{bcc}}$  is recalculated by adopting the fcc and bcc phases with the same site occupation of Mn to mimic the case without Mn diffusion. Herein,  $\Delta E_{\text{fcc} \rightarrow \text{bcc}}$  values calculated for Models I, II, III and IV are designated as  $\Delta E_{\text{fcc} \rightarrow \text{bcc}}^{\text{I}}$ ,  $\Delta E_{\text{fcc} \rightarrow \text{bcc}}^{\text{II}}$ ,  $\Delta E_{\text{fcc} \rightarrow \text{bcc}}^{\text{III}}$  and  $\Delta E_{\text{fcc} \rightarrow \text{bcc}}^{\text{IV}}$ , respectively.

Figure 12a displays the determined  $\Delta E_{\text{fcc} \rightarrow \text{bcc}}$  of  $\text{Fe}_{14}\text{Mn}_2$ . Despite the different values of  $\Delta E_{\text{fcc} \rightarrow \text{bcc}}^{\text{I}}$  to  $\Delta E_{\text{fcc} \rightarrow \text{bcc}}^{\text{IV}}$ , they are clustered around  $\Delta E_{\text{fcc} \rightarrow \text{bcc}}^0$  with a deviation at the level of  $\pm 10$  meV/atom. From Model IV to Model I, the absolute value of the energy difference between the fcc and the bcc phases gradually increases, implying an increase in the driving force of the fcc  $\rightarrow$  bcc phase transition. It is revealed that the high-temperature fcc phase prefers Model IV, while the low-temperature bcc phase favors Model I/II. Thus, during the phase transition from the fcc to the bcc phase, the Mn atoms prefer a diffusion from the site occupation in Model IV to that in Model I/II. Accompanied by this diffusion, the driving force of the phase transition increases with a value of  $\sim 12$  meV/atom (calculated by  $\Delta E_{\text{fcc} \rightarrow \text{bcc}}^0 - \Delta E_{\text{fcc} \rightarrow \text{bcc}}^{\text{IV}}$ ).

Figure 12b presents  $\Delta E_{\text{fcc} \rightarrow \text{bcc}}$  of the  $\text{Fe}_{16-x}\text{Mn}_x$  ( $x = 0, 1$  and  $2$ ) alloys plotted as a function of Mn content. For  $\text{Fe}_{14}\text{Mn}_2$ ,  $\Delta E_{\text{fcc} \rightarrow \text{bcc}}^0$  is displayed and the deviations of  $\Delta E_{\text{fcc} \rightarrow \text{bcc}}^{\text{I}}$  to  $\Delta E_{\text{fcc} \rightarrow \text{bcc}}^{\text{IV}}$  are plotted in open symbols. Clearly, with the increase in Mn content,  $\Delta E_{\text{fcc} \rightarrow \text{bcc}}$  shows a perfectly linear increasing tendency with a Pearson coefficient of near 1. An increase in  $\Delta E_{\text{fcc} \rightarrow \text{bcc}}$  suggests a decrease in driving force for the fcc  $\rightarrow$  bcc phase transition, corresponding to a lowered phase transition temperature. In other words, using a more colloquial expression, Mn tends to stabilize the high-temperature fcc phase (austenite) against the low-temperature bcc phase (e.g., ferrite), which is in good agreement with the experimental observations [52]. With the least square method, a linear relation between  $\Delta E_{\text{fcc} \rightarrow \text{bcc}}$  and the content of Mn is obtained, as follows:

$$\Delta E_{\text{fcc} \rightarrow \text{bcc}} = 40x - 147 \quad (3)$$

where  $x$  represents the substituted number of Mn atoms in the 16-atom superstructure.



**Figure 12.** Variation of  $\Delta E_{fcc \rightarrow bcc}$  against the Mn content. (a)  $\Delta E_{fcc \rightarrow bcc}$  of Fe<sub>14</sub>Mn<sub>2</sub> with different site occupations of Mn. (b) Dependence of  $\Delta E_{fcc \rightarrow bcc}$  on Mn content. The blocks in a and the open squares in (b) with various colors represent different occupation models of Fe<sub>14</sub>Mn<sub>2</sub>.

### 3.3.3. Key Factor Deciding Mn Tailored Phase Transition

In terms of lattice stability, the alloying of Mn tends to destabilize the bcc phase (Figure 3b) and stabilize the fcc phase (Figure 8b). Clearly, both effects of Mn alloying on the bcc phase and the fcc phase have the same sign as its impact on the fcc→bcc phase transition, i.e., decreasing the driving force from fcc to bcc. Thus, for Mn alloying in ferroalloys, both the destabilizing effect on the bcc phase and the stabilizing effect on the fcc phase contribute to the inhibited fcc→bcc phase transition. Note that when one more Mn atom is doped, as seen in Equation (3), the driving force of the fcc→bcc phase transition ( $\Delta E_{fcc \rightarrow bcc}$ ) increases to 40 meV/atom. According to Equations (1) and (2), it is evident that the destabilized effect on the bcc phase contributes ~10 meV, while the stabilized effect on the fcc phase contributes ~30 meV/atom. Clearly, the contribution of the stabilizing effect on the fcc phase is around three times larger than that of the destabilizing effect on the bcc phase. Therefore, the influence of Mn doping on the stability of the fcc phase, i.e., the strongly stabilizing effect, should dominate the inhibited role in the fcc→bcc phase transition.

Lastly, the mechanism behind the stabilizing effect of Mn in the fcc phase is discussed. As is known, valence electron concentration (VEC), lattice volume and magnetism are the three key factors deciding lattice stability [13–15]. When Mn replaces Fe, the VEC is decreased, owing to fewer valence electrons of Mn (7) against Fe (8). Generally, the lower the VEC, the weaker the stability of the fcc phase [15]. Thus, VEC is not the reason for the improved stability of the fcc phase. For lattice volume, it increases monotonically with the alloying of Mn. It is known that the expansion of lattice volume tends to weaken bonding strength and thus it also might not be the reason for the improved lattice stability of the fcc phase. As for magnetism, it is revealed that the doped Mn and the host Fe prefer to be antiferromagnetically coupled and the interaction strength is gradually enhanced with the increased doping concentration. It is well-recognized that antiferromagnetism generally strongly stabilizes the fcc structure [34,35]. Thus, antiferromagnetism could be responsible for the stabilizing effect of the fcc phase in Mn doping and further for the inhibition of the fcc→bcc phase transition.

#### 4. Conclusions

The impact of Mn alloying on magnetic and structural preferences, lattice stabilities, magnetic properties and electronic structures of the bcc and the fcc phases and the fcc→bcc phase transition is studied systematically by first-principles calculations. The main findings are as follows.

- (i) Mn prefers ferromagnetic and antiferromagnetic interaction with Fe in the bcc and fcc phases, respectively. In these two phases, the magnetic moment of Mn is smaller and larger than Fe, respectively. The local moment of Fe is decided by the Fe-Mn distance in the bcc phase, whereas in the fcc phase, it is determined by spatial orientation with Mn.
- (ii) Mn prefers different site occupations in the bcc and fcc phases, which can be understood from the electronic density of states near Fermi energy. This discrepancy implies the possibility of the redistribution of solute Mn in the Fe matrix during the fcc→bcc phase transition, which is favorable for increasing the driving force of transformation.
- (iii) Mn alloying tends to destabilize and stabilize the bcc and fcc phases, respectively. With the increase in Mn, the driving force of the fcc→bcc phase transition decreases, in which the stabilization in the fcc phase plays a dominant role. Antiferromagnetism is recognized as the key reason for the enhanced stability of the fcc phase by Mn alloying.

In conclusion, the present work clarifies the impact mechanisms of Mn alloying in the bcc and the fcc phases and the fcc→bcc phase transition in ferroalloys and thus is expected to design advanced ferroalloys.

**Author Contributions:** Conceptualization, H.-L.Y.; Methodology, H.-L.Y.; Software, H.Y., J.-H.Y. and Y.Z.; Formal analysis, H.M., Y.T., M.C., S.T., Y.L., X.Z., H.-L.Y. and L.Z.; Investigation, H.Y., J.-H.Y. and Y.Z.; Writing—original draft, H.Y., J.-H.Y., Y.Z. and H.-L.Y.; Writing—review & editing, H.Y., J.-H.Y., Y.Z., Y.T., Y.L. and H.-L.Y.; Visualization, H.Y., J.-H.Y. and Y.Z.; Funding acquisition, H.M., Y.T., X.Z., H.-L.Y. and L.Z. All authors have read and agreed to the published version of the manuscript.

**Funding:** This work is supported by the National Key R&D Program of China (2021YFA1200203), the National Natural Science Foundation of China (Grant No. 52274379) and the Fundamental Research Funds for the Central Universities (Grant No. N2202015).

**Institutional Review Board Statement:** Not applicable.

**Informed Consent Statement:** Not applicable.

**Data Availability Statement:** The data presented in this study are available on request from the corresponding author.

**Conflicts of Interest:** The authors declare no conflict of interest.

## References


- Hu, B.; Luo, H.; Yang, F.; Dong, H. Recent progress in medium-Mn steels made with new designing strategies, a review. *J. Mater. Sci. Technol.* **2017**, *33*, 1457–1464. [CrossRef]
- Lee, Y.K.; Han, J. Current opinion in medium manganese steel. *Mater. Sci. Technol.* **2015**, *31*, 843–856. [CrossRef]
- Zhang, H.; Cai, M.; Zhu, W.; Sun, S.; Yan, H.; Yao, S.; Luan, Y.; Tang, S.; Hodgson, P. Low-temperature superplastic deformation of cold-rolled Fe–5.6 Mn–1.1 Al–0.2 C steel. *Metall. Mater. Trans. A* **2022**, *53*, 3869–3880. [CrossRef]
- Mueller, J.; Hu, X.; Sun, X.; Ren, Y.; Choi, K.; Barker, E.; Speer, J.; Matlock, D.; De Moor, E. Austenite formation and cementite dissolution during intercritical annealing of a medium-manganese steel from a martensitic condition. *Mater. Des.* **2021**, *203*, 109598. [CrossRef]
- Li, C.M.; Sommer, F.; Mittemeijer, E.J. Characteristics of the  $\gamma \rightarrow \alpha$  transformation in Fe–Mn alloys. *Mater. Sci. Eng. A* **2002**, *325*, 307–319. [CrossRef]
- Sahin, O.; Calik, A.; Ekinici, A.; Ucar, N. Work hardening in Fe–Mn binary alloys. *Mater. Charact.* **2007**, *58*, 571–574. [CrossRef]
- Uenishi, A.; Teodosiu, C. Solid solution softening at high strain rates in Si-and/or Mn-added interstitial free steels. *Acta Mater.* **2003**, *51*, 4437–4446. [CrossRef]
- Lee, S.; De Cooman, B.C. On the selection of the optimal intercritical annealing temperature for medium Mn TRIP steel. *Metall. Mater. Trans. A* **2013**, *44*, 5018–5024. [CrossRef]
- Miyamoto, G.; Oh, J.; Hono, K.; Furuhashi, T.; Maki, T. Effect of partitioning of Mn and Si on the growth kinetics of cementite in tempered Fe–0.6 mass% C martensite. *Acta Mater.* **2007**, *55*, 5027–5038. [CrossRef]
- Sun, S.; Cai, M.; Ding, H.; Yan, H.; Tian, Y.; Tang, S.; Hodgson, P. Achieving high ductility in a 1.4 GPa grade medium Mn lightweight TRIP/TWIP steel with hierarchical lamellar structure. *Mater. Sci. Eng. A* **2022**, *858*, 144118. [CrossRef]
- Li, Z.; Pradeep, K.G.; Deng, Y.; Raabe, D.; Tسان, C.C. Metastable high-entropy dual-phase alloys overcome the strength–ductility trade-off. *Nature* **2016**, *534*, 227–230. [CrossRef] [PubMed]
- La Roca, P.; Baruj, A.; Sade, M. Shape-memory effect and pseudoelasticity in Fe–Mn-based alloys. *Shape Mem. Superelasticity* **2017**, *3*, 37–48. [CrossRef]
- Hu, G.; Cai, X.; Rong, Y. *Fundamentals of Materials Science*; Shanghai Jiao Tong University Press: Shanghai, China, 2010; pp. 19–57.
- Yan, H.L.; Liu, H.X.; Zhao, Y.; Jia, N.; Bai, J.; Yang, B.; Li, Z.; Zhang, Y.; Esling, C.; Zhao, X.; et al. Unraveling the abnormal dependence of phase stability on valence electron concentration in Ni-Mn-based metamagnetic shape memory alloys. *J. Appl. Phys.* **2020**, *128*, 045104. [CrossRef]
- Zayak, A.; Adeagbo, W.; Entel, P.; Rabe, K.  $e/a$  dependence of the lattice instability of cubic Heusler alloys from first principles. *Appl. Phys. Lett.* **2006**, *88*, 111903. [CrossRef]
- Kuang, W.; Wang, H.; Li, X.; Zhang, J.; Zhou, Q.; Zhao, Y. Application of the thermodynamic extremal principle to diffusion-controlled phase transformations in Fe–C–X alloys: Modeling and applications. *Acta Mater.* **2018**, *159*, 16–30. [CrossRef]
- Wang, D.; Wang, X.X.; Jin, M.L.; He, P.; Zhang, S. Molecular level manipulation of charge density for solid-liquid TENG system by proton irradiation. *Nano Energy* **2022**, *103*, 107819. [CrossRef]
- Zhang, B.; Hao, M.; Yao, Y.; Xiong, J.; Li, X.; Murphy, A.B.; Sinha, N.; Antony, B.; Ambalampitiya, H.B. Determination and assessment of a complete and self-consistent electron-neutral collision cross-section set for the C4F7N molecule. *J. Phys. D* **2023**, *56*, 134001. [CrossRef]
- Zhang, B.; Hao, M.; Xiong, J.; Li, X.; Koopman, J. Ab initio molecular dynamics calculations on electron ionization induced fragmentations of C4F7N and C5F10O for understanding their decompositions under discharge conditions. *Phys. Chem. Chem. Phys.* **2023**, *25*, 7540–7549. [CrossRef]
- Akai, H.; Akai, M.; Kanamori, J. Electronic structure of impurities in ferromagnetic iron. II. 3d and 4d impurities. *J. Phys. Soc. Japan* **1985**, *54*, 4257–4264. [CrossRef]
- Anisimov, V.I.; Antropov, V.P.; Liechtenstein, A.I.; Gubanov, V.A.; Postnikov, A.V. Electronic structure and magnetic properties of 3d impurities in ferromagnetic metals. *Phys. Rev. B* **1988**, *37*, 5598–5602. [CrossRef]
- Drittler, B.; Stefanou, N.; Blügel, S.; Zeller, R.; Dederichs, P.H. Electronic structure and magnetic properties of dilute Fe alloys with transition-metal impurities. *Phys. Rev. B* **1989**, *40*, 8203–8212. [CrossRef] [PubMed]
- Kulikov, N.I.; Demangeat, C. Spin polarization of disordered Fe–Cr and Fe–Mn alloys. *Phys. Rev. B* **1997**, *55*, 3533–3542. [CrossRef]
- Medvedeva, N.; Van Aken, D.; Medvedeva, J.E. Magnetism in bcc and fcc Fe with carbon and manganese. *J. Phys. Condens. Mat.* **2010**, *22*, 316002. [CrossRef] [PubMed]
- Medvedeva, N.; Van Aken, D.C.; Medvedeva, J.E. The effect of carbon distribution on the manganese magnetic moment in bcc Fe–Mn alloy. *J. Phys. Condens. Matter* **2011**, *23*, 326003. [CrossRef] [PubMed]
- Rahman, G.; Kim, I.G.; Bhadeshia, H.K.D.H.; Freeman, A.J. First-principles investigation of magnetism and electronic structures of substitutional 3d transition-metal impurities in bcc Fe. *Phys. Rev. B* **2010**, *81*, 184423. [CrossRef]
- Comesse, D.; Herper, H.C.; Hucht, A.; Entel, P. A first-principles study aided with Monte Carlo simulations of carbon doped iron-manganese alloys. *Eur. Phys. J. B* **2012**, *85*, 1–13. [CrossRef]
- King, D.J.; Middleburgh, S.C.; Burr, P.A.; Whiting, T.; Fossati, P.; Wenman, M.R. Density functional theory study of the magnetic moment of solute Mn in bcc Fe. *Phys. Rev. B* **2018**, *98*, 024418. [CrossRef]
- Schneider, A.; Fu, C.C.; Barreateau, C. Local environment dependence of Mn magnetism in bcc iron-manganese alloys: A first-principles study. *Phys. Rev. B* **2018**, *98*, 094426. [CrossRef]



30. Schneider, A.; Fu, C.C.; Waseda, O.; Barreateau, C.; Hickel, T. Ab initio based models for temperature-dependent magnetochemical interplay in bcc Fe-Mn alloys. *Phys. Rev. B* **2021**, *103*, 024421. [CrossRef]
31. Kou, B.; Kou, Z.; Liu, Y.; Han, P. First principles study on interstitial C and substitutional Mn in bcc iron: Structural stability and elastic properties. *Mater. Res. Innov.* **2014**, *18*, S2-775–S2-779. [CrossRef]
32. Music, D.; Takahashi, T.; Vitos, L.; Asker, C.; Abrikosov, I.A.; Schneider, J.M. Elastic properties of Fe–Mn random alloys studied by ab initio calculations. *Appl. Phys. Lett.* **2007**, *91*, 191904. [CrossRef]
33. Zhang, H.; Lu, S.; Zhou, M.; Punkkinen, M.P.; Johansson, B.; Vitos, L. Ab initio determination of the elastic properties of ferromagnetic body-centered cubic Fe-Mn-Al alloys. *J. Appl. Phys.* **2015**, *118*, 103904. [CrossRef]
34. Gebhardt, T.; Music, D.; Hallstedt, B.; Ekholm, M.; Abrikosov, I.A.; Vitos, L.; Schneider, J. Ab initio lattice stability of fcc and hcp Fe–Mn random alloys. *J. Phys. Condens. Matter* **2010**, *22*, 295402. [CrossRef] [PubMed]
35. Acciarri, M.; La Roca, P.; Guerrero, L.; Baruj, A.; Curiale, J.; Sade, M. Effect of FCC anti-ferromagnetic ordering on the stability of phases in Fe<sub>60–x</sub>Mn<sub>30</sub>Cr<sub>10</sub>Co<sub>10</sub> high entropy alloys. *J. Alloys Compd.* **2020**, *823*, 153845. [CrossRef]
36. Choi, Y.; Dong, Z.; Li, W.; Lizárraga, R.; Kwon, S.K.; Vitos, L. Density functional theory description of paramagnetic hexagonal close-packed iron. *Materials* **2022**, *15*, 1276. [CrossRef]
37. Nakano, J.; Jacques, P.J. Effects of the thermodynamic parameters of the hcp phase on the stacking fault energy calculations in the Fe–Mn and Fe–Mn–C systems. *Calphad* **2010**, *34*, 167–175. [CrossRef]
38. Wang, C.; Zu, W.; Wang, H.; Wang, Y. First-principles study on stacking fault energy of  $\gamma$ -Fe–Mn alloys. *Met. Mater. Int.* **2021**, *27*, 3205–3213. [CrossRef]
39. Okatov, S.V.; Kuznetsov, A.R.; Gornostyrev, Y.N.; Urtsev, V.N.; Katsnelson, M.I. Effect of magnetic state on the  $\gamma$ – $\alpha$  transition in iron: First-principles calculations of the Bain transformation path. *Phys. Rev. B* **2009**, *79*, 094111. [CrossRef]
40. Perdew, J.P.; Burke, K.; Ernzerhof, M. Generalized gradient approximation made simple. *Phys. Rev. Lett.* **1996**, *77*, 3865–3868. [CrossRef]
41. Kresse, G.; Furthmüller, J. Efficient iterative schemes for ab initio total-energy calculations using a plane-wave basis set. *Phys. Rev. B* **1996**, *54*, 11169–11186. [CrossRef]
42. Blöchl, P.E.; Jepsen, O.; Andersen, O.K. Improved tetrahedron method for Brillouin-zone integrations. *Phys. Rev. B* **1994**, *49*, 16223–16233. [CrossRef] [PubMed]
43. Herper, H.; Hoffmann, E.; Entel, P. Ab initio investigations of iron-based martensitic systems. *J. Phys.* **1997**, *7*, C5-71–C5-76. [CrossRef]
44. Kittel, C. Introduction to solid state physics, 6th ed. *Phys. Today* **1957**, *10*, 43–44. [CrossRef]
45. Wang, C.S.; Klein, B.M.; Krakauer, H. Theory of magnetic and structural ordering in Iron. *Phys. Rev. Lett.* **1985**, *54*, 1852–1855. [CrossRef]
46. Clementi, E.; Raimondi, D.L.; Reinhardt, W.P. Atomic screening constants from SCF functions. II. Atoms with 37 to 86 electrons. *J. Chem. Phys.* **2004**, *47*, 1300–1307. [CrossRef]
47. Schilfgaard, M.; Abrikosov, I.; Johansson, B. Origin of the Invar effect in iron–nickel alloys. *Nature* **1999**, *400*, 46–49. [CrossRef]
48. Yan, H.L.; Liu, H.X.; Zhao, Y.; Jia, N.; Bai, J.; Yang, B.; Li, Z.; Zhang, Y.; Esling, C.; Zhao, X.; et al. Impact of B alloying on ductility and phase transition in the Ni-Mn-based magnetic shape memory alloys: Insights from first-principles calculation. *J. Mater. Sci. Technol.* **2021**, *74*, 27–34. [CrossRef]
49. Abrahams, S.C.; Guttman, L.; Kasper, J.S. Neutron diffraction determination of antiferromagnetism in Face-centered cubic ( $\gamma$ ) iron. *Phys. Rev.* **1962**, *127*, 2052–2055. [CrossRef]
50. Lintzen, S.; von Appen, J.; Hallstedt, B.; Dronskowski, R. The Fe–Mn enthalpy phase diagram from first principles. *J. Alloys Compd.* **2013**, *577*, 370–375. [CrossRef]
51. Krauss, G.; Thompson, S.W. Ferritic microstructures in continuously cooled low-and ultralow-carbon steels. *ISIJ Int.* **1995**, *35*, 937–945. [CrossRef]
52. Calcagnotto, M.; Ponge, D.; Raabe, D. On the effect of manganese on grain size stability and hardenability in ultrafine-grained ferrite/martensite dual-phase steels. *Metall. Mater. Trans. A* **2012**, *43*, 37–46. [CrossRef]

**Disclaimer/Publisher’s Note:** The statements, opinions and data contained in all publications are solely those of the individual author(s) and contributor(s) and not of MDPI and/or the editor(s). MDPI and/or the editor(s) disclaim responsibility for any injury to people or property resulting from any ideas, methods, instructions or products referred to in the content.

# Prediction of Grain Size in a High Cobalt Nickel-Based Superalloy

Jingzhe Wang <sup>1,2</sup> , Siyu Zhang <sup>1,2</sup>, Liang Jiang <sup>3</sup>, Shesh Srivatsa <sup>4</sup> and Zaiwang Huang <sup>1,2,\*</sup>

<sup>1</sup> State Key Laboratory of Powder Metallurgy, Central South University, Changsha 410083, China; wangjingzhe@csu.edu.cn (J.W.)

<sup>2</sup> Powder Metallurgy Research Institute, Central South University, Changsha 410083, China

<sup>3</sup> Institute for Advanced Studies in Precision Materials, Yantai University, Yantai 264005, China

<sup>4</sup> Srivatsa Consulting LLC, Cincinnati, OH 45249, USA

\* Correspondence: huangzaiwang@csu.edu.cn; Tel.: +86-0731-88830938

**Abstract:** With the advancement in computational approaches and experimental, simulation, and modeling tools in recent decades, a trial-and-validation method is attracting more attention in the materials community. The development of powder metallurgy Ni-based superalloys is a vivid example that relies on simulation and experiments to produce desired microstructure and properties in a tightly controlled manner. In this research, we show an integrated approach to predicting the grain size of industrial forgings starting from lab-scale cylindrical compression by employing modeling and experimental validation. (a) Cylindrical compression tests to obtain accurate flow stress data and the hot working processing window; (b) double-cone tests of laboratory scale validation; (c) sub-scale forgings for further validation under production conditions; and (d) application and validation on full-scale industrial forgings. The procedure uses modeling and simulation to predict metal flow, strain, strain rate, temperature, and the resulting grain size as a function of thermo-mechanical processing conditions. The models are calibrated with experimental data until the accuracy of the modeling predictions is at an acceptable level, which is defined as the accuracy at which the results can be used to design and evaluate industrial forgings.

**Keywords:** high-temperature alloys; powder metallurgy; crystal structure; computer simulations; compression test; flow stress



**Citation:** Wang, J.; Zhang, S.; Jiang, L.; Srivatsa, S.; Huang, Z. Prediction of Grain Size in a High Cobalt Nickel-Based Superalloy. *Materials* **2023**, *16*, 5776. <https://doi.org/10.3390/ma16175776>

Academic Editor: Irina Hussainova

Received: 4 July 2023

Revised: 7 August 2023

Accepted: 21 August 2023

Published: 23 August 2023



**Copyright:** © 2023 by the authors. Licensee MDPI, Basel, Switzerland. This article is an open access article distributed under the terms and conditions of the Creative Commons Attribution (CC BY) license (<https://creativecommons.org/licenses/by/4.0/>).

## 1. Introduction

Powder metallurgy nickel-based superalloys are widely used to fabricate high-pressure turbine disks in aircraft due to their excellent performance at elevated temperatures. In past decades, the alloy compositions have always been optimized to meet higher operating temperatures. Controlling dynamic recrystallization grain size in a repeatable manner is a major concern during the hot working of structural materials, especially for large-scale components, since it significantly affects subsequent processing [1,2], heat treatment [3,4], and properties [5,6]. There is a need to accurately predict the dynamic recrystallization grain size, which depends on deformation temperature, strain, and strain rate [7,8]. To realize this, two concerns must be addressed: (1) precisely predicting local processing parameters throughout the component; (2) having precise dynamic recrystallization grain size models based on simulated local parameters and using experimental results to calibrate their accuracy. To date, an integrated approach that can be used to predict grain size using a step-wise method from lab-scale specimens to full-scale forgings is lacking.

Flow stress was often obtained using cylindrical compression specimens over a range of temperatures, strains, and strain rates. From the measured load-stroke curves, the corresponding true stress true strain data [9,10] (herein denoted by flow stress) were obtained [11]. The flow stress was then corrected by considering the effects of friction [12,13], adiabatic temperature rise, and non-homogeneous deformation [14,15]. The flow stress data were validated by conducting double-cone (DC) tests to generate a range of strain and

strain rates for a single specimen [16,17]. The measured load-stroke and final dimensions from the DC tests were compared with finite element models using the corrected flow stress data. When the difference between the predicted and experimental load-stroke data as well as the final specimen dimension was within an acceptable range, typically less than 5%, the flow stress and deformation models were believed to be accurate enough and could be used to simulate sub-scale and full-scale industrial forgings. The predicted strain, strain rate, and temperature can also be used in dynamic recrystallization grain size models. This procedure ensures that each step is validated before using the data in the subsequent step. If an attempt is made to directly validate the dynamic recrystallization grain size models, it is not difficult to isolate the cause of any discrepancy between the predicted and measured dynamic recrystallization grain sizes.

Certain positions on the deformed double cones were selected for experimental measurements and used to validate the simulated dynamic recrystallization grain size [18]. The positions were selected to cover a range of thermo-mechanical conditions that are typically encountered with industrial forgings [19]. When the difference between the experimentally observed and the simulated dynamic recrystallization grain size falls to an acceptable value, the dynamic recrystallization grain size model is considered validated and suitable for prediction at any position within the forging. In this research, we will provide an integrated approach to predicting dynamic recrystallization grain size using a step-wise method from laboratory specimens to full-scale industrial forgings.

## 2. Materials and Methods

A high-cobalt powder metallurgy Ni-based superalloy was designed by our research group [20,21]. The alloy powder was prepared by argon gas atomization and sieved using a mesh size of 10–63  $\mu\text{m}$ . The alloy powder was consolidated using hot isostatic pressing at 1100  $^{\circ}\text{C}$ /150 MPa for 4 h. Subsequently, hot extrusion was performed using an extrusion ratio of 6:1 at 1100  $^{\circ}\text{C}$ . To reduce the retained metallurgical strain, the extruded billet was heated at 1080  $^{\circ}\text{C}$  for 2 h and then air cooled. The cylindrical and double-cone specimens were machined from the extruded billets using electrical discharge machining.

Cylindrical specimens ( $\Phi 8 \times 12$  mm height) and double-cone (DC) specimens ( $\Phi 20 \times 16$  mm height) shown in Figure 1 were used for hot compression experiments. Three layers composed of boron nitride powder, mica, and graphite foil (as shown in Figure 2) were applied on the specimen's bottom and top ends to minimize interfacial friction between the dies and the specimen. Prior to hot compression, the furnace was heated to the test temperature, and then the specimen was loaded into the furnace until it reached the test temperature. The specimen was soaked for 15 min to obtain a uniform temperature.

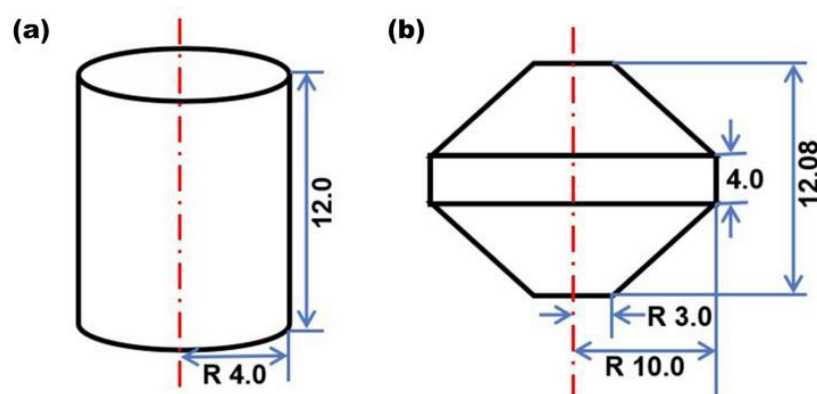
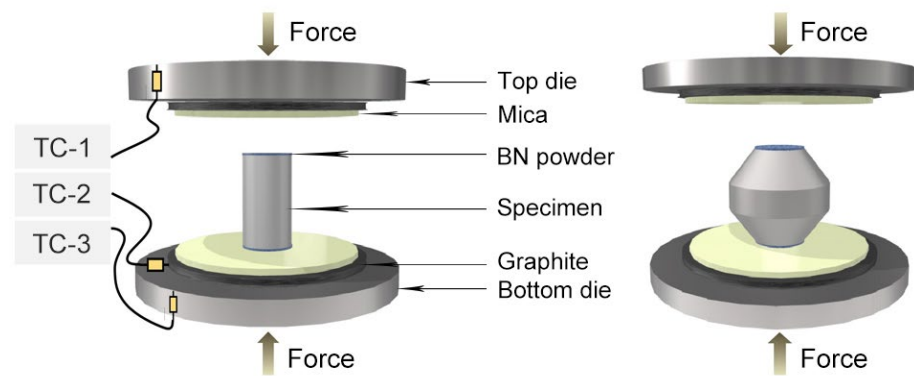


Figure 1. The geometry of cylinder (a) and double-cone specimens (b).



**Figure 2.** Schematic of cylindrical and double-cone specimens for hot compression. Three-layered structures composed of boron nitride powder, mica, and graphite foil are coated on the bottom and top planes of specimens.

Compression tests were conducted over a range of temperatures from 1010 °C to 1121 °C. Three strain rates ( $0.0032 \text{ s}^{-1}$ ,  $0.01 \text{ s}^{-1}$ , and  $0.032 \text{ s}^{-1}$ ) were chosen for compression, and the height reduction of the specimens was set to 50%, corresponding to a true effective compression strain of 69.3%. After compression, the specimens were immediately pulled out and quenched in the water to freeze the microstructure.

The compressed specimens were cut into two halves along the center-axis plane (along the compression direction) and prepared by mechanical grinding, polishing, and vibration polishing for electron backscatter diffraction (EBSD) observation (detector: Oxford instrument, software: AztecCrystal, data analysis software, HKL Channel 5). Under a scanning electron microscope (SEM), the acceleration voltage was 15 kV and the working current was 3 mA. Finite element modeling (FEM) was performed using DEFORM-2D software (Scientific Forming Technology Cooperation, Columbus, OH, USA).

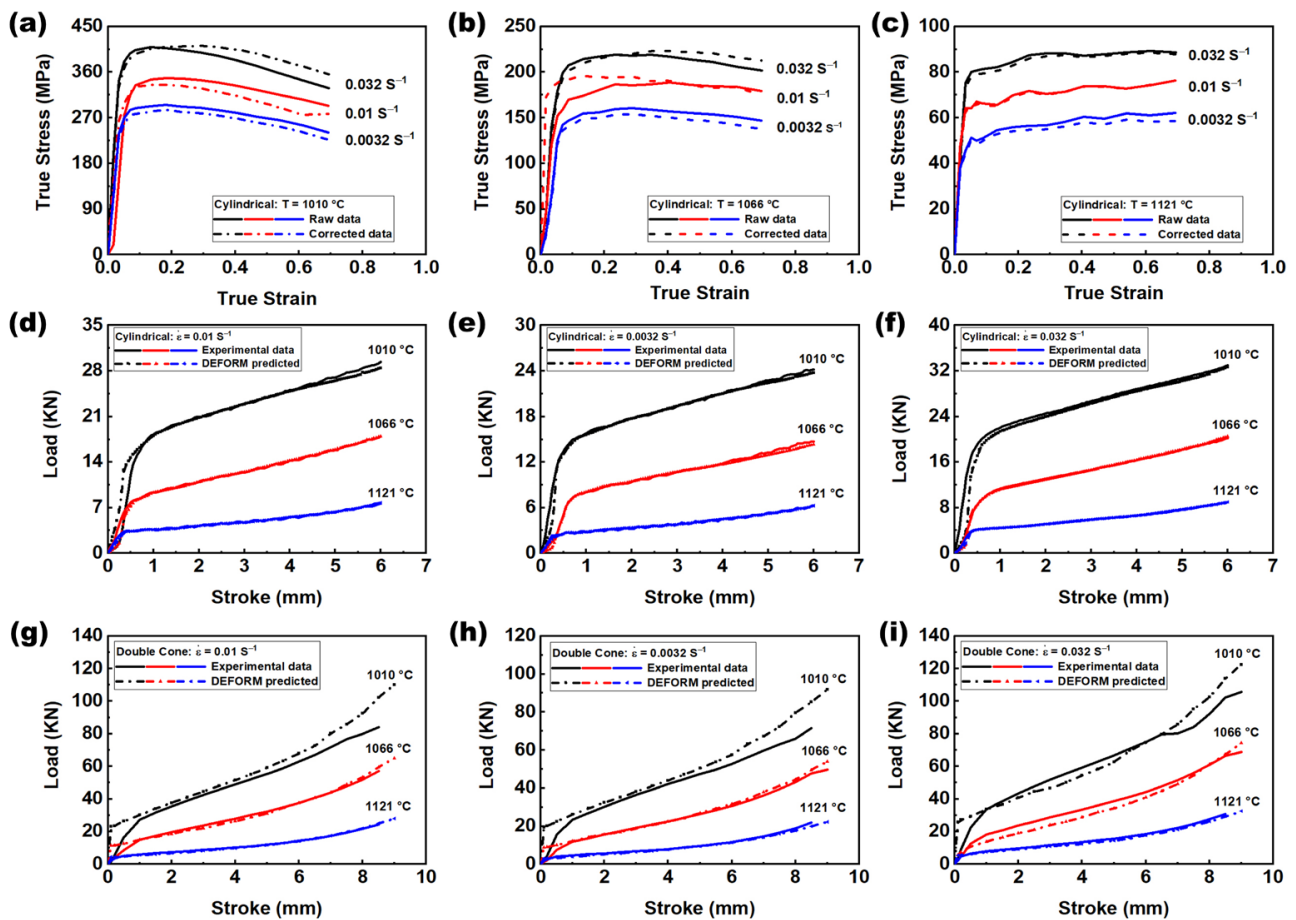
### 3. Results and Discussion

Figure 3 shows cylindrical compression true stress true strain curves (Figure 3a–c) over a range of temperatures and strain rates for the same nominal compressive strain of 50%. The flow stress is lower at higher temperatures and lower strain rates. As has been widely demonstrated in previous research, alloys compressed at a higher temperature and lower strain rate have lower strength [9,22]. The true stress true strain curves were obtained from the load-stroke curves after corrections due to interfacial friction and adiabatic temperature rise (the details of flow curve correction can be found in our previous work [21]). The load-stroke predicted by the corrected flow curve is shown in Figure 3d–f, which is in good agreement with the experimentally measured ones.

The corrected flow curve data were validated using DC compression data. Compression tests for lab-scale DC specimens can produce strains and strain gradients similar to full-scale forgings. Figure 3g–i show load-stroke data at different temperatures and strain rates. The predicted load-stroke data are very close to the experimental results. Hence, the simulated working parameters in the deformed DC specimens can be used with confidence for microstructure models. If the agreement with the predicted and measured loads is not at an acceptable level, the flow stress must be corrected again.

The calibration and validation of the constitutive model of the alloy and the finite-element hot deformation simulation are critical to predicting the location-specific process conditions within a laboratory specimen or a forging component. Thus, the accurate simulation of local deformation parameters is the primary aim since these are necessary to calculate microstructure information such as grain size and dynamic recrystallization (DRX) fraction [13]. Figure 4a shows geometric changes in the compression of a cylindrical specimen. The FEM results in Figure 4b show that there are strain gradients in the deformed specimen. Figure 4c shows the microstructure of the cylindrical specimen at positions  $P_1$  (hub area) and  $P_2$  (effective strain corresponds to 0.7), which are dependent on local

working parameters. Based on our simulation, the strain gradient between  $P_1$  and  $P_2$  is relatively small, corresponding to a small change in grain microstructures.



**Figure 3.** Correction of flow stress data. (a–c) True stress–true strain curves were obtained from load–stroke data after two-step correction. (d–f) Comparison of the measured load–stroke with that predicted by the corrected flow stress. (g–i) Prediction of load–stroke curves of double-cone specimens using corrected flow stress of cylindrical compression over a range of strain rate and temperature.

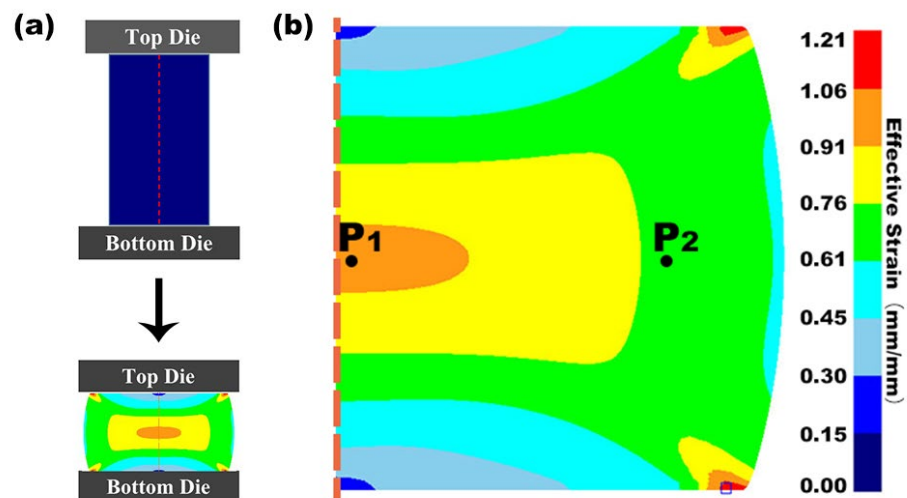


**Figure 4.** Cont.



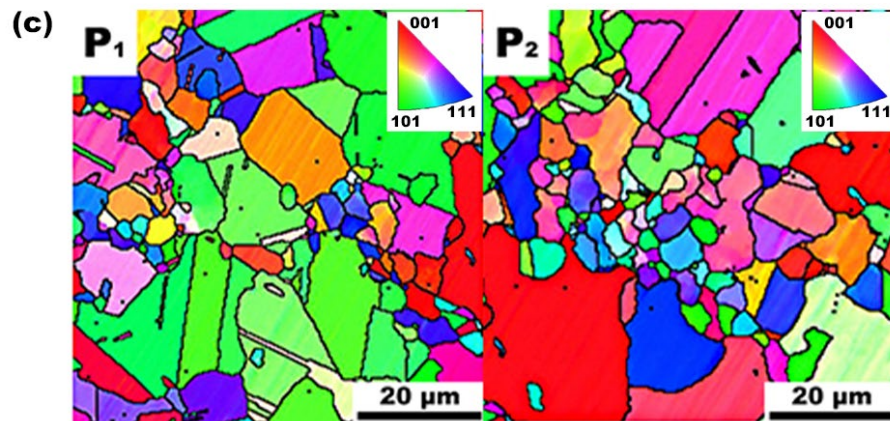


**Figure 4.** Dependence of grain size on the position inside a deformed cylindrical specimen. (a) Geometrical change of cylindrical specimen and effective strain distribution after 50% compression strain at 1121 °C and 0.01 s<sup>-1</sup>. (b) Effective strain varies from the rim to the core regions based on FEM. (c) EBSD measurement of grain size at two typical positions on a different effective strain.

As mentioned previously, accurate simulation of local deformation parameters is the prime aim of calculating microstructure information such as grain size and dynamic recrystallization fraction. Figure 5a shows geometric changes in the compression of the DC specimen. The finite element simulation (FES) results in Figure 5b show that there is a strain gradient from the hub to the rim of a compressed DC specimen at 1121 °C and 0.01 s<sup>-1</sup>. Figure 5c shows the effective strain variation curves of the center lines of the cylindrical and DC specimens. The central effective strain range of the DC specimen (0.21–1.2) is significantly larger than that of the cylindrical specimen (0.59–0.93). The change in the effective strain is small from the hub to the rim of the cylindrical specimen, and the change in the corresponding microstructure, such as grain size, is also small (Figure 5c,d). In contrast, multiple positions span a wide effective strain range from the hub to the rim of the deformed DC specimen. Five different locations (P<sub>1</sub>–P<sub>5</sub> assigned in Figure 5b) were selected, and the grain size and DRX fraction were measured using the EBSD method. Microscopic observations (Figure 5d) show that grain sizes are strongly dependent on position (local processing parameters).

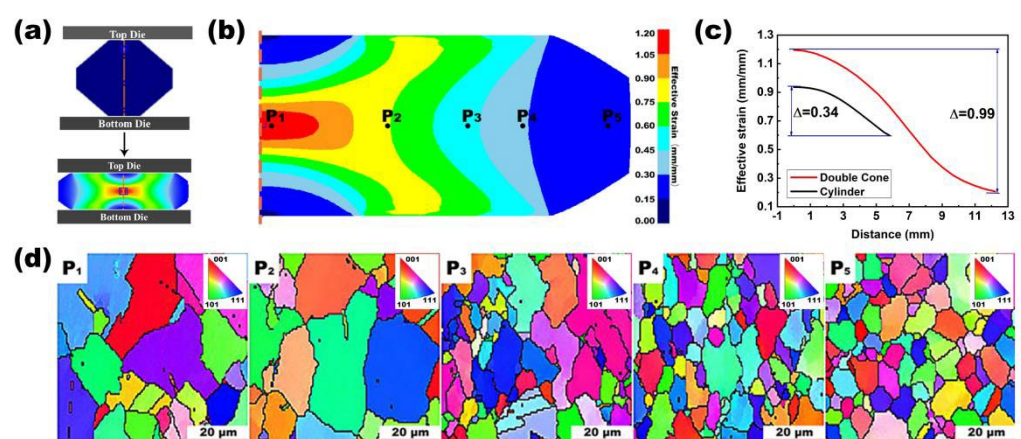


**Figure 5.** Dependence of grain size on the position inside a deformed double-cone specimen. (a) The geometry of the double-cone specimen and effective strain distribution after 50% compression strain at 1121 °C and 0.01 s<sup>-1</sup>. (b) Effective strain varies from the rim to the core regions based on FEM. (c) Comparison of the variation range of centerline equivalent strain between cylindrical and DC specimens. (d) EBSD measurement of the DC specimen's grain size at five typical positions with different effective strains.

Moreover, we can compare grain size information between cylindrical and DC specimens. The grain size information from cylindrical and DC specimens was compared.  $P_1$  and  $P_2$  in Figure 4c correspond to  $P_2$  and  $P_3$  in Figure 5d. The grain morphology and grain size of cylindrical and DC specimens are similar at the same effective strain position. With the increase in effective strain at the same hot compression temperature, the grain morphology evolves from equiaxed grain to non-equiaxed grain with an irregular shape, and many fine grains appear in the middle part. The appearance of these fine grains indicates the onset of recrystallization nucleation in the specimen.

The Avrami equations [23,24] (Equations (1)–(3)) are used to calculate the DRX volume fraction [25,26] and its average grain size [27], where  $A_1$ ,  $n_1$ ,  $A_2$ ,  $n_2$ ,  $A_3$ , and  $n_3$  are the material constants,  $Q_1$  and  $Q_2$  are the material activation energies,  $\dot{\epsilon}$  ( $s^{-1}$ ) is the strain rate,  $\epsilon$  is the true strain,  $\epsilon_c$  is the critical strain,  $\epsilon_{0.5}$  is the strain when the DRX volume fraction is 50%,  $R$  is the gas constant (8.314 J/(mol•K)), and  $T$  ( $^{\circ}C$ ) is the absolute temperature.

$$\epsilon_{0.5} = A_1 \dot{\epsilon}^{n_1} \exp\left(\frac{Q_1}{RT}\right) \quad (1)$$

$$X_{DRX} = 1 - \exp\left[A_2 \left(\frac{\epsilon - \epsilon_c}{\epsilon_{0.5}}\right)^{n_2}\right] \quad (2)$$

$$d_{DRX} = A_3 \dot{\epsilon}^{n_3} \exp\left(\frac{Q_2}{RT}\right) \quad (3)$$

Based on the alloy composition used in this research, these equations are determined:

$$\epsilon_{0.5} = 8.71 \times 10^{-6} \dot{\epsilon}^{-0.24} \exp\left(\frac{114071}{RT}\right) \quad (4)$$

$$X_{DRX} = 1 - \exp\left[-0.604 \left(\frac{\epsilon - \epsilon_c}{\epsilon_{0.5}}\right)^{0.401}\right] \quad (5)$$

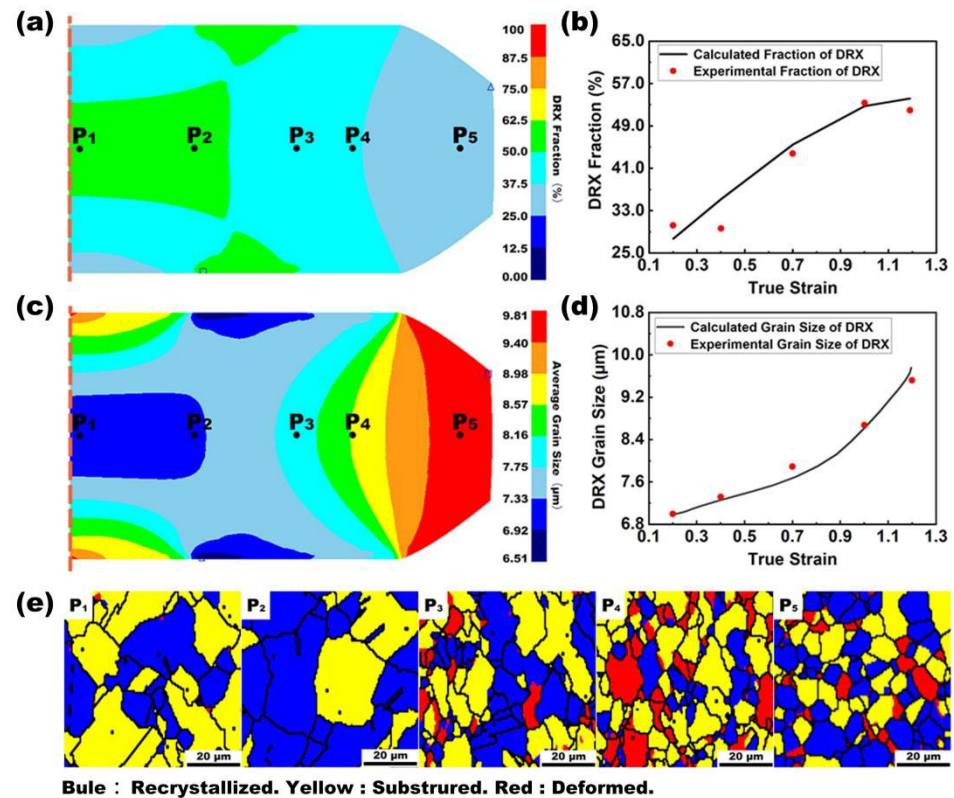
$$d_{DRX} = 1.88 \times 10^6 \dot{\epsilon}^{-0.17} \exp\left(\frac{167323}{RT}\right) \quad (6)$$

The equations were used as an input into FEM. To validate modeling results, experimental results were compared with the modeling results at five different positions (Figure 6a,c). The grain size can be determined based on EBSD measurements (Figure 6e). The difference should be less than 5% for the next step.

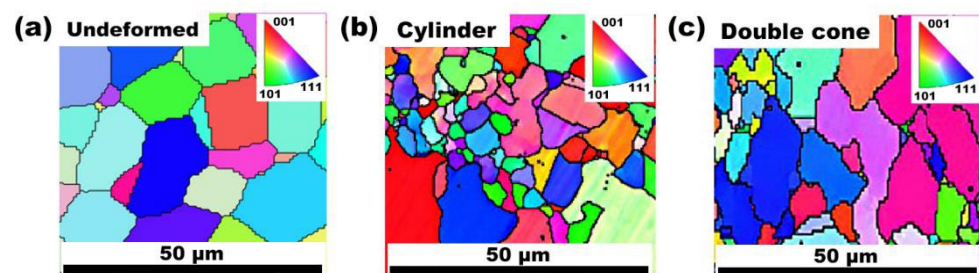
Figure 6a is a contour plot of dynamic recrystallization (DRX) volume fraction (DRVF) at different positions (Equations (4) and (5)). The DRVF decreases from the hub to the rim of the deformed DC specimen. A comparison of the experimental and predicted DRX volume fractions is shown in Figure 6b. Similarly, the average DRX grain size can be calculated using Equation (6), and the DRX grain size varies from the hub to the rim of the deformed specimen, as shown in Figure 6c. A comparison of the experimental and predicted results is shown in Figure 6d,e which show that the DRX, substructure, and deformed grains depend on local deformation parameters. The DRVF of the DC specimens increases with the increase in the true strain, but the slope rapidly decreases. In contrast, the grain size of the DRX shows similar behavior, but the slope increases with the increasing true strain. The prediction and experimental results of the DRX volume fraction and the grain size demonstrate the accuracy of the model and the feasibility of the method.

Figure 7 shows the result of the microstructural characterization of the material before and after the hot compression tests by EBSD. The results show that the initial microstructure is equiaxed with uniform grain size before the hot compression test. After the hot compression test, the initial microstructure of the specimen is deformed, and uniform equiaxed crystals almost do not exist. In their place are newly formed, dynamically recrystallized small grains and morphologically deformed, irregular large grains. Hot compression not only causes

the deformation of the original grain but also destroys the grain boundaries in the original material structure. The newly nucleated, dynamically recrystallized grains grow from the boundary of the original grain and gradually grow to replace the original grain.



**Figure 6.** Experimental and simulated results of DRX inside a double-cone specimen after 50% compression strain at 1121 °C and 0.01 s<sup>-1</sup>. (a) The DRX volume fraction varies from the hub to the rim of the deformed specimen. (b) Comparison of experimental and calculated DRX volume fractions. (c) DRX grain size varies from the hub to the rim of the deformed specimen. (d) Comparison of experimental and calculated DRX grain sizes. (e) DRX distribution obtained by EBSD.



**Figure 7.** The microstructural characterization of the material before and after the hot compression tests by EBSD. (a) The initial microstructure of the material before the hot compression tests. (b) The microstructure of the cylindrical specimen after the hot compression tests. (c) The microstructural characteristics of the double-cone specimen after the hot compression tests.

Figure 8 shows the workflow for predicting microstructures from cylindrical compression to DC compression and the forging of production-scale components.

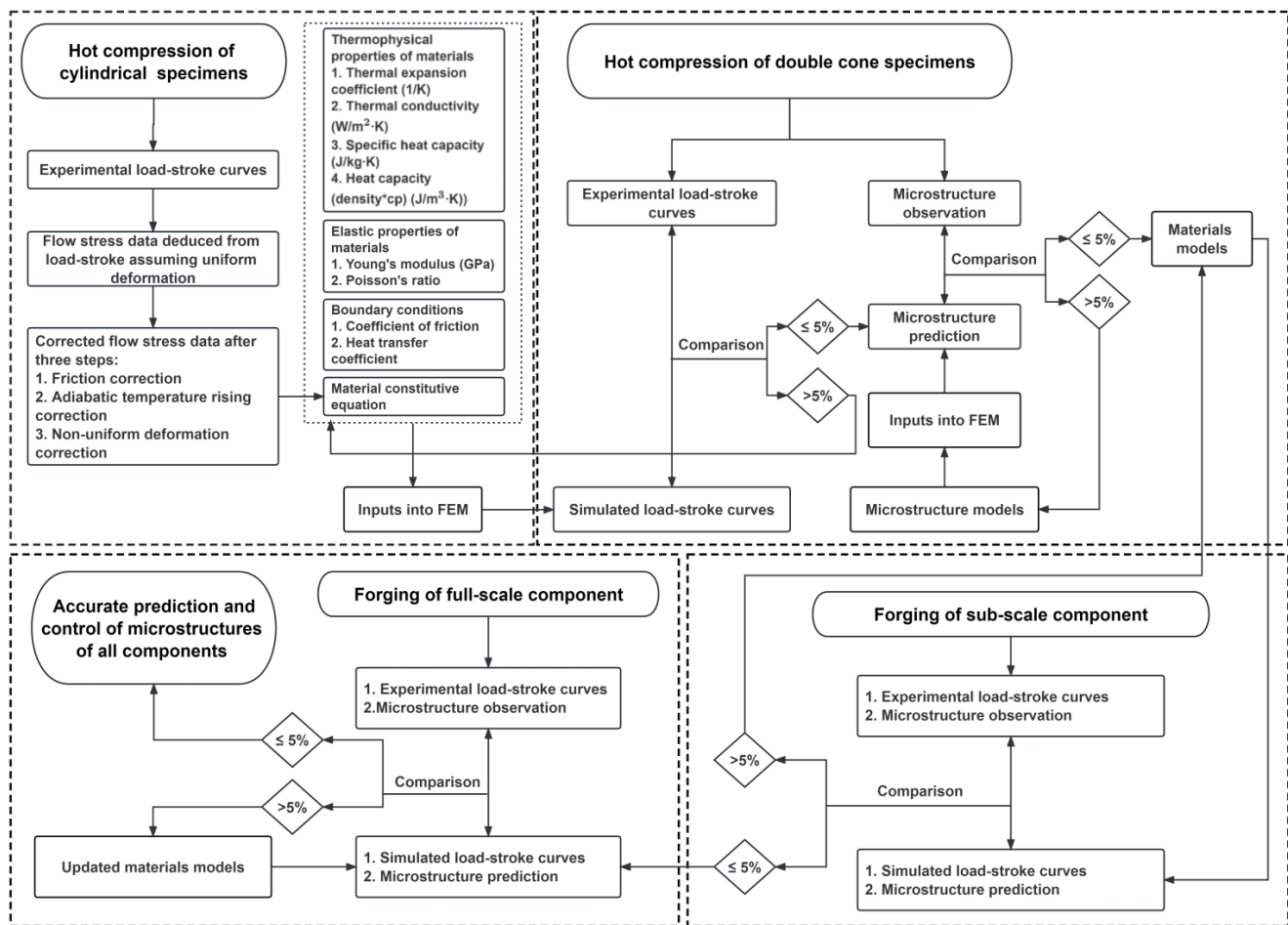


**Figure 8.** Workflow to predict microstructures of the full-scale component.

Firstly, flow curves were obtained using cylindrical compression specimens over a range of temperatures, strains, and strain rates. From the measured load-stroke curves, the corresponding true stress-true strain data [4], i.e., flow curves, were obtained [5]. The flow curves were then corrected to account for the effects of friction [6], adiabatic temperature rise, and non-homogeneous deformation [7,8], such that the constitutive models were established to describe alloy behavior during hot deformation and were integrated into the finite element simulation.

Secondly, double-cone (DC) specimen compression tests were conducted to generate a wider range of strain and strain rates [9] within a single specimen [10]. The measured load-stroke and final dimensions from the DC tests were compared with the finite element simulation using the corrected flow curve data. When the difference between the predicted and experimental load-stroke data and the final dimensions was within an acceptable range, typically less than 5%, the flow curves and finite element forging simulation were considered validated.

Thirdly, the grain microstructures of the compressed cylindrical specimens were characterized to calibrate the grain size model. The predicted processing conditions, including strain, strain rate, and temperature, were inputs for the grain size model to quantify the effect of processing parameters on the grain microstructure inside the DC specimen.

Furthermore, selected locations within the deformed double cones were experimentally characterized for grain microstructures and used to validate the simulated grain size [11]. The selected locations have processing conditions that cover a range of thermo-mechanical conditions that are typically encountered in industrial forgings [12]. When the



difference between the experimentally observed and the simulated grain size falls to an acceptable value, the grain size model is accepted.

This workflow is vital to establishing reliable prediction of grain microstructures from laboratory cylindrical compression testing to DC compression testing and production-scale component forging.

#### 4. Conclusions

A three-step procedure is outlined to establish modeling and simulation for the prediction of grain microstructures in laboratory specimens. The constitutive model and flow curve data for a powder-metallurgy high-cobalt superalloy are calibrated with the flow curve data of cylindrical compression specimens and with friction, adiabatic heating, and non-homogeneous deformation corrections. The hot deformation behavior and simulation tool are validated with double-cone specimens, which have a much broader range of effective strain; thus, the location-specific processing conditions are reliably predicted. The grain microstructures of the cylindrical and DC specimens are experimentally characterized, and they are used to calibrate and validate grain microstructure models. The effects of thermomechanical processing on the grain microstructure in a high-cobalt nickel-base superalloy are predicted and comparable with the experimental observations. To predict the grain microstructure during thermomechanical processing, this integrated experimental modeling approach enables the calibration and validation of constitutive models and simulation with cylindrical and DC compression specimens and provides modeling and computational capabilities that are capable of industrial forging simulations.

**Author Contributions:** L.J. and S.S.: Conceptualization, Methodology. J.W. and S.Z.: Data curation, Software, Visualization, Investigation, Validation. J.W.: Writing—Original draft preparation. Z.H.: Writing—Reviewing. All authors have read and agreed to the published version of the manuscript.

**Funding:** ①The National Key Research and Development Program of China (2018YFB0704100) and the Guangdong Province Key-Area Research and Development Program of China (Grant No. 2019B010943001). ②State Key Laboratory of Powder Metallurgy (Central South University, China).

**Institutional Review Board Statement:** Not applicable.

**Informed Consent Statement:** Not applicable.

**Data Availability Statement:** Data is contained within the article.

**Acknowledgments:** The research was supported by the National Key Research and Development Program of China (2018YFB0704100) and the Guangdong Province Key-Area Research and Development Program of China (Grant No. 2019B010943001). Z. H. appreciates the project supported by the State Key Laboratory of Powder Metallurgy (Central South University, China).

**Conflicts of Interest:** The authors declare no conflict of interest.

#### References

- Williams, J.C. Business Directions and Materials Challenges for the Aircraft Engine Industry. *Acta Metall. Sin.* **1996**, *9*, 407.
- Sah, J.P.; Richardson, G.J.; Sellars, C.M. Grain-Size Effects during Dynamic Recrystallization of Nickel Metal Science. *Met. Sci.* **1974**, *8*, 325–331. [CrossRef]
- Collins, D.M.; Conduit, B.D.; Stone, H.J.; Hardy, M.C.; Conduit, G.J.; Mitchell, R.J. Grain growth behaviour during near- $\gamma'$  solvus thermal exposures in a polycrystalline nickel-base superalloy. *Acta Mater.* **2013**, *61*, 3378–3391. [CrossRef]
- Semiatin, S.L.; McClary, K.E.; Rollett, A.D.; Roberts, C.G.; Payton, E.J.; Zhang, F.; Gabb, T.P. Microstructure evolution during supersolvus heat treatment of a powder metallurgy nickel-base superalloy. *Metall. Mater. Trans. A* **2012**, *43*, 1649–1661. [CrossRef]
- Mandal, S.; Jayalakshmi, M.; Bhaduri, A.K.; Subramanya Sarma, V. Effect of Strain Rate on the Dynamic Recrystallization Behavior in a Nitrogen-Enhanced 316L(N). *Metall. Mater. Trans. A* **2014**, *45*, 5645–5656. [CrossRef]
- Matsui, T.; Takizawa, H.; Kikuchi, H.; Wakita, S. The Microstructure Prediction of Alloy720LI for Turbine Disk Applications. In Proceedings of the Superalloys 2000, 9th International Symposium on Superalloys, Seven Springs, PA, USA, 17–21 September 2000; pp. 127–133. [CrossRef]
- Na, Y.S.; Yeom, J.T.; Park, N.K.; Lee, J.Y. Simulation of microstructures for Alloy 718 blade forging using 3D FEM simulator. *J. Mater. Process. Technol.* **2003**, *141*, 337–342. [CrossRef]



8. Ryan, N.D.; McQueen, H.J. Flow stress, dynamic restoration, strain hardening and ductility in hot working of 316 steel. *J. Mater. Process. Technol.* **1990**, *21*, 177–199. [CrossRef]
9. Wang, X.; Huang, Z.; Cai, B.; Zhou, N.; Magdysyuk, O.; Gao, Y.; Srivatsa, S.; Tan, L.; Jiang, L. Formation mechanism of abnormally large grains in a polycrystalline nickel-based superalloy during heat treatment processing. *Acta Mater.* **2019**, *168*, 287–298. [CrossRef]
10. Ebrahimi, R.; Najafizadeh, A. A new method for evaluation of friction in bulk metal forming. *J. Mater. Process. Technol.* **2004**, *152*, 136–143. [CrossRef]
11. Mandal, S.; Sivaprasad, P.V.; Dube, R.K. Kinetics, mechanism and modelling of microstructural evolution during thermomechanical processing of a 15Cr–15Ni–2.2Mo–Ti modified austenitic stainless steel. *J. Mater. Sci.* **2007**, *42*, 2724–2734. [CrossRef]
12. Yeom, J.T.; Lee, C.S.; Kim, J.H.; Park, N.K. Finite-element analysis of microstructure evolution in the cogging of an Alloy 718 ingot. *Mater. Sci. Eng. A* **2007**, *449–451*, 722–726. [CrossRef]
13. Sakui, S.; Sakai, T.; Takeishi, K. Hot Deformation of Austenite in a Plain Carbon Steel. *Trans. Iron Steel Inst. Jpn.* **1977**, *17*, 718–725. [CrossRef]
14. Shakib, M.; Perkins, K.M.; Bray, S.E.; Siviour, C.R. Development of a high temperature flow stress model for AerMet 100 covering several orders of magnitude of strain rate. *Mater. Sci. Eng. A* **2016**, *657*, 26–32. [CrossRef]
15. Solhjo, S. A note on “Barrel Compression Test”: A method for evaluation of friction. *Comput. Mater. Sci.* **2010**, *49*, 435–438. [CrossRef]
16. Kobayashi, S.; Kobayashi, S.; Oh, S.I.; Altan, T. *Metal Forming and the Finite-Element Method*; Oxford University Press: New York, NY, USA, 1989. [CrossRef]
17. Poliak, E.I.; Jonas, J.J. A one-parameter approach to determining the critical conditions for the initiation of dynamic recrystallization. *Acta Mater.* **1996**, *44*, 127–136. [CrossRef]
18. Semiatin, S.L.; Weaver, D.S.; Goetz, R.L.; Thomas, J.P.; Turner, T.J. Deformation and Recrystallization during Thermomechanical Processing of a Nickel-Base Superalloy Ingot Material. *Mater. Sci. Forum* **2007**, *550*, 129–140. [CrossRef]
19. Eriksson, E.; Hanning, F.; Andersson, J.; Colliander, M.H. The Effect of Grain Boundary Carbides on Dynamic Recrystallization During Hot Compression of Ni-Based Superalloy Haynes 282TM. *Metall. Mater. Trans. A* **2022**, *53*, 29–38. [CrossRef]
20. Tan, L.; Huang, Z.; Liu, F.; He, G.; Wang, X.; Huang, L.; Zhang, Y.; Jiang, L. Effects of strain amount and strain rate on grain structure of a novel high Co nickel-based polycrystalline superalloy. *Mater. Des.* **2017**, *131*, 60–68. [CrossRef]
21. Zhang, S.; Wang, J.; Huang, L.; Srivatsa, S.; Zhou, K.; Huang, Z.; Jiang, L. Correction of flow stress data due to non-homogeneous deformation and thermal conditions during hot compression testing of a polycrystalline nickel-base superalloy. *J. Mater. Sci.* **2021**, *56*, 7727–7739. [CrossRef]
22. Mejía, I.; Bedolla-Jacuinde, A.; Maldonado, C.; Cabrera, J.M. Determination of the critical conditions for the initiation of dynamic recrystallization in boron microalloyed steels. *Mater. Sci. Eng. A* **2011**, *528*, 4133–4140. [CrossRef]
23. Roberts, W.; Ahlblom, B. A nucleation criterion for dynamic recrystallization during hot working. *Acta Metall.* **1978**, *26*, 801–813. [CrossRef]
24. McQueen, H.J.; Ryan, N.D. Constitutive analysis in hot working. *Mater. Sci. Eng. A* **2002**, *322*, 43–63. [CrossRef]
25. Ravichandran, N. Application of Dynamic Recrystallization Model for the Prediction of Microstructure During Hot Working. *J. Mater. Eng. Perform.* **2003**, *12*, 653–655. [CrossRef]
26. Jonas, J.J. Dynamic Recrystallization—Scientific Curiosity of Industrial Tool? *Mater. Sci. Eng. A* **1994**, *184*, 155–165. [CrossRef]
27. Mandal, S.; Bhaduri, A.K.; Subramanya Sarma, V. Role of Twinning on Dynamic Recrystallization and Microstructure During Moderate to High Strain Rate Hot Deformation of a Ti-Modified Austenitic Stainless Steel. *Metall. Mater. Trans. A* **2012**, *43*, 2056–2068. [CrossRef]

**Disclaimer/Publisher’s Note:** The statements, opinions and data contained in all publications are solely those of the individual author(s) and contributor(s) and not of MDPI and/or the editor(s). MDPI and/or the editor(s) disclaim responsibility for any injury to people or property resulting from any ideas, methods, instructions or products referred to in the content.

## Article

# Influences of Fe Content and Cold Drawing Strain on the Microstructure and Properties of Powder Metallurgy Cu-Fe Alloy Wire

Xiaobo Yuan <sup>1,\*</sup> , Ping Zhang <sup>1,\*</sup> , Jianxiang Wang <sup>1</sup>, Biaobiao Yang <sup>1,2,3,\*</sup> and Yunping Li <sup>1</sup> 

<sup>1</sup> State Key Lab for Powder Metallurgy, Central South University, Changsha 410083, China; yuaxiaobo@csu.edu.cn (X.Y.); 223311073@csu.edu.cn (J.W.); lyping@csu.edu.cn (Y.L.)

<sup>2</sup> IMDEA Materials Institute, C/Eric Kandel 2, 28906 Getafe, Spain

<sup>3</sup> Department of Materials Science, Polytechnic University of Madrid, E.T.S. de Ingenieros de Caminos, 28040 Madrid, Spain

\* Correspondence: pingzhang@csu.edu.cn (P.Z.); biaobiao.yang@imdea.org (B.Y.)

**Abstract:** To study the effects of Fe content and cold drawing strain on the microstructure and properties, Cu-Fe alloys were prepared via powder metallurgy and hot extrusion. Scanning electron microscopy was applied to observe the Fe phase, and the ultimate tensile strength was investigated using a universal material testing machine. Alloying with an Fe content below 10 wt.% formed a spherically dispersed Fe phase via the conventional nucleation and growth mechanism, whereas a higher Fe content formed a water-droplet-like Fe phase via the spinodal decomposition mechanism in the as-extruded Cu-Fe alloy. Further cold drawing induced the fiber structure of the Fe phase (fiber strengthening), which could not be destroyed by subsequent annealing. As the Fe content increased, the strength increased but the electrical conductivity decreased; as the cold drawing strain increased, both the strength and the electrical conductivity roughly increased, but the elongation roughly decreased. After thermal–mechanical processing, the electrical conductivity and strength of the Cu-40Fe alloy could reach 51% IACS and 1.14 GPa, respectively. This study can provide insight into the design of high-performance Cu-Fe alloys by tailoring the size and morphology of the Fe phase.

**Keywords:** Cu-Fe wire; powder metallurgy; cold drawing; ultimate tensile strength; electrical conductivity; Fe phase



**Citation:** Yuan, X.; Zhang, P.; Wang, J.; Yang, B.; Li, Y. Influences of Fe Content and Cold Drawing Strain on the Microstructure and Properties of Powder Metallurgy Cu-Fe Alloy Wire. *Materials* **2023**, *16*, 5180. <https://doi.org/10.3390/ma16145180>

Academic Editors: Seong-Ho Ha, Shae-Kwang Kim and Hyun-Kyu Lim

Received: 25 June 2023

Revised: 17 July 2023

Accepted: 17 July 2023

Published: 23 July 2023



**Copyright:** © 2023 by the authors. Licensee MDPI, Basel, Switzerland. This article is an open access article distributed under the terms and conditions of the Creative Commons Attribution (CC BY) license (<https://creativecommons.org/licenses/by/4.0/>).

## 1. Introduction

Cu-X alloys, where X is a BCC-type metal element (Nb, Ta, Cr, or Fe), are generally recognized to exhibit both high strength and high electrical conductivity [1–5]. Among these BCC-type metal elements, Fe is the most abundant element in the Earth’s crust. In addition, the plastic flow behavior of Fe is similar to that of Cu; therefore, Cu-Fe alloys can be plastically deformed to high strain levels at room temperature [4,5]. Accordingly, Cu-Fe alloys are widely used in industrial fields [6–9]. The industrial applications of Cu-Fe wire are mainly in the electronics, electrical, and communication fields, such as wires and cables, where the focus is on strength and conductivity. Nevertheless, the Cu-Fe alloy is an immiscible binary alloy, and liquid phase separation takes place during solidification, especially in Cu-Fe alloys with a high Fe content [10,11]. Therefore, numerous defects are easily generated when casting Cu-Fe components [11]. Furthermore, a coarse Fe phase is also unfortunately inevitable, owing to the low cooling rate during solidification [12,13]. These aspects greatly lower the mechanical properties of Cu-Fe alloys, thus restricting their application.

Many attempts have been made to improve the mechanical performance of Cu-Fe alloys by refining the grain size (i.e., grain boundary strengthening) [14,15], work hardening

effect [16,17], and aging treatment (i.e., precipitation strengthening) [8,16]. In addition to the above methods, reducing the size of the Fe phase is another effective strategy to improve the comprehensive performance of Cu-Fe alloys. Pang et al. [7] reported that the ultimate tensile strength (UTS) and electrical conductivity (EC) of a cast Cu-10Fe alloy with an initial Fe phase size of 25  $\mu\text{m}$  were 466 MPa and 63% IACS, respectively. Wang et al. [8] reduced the Fe phase size of the same alloy to 20  $\mu\text{m}$  through dual-melt mixed casting and subsequent mechanical processing, leading to an enhancement in UTS to 608 MPa but a reduction in EC to 54%. The increased strength was due to grain boundary strengthening and dislocation strengthening, while the improved EC but reduced strength upon subsequent annealing could be ascribed to grain growth and reduced dislocation density [4]. Zou et al. [18] introduced a novel casting process with an alternating magnetic field to prepare a Cu-14Fe alloy with a finer Fe phase size of 18  $\mu\text{m}$ . The resultant UTS and EC could reach 605 MPa and 48% IACS, respectively. Recently, Wang et al. [19] prepared a Cu-15Fe alloy via spark plasma sintering (SPS) of atomized powder, refining the Fe phase size to  $\sim 2$   $\mu\text{m}$  after sintering. This led to a further increase in UTS to 750 MPa but a reduction in EC to 22% IACS.

Powder metallurgy is an effective method to enhance the mechanical performance of Cu-Fe alloys via reducing both the grain size of the Cu matrix and the Fe phase size, but this approach is generally detrimental to the EC. The reduced EC can be mainly attributed to the enhanced interface scattering, impurity scattering, and dislocation scattering [20]. The reduced EC of powder-metallurgy Cu-Fe alloys can be partly ascribed to its finer grain size, which leads to increased interface scattering. Moreover, due to the ultrahigh cooling rate during the atomization of powder, it becomes difficult to precipitate the Fe solute from the powder matrix, giving rise to a greater impurity scattering of electrons. Improving the EC becomes a key issue to improve the comprehensive performance of powder-metallurgy Cu-Fe alloys.

To this end, a combination of cyclic cold drawing and annealing was applied to powder-metallurgy Cu-Fe alloys with various cold drawing strain levels, aimed at enhancing the precipitation of Fe solute from the Cu matrix and improving the electrical conductivity by reducing the Fe impurity scattering of electrons. Therefore, in this study, Cu-Fe alloys with different Fe contents were prepared via powder metallurgy, and rod-shaped embryos were obtained via vacuum sintering. Cu-Fe alloy wires under different cold drawing strains were prepared via cold drawing and annealing treatments. The microstructure, EC, and mechanical properties of the wires with different Fe compositions and after various cold drawing strains were investigated in detail.

## 2. Materials and Methods

Powders of Cu-5Fe, Cu-10Fe, Cu-20Fe, and Cu-40Fe (wt.%) alloys were prepared via the Ar gas atomization process. The metal powders were placed into a rubber tube, the two ends of which were sealed. The rubber tube containing metal powders was compressed using cold isostatic pressure equipment (LDJ500/1500-300YS, Sichuan Airlines West Sichuan Machinery Co., Ltd., Ya'an, China) to obtain the metal embryos. The pressure of the cold isostatic press was set to 130–150 MPa. The embryos after cold isostatic pressing were subsequently placed into a tubular furnace (SK-G06123K-2R, Kejing Material Technology Co., Ltd., Hefei, China) for sintering under a nitrogen atmosphere containing 4% hydrogen. Sintering was conducted at 950 °C for 4 h, before cooling in the furnace. The embryo body was cylindrical with a length of 90 mm and a diameter of 20 mm. Then, the cylindrical embryos were hot-extruded to obtain rods with a diameter of 7.5 mm. The hot extrusion was performed at 900 °C. The rods ( $d = 7.5$  mm) were drawn into wires with various diameters at room temperature. The drawing equipment used in this experiment was a semiautomatic multi-station pipe-drawing machine (L-B70-A, Shengfei Mechanical Equipment Manufacturing Co., Ltd., Wuxi, China). The stretching mold used in this experiment

was a conical mold, and the drawing method was linear horizontal drawing. During cold drawing, the deformation strain is usually defined by the following formula:

$$\eta = \ln(A_0/A_f), \quad (1)$$

where  $A_0$  is the initial cross-sectional area and  $A_f$  is the final cross-sectional area.  $A_0$  in Equation (1) was 43.80 mm<sup>2</sup> before cold drawing. At cold drawing strains of 0, 1.26, 2.00, 2.64, and 4.03, the wires were taken out for annealing at 450 °C for 1 h to study the microstructure and properties of the Cu-Fe alloys, as schematically shown in Figure 1. An intermediate heat treatment between the cold drawing steps helped to appropriately eliminate a large amount of residual stress stored in the alloy due to deformation, thereby facilitating subsequent cold drawing. Furthermore, Equation (1) was utilized to calculate the deformation strain of the Fe phase ( $\eta_{Fe}$ ) under various cold drawing strains, by inputting both the initial and the final Fe phase areas.

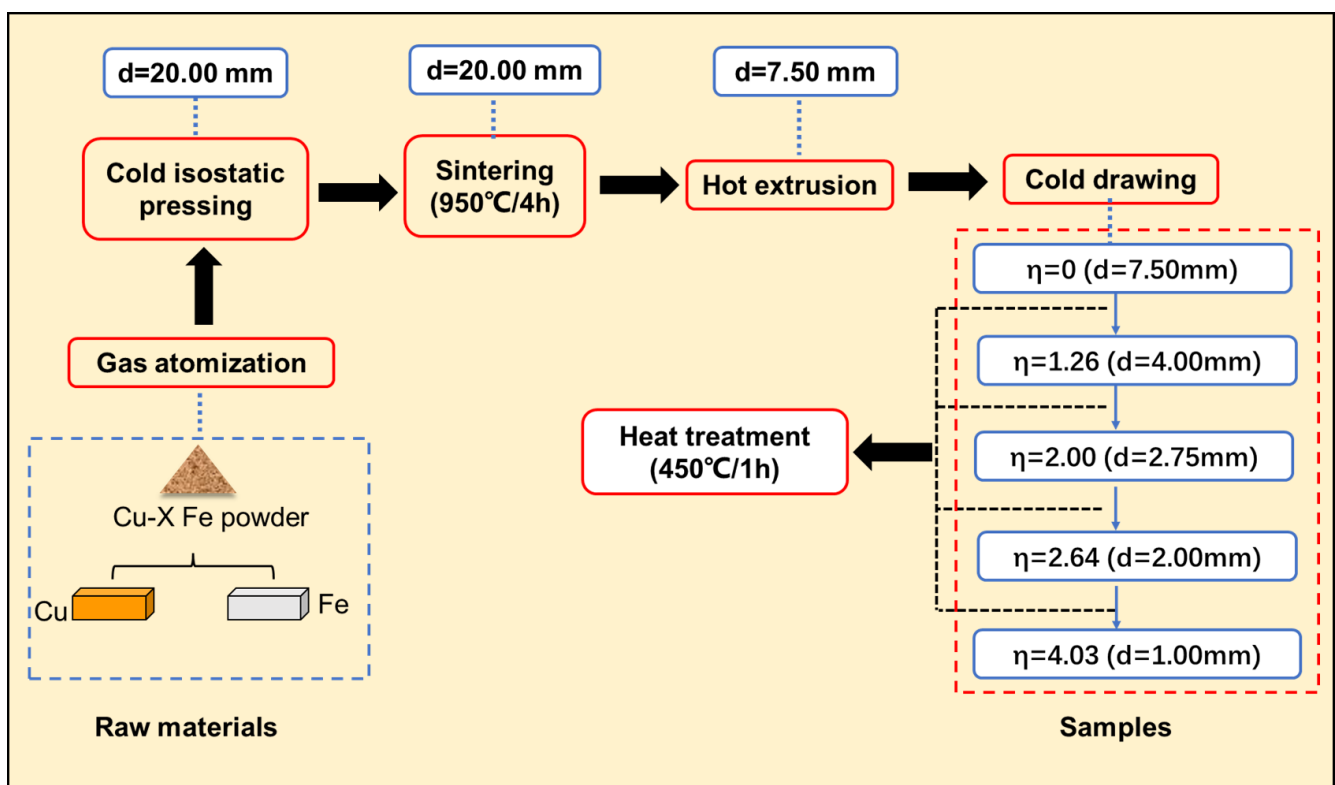


**Figure 1.** Thermal–mechanical processing flow.

A field emission scanning electron microscope (SEM, Quanta 650 FEG, FEI, Boston, MA, USA) was used for the microstructure observation. The surface morphologies of Cu-Fe alloys were observed using the scanning electron microscope through the backscattered electron (BSE) imaging mode, since the atomic numbers of Cu and Fe differ and the two phases can be clearly distinguished under this mode. The instrument used for EC in this work was the QJ36s direct-current low-resistance tester. We measured each sample three times and took the average value as the resistance value ( $R, \Omega$ ). Then, we converted the resistance ( $\rho, \Omega \cdot m$ ) into conductivity ( $\sigma, \%IACS$ ), according to the resistivity of annealed pure copper based on the international standard:

$$\sigma = \frac{\rho_{Cu}}{\rho} = \frac{\rho_{Cu} \cdot L}{S \cdot R} \quad (2)$$

where  $\sigma$  is the conductivity (%IACS),  $\rho_{Cu}$  is the resistivity of international standard annealed pure copper ( $\rho_{Cu} = 1.724 \Omega\cdot m$ ),  $\rho$  is the resistivity of the sample ( $\rho, \Omega\cdot m$ ),  $R$  is the resistance value of the sample ( $R, \Omega$ ), and  $L$  and  $S$  are the length ( $L, m$ ) and cross-sectional area of the tested sample ( $S, m^2$ ), respectively. Mechanical properties were investigated by using a universal material testing machine (INSTRON 5982, Instron, Norwood, MA, USA). An 80 mm long wire was cut; the upper and lower collets held 30 mm, respectively, leaving 20 mm as the gauge distance; and the strain rate was  $1.0 \times 10^{-3} s^{-1}$ . The conductivity and ultimate tensile strength were taken as the average of the three measured results.

### 3. Results and Discussion

#### 3.1. As-Textured Cu-Fe Alloys

Figure 2 shows the microstructures of various Cu-Fe alloys before the cold drawing. From the cross-sectional morphologies, a dark Fe phase is uniformly distributed, and no obvious dendrite structure of the Fe phase is observed in any Cu-Fe alloy. From the longitudinal section, for all alloys, the Fe phase is slightly elongated along the longitudinal direction during hot extrusion. Using Image-J 2.35 software, mean Fe phase sizes in Cu-5Fe, Cu-10Fe, Cu-20Fe, and Cu-40Fe are quantitatively determined to be 0.43, 0.85, 1.07, and 1.78  $\mu m$ , respectively, as shown in Figure 3. In both Cu-5Fe and Cu-10Fe alloys, the spherical Fe particles are observed to be randomly distributed in the Cu matrix. However, in Cu-20Fe and Cu-40Fe alloys with higher Fe contents, the Fe phase presents irregular shapes such as petal-like or water droplet shapes, which are interconnected together in the Cu matrix. This can be ascribed to the occurrence of phase separation in the liquid phase in Cu-Fe alloys [21–23].

A large metastable miscibility gap (i.e., bimodal curve) exists in the Cu-Fe binary system above 1200 °C [21]. The liquid phase separation of Cu and Fe has a strong impact on the resultant microstructure of the alloy during the solidification. Shi et al. believed that the concentration of solute elements plays a decisive role in the microstructure of binary alloys with spinodal decomposition [21]. They carried out a phase-field simulation on spinodal decomposition within a liquid droplet. The results showed that when the volume fraction of two phases differs greatly, the minority phase always forms discrete second-phase droplets embedded in the matrix of the major phase; if the volume fraction of the two phases is close, they will form an interpenetrating or bicontinuous morphology, in which each phase forms a continuous interconnection structure. The interconnected structures will break into a series of droplets during further solidification. Their simulation results are in good agreement with the morphologies of the Fe phase in the present work [21].

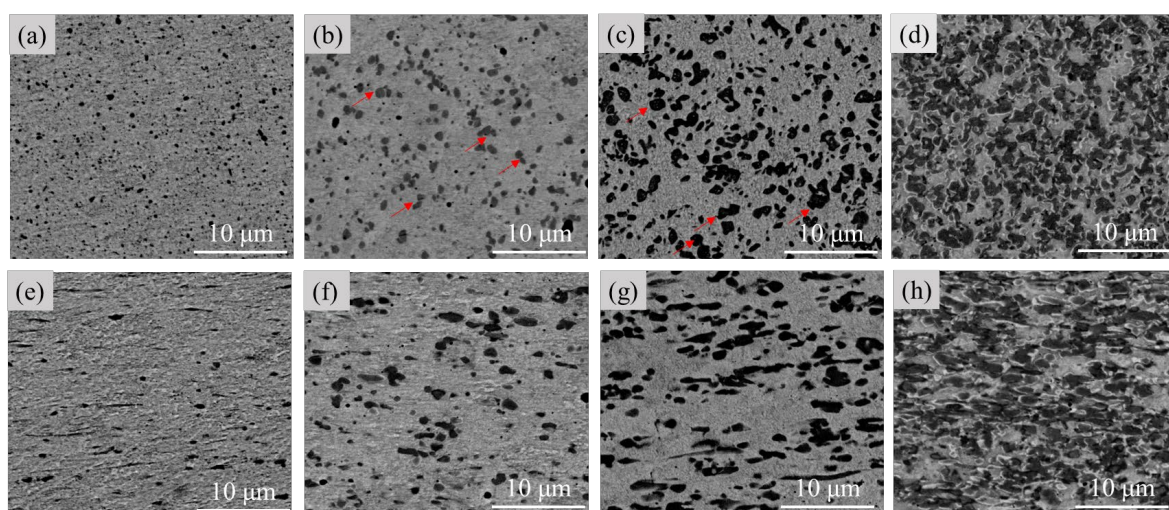


**Figure 2.** Microstructures of (a,e) Cu-5Fe, (b,f) Cu-10Fe, (c,g) Cu-20Fe, and (d,h) Cu-40Fe alloys in terms of (a–d) the cross-section and (e–h) the longitudinal section. Red arrows are used to point out the location of Fe phase.



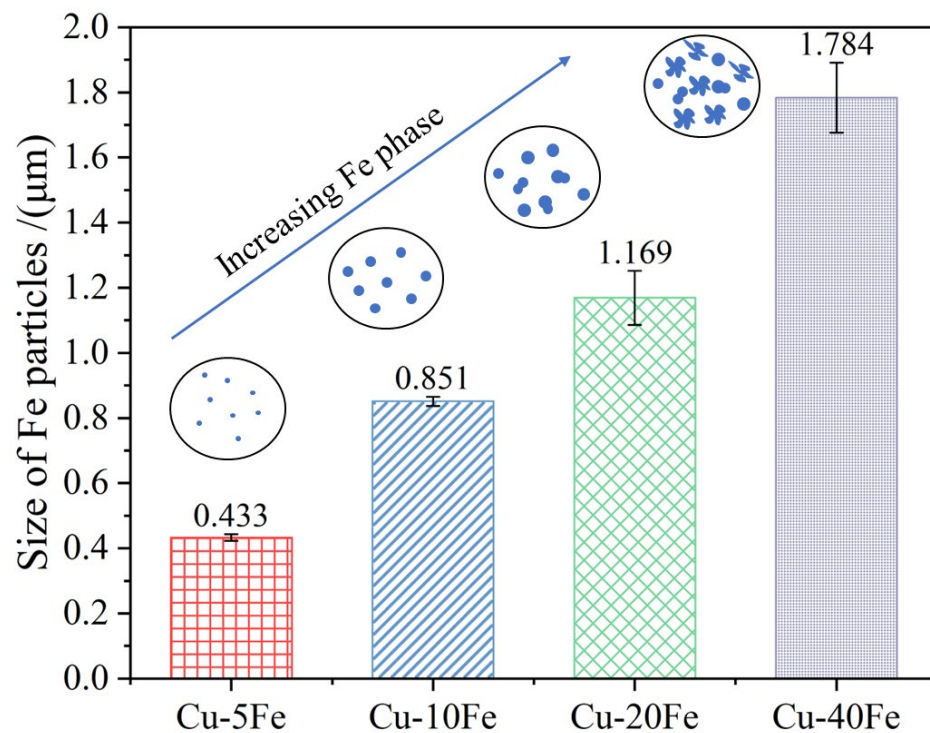


**Figure 3.** Size of Fe particles in Cu-Fe alloys after the hot extrusion.

A schematic figure describing the liquid phase separation and the resultant microstructure of the Cu-Fe alloy with different Fe contents is given in Figure 4. For the Cu-5Fe, Cu-10Fe, and Cu-20Fe alloys, the volume fraction of the Fe phase is lower in comparison with the Cu matrix (Figure 4a–d). During the liquid–liquid separation stage, the liquid droplets of the Fe phase are dispersed as the core in the Cu matrix (Figure 4b). Owing to the interface energy, some discrete droplets will gather to form a gourd-shaped or slightly larger spherical Fe phase (indicated by the red arrow in Figure 2b,c). Therefore, the Fe phase in the alloy presents a regular spherical dispersion in the Cu matrix (Figure 2a–c) during the process of atomization, where the cooling rate is extremely high. In the Cu-40Fe alloy with a close volume fraction of the Fe phase and Cu phase (Figure 4e–h), the two phases form a continuous interpenetrating structure in the liquid–liquid separation stage. Due to the different surface energy of the two phases, this interconnected structure will break, forming a series of incompletely agglomerated contours (Figure 4h). During the aging process at lower temperature, a small amount of secondary Fe phase precipitates from the Cu matrix (Figure 4d,h) [24,25]. The secondary Fe phase generally exhibits a size ranging from several to dozens of nanometers, which is much finer compared to the primary phase [6,8,9]. Since the fraction of the secondary Fe phase is extremely low, its influence on the main morphology of the Fe phase can be ignored. Therefore, the overall size and morphology of the Fe phase in the Cu-Fe alloy are mainly determined by the primary Fe phase. As shown in Figure 4, in the Cu-Fe alloy with a low Fe content, the phase separation takes place via the conventional nucleation and growth of the Fe phase [26,27]. In the Cu-Fe alloy with a high Fe content, the phase separation is characterized by spinodal decomposition [28,29] in a very short time [10], forming the water-droplet-like Fe phase.

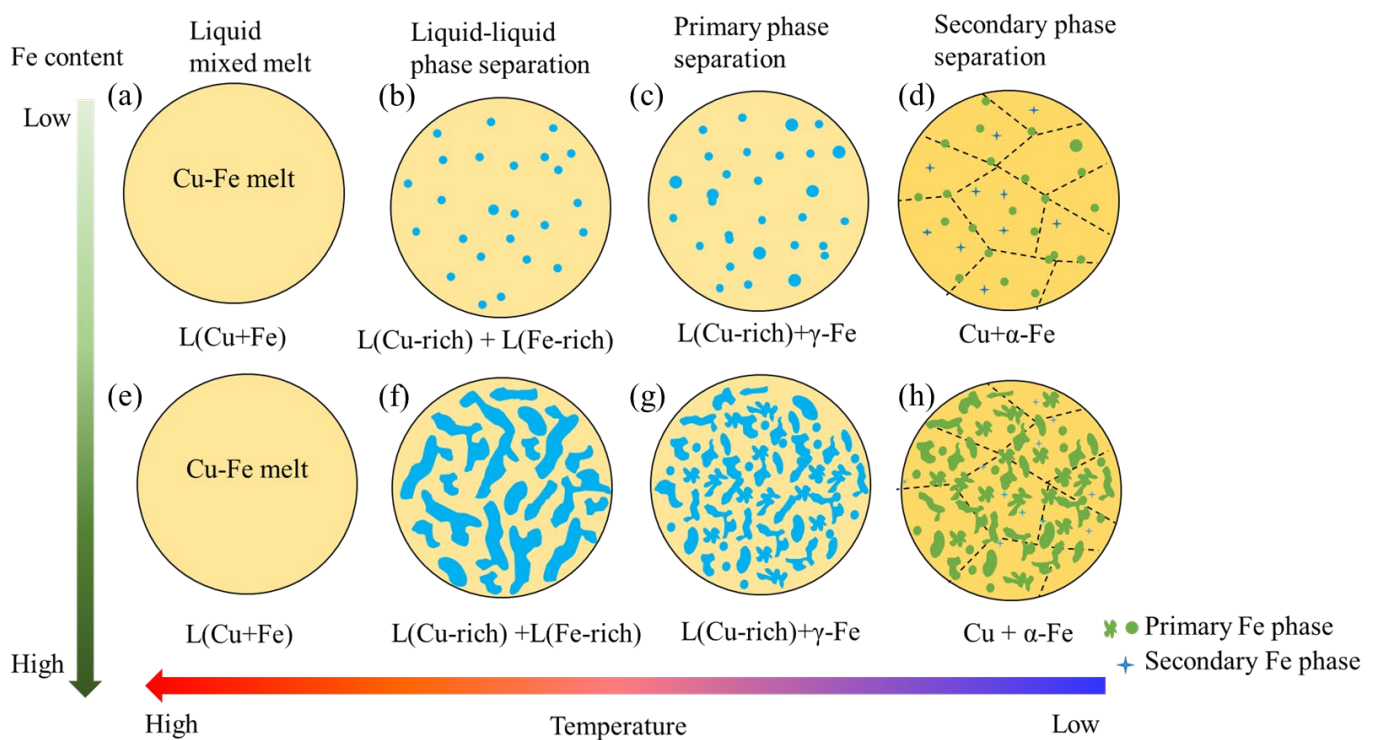


**Figure 4.** Schematic diagram of the solidification process of Cu-Fe alloys.

### 3.2. Cu-Fe Alloys after Cold Drawing and Annealing

Figures 5 and 6 show the cross-sectional and longitudinal microstructures of the four Cu-Fe alloys after cold drawing with various  $\eta$ , respectively. From the cross-sectional morphology, with increasing cold drawing strain ( $\eta$ ), the Fe phase gradually becomes finer (Figure 5) and is elongated significantly along the drawing direction (Figure 6). Figure 7a quantitatively plots the evolution of the Fe phase size with respect to  $\eta$ . As  $\eta$  increases from 0 to 4.03, the Fe phase in the Cu-40Fe alloy decreases from 1.78 to 0.72  $\mu\text{m}$ . As the Fe content decreases, the reduction rate/slope of the Fe phase size during drawing with respect to the cold drawing strain decreases obviously. The lowest reduction rate of Fe in the Cu-5Fe alloy is observed, i.e., from 0.43 ( $\eta = 0$ ) to 0.27  $\mu\text{m}$  ( $\eta = 4.03$ ). In addition, the reduction in the Fe phase slows down with the increase in strain. The deformation strain ( $\eta_{\text{Fe}}$ ) of the Fe phase—where the Fe phase in alloys before cold drawing is considered as the initial size—is plotted in Figure 7b with respect to the cold drawing strain. Obviously, under the same cold drawing strain, the  $\eta_{\text{Fe}}$  increases with the Fe content, except for Cu5Fe. A possible reason for the abnormal  $\eta_{\text{Fe}}$  of the Cu-5Fe alloy is that the initial cross-sectional area of the Fe phase is too small to determine the accurate  $\eta_{\text{Fe}}$  during cold drawing. Despite that, the deformation of the Fe phase is more severe in the Cu-Fe alloy with a higher Fe content.

Furthermore, another interesting point is that when  $\eta > 2$ , the  $\eta_{\text{Fe}}$  of Cu10Fe, Cu20Fe, and Cu40Fe alloys increases sharply (Figure 7b). This is because when the cold drawing strain is high enough, the Fe phase will fracture into several parts, greatly refining the size of the Fe phase and leading to the increase in  $\eta_{\text{Fe}}$ . Note that during the cold drawing, both plastic and fracture deformations may occur for the Fe phase, but which one is the dominant deformation mode depends on the morphology of the Fe phase to some extent. To be specific, for the Cu5Fe alloy, the Fe phase is regularly spherical; thus, it will extend uniformly along the drawing direction via the plastic deformation during the drawing process. However, for Cu20Fe and Cu40Fe alloys, the Fe phase is mostly presented in irregular-water-droplet and interconnected shapes; thus, it will tend to fracture during the drawing process. Typical experimental evidence can be found in Figure 6(b4,c3), where an obvious necking phenomenon takes place along the elongation direction of Fe-phase fibers. It must be mentioned that plastic deformation can reduce the Fe fiber spacing and fracture

deformation can decrease the Fe phase size. Stepanov et al. [30] reported that the tensile strength and the average spacing of the Fe fiber conform to the Hall–Patch relationship as [30,31]

$$\sigma_c = \sigma_0 + k \cdot \lambda^{-\frac{1}{2}} \quad (3)$$

where  $\sigma_0$  is a constant (MPa), usually close to the initial strength of the undeformed alloy [32];  $k$  is the coefficient of fiber strengthening ( $\text{MPa} \cdot \mu\text{m}^{-1/2}$ ); and  $\lambda$  is the spacing between the fibers ( $\mu\text{m}$ ).

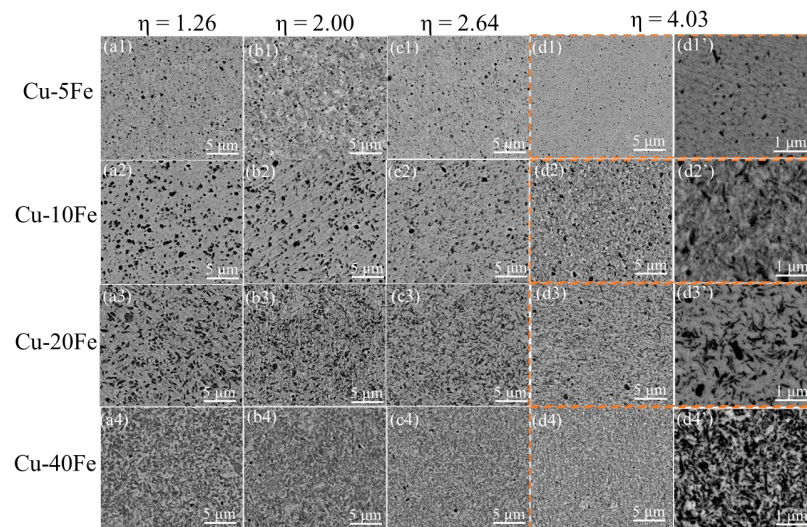


**Figure 5.** Cross-sectional structures of various Cu-Fe alloys after the cold drawing with various  $\eta$ . The structures of Cu-5Fe, Cu-10Fe, Cu-20Fe, and Cu-40Fe are shown in (a1–d1′), (a2–d2′), (a3–d3′), and (a4–d4′), respectively. The structures of Cu-Fe alloys under  $\eta$  of 1.26, 2.00, 2.64, and 4.03 are given in (a1–a4), (b1–b4), (c1–c4), and (d1–d4), (d1′–d4′), respectively.

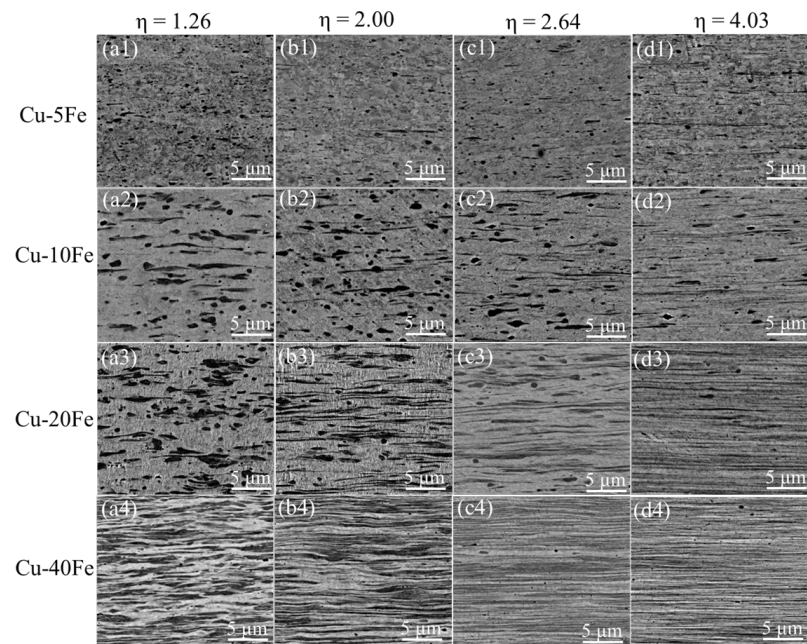


**Figure 6.** Longitudinal section structures of various Cu-Fe alloys after the cold drawing with various  $\eta$ . The structures of Cu-5Fe, Cu-10Fe, Cu-20Fe, and Cu-40Fe are shown in (a1–d1), (a2–d2), (a3–d3), and (a4–d4), respectively. The structures of Cu-Fe alloys under  $\eta$  of 1.26, 2.00, 2.64, and 4.03 are given in (a1–a4), (b1–b4), (c1–c4), and (d1–d4), respectively.



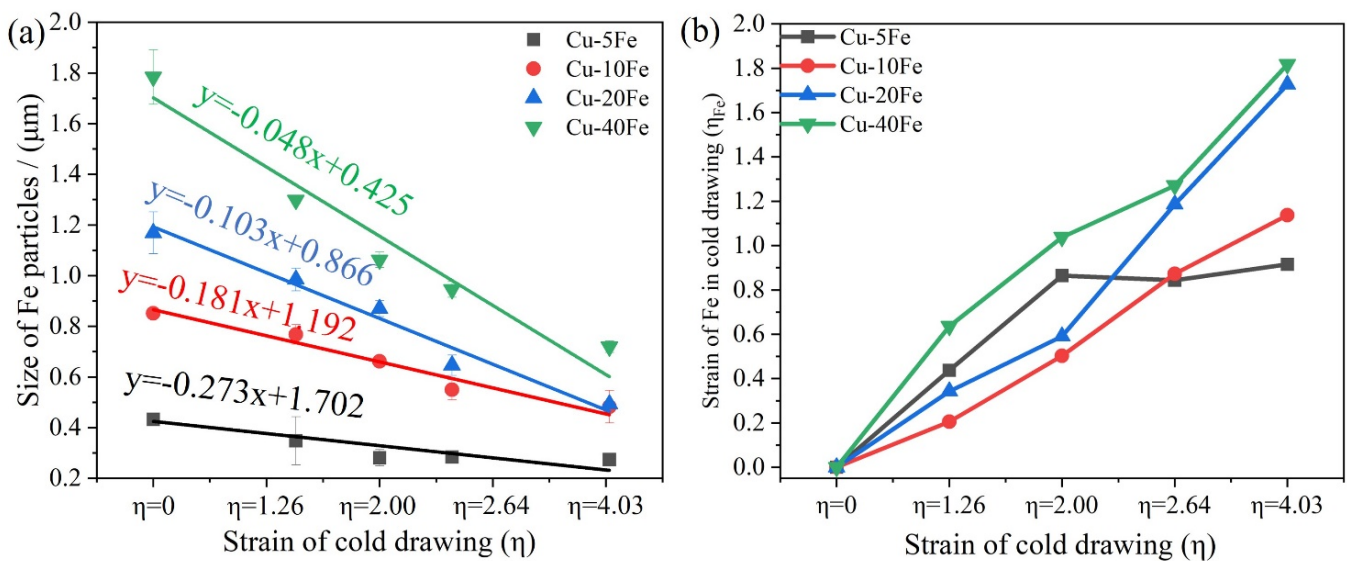


**Figure 7.** (a) The sizes of Fe particles and (b) the deformation strain of Fe particles ( $\eta_{Fe}$ ) in Cu-Fe alloys after the cold drawing with various  $\eta$ .

The tensile stress–strain curves of four Cu-Fe alloys with various  $\eta$  are shown in Figure 8, and the UTS, elongation, and electrical conductivity of the alloys are summarized in Figure 9. With the increase in  $\eta$ , for each Cu-Fe alloy, the UTS increases but the elongation decreases (Figure 9a), which could be ascribed to the reduced Fe fiber spacing and the refined Fe phase size. Note that with the increase in Fe content, the effect of fiber reinforcement is more obvious. That means that the Cu-Fe alloy with a higher Fe content is more suitable for the cold drawing deformation to improve mechanical strength. The Cu-10Fe alloy exhibits the largest elongation among all Cu-Fe alloys (Figure 9b). This may be correlated with the unique morphology of the Fe phase, i.e., slender fibers (Figure 6(d2)), which exhibits a good interface with the Cu matrix. Instead, it is difficult for the spherical or ellipsoidal Fe phase in the Cu-5Fe alloy to deform; thus, cracks may easily nucleate near the interface between the Fe phase and Cu matrix, while irregular-shaped and a vast Fe phase in Cu-20Fe and Cu-40Fe alloys presumably accelerates the propagation of cracks, both leading to the premature cracking of the Cu-Fe alloy. Despite that, with the increase in deformation strain, the elongation of the alloys in the tensile test decreases roughly due to more sessile dislocations stored in the alloy. In terms of the electrical conductivity, it increases gradually as the cold drawing strain increases from 0 to 2.64, but changes randomly as the cold drawing strain increases from 2.64 to 4.03 (Figure 9c).

The dissolved Fe atoms in the Cu matrix can greatly lower the electrical conductivity of alloys. Verhoeven et al. reported that the electrical resistivity increases by  $9.2 \mu\Omega/\text{cm}$  for each 1 wt.% Fe alloying in a Cu matrix [4]. For Cu-Fe alloys, the scattering effect of Fe solute in the Cu matrix and the interface between the Fe phase and Cu matrix are the main factors lowering the electrical conductivity. Note that after the cold drawing, the samples are subjected to heat treatment at  $450 \text{ }^\circ\text{C}$  for 1 h, which greatly improves the electrical conductivity of the alloy. A study by Niu et al. demonstrated that the critical temperature of drastic thermal grooving and rapid grain growth for the layered structure of Cu and Fe is  $500 \text{ }^\circ\text{C}$  [33]. This suggests in the study that the annealing cannot damage the Fe fibers; thus, it will not weaken the strengthening effect of Fe fibers. Meanwhile, annealing can improve the electrical conductivity of the alloy, presumably associated with the precipitation process and the dislocation short-circuit diffusion path of solute atoms [34]. The diffusion coefficients of Fe solute atoms during aging are calculated as [35]

$$D_0 = D_L \cdot (1 - f) + D_P \cdot f \quad (4)$$

where  $D_0$  is the diffusion coefficient,  $D_L$  is the diffusion coefficient of the lattice,  $f$  is the fraction of atoms in the dislocation, and  $D_p$  is the diffusion coefficient in the dislocation. The diffusion coefficient of atoms in the dislocation ( $D_p$ ) is much larger than that in the lattice ( $D_L$ ). After drawing deformation, the dislocations stored in the alloy provide a fast diffusion channel for the precipitation of Fe atoms. In addition, Li et al. reported that the greater the degree of deformation, the lower the activation energy of solute atom precipitation in the alloy [36]. With the gradual increase in cold drawing strain, the activation energy required for the precipitation of Fe solute atoms in the alloy is reduced gradually and it is easier for the precipitation behavior to occur. Therefore, the electrical conductivity increases with the increase in cold drawing strain (Figure 9c). Note that this argument may not work well at the high cold drawing strain of 4.03 (Figure 9c), presumably because of the large-deformation-induced mechanical alloying of Fe atoms from Fe fibers into the Cu matrix [30].

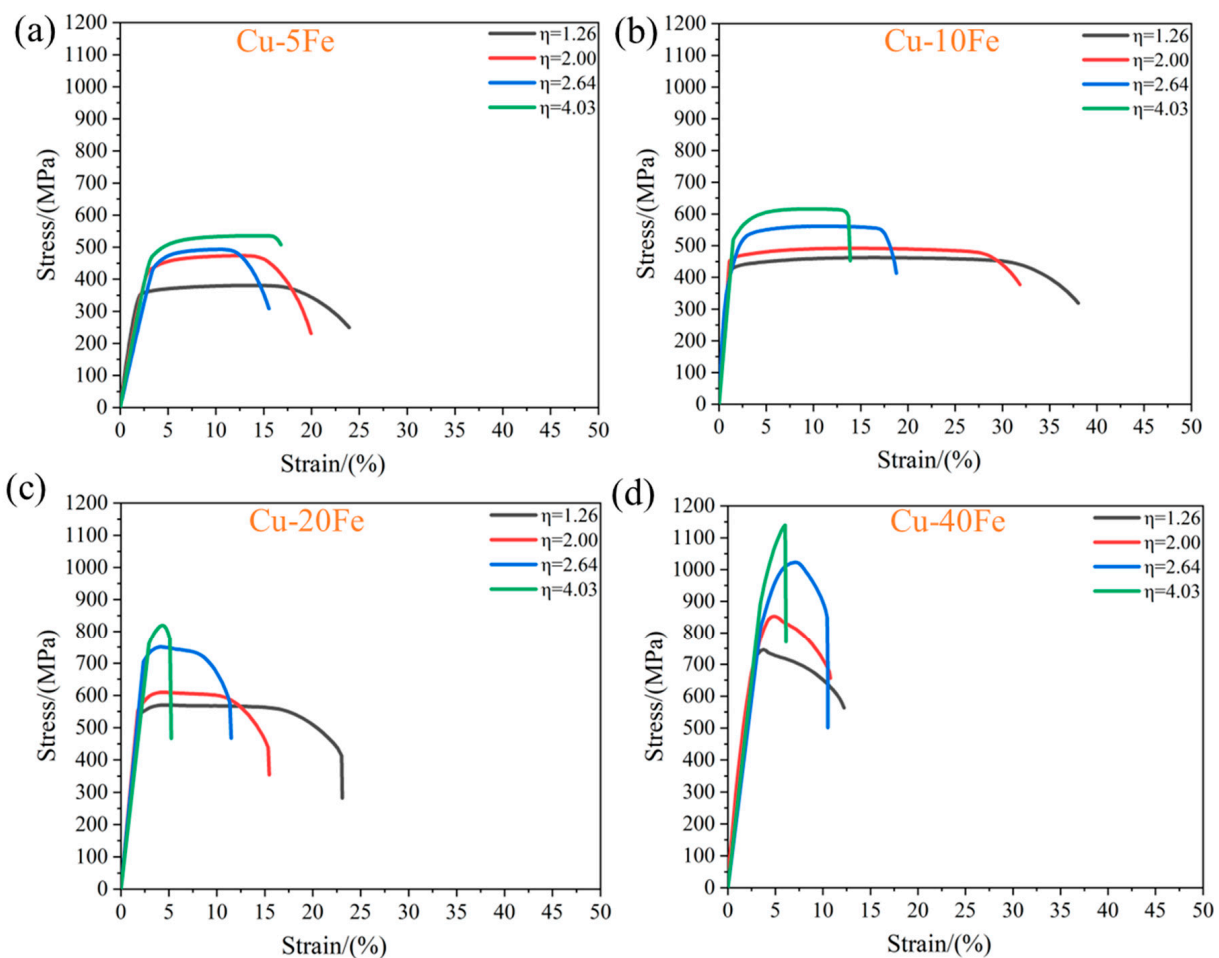


**Figure 8.** Engineering stress–engineering strain curves of Cu-Fe alloys after cold drawing with various  $\eta$ . (a) Cu-5Fe, (b) Cu-10Fe, (c) Cu-20Fe, and (d) Cu-40Fe.



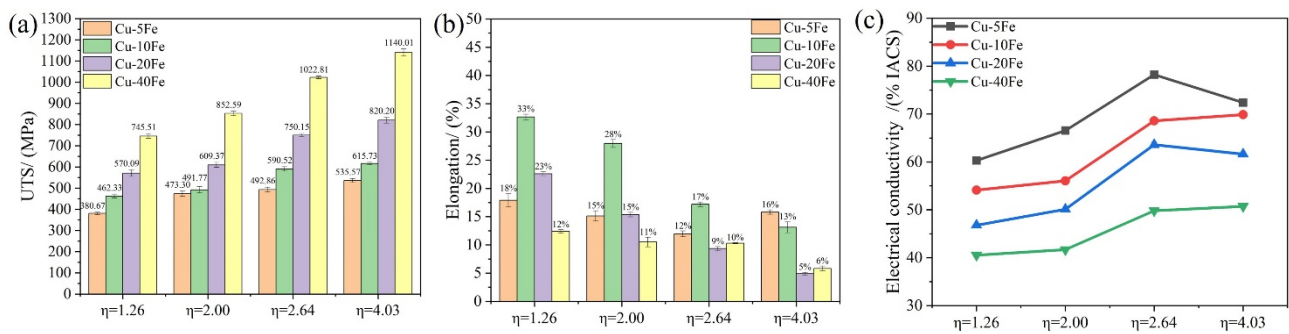


**Figure 9.** (a) The ultimate tensile strength (UTS), (b) elongation, and (c) electrical conductivity (EC) of various Cu-Fe alloys after cold drawing with various  $\eta$ .

### 3.3. Comparison of Properties

Ultimate tensile strength and electrical conductivity are important properties for Cu alloys. Synchronously increasing the mechanical strength and electrical conductivity of Cu alloys has been one of the research hotspots in recent decades. Pang et al. reported that the conductivity of a Cu-5Fe alloy prepared by casting and rolling is 63% IACS and the ultimate tensile strength is 466 MPa [7]. Zhang et al. reported that the conductivity of a Cu-30Fe alloy prepared by powder metallurgy and cold rolling was 38% IACS, and the strength was 826 MPa [37]. These, in combination with the previous studies, reveal a simple law: the Cu-Fe alloy with a low Fe content has a high EC but a low UTS, while the Cu-Fe alloy with a high Fe content tends to have a high UTS but a low EC [6,7,18,19,25,32,37–42].

In this study, a synchronous improvement in EC and UTS is achieved on the Cu-xFe ( $x = 5, 10, 20,$  and  $40$  wt.%) alloy wires, by the combination of the powder metallurgy technique, hot extrusion, cold drawing, and annealing treatments. For the Cu-5Fe alloy, the EC and UTS reach 72% IACS and 536MPa, respectively, while the EC and UTS of the Cu-40Fe alloy are 51% IACS and 1.14 GPa, respectively, which are obviously higher than those of previously reported Cu-Fe alloys with the same composition (Figure 10).

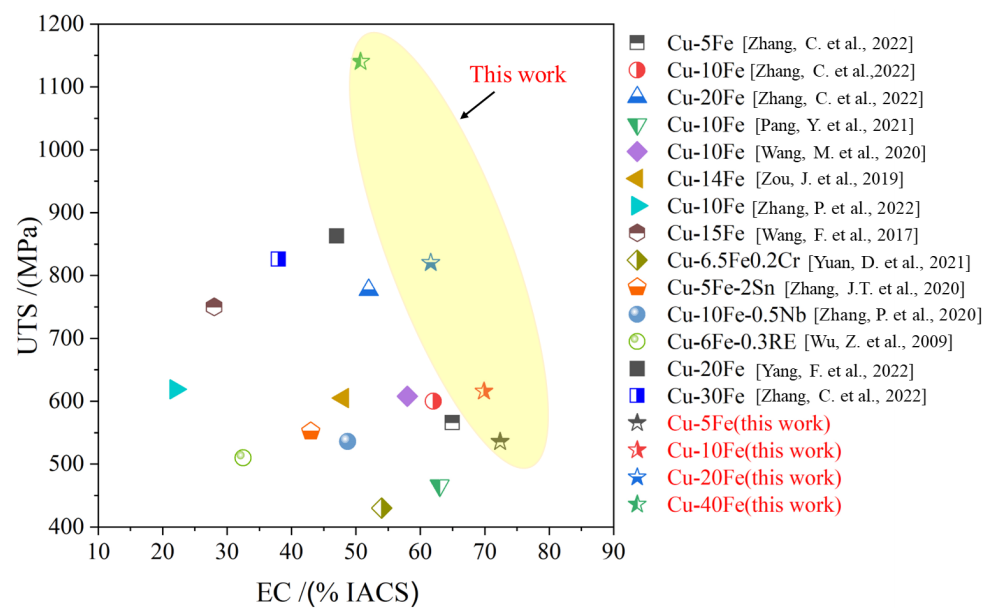


**Figure 10.** The UTS vs. EC map of the Cu-Fe alloys with different Fe contents [6,7,18,19,25,32,38–42].

### 4. Conclusions

In this study, Cu-xFe ( $x = 5, 10, 20,$  and  $40$  wt.%) alloy wires were prepared by powder metallurgy with the process of cold isostatic pressing, vacuum sintering, hot extrusion,

and cold drawing and annealing treatments. The microstructures, mechanical properties, and electrical conductivity of the alloys were analyzed. The conclusions can be drawn as follows:

- (1) The Fe phase in the as-extruded Cu-Fe alloys is uniformly dispersed. However, with the increase in Fe content, the Fe phase size increases, and the morphology of the Fe phase transforms from a discrete spheroid to interconnected water droplets, whose formation mechanism is the typical precipitation and spinodal decomposition, respectively.
- (2) During the cold drawing, the major deformation mechanism of the Fe phase is plastic deformation for Cu-Fe alloys with a low Fe content, while the combination of plastic and fracture deformations should be the dominant mechanism of the Fe phase for Cu-Fe alloys with a high Fe content. As the cold drawing strain increases, the Fe phase spacing is reduced and the Fe phase size is gradually refined, leading to the gradually enhanced mechanical strength of the alloy.
- (3) The combination of the powder metallurgy technique, hot extrusion, cold drawing, and annealing treatments achieves the synchronous improvement in electrical conductivity and mechanical strength of Cu-Fe alloys, which are superior to other reported Cu-Fe alloys.

**Author Contributions:** Conceptualization, Y.L.; methodology, P.Z.; formal analysis, X.Y and J.W.; investigation, X.Y.; writing—original draft preparation, X.Y. and P.Z.; writing—review and editing, Y.L. and B.Y.; supervision, Y.L. and J.W.; project administration, Y.L. All authors have read and agreed to the published version of the manuscript.

**Funding:** This investigation was supported by a grant from the Natural Science Foundation of China (51871244) and the Fundamental Research Funds for the Central Universities of Central South University (1053320190103).

**Institutional Review Board Statement:** Not applicable.

**Informed Consent Statement:** Not applicable.

**Data Availability Statement:** Data available on request from the authors.

**Acknowledgments:** B. Yang wishes to express his gratitude for the support of the China Scholarship Council (202106370122).

**Conflicts of Interest:** The authors declare no conflict of interest.

## References

1. Liu, S.; Jie, J.; Guo, Z.; Yue, S.; Li, T. A comprehensive investigation on microstructure and magnetic properties of immiscible Cu-Fe alloys with variation of Fe content. *Mater. Chem. Phys.* **2019**, *238*, 121909. [CrossRef]
2. Wang, M.; Yang, Q.-R.; Jiang, Y.-B.; Li, Z.; Xiao, Z.; Gong, S.; Wang, Y.-R.; Guo, C.-L.; Wei, H.-G. Effects of Fe content on microstructure and properties of Cu-Fe alloy. *Trans. Nonferrous Met. Soc. China* **2021**, *31*, 3039–3049. [CrossRef]
3. Biselli, C.; Morris, D. Microstructure and strength of Cu-Fe in Situ composites after very high drawing strains. *Acta Mater.* **1996**, *44*, 493–504. [CrossRef]
4. Verhoeven, J.D.; Chueh, S.C.; Gibson, E.D. Strength and conductivity of in situ Cu-Fe alloys. *J. Mater. Sci.* **1989**, *24*, 1748–1752. [CrossRef]
5. Jerman, G.A.; Anderson, I.E.; Verhoeven, J.D. Strength and electrical conductivity of deformation-processed Cu-15 Vol Pct Fe alloys produced by powder metallurgy techniques. *Met. Trans. A* **1993**, *24*, 35–42. [CrossRef]
6. Zhang, P.; Lei, Q.; Yuan, X.; Sheng, X.; Jiang, D.; Li, Y.; Li, Z. Microstructure and mechanical properties of a Cu-Fe-Nb alloy with a high product of the strength times the elongation. *Mater. Today Commun.* **2020**, *25*, 101353. [CrossRef]
7. Pang, Y.; Chao, G.; Luan, T.; Gong, S.; Wang, Y.; Jiang, Z.; Xiao, Z.; Jiang, Y.; Li, Z. Microstructure and properties of high strength, high conductivity and magnetic Cu-10Fe-0.4Si alloy. *Mater. Sci. Eng. A* **2021**, *826*, 142012. [CrossRef]
8. Wang, M.; Zhang, R.; Xiao, Z.; Gong, S.; Jiang, Y.; Li, Z. Microstructure and properties of Cu-10 wt%Fe alloy produced by double melt mixed casting and multi-stage thermomechanical treatment. *J. Alloys Compd.* **2020**, *820*, 153323. [CrossRef]
9. Li, Y.; Yuan, X.; Yang, B.; Ye, X.; Zhang, P.; Lang, H.; Lei, Q.; Liu, J.; Li, Y. Hierarchical microstructure and strengthening mechanism of Cu-36.8Fe alloy manufactured by selective laser melting. *J. Alloys Compd.* **2022**, *895*, 162701. [CrossRef]
10. Ratke, L.; Diefenbach, S. Liquid immiscible alloys. *Mater. Sci. Eng. R Rep.* **1995**, *15*, 263–347. [CrossRef]

11. Ohnuma, I.; Saegusa, T.; Takaku, Y.; Wang, C.; Liu, X.; Kainuma, R.; Ishida, K. Microstructural Evolution of Alloy Powder for Electronic Materials with Liquid Miscibility Gap. *J. Electron. Mater.* **2009**, *38*, 2–9. [CrossRef]
12. Zhang, S.; Wang, F.; Huang, P. Enhanced Hall-Petch strengthening in graphene/Cu nanocomposites. *J. Mater. Sci. Technol.* **2021**, *87*, 176–183. [CrossRef]
13. Hansen, N. Hall-Petch relation and boundary strengthening. *Scr. Mater.* **2004**, *51*, 801–806. [CrossRef]
14. Huang, J.; Xiao, Z.; Dai, J.; Li, Z.; Jiang, H.; Wang, W.; Zhang, X. Microstructure and Properties of a Novel Cu-Ni-Co-Si-Mg Alloy with Super-high Strength and Conductivity. *Mater. Sci. Eng. A* **2019**, *744*, 754–763. [CrossRef]
15. Li, Y.; Tao, N.; Lu, K. Microstructural evolution and nanostructure formation in copper during dynamic plastic deformation at cryogenic temperatures. *Acta Mater.* **2008**, *56*, 230–241. [CrossRef]
16. Song, J.; Hong, S. Strength and electrical conductivity of Cu-9Fe-1.2Co filamentary microcomposite wires. *J. Alloys Compd.* **2000**, *311*, 265–269. [CrossRef]
17. Hong, S.; Song, J.; Kim, H. Thermo-mechanical processing and properties of Cu-9Fe-1.2Co microcomposite wires. *Scr. Mater.* **2001**, *45*, 1295–1300. [CrossRef]
18. Zou, J.; Lu, D.-P.; Fu, Q.-F.; Liu, K.-M.; Jiang, J. Microstructure and properties of Cu-Fe deformation processed in-situ composite. *Vacuum* **2019**, *167*, 54–58. [CrossRef]
19. Wang, F.; Wakoh, K.; Li, Y.; Ito, S.; Yamanaka, K.; Koizumi, Y.; Chiba, A. Study of microstructure evolution and properties of Cu-Fe microcomposites produced by a pre-alloyed powder method. *Mater. Des.* **2017**, *126*, 64–72. [CrossRef]
20. Gao, H.; Wang, J.; Shu, D.; Sun, B. Effect of Ag on the microstructure and properties of Cu-Fe in situ composites. *Scr. Mater.* **2005**, *53*, 1105–1109. [CrossRef]
21. Shi, R.; Wang, C.; Wheeler, D.; Liu, X.; Wang, Y. Formation mechanisms of self-organized core/shell and core/shell/corona microstructures in liquid droplets of immiscible alloys. *Acta Mater.* **2013**, *61*, 1229–1243. [CrossRef]
22. Wang, Y.; Gao, H.; Han, Y.; Dai, Y.; Wang, J.; Sun, B. First-principles study on the solubility of iron in dilute Cu-Fe-X alloys. *J. Alloys Compd.* **2017**, *691*, 992–996. [CrossRef]
23. Liu, S.; Jie, J.; Dong, B.; Guo, Z.; Wang, T.; Li, T. Novel insight into evolution mechanism of second liquid-liquid phase separation in metastable immiscible Cu-Fe alloy. *Mater. Des.* **2018**, *156*, 71–81. [CrossRef]
24. Yuan, D.; Zeng, H.; Xiao, X.; Wang, H.; Han, B.; Liu, B.; Yang, B. Effect of Mg addition on Fe phase morphology, distribution and aging kinetics of Cu-6.5Fe alloy. *Mater. Sci. Eng. A* **2021**, *812*, 141064. [CrossRef]
25. Zhang, P.; Yuan, X.; Li, Y.; Zhou, Y.; Lai, R.; Li, Y.; Lei, Q.; Chiba, A. Influence of minor Ag addition on the microstructure and properties of powder metallurgy Cu-10 wt% Fe alloy. *J. Alloys Compd.* **2022**, *904*, 163983. [CrossRef]
26. Thanh, N.T.K.; Maclean, N.; Mahiddine, S. Mechanisms of Nucleation and Growth of Nanoparticles in Solution. *Chem. Rev.* **2014**, *114*, 7610–7630. [CrossRef]
27. Bonvalet, M.; Sauvage, X.; Blavette, D. Intragranular nucleation of tetrahedral precipitates and discontinuous precipitation in Cu-5wt%Ag. *Acta Mater.* **2019**, *164*, 454–463. [CrossRef]
28. Cahn, J.W. On spinodal decomposition. *Acta Met.* **1961**, *9*, 795–801. [CrossRef]
29. Emo, J.; Pareige, C.; SAILLET, S.; Domain, C.; Pareige, P. Kinetics of secondary phase precipitation during spinodal decomposition in duplex stainless steels: A kinetic Monte Carlo model—Comparison with atom probe tomography experiments. *J. Nucl. Mater.* **2014**, *451*, 361–365. [CrossRef]
30. Stepanov, N.; Kuznetsov, A.; Salishchev, G.; Khlebova, N.; Pantsyrny, V. Evolution of microstructure and mechanical properties in Cu-14%Fe alloy during severe cold rolling. *Mater. Sci. Eng. A* **2013**, *564*, 264–272. [CrossRef]
31. Guo, J.; Shao, Q.; Renk, O.; Li, L.; He, Y.; Zhang, Z.; Pippin, R. Combined Fe and O effects on microstructural evolution and strengthening in Cu-Fe nanocrystalline alloys. *Mater. Sci. Eng. A* **2020**, *772*, 138800. [CrossRef]
32. Zhang, C.; Chen, C.; Liu, X.; Yan, M.; Qi, M.; Li, X.; Li, Y.; Zhang, H.; Yang, F.; Wang, W.; et al. High strength and high electrical conductivity in Cu-Fe alloys with nano and micro Fe particles. *Mater. Sci. Eng. A* **2022**, *855*, 143948. [CrossRef]
33. Niu, T.; Zhang, Y.; Cho, J.; Li, J.; Wang, H.; Zhang, X. Thermal stability of immiscible Cu-Ag/Fe triphase multilayers with triple junctions. *Acta Mater.* **2021**, *208*, 116679. [CrossRef]
34. Humphreys, F.J.; Hirsch, P.B. The deformation of single crystals of copper and copper-zinc alloys containing alumina particles—II. Microstructure and dislocation-particle interactions. *Proc. R. Soc. Lond. Ser. A Math. Phys. Sci.* **1970**, *318*, 73–92. [CrossRef]
35. Yu, Y.; Wang, C.; Liu, X.; Kainuma, R.; Ishida, K. Thermodynamics and kinetics in liquid immiscible Cu-Cr-Si ternary system. *Mater. Chem. Phys.* **2011**, *127*, 28–39. [CrossRef]
36. Li, Y.; Yang, B.; Zhang, P.; Nie, Y.; Yuan, X.; Lei, Q.; Li, Y. Cu-Cr-Mg alloy with both high strength and high electrical conductivity manufactured by powder metallurgy process. *Mater. Today Commun.* **2021**, *27*, 102266. [CrossRef]
37. Zhang, C.; Chen, C.; Li, P.; Yan, M.; Qin, Q.; Yang, F.; Wang, W.; Guo, Z.; Volinsky, A.A. Microstructure and properties evolution of rolled powder metallurgy Cu-30Fe alloy. *J. Alloys Compd.* **2022**, *909*, 164761. [CrossRef]
38. Wang, M.; Jiang, Y.; Li, Z.; Xiao, Z.; Gong, S.; Qiu, W.; Lei, Q. Microstructure evolution and deformation behaviour of Cu-10 wt%Fe alloy during cold rolling. *Mater. Sci. Eng. A* **2020**, *801*, 140379. [CrossRef]
39. Yuan, D.; Xiao, X.; Chen, J.; Han, B.; Huang, H.; Yang, B. Influence of Ag addition on the microstructure and properties of Cu-6.5Fe-0.2Cr alloy prepared by upward continuous casting. *J. Alloys Compd.* **2021**, *887*, 161458. [CrossRef]
40. Yang, F.; Dong, L.; Zhou, L.; Zhang, N.; Zhou, X.; Zhang, X.; Fang, F. Excellent strength and electrical conductivity achieved by optimizing the dual-phase structure in Cu-Fe wires. *Mater. Sci. Eng. A* **2022**, *849*, 143484. [CrossRef]

41. Wu, Z.; Zhang, J.; Chen, Y.; Meng, L. Effect of rare earth addition on microstructural, mechanical and electrical characteristics of Cu-6%Fe microcomposites. *J. Rare Earths* **2009**, *27*, 87–91. [CrossRef]
42. Zhang, J.T.; Lin, J.; Wang, Q.; Du, X.L.; Wang, Y.H. Recrystallization behaviour during annealing of cold-rolled Cu-5Fe-2Sn alloy. *Mater. Sci. Technol.* **2020**, *36*, 1162–1168. [CrossRef]

**Disclaimer/Publisher's Note:** The statements, opinions and data contained in all publications are solely those of the individual author(s) and contributor(s) and not of MDPI and/or the editor(s). MDPI and/or the editor(s) disclaim responsibility for any injury to people or property resulting from any ideas, methods, instructions or products referred to in the content.

Article

# Microstructural Considerations of a Multi-Pass Rolled Ti-Nb-Ta-Zr Alloy

Doina Răducanu <sup>1</sup>, Anna Nocivin <sup>2</sup>, Vasile Dănuț Cojocaru <sup>1</sup>, Nicolae Șerban <sup>1</sup>, Nicoleta Zărnescu-Ivan <sup>1</sup>, Raluca Elena Irimescu <sup>1,\*</sup> and Bogdan Mihai Gălbinașu <sup>3</sup>

<sup>1</sup> Department of Metallic Materials Processing and Environmental Engineering, University Politehnica of Bucharest, 060042 Bucharest, Romania; doina.raducanu@upb.ro (D.R.); dan.cojocaru@upb.ro (V.D.C.); nicolae.serban@upb.ro (N.Ș.); nicoleta.zarnescu@upb.ro (N.Z.-I.)

<sup>2</sup> Faculty of Mechanical, Industrial and Maritime Engineering, Ovidius University of Constanta, 900527 Constanța, Romania; anocivin@univ-ovidius.ro

<sup>3</sup> Dental Medicine Faculty, University of Medicine and Pharmacy “Carol Davila” Bucharest, 020021 Bucharest, Romania; bogdan.galbinașu@umfcd.ro

\* Correspondence: raluca.irimescu@stud.sim.upb.ro; Tel.: +40-21-402-9531

**Abstract:** The microstructural characteristic evolution was investigated during thermomechanical processing of Ti-29Nb-9Ta-10Zr (wt %) alloy, which consisted of, in a first stage, in a Multi-Pass Rolling with increasing thickness reduction of 20%, 40%, 60%, 80%, and 90%; in step two, the multi-pass rolled sample with the highest thickness reduction (90%) was subjected to a series of three variants of static short recrystallization and then to a final similar aging. The objective was to evaluate the microstructural features evolution during thermomechanical processing (phase's nature, morphology, dimensions, and crystallographic characteristics) and to find the optimal heat treatment variant for refinement of the alloy granulation until ultrafine/nanometric level for a promising combination of mechanical properties. The microstructural features were investigated by X-ray diffraction and SEM techniques through which the presence of two phases was recorded: the  $\beta$ -Ti phase and the  $\alpha''$ -Ti martensitic phase. The corresponding cell parameters, dimensions of the coherent crystallite and the micro-deformations at the crystalline network level for both recorded phases were determined. The majority  $\beta$ -Ti phase underwent a strong refinement during the Multi-Pass Rolling process until ultrafine/nano grain dimension (about 9.8 nm), with subsequent slow growing during recrystallization and aging treatments, hindered by the presence of sub-micron  $\alpha''$ -Ti phase dispersed inside  $\beta$ -Ti grains. An analysis concerning the possible deformation mechanisms was performed.

**Keywords:** beta-titanium alloys; multi-pass rolling; recrystallization; XRD; SEM



**Citation:** Răducanu, D.; Nocivin, A.; Cojocaru, V.D.; Șerban, N.; Zărnescu-Ivan, N.; Irimescu, R.E.; Gălbinașu, B.M. Microstructural Considerations of a Multi-Pass Rolled Ti-Nb-Ta-Zr Alloy. *Materials* **2023**, *16*, 3208. <https://doi.org/10.3390/ma16083208>

Academic Editors: Seong-Ho Ha, Shae-Kwang Kim and Hyun-Kyu Lim

Received: 13 March 2023

Revised: 5 April 2023

Accepted: 12 April 2023

Published: 19 April 2023



**Copyright:** © 2023 by the authors. Licensee MDPI, Basel, Switzerland. This article is an open access article distributed under the terms and conditions of the Creative Commons Attribution (CC BY) license (<https://creativecommons.org/licenses/by/4.0/>).

## 1. Introduction

For hard tissue replacement, titanium and its alloys represent an important metallic biomaterial due to its excellent biocompatibility and high mechanical strength, comparable to that of cobalt alloys or stainless steel, but with low Young modulus that favors the reducing of the well-known “stress shielding effect” [1–3]. For permanent bone implants that require high strength coupled with low elastic modulus, the  $\beta$ -type titanium alloys are most appreciated among other two possible types,  $\alpha$ - or  $\alpha/\beta$ -type Ti-alloys [4–7]. Therefore,  $\beta$ -Titanium alloys with non-toxic Nb, Ta, and Zr alloying elements are of maximum interest nowadays [1,2,8–10]. The TNTZ (Ti-Nb-Ta-Zr) alloys represent an appreciated selection of  $\beta$ -Ti alloys not only for their non-toxic and biocompatibility character, but also for good  $\beta$ -stabilizing capacity of alloying elements which is required knowing that the single  $\beta$ -phase structure has an easier ability for mechanical processing [11,12]. The  $\beta$ -stabilizing character of niobium has been well known for a long time [9,10]. The same applies for the tantalum [13,14]. Regarding zirconium, even if it is classified as a neutral alloying element, it can favor the stabilization of the  $\beta$  phase in the presence of  $\beta$  stabilizers [15], in this



case Nb and Ta. Also, the toughness of titanium alloys can be increased by zirconium, as niobium does [16,17], and the association of both, niobium and zirconium, facilitate a decrease of the elastic modulus [2]; finally, the suppression of the formation of the omega phase assured by zirconium presence [18] represents another important benefit of TNTZ alloys. Thus, referring entirely to the improvement of the mechanical biocompatibility of  $\beta$ -type TNTZ alloys, apart from the above chemical composition, one of the most used and recognized as beneficial methods is the thermomechanical processing, which includes, among others, the grain refinement of the alloy to ultrafine or even nanometer dimensions [3,19–21]; this nanometric structure can assure the alloy necessary bio-structural and bio-mechanical properties dictated by particular implant destination/localization and by other mechanical and biochemical demands. A single  $\beta$ -phase structure has an easy ability for mechanical processing, and can achieve a low elastic modulus, but with a moderate mechanical strength [20,22–24]; generally, the obtained elastic modulus can be around 55 GPa, which is a satisfactory value comparative to that for cortical bone of about 30–35 GPa [25], but with not-so-high strength, generally not exceeding 550 MPa, which may be insufficient for hip implant applications [14]. For higher strength values, a suitable way may be a structural combination of two phases [26,27]: the majority  $\beta$  phase and a small amount of orthorhombic  $\alpha''$  martensitic phase, depending on the  $\beta$ -phase stability, sufficient to ensure a desirable increase in the mechanical strength of the  $\beta$  phase, but with keeping the low modulus of elasticity through a controllable dispersion, dimension, and quantity of  $\alpha''$  phase [12,28–30]. Comparative to hexagonal- $\alpha'$  martensitic phase or to  $\omega$  phase, the orthorhombic- $\alpha''$  martensitic phase has the lowest Young modulus [18], even comparable to that of the  $\beta$  phase [31], but with the possibility of strength enhancing.

Thus, it follows that, by combining the two aspects, i.e., the creation of a structure consisting of  $\beta$  phase with a small/controllable amount of orthorhombic martensitic  $\alpha''$  phase, on the one hand, and the refinement of the structure granulation, on the other hand, an efficient method can result for improving the mechanical biocompatibility of TNTZ alloys. The present study follows this objective and proposes for the experimental program the Ti-29Nb-9Ta-10Zr (wt %) alloy, that is, part of the  $\beta$ -type TNTZ system which has been shown the most appreciated results regarding good biocompatibility and low Young modulus [32,33]. The chemical composition has been selected based on the abovementioned considerations regarding the influence of Nb, Ta, and Zr as alloying elements; thus, to ensure a high stability of  $\beta$  phase, the related literature reports the following necessary intervals: Nb between 20 and 40 wt %, Ta between 7 and 13 wt %, and Zr between 3 and 10 wt % [12,34–36]. The selection of the proposed chemical composition also took into account the promising results of already-experimented alloys with close chemical compositions: Ti-29Nb-13Ta-4.6Zr [7], Ti-30Nb-6Zr-5Ta [7,21], Ti-36Nb-2Ta-3Zr-0.3O [22], Ti-29Nb-13Ta-5Zr [37], and Ti-35Nb-3Zr-2Ta [38].

As concerning obtaining an efficient grain refinement combined with a controllable stress-induced martensitic phase formation, in general, one of the severe plastic deformations (SPD) methods can be applied: *multi-pass rolling* (MPR), *accumulative roll bonding* (ARB), *equal-channel angular pressing* (ECAP), and *high-pressure torsion* (HPT) [39–42]. The desired grain refinement can be achieved through one or more SPD structural mechanisms such as dislocation slip, twinning, and *stress-induced martensite* (SIM) formation [36,43], depending on the stability of the  $\beta$  phase and of the deformation extent [39,40,44]. For the present study, the MPR method has been selected as a part of a complex thermomechanical process proposed for experiments together with a static short recrystallization and aging treatments capable of obtaining ultrafine/nanometric grains with an optimal combination of mechanical properties. Consequently, the aim of the present study is to examine the effects of MPR severe plastic deformation in conjunction with some heat treatments (recrystallization and aging) on the evolution of the Ti-29Nb-9Ta-10Zr alloy microstructure through XRD analysis and SEM visualizations.

## 2. Materials and Methods

The experimental program (Figure 1) comprises the following stages: the obtaining of the initial sample—S-1, with the proposed chemical composition necessary to perform the multi-pass rolling (MPR) procedure; the applying of the MPR process to the initial stage with increasing deformation degree using a total thickness reduction of 20%, 40%, 60%, 80%, and 90% in order to reduce the grain size step-by-step, until ultrafine/nanometric size, by severe plastic deformation; the applying of a series of short recrystallizations and aging treatments on the highest deformed sample (90%) in order to study the process of microstructure remodeling after a heavy deforming and hardening of the sample; the microstructural analysis of all experimented stages through XRD analysis and SEM visualizations in order to establish the phase nature changing with all dimensional and morphological evolutions.

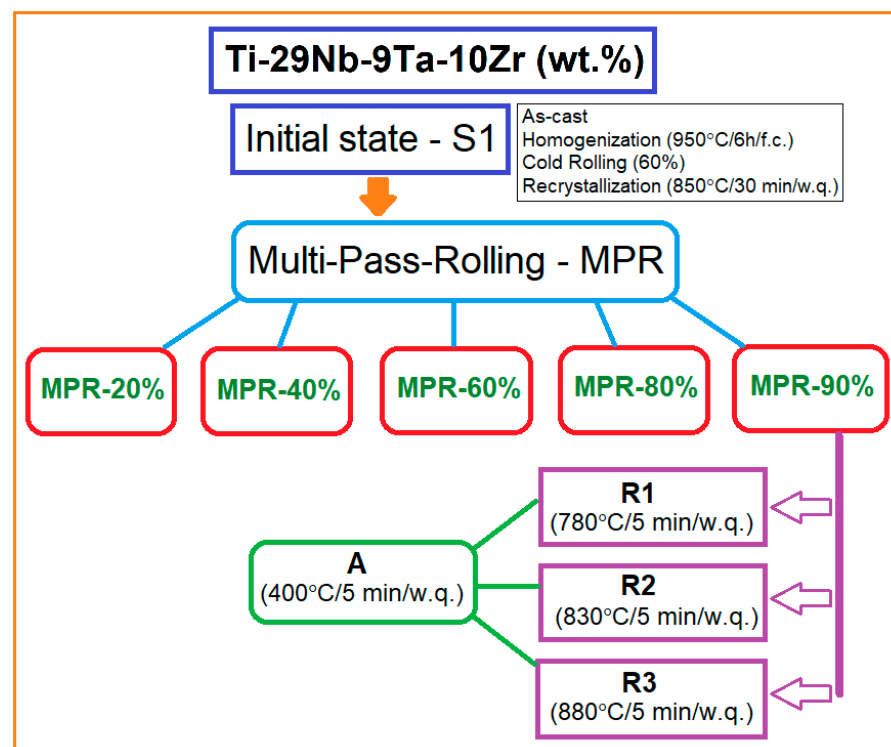


**Figure 1.** The experimental thermomechanical processing schema of the studied Ti-29Nb-9Ta-10Zr (wt %) alloy.

The proposed alloy for the experimental program has the following chemical composition (wt %): Titanium—52%; Niobium—29%; Tantalum—9%; Zirconium—10%. Considering that the elements amount with  $\beta$ -stabilizing character represents almost one half of the entire composition, it is expected that the structure of the studied alloy can be included in the class of near-beta titanium alloys. This aspect will be analysed by XRD envisaged analysis. The obtaining of the initial sample lot (S-1) of the studied alloy starts from high-purity elemental components and comprises the following stages: the alloy synthesis in a levitation induction melting furnace, FIVE CELES—MP25 (Five’s Group Company, Paris, France), with a nominal power of 25 kW, melting capacity of 30 cm<sup>3</sup>, and using a high vacuum of 10<sup>-4</sup>–10<sup>-5</sup> mbar. Then, the obtained sample lot in as-cast condition was subjected to a homogenisation treatment at 1223 K (950 °C) with holding time of 6 h, followed by furnace cooling for obtaining a homogeneous structure without casting defects. After that, for refinement of the coarse homogenised microstructure, a plastic deformation by cold rolling was applied with a total thickness reduction of about 60%. Finally, prior to the multi-pass rolling (MPR) procedure, a completely alloy recrystallization was performed

at 1123 K (850 °C)/30 min/water quenching (w.q.). The whole above thermo-mechanical processing route applied for obtaining the S-1 structural state has been established based on prior results [45–47]. The cold rolling was applied using a Mario di Maio LQR120AS rolling mill (Mario di Maio Inc., Milano, Italy) with a 3 m/min rolling speed and no lubrication; before this procedure, the homogenized alloy was cleaned using an ultrasonic bath at 60 °C in ethylic alcohol. The applied heat treatments were realized in a GERO SR 100 × 500-type oven (Carbolite-Gero Inc., Neuhausen, Germany) under a high vacuum.

The MPR process of the above-established S-1, measuring 20 mm × 20 mm × 60 mm, was applied using the same Mario di Maio LQR120AS rolling mill with a 3 m/min rolling speed and no lubrication. The total reduction degree ( $\epsilon_{\text{tot}}$ ) for each of five applied steps was successively increased from 20% to 40%, 60%, 80%, and finally 90%. For each of these variants, the MPR process was performed with a reduction of 10% per pass.

The samples processed by MPR with  $\epsilon_{\text{tot}} = 90\%$  were subjected to a series of three variants of static short recrystallization, R1 (780 °C/5 min/w.q.), R2 (830 °C/5 min/w.q.), and R3 (880 °C/5 min/w.q.), and a final aging-A (400 °C/5 min/w.q.) similar for all recrystallization variants (R1 + A; R2 + A; R3 + A) in order to find the optimal variant for reforming the strong deformed shape of the grain in an equiaxial one by kipping as much as possible the obtained ultrafine/nanometric size of the grains. The same GERO SR 100 × 500-type oven (Carbolite-Gero Inc., Neuhausen, Germany) under a high vacuum as for the homogenization treatment was used for these heat treatments too; the rate of temperature increase was about 15 °C/s.

The microstructural features evolution was highlighted through X-ray diffraction (XRD) analysis completed with scanning electron microscopy (SEM) analysis. The XRD analysis was performed at room temperature using a Philips PW 3710 diffractometer, with Cu K $\alpha$ 12 radiation source), and with a scanning interval in the range of 30–90° for the 2 $\theta$  (°) using a step size of 0.02°. The rolling direction was set to be parallel to the direction of X-rays projected onto the sample surface. The main objective of this analysis was to determine the formed phases with their crystallographic characteristics. Therefore, the recorded XRD patterns were simulated and fitted. For the XRD pattern simulation has been used the MAUD v2.33 software package, by which the phase lattice parameters were calculated. The fitting procedure was performed using the PeakFit v4.12 software package for determining the position and intensity of each peak, and the peak broadening—FWHM (*Full Width at Half Maximum*). It must be mentioned that, in the fitting procedure, a pseudo-Voigt diffraction line profile was used.

The microstructural analysis was completed by scanning electron microscopy (SEM) visualization using a SEM microscope—TESCANVEGA II—XMU (Tescan Orsay Holding, Brno, Czech Republic). For better observing the evolution of the grain texturing/deformation, the MPR samples were examined mainly in the RD–ND cross section (RD—rolling direction; ND—normal direction).

For preparing the metallographic samples for microscopically observation and the test surfaces for XRD, the following stages were applied: the alloy cutting using a Metkon MICRACUT 200-type machine (Metkon Instruments Inc., Bursa, Turkey) with diamond cutting disks; the fixing of the obtained specimens on a specific epoxy resin of a Buehler Sampl-Kwick type, abraded with 1200-grit SiC paper using a Metkon Digi prep ACCURA machine (Metkon Instruments Inc., Bursa, Turkey); the mechanical polishing of the obtained metallographic samples using 6, 3, and 1  $\mu\text{m}$  polycrystalline diamond suspension first, and 0.03  $\mu\text{m}$  colloidal silica secondly, on a Buehler VibroMet2 machine (Buehler Ltd., Lake Bluff, IL, USA).

### 3. Results and Discussion

The microstructural characterization of the studied Ti-29Nb-9Ta-10Zr (wt %) alloy was made based on X-ray diffraction analysis and SEM imaging. All resulted data were discussed and compared for evaluating the structural stability of the majority  $\beta$ -solid solution, the grain-refinement capability during the applied MPR process of deforma-

tion, and the grain morphology evolution during the short recrystallizations and aging applied afterwards.

In order to ensure a complete analysis of the microstructural characteristics of the tested samples, it was considered useful to determine the two characteristic temperatures, important for a  $\beta$ -type titanium alloy: the  $\beta$ -transus temperature— $T_\beta$  and the starting temperature of the martensitic transformation— $M_s$ .

Considering the temperature  $T_\beta$ , it strongly depends on the type of alloying elements used,  $\alpha$ -stabilizers or  $\beta$ -stabilizers, since the former increase  $T_\beta$  and the others decrease  $T_\beta$ . Neutral elements have no influence on  $T_\beta$  [48]. Consequently, for the determination of  $T_\beta$ , the established equation from [49] was applied, based on which it results that  $T_\beta = 813^\circ\text{C}$  for the currently studied alloy.

Referring to the second characteristic temperature— $M_s$ , it can be calculated depending on the alloy composition using the equation in [50], a special formula that was determined with particular reference to  $\beta$ -Ti alloys with high  $\beta$  stability. By applying this formula, it follows that  $M_s = -40^\circ\text{C}$  for the currently studied alloy.

### 3.1. The Phase Analysis Resulted from X-ray Diffraction Investigation

The investigations and analysis by XRD diffraction were made on all experimented samples, beginning with the initial state one (S-1) and continuing with samples obtained after each MPR stage, then after MPR (90%) plus three different variants of recrystallization (R1, R2, and R3), and, finally, after MPR (90%) with three recrystallizations and a similar aging (R1 + A; R2 + A; R3 + A). All obtained XRD patterns were fitted to deconvolute observed cumulative diffraction peaks and to obtain for each constitutive peak its position, intensity, and broadening. Figures 2 and 3 present the recorded XRD patterns; in addition, the Supplementary Materials present the detailed zooms of cumulative diffraction peaks and the Rietveld plots for all examined samples (Figures S1–S12).

For all analyzed samples, the presence of two phases in variable proportions,  $\beta$ -Ti solid solution and  $\alpha''$ -Ti martensitic phase, can be observed as a microstructural common denominator. No other secondary phases were recorded. By indexing, it results that the  $\beta$ -Ti phase corresponds to the body-centered cubic (bcc) system— $Im\text{-}3m$  space group, and the  $\alpha''$ -Ti phase corresponds to the orthorhombic system— $Cmcm$  space group. For both presented phases, the corresponding lattice parameters ( $a$  for  $\beta$  phase, and  $a, b, c$  for  $\alpha''$  phase) were calculated based on data corresponding to peaks' position; the obtained data are indicated in Table 1.

The major diffraction peaks observed for the  $\beta$ -Ti phase are (110) and (211), and for the  $\alpha''$ -Ti phase major peaks are (020), (002), (220), and (202). To better highlight these observations, detailed zooms of cumulative diffraction peaks corresponding to  $2\theta = (37\text{--}40^\circ)$  and  $2\theta = (68\text{--}72^\circ)$  scattering angles were realized for all samples (Figures 2 and 3). For the magnified interval  $2\theta = (37\text{--}40^\circ)$  of scattering domain, the sequence order of the cumulative indexed peaks is:  $\alpha''(020)\text{--}\beta(110)\text{--}\alpha''(002)$ ; for the second magnified interval  $2\theta = (68\text{--}72^\circ)$  of scattering domain, the sequence is  $\alpha''(220)\text{--}\beta(211)\text{--}\alpha''(202)$ .

As concerning the intensities of the major diffraction peaks, those corresponding to  $\beta$ -solid solution are evidently much higher than for the martensitic  $\alpha''$  phase, showing by this the stability of  $\beta$  phase and its majority presence. Another interesting aspect concerns the dominant  $\beta$ -phase peak intensities, the (110) and (211) peaks, observed for all experimented variants: the strongest peak among the  $\beta$  planes in all samples is the (110) peak constantly, followed by the (211) peak. It is well known that the common rolling textures of strong  $\{001\}_\beta \langle 110 \rangle_\beta$  and weak  $\{211\}_\beta \langle 110 \rangle_\beta$  for body-centered cubic (bcc) metals are formed by cold rolling [51]; however, the (211) peak becomes, vice versa, greater than (110) for the sample MPR 90% + R1, indicating by this that the texture is changed in this case, a phenomenon which could be correlated with the heating temperature applied for R1 ( $780^\circ\text{C}$ ), which is lower than the  $\beta$ -transus temperature determined above ( $813^\circ\text{C}$ ); for the following two recrystallizations, the heating temperatures are higher than  $\beta$ -transus ( $830^\circ\text{C}$  and  $880^\circ\text{C}$ , respectively).

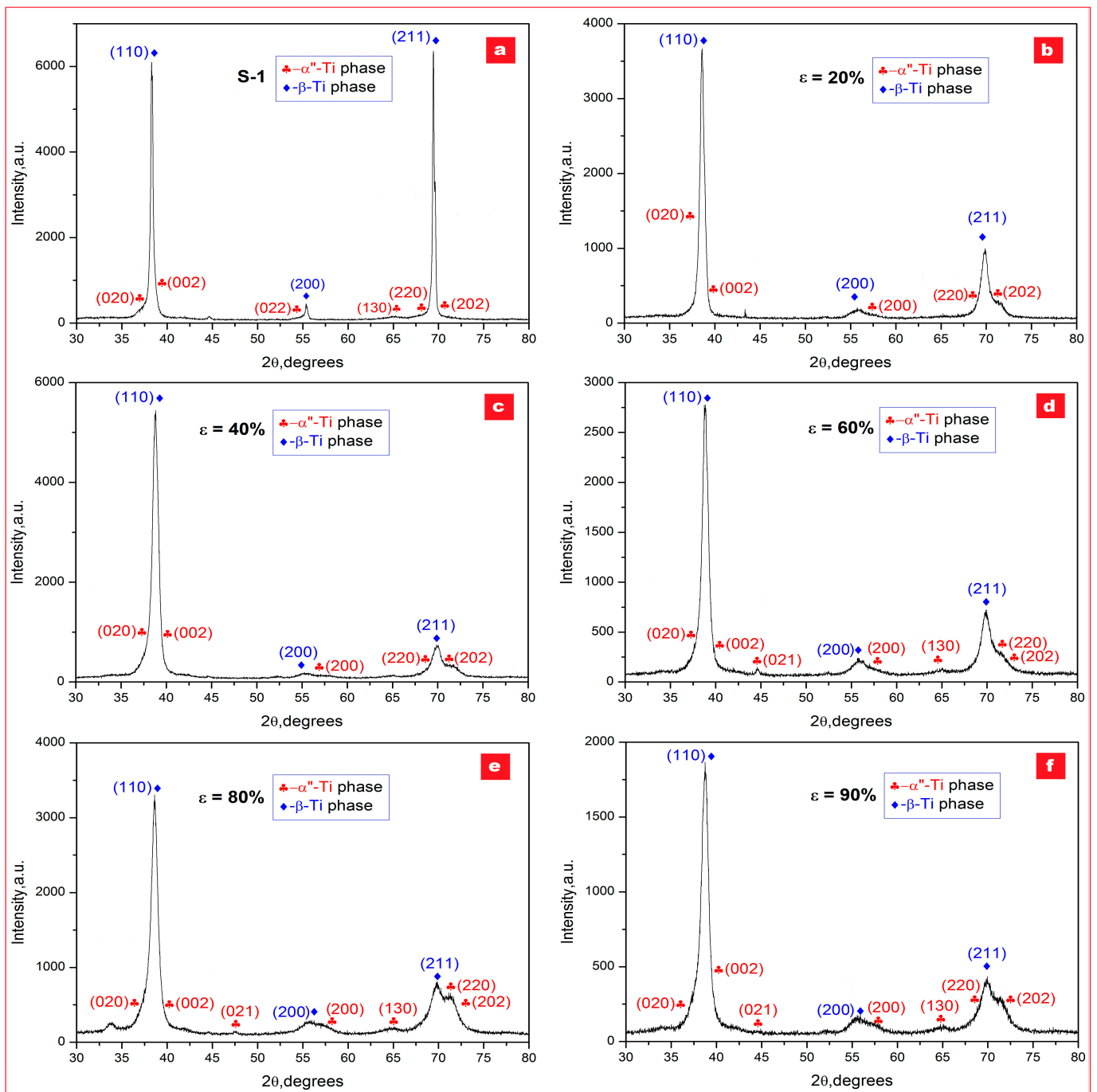


**Figure 2.** XRD patterns of the Ti<sub>29</sub>Nb-9Ta-10Zr alloy corresponding to following stages: (a) initial state—S-1; (b) MPR processed with  $\varepsilon = 20\%$ ; (c) MPR processed with  $\varepsilon = 40\%$ ; (d) MPR processed with  $\varepsilon = 60\%$ ; (e) MPR processed with  $\varepsilon = 80\%$ ; (f) MPR processed with  $\varepsilon = 90\%$ .

The data from Table 1 indicate that the crystallographic cell parameter (a) of the  $\beta$  phase remains essentially constant ( $\sim 0.330$  nm), the applied severe deformation being accommodated either by a twinning process, which is reported to help active the  $\beta$ -Ti bcc grain refinement during the SPD process [34,52,53], and by a SIM process, reported also to occur in some  $\beta$ -Ti alloys [35,54,55]. The SIM process is proved by XRD patterns, but, due to tiny and broad peaks of the recorded orthorhombic- $\alpha''$  martensitic phase, the proportion of the formed phase is smaller than for the  $\beta$  phase. The same observation and correlation of constantly preserving the  $\beta$ -phase cell parameter (a) at about 0.330 nm corresponds



to recrystallized and aged samples also, when the relaxation of the micro-deformations, internal to the  $\beta$  phase, occur. As for the  $\alpha''$  orthorhombic phase, the three corresponding lattice parameters,  $a$ ,  $b$ , and  $c$ , have a slight variation: a small decrease during the MPR process, when a crystallographic texture can develop for the samples highly deformed, and a return during recrystallization and aging.

Comparative to other  $\beta$ -Ti alloys with a more active SIM process during severe plastic deformation [34,54,55], the present studied alloy does not record a substantial activity of this process due to very small recorded diffraction peaks of the  $\alpha''$  phase. Reports about correlations between the Nb, Ta, and Zr chemical amounts, and  $\alpha''$  martensitic phase volume fraction show that the last one decreases (or even its formation can be suppressed) if the Nb content is between 23 and 38 wt %, Ta between 4 and 7 wt %, and Zr is higher than 4 wt % [34,52].

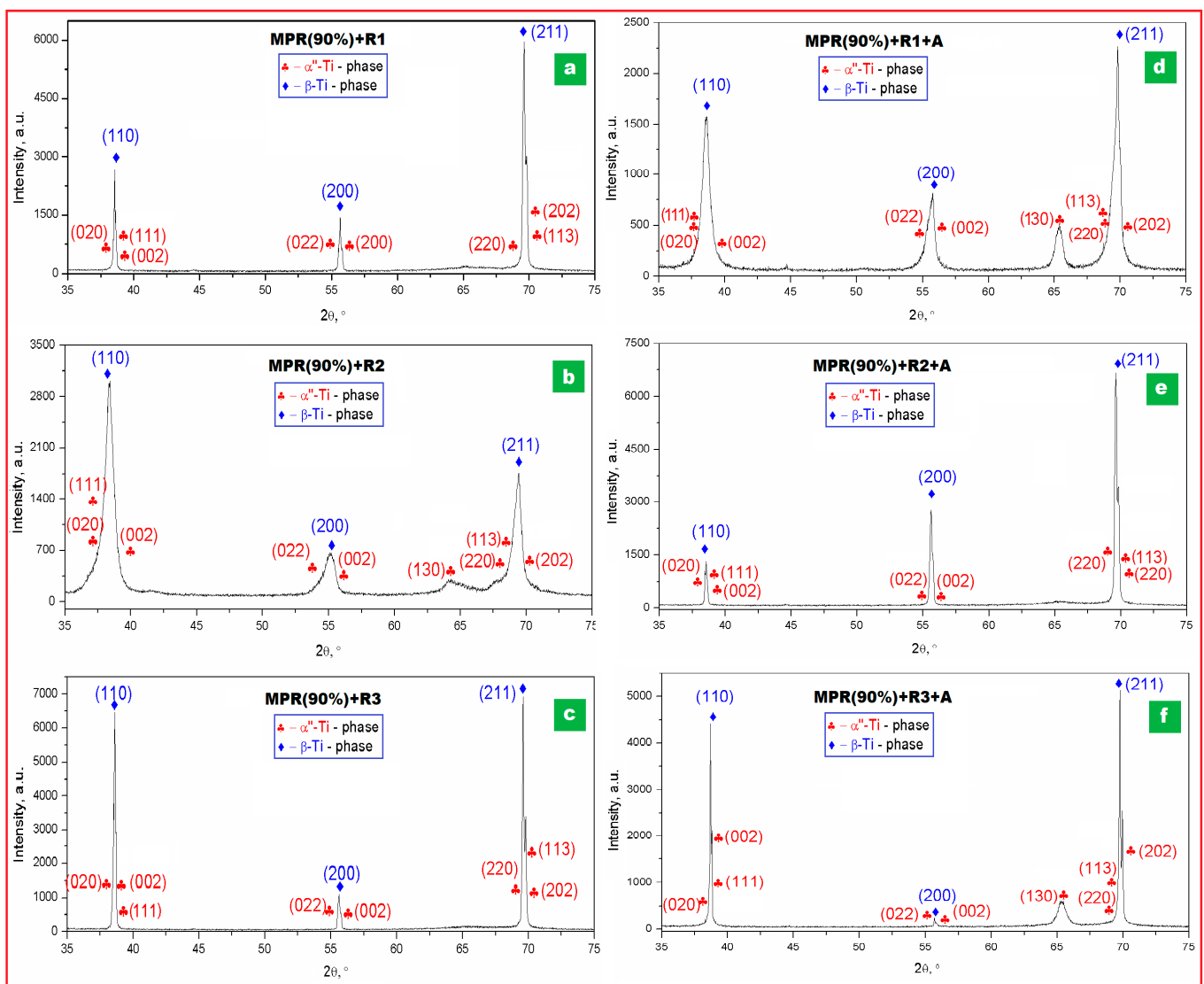


**Figure 3.** XRD patterns of the Ti<sub>29</sub>Nb-9Ta-10Zr alloy corresponding to following stages: (a) MPR (90%) + R1 (780 °C/5 min/w.q.); (b) MPR (90%) + R2 (830 °C/5 min/w.q.); (c) MPR (90%) + R3 (880 °C/5 min/w.q.); (d) MPR (90%) + R1 + A (400 °C/5 min/w.q.); (e) MPR (90%) + R2 + A (400 °C/5 min/w.q.); (f) MPR (90%) + R3 + A (400 °C/5 min/w.q.).

**Table 1.** Average crystalline network parameters corresponding to  $\beta$ -Ti and  $\alpha''$ -Ti phases identified for all analyzed stages of the studied alloy (MPR—multi-pass rolled sample; R—recrystallized sample; A—aged sample).

Structural State	$\beta$ -Ti Phase		$\alpha''$ -Ti Phase	
	a [nm]	a [nm]	b [nm]	c [nm]
S-1: Initial Sample	0.330	0.329	0.478	0.462
MPR ( $\epsilon_{\text{tot}} = 20\%$ )	0.330	0.323	0.474	0.462
MPR ( $\epsilon_{\text{tot}} = 40\%$ )	0.330	0.323	0.472	0.462
MPR ( $\epsilon_{\text{tot}} = 60\%$ )	0.330	0.321	0.470	0.460
MPR ( $\epsilon_{\text{tot}} = 80\%$ )	0.330	0.322	0.472	0.462
MPR ( $\epsilon_{\text{tot}} = 90\%$ )	0.329	0.321	0.471	0.461
MPR ( $\epsilon_{\text{tot}} = 90\%$ ) + R1	0.331	0.330	0.476	0.466
MPR ( $\epsilon_{\text{tot}} = 90\%$ ) + R2	0.331	0.333	0.479	0.469
MPR ( $\epsilon_{\text{tot}} = 90\%$ ) + R3	0.330	0.326	0.476	0.448
MPR ( $\epsilon_{\text{tot}} = 90\%$ ) + R1 + A	0.330	0.326	0.477	0.469
MPR ( $\epsilon_{\text{tot}} = 90\%$ ) + R2 + A	0.331	0.331	0.475	0.465
MPR ( $\epsilon_{\text{tot}} = 90\%$ ) + R3 + A	0.330	0.333	0.478	0.464

For the samples processed by MPR (Figure 2), the intensity of the  $\alpha''$ -phase diffraction peaks (very tiny at the beginning) starts to gradually grow, but slowly, remaining of much lower intensity compared to those of the  $\beta$  phase, resulting that the  $\alpha''$  phase formed by the “stress induced martensite” (SIM) process during the severe plastic deformation—MPR remains a secondary and minor phase. Conversely, the main action is proved to be the refinement of the  $\beta$  grains based on constantly decreasing the  $\beta$ -phase peaks intensity, with visible peaks width broadening. For the Figure 3 corresponding to samples processed by MPR followed by a short recrystallization with three different heating temperatures (780 °C, 830 °C, and 880 °C) and similar short holding time (5 min), and a short aging (400 °C/5 min/w.q.), the intensity of the  $\beta$ -phase diffraction peaks gradually returns to higher values, with sharper peaks, denoting a gradual growing of the  $\beta$  grains.

Table 2 indicate the dimensions of the coherent crystallite ( $D$ , nm) and the micro-deformations ( $\epsilon$ , %) at the crystalline network level corresponding to both  $\beta$ -Ti and  $\alpha''$ -Ti phases that were determined using the Williamson–Hall equation [51] for the FWHM parameter. It can be observed that the coherent crystallite dimensions ( $D$ , nm) of the  $\beta$  phase decrease constantly with increasing of the deformation degree due to the abovementioned strong refinement process; the diminution is about three times, from 26.92 nm to ultrafine/nanometric size of 9.84 nm. This can be considered the most important result of the present experimental program.

Regarding the micro-deformations ( $\epsilon$ , %) corresponding to  $\beta$ -Ti and  $\alpha''$ -Ti phases, the values from Table 2 show that those of the  $\beta$  phase gradually decrease with the deformation degree enhancement (until MPR-60%), from 0.28% to 0.14%, due to twinning accumulation inside  $\beta$  grains followed by their splitting for  $\beta$ -grains refinement; after that, the micro-deformations begin to increase slowly (from 0.14% to 0.22%) due to  $\alpha''$ -grain gradual formation. The twinning process is also validated by SEM images. On the contrary, the micro-deformation corresponding to the  $\alpha''$  phase gradually increases with the enhancement of the deformation degree because of the predisposition of the  $\alpha''$  crystallites (even in poor quantities), first to forming and then to accommodate between/inside the  $\beta$  grains. After recrystallization and aging, the  $\beta$  grains increase in size while the  $\alpha''$ -martensitic grains dissolve in the  $\beta$  phase and diminish in quantity; therefore, the micro-deformations decrease drastically for both phases present, to a minimum of about 0.04%.

**Table 2.** The average dimensions of the coherent crystallite ( $D$ , nm) and micro-deformations ( $\epsilon$ , %) corresponding to  $\beta$ -Ti and  $\alpha''$ -Ti phases identified for all analyzed stages of the studied alloy (MPR—multi-pass rolled sample; R—recrystallized sample).

Structural State	$\beta$ -Ti Phase			$\alpha''$ -Ti Phase		
	$\epsilon$ [%]	$D$ [nm]	Phase's %	$\epsilon$ [%]	$D$ [nm]	Phase's %
S-1: Initial Sample	0.05	26.92	99.52 $\pm$ 0.61%	0.06	-	0.48 $\pm$ 0.12%
MPR ( $\epsilon_{\text{tot}} = 20\%$ )	0.28	24.16	97.79 $\pm$ 1.17%	0.22	7.32	2.21 $\pm$ 0.68%
MPR ( $\epsilon_{\text{tot}} = 40\%$ )	0.26	11.72	94.19 $\pm$ 1.84%	0.28	6.84	5.81 $\pm$ 1.09%
MPR ( $\epsilon_{\text{tot}} = 60\%$ )	0.14	11.48	91.38 $\pm$ 1.31%	0.35	8.43	8.62 $\pm$ 1.01%
MPR ( $\epsilon_{\text{tot}} = 80\%$ )	0.18	10.19	89.67 $\pm$ 1.27%	0.89	7.65	10.33 $\pm$ 1.89%
MPR ( $\epsilon_{\text{tot}} = 90\%$ )	0.22	9.84	89.35 $\pm$ 1.48%	0.92	9.12	10.65 $\pm$ 1.04%
MPR ( $\epsilon_{\text{tot}} = 90\%$ ) + R1	0.36	108.22	95.54 $\pm$ 0.85%	0.44	9.33	4.46 $\pm$ 0.66%
MPR ( $\epsilon_{\text{tot}} = 90\%$ ) + R2	0.39	112.63	97.15 $\pm$ 0.94%	0.42	9.64	2.85 $\pm$ 0.38%
MPR ( $\epsilon_{\text{tot}} = 90\%$ ) + R3	0.40	138.65	97.87 $\pm$ 1.25%	0.41	10.08	2.13 $\pm$ 0.07%
MPR ( $\epsilon_{\text{tot}} = 90\%$ ) + R1 + A	0.04	138.82	93.66 $\pm$ 1.34%	0.06	9.31	6.34 $\pm$ 0.54%
MPR ( $\epsilon_{\text{tot}} = 90\%$ ) + R2 + A	0.07	156.76	97.73 $\pm$ 0.96%	0.04	7.83	2.27 $\pm$ 0.11%
MPR ( $\epsilon_{\text{tot}} = 90\%$ ) + R3 + A	0.09	186.33	97.94 $\pm$ 0.47%	0.04	8.24	2.06 $\pm$ 0.09%

### 3.2. The Phase Analysis Resulted from SEM Imaging

The SEM images obtained after analysis using a scanning electron microscope were grouped in two: Figure 4 for the samples processed by MPR with different deformation degree, and Figure 5 for the samples processed by MPR (90%), followed by three variants of short recrystallization and short aging. The SEM images from Figures 4 and 5 correspond to the RD-ND examined cross section and show the characteristic microstructural features for each tested sample.

The first important aspect to emphasize is related to the fact that the SEM images indicate the majority presence of the  $\beta$  phase. By the presence of a high amount of  $\beta$ -stabilizing alloying elements, 48% cumulative for Nb, Ta, and Zr, it was to be expected that the resulted microstructure will be formed of the majority  $\beta$  phase.

Another important aspect relates to the observation that the cold severe rolled microstructure, composed of visible deformed  $\beta$  grains, becomes more and more elongated and textured along the RD direction (Figure 4); also, at high deformation degree, it becomes fragmented due to shear deformation produced by MPR processing. Starting with the first stage of MPR processing, MPR (20%), the  $\beta$  grains have a visible twinning tendency which favors an increasing successive grain refinement [14,20,51]. The sub-micron grains of the  $\alpha''$ -Ti phase, formed by SIM process, are dispersed inside  $\beta$ -Ti grains, but they are not visible from the SEM images due to their nanometric dimensions. The visible elongated microstructural features corresponding to the  $\beta$  phase are in agreement with the XRD results already discussed, showing a cumulative deformation mechanism (more active twinning and additionally active SIM transformation). Following the recrystallization (Figure 5), the  $\beta$ -grain dimension begins to increase back constantly with enhancing of the recrystallization temperature. Thus, the gradual morphological rehabilitation of the previously highly deformed and textured nanometric  $\beta$  grains to an equiaxial shape, with gradually increasing sizes to about 108 nm and 186 nm, preserve however the ultrafine character of the final obtained microstructure. This part of the experiments could make it possible to find an optimal final variant of thermo-mechanical processing, with a good balance of necessary mechanical properties.

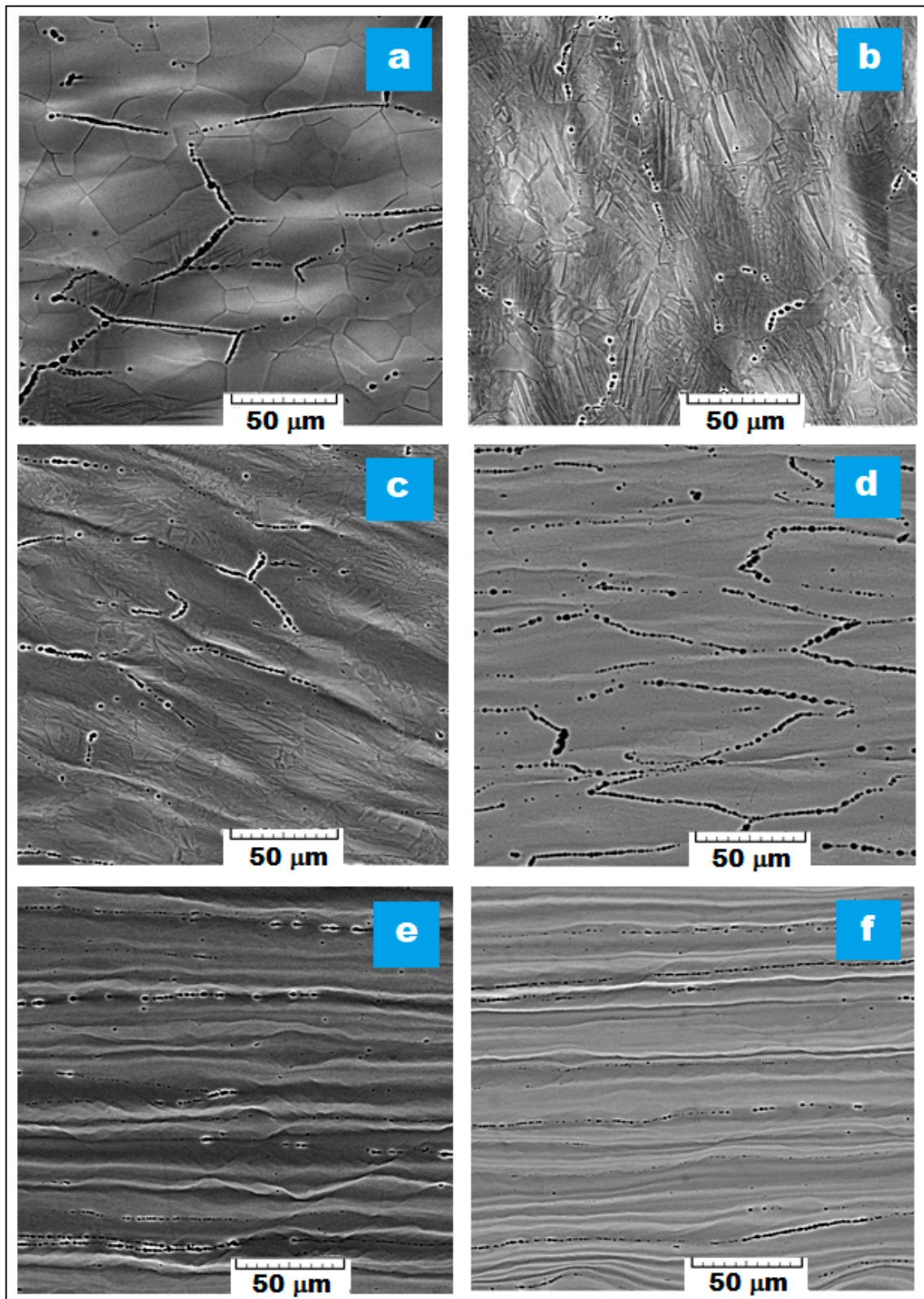


**Figure 4.** SEM images of the Ti99Nb-9Ta-10Zr alloy corresponding to the following stages: (a) initial state—S-1; (b) MPR processed with  $\epsilon = 20\%$ ; (c) MPR processed with  $\epsilon = 40\%$ ; (d) MPR processed with  $\epsilon = 60\%$ ; (e) MPR processed with  $\epsilon = 80\%$ ; (f) MPR processed with  $\epsilon = 90\%$ .



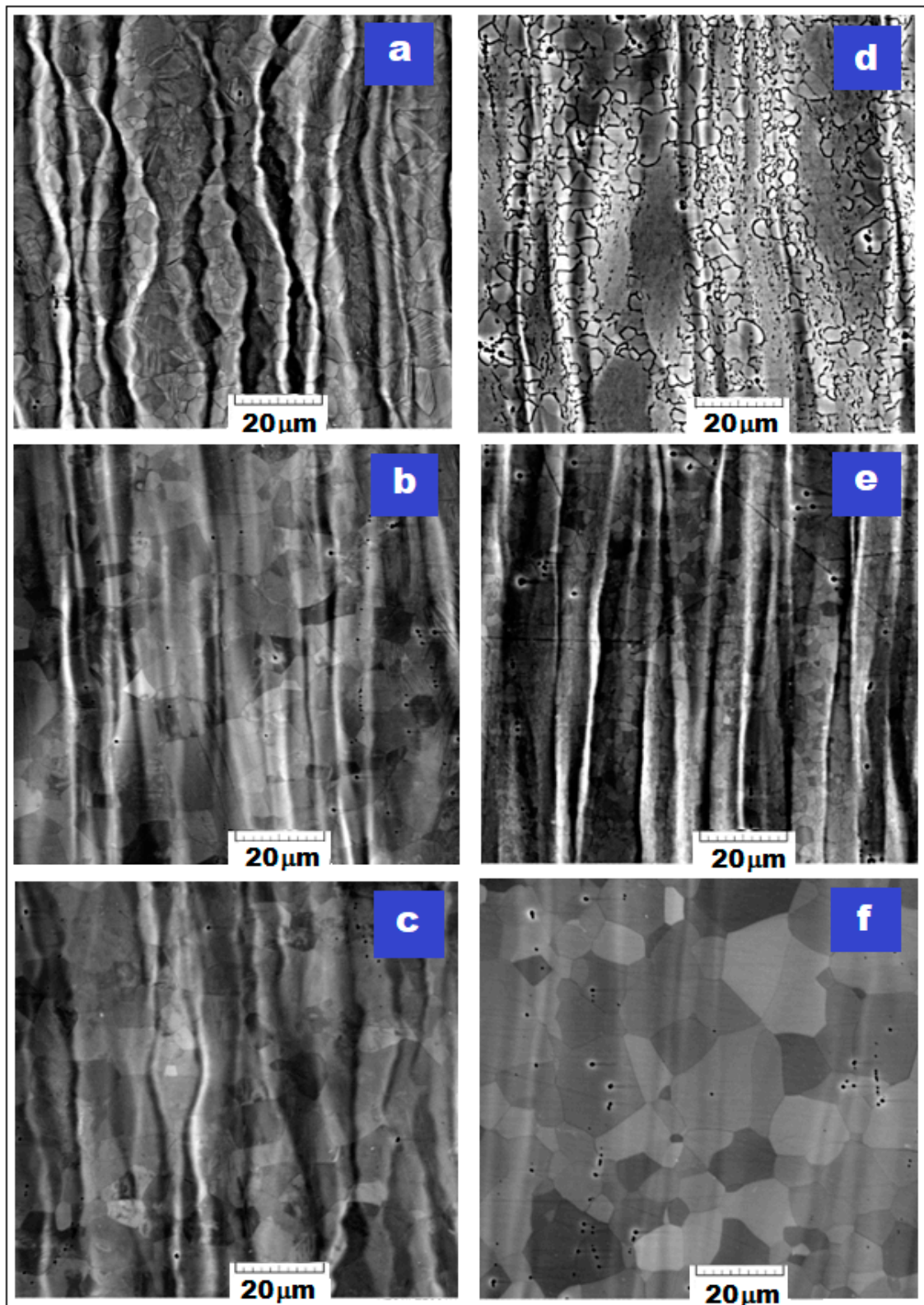


**Figure 5.** XRD patterns of the Ti<sub>29</sub>Nb-9Ta-10Zr alloy corresponding to the following stages: (a) MPR (90%) + R1 (780 °C/5 min/w.q.); (b) MPR (90%) + R2 (830 °C/5 min/w.q.); (c) MPR (90%) + R3 (880 °C/5 min/w.q.); (d) MPR (90%) + R1 + A (400 °C/5 min/w.q.); (e) MPR (90%) + R2 + A (400 °C/5 min/w.q.); (f) MPR (90%) + R3 + A (400 °C/5 min/w.q.).



As concerning the  $\alpha''$ -grain size (Table 2), no significant dimensional variations are observed as in the case of the  $\beta$  phase. However, an interesting variation during the MPR process can be noted, from 7.32 nm (for MPR 20%) to a smaller one 6.84 nm (for MPR 40%), and again to larger dimensions (9.12 nm for MPR 90%). The reason for such variable evolution may be that the  $\alpha''$  grains decrease during MPR, due to an inevitable crushing process (achieving 6.84 nm for the MPR-40%); concomitantly, new  $\alpha''$  grains are forming by SIM process in the following MPR stage, with again increased dimension (8.43 nm for MPR-60%), which will be also crushed subsequently; so, an alternative forming-crushing process occurs with variable  $\alpha''$ -grains dimensions, but not significantly.

After recrystallization, the grains of the  $\alpha''$  phase preserve some constancy of their values, but with a strong decrease in the amount of phase, from 10.65% to 2.13%, due to their dissolution process in the  $\beta$  phase. Compared to similar variants of recrystallization and aging, the SEM image corresponding to the [MPR-90% + R1 + A] stage (Figure 5d) shows visibly thicker limits of the  $\beta$  phase due to a higher amount of secondary  $\alpha''$  phase present here (6.34% versus 2.27% or 2.06%), because the heating temperature of 780 °C is lower than  $\beta$ -transus (813 °C) and allows a somewhat more pronounced precipitation of the  $\alpha''$  secondary phase, compared to similar treatments but with higher temperatures than  $\beta$ -transus (830 °C and 880 °C, respectively).

Thus, a distinction should be made between the  $\alpha''$  phase that forms following the SIM transformation by applying a severe plastic deformation, and the same  $\alpha''$  phase that once dissolves into the  $\beta$  phase upon recrystallization and can then precipitate through aging, but not consistently, because the treatment is of short duration (5 min).

In the end, the experimental validation of the microstructural features and other detailed aspects concerning the  $\beta$ -phase stability and its accented refinement process by combining MPR with recrystallization/aging until nanometric dimensions is obtained mainly by XRD data acquisition and processing, and by some relevant SEM imaging. The refinement process of the  $\beta$  phase until nanometric grain dimensions through the experimented thermomechanical process permits the selection of a suitable processing variant function of possible particular aspects of a real application/situation.

#### 4. Conclusions

A  $\beta$ -type Ti-based alloy was studied concerning the  $\beta$ -phase stability evolution and the microstructural and crystallographic features evolution when subjected to severe plastic deformation, a MPR processing in this case, and a subsequent combination of short recrystallization and aging.

Using XRD analysis and SEM imaging, the  $\beta$ -phase stability and the ability of  $\alpha''$ -martensitic phase formation through stress-induced martensitic transformation were evaluated.

For both recorded phases, the  $\beta$ -Ti phase and  $\alpha''$  martensitic phase, the crystallographic cell parameters, the coherent crystallite dimensions, the phase quantities and the micro-deformations at the crystalline network level were determined by analyzing and processing the data obtained through X-ray diffraction. For verifying and validating the XRD results, the relevant SEM images corresponding to each experimented stage were added.

As a consequence, based on the provided analysis, it has been established/highlighted the following: a good  $\beta$ -phase stability during the entire thermo-mechanical proposed process; the deformation mechanism during MPR process, mainly by twinning and seconded by SIM transformation; the pronounced refinement of the  $\beta$  phase until nanometric grain dimensions. Further studies need to clarify more exactly the involvement, intensity and sequence of the plastic deformation mechanisms that take place in the alloy microstructure by studying the evolution of the mechanical properties.

However, at this stage, the present study provides useful data to start the design of an optimal processing route for the Ti<sub>29</sub>Nb-9Ta-10Zr alloy, with a good selection of possible ultrafine/nanometric grains capable of suitable mechanical properties.

**Supplementary Materials:** The following supporting information can be downloaded at: <https://www.mdpi.com/article/10.3390/ma16083208/s1>, Figures S1 to S12: The detailed zooms of cumulative diffraction peaks (top) and the Rietveld plot (down) for the Ti<sub>29</sub>Nb-9Ta-10Zr alloy corresponding to initial state—Figure S1; MPR (20%)—Figure S2; MPR (40%)—Figure S3; MPR (60%)—Figure S4; MPR (80%)—Figure S5; MPR (90%)—Figure S6; MPR (90%) + R1 (780 °C/5 min/w.q.)—Figure S7; MPR (90%) + R2 (830 °C/5 min/w.q.)—Figure S8; MPR (90%) + R3 (880 °C/5 min/w.q.)—Figure S9; MPR (90%) + R1 (780 °C/5 min/w.q.) + A (400 °C/5 min/w.q.)—Figure S10; MPR (90%) + R2 (830 °C/5 min/w.q.) + A (400 °C/5 min/w.q.)—Figure S11; MPR (90%) + R3 (880 °C/5 min/w.q.) + A (400 °C/5 min/w.q.)—Figure S12.

**Author Contributions:** Conceptualization, D.R., A.N. and R.E.I.; methodology, D.R. and V.D.C.; software, V.D.C.; validation, A.N., D.R. and R.E.I.; formal analysis, R.E.I.; investigation, R.E.I., N.Z.-I. and N.Ş.; resources, V.D.C.; data curation, N.Z.-I., N.Ş. and B.M.G.; writing—original draft preparation, A.N.; writing—review and editing, D.R. and A.N.; visualization, D.R., A.N. and R.E.I.; supervision, D.R., A.N. and V.D.C.; project administration, D.R.; funding acquisition, V.D.C. All authors have read and agreed to the published version of the manuscript.

**Funding:** This research was funded by the Romanian National Authority for Scientific Research CCCDI-UEFISCDI, Project ERANET-MANUNET-III/grant No. 143/2020. The APC was funded by MDPI-discount vouchers and by the University POLITEHNICA of Bucharest.

**Institutional Review Board Statement:** Not applicable.

**Informed Consent Statement:** Not applicable.

**Data Availability Statement:** The data presented in this study are available on request from the corresponding author.

**Acknowledgments:** The authors acknowledge financial support for this research by the Romanian National Authority for Scientific Research CCCDI-UEFISCDI, Project ERANET-MANUNET-III/grant No. 143/2020.

**Conflicts of Interest:** The authors declare no conflict of interest. The funders had no role in the design of the study; in the collection, analyses, or interpretation of data; in the writing of the manuscript; or in the decision to publish the results.

## References

1. Festas, A.; Ramos, A.; Davim, J. Medical devices biomaterials—A review. *Proc. Inst. Mech. Eng. L J. Mater. Des. Appl.* **2020**, *234*, 218–228. [CrossRef]
2. Carobolante, J.P.A.; Pereira Júnior, A.; Bortolini Junior, C.; Barboza da Silva, K.; Sabino, R.M.; Popat, K.C.; Claro, A.P.R.A. Processing and Characterization of a New Quaternary Alloy Ti<sub>10</sub>Mo<sub>8</sub>Nb<sub>6</sub>Zr for Potential Biomedical Applications. *Materials* **2022**, *15*, 8636. [CrossRef] [PubMed]
3. Wang, H.; Yuan, X.; Wu, K.; Xu, C.; Jiao, Y.; Ge, W.; Luo, J. Effect of high energy shot-peening on the microstructure and mechanical properties of Al<sub>50</sub>Si<sub>2</sub>/Ti<sub>6</sub>Al<sub>4</sub>V lap joints. *J. Mater. Process. Technol.* **2018**, *255*, 76–85. [CrossRef]
4. Zheng, Y.; Wang, D.; Banerjee, R.; Banerjee, D.; Wang, Y.; Fraser, H.L. Exploration of Nano-scale Structural Instabilities in Metastable  $\beta$  Titanium Alloys Using Advanced Electron Microscopy. In *MATEC Web of Conferences*; EDP Sciences: Les Ulis, France, 2020; Volume 321, p. 12001.
5. Wang, T.; Feng, Y.; Liu, X.; Wang, K.; Li, S.; Zhao, F. Phase Composition Effects on Dynamic Behavior and Strain Rate Sensitivity in Metastable  $\beta$ -Ti Alloys. *Materials* **2022**, *15*, 4068. [CrossRef] [PubMed]
6. Li, Y.; Yang, C.; Zhao, H.; Qu, S.; Li, X.; Li, Y. New Developments of Ti-Based Alloys for Biomedical Applications—A review. *Materials* **2014**, *7*, 1709–1800. [CrossRef]
7. Niinomi, M.; Nakai, M.; Hieda, J. Development of new metallic alloys for biomedical applications. *Acta Biomater.* **2012**, *8*, 3888–3903. [CrossRef]
8. Capellato, P.; Vilela, F.B.; Fontenele, A.H.P.; da Silva, K.B.; Carobolante, J.P.A.; Bejarano, E.G.M.; de Lourdes Noronha Motta Melo, M.; Claro, A.P.R.A.; Sanchs, D. Evaluation of microstructure and mechanical properties of a Ti<sub>10</sub>Mo<sub>8</sub>Nb alloy for biomedical applications. *Metals* **2022**, *12*, 1065. [CrossRef]
9. Zhang, S.; Wang, Q.; Cheng, X.; Han, J.; Zhang, W.; Zhang, C.; Wu, J. Static Recrystallization Behavior and Texture Evolution during Annealing in a Cold Rolling Beta Titanium Alloy Sheet. *Metals* **2022**, *12*, 899. [CrossRef]
10. Qu, W.; Sun, X.; Yuan, B.; Xiong, C.; Zhang, F.; Li, Y.; Sun, B. Microstructures and phase transformations of Ti-30Zr-xNb (x = 5, 7, 9, 13 at.%) shape memory alloys. *Mater. Charact.* **2016**, *122*, 1–5. [CrossRef]
11. Keshtta, A.; Gepreel, M.A.H. Superelasticity Evaluation of the Biocompatible Ti-17Nb-6Ta Alloy. *J. Healthc. Eng.* **2019**, *2019*, 8353409. [CrossRef]

12. Ozan, S.; Lin, J.; Li, Y.; Wen, C. New Ti-Ta-Zr-Nb alloys with ultrahigh strength for potential orthopedic implant applications. *J. Mech. Behav. Biomed. Mater.* **2017**, *75*, 119–127. [CrossRef] [PubMed]
13. Gepreel, M.A.; Niinomi, M. Biocompatibility of Ti-alloys for long-term implantation. *J. Mech. Behav. Biomed. Mater.* **2013**, *20*, 407–415. [CrossRef]
14. Kopova, I.; Stráský, J.; Hrcuba, P.; Landa, M.; Janeček, M.; Bačáková, L. Newly developed Ti–Nb–Zr–Ta–Si–Fe biomedical beta titanium alloys with increased strength and enhanced biocompatibility. *Mater. Sci. Eng. C* **2016**, *60*, 230–238. [CrossRef] [PubMed]
15. Slokar, L.; Štrkalj, A.; Glavaš, Z. Synthesis of Ti-Zr alloy by powder metallurgy. *Eng. Rev.* **2019**, *39*, 115–123. [CrossRef]
16. Medvedev, A.E.; Molotnikov, A.; Lapovok, R.; Zeller, R.; Berner, S.; Habersetzer, P.; Torre, F.D. Microstructure and mechanical properties of Ti–15Zr alloy used as dental implant material. *J. Mech. Behav. Biomed. Mater.* **2016**, *62*, 384–398. [CrossRef]
17. Grandin, H.M.; Berner, S.; Dard, M. A review of Titanium Zirconium (TiZr) alloys for use in endosseous dental implants. *Materials* **2012**, *5*, 1348–1360. [CrossRef]
18. Pang, E.L.; Pickering, E.J.; Baik, S.I.; Seidman, D.N.; Jones, N.G. The effect of zirconium on the omega phase in Ti-24Nb-[0–8]Zr (at.%) alloys. *Acta Mater.* **2018**, *153*, 62–70. [CrossRef]
19. Sulkowski, B.; Panigrahi, A.; Ozaltin, K.; Lewandowska, M.; Mikułowski, B.; Zehetbauer, M. Evolution of strength and structure during SPD processing of Ti-45Nb alloys: Experiments and simulations. *J. Mater. Sci.* **2014**, *49*, 6648. [CrossRef]
20. Zhang, J.; Li, J.; Chen, G.; Liu, L.; Chen, Z.; Meng, Q.; Shen, B.; Sun, F.; Prima, F. Fabrication and characterization of a novel  $\beta$  metastable Ti-Mo-Zr alloy with large ductility and improved yield strength. *Mater. Charact.* **2018**, *139*, 421–427. [CrossRef]
21. Niinomi, M.; Nakai, M.; Hendrickson, M.; Nandwana, P.; Alam, T.; Choudhuri, D.; Banerjee, R. Influence of oxygen on omega phase stability in the Ti-29Nb-13Ta-4.6Zr alloy. *Scripta Mater.* **2016**, *123*, 144–148. [CrossRef]
22. Xie, K.Y.; Wang, Y.B.; Zhao, Y.H.; Chang, L.; Wang, G.C.; Chen, Z.B.; Cao, Y.; Liao, X.Z.; Lavernia, E.J.; Valiev, R.Z.; et al. Nanocrystalline  $\beta$ -Ti alloy with high hardness, low Young's modulus and excellent in vitro biocompatibility for biomedical applications. *Mater. Sci. Eng. C* **2013**, *33*, 3530–3536. [CrossRef]
23. Zhao, D.; Ebel, T.; Yan, M.; Qian, M. Trace Carbon in Biomedical Beta-Titanium Alloys: Recent Progress. *JOM* **2015**, *67*, 2236. [CrossRef]
24. Sun, J.; Ke, Q.; Chen, W. Material instability under localized severe plastic deformation during high-speed turning of titanium alloy Ti-6.5Al-2Zr-1Mo-1V. *J. Mater. Process Technol.* **2019**, *264*, 119. [CrossRef]
25. Niinomi, M.; Yi, L.; Nakai, M.; Liu, H.; Hua, L. Biomedical titanium alloys with Young's moduli close to that of cortical bone. *Regener. Biomater.* **2016**, *3*, 173–185. [CrossRef]
26. Matlakhova, L.A.; Matlakhov, A.N.; Monteiro, S.N.; Fedotov, S.G.; Goncharenko, B.A. Properties and structural characteristics of Ti–Nb–Al alloys. *Mater. Sci. Eng. A* **2005**, *393*, 320–326. [CrossRef]
27. Zhou, Y.L.; Niinomi, M.; Akahori, T. Effects of Ta content on Young's modulus and tensile properties of binary Ti–Ta alloys for biomedical applications. *Mater. Sci. Eng. A* **2004**, *371*, 283. [CrossRef]
28. Majchrowicz, K.; Sotniczuk, A.; Malicka, J.; Choinska, E.; Garbacz, H. Thermal Stability and Mechanical Behavior of Ultrafine-Grained Titanium with Different Impurity Content. *Materials* **2023**, *16*, 1339. [CrossRef]
29. Kriegel, M.J.; Rudolph, M.; Kilmametov, A.; Straumal, B.B.; Ivanisenko, J.; Fabrichnaya, O.; Hahn, H.; Rafaja, D. Formation and Thermal Stability of  $\omega$ -Ti(Fe) in  $\alpha$ -Phase-Based Ti(Fe) Alloys. *Metals* **2020**, *10*, 402. [CrossRef]
30. Sajadifar, S.V.; Maier, H.J.; Niendorf, T.; Yapici, G.G. Elevated Temperature Mechanical Characteristics and Fracture Behavior of a Novel Beta Titanium Alloy. *Crystals* **2023**, *13*, 269. [CrossRef]
31. Hao, Y.L.; Yang, R.; Niinomi, M.; Kuroda, D.; Zhou, Y.L.; Fukunaga, K.; Suzuki, A. Young's modulus and mechanical properties of Ti-29Nb-13Ta-4.6Zr in relation to  $\alpha''$  martensite. *Metall. Mater. Trans. A* **2002**, *33*, 3137–3144. [CrossRef]
32. Haftlang, F.; Zarei-Hanzaki, A.; Abedi, H.R.; Kalaei, M.A.; Nemecek, J.; Málek, J. Room-temperature micro and macro mechanical properties of the metastable Ti–29Nb–14Ta–4.5Zr alloy holding nano-sized precipitates. *Mater. Sci. Eng. A* **2019**, *771*, 138583. [CrossRef]
33. Baltatu, M.S.; Vizureanu, P.; Geanta, V.; Tugui, C.A.; Voiculescu, I. Mechanical tests for Ti-based alloys as new medical materials. *IOP Conf. Ser. Mater. Sci. Eng.* **2019**, *572*, 012029. [CrossRef]
34. Kolli, R.P.; Devaraj, A. A Review of Metastable Beta Titanium Alloys. *Metals* **2018**, *8*, 506. [CrossRef]
35. Hua, K.; Zhang, Y.; Tong, Y.; Zhang, F.; Kou, H.; Li, X.; Wang, H.; Li, J. Enhanced mechanical properties of a metastable  $\beta$  titanium alloy via optimized thermomechanical processing. *Mater. Sci. Eng. A* **2022**, *840*, 142997. [CrossRef]
36. Valiev, R.Z.; Estrin, Y.; Horita, Z.; Langdon, T.G.; Zehetbauer, M.J.; Zhu, Y.T. Fundamentals of superior properties in bulk nano SPD materials. *Mater. Res. Lett.* **2016**, *4*, 1–21. [CrossRef]
37. Yilmazer, H.; Niinomi, M.; Nakai, M.; Cho, K.; Hieda, J.; Todaka, Y.; Miyazaki, T. Mechanical properties of a medical  $\beta$ -type titanium alloy with specific microstructural evolution through high-pressure torsion. *Mater. Sci. Eng. C* **2013**, *33*, 2499–2507. [CrossRef]
38. Lin, Z.; Wang, L.; Xue, X.; Lu, W.; Qin, J.; Zhang, D. Microstructure evolution and mechanical properties of a Ti–35Nb–3Zr–2Ta biomedical alloy processed by equal channel angular pressing (ECAP). *Mater. Sci. Eng. C* **2013**, *33*, 4551–4561. [CrossRef]
39. Wang, Y.; Zhao, J.; Dai, S.; Chen, F.; Yu, X.; Zhang, Y. Influence of cold rolling and ageing treatment on microstructure and mechanical properties of Ti-30Nb-5Ta-6Zr alloy. *J. Mech. Behav. Biomed. Mater.* **2013**, *27*, 33–42. [CrossRef]
40. Yang, Y.; Wu, S.Q.; Li, G.P. Evolution of deformation mechanisms of Ti–22.4Nb–0.73Ta–2Zr–1.34O alloy during straining. *Acta Mater.* **2010**, *58*, 2778. [CrossRef]

41. Angelescu, M.L.; Dan, A.; Ungureanu, E.; Zarnescu-Ivan, N.; Galbinasu, B.M. Effects of Cold Rolling Deformation and Solution Treatment on Microstructural, Mechanical, and Corrosion Properties of a Biocompatible Ti-Nb-Ta-Zr Alloy. *Metals* **2022**, *12*, 248. [CrossRef]
42. Valiev, R.Z.; Estrin, Y.; Horita, Z.; Langdon, T.G.; Zehetbauer, M.J.; Zhu, Y.T. Producing bulk ultrafine-grained materials by severe plastic deformation: Ten years later. *JOM* **2016**, *68*, 1216–1226. [CrossRef]
43. Raducanu, D.; Cojocaru, V.D.; Nocivin, A.; Cinca, I.; Serban, N.; Cojocaru, E.M. Contributions to Mechanical Characteristics Improvement of Some Biomedical TNTZ Alloys by Adding Fe, Si, and O: A Comparative Study. *JOM* **2019**, *71*, 264–271. [CrossRef]
44. Valiev, R.Z.; Prokofiev, E.A.; Kazarinov, N.A.; Raab, G.I.; Minasov, T.B.; Stráský, J. Developing Nanostructured Ti Alloys for Innovative Implantable Medical Devices. *Materials* **2020**, *13*, 967. [CrossRef]
45. Nocivin, A.; Raducanu, D.; Vasile, B.; Trisca-Rusu, C.; Cojocaru, E.M.; Dan, A.; Irimescu, R.; Cojocaru, V.D. Tailoring a Low Young Modulus for a Beta Titanium Alloy by Combining Severe Plastic Deformation with Solution Treatment. *Materials* **2021**, *14*, 3467. [CrossRef]
46. Raducanu, D.; Cojocaru, V.D.; Nocivin, A.; Cinca, I.; Serban, N.; Cojocaru, E.M. Beta-Phase Stability of Two Biomedical b-Titanium Alloys during Severe Plastic Deformation. *JOM* **2020**, *72*, 2937–2948. [CrossRef]
47. Nocivin, A.; Raducanu, D.; Cinca, I.; Trisca-Rusu, C.; Butu, M.; Thibon, I.; Cojocaru, V.D. X-ray Diffraction Study and Texture Evolution for a Ti-Nb-Ta Biomedical Alloy processed by Accumulative Roll Bonding. *J. Mater. Eng. Perform.* **2015**, *24*, 1587–1601. [CrossRef]
48. Soundararajan, S.R.; Vishnu, J.; Manivasagam, G.; Muktinutalapati, N.R. Heat Treatment of Metastable Beta Titanium Alloys. In *Metal Heat Treatments*; IntechOpen: London, UK, 2020; Available online: <https://www.intechopen.com/chapters/72078> (accessed on 10 January 2023). [CrossRef]
49. Naresh Kumar, K.; Muneshwar, P.; Singh, S.K.; Jha, A.K.; Pant, B. Thermomechanical working and heat treatment studies on meta-stable beta titanium alloy (Ti15V3Al3Sn3Cr) plates. *Mater. Sci. Forum.* **2015**, *830–831*, 151–155. [CrossRef]
50. Neelakantan, S.; Rivera-Diaz-del-Castillo, P.E.J.; van der Zwaag, S. Prediction of the martensite start temperature for beta titanium alloys as a function of composition. *Scripta Mater.* **2009**, *60*, 611–614. [CrossRef]
51. Hendri, H.; Abdullah, B.; Tahir, D. Analysis of structural properties of X-ray diffraction for composite copper-activated carbon by modified Williamson-Hall and size-strain plotting methods. *J. Phys. Conf. Ser.* **2018**, *1080*, 012007.
52. Ahmed, M.; Wexler, D.; Casillas, G.; Ivasishin, O.M.; Pereloma, E.V. The influence of  $\beta$  phase stability on deformation mode and compressive mechanical properties of Ti-10V-3Fe-3Al alloy. *Acta Mater.* **2015**, *84*, 124–135. [CrossRef]
53. Azadmanjiri, J.; Berndt, C.C.; Kapoor, A.; Wen, C. Development of Surface Nano-Crystallization in Alloys by Surface Mechanical Attrition Treatment (SMAT). *Crit. Rev. Solid State Mater. Sci.* **2015**, *40*, 164–181. [CrossRef]
54. Ma, X.; Chen, Z.; Xiao, L.; Lu, W.; Luo, S.; Mi, Y. Compressive deformation of a metastable  $\beta$  titanium alloy undergoing a stress-induced martensitic transformation: The role of  $\beta$  grain size. *Mater. Sci. Eng. A* **2020**, *794*, 139919. [CrossRef]
55. Wang, Q.; Ren, J.Q.; Xin, C.; Sang, B.; Chen, D.J.; Lu, X.F.; Zhang, L.; Zhang, Y.H. Charpy impact behaviors of metastable  $\beta$ -Ti alloys: Transformation induce plasticity versus twinning induce plasticity. *Mater. Sci. Eng. A* **2023**, *867*, 144753. [CrossRef]

**Disclaimer/Publisher’s Note:** The statements, opinions and data contained in all publications are solely those of the individual author(s) and contributor(s) and not of MDPI and/or the editor(s). MDPI and/or the editor(s) disclaim responsibility for any injury to people or property resulting from any ideas, methods, instructions or products referred to in the content.

## Article

# Microstructure Evolution and Mechanical Properties of Al–Cu–Mg Alloys with Si Addition

Abdul Wahid Shah <sup>1,2</sup>, Seong-Ho Ha <sup>2,\*</sup>, Jabir Ali Siddique <sup>1,2</sup>, Bong-Hwan Kim <sup>1,2</sup>, Young-Ok Yoon <sup>2</sup>, Hyun-Kyu Lim <sup>2</sup> and Shae K. Kim <sup>1,2</sup>

<sup>1</sup> Industrial Technology, University of Science and Technology, Daejeon 34113, Republic of Korea; abdulwahid.shah799@gmail.com (A.W.S.)

<sup>2</sup> Industrial Materials Processing R&D Department, Korea Institute of Industrial Technology, Incheon 21999, Republic of Korea

\* Correspondence: shha@kitech.re.kr

**Abstract:** The aim of this study was to investigate the impact of the addition of a minor quantity of Si on the microstructure evolution, heat treatment response, and mechanical properties of the Al–4.5Cu–0.15Ti–3.0Mg alloy. The microstructure analysis of the base alloy revealed the presence of  $\alpha$ -Al grains, eutectic  $\alpha$ -Al–Al<sub>2</sub>CuMg (S) phases, and Mg<sub>32</sub>(Al, Cu)<sub>49</sub> (T) phases within the Al grains. In contrast, the Si-added alloy featured the eutectic  $\alpha$ -Al–Mg<sub>2</sub>Si phases, eutectic  $\alpha$ -Al–S–Mg<sub>2</sub>Si, and Ti–Si-based intermetallic compounds in addition to the aforementioned phases. The study found that the Si-added alloy had a greater quantity of T phase in comparison to the base alloy, which was attributed to the promotion of T phase precipitation facilitated by the inclusion of Si. Additionally, Si facilitated the formation of S phase during aging treatment, thereby accelerating the precipitation-hardening response of the Si-added alloy. The as-cast temper of the base alloy displayed a yield strength of roughly 153 MPa, which increased to 170 MPa in the Si-added alloy. As a result of the aging treatment, both alloys exhibited a notable increase in tensile strength, which was ascribed to the precipitation of S phases. In the T6 temper, the base alloy exhibited a yield strength of 270 MPa, while the Si-added alloy exhibited a significantly higher yield strength of 324 MPa. This novel Si-added alloy demonstrated superior tensile properties compared to many commercially available high-Mg-added Al–Cu–Mg alloys, making it a potential replacement for such alloys in various applications within the aerospace and automotive industries.

**Keywords:** Al–Cu–Mg alloy; Si addition; microstructure; heat treatment; tensile properties



**Citation:** Shah, A.W.; Ha, S.-H.; Siddique, J.A.; Kim, B.-H.; Yoon, Y.-O.; Lim, H.-K.; Kim, S.K. Microstructure Evolution and Mechanical Properties of Al–Cu–Mg Alloys with Si Addition. *Materials* **2023**, *16*, 2783. <https://doi.org/10.3390/ma16072783>

Academic Editor: Bolv Xiao

Received: 12 March 2023

Revised: 27 March 2023

Accepted: 29 March 2023

Published: 30 March 2023



**Copyright:** © 2023 by the authors. Licensee MDPI, Basel, Switzerland. This article is an open access article distributed under the terms and conditions of the Creative Commons Attribution (CC BY) license (<https://creativecommons.org/licenses/by/4.0/>).

## 1. Introduction

Aluminum–copper–magnesium (Al–Cu–Mg)-based alloys, such as A201 and A206, are the strongest casting alloys of aluminum [1]. The copper content in these alloys varies between 4 and 10% by weight, with most alloys containing around 4.5%. Magnesium is an essential component of these alloys, and depending on the amount of magnesium present, they can be categorized into low-magnesium- and high-magnesium-containing Al–Cu–Mg alloys [1,2]. Aluminum alloys such as A201 and A206, which have a magnesium content below 1%, are renowned for their high strength and toughness. They also possess excellent corrosion resistance, and their precipitation hardening during heat treatment results in the highest tensile strength among all aluminum casting alloys [1–5]. However, these alloys have some disadvantages, including a relatively high tendency to hot tearing and low corrosion resistance [6–10]. Alloys with higher magnesium content (1.5~6%), such as 240, 242, and 243 alloys, are renowned for their superior hardness, high specific strength, and thermal stability at elevated temperatures. These alloys are commonly employed in applications where wear resistance and thermal stability are crucial factors, such as the production of pistons for internal combustion engines (e.g., 242 and A242 alloys) and



air-cooled cylinder heads for aircraft engines [1]. Alloys with high magnesium content (such as 240, 242, and 243) exhibit better fluidity and resistance to hot tearing than those with low magnesium content (such as A201 and A206) [1,2].

In the Al–Cu–Mg ternary phase diagram, the Al<sub>2</sub>CuMg (S) intermetallic compound (IMC) is comparable to Mg<sub>2</sub>Si in the Al–Mg–Si ternary phase diagram. It divides the diagram into two sections on the Al-rich corner:  $\alpha$ -Al + Al<sub>2</sub>Cu ( $\theta$ ) + S and  $\alpha$ -Al + Mg<sub>32</sub>(Al, Cu)<sub>49</sub> (T) + S. A quasi-binary eutectic reaction ( $L \Rightarrow \alpha$ -Al + S) occurs at a Cu/Mg ratio of 2.40, resulting in various non-variant reactions in the Al-rich corner of Al–Cu–Mg ternary alloys [2]. Low-Mg-containing alloys in the  $\alpha$ -Al +  $\theta$  + S section of the diagram are primarily composed of a primary  $\alpha$ -Al matrix and eutectic  $\alpha$ -Al- $\theta$  phases, along with a small amount of eutectic  $\alpha$ -Al-S phases [3,5,11–20]. High-Mg-containing Al–Cu–Mg commercial alloys have compositions lying in the  $\alpha$ -Al + S +  $\theta$  and  $\alpha$ -Al + S sections of the diagram [1,2,19–21]. However, due to their higher Mg content, these alloys have a significantly greater amount of eutectic  $\alpha$ -Al-S phases than low-Mg-containing alloys.

However, the development of Al–Cu–Mg alloys with compositions in the  $\alpha$ -Al + S + T section of the Al–Cu–Mg ternary phase diagram has received very little attention so far, according to the authors' knowledge [19–21]. High-Mg-containing Al–Cu–Mg alloys exhibit significantly higher tensile strength compared to Al–Si-based commercial alloys in the as-cast condition. However, compared to other heat-treated Al alloys such as A356 and A206 alloys, their response to heat treatment is less effective [1]. This is because the high Mg content leads to the formation of a higher amount of S phases in the as-cast microstructure, which do not dissolve during solution heat treatment, thus decreasing the heat treatment response of these alloys [20]. However, selecting a composition within the  $\alpha$ -Al + S + T section of the Al–Mg–Cu ternary phase diagram results in the formation of T precipitates that can be dissolved during solution heat treatment, thus improving the precipitation hardening of high-Mg-containing alloys. In addition, the incorporation of minor quantities of other elements (such as Si, Ag, Mn, Zn, Ge, and Sn) has been reported to have a significant impact on the microstructure evolution and heat treatment response of Al–Cu–Mg alloys with low Mg content [11–19,21]. Despite extensive studies on Al–Cu–Mg alloys with low Mg content, there has been limited research on how alterations in chemical composition impact the microstructure evolution and heat treatment response of Al–Cu–Mg alloys that contain a high Mg content.

The enhancement in tensile strength through the development of new Al–Cu–Mg alloys with high Mg content is of great importance to the aerospace and automotive industries, given their good thermal stability at elevated temperatures. The primary objective of this study was to modify the chemical composition of these alloys to enhance their strength. Specifically, the study aimed to investigate the impact of adding small amounts of other elements to the Al–Cu–Mg alloys with high magnesium content, located in the  $\alpha$ -Al + S + T section of the Al–Mg–Cu ternary phase diagram. The study focused on analyzing the solidification behavior, microstructure evolution, heat treatment response, and mechanical properties of the Al–4.5Cu–0.15Ti–3.0Mg alloy with the inclusion of a small amount of Si.

## 2. Materials and Methods

The chemical composition of the experimental alloys utilized in the investigation is presented in Table 1. The base material employed in the study was high-purity aluminum ingots with a purity level of 99.99%. To form the experimental alloys, copper, magnesium, titanium, and silicon were introduced into the melt through the use of Al–50%Cu, Mg + Al<sub>2</sub>Ca, Al–5%Ti–1%B, and Al–25%Si master alloys, respectively. The melting process involved melting an aluminum ingot in an induction furnace at ambient atmosphere, followed by alloying at temperatures of 760–800 °C. After melting the pure aluminum, the melt was maintained at around 750 °C for a brief duration to ensure the uniform distribution of the alloying elements. To remove hydrogen gas and oxide inclusions, gas bubbling filtration (with Ar gas) was utilized for a duration of 15 min. The temperature

was kept at approximately 700 °C throughout the degassing process. After degassing, the melt was held at approximately 690 °C for 5 min before being poured into a preheated steel mold at the same temperature for all alloys. The experimental alloys underwent a two-step heat treatment. The first step was a solution heat treatment at a temperature of 477 °C for 10 h, followed by water quenching. The second step was an aging treatment, which was carried out at 200 °C for 20 h. For the hardness measurements at various aging times, the Brinell hardness machine from Buehler (Uzwil, Switzerland) was employed. For each condition, five measurements were taken for every specimen, and the mean of these five measurements is presented.

**Table 1.** Nominal composition of the alloys that were investigated.

Alloy	Compositions (Mass%)				
	Cu	Mg	Ti	Si	Al
B43	4.5	3.0	0.15	-	bal.
S43	4.5	3.0	0.15	0.5	bal.

The theoretical calculations were performed using JMatPro 11.2 software. The differential scanning calorimetry (DSC, TA Q1000 instrument, TA instruments, Milford, MA, USA) experiments involved heating the samples of each alloy in an alumina pan within a furnace, and the specimens were heated at a rate of 10 °C per minute in an argon atmosphere ranging from 100 °C to 700 °C. For the precipitation behavior of the investigated alloys, the as-quenched samples were heated between 30 °C and 580 °C under an argon atmosphere at a rate of 10 °C per minute while placed in pure aluminum pans in the furnace. The microstructure of the experimental alloys was examined using optical microscopy (OM, Nikon, Tokyo, Japan) and field emission-scanning electron microscopy (FE-SEM, FEI model Quanta 200 F) with energy-dispersive spectroscopy (EDS, EDAX, Pleasanton, CA, USA). Prior to OM observation, the samples were prepared by grinding, micro-polishing, and etching in Keller's reagent. FE-SEM analysis was conducted under specific conditions, including an accelerating voltage of 20 KV and a working distance of 10.0 mm. The tensile samples were prepared as per ASTM standard B557 and tested using a universal tensile testing machine (DTU-900MHN, Daekyung Tech, Gumisi, Republic of Korea) with a strain rate of 1.5 mm/min and an extensometer gauge length of 30 mm.

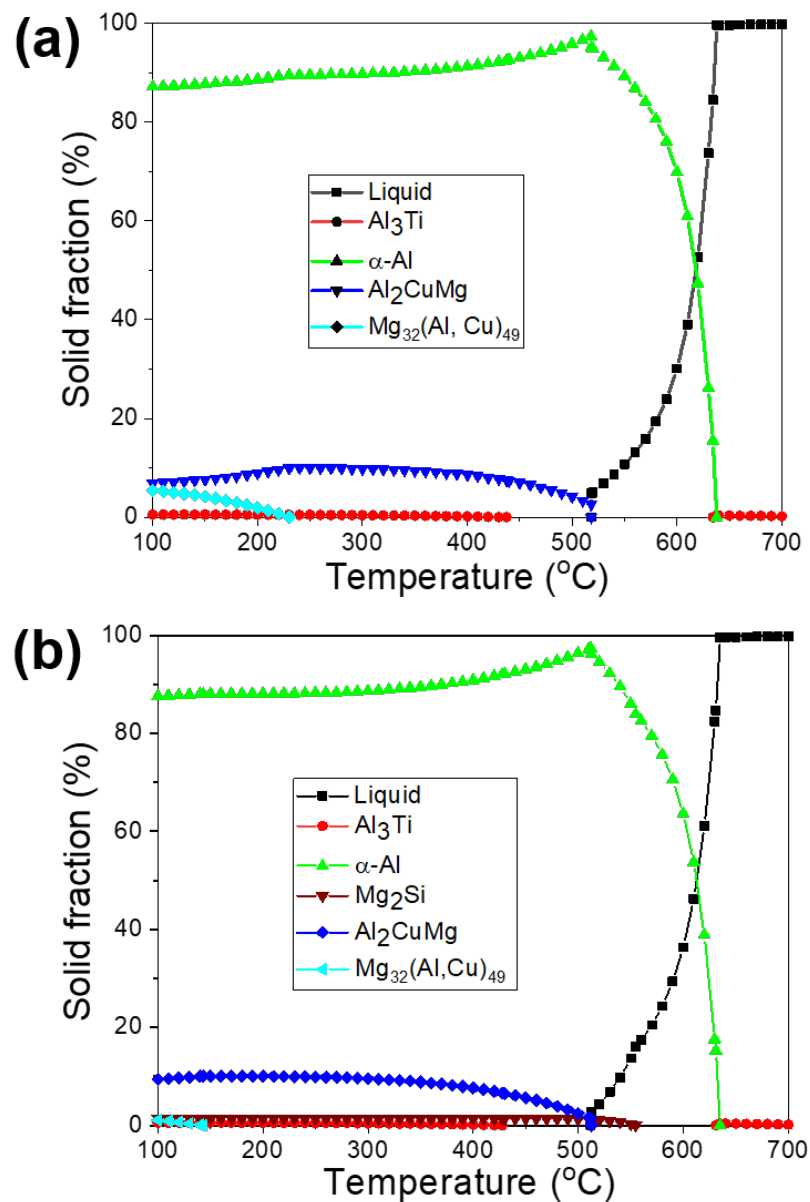
### 3. Results and Discussion

Table 2 shows all of the non-variable eutectic reactions that have taken place on the aluminum-rich corner of the Al–Cu–Mg–Si quaternary phase diagram [2]. The introduction of a small quantity of silicon into the Al–Cu–Mg ternary system results in the development of Mg<sub>2</sub>Si phases through either a ternary reaction ( $L \Rightarrow \alpha\text{-Al} + S + \text{Mg}_2\text{Si}$ ) or a quaternary reaction ( $L \Rightarrow \alpha\text{-Al} + \text{Al}_2\text{Cu} + \text{Al}_2\text{CuMg} (S) + \text{Mg}_2\text{Si}$ ), depending on the ratio of Cu to Mg and the amount of Si (as presented in Table 2). In this study, theoretical calculations were conducted using JMatPro 7.0 software (based on equilibrium cooling) to explore the formation of different phases in the alloys examined during the solidification process. Based on the theoretical calculations shown in Figure 1a, it is predicted that the B43 (Al–4.5Cu–0.15Ti–3.0Mg) alloy consists of  $\alpha$ -Al, eutectic  $\alpha$ -Al–S, Al<sub>3</sub>Ti intermetallic compounds (IMCs), and T phases. A univariant eutectic ( $L \Rightarrow \alpha\text{-Al} + S$ ) reaction is predicted to end the solidification process in this alloy. Additionally, it is predicted that the T phases precipitate out once the solidification process is completed and the temperature decreases to 250 °C. On the other hand, apart from the phases observed in the B43, the formation of Mg<sub>2</sub>Si phases is also predicted in the S43 (Al–4.5Cu–0.15Ti–3.0Mg–0.5Si) alloy (Figure 1b) through the following univariant reaction:  $L \Rightarrow \alpha\text{-Al} + \text{Mg}_2\text{Si}$  at around 560 °C. Furthermore, it is predicted that the addition of silicon decreases the precipitation temperature of the T phases to below 150 °C and reduces their amount compared to the B43 base alloy (Figure 1a). A decrease in the amount of T phases in the Si-added alloy (S43) is linked to

the consumption of magnesium in the creation of eutectic  $\alpha$ -Al-Mg<sub>2</sub>Si phases, resulting in a lower amount of magnesium within the Al matrix for the precipitation of T phases.

**Table 2.** Non-variant reactions that are formed at the Al-rich corner of the Al–Cu–Mg–Si quaternary phase diagram, as documented in reference [2].

Eutectic Reaction	Composition (Mass%)			Temperature (°C)
	Cu	Mg	Si	
L => Al + Al <sub>2</sub> CuMg (quasi-binary eutectic)	24.5	10.1	-	518
L + Al <sub>2</sub> CuMg (S) => Al + Mg <sub>32</sub> (Al, Cu) <sub>49</sub> (T)	10	26	-	467
L => Al + Al <sub>2</sub> Cu + Al <sub>2</sub> CuMg (S) + Mg <sub>2</sub> Si	33	6–7	0.3	500
L => Al + Mg <sub>2</sub> Si + Al <sub>2</sub> CuMg (S)	23	10.3	0.3	516
L + Al <sub>2</sub> CuMg (S) => Al + Mg <sub>32</sub> (Al, Cu) <sub>49</sub> (T) + Mg <sub>2</sub> Si	10	25	0.3	467



**Figure 1.** Results of theoretical calculations conducted using JMatPro 7.0 to evaluate different phases during the solidification process of the B43 and S43 alloys, as shown in (a) and (b), respectively.

Figure 2 shows the DSC results of the B43 and S43 alloys, revealing solidus temperatures of approximately 493 °C and 500 °C, respectively. In the B43 alloy, a eutectic peak was detected in addition to the peak related to the  $\alpha$ -Al matrix, indicating the formation of a quasi-binary eutectic reaction ( $L \Rightarrow \alpha\text{-Al} + S$ ). The S43 alloy exhibited an additional peak, likely indicating the formation of binary eutectic ( $\alpha\text{-Al-Mg}_2\text{Si}$ ) phases due to the addition of 0.5%Si. These results suggest that the solidification process in the B43 base alloy ends with an univariant binary ( $\alpha\text{-Al-S}$ ) reaction, while in the S43 alloy, solidification ends with either a binary ( $\alpha\text{-Al-S}$ ) or a ternary ( $\alpha\text{-Al-Mg}_2\text{Si-S}$ ) eutectic reaction (as per Table 2). Both alloys showed exothermic peaks below 300 °C, with peak #1 likely indicating the precipitation of T phases, consistent with the phase diagram in Figure 1. Notably, the formation temperatures of both alloys were almost identical, contrary to the theoretical calculations. Peak #2 may be linked to the formation of GPB zones or solute clusters. Peak #3 observed between 250 and 280 °C could be associated with the precipitation of  $S''$  or  $S'$  phases, as suggested in prior research [20–23].

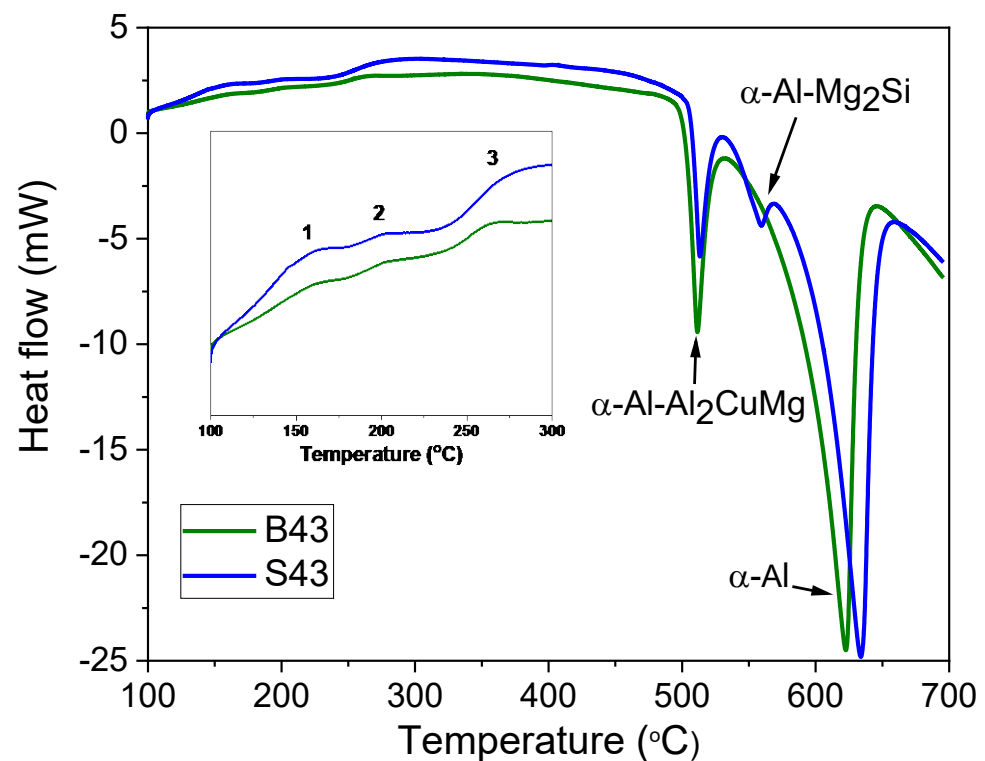


**Figure 2.** Differential scanning calorimetry (DSC) curves of the investigated alloys, which were heated at a rate of 10 °C per minute.

The optical microscopy (OM) micrographs of the investigated alloys showed that the microstructures primarily consisted of globular grains of  $\alpha$ -Al matrix with eutectic  $\alpha\text{-Al-S}$  or  $\alpha\text{-Al-S}$  and  $\alpha\text{-Al-S-Mg}_2\text{Si}$  phases at the grain boundaries and T precipitates within the  $\alpha$ -Al matrix, as seen in Figure 3. The globular grains present in the B43 alloy had a size of 36.4  $\mu\text{m}$ , which was reduced to 29.7  $\mu\text{m}$  in the S43 alloy. The size of the globular grains in the S43 alloy (Figure 3b) was slightly smaller than that in the base alloy (Figure 3a) due to the addition of silicon, which increased the solute concentration on the solid/liquid interface and the formation of binary eutectic  $\alpha\text{-Al-Mg}_2\text{Si}$  phases at higher temperature, suppressing the grain growth. The scanning electron microscopy (SEM) analysis shown in Figures 4 and 5 confirmed that the microstructure of the base alloy consisted of  $\alpha$ -Al grains (#1), eutectic  $\alpha\text{-Al-S}$  phases (#2), and T phases (#3) within the Al grains. In contrast, the Si-added alloy featured the eutectic  $\alpha\text{-Al-Mg}_2\text{Si}$  phases, eutectic  $\alpha\text{-Al-S-Mg}_2\text{Si}$ , and Ti-Si based intermetallic compounds (#4) in addition to the aforementioned phases. The SEM-EDS analysis of the second phases also confirmed that the eutectic Al-Mg<sub>2</sub>Si phases were formed

through an univariant eutectic ( $L \Rightarrow \alpha\text{-Al} + \text{Mg}_2\text{Si}$ ) reaction. The elemental composition of these second phases was determined by SEM-EDS analysis. The morphology of eutectic phases (Figure 4a,b) was significantly changed with the addition of silicon (Figure 4d,e), indicating that an univariant eutectic ( $\alpha\text{-Al-S-Mg}_2\text{Si}$ ) reaction ended solidification in the S43 alloy instead of the quasi-binary eutectic ( $L \Rightarrow \alpha\text{-Al} + \text{S}$ ) reaction. The addition of Si also caused the formation of coarse Ti-Si based IMCs, which are undesirable as they decrease the grain refinement efficiency of Ti by decreasing the amount of free Ti in the alloy melt.

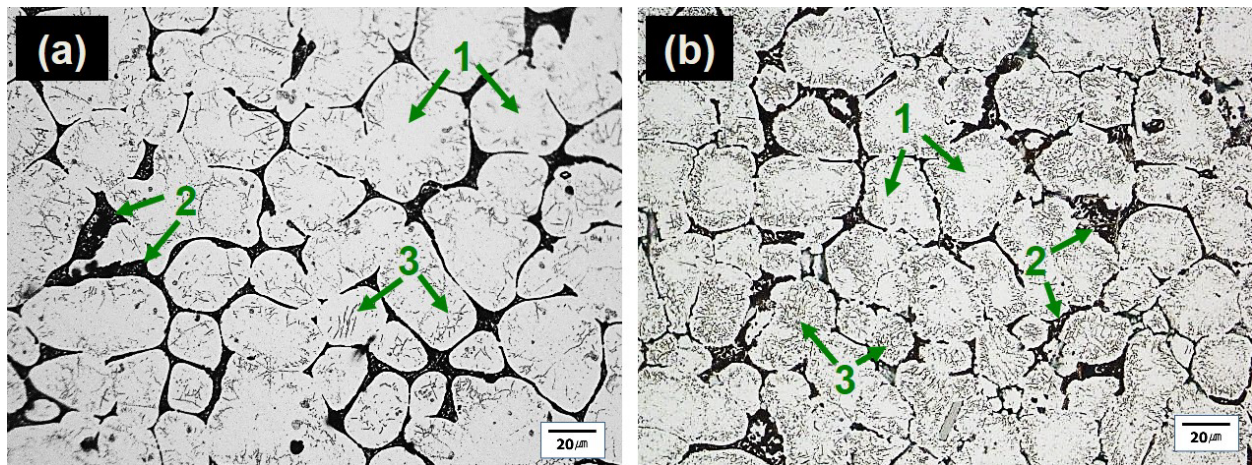


**Figure 3.** Optical micrographs of the investigated alloys in their as-cast condition. The micrographs show (a) the B43 alloy and (b) the S43 alloy. Here, (1), (2), and (3) indicate the  $\alpha\text{-Al}$  grains, eutectic Al-S/Al-S and Al-Mg<sub>2</sub>Si phases, and T precipitates, respectively.

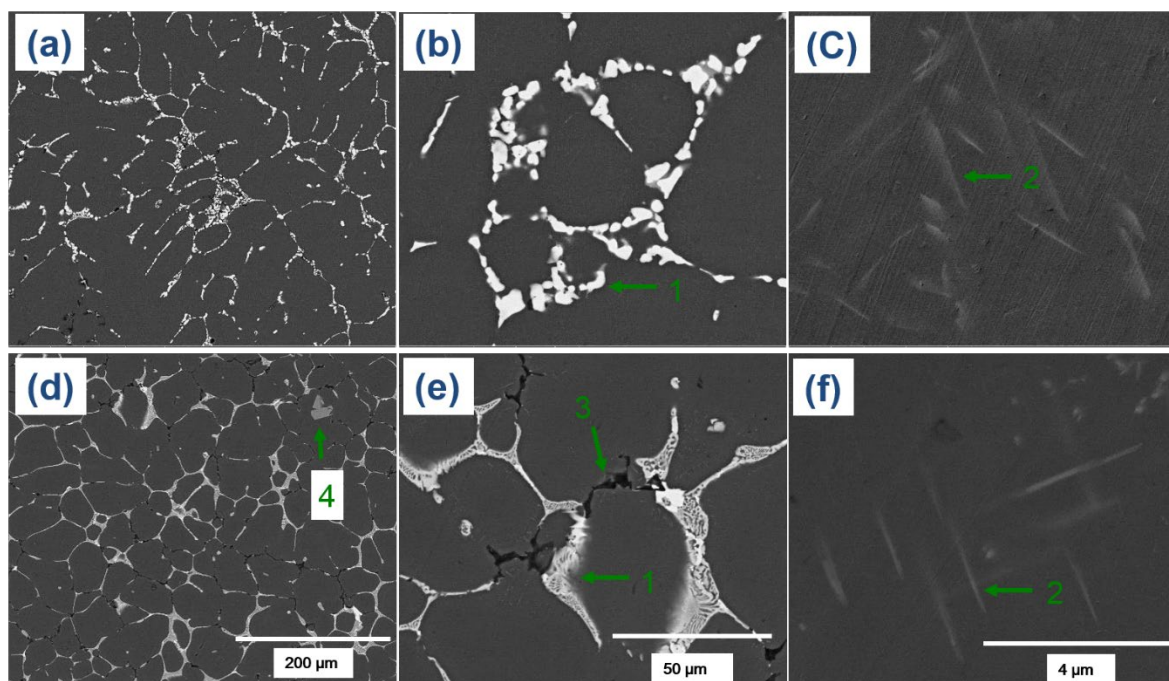


**Figure 4.** FE-SEM micrographs of the investigated alloys in their as-cast condition. The microstructures of the B43 alloy are shown in (a–c), while (d–f) show the microstructures of the S43 alloy. The annotations (1), (2), (3), and (4) indicate the eutectic Al-S, T precipitates, eutectic Al-Mg<sub>2</sub>Si, and Ti-based intermetallic phases, respectively.



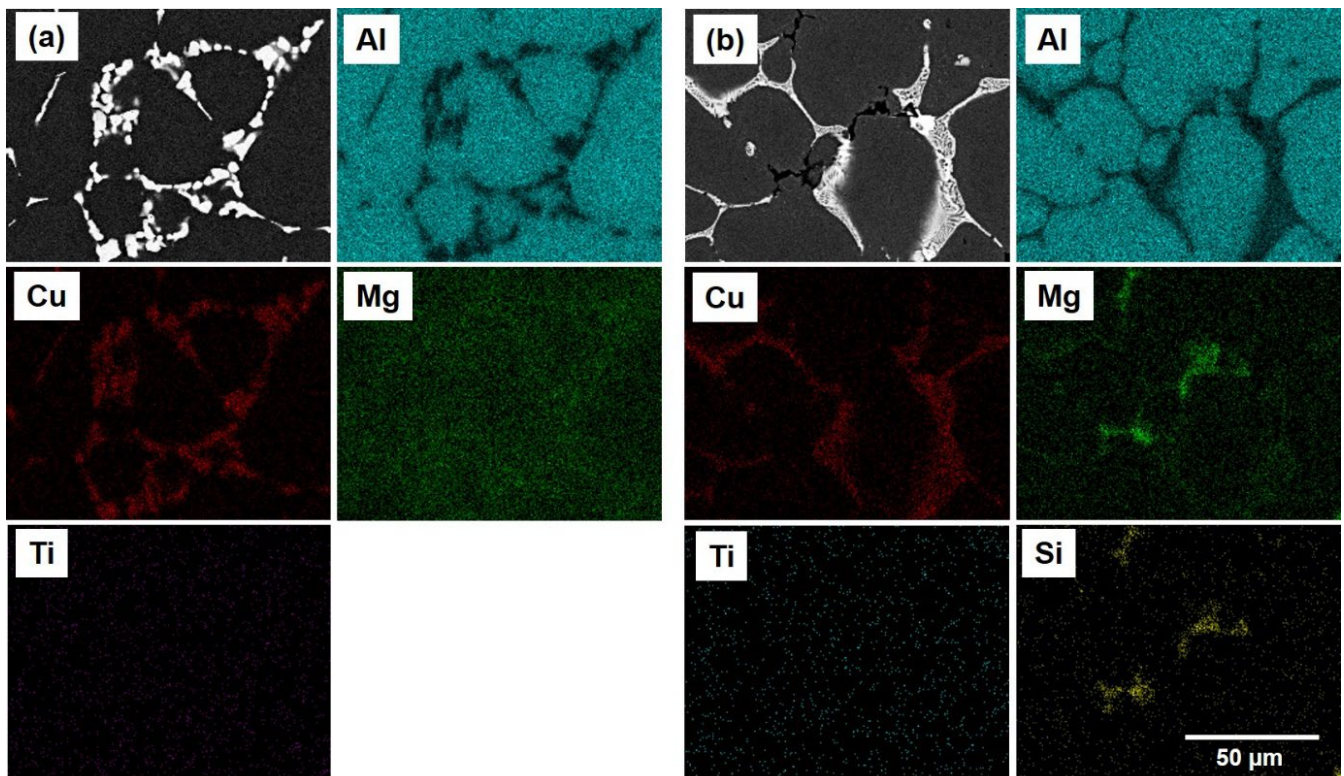


**Figure 5.** FE-SEM micrographs of (a) the B43 alloy and (b) the S43 alloy, along with their corresponding EDS mapping analyses.

The T phases (#2) were formed (Figure 4c,f) during the solidification process, when the temperature fell below the solidus temperature, as mentioned earlier. Although the theoretical calculations in Figure 1 showed that the addition of Si decreased the amount of T precipitates, the OM micrographs of the B43 alloy (Figure 3a) and S43 alloy (Figure 3b) revealed a noteworthy rise in the amount of T phase in the Si-added alloy. The Al matrix in the B43 alloy contained approximately 5.0 at% Mg (#1 and #2), which decreased to about 2.80 at% (#3 and #4) in the S43 alloy, as shown in Figure 6. This reduction in the amount of Mg contents in the Al matrix can be related to the formation of eutectic  $\alpha$ -Al-Mg<sub>2</sub>Si phases and an increasing amount of T precipitates. Previous studies on Si addition in Al-Cu-Mg with a low Mg/Cu ratio showed that Si addition significantly reduced the dislocation density and stabilized GPB zones, resulting in a more uniform distribution of fine precipitates than Si-free alloys [19,21]. A similar mechanism is more likely in the current Si-added alloy, leading to a significant increase in the amount of T phase in Figure 3b. Therefore, it can be concluded that the addition of Si encourages the precipitation of T phases within the Al matrix.

Figure 7 displays the OM micrographs of the investigated alloys in both the as-cast and as-quenched tempers. The investigation revealed that very little modification in the eutectic  $\alpha$ -Al-S,  $\alpha$ -Al-Mg<sub>2</sub>Si, and  $\alpha$ -Al-S-Mg<sub>2</sub>Si phases occurred upon exposing these alloys to the solution heat treatment, causing a significant amount of remnant phases in the as-quenched alloys (Figure 7c,d). However, a considerable dissolution of T precipitates was achieved after the solution heat treatment. Figure 8 shows the variation in hardness values against aging time for the investigated alloys. There was a considerable difference in the hardness of the alloys in the as-quenched states, with B43 and S43 alloys exhibiting hardness values of 27 and 62 HBR, respectively. This difference can be ascribed to the existence of Mg<sub>2</sub>Si phases in the S43 alloy, which did not dissolve during the solution treatment, thus maintaining the same yield strength achieved in the as-cast condition. Nonetheless, a significant increase in the hardness of the B43 alloy was observed after only 1 h of aging treatment, reaching a peak hardness of 65 HRB after 8 h of aging treatment.

Thereafter, a slight decrease in hardness was observed before becoming almost constant for the rest of the aging time. In contrast, the S43 alloy initially exhibited a decrease in hardness values for up to 2 h before bouncing back upward. Upon further exposure of the S43 alloy at 200 °C, the hardness slightly decreased before starting to increase again and reaching a peak hardness value of ~73 HRB at ~16 h of aging treatment. These results clearly reveal that the minor Si addition in the S43 alloy resulted in a more noteworthy increase in the peak hardness value than the B43 base alloy.

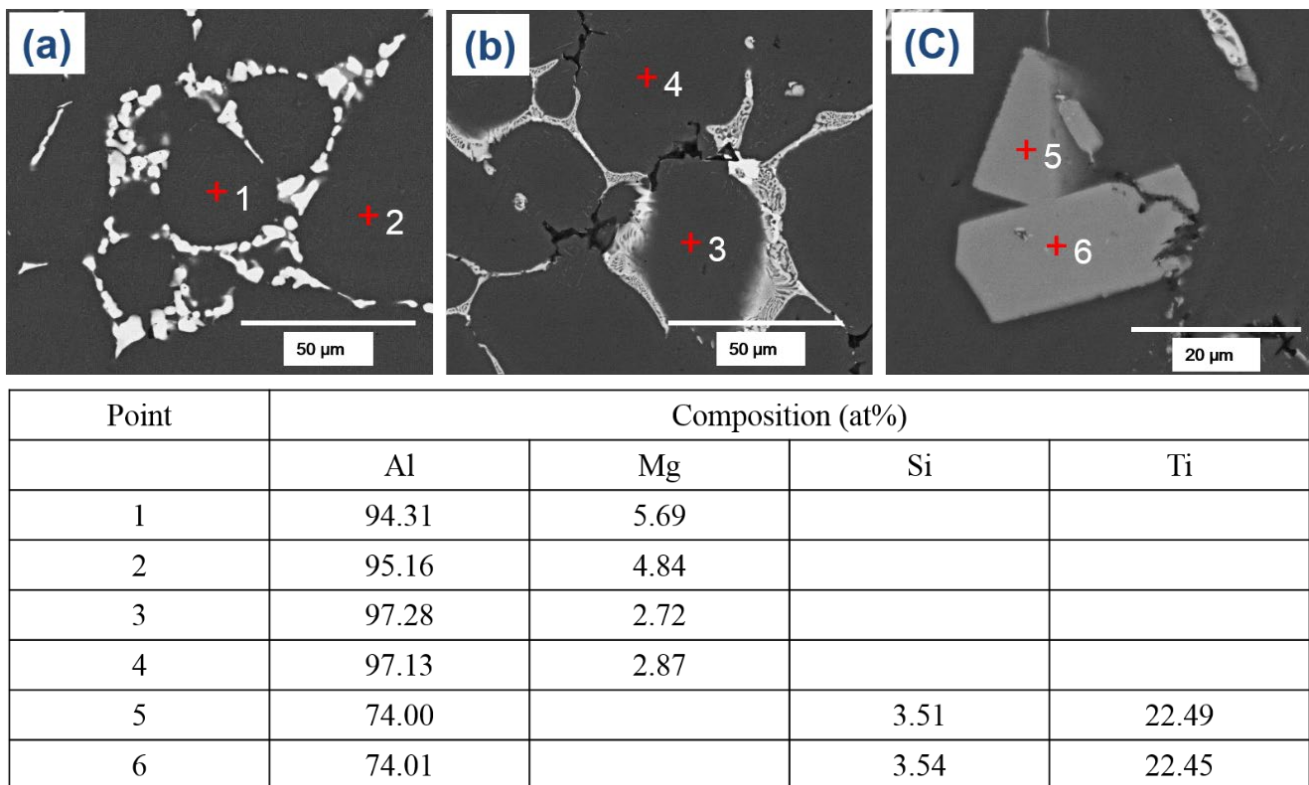


**Figure 6.** FE-SEM micrographs of (a) the B43 alloy and (b,c) the S43 alloy in their as-cast condition. The table below the micrographs provides the composition of the points indicated in the micrographs.

The existing literature [19–23] suggests that as-quenched Al–Cu–Mg alloys consist of a supersaturated solid solution (SSSS), which is a high-energy state that transforms into GPB zones as the first stage of precipitation hardening. The growth in these GPB zones leads to the formation of the S'' metastable phase, which subsequently converts to another metastable phase (S' phase) over time. Eventually, the S phase, which represents the stable phase, is formed through the growth of the S' phase. While this sequence is most commonly reported, some studies [21–23] have reported solute clusters as the starting point for precipitate formation instead of GPB zones. In these cases, atomic clusters are observed as the first stage of precipitate formation, which are distinct from GPB zones as they lack well-defined characteristics such as proper shape, composition, and crystal structure. Regarding the evolution of hardness during the aging treatment, prior research [20–23] has identified two distinct peaks in Al–Mg–Cu alloys. The initial peak in hardness is linked to the formation of atomic clusters or GPB zones, which account for up to 60% of the total hardening attained during aging. The subsequent precipitation of S'' and S phases corresponds to the second stage of precipitation hardening, occurring later in the aging process.



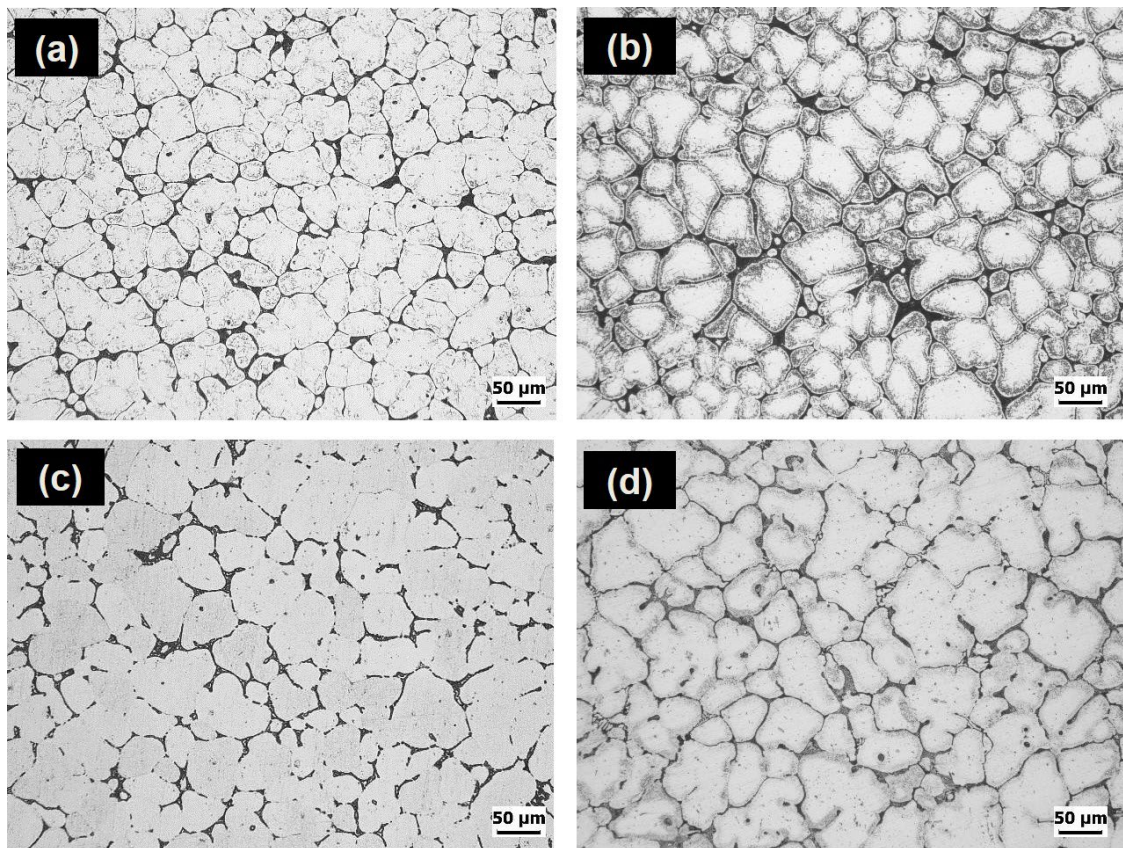


**Figure 7.** Optical micrographs of the investigated alloys in different temper conditions. Microstructures of the B43 alloy are displayed in (a,c), while (b,d) show the as-cast and as-quenched microstructures of the S43 alloy, respectively.

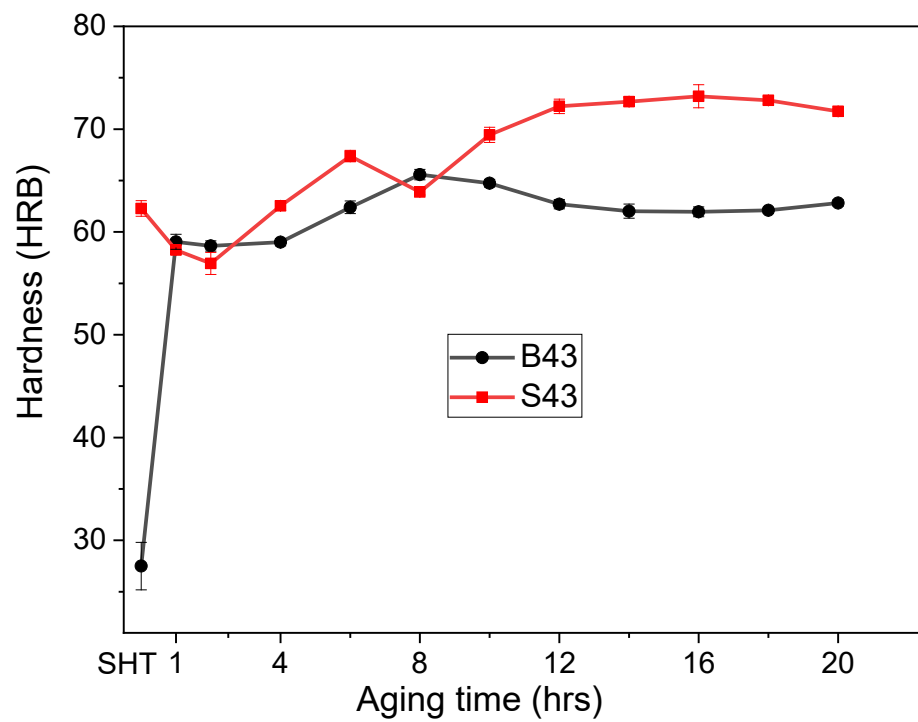


**Figure 8.** Change in the hardness values for both examined alloys as a function of aging time.

The DSC analysis (Figure 9) of the as-quenched alloys showed three distinct endothermic peaks (A, C, and D) and one exothermic peak (B) for both B43 and S43 alloys. Previous studies on Al–Cu–Mg alloys with high Mg content have also reported similar DSC curves [20–22]. According to these studies, endothermic peak A is related to the dissolution of atomic clusters (GPB/S''/T phases), while peaks C and D represent the dissolution of S precipitates and partial melting of S + T phases, respectively. Exothermic peak B represents the formation of S phases. The area of peak B, representing the formation of S phases, increased significantly in the S43 alloy compared to the B43 alloy, indicating a considerable increase in the precipitation of S phases. Previous studies have shown that the addition of Si in Al–Mg–Cu alloys enhances the precipitation of the S phase by stabilizing GPB zones, resulting in a more uniform precipitation of fine S precipitates and higher peak hardness [19,21]. Based on the current results and previous studies, it can be concluded that the higher hardness of the S43 alloy compared to the B43 alloy can be attributed to Si-induced uniform precipitation of S''/S phases in the former alloy. The Si addition in the S43 alloy is believed to have reduced the number of dislocations and forced the S phases to nucleate on homogeneously distributed GPB zones, resulting in a more uniform distribution of fine S precipitates and higher peak hardness [19,21].

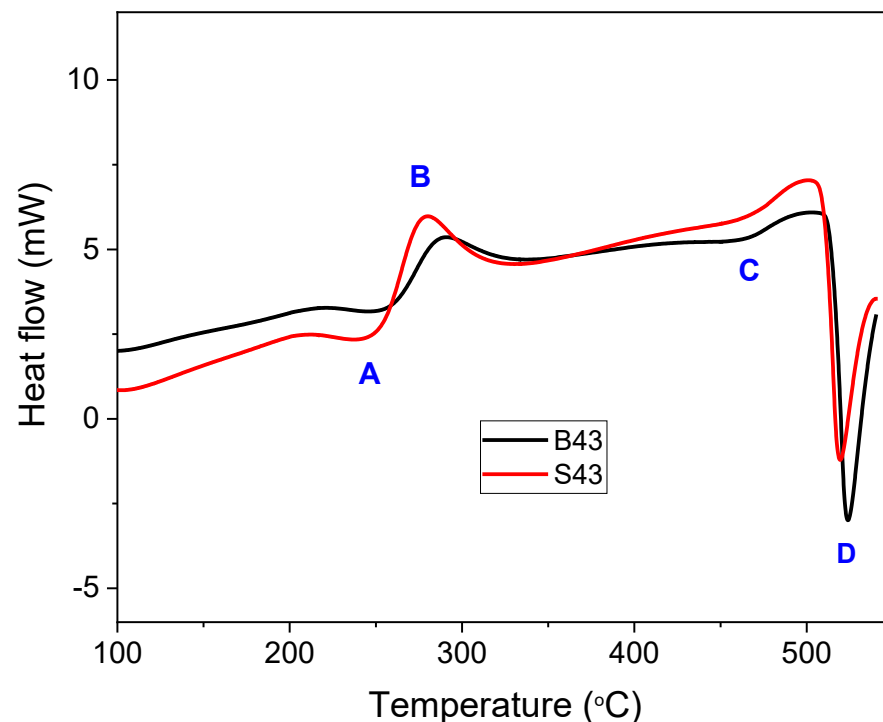


**Figure 9.** DSC curves of the investigated alloys, which were heated at a rate of 10 °C per minute.

Figure 10 displays the tensile properties of the investigated alloys in different tempers. In the as-cast condition, the B43 alloy achieved a yield strength of around 153 MPa, while the S43 alloy achieved a yield strength of 170 MPa (Figure 10a). This increase in tensile strength can be attributed to the presence of Mg<sub>2</sub>Si phases and an increasing amount of T precipitates within the Al matrix of the S43 alloy. However, this improvement in tensile strength in the S43 alloy comes at the cost of ductility, as elongation decreased to 0.5%. After undergoing the solution heat treatment process, the B43 alloy exhibited a decrease in yield strength but a significant increase in ultimate tensile strength and elongation (Figure 10b). Additionally, the S43 alloy showed a higher yield strength in the as-quenched condition compared to that achieved in the as-cast condition. This trend is similar to that reported in Al–Mg–Si ternary alloys with high Mg content, and it is attributed to the breaking of eutectic phases and redistribution of Mg<sub>2</sub>Si phases [24]. Furthermore, subjecting these

alloys to the aging treatment at 200 °C led to a significant increase in their tensile strengths compared to those achieved in the as-cast and as-quenched conditions. These enhanced strengths were achieved with improved elongations compared to the as-cast condition. After an exposure time of 8 h, the B43 alloy reached a yield strength of 234 MPa, while the S43 alloy attained a yield strength of 245 MPa (Figure 10c). Moreover, a longer exposure time of 16 h led to a further significant enhancement in the yield strengths in both alloys, resulting in a yield strength of 270 MPa in the B43 alloy and 324 MPa in the S43 alloy (Figure 10d). However, this enhancement was associated with a decrease in elongation, which decreased to below 1% for both alloys. Nevertheless, both alloys, and the Si-added alloy in particular, exhibited much better tensile properties than many commercial alloys such as A240, A242, and A243 alloys [1].

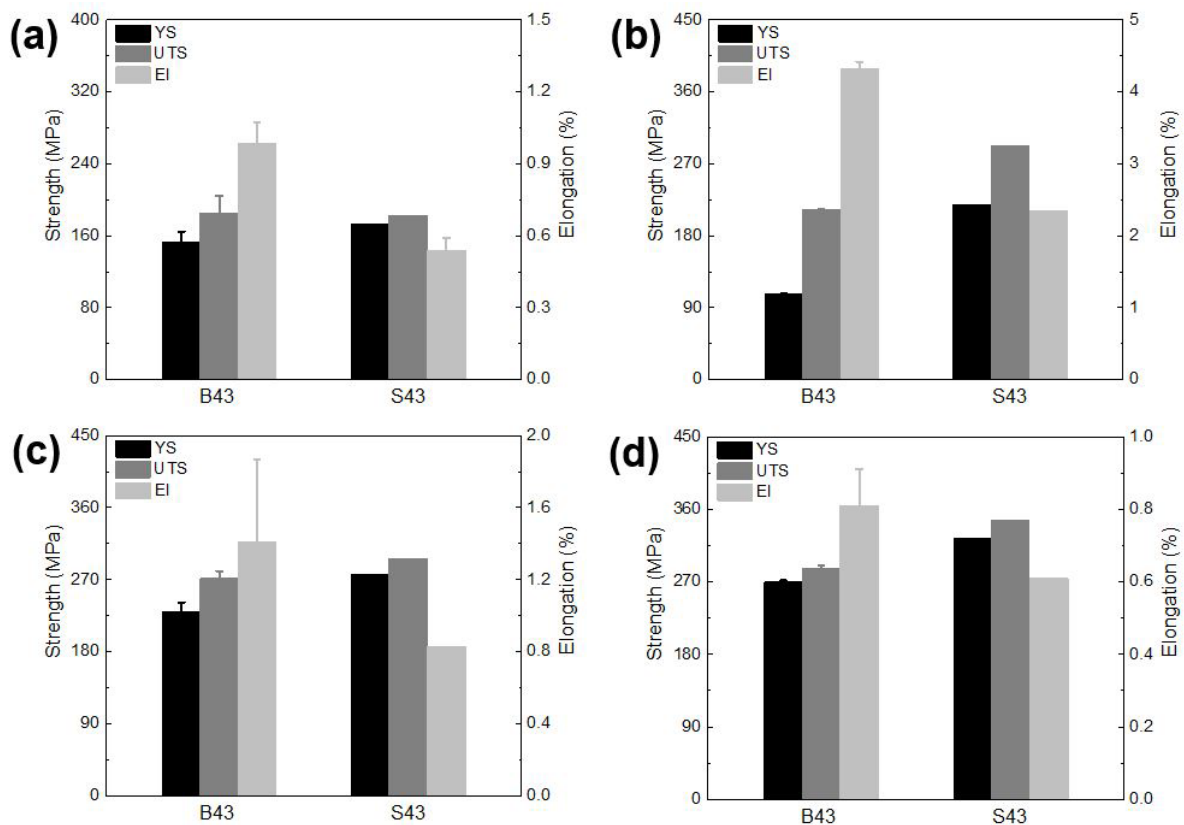


**Figure 10.** Tensile properties of the investigated alloys in different temper conditions: (a) as-cast, (b) as-quenched, (c) aged at 200 °C for 8 h, and (d) aged at 200 °C for 16 h.

#### 4. Conclusions

This study aimed to explore how the addition of a small amount of Si impacts the microstructure evolution, heat treatment response, and mechanical properties of the Al–4.5Cu–0.15Ti–3.0Mg alloy. The following conclusions can be inferred from this research:

The microstructure analysis of the base alloy revealed the presence  $\alpha$ -Al grains, eutectic  $\alpha$ -Al-S phases, and T phases within the Al grains. In contrast, the Si-added alloy featured the eutectic  $\alpha$ -Al-Mg<sub>2</sub>Si phases, eutectic  $\alpha$ -Al-S-Mg<sub>2</sub>Si, and Ti-Si-based intermetallic compounds in addition to the aforementioned phases. The study found that the Si-added alloy had a greater quantity of T phase in comparison to the base alloy, which was attributed to the promotion of T phase precipitation facilitated by the inclusion of Si. Additionally, Si facilitated the formation of S phase during the aging treatment, thereby accelerating the precipitation hardening response of the Si-added alloy.

The as-cast temper of the base alloy displayed a yield strength of roughly 153 MPa, which increased to 170 MPa in the Si-added alloy. As a result of the aging treatment, both alloys



exhibited a notable increase in tensile strength, which was ascribed to the precipitation of S phases. In the T6 temper, the base alloy exhibited a yield strength of 270 MPa, while the Si-added alloy exhibited a significantly higher yield strength of 324 MPa. This novel Si-added alloy demonstrated superior tensile properties compared to many commercially available high Mg-added Al–Cu–Mg alloys, making it a potential replacement for such alloys in various applications within the aerospace and automotive industries.

**Author Contributions:** Conceptualization: A.W.S. and S.-H.H.; methodology: A.W.S.; Data curation: A.W.S. and J.A.S.; Formal analysis: A.W.S. and J.A.S.; Original draft preparation: A.W.S. and S.-H.H. writing—review and editing: B.-H.K., Y.-O.Y., H.-K.L. and S.K.K.; supervision: S.-H.H.; B.-H.K., Y.-O.Y., H.-K.L. and S.K.K. All authors have read and agreed to the published version of the manuscript.

**Funding:** This study has been conducted with the support of the Ministry of Trade, Industry and Energy as “Materials & Components Technology Development Program (20011420)”.

**Institutional Review Board Statement:** Not applicable.

**Informed Consent Statement:** Not applicable.

**Data Availability Statement:** Available upon request from the corresponding author.

**Conflicts of Interest:** The authors declare no conflict of interest.

## References

- Hatch, J.E. *Aluminum: Properties and Physical Metallurgy*; ASM International: Geauga County, OH, USA, 1984; pp. 333–338.
- Glazoff, M.V.; Khvan, A.; Zolotarevsky, V.S.; Belov, N.A.; Dinsdale, A.T. *Casting Aluminum Alloys: Their Physical and Mechanical Metallurgy*, 2nd ed.; Elsevier: Oxford, UK, 2018; pp. 56–58, 85–87.
- Kamga, H.K.; Larouche, D.; Bournane, M.; Rahem, A. Solidification of Aluminum-Copper B206 alloys with Iron and Silicon Additions. *Metall. Mater. Trans. A* **2010**, *41*, 2844–2855. [CrossRef]
- Fentazi, S.; Bournane, M.; Ragab, K.A.; Mehdi, B. Influence of Mg Additions on Solidification and Performance of B206-Type Aluminum Castings of High Fe and Si Contents. *Int. J. Cast Met. Res.* **2018**, *31*, 14–19. [CrossRef]
- Liu, K.; Cao, X.; Chen, X. Effect of Mn, Si, and Cooling Rate on the Formation of Iron-Rich Intermetallics in 206 Al-Cu Cast Alloys. *Metall. Mater. Trans. B* **2012**, *43*, 1231–1240. [CrossRef]
- D’Elia, F.; Ravindran, C.; Sediako, D.; Kainer, K.U.; Hort, N. Hot Tearing Mechanisms of B206 Aluminum–Copper Alloy. *Mater. Des.* **2014**, *64*, 169–180. [CrossRef]
- D’Elia, F.; Ravindran, C.; Sediako, D. Interplay Among Solidification, Microstructure, Residual Strain and Hot Tearing in B206 Aluminum Alloy. *Mater. Sci. Eng. A* **2015**, *624*, 169–180. [CrossRef]
- Kang, B.K.; Sohn, I. Effects of Cu and Si Contents on the Fluidity, Hot Tearing, and Mechanical Properties of Al-Cu-Si Alloys. *Metall. Mater. Trans. A* **2018**, *49*, 5137. [CrossRef]
- Masoumi Khalilabad, M.; Zedanb, Y.; Texier, D.; Jahazi, M.; Bocher, P. Effect of heat treatments on microstructural and mechanical characteristics of dissimilar friction stir welded 2198/2024 aluminum alloys. *J. Alloys Compd.* **2022**, *36*, 221–239. [CrossRef]
- Girgis, A.; Abdelaziz, M.H.; Samuel, A.M.; Valtierra, S.; Samuel, F.H. On the Enhancement of the Microstructure and Tensile Properties of an Al-Cu Based Cast Alloy. *Metall. Microstruct. Anal.* **2019**, *8*, 757–769. [CrossRef]
- Cai, Q.; Mendis, C.L.; Wang, S.; Chang, I.T.H.; Fan, Z. Effect of Heat Treatment on Microstructure and Tensile Properties of Die-Cast Al-Cu-Si-Mg Alloys. *J. Alloys Compd.* **2021**, *881*, 160559. [CrossRef]
- Kang, S.J.; Kim, Y.W.; Kim, M.; Zuo, J.M. Determination of Interfacial Atomic Structure, Misfits and Energetics of X Phase in Al-Cu-Mg-Ag Alloy. *Acta Mater.* **2014**, *81*, 501–511. [CrossRef]
- Cai, Q.; Mendis, C.L.; Chang, I.T.H.; Fan, Z. Microstructure and Mechanical Properties of New Die-Cast Quaternary Al-Cu-Si-Mg Alloys. *Mater. Sci. Eng. A* **2021**, *800*, 140357. [CrossRef]
- Souissi, M.; Fang, C.M.; Sahara, R.; Fan, Z. Formation Energies of  $\theta$ -Al<sub>2</sub>Cu Phase and Precursor Al-Cu Compounds: Importance of On-Site Coulomb Repulsion. *Comput. Mater. Sci.* **2021**, *194*, 110461. [CrossRef]
- Zheng, Z.Q.; Liu, W.Q.; Liao, Z.Q.; Ringer, S.P.; Sha, G. Solute Clustering and Solute Nanostructures in an Al-3.5Cu-0.4Mg-0.2Ge Alloy. *Acta Mater.* **2013**, *61*, 3724–3734. [CrossRef]
- Chen, Y.; Hu, Q.; Pan, S.; Zhang, H.; Liu, H.; Zhu, B.; Liu, X.; Liu, W. Influences of Cu Content on the Microstructure and Strengthening Mechanisms of Al-Mg-Si-xCu Alloys. *Metals* **2019**, *9*, 524. [CrossRef]
- Fang, C.; Souissi, M.; Que, Z.; Fan, Z. Crystal Chemistry and Electronic Properties of the Al-Rich Compounds, Al<sub>2</sub>Cu,  $\omega$ -Al<sub>7</sub>Cu<sub>2</sub>Fe and  $\theta$ -Al<sub>13</sub>Fe<sub>4</sub> with Cu Solution. *Metals* **2022**, *12*, 329. [CrossRef]
- Kamga, H.; Larouche, D.; Bournane, M.; Rahem, A. Mechanical Properties of Aluminum-Copper B206 Alloys with Iron and Silicon Additions. *Int. J. Cast Met. Res.* **2012**, *25*, 15–25. [CrossRef]
- Chen, Z.; Zhang, J.; Shu, J.; Sha, G.; Xia, J.; Wang, S.; Ringer, S.P. Effects of Si Addition on the Microstructure Evolution of Al-Cu-Mg Alloys in the  $\alpha + S + T$  Phase Field. *Philos. Mag. Lett.* **2013**, *93*, 648–654. [CrossRef]

20. Shah, A.W.; Ha, S.H.; Kim, B.H.; Yoon, Y.O.; Lim, H.K.; Kim, S.K. Effect of Cu Addition on the Precipitation Hardening and Mechanical Properties of Al–Mg Based Cast Alloys. *J. Nanosci. Nanotechnol.* **2021**, *21*, 1943–1947.
21. Li, C.; Sha, G.; Gun, B.; Xia, J.H.; Liu, X.F.; Wu, Y.Y.; Birbilis, N.; Ringer, S.P. Enhanced age-hardening response of Al–4Mg–1 Cu (wt.%) micro-alloyed with Ag and Si. *Scr. Mater.* **2013**, *68*, 857–860. [CrossRef]
22. Wang, S.C.; Starink, M.J.; Gao, N. Precipitation hardening in Al–Cu–Mg alloys revisited. *Scr. Mater.* **2006**, *54*, 287–291. [CrossRef]
23. Wang, S.C.; Starink, M.J. Two types of S phase precipitates in Al–Cu–Mg alloys. *Acta Mater.* **2007**, *55*, 933–941. [CrossRef]
24. Shah, A.W.; Ha, S.H.; Kim, B.H.; Yoon, Y.O.; Lim, H.K.; Kim, S.K. Influence of Si Content on Tensile Properties and Fractography of Al–Mg–Si Ternary Alloys. *J. Nanosci. Nanotechnol.* **2021**, *21*, 2005–2009.

**Disclaimer/Publisher’s Note:** The statements, opinions and data contained in all publications are solely those of the individual author(s) and contributor(s) and not of MDPI and/or the editor(s). MDPI and/or the editor(s) disclaim responsibility for any injury to people or property resulting from any ideas, methods, instructions or products referred to in the content.

MDPI AG  
St. Alban-Anlage 66  
4052 Basel  
Switzerland  
[www.mdpi.com](http://www.mdpi.com)

*Materials* Editorial Office  
E-mail: [materials@mdpi.com](mailto:materials@mdpi.com)  
[www.mdpi.com/journal/materials](http://www.mdpi.com/journal/materials)



Disclaimer/Publisher's Note: The title and front matter of this reprint are at the discretion of the . The publisher is not responsible for their content or any associated concerns. The statements, opinions and data contained in all individual articles are solely those of the individual Editors and contributors and not of MDPI. MDPI disclaims responsibility for any injury to people or property resulting from any ideas, methods, instructions or products referred to in the content.





Academic Open  
Access Publishing

[mdpi.com](http://mdpi.com)

ISBN 978-3-7258-1219-6